



Contaminant Transport Parameters for the Groundwater Flow and Contaminant Transport Model of Corrective Action Units 101 and 102: Central and Western Pahute Mesa, Nye County, Nevada



Revision No.: 0

August 2003

Prepared for U.S. Department of Energy under Contract No. DE-AC08-97NV13052.

Approved for public release; further dissemination unlimited.

Available for public sale, in paper, from:

U.S. Department of Commerce
National Technical Information Service
5285 Port Royal Road
Springfield, VA 22161
Phone: 800.553.6847
Fax: 703.605.6900
Email: orders@ntis.fedworld.gov
Online ordering: <http://www.ntis.gov/ordering.htm>

Available electronically at <http://www.doe.gov/bridge>

Available for a processing fee to U.S. Department of Energy and its contractors,
in paper, from:

U.S. Department of Energy
Office of Scientific and Technical Information
P.O. Box 62
Oak Ridge, TN 37831-0062
Phone: 865.576.8401
Fax: 865.576.5728
Email: reports@adonis.osti.gov

Reference herein to any specific commercial product, process, or service by trade name, trademark, manufacturer, or otherwise, does not necessarily constitute or imply its endorsement, recommendation, or favoring by the United States Government or any agency thereof or its contractors or subcontractors.



**CONTAMINANT TRANSPORT
PARAMETERS FOR THE GROUNDWATER
FLOW AND CONTAMINANT TRANSPORT
MODEL OF CORRECTIVE ACTION UNITS
101 AND 102: CENTRAL AND WESTERN
PAHUTE MESA, NYE COUNTY, NEVADA**

Revision No.: 0

August 2003

K. Rehfeldt, W. Drici, D. Sloop, J. Watrus, T. Beard, M. Sully,
C. Benedict, A. Wolfsberg, and P. Reimus

Shaw Environmental, Inc.
P.O. Box 93838
Las Vegas, Nevada 89193-3838

Prepared for U.S. Department of Energy under Contract No. DE-AC08-97NV13052.

Approved for public release; further dissemination unlimited.

**CONTAMINANT TRANSPORT PARAMETERS
FOR THE GROUNDWATER FLOW AND CONTAMINANT TRANSPORT MODEL
OF CORRECTIVE ACTION UNITS 101 AND 102:
CENTRAL AND WESTERN PAHUTE MESA, NYE COUNTY, NEVADA**

Approved by: _____

Kenneth Wall, Project Manager
Shaw Environmental, Inc.

Date: _____

Table of Contents

List of Figures	xi
List of Plates	xviii
List of Tables	xix
List of Acronyms and Abbreviations	xxii
1.0 Introduction	1-1
1.1 Background	1-1
1.1.1 Project Background	1-1
1.1.2 Pahute Mesa Background	1-4
1.2 Task Purpose and Scope	1-5
1.2.1 Purpose	1-5
1.2.2 Scope of Work	1-5
1.3 Quality Assurance	1-6
1.4 CAU Model Documentation	1-9
1.5 Document Organization	1-9
2.0 Selected Components of the Pahute Mesa Conceptual Model	2-1
2.1 Regional Setting	2-1
2.1.1 Regional Hydrogeologic Framework	2-1
2.1.1.1 Hydrogeologic Units	2-3
2.1.1.2 Hydrostratigraphic Units	2-6
2.1.2 Groundwater Occurrence and Movement	2-9
2.1.2.1 Groundwater Occurrence	2-9
2.1.2.2 Groundwater Movement	2-10
2.2 Hydrogeologic Framework of the Pahute Mesa-Oasis Valley Area	2-11
2.2.1 HSU Model Development	2-11
2.2.2 HSU Alternative Model Screening	2-13
2.2.3 Base HSU Model	2-13
2.2.3.1 Structural Features	2-15
2.2.3.2 Hydrogeologic Units	2-15
2.2.3.3 Hydrostratigraphic Units	2-17
2.2.3.4 Mineralogical Data in the PM-OV Model Area	2-17
2.2.4 Silent Canyon Caldera Complex HSU Model	2-20
2.2.4.1 Structure	2-20
2.2.4.2 Hydrostratigraphy	2-22
2.3 Groundwater Chemistry	2-26
2.4 Contamination Sources and Extent	2-26

Table of Contents (Continued)

2.4.1	Contamination Sources	2-27
2.4.1.1	Underground Nuclear Tests	2-27
2.4.1.2	Radiologic Source Term and Potential Contaminants	2-27
2.4.1.3	Hydrologic Source Term	2-29
2.4.1.4	Simplified Hydrologic Source Term	2-31
2.4.2	Contamination Extent	2-31
3.0	CAU Modeling Approach and Data Needs	3-1
3.1	Overview of CAU Modeling Approach	3-1
3.1.1	Selected Code	3-1
3.1.2	Data Requirements for the Pahute Mesa CAU Model	3-3
3.2	Contaminant Transport Modeling Approach and Data Requirements	3-3
3.2.1	Modeling Approach	3-3
3.2.1.1	Objectives	3-4
3.2.1.2	Modeling Process	3-4
3.2.2	Data Requirements	3-6
4.0	Data Analysis Approach	4-1
4.1	Data Compilation	4-1
4.1.1	Data Types	4-1
4.1.1.1	General Description	4-1
4.1.1.2	Description of Contaminant Transport Parameters	4-2
4.1.1.2.1	Porosity	4-2
4.1.1.2.2	Dispersivity	4-3
4.1.1.2.3	Matrix Diffusion Coefficient	4-3
4.1.1.2.4	Matrix and Fracture Sorption Parameters	4-4
4.1.1.2.5	Colloid-Facilitated Transport Parameters	4-5
4.1.2	Data Sources	4-5
4.2	Data Transfer Methodology	4-6
4.2.1	Factors Influencing Flow and Transport	4-6
4.2.2	General Transfer Methodology	4-7
4.2.3	YMP Data Transfer	4-8
4.3	Data Documentation Evaluation	4-8
4.4	Data Quality Evaluation	4-9
4.5	Development of Transport Parameter Distributions	4-10
4.6	Scaling Philosophy	4-10
4.7	Data Analysis Limitations	4-11
5.0	Matrix Porosity	5-1
5.1	Role of Matrix Porosity in Contaminant Transport	5-1
5.2	Data Compilation	5-2

Table of Contents (Continued)

5.2.1	Data Types	5-2
5.2.2	Data Sources	5-3
5.2.3	Data Documentation Evaluation	5-3
5.3	Data Description and Evaluation	5-3
5.3.1	Comparison of Core- and Geophysical Log-Derived Porosity	5-3
5.3.2	Assessment of Porosity Changes with Depth	5-8
5.4	Development of Parameter Distributions	5-11
5.4.1	Approach	5-11
5.4.2	Distribution of Porosity Values Based on HSUs	5-12
5.4.3	Distribution of Porosity Values Based on Alteration	5-20
5.4.4	Distribution of Matrix Porosity Values Based on Lithology	5-21
5.5	Data Limitations	5-39
5.6	Scaling Considerations	5-39
5.7	Summary of Matrix Porosity by Hydrostratigraphic Unit	5-40
6.0	Effective Porosity	6-1
6.1	Role of Effective Porosity in Contaminant Transport	6-1
6.2	Effective Porosity for the Alluvial Aquifer	6-2
6.2.1	Data Compilation	6-2
6.2.1.1	Data Types	6-2
6.2.1.2	Data Sources	6-3
6.2.1.3	Data Documentation Evaluation	6-3
6.2.1.4	Dataset Description	6-4
6.2.2	Data Evaluation	6-4
6.2.3	Development of Parameter Distributions	6-5
6.2.4	Data Limitations	6-6
6.2.5	Scaling Considerations	6-7
6.3	Effective Porosity for the Fractured Volcanic Aquifers	6-8
6.3.1	Data Compilation	6-8
6.3.1.1	Data Types	6-8
6.3.1.2	Data Sources	6-9
6.3.1.3	Data Documentation Evaluation	6-9
6.3.2	Dataset Description and Data Evaluation	6-11
6.3.2.1	Dataset Description	6-11
6.3.2.2	Data Evaluation	6-11
6.3.2.2.1	Parallel Plate Model	6-13
6.3.2.2.2	BULLION FGE	6-14
6.3.2.2.3	Simulation of Plutonium Migration from the BENHAM Test	6-15

Table of Contents (Continued)

6.3.2.2.4	YMP Estimates of Fracture and Effective Porosity	6-16
6.3.3	Development of Parameter Distributions	6-17
6.3.4	Data Limitations	6-20
6.3.5	Scaling Considerations	6-22
6.4	Effective Porosity for Carbonate Aquifers and Confining Units	6-22
6.4.1	Data Compilation	6-23
6.4.1.1	Data Types	6-23
6.4.1.2	Data Sources	6-23
6.4.1.3	Data Documentation Evaluation	6-24
6.4.2	Data Evaluation	6-25
6.4.2.1	Dataset Description	6-25
6.4.2.2	Data Generation	6-27
6.4.3	Development of Parameter Distributions	6-32
6.4.4	Data Limitations	6-32
6.4.5	Scaling Considerations	6-32
6.5	Summary of Effective Porosity by Hydrostratigraphic Unit	6-33
7.0	Dispersivity	7-1
7.1	Role of Dispersion in Contaminant Transport	7-1
7.2	Data Compilation	7-2
7.2.1	Data Types	7-2
7.2.2	Data Sources	7-2
7.2.3	Data Documentation Evaluation	7-2
7.3	Data Evaluation	7-3
7.3.1	Dataset Description	7-3
7.3.1.1	NTS Data	7-3
7.3.1.1.1	BULLION Site	7-3
7.3.1.1.2	C-Well Complex Site	7-5
7.3.1.1.3	Amargosa Tracer Calibration Site	7-6
7.3.1.1.4	C-Well Site, Yucca Flat	7-7
7.3.1.1.5	CAMBRIC Site Test	7-9
7.3.2	Non-NTS Dispersion Studies	7-16
7.3.3	Dispersivity Estimation Through Modeling	7-17
7.4	Data Evaluation	7-19
7.4.1	Data Quality Evaluation	7-19
7.4.2	Evaluation of Scale Dependency	7-19
7.5	Scaling Considerations	7-24
7.6	Probability Distributions	7-24
7.7	Data Limitations	7-25

Table of Contents (Continued)

8.0	Matrix Diffusion Parameters	8-1
8.1	Role of Matrix Diffusion in Contaminant Transport	8-1
8.2	Data Compilation	8-1
8.2.1	Data Types	8-1
8.2.2	Data Sources	8-2
8.2.3	Data Documentation Evaluation	8-2
8.3	Data Evaluation	8-2
8.3.1	Dataset Description	8-2
8.3.2	Parameter Generation	8-2
8.4	Development of Parameter Distributions	8-6
8.4.1	Matrix Diffusion Coefficients as a Function of Matrix Porosity and Permeability	8-7
8.4.2	Matrix Diffusion Coefficients as a Function of Matrix Porosity	8-9
8.4.3	Cumulative Distribution of Matrix Diffusion Coefficients with No Dependence on Matrix Porosity or Permeability	8-11
8.4.4	Adjusting Matrix Diffusions Coefficient for Different Species, Temperature, and Ionic Strength	8-12
8.5	Diffusion Coefficients Estimated per HSU	8-14
8.6	Data Limitations	8-14
8.7	Scaling Considerations	8-18
9.0	Matrix Sorption Parameters	9-1
9.1	The Role of Matrix Sorption in Contaminant Transport Models	9-1
9.1.1	The K_d Parameter	9-2
9.1.2	Limitations of the K_d Parameter	9-2
9.2	Matrix K_d Data Compilation	9-2
9.2.1	Data Types	9-3
9.2.1.1	K_d Derived From Upscaled Mechanistic Sorption Models	9-3
9.2.1.2	Directly Measured K_d	9-5
9.2.2	Sources of K_d Data	9-6
9.2.2.1	K_d s Derived From Mechanistic Modeling Studies	9-6
9.2.2.2	Measured K_d Values	9-6
9.2.3	Data Documentation Evaluation	9-7
9.3	Data Evaluation	9-7
9.3.1	Dataset Descriptions	9-8
9.3.1.1	K_d Derived From Scaled Mechanistic Models	9-8
9.3.1.2	Measured K_d Values for Pahute Mesa Samples	9-9
9.3.1.3	Measured K_d Values for Alluvium	9-10
9.3.1.4	Measured K_d Distributions Derived From YMP Databases	9-10

Table of Contents (Continued)

	9.3.1.4.1	Radionuclides Considered	9-11
	9.3.1.4.2	Rock Types	9-12
	9.3.1.4.3	Water Types Used in YMP Sorption Experiments	9-13
	9.3.1.4.4	YMP Laboratory Sorption Data Obtained Prior to 1993	9-13
	9.3.1.4.5	YMP Laboratory Sorption Data Obtained After 1993	9-13
	9.3.1.5	Measured K_d Values for Carbonate Rock Material	9-14
	9.3.1.6	Measured K_d Values for Granite	9-14
	9.3.2	Parameter Generation	9-14
9.4		Development of K_d Distributions: YMP Database	9-15
	9.4.1	Plutonium	9-15
	9.4.1.1	Review of YMP Studies	9-15
	9.4.1.2	Plutonium K_d Distributions Fit to YMP Data	9-16
	9.4.2	Neptunium	9-18
	9.4.2.1	Neptunium K_d Distributions Fit to YMP Data	9-19
	9.4.3	Strontium and Cesium	9-20
	9.4.3.1	Strontium	9-20
	9.4.3.2	Cesium	9-21
	9.4.4	Uranium	9-22
	9.4.4.1	Summary of Former YMP Evaluation	9-22
	9.4.4.2	Analyses of YMP TDMS Database For Uranium Sorption	9-22
9.5		Data Limitations	9-23
9.6		Summary: K_d s by HSU	9-23
9.7		Scaling Considerations	9-24
9.8		Figures	9-24
9.9		Tables	9-24
10.0		Fracture Sorption Parameter	10-1
10.1		The Role of Fracture Sorption in Contaminant Transport	10-1
10.2		Data Compilation and Evaluation	10-2
	10.2.1	Data Types	10-2
	10.2.2	Data Sources	10-3
10.3		Data Evaluation	10-3
	10.3.1	Dataset Descriptions	10-3
	10.3.1.1	Derivation by Wolfsberg et al. (2002)	10-3
	10.3.1.2	Derivation by Zavarin et al. (2002)	10-5
	10.3.2	Fracture Retardation Factor Summary and Integration	10-5
11.0		Colloid-Facilitated Transport Parameters	11-1

Table of Contents (Continued)

11.1	Role of Colloids in Contaminant Transport	11-1
11.2	Colloid Types, Concentrations, and Size Distributions	11-1
11.2.1	Data Compilation and Evaluation	11-2
11.2.2	Development of Parameter Distributions	11-2
11.2.2.1	Colloid Types (Mineralogy)	11-2
11.2.2.2	Colloid Concentrations and Size Distributions	11-3
11.2.3	Data Limitations	11-8
11.2.4	Scaling Considerations	11-9
11.3	Actinide Distribution Coefficients and Sorption Rates onto Colloids	11-9
11.3.1	Data Compilation and Evaluation	11-9
11.3.2	Development of Parameter Distributions	11-9
11.3.2.1	Distribution Coefficients (K_d values)	11-9
11.3.2.2	Radionuclide Sorption Rates Onto Colloids	11-16
11.3.2.3	Radionuclide Desorption Rates from Colloids	11-17
11.3.2.4	Recommendations for Radionuclide Sorption and Desorption Rates From Colloids	11-20
11.3.3	Data Limitations	11-20
11.3.4	Scaling Considerations	11-21
11.4	Colloid Filtration and Retardation Parameters	11-21
11.4.1	Data Compilation and Evaluation	11-21
11.4.2	Data Evaluation	11-21
11.4.3	Development of Parameter Distributions	11-22
11.4.3.1	Colloid Filtration Rate Constants	11-22
11.4.3.2	Colloid Retardation Factors	11-26
11.4.4	Data Limitations	11-28
11.4.5	Scaling Considerations	11-28
11.5	Summary	11-28
12.0	References	12-1

Appendix A - Hydrostratigraphic Model Supporting Information

A.1.0	Description of the Pahute Mesa-Oasis Valley Model Layers	A-1
A.2.0	References	A-1

Appendix B - Use of Yucca Mountain Site Characterization Project Data for Developing Pahute Mesa Corrective Action Unit Model Parameter Distributions

B.1.0	Introduction	B-1
B.2.0	Deposition and Alteration of Volcanic Rocks	B-2

Table of Contents (Continued)

B.2.1	Deposition	B-2
B.2.2	Alteration	B-5
B.3.0	Factors Influencing Flow and Transport Parameters of Fractured Rock	B-5
B.3.1	Influences on Flow Parameters	B-5
B.3.2	Influences on Transport Parameters	B-7
B.3.3	Basis for Correlation Between Sites	B-7
B.4.0	Transferability Rationale	B-8
B.4.1	Geologic Setting	B-8
B.4.2	Lithology	B-9
B.4.3	Alteration	B-10
B.4.4	Influence of Stress	B-10
B.4.5	Groundwater Chemistry	B-12
B.4.6	Summary	B-13
B.5.0	Uncertainties in Data Transfer	B-13
B.6.0	References	B-15

Appendix C - Description of BestFit Software

C.1.0	Introduction	C-1
C.2.0	BestFit Software Overview	C-1
C.3.0	Distribution Descriptions	C-2
C.4.0	References	C-2

Appendix D - Description of Matrix Porosity Dataset

D.1.0	Introduction	D-1
D.2.0	Dataset Summary	D-1
D.3.0	Table Structure	D-1
D.4.0	Access to Dataset	D-3
D.5.0	References	D-3

Appendix E - Description of Effective Porosity Dataset

E.1.0	Introduction	E-1
E.2.0	Dataset Summary	E-1
E.3.0	Table Structure	E-1
E.4.0	Access to Dataset	E-3

Table of Contents (Continued)

E.5.0	References	E-3
-------	----------------------	-----

Appendix F - Description of Dispersivity Dataset

F.1.0	Introduction	F-1
F.2.0	Dataset Summary	F-1
F.3.0	Table Structure	F-1
F.4.0	Access to Dataset	F-3

Appendix G - Description of Matrix Diffusion Dataset

G.1.0	Introduction	G-1
G.2.0	Dataset Summary	G-1
G.3.0	Table Structure	G-1
G.4.0	Access to Dataset	G-2

Appendix H - Description of Matrix Sorption Parameter Datasets

H.1.0	Introduction	H-1
H.2.0	Dataset Summary	H-1
H.3.0	Table Structure	H-2
H.4.0	Access to Datasets	H-8

Appendix I - Description of Fracture Sorption Datasets

I.1.0	Introduction	I-1
I.2.0	Dataset Summary	I-1
I.3.0	Table Structure	I-1
I.4.0	Access to Datasets	I-2

Appendix J - Description of Colloid-Facilitated Transport Parameter Dataset

J.1.0	Introduction	J-1
J.2.0	Dataset Summary	J-1
J.3.0	Table Structure	J-2
J.4.0	Access to Dataset	J-4

Table of Contents *(Continued)*

Appendix K - Supplemental Information

K.1.0	Introduction	K-1
K.2.0	Data Summary	K-1
K.3.0	Access to Data	K-2
K.4.0	References	K-3

CD Containing Datasets and Supplemental Information

List of Figures

Number	Title	Page
1-1	Location of the Pahute Mesa Corrective Action Units	1-2
1-2	Investigation and Pahute Mesa-Oasis Valley Areas for the Pahute Mesa Corrective Action Units (DOE/NV, 1999)	1-7
2-1	Features of the Nevada Test Site Regional Groundwater Flow System.	2-2
2-2	Three-Dimensional View of the Base Hydrostratigraphic Model of the Pahute Mesa-Oasis Valley Area (BN, 2002)	2-14
2-3	Comparison of Silent Canyon Caldera Margins: Base Model and SCCC Alternative (BN, 2002)	2-23
2-4	Typical West - East Cross-Section through the Silent Canyon Caldera for the SCCC Model (BN, 2002)	2-25
2-5	Location of Underground Nuclear Tests on Pahute Mesa	2-28
5-1	Crossplots of Geophysical Log-Derived and Core-Derived Porosity Values	5-4
5-2	Comparison of Core-Derived and Geophysical Log-Derived Porosity Values for UE-20ae.	5-5
5-3	Comparison of Core-Derived and Geophysical Log-Derived Porosity Values for UE-20ad.	5-6
5-4	Comparison of Core-Derived and Geophysical Log-Derived Porosity Values for UE-18t.	5-7
5-5	Comparison of Core-Derived and Geophysical Log-Derived Porosity Values for UE-19t and U-19t	5-7
5-6	Comparison of Core-Derived and Geophysical Log-Derived Porosity Values for WW-8	5-8
5-7	Porosity vs. Depth Trend: Bedded and Nonwelded Tuff (Depth in Meters).	5-9
5-8	Porosity vs. Depth: Lava Flow, Moderately Welded Tuff, and Densely Welded Tuff.	5-10
5-9	Porosity vs. Depth: Flow Breccia and Tuff Breccia	5-10
5-10	Porosity vs. Depth: Pumiceous Lava and Partially Welded Tuff	5-11
5-11	PFD of Porosity Data (in Percent): Timber Mountain Aquifer HSU (648 Samples)	5-14
5-12	PFD of Porosity Data (in Percent): Benham Aquifer HSU (154 Samples).	5-14
5-13	PFD of Porosity Data (in Percent): Paintbrush Vitric Tuff Aquifer HSU (325 Samples).	5-15
5-14	PFD of Porosity Data (in Percent): Calico Hills Vitric Tuff Aquifer HSU (71 Samples).	5-15
5-15	PFD of Porosity Data (in Percent): Paintbrush Lava-Flow Aquifer HSU (54 Samples).	5-16
5-16	PFD of Porosity Data (in Percent): Thirsty Canyon Volcanic Aquifer HSU (146 Samples)	5-16
5-17	PFD of Porosity Data (in Percent): Belted Range Aquifer HSU (48 Samples).	5-17
5-18	PFD of Porosity Data (in Percent): Calico Hills Zeolitized Composite Unit HSU (430 Samples)	5-18

List of Figures (Continued)

Number	Title	Page
5-19	PFD of Porosity Data (in Percent): Timber Mountain Composite Unit HSU (364 Samples)	5-18
5-20	PFD of Porosity Data (in Percent): Calico Hills Vitric Composite Unit HSU (83 Samples)	5-19
5-21	PFD of Porosity Data (in Percent): Pre-Belted Range Composite Unit HSU (37 Samples)	5-19
5-22	PFD of Porosity Data (in Percent): Lower Carbonate Aquifer HSU (15 Samples)	5-20
5-23	PFD of Porosity Data (in Percent): Intrusive Confining Unit HSUs (55 Samples)	5-21
5-24	PFD of Porosity Data (in Percent): Vitric Alteration (509 Samples)	5-22
5-25	PFD of Porosity Data (in Percent): Devitrified Alteration (771 Samples)	5-22
5-26	PDF and CDF Curve Fits for Group 1: Lognormal (Format 2) Distribution (Matrix Porosity in Percent)	5-25
5-27	Comparison of Group 1 PDF Root Mean Squared Errors	5-27
5-28	PDF and CDF Curve Fits for Group 2: Normal Distribution (Matrix Porosity in Percent)	5-28
5-29	Comparison of Group 2 PDF Root Mean Squared Errors	5-30
5-30	PDF and CDF Curve Fits for Group 2: Logistic Distribution (Matrix Porosity in Percent)	5-31
5-31	PDF and CDF Curve Fits for Group 3: Normal Distribution (Matrix Porosity in Percent)	5-33
5-32	Comparison of Group 3 PDF Root Mean Squared Errors	5-35
5-33	PDF and CDF Curve Fits for Group 4: Normal Distribution (Matrix Porosity in Percent)	5-36
5-34	Comparison of Group 4 PDF Root Mean Squared Errors	5-38
6-1	PFD of Porosity Data: Alluvium HSU (208 Samples)	6-5
6-2	Minimum Fracture Porosity (HGU)	6-19
6-3	Maximum Fracture Porosity (HGU)	6-19
6-4	Minimum Fracture Porosity (HSU)	6-21
6-5	Maximum Fracture Porosity (HSU)	6-21
6-6	PFD of Porosity Data: Bedded Tuff Lithology (868 Samples)	6-28
6-7	PFD of Porosity Data: Nonwelded Tuff Lithology (264 Samples)	6-28
6-8	PFD of Porosity Data: Vitric Tuff Lithology (20 Samples)	6-29
7-1	Illustration of the Breakthrough-Curve, Pulse-Width Method of Analysis (Welty and Gelhar, 1989)	7-9

List of Figures (Continued)

Number	Title	Page
7-2	Conceptualized Breakthrough Curve	7-9
7-3	Tritium Concentration in Water Pumped from Well RNM-2S versus Volume Pumped (Thompson, 1991; activity concentrations corrected to CAMBRIC zero time).....	7-11
7-4	The ⁸⁵ Kr Concentration in Water Pumped from Well RNM-2S versus Volume Pumped (Thompson, 1991; activity concentrations corrected to CAMBRIC zero time).....	7-11
7-5	Type Curves for Instantaneous Tracer Injection in Radial Converging Flow Field: Comparison with Derivative of Imposed Step Function (Sauty, 1980).....	7-13
7-6	Tritium Concentration Data (X) for Well RNM-2S Water and Calculated Elution of Tracer after Instantaneous Tracer Injection in a Radial Converging Flow Field for Peclet Number 10 (Daniels and Thompson, 1984).....	7-14
7-7	Elution of Tritium and Cl-36 from Well RNM-2S (Thompson, 1988)	7-15
7-8	Elution of Tritium Compared with Sauty Model (Thompson, 1988).....	7-15
7-9	Elution of Cl-36 Compared with Sauty Model (Thompson, 1988)	7-16
7-10	Longitudinal Dispersivity Versus Tracer Test Scale	7-20
7-11	Transverse Horizontal Dispersivity Versus Tracer Test Scale	7-20
7-12	Transverse Vertical Dispersivity Versus Tracer Test Scale	7-21
7-13	NTS Data as Compared to Non-NTS Data for Longitudinal Dispersivity	7-23
7-14	Probability Density Functions for Dispersivity	7-25
8-1	Log Matrix Diffusion Coefficients as a Function of Both Matrix Porosity and Log Matrix Permeability for ³ H ₂ O in Pahute Mesa Rocks (Reimus et al., 2002a), for Bromide in Rocks From the UE25 C-Wells (Reimus et al., 1999), and for Iodide in Rocks From ER-20-6 #1 (Reimus et al., 2000).	8-8
8-2	Log Matrix Diffusion Coefficients as a Function of Matrix Porosity (Fraction) Determined From Diffusion Cell Tests (Triangles) and Fracture Transport Tests (Squares). The Least-Squares Linear Regressions Indicate Relatively Poor Fits to the Individual Datasets.....	8-10
8-3	Log (nD _m) Values as a Function of Matrix Porosity (Fraction), and a Logarithmic Fit to the Data. The Dashed Lines Represent 95 Percent Confidence Intervals	8-10
8-4	Cumulative Probability Distribution of Matrix Diffusion Coefficients from Figure 8-3 with No Regard to Matrix Porosity or Matrix Permeability. The Line Represents a Normal Distribution with a Mean of -6.48 and a Standard Deviation of 0.49.....	8-12

List of Figures (Continued)

Number	Title	Page
8-5	Matrix Diffusion Mass Transfer Coefficients for Halides and Tritium Obtained in Laboratory Fracture Transport Experiments and Field Tracer Tests in Volcanic Rocks From the Nevada Test Site. There is a Tendency for Smaller Mass Transfer Coefficients as Time Scales Increase. Laboratory and Field Data for C-hole Rocks are from Reimus et al. (1999); Laboratory Data for ER-20-6 Rocks are from Reimus and Haga (1999). The Horizontal Lines for the Field Data Reflect the Range of Uncertainty in Mean Residence Times in These Tests.	8-19
9-1	YMP PDF Distributions for Pu Sorption on Volcanic Tuff (Conca, 2000, Table 2b; Table 9-10 this Report); Vertical Lines Indicate the 95 Percent Confidence Intervals	9-25
9-2	Distributions Fit to All Pu Sorption Data for Three Different Rock Types Using YMP Data in YMP (1996) DTN: LAIT831341AQ96.001	9-25
9-3	PDF and CDF of Pu K_d on Vitric Tuff in J-13 Water at 20°C: Triangular Distribution Shown with Red Line; Symbols Indicate Experimental Atmosphere for Individual Data Points in Distribution (Note: Benchtop Conditions are Atmospheric with pH Approximately 8.4).....	9-26
9-4	CDF of Pu K_d on Vitric Tuff in J-13 Water at 20°C: Triangular Distribution Shown with Red Line; Distribution Only for Air Environment (pH >8) Experiments	9-27
9-5	PDF and CDF of Pu K_d on Vitric Tuff in p#1 Water at 20°C: Triangular Distribution Shown with Red Line; Symbols Indicate Experimental Atmosphere for Individual Data Points in Distribution.	9-28
9-6	PDF and CDF of Pu K_d on Devitrified Tuff in J-13 Water at 20°C: Lognormal Distribution Shown with Red Line; Symbols Indicate Experimental Atmosphere for Individual Data Points in Distribution.	9-29
9-7	Relationship Between Duration of Experiment and K_d Value for Pu on Devitrified Tuff in J-13 Water	9-30
9-8	PDF and CDF of Pu K_d on Devitrified Tuff in p#1 Water at 20-25°C: Exponential Distribution Shown with Red Line; Components of Distribution Associated with CO ₂ Atmosphere Circled in Green in Upper Plot; Middle and Lower Plot are for Air Atmosphere Experiments Only	9-31
9-9	PDF and CDF of Pu K_d on Zeolitic Tuff in J-13 Water at 20-25°C: Logistic Distribution Shown with Red Line; Symbols Indicate Experimental Atmosphere for Individual Data Points in Distribution	9-32
9-10	PDF and CDF of Pu K_d on Zeolitic Tuff in p#1 Water at 20-25°C: Lognormal Distribution Shown with Red Line (Logistic Distribution Shown with Blue Line for Comparison with Figure 9-9); Symbols Indicate Experimental Atmosphere for Individual Data Points in Distribution	9-33
9-11	YMP PDF Distributions for Np Sorption on Volcanic Tuff (Conca, 2000, Table 2b).....	9-34
9-12	Np K_d Distributions Fit to YMP TDMS Data for All Experimental Conditions Included in YMP (1996) DTN: LAIT831341AQ96.001	9-34

List of Figures (Continued)

Number	Title	Page
9-13	PDF and CDF of Np K_d on Vitric Tuff in J-13 Water at All Temperatures (20-90°C): Symbols Indicate Experimental Atmosphere for Individual Data Points in Distribution (Note: All But 4 Experiments Conducted at 20-25°C)	9-35
9-14	PDF and CDF of Np K_d on Vitric Tuff in p#1 Water at All Temperatures (20-60°C): Symbols Indicate Experimental Atmosphere for Individual Data Points in Distribution (Note: All But 1 Experiment Conducted at 20-25°C)	9-36
9-15	PDF and CDF of Np K_d on Devitrified Tuff in J-13 Water; Symbols Indicate Experimental Atmosphere and Temperature (for Experiments Conducted at High Temperature) for Individual Data Points in Distribution.	9-37
9-16	PDF and CDF of Np K_d on Devitrified Tuff in p#1 Water; Symbols Indicate Experimental Atmosphere and Temperature for Individual Data Points in Distribution.	9-38
9-17	CDF of Np K_d on Devitrified Tuff in p#1 Water; Distribution for 20-25°C Only, and Upper 4 K_d Values (> 18) are Rejected.	9-39
9-18	Np K_d on Zeolitic Tuff in J-13 Water at 20-25°C	9-40
9-19	Np K_d on Zeolitic Tuff in J-13 Water at 20-60°C	9-41
9-20	Np K_d on Zeolitic Tuff in J-13 Water at 20-90°C	9-42
9-21	Np K_d on Zeolitic Tuff in J-13 Water at 90°C.	9-43
9-22	Np K_d on Zeolitic Tuff in p#1 Water at 20-90°C.	9-44
9-23	Np K_d on Zeolitic Tuff in p#1 Water at 20-25°C.	9-45
9-24	CDF of Np K_d Alluvium	9-46
9-25	Strontium Sorption on Devitrified Tuff in J-13 Water; Red Line Shows Lognormal Distribution to YMP TDMS Data (YMP [1996] DTN: LAIT831341AQ96.001); Green Line Shows YMP Distribution (Table 9-10)	9-47
9-26	Strontium Sorption on Vitric Tuff in J-13 Water; Red Line Shows Normal Distribution to YMP TDMS Data (YMP [1996] DTN: LAIT831341AQ96.001); Green Line Shows YMP Distribution (Table 9-10)	9-48
9-27	Strontium Sorption on Zeolitic Tuff in J-13 Water; Red Line Shows Lognormal Distribution to YMP TDMS Data (YMP [1996] DTN: LAIT831341AQ96.001); Green Line Shows YMP Distribution (Table 9-10)	9-49
9-28	Temperature Dependence of Sr K_d for (a) Devitrified Tuff, (b) Vitric Tuff, and (c) Zeolitic Tuff	9-50
9-29	Cesium Sorption on Devitrified Tuff in J-13 Water; Red Line Shows Normal Distribution to YMP TDMS Data (YMP [1996] DTN: LAIT831341AQ96.001); Green Line Shows YMP Distribution (Table 9-10)	9-51
9-30	Cesium Sorption on Vitric Tuff in J-13 Water; Red Line Shows Normal Distribution to YMP TDMS Data (YMP [1996] DTN: LAIT831341AQ96.001); Green Line Shows YMP Distribution (Table 9-10).	9-52

List of Figures (Continued)

Number	Title	Page
9-31	Cesium Sorption on Zeolitic Tuff in J-13 Water; Red Line Shows Lognormal Distribution to YMP TDMS Data (YMP [1996] DTN: LAIT831341AQ96.001); Green Line Shows YMP Distribution (Table 9-10)	9-53
9-32	Uranium Sorption on Devitrified Tuff in J-13 Water; Red Line Shows Exponential Distribution to YMP TDMS Data (YMP [1996] DTN: LAIT831341AQ96.001); Green Line Shows YMP Distribution (Table 9-10)	9-54
9-33	Uranium Sorption on Devitrified Tuff in p#1 Water; Red Line Shows Exponential Distribution to YMP TDMS Data (YMP [1996] DTN: LAIT831341AQ96.001); Green Line Shows YMP Distribution (Table 9-10)	9-55
9-34	Uranium Sorption on Vitric Tuff in J-13 Water; Red Line Shows Exponential Distribution to YMP TDMS Data (YMP [1996] DTN: LAIT831341AQ96.001); Green Line Shows YMP Distribution (Table 9-10)	9-56
9-35	Uranium Sorption on Vitric Tuff in p#1 Water; Red Line Shows Exponential Distribution to YMP TDMS Data (YMP [1996] DTN: LAIT831341AQ96.001); Green Line Shows YMP Distribution (Table 9-10)	9-57
9-36	Uranium Sorption on Zeolitic Tuff in J-13 Water; Red Line Shows Exponential Distribution to YMP TDMS Data (YMP [1996] DTN: LAIT831341AQ96.001); Green Line Shows YMP Distribution (Table 9-10)	9-58
9-37	Uranium Sorption on Zeolitic Tuff in p#1 Water; Red Line Shows Exponential Distribution to YMP TDMS Data (YMP [1996] DTN: LAIT831341AQ96.001); Green Line Shows YMP Distribution (Table 9-10)	9-59
9-38	pH and K_d Relationships for U Sorption on Vitric Tuff in p#1 and J-13 Water	9-60
9-39	pH and K_d Relationships for U Sorption on Devitrified Tuff in p#1 and J-13 Water	9-60
9-40	pH and K_d Relationships for U Sorption on Zeolitic Tuff in p#1 and J-13 Water	9-61
11-1	Cumulative Probability Distribution of Log Colloid Concentrations in NTS Fractured Volcanics	11-5
11-2	Log Colloid Concentrations Versus Log ($[CA]+[Mg]$) (M) in Saturated Alluvium near Yucca Mountain	11-5
11-3	Normalized Size Distributions of Colloids in Wells Located on the Nevada Test Site and Vicinity	11-6
11-4	Mean Normalized Size Distribution of Colloids in Wells Located on the Nevada Test Site and Vicinity	11-7
11-5	Standard Deviations of Normalized Concentrations Versus Colloid Diameter	11-8
11-6	Ranges of K_d Values Measured for Actinide Sorption Onto Colloids	11-11
11-7	Distribution Coefficient (K_d) Calculated for Pu(V) Sorbed Onto Various Mineral Colloids (Source: Kersting et al., 2002b)	11-15

List of Figures (Continued)

Number	Title	Page
11-8	Yucca Mountain Pu Desorption Experiments using Smectite and Silica Colloids (Lu et al., 1998b)	11-19
11-9	CML Microsphere and Inorganic Colloid Filtration Rate Constants as a Function of Time to Solute Peak Concentration.	11-23
11-10	Cumulative Probability Distribution of Log Colloid Filtration Rate Constants.	11-25
11-11	Cumulative Probability Distribution of Log Colloid Retardation Factors	11-26
11-12	Cumulative Probability Distribution of Log Colloid Retardation Factors and a “fit” of a Lognormal Distribution to the Data.	11-27
B.1-1	Location of Pahute Mesa, Yucca Mountain Site, and Relevant Caldera Complexes of the Southwestern Nevada Volcanic Field.	B-3
B.3-1	Factors Influencing Flow and Transport Parameters in Fractured Rock	B-6
B.4-1	Maximum Excess Horizontal Stress from Yucca Mountain Boreholes (Stock and Healy, 1988) and Rainier Mesa (Carr, 1974)	B-12
B.4-2	Trilinear Diagram Showing Relative Major Ion Percentages for Groundwater from Pahute Mesa and Yucca Mountain (IT, 2001)	B-14

List of Plates

Number	Title
1	Hydrostratigraphic Units for the Pahute Mesa-Oasis Valley Area Pocket
2	Southwest to Northeast Hydrostratigraphic Cross Section J-J' through the Pahute Mesa-Oasis Valley Area Pocket
3	West to East Hydrostratigraphic Cross Section C-C' through the Pahute Mesa-Oasis Valley Area Pocket
4	Contaminant Transport Data Availability Within the Pahute Mesa-Oasis Valley Area and Vicinity Pocket

List of Tables

Number	Title	Page
2-1	Hydrogeologic Units of the UGTA Regional Model in the PM-OV Model Area	2-4
2-2	Hydrostratigraphic Units of the Pahute Mesa-Oasis Valley Area Included in the Regional Hydrostratigraphic Framework Model	2-8
2-3	Ranges of Hydraulic Conductivity for the Major Aquifers of the Nevada Test Site Region.	2-9
2-4	Estimated Steady-State Groundwater Budget for the Nevada Test Site Regional Groundwater Flow System	2-11
2-5	Additional and Modified Hydrogeologic Units of the PM-OV Model	2-16
2-6	Correlation of Hydrostratigraphic Units of the Pahute Mesa-Oasis Valley Model and Earlier Models	2-18
2-7	Mineralogical Analyses within PM-OV Model Area (by HSU)	2-21
2-8	Correlation of Hydrostratigraphic Units Between the Silent Canyon Caldera Complex Model and the Base HSU Model	2-24
2-9	Radionuclide Summary for Areas 19 and 20 of the Nevada Test Site	2-30
5-1	Test Statistics for the Comparison of Rainier Mesa and PM-OV Porosity Data as a Function of HSU.	5-13
5-2	Test Statistics for the Comparison of Rainier Mesa and PM-OV Porosity Data Based on Lithology	5-23
5-3	Group 1 Summary Statistics	5-26
5-4	Group 2 Summary Statistics	5-29
5-5	Group 3 Summary Statistics	5-34
5-6	Group 4 Summary Statistics	5-37
5-7	Pahute Mesa - Matrix Porosity - Dominant Lithology for Each HSU	5-41
6-1	Pahute Mesa-Oasis Valley and Yucca Flat Lithologic Comparison.	6-3
6-2	Sources for Data Required for Estimation of Fracture Porosity of Volcanic Aquifers	6-10
6-3	Sources for Data for Estimation of Effective Porosity of Volcanic Aquifers.	6-10
6-4	Data Documentation Evaluation Flags for Parameters Required to Estimate Fracture Porosity of Volcanic Aquifers.	6-10
6-5	Data Documentation Flags for Tracer Migration Experiments	6-10
6-6	Fracture Porosity of Volcanic Aquifers Estimated Using Parallel Plate Models	6-12
6-7	Fracture Porosity Obtained from the Study of Volcanic Core	6-13
6-8	Effective Porosity for Volcanic Aquifers Obtained from the BULLION Forced-Gradient Experiment	6-13
6-9	Fracture Porosities Used by Wolfsberg et al. (2002)	6-15

List of Tables (Continued)

Number	Title	Page
6-10	Sources for Data Required to Estimate Fracture Porosity of Tuff Confining Unit	6-24
6-11	Data Sources for the Effective Porosity of the Carbonate Aquifer.	6-24
6-12	Data Documentation Flags for Tracer Migration Experiments	6-25
6-13	Estimate of Fracture Porosity for the Tuff Confining Unit	6-26
6-14	Effective Porosity of the Carbonate Aquifer	6-26
6-15	Pahute Mesa - Effective Porosity - Dominant Lithology for Each HSU	6-34
7-1	Dispersivity Information Summary from the Nevada Test Site and Vicinity	7-4
7-2	Dispersivity from Hypothetical Transport Simulations for Frenchman Flat Underground Test Areas.	7-18
8-1	Summary of Diffusion Cell Experiments, Including Rocks Samples, Matrix Porosities and Permeabilities, and Solutes for Which Diffusion Coefficients Were Measured.	8-3
8-2	Fracture Transport Experiment Rock Samples, Solutes Tested, and Number of Experiments In Each Fracture	8-5
8-3	Factor by Which Diffusion Coefficients Change as a Function of Temperature In Water.	8-13
8-4	Pahute Mesa - Matrix Diffusion Coefficient (cm ² /s) - Dominant Lithology for Each HSU	8-15
9-1	Descriptions of Stratigraphy, Hydrogeologic Units (HGUs), Lithology, and Alteration Considered in This Section	9-62
9-2	Theoretically Computed Matrix K _d Distributions by Stratigraphy (Data from Zavarin et al., 2002)	9-64
9-3	Predicted Average Log K _d for Selected Regional Hydrostratigraphic Units from Zavarin et al. (2002).	9-66
9-4	Predicted Radionuclide K _d s (mL/g) for Frenchman Flat Alluvium by Zavarin et al. (2002).	9-66
9-5	Cs K _d s Reported by Papeilis and Um (2002) for Crushed Pahute Mesa Material and for Intact Plugs Used in Diffusion Experiments	9-67
9-6	Pb K _d s Reported by Papeilis and Um (2002) for Crushed Pahute Mesa Material and for Intact Plugs Used in Diffusion Experiments	9-67
9-7	Sr and Pb K _d s Reported by Um and Papeilis (2001b) for Zeolitized Tuff from Rainier Mesa.	9-68
9-8	Sr and Pb K _d s Reported by Sloop (1998) for Zeolitized Tuff from Rainier Mesa.	9-68
9-9	Chemical Composition (mg/L) of Water in J-13, p#1, and Two Locations on Pahute Mesa.	9-68
9-10	YMP Sorption Coefficient Distributions for Saturated Zone Units (Conca, 2000; Table 2b)	9-69

List of Tables (Continued)

Number	Title	Page
9-11	Carbonate Sorption K_d Ranges	9-70
9-12	Summary of Distributions Fit for Pu Sorption Using YMP Data - Minimum and Maximum of Dataset Listed in Parentheses When Different from Distribution	9-70
9-13	Summary of Distributions Fit for Np Sorption Using YMP Data	9-71
9-14	Summary of Distributions Fit for Sr Using YMP Data	9-72
9-15	Summary of Distributions Fit for Cs Using YMP Data	9-72
9-16	Summary of Distributions Fit for U Using YMP Data	9-72
9-17	HSUs and Corresponding HGUs, Alteration, Lithology, and Stratigraphy	9-73
9-18	K_d Distributions Based on Laboratory Experiments Characterized by Material Alteration	9-76
9-19	Summary of K_{ds} Estimated by Stratigraphy with Mechanistic Model, Correlated to HSUs (Data in Zavarin et al., 2002)	9-79
10-1	Radionuclide Classes in Wolfsberg et al. (2002)	10-4
10-2	Fracture Retardation Factors from Wolfsberg et al. (2002) (Class I has $R=1$)	10-4
10-3	Fracture Retardation Factors, $\log(R)$, Estimated for Regional HSUs by Zavarin et al., 2002	10-5
10-4	Summary of Fracture Retardation Factors for HSUs	10-7
11-1	Wells Sampled for Colloid Concentration and Size Distribution Analyses	11-4
11-2	Ranges of Rate Constants (hr^{-1}) for Sorption and Desorption of Actinides Onto Colloids (Assuming Only a Single Type of Sorption Site) from UGTA and Yucca Mountain Experiments	11-10
A.1-1	Hydrostratigraphic Units of the Pahute Mesa-Oasis Valley Hydrostratigraphic Framework Model	A-2
A.1-2	Hydrogeologic Units of the UGTA Regional Model in the PM-OV Model Area	A-8
A.1-3	Additional and Modified Hydrogeologic Units of the PM-OV Model	A-8

List of Acronyms and Abbreviations

ac-ft/yr	Acre-feet per year
Am	Americium
ASTM	American Society for Testing and Materials
BA	Benham Aquifer
bgs	Below ground surface
BHTV	Borehole televiewer
BN	Bechtel Nevada
Br ⁻	Bromide
BRA	Belted Range Aquifer
BRT	Belted Range Thrust
BZA	Breathing zone apparatus
C	Carbon
Ca	Calcium
CADD	Corrective Action Decision Document
CAI	Corrective Action Investigation
CAIP	Corrective Action Investigation Plan
CAP	Corrective Action Plan
CAS	Corrective Action Site
CAU	Corrective Action Unit
CD	Compact disc
CDF	Cumulative distribution function
CFD	Cumulative frequency distribution
CHVTA	Calico Hills Vitric Tuff Aquifer
CHZCM	Calico Hills Zeolitized Composite Unit
Cl ⁻	Chloride
cm	Centimeter
Cm	Curium
cm ² /s	Square centimeter per second
CML	Carboxylate-modified polystyrene latex
Co	Cobalt
CO ₂	Carbon dioxide
CR	Closure Report

List of Acronyms and Abbreviations (Continued)

Cs	Cesium
DDE_F	Data Documentation Evaluation Flags
DFN	Discrete fracture network
D _m	Matrix diffusion coefficient
DoD	U.S. Department of Defense
DOE	U.S. Department Energy
DOT	U.S. Department of Transportation
DQO	Data Quality Objective
DQE_F	Data Quality Evaluation Flags
DRI	Desert Research Institute
DTN	Data tracking number
EPA	U.S. Environmental Protection Agency
ERP	Environmental Restoration Program
ESF	Exploratory Studies Facility
ET	Evapotranspiration
Eu	Europium
FCCM	Fortymile Canyon Composite Unit
FEHM	Finite-element heat mass transfer code
FFACO	<i>Federal Facility Agreement and Consent Order</i>
FGE	Forced-Gradient Experiment
FMI	Formation microimage
FMS	Micro-resistivity electronic scanner
ft/d	Foot (feet) per day
ft	Foot (feet)
g/cm ³	Grams per cubic centimeter
GCU	Granite Confining Unit
gpm	Gallon per minute
HCO ₃ ⁻	Bicarbonate
HGU	Hydrogeologic unit
³ HHO	Tritiated water
Ho	Holmium
hr	Hour
HRMP	Hydrology/Radionuclide Migration Project

List of Acronyms and Abbreviations (Continued)

HSLIS	High sensitivity liquid <i>in situ</i> particle spectrometry
HST	Hydrologic source term
HSU	Hydrostratigraphic Unit
I ⁻	Iodide
ICU	Intrusive Confining Unit
IICU	Intra-Caldera Intrusive Confining Unit
in.	Inch
K	Hydraulic Conductivity
K ⁺	Potassium
K _d	Distribution coefficient
kg/m ³	Kilograms per cubic meter
km	Kilometer
km ²	Square kilometer
Kr	Krypton
L	Length
LaGriT	Los Alamos Grid Toolbox
LANL	Los Alamos National Laboratory
LCA	Lower Carbonate Aquifer
LCCU	Lower Carbonate Confining Unit
LFA	Lava flow aquifer
Li	Lithium
LLNL	Lawrence Livermore National Laboratory
m	Meter
M	Molar
mbgs	Meters below ground surface
m/d	Meter per day
m ² /day	Square meters per day
m ³	Cubic meter
m ³ /d	Cubic meter per day
m ³ /min	Cubic meter per minute
m ³ /yr	Cubic meters per year
m/s ²	Meters per square second
Mg	Magnesium

List of Acronyms and Abbreviations (Continued)

mg/L	Milligram per liter
Mg/m ³	Megagram per cubic meter
mi	Mile
mi ²	Square mile
mL/g	Milliliters per gram
Mn	Manganese
MTC	Mass Transfer Coefficient
Na	Sodium
NaNO ₃	Sodium Nitrate
Nb	Niobium
NDEP	Nevada Division of Environmental Protection
NEPA	<i>National Environmental Policy Act</i>
NH ₄ ⁺	Ammonium
Ni	Nickel
NNSA/NSO	U.S. Department of Energy, National Nuclear Security Administration Nevada Site Office
nm	Nanometer
Np	Neptunium
NpO ₂	Neptunium dioxide
NTS	Nevada Test Site
NTSWAC	Nevada Test Site Waste Acceptance Criteria
OSHA	Occupational Safety and Health Administration
OV	Oasis Valley
p	Partial pressure
Pa-s	Pascal-second
Pb	Lead
PBRCM	Pre-Belted Range Composite Unit
pCi/L	Picocurie per liter
PDF	Probability density function
PFBA	Pentafluorobenzoate
PDF	Probability Frequency Distribution
PLFA	Paintbrush Lava Flow Aquifer
PM-OV	Pahute Mesa-Oasis Valley
PPE	Personal protective equipment

List of Acronyms and Abbreviations (Continued)

Pu	Plutonium
PuO ₂	Plutonium dioxide
PVC	Polyvinyl chloride
PVTA	Paintbrush Volcanic Tuff Aquifer
QA	Quality assurance
QAPP	Quality assurance project plan
QC	Quality control
R	Retardation factors
Redox	Reduction/oxidation
RMS	Root-mean squared
Ru	Ruthenium
RWMS	Radioactive Waste Management Site
Sb	Antimony
SCCC	Silent Canyon Caldera Complex
SDWA	<i>Safe Drinking Water Act</i>
SEM	Scanning electron microscope
S _h	Principle stress
Shaw	Shaw Environmental, Inc.
Sm	Samarium
Sn	Tin
SOP	Standard Operating Procedure
Sr	Strontium
SSHASP	Site-Specific Health and Safety Plan
SSM	Simplified Source Term Model
SWIFT	Sandia Waste Isolation Flow and Transport
SWNVF	Southwestern Nevada Volcanic Field
SZ	Saturated Zone
T	Time
Tc	Technetium
TcO ₄ ⁻	Technetium Oxide
TCU	Tuff Confining Unit
TCVA	Thirsty Canyon Volcanic Aquifer
TDMS	Technical Data Management System

List of Acronyms and Abbreviations (Continued)

Th	Thorium
TMA	Timber Mountain Aquifer
TMCM	Timber Mountain Composite Unit
TSA	Topapah Spring Aquifer
TWG	Technical Working Group
U	Uranium
UBI	Ultrasonic borehole imager
UCCU	Upper Clastic Confining Unit
UGTA	Underground Test Area
USGS	U.S. Geological Survey
UZ	Unsaturated Zone
VA	Volcanic Aquifer
VOIA	Value of Information Analysis
VTA	Volcanic Tuff Aquifer
VU	Volcanics Undifferentiated
WIPP	Waste Isolation Pilot Plan
WTA	Welded Tuff Aquifer
XRD	X-ray diffraction
YMP	Yucca Mountain Project
Zr	Zirconium
°C	Degree(s) Centigrade
3-D	Three dimensional
2-D	Two dimensional
1-D	One dimensional
μm	Micrometer
μCi/mL	Microcuries per milliliter

1.0 Introduction

This report documents the analysis of the available transport parameter data conducted in support of the development of a Corrective Action Unit (CAU) groundwater flow model for Central and Western Pahute Mesa: CAUs 101 and 102. Central and Western Pahute Mesa constitute two areas of the Nevada Test Site (NTS) used for underground nuclear testing (Figure 1-1). These nuclear tests resulted in groundwater contamination in the vicinity of the underground test areas. As a result, the U.S. Department of Energy (DOE), National Nuclear Security Administration Nevada Site Office (NNSA/NSO) is currently conducting a corrective action investigation of the Pahute Mesa underground test areas. The CAU groundwater flow model is a component of the CAU model, a major part of the Underground Test Area (UGTA) strategy (FFACO, 1996). A brief summary of the project background is provided, followed by a presentation of the purpose and scope of the work described in this document. Brief descriptions of the CAU model's documentation and this document's contents are provided at the end of this section.

The reader who is familiar with the UGTA Project may wish to skip Sections 1.0 through 4.0 and read Sections 5.0 through 11.0, which describe the data analysis activities and their results.

1.1 Background

A brief overview of the project and site background are presented in this section.

1.1.1 Project Background

Between 1951 and 1992, the DOE and the U.S. Department of Defense (DoD) conducted underground nuclear testing at the NTS. To ensure protection of the public and the environment, the NNSA/NSO and its predecessors established a long-term program to monitor groundwater for the presence of radionuclides, and the UGTA Project to investigate and remediate the underground test areas. The UGTA Project is a component of NNSA/NSO's Environmental Restoration Program (ERP).

The UGTA Project activities are conducted under the direction of the NNSA/NSO UGTA Project Manager. A Technical Working Group (TWG) was formed to serve as a technical advisory group and assist the NNSA/NSO UGTA Project Manager with technical management issues. The TWG consists of representatives from the participating organizations which include Bechtel Nevada (BN), Desert

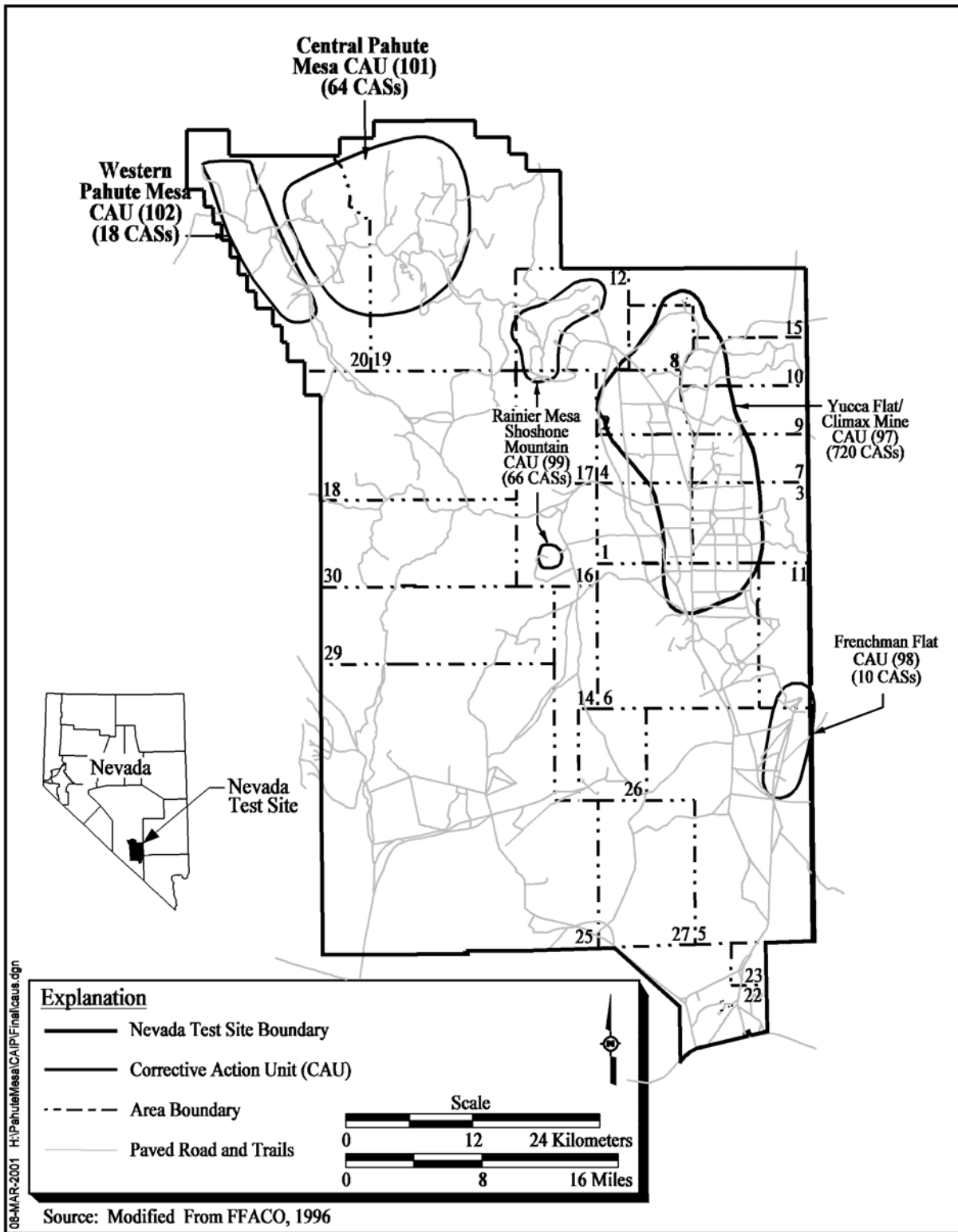


Figure 1-1
Location of the Pahute Mesa Corrective Action Units

Research Institute (DRI), Shaw Environmental, Inc. (Shaw), Lawrence Livermore National Laboratory (LLNL), Los Alamos National Laboratory (LANL), and the U.S. Geological Survey (USGS). Tasks assigned to the TWG committee include providing technical recommendations to NNSA/NSO, providing expert technical support in specific UGTA tasks via subcommittees, and serving as internal peer reviewers of UGTA products.

Since 1996, the Nevada Division of Environmental Protection (NDEP) has regulated NNSA/NSO's corrective actions through the *Federal Facility Agreement and Consent Order* (FFACO) (1996). The individual locations covered by the agreement are known as Corrective Action Sites (CASs), and they are grouped into Corrective Action Units. The UGTA CAUs are Frenchman Flat, Central Pahute Mesa, Western Pahute Mesa, Yucca Flat, and the Rainier Mesa/Shoshone Mountain CAUs (Figure 1-1). Central Pahute Mesa (CAU 101) and Western Pahute Mesa (CAU 102) are addressed together due to their adjacent locations and common groundwater regime as well as similarities in testing practices, geology, and hydrology.

Appendix VI of the FFACO, "*The Corrective Action Strategy*," describes the processes that will be used to complete corrective actions, including those in the UGTA Project. The UGTA corrective action strategy, described in Section 3.0 of Appendix VI of the FFACO (1996), was revised in 2000. The UGTA strategy was modified following completion of the DOE review of the Frenchman Flat CAU model. Any subsequent references to the FFACO or its appendices in this document will be made to the FFACO as a whole (i.e., FFACO, 1996).

The UGTA corrective action strategy consists of two major phases: a regional evaluation of all the UGTA CAUs and a corrective action process for each of the CAUs. The CAU-specific corrective action process includes six major components: Corrective Action Investigation Plan (CAIP), Corrective Action Investigation (CAI), Corrective Action Decision Document (CADD), Corrective Action Plan (CAP), Closure Report (CR), and long-term monitoring.

- The regional groundwater flow and contaminant transport model encompasses the NTS and the groundwater flow systems extending to downgradient discharge areas. The regional model is designed to support the entire UGTA program and is developed prior to any CAU-specific activities.
- The CAI planning is documented in the CAIP, an FFACO-required document which provides or references all specific information for planning investigation activities associated with corrective action units or sites.
- The corrective action investigation includes the collection of new data, the evaluation of new and existing data, and the development and use of CAU-specific groundwater flow and transport model(s).
- The CADD is a required report that documents the corrective action investigation. It describes the results of the CAI, the corrective action

alternatives considered, the results of their comparative evaluation, the selected corrective action, and the rationale for its selection.

- The CAP is prepared to describe how the selected remedial alternative is to be implemented. The CAP will contain the engineering design and all specifications necessary to implement the selected remedial alternative.
- The UGTA strategy has provisions for CAU closure only if the long-term monitoring alternative is selected. Closure activities include the preparation of a CR, a review of the CR by NDEP, and long-term closure monitoring by DOE.
- The long-term, post-closure monitoring is designed to ensure the compliance boundary is not violated.

Details on the UGTA corrective action strategy, including the decision process, may be found in Section 3.0 of Appendix VI of the FFACO (1996).

1.1.2 Pahute Mesa Background

Brief overviews of the operational history and work conducted to date are presented in this section.

Pahute Mesa was used as an underground nuclear testing area of the NTS for 27 years. Nuclear testing on Pahute Mesa began with Operation Whetstone in 1965 and ended with Operation Julin in 1992 (DOE/NV, 2000b). Nuclear tests conducted at Pahute Mesa that are of interest to the UGTA Project were detonated in deep vertical shafts, drilled into volcanic rock near or below the water table. A total of 82 such underground nuclear tests were conducted in Pahute Mesa. Sixty-four of these tests were detonated on Central Pahute Mesa (CAU 101), and 18 tests were detonated in Western Pahute Mesa (CAU 102) (DOE/NV, 1999). Media contaminated by the underground nuclear tests of Pahute Mesa are subsurface soils within the unsaturated and saturated zones. Transport in groundwater is the primary mechanism of migration for the subsurface contamination away from the Pahute Mesa underground nuclear tests.

The following is a summary of the activities completed prior to the time of preparation of this document:

- The regional model (IT, 1996 a through f; 1997 a and b; DOE/NV, 1997) was completed prior to the initiation of CAU-specific activities. It was used during the planning and execution of the Pahute Mesa CAI.
- The CAI planning step included the preparation of CAU-specific Data Quality Objectives (DQOs) and the preparation of the CAIP. A Value of Information Analysis (VOIA) (IT, 1998b) using the regional model (DOE/NV, 1997) was conducted to help identify data-collection activities in support of the DQO process. This step is documented in the CAIP (DOE/NV, 1999).

- New data have been collected and added to the data sets. Eight wells have been installed and tested (IT, 2002a through h and k). A tracer test was conducted (IT, 1998a). Major steps of the data analysis process completed at this point include the assessment of geologic data and that of hydrologic data (BN, 2002; Rehfeldt et al., 2003). The assessment of geologic data which resulted in the construction of a CAU-specific Hydrostratigraphic Unit (HSU) model is documented in the HSU model report (BN, 2002). A summary of the Pahute Mesa HSU model is presented in [Section 2.0](#) of this document. The assessment of hydrologic data is documented in a data analysis report by Rehfeldt et al. (2003).

1.2 Task Purpose and Scope

The purpose and scope of the analysis of transport parameter data for the Pahute Mesa CAUs are presented.

1.2.1 Purpose

The purpose of the tasks documented in this report was to analyze relevant information available for the simulation of radionuclide transport within the groundwater flow system of Pahute Mesa and vicinity. The information will be used to develop the Pahute Mesa CAU model.

Specific task objectives were as follows:

- Compile available transport parameter data and supporting information that may be relevant to the Pahute Mesa corrective action investigation.
- Assess the level of quality of the data and associated documentation.
- Analyze the data to derive expected values of transport parameters and estimates of the associated uncertainty and variability.

1.2.2 Scope of Work

The scope of this task includes the assessment of data and information relevant to groundwater flow in the Pahute Mesa subsurface. Transport Parameter data described in the NTS regional model documentation (IT, 1997a; DOE/NV, 1997) and the Pahute Mesa CAIP (DOE/NV, 1999) are supplemented with existing data that were not used and newly-acquired data.

Parameters of interest include effective porosity, dispersivity, matrix porosity, matrix diffusion coefficient, matrix sorption, fracture sorption, and colloid-facilitated transport parameters. Descriptions of these parameters are provided in [Section 4.0](#).

Data analysis includes: (1) literature searches, (2) data/information compilation, (3) data documentation, (4) data documentation qualification, (5) data quality evaluation, and (6) data assessment and interpretation activities. Data analysis includes the use of scientific software to assist in developing probability distributions for each of the transport parameters of interest.

The area of investigation, as described in the CAIP ([Figure 1-2](#)), was selected to encompass the Pahute Mesa CAUs and areas located downgradient that may be impacted by these CAUs. This area includes the Pahute Mesa-Oasis Valley (PM-OV) area and a portion of the Amargosa Desert located downgradient of the Pahute Mesa CAUs. Preliminary radionuclide transport simulations revealed that within the 1,000-year period, the maximum extent of contamination will remain within the PM-OV area ([Figure 1-2](#)). This area of over 2,700 square kilometers encompasses the northwestern portion of the NTS and adjacent lands to the west managed by the U.S. Air Force and the Bureau of Land Management. The PM-OV area includes Timber Mountain, Black Mountain, most of Oasis Valley, and the northern parts of Yucca Mountain and Fortymile Canyon. The groundwater flow model area is virtually the same as the PM-OV area ([Figure 1-2](#)).

Even though the area of interest is limited to the PM-OV area, information considered to be relevant to this task may be obtained from other nearby sites. Nearby sites include other underground test areas, the Yucca Mountain Site, and other sites located within the NTS region. The justification for the transfer of data from other sites was documented. The available data have been collected at various scales ranging from core-scale to field-scale experiments. The available data were compiled and analyzed at their original scale. The issue of upscaling the data to the scale of the CAU groundwater flow and transport model is addressed in [Section 4.0](#). A discussion of parameter-specific scaling considerations is also included in each of the data analysis sections ([Sections 5.0 through 11.0](#)).

1.3 Quality Assurance

Quality assurance measures consistent with the UGTA Project Quality Assurance Project Plan (QAPP) (DOE/NV, 2000a) have been taken to control quality during the performance of all UGTA data analysis tasks. Measures used include data documentation qualification, data quality evaluation, checking procedures, software quality assurance, use of standard methodologies, technical and peer reviews, and corroboration through models.

Data Documentation Evaluation

Each data record or group of similar records evaluated by Shaw was assigned a data documentation evaluation flag (DDE_F) designed to indicate the level of documentation available. The five levels of data documentation evaluation flags are described in [Section 4.0](#).

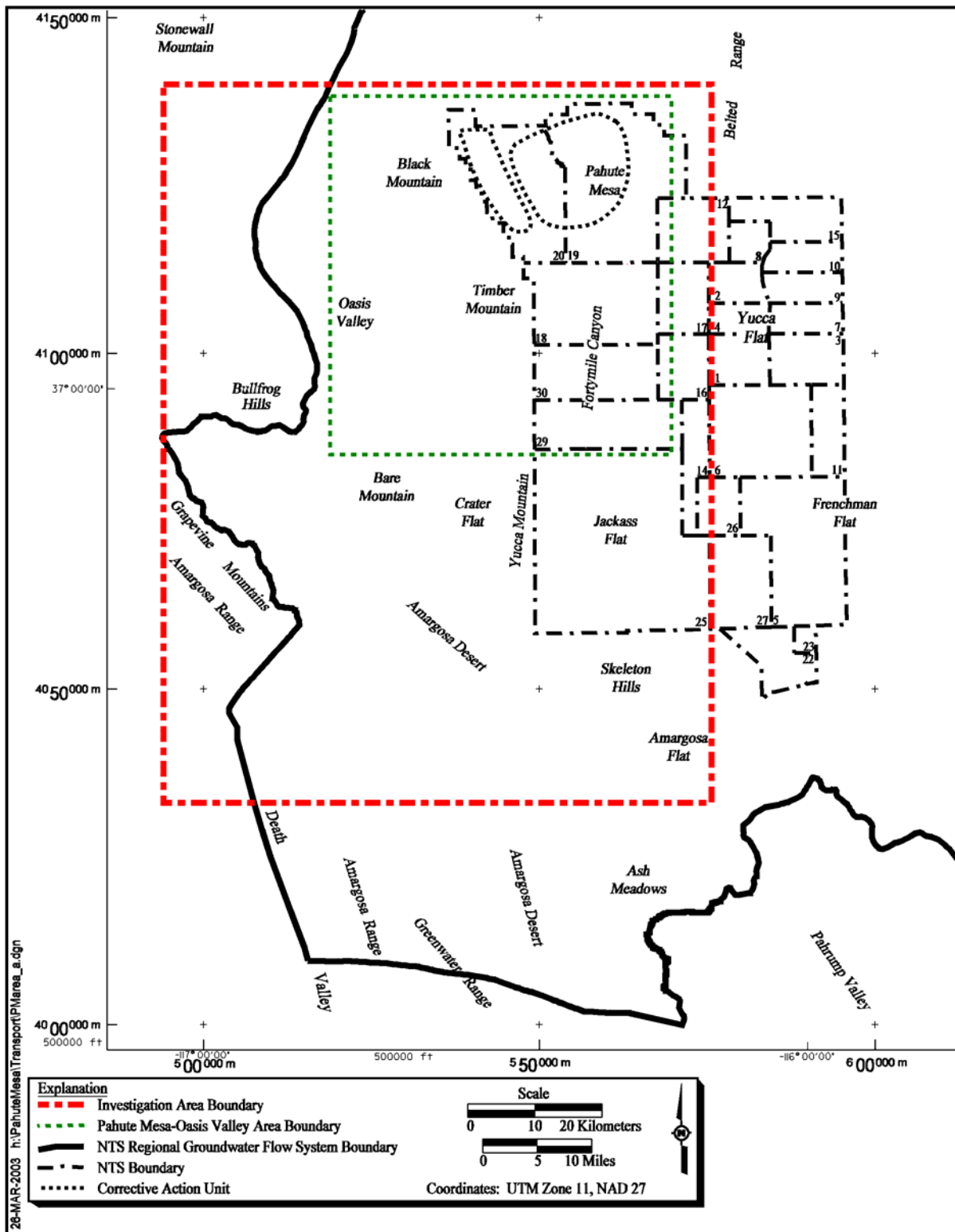


Figure 1-2
Investigation and Pahute Mesa-Oasis Valley Areas for the
Pahute Mesa Corrective Action Units (DOE/NV, 1999)

Data Quality Assessment

The criteria used to assess the quality of the different types of required data are dependent on the type and the intended use of the data. The general procedure used by Shaw includes assigning one or more flags to each record or group of similar records compiled in the dataset, indicating the data quality or suitability of the individual data record for the intended usage. Data-type specific quality evaluation procedures are described in the corresponding section of this document.

Checking Procedures

Various checking procedures were designed for quality control purposes. Checking procedures applicable to the UGTA data analysis include those developed for transcription of data, generation of figures, tables and logs, and performance of calculations. Data compiled by project personnel are subjected to the checking procedures before inclusion in the appropriate dataset. However, the bulk of the available data is comprised of data gathered and compiled by agencies external to the UGTA project. Internal procedures do not govern other UGTA participants; therefore, their data were not subjected to the checking procedures described here.

Standard Methodologies

Only standard and widely accepted methodologies have been used in the development of the interpretive products. The various methodologies used are too numerous to list here; however, they are described and referenced in the sections of this document which discuss their use in the data analysis process.

Technical and Peer Reviews

The review process constitutes an important measure of product quality, and is used throughout the performance of the data analysis activities. The review process may include internal and external technical reviews. The internal reviews are performed by individuals who did not directly contribute to the preparation of the product. These reviews may include representatives of BN, USGS, DRI, LANL, LLNL, GeoTrans, and Shaw. External reviews may be conducted as directed by NNSA/NSO.

Corroboration of Data Through Models

This step is completed during the development of the groundwater flow and transport model(s). For example, during the CAU groundwater flow model calibration process, geologic and hydrologic data interpretations are tested and modified as required. This may be accomplished by modifying the extent or thickness of a given HSU or modifying its hydraulic conductivity in areas where no data are available.

1.4 CAU Model Documentation

The Pahute Mesa CAU model is documented in a series of reports describing the data analysis and modeling tasks. The CAU model documentation consists of the following reports:

- A report describing the assessment of geologic data and the resulting hydrostratigraphic model titled: *A Hydrostratigraphic Model and Alternatives for the Groundwater Flow and Contaminant Transport Model of Corrective Action Units 101 and 102: Central and Western Pahute Mesa, Nye County, Nevada* (BN, 2002).
- A report describing the assessment of hydrologic data in support of the CAU groundwater flow model titled *Hydrologic Data for the Groundwater Flow and Contaminant Transport Model of Corrective Action Units 101 and 102: Central and Western Pahute Mesa, Nye County, Nevada* (Rehfeldt et al., 2003).
- This report which describes the assessment of contaminant transport parameter data in support of the CAU radionuclide transport model.
- A report describing the assessment of the data available on the unclassified hydrologic source term and radionuclide concentrations for the PM-OV area.
- A report describing the groundwater flow model developed for the PM-OV area.
- A report describing the radionuclide transport model developed for the PM-OV area.
- A report summarizing all data analysis and modeling activities. This document includes a summary of the information presented in the six documents listed above.

1.5 Document Organization

This document consists of 12 sections and 7 appendices. As stated previously, readers who are familiar with the UGTA Project may skip to [Sections 5.0](#) through [11.0](#), which describe the data analysis activities and their results.

Summaries of the section contents follow:

- [Section 1.0](#) provides a description of the project background, the purpose and scope of this data analysis task, QA and quality control (QC) considerations, and a description of the documentation of the CAU model.

- [Section 2.0](#) describes components of the conceptual model of the Pahute Mesa CAUs including the regional setting and the local hydrostratigraphic and mineralogic frameworks of the PM-OV area. These descriptions are presented to support the analysis of the transport parameter data described in this document.
- [Section 3.0](#) provides a brief overview of the modeling strategy proposed for the Pahute Mesa CAUs, and a more detailed description of the approach that will be used to simulate radionuclide transport in groundwater.
- [Section 4.0](#) presents the approach used to assess the available transport parameter data.
- [Section 5.0](#) describes the analysis of the available matrix porosity data.
- [Section 6.0](#) describes the analysis of effective porosity data for the alluvial, volcanic, and carbonate aquifers; and for confining units.
- [Section 7.0](#) describes the analysis of the available dispersivity data.
- [Section 8.0](#) describes the analysis of matrix diffusion coefficient data.
- [Section 9.0](#) describes the analysis of matrix sorption coefficient data.
- [Section 10.0](#) describes the analysis of fracture sorption coefficient data.
- [Section 11.0](#) describes the analysis of data relating to the colloid-facilitated transport parameters.
- [Section 12.0](#) provides a list of references used in the document.
- [Appendix A](#) contains information in support of the HSU model and alternatives described in [Section 2.0](#).
- [Appendix B](#) contains a justification of the use of Yucca Mountain site characterization data for developing parameter distributions for the Pahute Mesa modeling effort.
- [Appendix C](#) contains a description of the BestFit software package used to develop parameter distributions.
- [Appendices D through J](#) contain descriptions of the data available for each of the transport parameters considered.
- [Appendix K](#) provides supplemental information including a gallery of visualizations of the PM-OV HSU model.

2.0 Selected Components of the Pahute Mesa Conceptual Model

Selected components of the Pahute Mesa flow system conceptual model are summarized in this section to support the assessment of transport parameter data presented in this report. Components described in this section include the regional setting, the local hydrostratigraphic framework, the geochemical environment, and the sources of contamination.

2.1 Regional Setting

The PM-OV flow system is part of the NTS regional flow system ([Figure 2-1](#)), which is part of the Death Valley flow system. A conceptual model of the regional groundwater flow system of the NTS was developed during the regional evaluation (DOE/NV, 1997). Summary descriptions of the regional hydrogeologic framework and groundwater occurrence and movement, as conceptualized in the regional flow model (DOE/NV, 1997), are presented in this section.

2.1.1 Regional Hydrogeologic Framework

The hydrogeologic framework used in the UGTA regional model is based on the conceptual hydrologic system established for the NTS area by Winograd and Thordarson (1975) and Blankennagel and Weir (1973). This early work was summarized and updated by Laczniaik et al. (1996), and has further been developed by the UGTA hydrostratigraphic regional modeling team (IT, 1996d).

The rocks of the NTS have been classified using a two-level classification scheme, in which hydrogeologic units (HGUs) are grouped to form HSUs (IT, 1996d). The HGUs are used to categorize rocks according to their ability to transmit groundwater, which is mainly a function of the rocks' primary lithologic properties, degree of fracturing, and secondary mineral alteration. The complex hydrologic properties of the volcanic rocks of the NTS and vicinity are best addressed in terms of HGUs (Blankennagel and Weir, 1973; Winograd and Thordarson, 1975). The concept of HSUs that are made up of groups of similar HGUs is also very useful in volcanic terrains because stratigraphic units can differ greatly in hydrologic character both laterally and vertically. The HSUs serve as “layers” in the UGTA regional and CAU-scale hydrostratigraphic framework models.

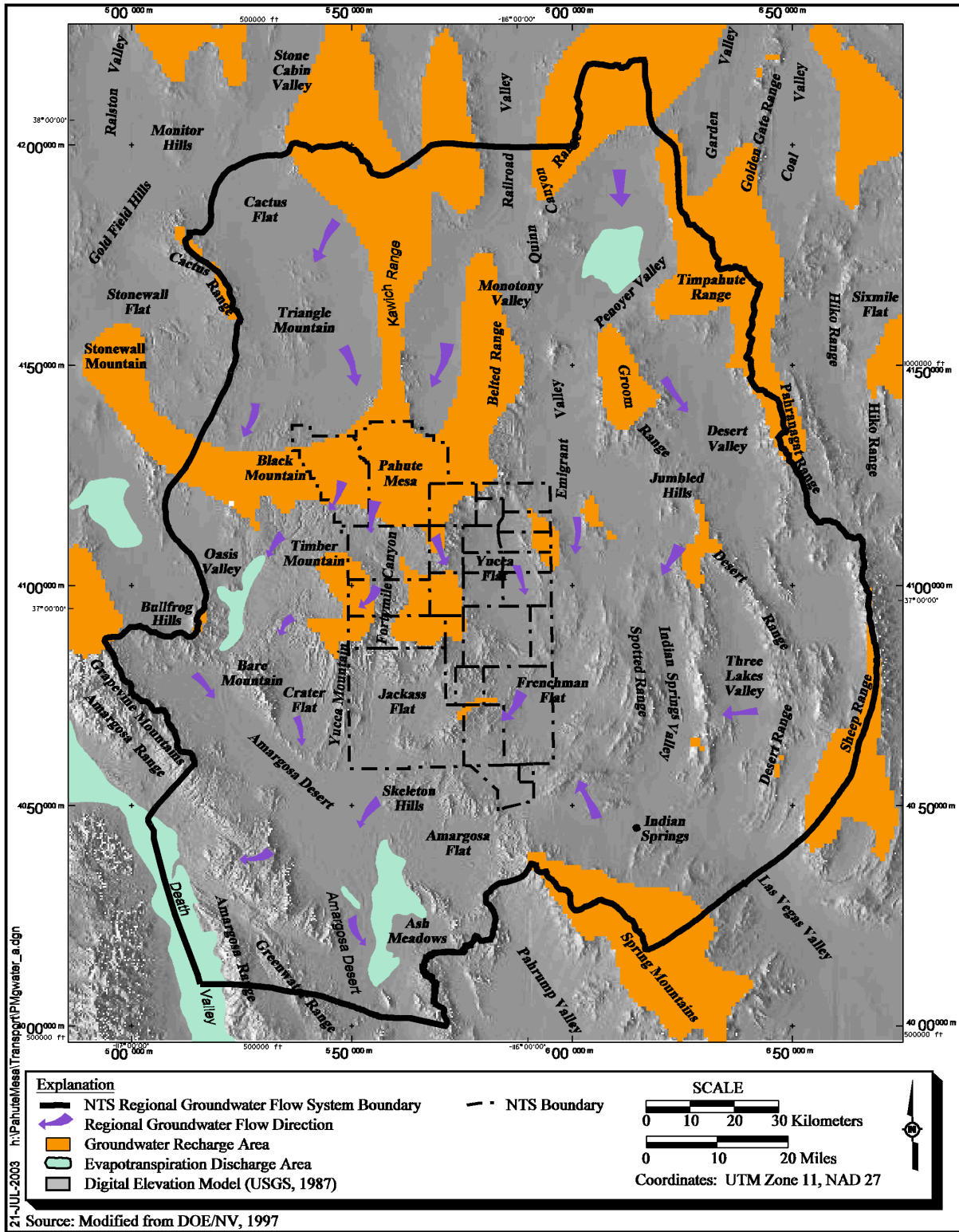


Figure 2-1
Features of the Nevada Test Site Regional Groundwater Flow System

The mineralogical properties of rocks at the NTS are important characteristics that influence the reactivity of the geological media relative to groundwater. These properties include the nature and distribution of reactive mineral phases that are present within rock matrices, as coatings on fracture surfaces, and/or as fine particles derived mechanically from or by incongruent dissolution of the geological media and suspended in groundwater (i.e. colloids). The formation of these minerals is controlled by primary rock-forming processes and secondary alteration and/or weathering processes. The geochemical influence of geological media is evident in the chemical characteristics of groundwater in the vicinity of Pahute Mesa (e.g., Winograd and Thordarson, 1975; Blankennagel and Weir, 1973; Schoff and Moore, 1964) and the varying affinity of different rock-forming, alteration, fracture-coating, or colloidal minerals to interact with dissolved solutes (as will be discussed in [Section 9.0](#), [Section 10.0](#), and [Section 11.0](#)). The mineralogical characteristics of the various HGUs (and HSUs) will influence both the geochemical characteristics of groundwater associated with a given HGU (or HSU) as well as the affinity (expressed as a distribution coefficient or K_d) of that particular HGU (or HSU) for specific dissolved solutes.

The following paragraphs summarize the hydrogeologic framework of the NTS, first addressing HGUs, then describing HSUs.

2.1.1.1 Hydrogeologic Units

All rocks of the NTS and vicinity can be classified as one of eight hydrogeologic units, which include the alluvial aquifer, four volcanic HGUs, an intrusive HGU, and two HGUs that represent the pre-Tertiary sedimentary and metasedimentary rocks ([Table 2-1](#)).

Alluvium

The deposits of alluvium (alluvial aquifer) fill the main basins of the NTS, and generally consist of a loosely consolidated mixture of boulders, gravel, and sand derived from volcanic and Paleozoic sedimentary rocks (Slate et al., 1999).

Alluvial deposits are not extensive in the Pahute Mesa area and have not been subject to detailed mineralogical evaluation. Detailed mineralogical data for alluvial deposits elsewhere at NTS are limited (e.g. Warren et al., 2002).

Volcanic HGUs

The volcanic rocks within the study area can be categorized into four HGUs based on primary lithologic properties, degree of fracturing, and secondary mineral alteration. In general, the altered volcanic rocks (typically zeolitic, or hydrothermally altered near caldera margins) act as confining units, and the unaltered rocks form aquifers. The aquifer units can be further divided into welded-tuff and vitric-tuff aquifers (depending on degree of welding) and lava-flow aquifers. Denser rocks, such as welded ash-flow tuffs and lava flows, tend to fracture more readily; therefore, they have relatively high permeability (Blankennagel and Weir, 1973; Winograd and Thordarson, 1975; Laczniaik et al., 1996; IT, 1996d; Prothro and Drellack, 1997).

Table 2-1
Hydrogeologic Units of the UGTA Regional Model in the PM-OV Model Area
 (Page 1 of 2)

Hydrogeologic Unit	Typical Lithologies	Hydrologic Significance	Mineralogical Significance
Alluvial aquifer (AA) (AA is also an HSU in hydrogeologic models.)	Unconsolidated to partially consolidated gravelly sand, aeolian sand, and colluvium; thin, basalt flows of limited extent	Has characteristics of a highly conductive aquifer, but less so where lenses of clay-rich paleocolluvium or playa deposits are present	Significant mineral phases (include feldspars, silica polymorphs, iron and manganese oxides, mica-group minerals, clay minerals, calcite and/or dolomite, and zeolites) as often fine-grained matrix and clast coatings with high reactive surface areas, intra-clast phases may be isolated from interaction with groundwater
Welded-tuff aquifer (WTA)	Welded ash-flow tuff; vitric to devitrified	Degree of welding greatly affects interstitial porosity (less porosity as degree of welding increases) and permeability (greater fracture permeability as degree of welding increases)	The predominance of significant mineral phases (include feldspars, silica polymorphs, iron and/or manganese oxides, clay minerals, calcite and/or dolomite, zeolites) is determined by stratigraphic unit and secondary alteration and weathering processes, distribution and accessibility (to groundwater) of significant mineral phases strongly influenced by degree of welding and consequent tendency for fracture formation (and development of secondary fracture coatings)
Vitric-tuff aquifer (VTA)	Bedded tuff; ash-fall and reworked tuff; vitric	Constitutes a volumetrically minor HGU; generally does not extend far below the static water level due to tendency of tuffs to become zeolitic (which drastically reduces permeability) under saturated conditions; significant interstitial porosity (20 to 40 percent); generally insignificant fracture permeability	The predominance of significant minerals phases (include glass, feldspars, silica polymorphs, zeolites, calcite, clay minerals, iron and/or manganese oxides) is determined by stratigraphic unit and secondary alteration and weathering processes, typical low accessibility (under saturated conditions) of significant mineral phases dependent on development of secondary permeability associated with fracturing (and accompanying potential for formation of secondary fracture coatings)
Lava-flow aquifer (LFA)	Rhyolite lava flows; includes flow breccias (commonly at base) and pumiceous zones (commonly at top)	Generally a caldera-filling unit; hydrologically complex, wide range of transmissivities, fracture density and interstitial porosity differ with lithologic variations	The predominance of significant mineral phases (include feldspars, silica polymorphs, iron and manganese oxides, glass, zeolites) is determined by 'stratigraphic' unit and secondary alteration and weathering processes, distribution and accessibility (to groundwater) of significant mineral phases strongly influenced by degree of fracturing and/or brecciation (and development of secondary fracture coatings)

Table 2-1
Hydrogeologic Units of the UGTA Regional Model in the PM-OV Model Area
 (Page 2 of 2)

Hydrogeologic Unit	Typical Lithologies	Hydrologic Significance	Mineralogical Significance
Tuff confining unit (TCU)	Zeolitic bedded tuff with interbedded, but less significant, zeolitic, nonwelded to partially welded ash-flow tuff	May be saturated but measured transmissivities are very low; may cause accumulation of perched and/or semi-perched water in overlying units	The predominance of significant mineral phases (include zeolites, iron and/or manganese oxides, calcite) is determined by stratigraphic unit and secondary alteration and weathering processes (i.e. the degree of zeolitization), typical low accessibility (to groundwater) of significant mineral phases dependent on development of secondary permeability associated with fracturing (with potential for formation of secondary fracture coatings)
Intrusive confining unit (ICU)	Granodiorite, quartz monzonite	Relatively impermeable; forms local bulbous stocks, north of Rainier Mesa, Yucca Flat, and scattered elsewhere in the regional model area; may contain perched water	The predominance of significant mineral phases (include clay, calcite, iron and/or manganese oxides) is determined by 'stratigraphic' unit and secondary alteration and weathering processes, typical low accessibility (to groundwater) of significant mineral phases dependent on development of local secondary permeability associated with fracturing (with potential for formation of secondary fracture coatings)
Clastic confining unit (CCU)	Argillite, siltstone, quartzite	Clay-rich rocks are relatively impermeable; more siliceous rocks are fractured, but with fracture porosity generally sealed due to secondary mineralization	The predominance of significant mineral phases (include calcite, clay, iron and/or manganese oxides) is determined by stratigraphic unit and secondary alteration and weathering processes, typical low accessibility (to groundwater) of significant mineral phases dependent on development of secondary permeability associated with fracturing (with potential for formation of secondary fracture coatings)
Carbonate aquifer (CA)	Dolomite, limestone	Transmissivity values vary greatly and are directly dependent on fracture frequency	The predominance of significant mineral phases (include calcite and/or dolomite, iron and/or manganese oxides) is determined by stratigraphic unit and secondary alteration and weathering processes, typical low primary permeability limits groundwater accessibility to fracture and solution cavity coatings

Source: Adapted from IT (1996d); BN (2002); IT (2002i); Warren et al. (2003)

The numerous and diverse volcanic stratigraphic units comprising volcanic HGUs in the Pahute Mesa area have been subject to mineralogical and chemical evaluation, initially as part of the containment program during underground testing and later during characterization activities conducted as part of the UGTA project. Data generated during the analysis of primary and secondary rock matrix mineralogical characteristics have been compiled into a relational database focusing on the Southwestern Nevada Volcanic Field (SWNVF) (Warren et al., 2003). Data generated during the micrographic analysis of fracture coatings on rocks from the Pahute Mesa area have been compiled by IT (2002i).

Pre-Tertiary HGUs

The pre-Tertiary rocks beneath the study area are also categorized as aquifer or confining unit HGUs based on lithology. The silicic clastic rocks (quartzites, siltstones, shales) typically are aquitards or confining units, while the carbonates (limestone and dolomite) tend to be aquifers (Winograd and Thordarson, 1975; Laczniak et al., 1996).

Pre-Tertiary rocks do not comprise significant drill intercepts or surface exposures within the Pahute Mesa area. This relative scarcity is reflected in the amount of mineralogical data that are available for these rock types (Warren et al., 2003).

Intrusives

The intrusive confining unit (ICU) category includes the Mesozoic granite stocks north of Rainier Mesa and Yucca Flat and several intrusives scattered throughout the model area (mostly to the north of the NTS). These rocks are considered to behave as a confining unit. The ICU is the eighth HGU in the regional model area.

Intrusive rocks that have been identified within the Pahute Mesa are limited to the Gold Meadows stock in the northeastern portion of the PM-OV model area. There are no mineralogical data currently available for these rock types (Warren et al., 2003).

2.1.1.2 Hydrostratigraphic Units

Hydrostratigraphic units are groupings of contiguous stratigraphic units that have a particular hydrogeologic character, such as aquifer (unit through which water moves readily) or confining unit (unit that generally is impermeable to water movement). An HSU may contain several HGUs but is defined so that a single general type of HGU dominates (for example, mostly welded-tuff and vitric-tuff aquifers or mostly tuff confining units). Twenty HSUs were defined in the UGTA regional geologic model (IT, 1996d).

Structure played a major role in hydrostratigraphy differentiation within the Pahute Mesa-Timber Mountain caldera complex, which is part of the SWNVF. As defined for the regional model, the Pahute Mesa-Timber Mountain caldera complex includes the nested calderas comprising the Silent Canyon Caldera Complex on Pahute Mesa and the Timber Mountain Caldera. A structural block model covering an area larger than the Pahute Mesa/Timber Mountain caldera

areas was used to differentiate volcanic hydrostratigraphic units within the SWNVF. The volcanic stratigraphy differentiation was made based on the HSUs stratigraphic position within the volcanic rocks, their lithologic properties related to depositional environment, post-depositional alteration, and degree of welding. Outside the caldera complex, structural relationships depicted on the hand-drawn cross sections were used to map volcanic HSUs. The block model was used as guidance in this area. Volcanic units within the caldera complex were mapped as horizontal layers because they have very low dips. The rationale for the block model is presented in Appendix E-3 of the regional geologic model report (IT, 1996d).

In the Pahute Mesa-Timber Mountain caldera complex area, the rocks were divided into six Tertiary volcanic HSUs, one intrusive HSU, and five pre-Tertiary HSUs. The volcanic rocks west of the NTS caldera complex were not subdivided and are represented by a single HSU, VU. The HSUs defined for the regional model that are within the PM-OV model area are listed in [Table 2-2](#). These units are listed in approximate order from surface to basement, although some are laterally rather than vertically contiguous, and not all units are present in all parts of the model area. Because the model is very large, geologically and hydrologically complex, with little subsurface data, various simplification steps had to be employed. The entire model area was divided into four geographical areas based on geology and availability of subsurface data (IT, 1996d; Warren et al., 2000a). A hydrostratigraphic nomenclature scheme was developed separately for each of the four areas. Consequences of this procedure are artificial changes at the boundaries of the four geographic mapping areas. Such changes reflect the different HSU nomenclatures and level of detail for the separate geologic domains. For example, the six volcanic HSUs differentiated within the NTS caldera complex become VU to the west and north.

Additionally, the dominant lithology of some units may change or pinch out laterally (e.g., Lava Flow Aquifer [LFA] close to the source vents, Welded-Tuff Aquifer [WTA] further away, and finally nonwelded Tuff Confining Unit [TCU] or Volcanic Tuff-Aquifer [VTA] at distal edges). Another simplification addresses the caldera roots. For the UGTA regional model, the plutonic or hypabyssal igneous rocks that likely occur at a depth below the calderas are modeled as the lower clastic confining unit (LCCU).

Based on data used in the UGTA regional model (IT, 1996b; and DOE/NV, 1997), hydraulic conductivity ranges for the main aquifers are as summarized in [Table 2-3](#). The mean hydraulic conductivity of the Alluvial Aquifer is less than that of carbonate aquifers, but greater than that of the volcanic aquifers. The ranges extend over orders of magnitude. For example, within the Lower Carbonate Aquifer (LCA), the range of hydraulic conductivity is estimated to be between 0.0008 and 1,570 meters per day (m/d) (0.003 and 5,150 feet per day [ft/d]), representing interstitial and fracture porosity. This large range suggests that at the local scale, large variability in hydraulic conductivity can be expected. At the larger scales, the degree of fracturing controls the heterogeneity. It was also found that a linear trend exists in the logarithm of hydraulic conductivity with increased depth. The data, however, displayed a significant level of scatter.

**Table 2-2
Hydrostratigraphic Units of the Pahute Mesa-Oasis Valley Area Included in the Regional Hydrostratigraphic Framework Model**

Model Layer Number ^a	Hydrostratigraphic Unit (Symbol)	Dominant Hydrogeologic Unit(s) ^b	Stratigraphic Unit Map Symbols ^c	General Description
20	Alluvial Aquifer (AA) (this term is also used to designate a hydrogeologic unit)	AA	Qay, QTc, Qs, Qam, QTa, QTu, Qb, Tgy, Tgc, Tgm, Tgyx, Tt	Consists mainly of alluvium that fills extensional basins such as Gold Flat, Crater Flat, Kawich Valley, and Sarcobatus Flat. Also includes generally older Tertiary gravels, tuffaceous sediments, and nonwelded tuffs (where thin) that partially fill other basins such as Oasis Valley and the moat of the Timber Mountain caldera complex.
19	Timber Mountain Aquifer (TMAQ)	Mostly WTA, minor VTA; TCU within the Tm caldera complex	Tt, Tf, Tm	"The uppermost welded tuffs" in the PM-OV model area. Consists mainly of extra-caldera welded ash-flow tuffs (aquifer-like lithologies). However, the altered intra-caldera equivalent rocks within the Timber Mountain caldera are modeled as confining units.
18	Tuff Cone (TC)	LFA, TCU	Tp, Th (formerly Ta), Tc	Complex three-dimensional distribution of rhyolite lava and zeolitic nonwelded tuff of the Paintbrush Group, Calico Hills Formation or Crater Flat Group. Present in the northern portion of the PM-OV model area beneath most of eastern and central Area 20.
17	Bullfrog Confining Unit (TCB)	TCU	Tcb	Major confining unit differentiated within the NTS caldera complex area. Unit consists of thick intra-caldera, zeolitic, mostly nonwelded tuff of the Bullfrog Formation.
16	Belted Range Aquifer (TBAQ)	LFA and WTA, with lesser TCU	Tub, Tcbs, Tr	Consists of welded ash-flow tuff and lava of the Belted Range Group (Tb) above the Grouse Canyon Tuff (Tbg), but may also include the lava flow lithofacies of the commendite of Split Ridge (Tbgs) and the commendite of Quartet Dome (Tbq) where present. Differentiated within the NTS caldera complex area.
15	Basal Confining Unit (BCU)	TCU	Tn, Tub, To, Tr, Tq	Mostly zeolitized nonwelded tuffs differentiated in the NTS caldera complex area.
14	Basal Aquifer (BAQ)	WTA	To, Tlt, Tqm	Mostly aquifer-like older volcanic rocks. Differentiated within the NTS caldera complex area.
11	Volcanics Undifferentiated (VU)	WTA, TCU, lessor LFA	Potentially includes all Tertiary volcanic units	All Quaternary and Tertiary volcanic units outside the NTS proper and the proximal NTS caldera complex.
8	Upper Clastic Confining Unit (UCCU)	CCU	MDC, MDE	Late Devonian through Mississippian siliciclastic rocks. Present in the eastern third of the PM-OV model area.
7	Lower Carbonate Aquifer (LCA)	CA	Dg through Cc	Cambrian through Devonian mostly limestone and dolomite. Widespread throughout the PM-OV area.
6	Lower Clastic Confining Unit (LCCU)	CCU	Cc, Cz, Czw, Zs, Zj	Late Proterozoic through Early Cambrian siliciclastic rocks. Widespread throughout the PM-OV area.
5	Lower Carbonate Aquifer - Thrust Plate (LCA1)	CA	Dg through Cc	Cambrian through Devonian, mostly limestone and dolomite, rocks that occur in the hanging wall of the Belted Range thrust fault.
4	Lower Clastic Confining Unit - Thrust Plate (LCCU1)	CCU	Cc, Cz, Czw, Zs	Late Proterozoic to Early Cambrian siliciclastic rocks that occur within the hanging wall of the Belted Range thrust fault.
1	Intrusives (I)	ICU	Ti, Kg	Consists of granitic rocks that comprise the Gold Meadows stock along the northeastern margin of the PM-OV area and intrusives greater than 2 kilometers in size elsewhere in the regional model.

^aUGTA regional geologic model (IT, 1996d)

^bSee Table 2-1 for definitions of HGUs.

^cRefer to Slate et al. (1999) and Ferguson et al. (1994) for definitions of stratigraphic unit map symbols.

Source: Adapted from IT, 1996d

Table 2-3
Ranges of Hydraulic Conductivity for the Major Aquifers
of the Nevada Test Site Region

Aquifer	Hydraulic Conductivity	
	Mean (m/d)	Range (m/d)
Alluvial Aquifer	8.44	0.00006-83
Volcanic Aquifers	1.18	0.0003-12
Carbonate Aquifers	31.71	0.0008-1,570

Source: DOE/NV, 1997; and IT, 1996b

Hydraulic property data for rocks relevant to the PM-OV area have been assessed and are presented in the hydrologic data report (Rehfeldt et al., 2003).

2.1.2 Groundwater Occurrence and Movement

A brief description of the NTS regional flow system is provided. Detailed descriptions of the hydrologic components of the Pahute Mesa flow system may be found in the hydrologic data report (Rehfeldt et al., 2003). [Figure 2-1](#) is a map depicting the characteristics of the regional groundwater flow system including the flow system boundary, areas of recharge, and evapotranspiration (ET) areas. The descriptions provided in this section are based on the data gathered during the regional evaluation (IT, 1996c; and DOE/NV, 1997).

2.1.2.1 Groundwater Occurrence

Groundwater occurrence within the NTS regional flow system is discussed based on the water level dataset compiled during the regional evaluation (IT, 1996c; and DOE/NV, 1997).

Within the NTS region, groundwater occurs in alluvial, volcanic, and carbonate materials. Saturated alluvial materials are present in central and southern Yucca Flat, Frenchman Flat, and Jackass Flats on the NTS and in the basins located throughout the flow system. Saturated Tertiary volcanics are present in the western section of the region. The distribution and thickness of alluvial and volcanic aquifers are highly variable throughout the region and are not interpreted to be continuous. In most instances, an alluvial aquifer is confined to a basin by surrounding mountain ranges. In some basins, alluvial aquifers are discontinuous due to structural controls elevating the bottom of the alluvium above the water table. In general, alluvial and volcanic aquifers are considered depositional elements overlying the regional flow system and only influence regional flow in localized areas. The underlying LCA is the principal aquifer of the regional flow system. The LCA forms a nearly continuous aquifer across the region except

where interrupted by calderas, truncated by structural controls, or penetrated by intrusive rocks.

Based on the water level dataset compiled during the regional evaluation (IT, 1996c and DOE/NV, 1997), depths to groundwater beneath the NTS and surrounding region vary greatly. Groundwater depths in the southern NTS range from about 23 meters (m) (75 feet [ft]) beneath upper Fortymile Wash to 157 m (515 ft) beneath Frenchman Lake compared to more than 610 m (2,000 ft) beneath Pahute Mesa in the northern NTS (IT, 1996c and DOE/NV, 1997). Perched groundwater is found locally throughout the NTS and occurs within the tuff confining units and, to some extent, overlying units. In the highlands, springs emerge from perched groundwater lenses. Spring discharge rates are low and this water is used only by wildlife.

2.1.2.2 Groundwater Movement

Within the NTS regional flow system, groundwater movement is controlled by structural and geologic conditions, and the distribution of recharge and discharge locations.

The general direction of groundwater flow in the regional flow system is from north to south and east to southwest (Figure 2-1). The direction of groundwater flow is locally influenced in areas where structural and geologic conditions have controlled the distribution and thickness of the Lower Carbonate Aquifer. In some areas of the regional flow system, groundwater encounters structural and geologic conditions (e.g., as structural highs of the Lower Clastic Confining Unit) that promote an upward flow component. The upward flow component brings water to discharge at the surface in the form of a wet playa or springs. Groundwater flow between basins occurs in the form of subsurface inflow and outflow.

Horizontal hydraulic gradients are very low to the east and west of the NTS. In other areas, the prevailing flow direction and hydraulic gradients may locally be influenced by the structural position of geologic units with significantly lower transmissivity than that of the LCA. If the low transmissive units are structurally oriented so that they are perpendicular to flow, flow might be significantly altered, causing large hydraulic gradients. If these units are not extensive and their structural orientation is parallel to the prevailing flow direction, their effect may be insignificant. Structural uplifts of the LCCU and the distribution of the Upper Clastic Confining Unit have caused several of the observed steep gradients within the flow system. Low-permeability sediments along the Funeral Mountains, such as the Tertiary and Death Valley Section sediments, also cause a steep hydraulic gradient between Amargosa Desert and Death Valley.

Groundwater recharge results from precipitation at higher elevations and infiltration along stream courses and in playas. Recharge rates and distribution are, however, highly uncertain. The recharge model used in the regional flow model was based on the Maxey-Eakin method (Maxey and Eakin, 1949). Several new models have recently been proposed and are described in Section 6.0 of the Pahute Mesa hydrologic data report (Rehfeldt et al., 2003).

Groundwater discharges to the surface in the form of springs and seeps and evapotranspiration in several areas. Major areas of natural groundwater discharge include Oasis Valley, Ash Meadows, Alkali Flat, Death Valley, and Penoyer Valley. Estimates of ET have recently been updated by the USGS for the first four areas listed above (Laczniak et al., 2001). Within the NTS region, artificial discharge occurs as groundwater pumpage from drinking water supply wells (public and domestic), agricultural wells, and industrial wells. Public, domestic, and industrial water supply wells for the NTS produce water from the carbonate, volcanic, and valley-fill aquifers. South of the NTS, private and public water supply wells are completed in the valley-fill aquifer. Discharge from the Pahute Mesa-Oasis Valley area is discussed in [Section 7.0](#) of this document.

An estimate of the regional, steady-state, groundwater budget used in the regional model (DOE/NV, 1997) is provided in [Table 2-4](#). Groundwater pumpage is not included in the budget because the regional flow model was designed to simulate predevelopment conditions. Updated regional recharge and discharge volumes are provided in [Appendix F](#) of the Pahute Mesa hydrologic data report (Rehfeldt et al., 2003).

Table 2-4
Estimated Steady-State Groundwater Budget
for the Nevada Test Site Regional Groundwater Flow System

Recharge	
Recharge from precipitation	177,484 - 289,410 m ³ /d
Subsurface inflow	5,405 - 70,100 m ³ /d
Total Natural Recharge	182,889 - 359,510 m³/d
Discharge	
Surface discharge (ET)	135,340 - 300,700 m ³ /d
Subsurface outflow	850 - 5,100 m ³ /d
Total Natural Discharge	136,190 - 305,800 m³/d

m³/d = Cubic meters per day

2.2 Hydrogeologic Framework of the Pahute Mesa-Oasis Valley Area

A three-dimensional (3-D) hydrostratigraphic framework model and alternatives have been built for the PM-OV area. The processes of HSU model development and screening are summarized along with the models retained for use in the CAU groundwater flow and transport model. The details may be found in the HSU model report (BN, 2002).

2.2.1 HSU Model Development

The approach used to develop the base HSU model and alternatives is described in this section. The HSU model area coincides with the PM-OV area described in [Section 1.0](#) ([Figure 1-2](#)).

The PM-OV area HSU model(s) were constructed using EarthVision® (Version 5.1, by Dynamic Graphics), a 3-D geologic model building and visualization software package. Input data included drill-hole data, digital elevation model data, and outcrop and fault data from surface geologic map. Where deemed necessary, the data were supplemented with interpretations in the form of “pseudo drill holes,” cross sections, and structure-contour maps.

A preliminary base HSU model was constructed based on the conceptual model of the NTS hydrologic system described by Winograd and Thordarson (1975). Further developments made by Lacznik et al. (1996), and IT (1996d), were also used in the UGTA base HSU model.

To capture the uncertainty associated with the HSU framework, a number of alternative interpretations were considered in addition to the base HSU model (BN, 2002). These alternatives were then evaluated and organized into four groups as follows:

- Group A - Recommended changes to the preliminary base model: Alternatives of this group were used to improve the base HSU model.
- Group B - Viable alternative scenarios: These were further developed as alternative HSU models.
- Group C - Proposed Alternatives to address during the Hydrologic Modeling Phase: It was decided that these alternatives would be better addressed during the hydrologic modeling phase.
- Group D - Suggested alternatives that were deemed to be of low priority or not necessary to model

The main criterion for selecting alternatives for full development was the potential impact of the alternative interpretation on groundwater flow and the transport of contaminants in groundwater.

Following this evaluation of the alternatives, the base HSU model was updated using the Group A alternatives, and the alternatives placed under Group B were further developed into EarthVision® models. These alternatives are listed below in descending order of inferred potential impact (BN, 2002):

- Alternative #1 - Silent Canyon Caldera Complex (SCCC): Develop structurally uncoupled alternative model for the Silent Canyon caldera complex.
- Alternative #2 - Area between the Timber Mountain Caldera and the Silent Canyon Caldera Complex: Explore variations in the interpretation of the basement “ridge” (gravity high) between Timber Mountain and Silent Canyon caldera complexes.
- Alternative #3 - Thirsty Canyon Lineament: Explore variations of the Thirsty Canyon lineament.

- Alternative #4 - Depth to the Pre-Tertiary Surface: Vary depth to basement/pre-Tertiary surface.
- Alternative #5 - Contiguous Sheet of LCA3 Rocks: Change extent and thickness of LCA3 and LCCU1 in the southeastern portion of model.
- Alternative #6 - Deeply Rooted Belted Range Thrust Fault: Develop a scenario with a deeply rooted Belted Range Thrust (BRT) fault.

For a detailed description of the alternative HSU models, see report titled: *Hydrostratigraphic Model for the Groundwater Flow and Contaminant Transport Model of Corrective Action Units 101 and 102: Central and Western Pahute Mesa, Nye County, Nevada* (BN, 2002).

2.2.2 HSU Alternative Model Screening

The development of groundwater water flow and contaminant transport models for all alternative HSU models would require considerable resources. Therefore, a screening process was developed to evaluate the impact of each alternative on contaminant transport, using simplified transport models (see Section A.3.0 of Appendix A of the hydrologic data report [Rehfeldt et al., 2003]).

These simplified models were developed using Finite-Element Heat Mass Transfer (FEHM) Computer Code (Zyvoloski et al., 1997a and b). The “particle-tracking” capability of FEHM was used to approximate the transport of radionuclides in groundwater using the base HSU model and the six alternatives.

Except for the SCCC alternative (Alternative 1), the results of the “particle-tracking” analyses for the other five alternatives were statistically similar to those of the base HSU model. The results of the SCCC alternative produced results that were clearly different from those produced by the base HSU model (Section A.3.0 of Appendix A of the hydrologic data report [Rehfeldt et al., 2003]). Therefore, only the base HSU model and the SCCC alternative will be used to develop alternative CAU models. The other five HSU model alternatives have been eliminated for further consideration. Details of the HSU model screening process and results are presented in Section A.3.0 of Appendix A of the hydrologic data report (Rehfeldt et al, 2003). Summary descriptions of the base HSU and the SCCC alternative models follow.

2.2.3 Base HSU Model

The structural features, hydrogeologic units, and hydrostratigraphic units of the base HSU model developed for the PM-OV area are described in this section. A 3-D view of this model is shown in [Figure 2-2](#).

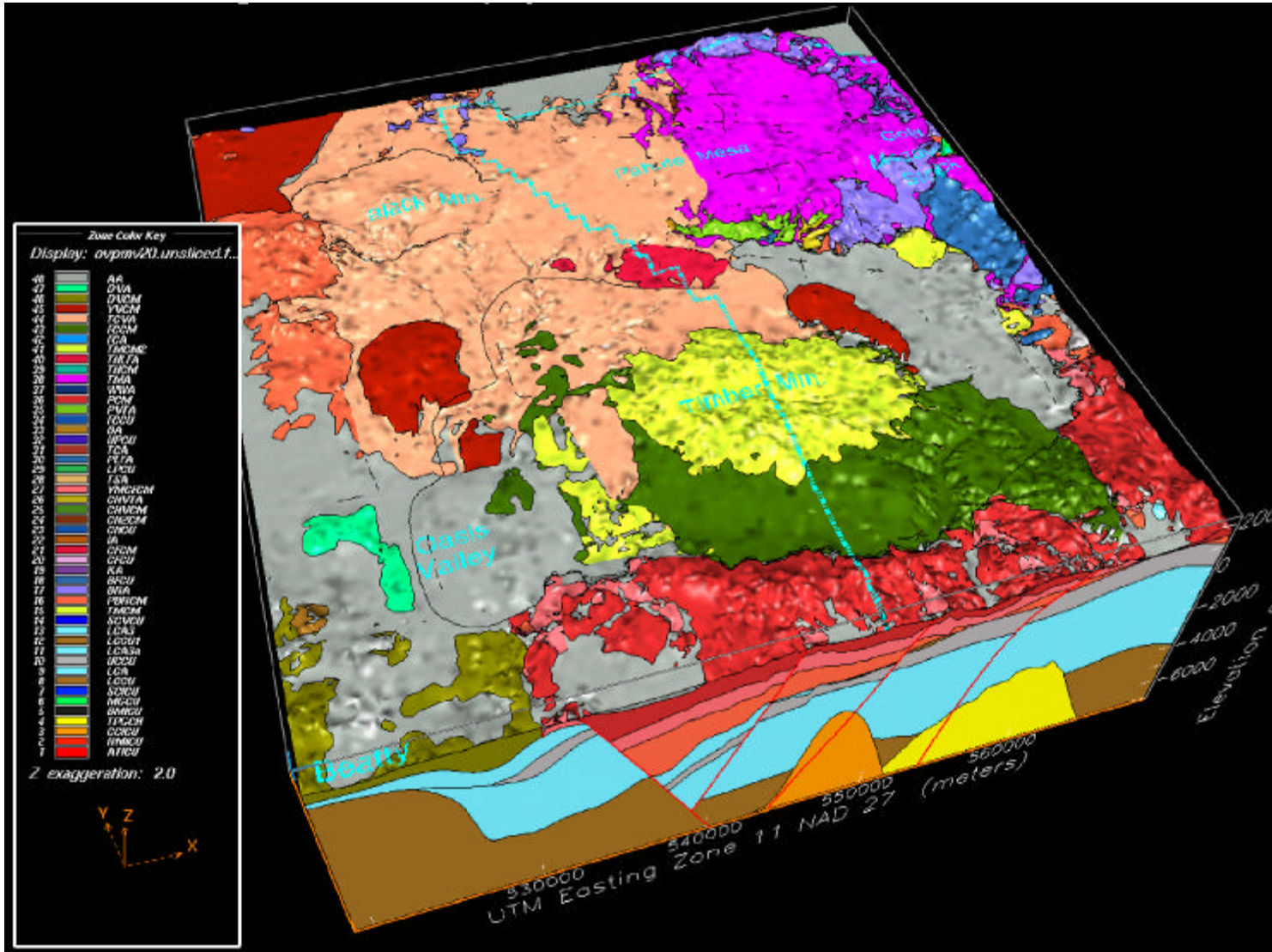


Figure 2-2
 Three-Dimensional View of the Base Hydrostratigraphic Model
 of the Pahute Mesa-Oasis Valley Area (BN, 2002)

2.2.3.1 Structural Features

Geologic structural features are an important part of the hydrologic framework of the groundwater flow system of the PM-OV area. They define the geometric configuration of the flow domain, including the distribution, thickness, and orientation of rock units. The depositional patterns of the geologic units occurring in the area were strongly influenced by syn-volcanic structures, including caldera faults and some normal faults. Faulting, for example, may result in juxtaposition of units with different hydrologic properties. Structures themselves may influence flow patterns by acting as conduits for flow or barriers to flow (BN, 2002).

The structure of the base HSU model is based on the conceptual model developed by Ferguson et al. (1994) and Warren (1994a and b). Ferguson et al. (1994) developed a detailed structural model of the SCCC using seismic refraction, gravity, and drill hole data. Warren (1994a and b) extended the work of Ferguson et al. (1994) to the area surrounding the SCCC. The work of Warren (1994a and b) was later published by Warren et al. (2000a and b).

The base HSU model includes a total of 47 structural elements which are either faults or calderas. Only faults that were considered to be significant were included in the model. These include the larger ones and the ones that seem to form significant structural boundaries. Six calderas have been identified in the PM-OV model area, two of which are buried. These calderas reflect a variety of geometries and collapse processes. Caldera-collapse processes include the “piston,” down-sag, trap-door, and piecemeal collapse. Some calderas seem to have collapsed along pre-existing linear faults, resulting in polygonal boundaries (Kane et al., 1981; Ferguson et al., 1994). Of particular interest is the SCCC, an important and uncertain geologic feature of the PM-OV area. As stated previously, an alternative scenario was developed to evaluate the effect of caldera shape (see following subsection).

In the base HSU model, the SCCC includes two calderas: the Grouse Canyon and Area 20 calderas. As described by BN (2002), *“the caldera-forming faults coincide with north-south striking basin-and-range faults mapped at the surface and with inferred, buried, west-northwest-trending structural zones, which effectively segment the SCCC into numerous fault-bounded sub-basins having the general configuration of half grabens. Thus, the base HSU model incorporates many faults with episodic movements that were synchronous with and associated with caldera formation. Consequently, many of the faults in the base HSU model have significant influence on the distribution of volcanic units.”* The base HSU model for the SCCC area also includes 20 faults and structural zones in addition to the caldera-forming faults. Thirteen of these 20 structural features are basin-and-range type faults mapped at the surface.

2.2.3.2 Hydrogeologic Units

The hydrogeologic framework for PM-OV model established by Blankennagel and Weir (1973) provided the foundation for most subsequent hydrogeologic studies in the area. As described in [Section 2.1](#), the rocks of the NTS have been

classified for hydrologic modeling using a two-level classification scheme in which HGUs are grouped to form HSUs (IT, 1996d). New units and additional detail have been added to the basic framework definition, but the systems developed by these early workers remain the best way to understand the groundwater of the NTS region.

The HGU scheme used for CAU-scale modeling, including the PM-OV framework model, included nine HGUs; the initial eight used in the regional model mentioned in [Section 2.1](#), and an additional ICU. The nomenclature for the intrusive was also modified to Granite Confining Unit (GCU) ([Table 2-5](#)).

**Table 2-5
Additional and Modified Hydrogeologic Units of the PM-OV Model**

Hydrogeologic Unit	Typical Lithologies	Hydrologic Significance
Intra-caldera intrusive confining unit (IICU)	Highly altered, highly injected/intruded country rock and granitic material	Assumed to be impermeable. Conceptually underlies each of the SWNVF calderas and Calico Hills. Developed for this study to designate basement beneath calderas as different from basement outside calderas.
Granite confining unit (GCU)	Granodiorite, quartz monzonite	Relatively impermeable; forms local bulbous stocks, north of Rainier Mesa and Yucca Flat; may contain perched water.

Source: Adapted from BN, 2002

The intra-caldera intrusive confining unit (IICU) was initially defined for the PM-OV hydrostratigraphic framework model (BN, 2002). Conceptually, an IICU underlies each of the SWNVF calderas, and one other IICU is depicted as the Calico Hills intrusive. Although modeled as single intrusive masses, the exact nature of the rocks beneath the calderas is unknown, as no drill holes penetrate these rocks. It is assumed that these bodies may range from highly altered, highly injected/intruded country rock to granite. The IICUs are considered to behave as confining units due to low primary porosity and low permeability where measured (such as in the granite of Climax stock [Walker, 1962]). Most fractures are probably filled with secondary minerals and/or are poorly connected. The Climax stock in extreme northern Yucca Flat (Houser et al., 1961; Walker, 1962; Maldonado, 1977) and the Gold Meadows stock in the extreme eastern part of the PM-OV model area (Snyder, 1977) may serve as analogs to the IICUs.

Intra-Caldera Intrusive Confining Unit (IICU)

This units includes highly altered, highly injected/intruded country rock and granitic material. It is assumed to be impermeable. Conceptually, it underlies each of the SWNVF calderas and Calico Hills. It was developed for this study to designate basement beneath calderas as different from basement outside calderas.

Granite Confining Unit (GCU)

This unit includes granodiorite and quartz monzonite, and is relatively impermeable. It forms local bulbous stocks north of Rainier Mesa and Yucca Flat. It may contain perched water.

2.2.3.3 Hydrostratigraphic Units

Brief descriptions of all the HSUs used to construct the PM-OV model are provided in [Table A.1-1 \(Appendix A\)](#). They are listed in approximate order from surface to basement, although some are laterally rather than vertically contiguous, and not all units are present in all parts of the model area.

[Table 2-6](#) shows the correlation of PM-OV HSUs with HSUs from earlier hydrostratigraphic models for this region. [Plate 1](#) is a map showing a plan view of the surficial hydrostratigraphy for the PM-OV model area. A northeast-southwest hydrostratigraphic cross section, along the general flow direction, is provided in [Plate 2](#). A west-east hydrostratigraphic cross section through Pahute Mesa (perpendicular to the general groundwater flow direction) is presented in [Plate 3](#). Both of these cross sections are from the PM-OV 3-D framework documentation package (BN, 2002), where additional cross sections and detailed information regarding this CAU-scale model can be found.

As can be seen from the information presented in this section, the PM-OV hydrostratigraphic framework model (BN, 2002) includes considerable structural detail and stratigraphic enhancement over the regional geologic model (IT, 1996d). The total number of HSUs increased from 20 to 46; most of the increase affected the Tertiary volcanic section. The six Tertiary volcanic HSUs in the Pahute Mesa and Timber Mountain caldera complex and the single volcanics undifferentiated outside the caldera complex (of the regional model) were subdivided into 40 HSUs for the PM-OV model. Except for geometry details, the five pre-Tertiary HSUs remain as initially defined.

The concept of a “composite unit” was first used while developing the PM-OV model. Composite units comprise a mixture of hydraulically variable units. A good example is the Calico Hills Zeolitized Composite Unit (CHZCM). The CHZCM consists of lava-flow aquifers embedded within a zeolitic bedded tuff. The relative distribution of each HGU component of a composite unit is uncertain either due to natural variation or due to lack of definitive subsurface data.

2.2.3.4 Mineralogical Data in the PM-OV Model Area

The nature and distribution of mineral phases in groundwater systems can exert a significant influence on water composition (e.g., major ion chemistry, pH) and the mobility of solutes of potential concern. Potentially reactive minerals occur in three distinct settings within the PM-OV model area. These include minerals within rock matrices, minerals occurring as coatings on fracture surfaces, and fine-grained mineral particles occurring as colloids suspended in groundwater. Matrix minerals are formed as a result of primary rock-forming processes but are also subject to modification in response to subsequent alteration processes (such as hydrothermal alteration associated with caldera formation). Fracture-coating minerals tend to occur along transmissive fracture or joint surfaces in competent rock types (e.g., welded tuff) as a result of interaction with hydrothermal or groundwater solutions (Benedict et al., 2001). Available data (Brachmann and

Table 2-6
Correlation of Hydrostratigraphic Units of the Pahute Mesa-Oasis Valley Model and Earlier Models^a
 (Page 1 of 2)

Layer No. ^b	Hydrostratigraphic Unit	Symbol This Report ^b	Correlation with PM-300 Model ^c	Correlation with UGTA Phase I ^d	Correlation with YMP ^e (Lithostratigraphic Units)
46	Alluvial aquifer	AA	TMA	AA	QAL, TPAL, TLIM
45	Younger volcanic composite unit	YVCM	NP ^f	VU	B
44	Thirsty Canyon volcanics aquifer	TCVA	TMA	TMA, VU	NP
43	Detached volcanic aquifer	DVA	NP	VU	
42	Detached volcanics composite unit	DVCM			
41	Fortymile Canyon composite unit	FCCM	TMA	TMA, VA	NP
40	Fortymile Canyon aquifer	FCA	NP	VU	
39	Timber Mountain composite unit	TMCM	TMCU	TMA	
38	Tannenbaum Hill lava-flow aquifer	THLFA	TMA		
37	Tannenbaum Hill composite unit	THCM			
36	Timber Mountain aquifer	TMA		TMA, VA	UVA
35	Subcaldera volcanic confining unit	SCVCU	PreT	BCU	NR
34	Fluorspar Canyon confining unit	FCCU	TMA	TMA, VA	NP
33	Windy Wash aquifer	WWA	WWA	TMA	
32	Paintbrush composite unit	PCM	NP	TMA, VA, TC	UVA
31	Paintbrush vitric-tuff aquifer	PVTA	PVTA	TMA, TC, VA	
30	Benham aquifer	BA	BA	TC	NP
29	Upper Paintbrush confining unit	UPCU	UPCU		NR
28	Tiva Canyon aquifer	TCA	TCA	TMA, TC, VA	UVA
27	Paintbrush lava-flow aquifer	PLFA	PLFA	TC	NP
26	Lower Paintbrush confining unit	LPCU	LPCU	TC	NR
25	Topopah Spring aquifer	TSA	TSA	TC, VA	UVA
24	Yucca Mt. Crater Flat composite unit	YMCFCM	NP	VA, VU	UVCU, MVA
23	Calico Hills vitric-tuff aquifer	CHVTA	CHVTA	TC	MVA
22	Calico Hills vitric composite unit	CHVCM	CHVCM		
21	Calico Hills zeolitic composite unit	CHZCM	CHZCM		
20	Calico Hills confining unit	CHCU	CHCU	TC	NR

Table 2-6
Correlation of Hydrostratigraphic Units of the Pahute Mesa-Oasis Valley Model and Earlier Models^a
 (Page 2 of 2)

Layer No. ^b	Hydrostratigraphic Unit	Symbol This Report ^b	Correlation with PM-300 Model ^c	Correlation with UGTA Phase I ^d	Correlation with YMP ^e (Lithostratigraphic Units)
19	Inlet aquifer	IA	IA	TC, VA	NP
18	Crater Flat composite unit	CFCM	CFCM	TC, VU	MVA
17	Crater Flat confining unit	CFCU	CFCU		NR
16	Kersarge aquifer	KA	KA	TC	NP
15	Bullfrog confining unit	BFCU	BFCU	TCB	
14	Belted Range aquifer	BRA	BRA	TBA	NR
13	Pre-Belted Range composite unit	PBRCM	PBRCM	BAQ, BCU	MVCU, LVA, LVCU, LCU
12	Black Mountain intrusive confining unit	BMICU	NP	VU	NP
11	Ammonia Tanks intrusive confining unit	ATICU	TMCM	TMA	
10	Rainier Mesa intrusive confining unit	RMICU			
9	Claim Canyon intrusive confining unit	CCICU	NP	VA	NR
8	Calico Hills intrusive confining unit	CHICU		I	NP
7	Silent Canyon intrusive confining unit	SCICU	PreT	LCCU	
6	Mesozoic granite confining unit	MGCU		I	
5	Lower carbonate aquifer–thrust plate	LCA3	NP	LCA3	NR
4	Lower clastic confining unit–thrust plate	LCCU1	PreT	LCCU1	
3	Upper clastic confining unit	UCCU	NP	UCCU	ECU
2	Lower carbonate aquifer	LCA	PreT	LCA	LCA
1	Lower clastic confining unit	LCCU		LCCU	QCU

^aIf correlative to more than one HSU, all HSUs are listed.

^bSee BN (2002) and [Table A.1-1](#) of this report for explanation of PM-OV model HSU nomenclature.

^cSee BN (2002) for explanation of PM-300 HSU nomenclature.

^dSee IT (1996d) for explanation of the UGTA Phase I HSU nomenclature.

^eSee CRWMS M&O (1997 and 2000b) for explanation of the YMP lithostratigraphic unit nomenclature.

^fNot present

^gNot recognized as a separate HSU

Kersting, 2002) suggest that colloids in NTS groundwater are indicative of the host geologic media.

The availability of mineralogical data for the PM-OV model area is summarized in [Table 2-7](#). Matrix mineralogy data generated by X-ray diffraction (XRD) from more than 1,300 samples from stratigraphic units comprising the PM-OV HSUs are contained in Warren et al. (2003). XRD data exist for 19 of the HSUs within the PM-OV model. As discussed in [Section 9.0](#), matrix mineralogical data support the application of the LLNL mechanistic model (Zavarin et al., 2002) to estimate K_d values for HSUs where correlative laboratory derived data are unavailable. Fracture-coating mineralogy characterization data generated using the scanning electron microscope (SEM) from more than 80 samples are compiled in IT (2002i). Fracture-coating characterization has been conducted in support of the geochemical evaluation of groundwater flow paths in the PM-OV flow system (Rose et al. 2003; Thomas et al., 2002) and radionuclide transport experiments in fractured volcanic rocks from Pahute Mesa (Reimus et al., 2002a). These data consist of fracture coating mineral characteristics on naturally occurring fractures in 14 of the HSUs within the PM-OV model. As discussed in [Section 10.0](#), fracture-coating mineral data support the prediction (Wolfsberg et al., 2002; Zavarin and Bruton, 2002a and b) of solute retardation during groundwater fracture flow. Colloid data have been collected from wells in hydraulic communication with 16 of the different HSUs present in the PM-OV model area. Since many of these samples are composite samples or samples collected from wells with screened intervals that cross HSU boundaries, the data generated are considered to represent composite or multiple HSUs. Mineralogical data (Brachmann and Kersting, 2002) for colloids in NTS groundwater are available for samples from two individual wells (ER-20-5#1 and ER-20-5#3).

2.2.4 Silent Canyon Caldera Complex HSU Model

The alternative SCCC model is based on the same HGUs as the base HSU model. Despite the considerable differences in basic concepts such as style of caldera formation and number and activity of faults, as well as in scale and level of detail, both models honor the available drill hole and outcrop data. Differences between the two models relate to the structural model used and the categorizing of HGUs into HSUs. Descriptions of these features are summarized from the HSU model report (BN, 2002).

2.2.4.1 Structure

The alternative structural model of the SCCC is more simplified than the base HSU model. This structural model is based on previous models of calderas of the Pahute Mesa region developed by Noble et al. (1968) and Orkild et al. (1969), and analogies with other calderas of the world.

The SCCC HSU model includes an elliptical ring-fracture fault system elongated to the north-northeast ([Figure 2-3](#)). Major structural differences with the base

Table 2-7
Mineralogical Analyses within PM-OV Model Area (by HSU)
 (Page 1 of 2)

HSU #	HSU Name	HGUs	Number of Available Mineralogical Analyses (XRD, from Warren et al., 2003) ^a	Number of Available Fracture-Coating Mineralogical Analyses (from IT, 2002i) ^b	Number of Available Groundwater Colloid Analyses (from IT, 2002j) ^c
1	LCCU	CCU	0	0	0
2	LCA	CA	0	0	0
3	UCCU	CCU/SCU	0	0	0
4	LCCU1	CCU/SCU	0	0	0
5	LCA3	CA	3	0	0
6	MGCU	GCU	0	0	0
7-12	SCICU, CHICU, CCICU, RMICU, ATICU, BMICU	IICU	0	0	0
13	PBRM	TCU, WTA, LFA	173	9	3
14	BRA	LFA, WTA, TCU, VTA,	0	2	3
15	BFCU	TCU	106	0	3
16	KA	LFA, TCU	0	0	0
17	CFCU	TCU, LFA, VTA	0	0	0
18	CFCM	Mostly LFA, some TCU	0	2	2
19	IA	LA	0	0	0
20	CHCU	TCU, LFA	144	1	4
21	CHZCM	LFA, TCU, VTA	39	1	3 ^d
22	CHVCM	VTA, LFA, TCU	98	0	4
23	CHVTA	VTA, TCU	103	0	0
24	YMCFCM	TCU, LFA, WTA, unk	275	0	4
25	TSA	WTA, TCU, unk	2	13	8 ^d
26	LPCU	TCU, unk	64	0	2
27	PLFA	LFA, WTA, TCU, VTA, unk	7	0	0
28	TCA	WTA	4	3	4
29	UPCU	TCU, VTA, LFA, unk	51	0	4
30	BA	LFA, TCU, unk	3	2	4
31	PVTA	VTA, WTA, LFA, TCU, unk	51	1	0
32	PCM	WTA, VTA, TCU, LFA, unk, AA	145	0	0
33	WWA	LFA, unk	0	0	0
34	FCCU	TCU	4	0	0
35	SCVCU	NA	0	0	0
36	TMA	WTA, VTA, unk, TCU, LFA, ICU, AA	30	13	0
37	THCM	TCU, WTA, VTA	7	0	0
38	THLFA	LFA, AA	0	0	0
39	TMCM	TCU, WTA, VTA, LFA, AA	0	26	8
40	FCA	NA	0	0	0
41	FCCM	LFA, TCU, WTA, VTA, AA	0	5	7
42	DVA	NA	0	0	0
43	DVCM	TCU, WTA	0	0	0

Table 2-7
Mineralogical Analyses within PM-OV Model Area (by HSU)
 (Page 2 of 2)

HSU #	HSU Name	HGUs	Number of Available Mineralogical Analyses (XRD, from Warren et al., 2003) ^a	Number of Available Fracture-Coating Mineralogical Analyses (from IT, 2002i) ^b	Number of Available Groundwater Colloid Analyses (from IT, 2002j) ^c
44	TCVA	WTA, VTA, LFA, TCU, AA	0	2	1
45	YVCM	LFA, WTA, AA	0	0	0
46	AA	AA, VTA, WTA, LFA, TCU	0	1	0

^aAdditional X-ray diffraction (XRD) data exist and are pending integration into database

^bAdditional scanning electron microscope (SEM) and XRD data exist and are pending integration into the database

^cColloid size fraction data are assigned to HSU based on completion specifics of wells sampled where known, in the event of multiple or composite completions samples are assigned to multiple HSUs, total number of colloid samples = 48

^dMineralogical characterization of one colloid sample available for this HSU from Kersting and Reimus (2003)

HSU model include the locations of caldera-forming faults and the number depth of the faults considered.

The locations of the SCCC margins are different on the eastern and western sides of the complex (Figure 2-3). In the alternative HSU model, these two margins are located 1 to 3 km farther west and east than in the base HSU model.

The number of faults is different. The SCCC HSU model includes the single caldera ring-fracture system, and only 11 of the basin-and-range faults mapped at the surface. Another difference is that the faults in the SCCC HSU model end at shallower depths than in the base HSU model.

2.2.4.2 Hydrostratigraphy

Hydrostratigraphic differences between the two models of the SCCC area are the number of HSUs, their definition, and their distribution (BN, 2002). Whereas in the base HSU model, the SCCC area includes 25 HSUs; the alternative model includes only 12 in the SCCC (Table 2-8). Six post-Paintbrush HSUs are lumped together in the alternative model. This simplification may not be important because these units are mostly unsaturated, but other simplifications such as the lumping of the four Calico Hills HSUs may be important (BN, 2002).

Significant differences also exist in the configuration of the HSU surfaces. The surfaces of the HSUs are less rugged in the SCCC model than in the base HSU model. The surfaces of the HSUs in the base HSU model are much more rugged than the surfaces in the alternative HSU model. Within the SCCC area, the upper surfaces of HSUs in the alternative HSU model are generally bowl-shaped, and dip more gently than those in the base HSU (Figure 2-4). Upper surfaces of HSUs in the alternative HSU model are also higher along the down-thrown sides of faults, and lower along the up-thrown sides (BN, 2002).

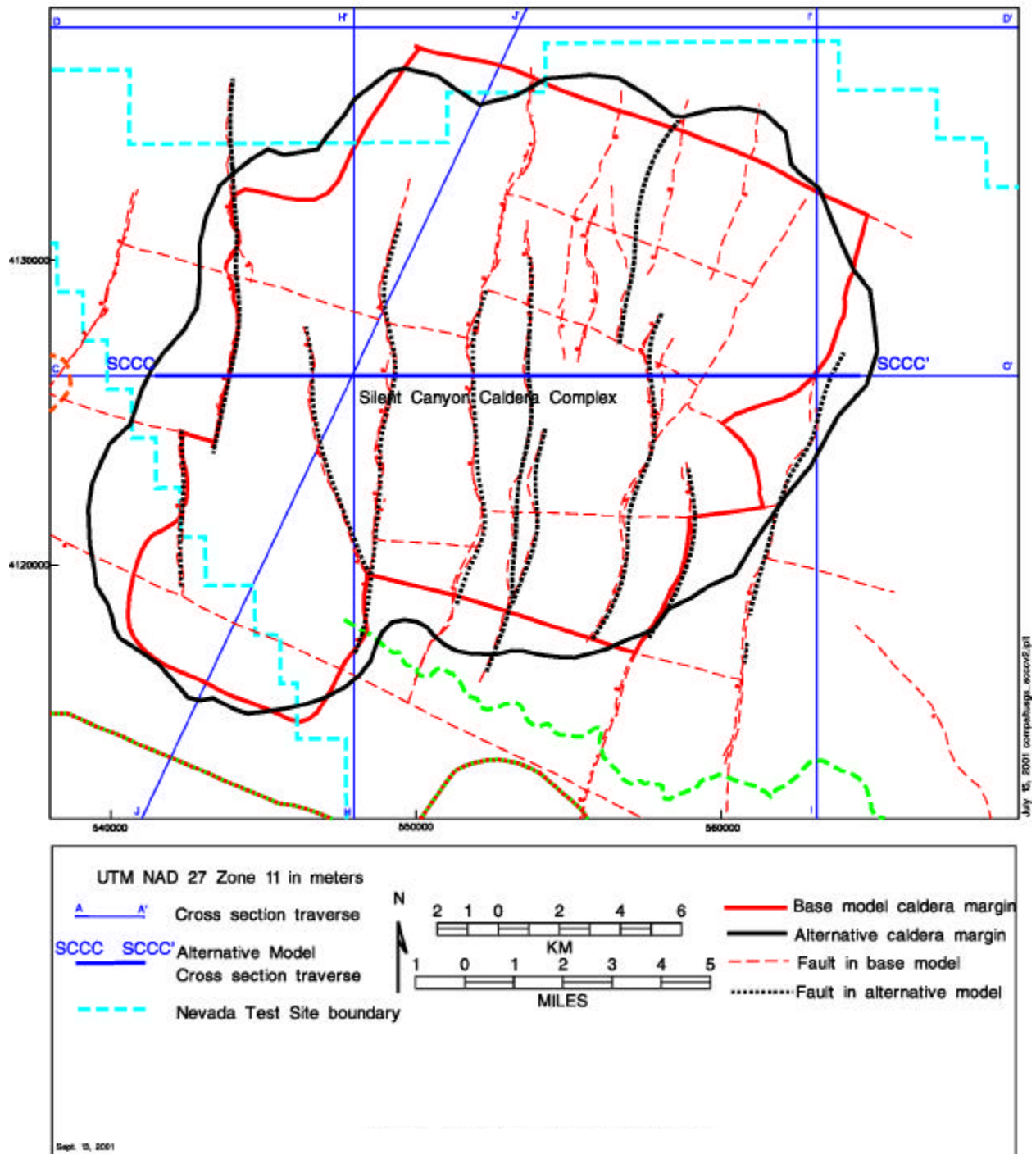


Figure 2-3
Comparison of Silent Canyon Caldera Margins:
Base Model and SCCC Alternative (BN, 2002)

**Table 2-8
Correlation of Hydrostratigraphic Units Between
the Silent Canyon Caldera Complex Model and the Base HSU Model**

UGTA Base Model HSUs	Alternative SCCC Model HSUs
Thirsty Canyon volcanic aquifer	Silent Canyon Timber Mountain composite unit
Tannenbaum Hill lava-flow aquifer	
Tannenbaum Hill composite unit	
Timber Mountain aquifer	
Fluorspar Canyon confining unit	
Windy Wash aquifer	
Paintbrush vitric-tuff aquifer	
Benham aquifer	Silent Canyon Benham aquifer
Upper Paintbrush confining unit	
Tiva Canyon aquifer	Silent Canyon Tiva Canyon aquifer
Paintbrush lava-flow aquifer	Silent Canyon Lower Paintbrush confining unit
Lower Paintbrush confining unit	
Topopah Spring aquifer	Silent Canyon Topopah Spring aquifer
Calico Hills vitric-tuff aquifer	Silent Canyon Calico Hills composite unit
Calico Hills vitric composite unit	
Calico Hills zeolitic composite unit	
Calico Hills confining unit	
Inlet aquifer	Silent Canyon Inlet aquifer
Crater Flat composite unit	Silent Canyon Crater Flat composite unit
Crater Flat confining unit	
Kearsarge aquifer	
Bullfrog confining unit	Silent Canyon Bullfrog confining unit
Belted Range aquifer	Silent Canyon Belted Range aquifer
Pre-Belted Range composite unit	Silent Canyon Pre-Belted Range composite unit
Silent Canyon intrusive confining unit	Silent Canyon intrusive confining unit

Source: BN, 2002

Note: The HSU names used in the alternative model were modified by adding the prefix "Silent Canyon" for differentiation purposes.

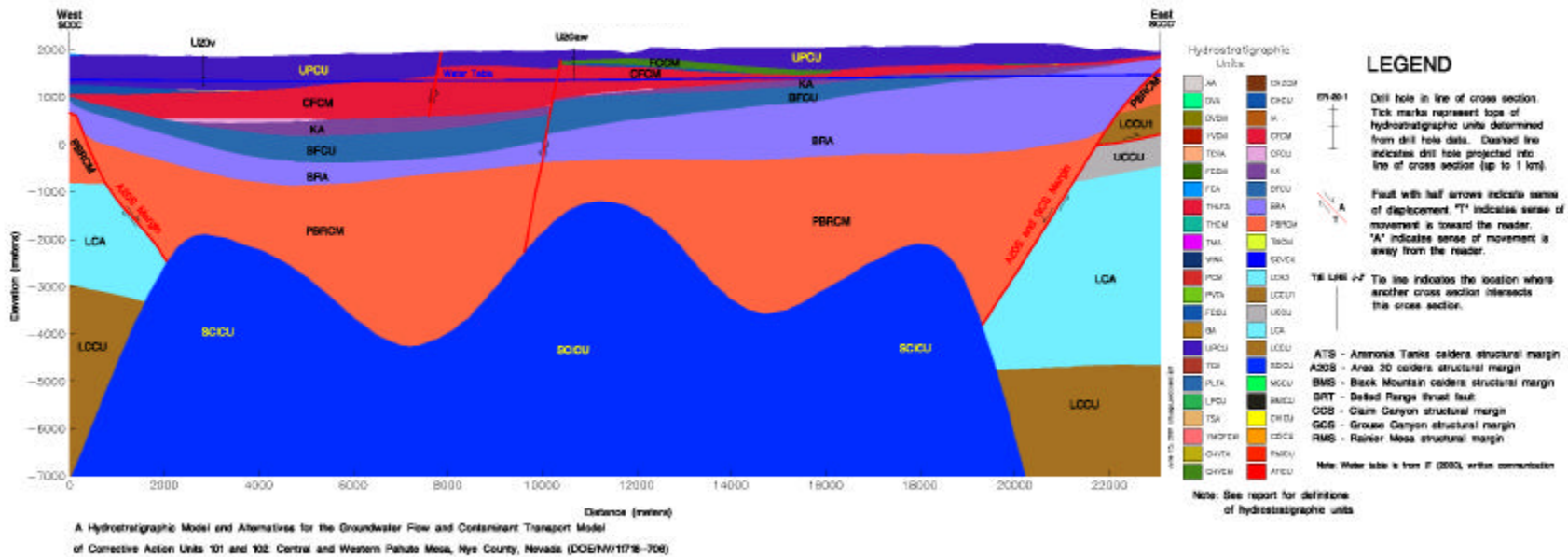


Figure 2-4
 Typical West - East Cross-Section through the Silent Canyon Caldera for the SCCC Model (BN, 2002)

The differences in the locations of caldera margins and in structure result in differences in HSU thicknesses. Generally, the thicknesses of HSUs located within the SCCC vary to a greater degree in the base HSU model. In comparison, in the SCCC model, the HSUs are generally lens-shaped. These lenses are thick in the middle and thin out towards the margins of the SCCC (BN, 2002).

In the alternative HSU model, the HSUs were defined using the drill hole stratigraphy data, without considering lithologic differences present. This led to some differences in the definition of the HSUs. For example, the distribution and composition of the Topopah Springs Aquifer (TSA) HSU are different in the two models. In the base HSU model, the TSA includes only the welded ash-flow tuff of the Topopah Spring Tuff, whereas the TSA in the alternative HSU model also includes Topopah Spring vitric and zeolitic, nonwelded, and some bedded tuff.

The hydrogeologic importance of the Calico Hills Formation in the SCCC area is recognized in both the base and SCCC models. It is, however, handled differently in the two models. In the base HSU model, the Calico Hills Formation is subdivided into four HSUs based on differences in lithologic composition and alteration effects, whereas it is treated as a single composite unit in the SCCC alternative model (Table 2-8). A more detailed discussion of the SCCC alternative model may be found in the HSU model report (BN, 2002).

2.3 Groundwater Chemistry

Geochemical data provide a corroborative, yet independent (of hydraulic data), means to verify groundwater flow paths, apparent travel times, and water-rock interaction processes. Groundwater chemistry data are also an important consideration in the determination of K_d values (see discussion in sections 9.0 and 10.0 of this document). Viable groundwater source areas, flow paths and apparent travel times have been identified using geochemical data (Rose et al., 2003) for the PM-OV flow system. Two chemically and isotopically distinct groundwater masses were identified in association with a known water level discontinuity near the Purse Fault, in western Pahute Mesa. These distinct water masses appear to mix in the region down gradient from Pahute Mesa. Within the discharge area of Oasis Valley, further changes in groundwater chemistry are associated with evapotranspiration.

Groundwater chemistry data for the PM-OV area are compiled in the UGTA Groundwater Chemistry Database (IT, 2002j). The PM-OV groundwater chemistry data are included and discussed in greater detail as part of the Pahute Mesa hydrologic data report (Rehfeldt et al., 2003).

2.4 Contamination Sources and Extent

This section includes summary descriptions of the sources and extent of the radioactive contamination present at the Pahute Mesa CAUs. A more detailed

description of the sources and extent of contamination may be found in the unclassified source term and radionuclide data report.

2.4.1 Contamination Sources

This section describes the sources of radioactive contamination present at the Pahute Mesa CAUs. Brief descriptions of the underground nuclear tests, the radiologic source term, the hydrologic source term, and the simplified hydrologic source term are provided.

2.4.1.1 Underground Nuclear Tests

A total of 82 underground nuclear tests (shaft nuclear devices) were conducted on Pahute Mesa. Shaft nuclear devices were exploded at the bottom of a drilled or mined vertical hole. Sixty-four tests were detonated on Central Pahute Mesa (CAU 101), and 18 tests were detonated on Western Pahute Mesa (CAU 102). In the FFACO (1996), each of the 82 underground nuclear tests corresponds to a corrective action site. The locations of the underground nuclear tests are shown in [Figure 2-5](#). Tests that were conducted in the shallow subsurface of Pahute Mesa are not part of the UGTA Project because they are not considered to be underground nuclear tests. These tests are PALANQUIN, CABRIOLET, and SCHOONER and are addressed under the Soils Project.

To reduce the number of source terms to consider in the model, Pawloski et al. (2002) investigated the categorization of the underground nuclear tests of Pahute Mesa. They found that classification by HSU appeared to be a reasonable approach. Pawloski et al. (2002) grouped the underground tests into four classes based on the HSU adjacent to the cavity and overlying HSUs: (1) tests in aquifers, (2) tests in aquifers with overlying aquifers, (3) tests in confining units, and (4) tests in confining units with overlying aquifers. For the purposes of this study, an overlying aquifer is any HSU identified as an aquifer or composite unit that is present above the 2-radii distance from the working point. For a detailed description of the source categorization, see the unclassified source term and radionuclide data report and the test categorization report (Pawloski et al., 2002).

Based on this grouping, thirteen tests located in Area 19 and two tests located in Area 20 have been eliminated from further analysis because they were conducted in confining units. Such tests will never contribute radionuclides to the contaminant boundary because migration from these is very slow relative to migration from tests conducted in aquifer units.

2.4.1.2 Radiologic Source Term and Potential Contaminants

The most recent inventory of the radiologic source term may be found in an unclassified report titled, *Nevada Test Site Radionuclide Inventory, 1951-1992* (Bowen et al., 2001). The inventory includes radionuclides produced by the

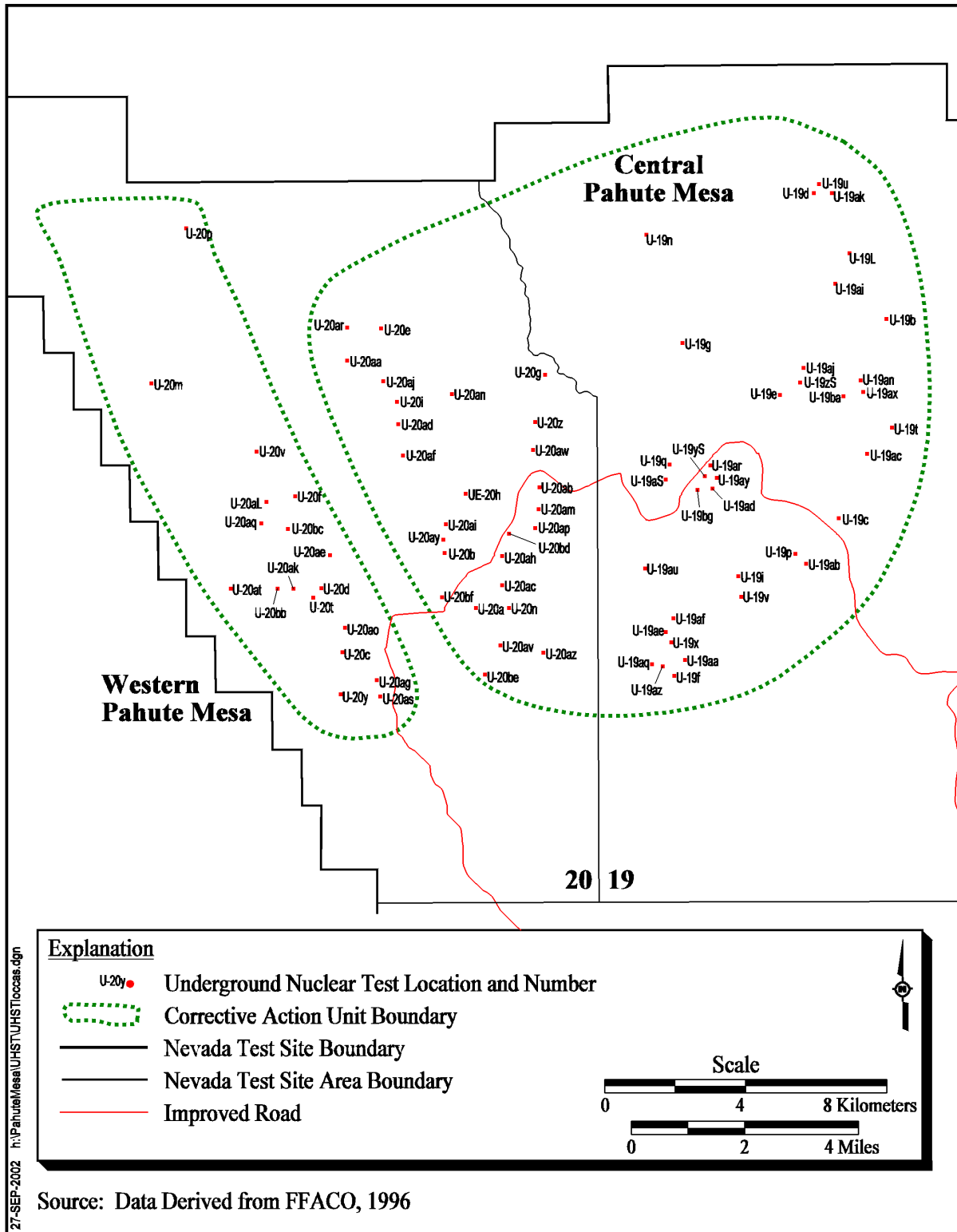


Figure 2-5
Location of Underground Nuclear Tests on Pahute Mesa

828 underground nuclear tests conducted at the NTS between 1951 and 1992. The inventory was subdivided into five areas roughly corresponding to the UGTA CAUs. The inventory for Yucca Flat was further subdivided by tests based on the depth of the working point relative to that of the water table. The inventory for Pahute Mesa was subdivided by NTS area. The inventory includes tritium, fission products, actinides, and activation products. This inventory also provides an estimate of radioactivity remaining underground after nuclear testing.

The source term inventory does not include all of the radionuclides produced during a nuclear test. Bowen et al. (2001) developed criteria to exclude nuclides that are not considered to be of interest from the perspective of risk assessment. Nuclides were excluded from the inventory if they have half-lives of less than 10 years (with the exception of europium-154 [Eu-154] at 8.6 years), and if their abundance is so low that they do not present a significant risk to human health. A detailed description of the criteria for inclusion of radionuclides in the inventory may be found in the report prepared by Bowen et al. (2001).

The list of nuclides including the remaining radioactivity values for Areas 19 and 20 of Pahute Mesa is provided in [Table 2-9](#). The list includes 43 radiological contaminants. Remaining radioactivity values have been decay-corrected to September 23, 1992, the date of the last underground nuclear test at the NTS. The list provided in [Table 2-9](#) serves as the preliminary list of potential contaminants for the Pahute Mesa CAUs. This list supersedes the list of potential contaminants presented in the Pahute Mesa CAIP. Lead has previously been included in the list of potential contaminants for the Pahute Mesa CAUs because it is known to have been used in significant quantities in underground nuclear tests (DOE/NV, 1999). Lead was subsequently deleted from the list because it has not been found in groundwater samples.

To minimize the computational effort involved in generating the source term values, the 43 radionuclides considered in the inventory were combined into three sets of basis species. Basis species are radionuclides representing a group of radionuclides having similar partitioning and transport behavior. The three groups are as follows:

- Tracers: all non-sorbing radionuclides that partitioned in different ratios between the melt glass and the exchange volume and colloids.
- Sorbing Radionuclides: without consideration of daughter product production.
- Radionuclides with daughter products of concern and their associated daughter products.

2.4.1.3 Hydrologic Source Term

The hydrologic source term is defined as the radionuclides that are available for transport in groundwater. It represents a portion of the radiologic source term, which includes all radioactive material remaining after a nuclear test.

Table 2-9
Radionuclide Summary for Areas 19 and 20 of the Nevada Test Site

Radionuclide	Curies ^a	Atoms ^a	Curies ^a	Atoms ^a
	Area 19	Area 19	Area 20	Area 20
Tritium	1.778E+07	3.689E+26	5.903E+07	1.225E+27
Carbon-14	2.193E+02	2.111E+24	4.693E+02	4.518E+24
Aluminum-26	8.975E-04	1.073E+21	8.370E-03	1.001E+22
Chlorine-36	9.108E+01	4.618E+25	1.573E+02	7.973E+25
Argon-39	6.398E+02	2.899E+23	1.247E+03	5.652E+23
Potassium-40	1.588E+02	3.398E+29	3.171E+02	6.783E+29
Calcium-41	5.050E+02	8.763E+25	1.273E+03	2.208E+26
Nickel-59	1.596E+01	2.043E+24	2.976E+01	3.810E+24
Nickel-63	1.724E+03	2.904E+23	3.126E+03	5.266E+23
Krypton-85	4.981E+04	9.028E+23	5.706E+04	1.034E+24
Strontium-90	5.804E+05	2.814E+25	6.835E+05	3.314E+25
Zirconium-93	1.887E+01	4.767E+25	2.372E+01	5.993E+25
Niobium-93m	2.969E+03	8.053E+22	5.100E+03	1.383E+23
Niobium-94	7.938E+01	2.674E+24	9.852E+01	3.31.9E+25
Technetium-99	1.344E+02	4.821E+25	1.782E+02	6.394E+25
Palladium-107	5.957E-01	6.523E+24	1.002E+00	1.097E+25
Cadmium-113m	5.017E+02	1.192E+22	7.469E+02	1.774E+22
Tin-121m	1.782E+03	1.651E+23	2.667E+03	2.470E+23
Tin-126	8.085E+00	3.405E+24	1.188E+01	5.002E+24
Iodine-129	4.153E-01	1.098E+25	5.596E-01	1.480E+25
Cesium-135	1.393E+01	5.397E+25	1.838E+01	7.120E+25
Cesium-137	6.971E+05	3.531E+25	8.957E+05	4.537E+25
Samarium-151	2.307E+04	3.498E+24	3.568E+04	5.409E+24
Europium-150	7.805E+01	4.733E+21	1.069E+03	6.483E+22
Europium-152	1.151E+04	2.626E+23	2.970E+04	6.774E+23
Europium-154	7.099E+03	1.028E+23	1.327E+04	1.921E+23
Holmium-166m	3.083E+01	6.231E+22	2.892E+01	5.846E+22
Thorium-232	1.147E+01	2.706E+29	2.319E+01	5.468E+29
Uranium-232	8.730E+01	1.026E+22	1.738E+02	2.044E+22
Uranium-233	6.508E+01	1.745E+25	1.176E+02	3.154E+25
Uranium-234	1.421E+02	5.888E+25	1.179E+02	4.885E+25
Uranium-235	1.293E+00	1.533E+27	1.343E+00	1.592E+27
Uranium-236	2.213E+00	8.730E+25	2.647E+00	1.044E+26
Uranium-238	6.826E+00	5.140E+28	1.250E+01	9.411E+28
Neptunium-237	1.196E+01	4.310E+25	2.476E+01	8.923E+25
Plutonium-238	2.857E+03	4.220E+23	4.768E+03	7.043E+23
Plutonium-239	7.684E+03	3.119E+26	1.262E+04	5.123E+29
Plutonium-240	2.041E+03	2.256E+25	4.405E+03	4.867E+25
Plutonium-241	2.946E+04	7.145E+23	6.952E+04	1.686E+24
Plutonium-242	1.367E+00	8.637E+23	2.279E+00	1.440E+24
Americium-241	1.299E+03	9.468E+23	3.567E+03	2.600E+24
Americium-243	1.203E-02	1.493E+20	1.772E-01	2.200E+21
Curium-244	1.190E+03	3.629E+22	2.197E+03	6.700E+22
Total	1.920E+07	6.646E+29	6.086E+07	1.324E+30

^aDecay Corrected to September 23, 1992 (date of last underground nuclear test)

Source: Modified from Bowen et al., 2001

Detailed process models have been developed by LLNL to simulate the Hydrologic Source Term (Tompson et al., 1999 and 2002; Pawloski et al., 2002). These models are designed to simulate the chemical and physical processes that govern the migration of radionuclides from the underground test cavities. These process models have the potential to simulate the release from a specific underground test assuming adequate site-specific data exist.

However, the HST models require large amounts of information and resources. Thus, it is impractical to use them to generate hydrologic source terms for the underground tests on Pahute Mesa. The development of a simplified method was, therefore, necessary.

2.4.1.4 Simplified Hydrologic Source Term

A Simplified Source Term Model (SSM) was constructed using GoldSim (Golder, 2002a and b). The SSM will be used to generate generic cavity source flux terms for use in the CAU-scale radionuclide transport model of the Pahute Mesa CAUs. The generic cavity source flux terms will then be used to derive hydrologic source terms for the Pahute Mesa CAUs.

The SSM consists of several components representing sections of the detailed process model presented in Tompson et al. (1999 and 2002) and Pawloski et al. (2002). The SSM is used to generate a series of generic radionuclide mass flux curves representing the release of radionuclides from the exchange volume and the melt glass. The SSM accounts for radionuclides with different mass partitioning between melt glass and exchange volume. The SSM approximates the release of radionuclides as tracers or as colloids, but can also simulate the release of reactive radionuclides. Finally, the SSM has the capability to simulate the mass flux of daughter products. SSM simulations account for uncertainty by treating many of the input parameters as random variables.

A normalized inventory of 1.0 is used for each radionuclide considered in the SSM to generate the series of generic radionuclide mass flux curves. Hydrologic source terms specific to each nuclear test or a group of similar tests are then generated using site-specific or group-averaged inventory data. For more details on the hydrologic source term for the CAU transport model, see the unclassified hydrologic source term and radionuclide data report.

2.4.2 Contamination Extent

This section describes the extent of radioactive contamination in the flow system of the PM-OV area.

Radionuclide data are available for 98 groundwater sampling locations within the PM-OV area. Nineteen of these sampling locations are considered to be near-field and seventy-nine far-field. For the purposes of this evaluation, sites located within two cavity radii are considered to be “near-field” locations. All post-shot holes are

considered to be “near-field” regardless of their locations at land surface. All others are considered to be far-field locations.

The available data show that radionuclides related to underground nuclear testing are present at detectable levels in groundwater at Pahute Mesa. The radiological contamination has, however, only been observed in areas relatively close to the nuclear test locations (DOE/NV, 1999). The farthest radionuclide migration is known to have occurred on Pahute Mesa between BENHAM and TYBO. Radioactivity was found in groundwater samples collected at wells #1 and #3 of the ER-20-5 well cluster, located near the TYBO test. The data indicated that a large fraction of the total activity of each radionuclide was associated with colloidal material. However, non-sorbing species were also present in solution. Evaluation of the plutonium-239 (Pu-239)/Pu-240 data indicated that the source of radionuclides in Well ER-20-5 groundwater was the BENHAM test, not TYBO. BENHAM (U-20c) is located approximately 1,300 m north of the ER-20-5 well cluster. These findings imply that low-solubility radionuclides may migrate an appreciable distance from the nuclear test where they originated (Thompson, 1998; Kersting et al., 1998). These radionuclides are associated with the particulate/colloidal fraction and are not dissolved species.

3.0 CAU Modeling Approach and Data Needs

This section presents an overview of the CAU modeling approach and descriptions of the groundwater flow modeling approach and data requirements.

3.1 Overview of CAU Modeling Approach

Given the complexity of the NTS flow system, the sources of contamination, and the processes controlling transport, computer models will be required as a tool to meet the objectives of the FFACO strategy. The modeling approach used to develop an integrated 3-D model for flow and transport begins with characterization of the flow system, development of conceptual models based on assumptions of system processes, and representation of these processes mathematically. Mathematical models are then implemented on computers to represent the system.

The CAU model will consist of an integrated set of component models. Some of these models focus on small-scale (relative to the CAU) processes such as radionuclide release from source regions, and others simplifying CAU-scale processes such as reactive transport in fractures.

The CAU groundwater flow and transport model will be developed at the CAU scale and will be used to simulate radionuclide concentrations for the 1,000-year timeframe. The CAU-scale model will be a numerical 3-D finite-element flow and transport simulator that captures the complex geologic structure including units of variable thickness, faults, and offsets as well as complex transport processes associated with reactive solutes and fractured rock. The CAU-scale model will consist of two integrated components: the CAU-scale flow model and the CAU-scale transport model. The regional-scale flow model and the recharge model are the component models required for the CAU-scale flow model.

3.1.1 Selected Code

The FEHM code (Zyvoloski et al., 1997a and b), developed by LANL, was chosen for the Pahute Mesa CAU-scale flow and transport model. FEHM simulates 3-D, time-dependent, multiphase, nonisothermal flow and multicomponent, reactive solute transport through porous and fractured media. FEHM's finite element formulation provides an accurate representation of complex 3-D geologic media

and structures and their effects on subsurface flow and transport. Specific capabilities include:

- 3-D
- Flow of air, water, and heat
- Multiple chemically reactive and sorbing tracers
- Colloid transport
- Finite element/finite volume formulation
- Coupled stress module
- Saturated and unsaturated media
- Preconditioned conjugate gradient solution of coupled nonlinear equations
- Double porosity and double porosity/double-permeability capabilities
- Complex geometries with unstructured grids
- Two different, reactive, dual-porosity, particle-tracking modules
- Coupled to PEST parameter estimation software (Watermark Computing, 2000)
- Linked with LaGriT grid generation software (George, 1997)
- Supported on SUN, SGI, ALPHA, and Intel (Windows®)

Documentation includes a description of the mathematical models and numerical methods used by FEHM (Zyvoloski et al., 1997a), the user's manual (Zyvoloski et al., 1997b), documentation of the functional and performance requirements for FEHM, description of the FEHM software, and verification and validation reports (Dash et al., 1997; Dash, 2000 and 2001). Further, the software is maintained in configuration management at LANL. With each new release, the software is subjected to a rigorous verification test to ensure accuracy and functionality of all capabilities.

Assumptions for the flow and energy transport models in FEHM include fluid flow governed by Darcy's law, thermal equilibrium between fluid and rock, immovable rock phase, and negligible viscous heating. Specific assumptions are discussed further by Zyvoloski, et al. (1997a).

Inputs to the flow model include the finite-element grid, initial conditions, lateral boundary conditions, recharge, and material properties for HSUs and faults. For

application to isothermal groundwater flow, the calibrated FEHM model produces values of hydraulic head or pressure for each node in the grid.

Input to the transport model include the sources of contamination and transport parameters describing the processes to be simulated.

3.1.2 Data Requirements for the Pahute Mesa CAU Model

Data requirements for the CAU model fall into the three categories listed below.

Groundwater Flow

Data types required for the groundwater flow model include the hydrostratigraphic framework, hydraulic conductivity, storage, surface recharge and discharge, lateral boundary fluxes, hydraulic heads, and groundwater chemistry. The hydrostratigraphic framework is available in the PM-OV HSU model report (BN, 2002). The hydrologic data types are the subject of the hydrologic data report for the Pahute Mesa CAUs (Rehfeldt et al., 2003).

Contamination Sources and Extent

Potential contaminants are currently located in the 82 test locations and downgradient areas in Western and Central Pahute Mesa. Considering the 1,000-year time frame of interest, the potential contaminants may extend from a few hundred meters away from an underground test to as far as Oasis Valley and the northern area of Yucca Mountain. The source term and contamination extent are documented in the unclassified hydrologic source term and radionuclide data report for Pahute Mesa.

Transport Parameters

Major data types of interest include effective porosity, dispersivity, matrix porosity, matrix diffusion coefficients, sorption coefficients, radioactive decay constants, and colloid-facilitated transport parameters. Details for these parameters are the subject of this document.

3.2 Contaminant Transport Modeling Approach and Data Requirements

This section describes the approach used for modeling the transport of contaminants in the groundwater flow system of the PM-OV area. The associated data requirements are also described.

3.2.1 Modeling Approach

The CAU transport model will be built upon the groundwater flow model using the contaminant transport capabilities of the FEHM code (Zyvoloski et al., 1997b). The CAU transport model will then be used to simulate the transport of radionuclides in the aquifer system of Pahute Mesa and vicinity. The objectives and modeling process are briefly described.

3.2.1.1 Objectives

Using the CAU transport model, mass fluxes and concentrations of radionuclides will be calculated for specified points located downgradient from the underground nuclear tests of Pahute Mesa. Simulated concentrations will then be used to estimate the location of the contaminant boundary as defined in the FFACO (1996).

3.2.1.2 Modeling Process

The modeling process will consist of the following steps:

- Identifying radionuclide transport processes at work
- Designing of a simulation strategy
- Conducting transport model simulations
- Conducting sensitivity analyses
- Conducting uncertainty analysis

Transport Processes

The Pahute Mesa CAU transport model will need to account for the following processes:

- Advective and dispersive solute transport
- Diffusion of solutes from fractures into matrix material
- Retardation of solutes on fracture minerals
- Retardation of solutes on matrix minerals
- Enhanced mobility of solutes due to colloids
- Retardation of colloids via filtration and attachment to fracture walls

Simulation Strategy

The strategy for simulating the transport of radionuclides at the CAU scale will include both a fully-coupled reactive transport methodology, and an abstraction model based on streamline particle tracking. The fully-coupled model will be used to investigate process sensitivity and design parameter ranges for the more efficient particle-tracking model. The particle-tracking model will be suitable for the multiple simulations needed to investigate multiple geologic interpretations and ranges of uncertainty of all other groundwater flow and transport parameters.

Saturated zone transport can be simulated with continuity equations on a finite-element grid, with discrete particle-tracking techniques, or with continuity equations along one-dimensional (1-D) grids, mapped to coincide with particle pathways in a 3-D flow field.

Solving the continuity equations in 3-D or along 1-D pathways allows for the greatest flexibility in specifying reactive processes. Fully coupled kinetic and equilibrium reactions describing multicomponent, aqueous-aqueous, and aqueous-solid reactions can be accommodated with a dual-porosity methodology suitable for capturing fracture-matrix interactions. However, such simulations are

computationally demanding and may not be appropriate for CAU-scale simulations, particularly when uncertainty is addressed with Monte Carlo-type simulations. Although slightly more limited in the reactions that can be addressed, the 3-D streamline particle-tracking transport algorithm is significantly more efficient than finite-element solutions of the continuity equations.

The particle-tracking model is a full, dual-porosity method for simulating transport in fractured rock. It can be used to simulate dual-porosity transport with: (a) diffusion into the matrix, (b) solute retardation on fracture minerals, and (c) solute reaction with matrix minerals. Fracture properties such as aperture, spacing, and reactivity can vary spatially as can matrix reactivity.

The limitation of the particle-tracking solver compared to the continuity equation solver is that solute-solute reactions cannot be simulated with the particle-tracking model. This means that an abstraction of complex processes such as solute-colloid reactions must be developed prior to the simulations. Such an abstraction can be developed with a limited number of simulations of the complete set of continuity equations. It involves identifying the transport parameters associated with a new species, plutonium-colloid. The parameters govern the retardation and the maximum aqueous concentration. The new species can then be simulated independently, and somewhat conservatively relative to the fully-coupled model. Another limitation of the particle-tracking model is that it is incapable of considering kinetic sorption processes and filtration of colloids. Thus, an abstraction will use the fully-coupled process model to justify equilibrium retardation factors for such processes as colloid attachment and detachment to fracture walls, while maintaining conservatism.

Radionuclide Transport Simulations

Deterministic transport simulations will be conducted to predict the movement of contaminants in the groundwater.

First, the finite-element mesh will be refined around the contamination sources and within the plume domains. Second, a limited number of simulations will be conducted using the finite-element, dual-porosity, reactive transport module (1-D and 3-D) to develop abstractions of complex processes. These simulations will be used to condition and validate parameters that will be used in the particle-tracking simulations. They will also be used to condition and validate conceptual models. Third, predictive simulations will be made using the dual-porosity, streamline, particle-tracking module of FEHM.

Important inputs for transport simulations are: (1) groundwater fluxes, (2) transport parameter distributions, (3) integrated-source release model, and (4) natural geochemical system.

Sensitivity Analyses

Sensitivity analyses will be performed after the deterministic part of the contaminant transport model is completed. The objective of the sensitivity analyses is to assess the response of the predicted concentration values as a result of changes in input parameter values.

The results of the sensitivity analyses will be used to guide potential additional data collection efforts or model validation data to ensure that meaningful data are collected. Results of the sensitivity analyses may also help define monitoring locations and the type of data to be collected for the monitoring network design.

For the transport calculations where predictions extend well into the future, the sensitivity provides different information. The most sensitive parameters for contaminant transport do not have reduced uncertainty because it is not possible to calibrate to future events. The most sensitive transport parameters identify the parameters of most concern because the range of uncertainty must be constrained by information external to the transport model.

Uncertainty Analyses

Uncertainty analyses will follow the sensitivity analyses. The purpose of these analyses is to quantify the level of uncertainty associated with the CAU-modeling results. The uncertainty of the predicted contaminant concentrations and the location of the contaminant boundary is caused by the uncertainties in the data used to build the CAU model. Model result uncertainties caused by uncertainties in the HSU model, hydrologic source term, transport parameter values, or boundary conditions will be evaluated.

The approach to quantifying the uncertainty in the hydrologic source term and transport parameter values is via the Monte Carlo approach. One Monte Carlo realization will consist of a set of input parameters sampled from their respective probability distributions, and a simulation using FEHM. The probability distribution of model response (contaminant concentrations) is determined from the simulations and provides an assessment of uncertainty in the model predictions. The Monte Carlo method can provide a quantitative measure of the uncertainty in the location of the contaminant boundary.

Assessment of sources of uncertainty that cannot be described via a probability distribution will be included in a different manner. For example, the alternative interpretations of the HSU model will actually be evaluated using separate models. In this case, the simulation of contaminant concentrations for each alternative provides a quantitative change in a measure, such as the contaminant boundary. Other sources of uncertainty that cannot be described by a probability function will be treated in a similar manner.

3.2.2 Data Requirements

A wide variety of data types are required to simulate radionuclide transport in the groundwater system. The data types needed for the contaminant transport model include: the hydrologic source term and transport parameters including effective porosity, dispersivity, radioactive decay coefficients, distribution coefficients, matrix diffusion coefficients, matrix porosity, a description of the fracture geometry, and a description of colloid-facilitated transport.

Hydrologic Source Term

Two source-term datasets will be defined for Pahute Mesa. One source term will be based on unclassified data and will be extrapolated to all underground tests on Pahute Mesa. Later, a classified dataset (based on information from individual tests) will be used to calculate the final location of the contaminant boundary.

For the unclassified data, the source of radionuclides for the CAU transport model will be abstracted release functions from the underground nuclear tests of Pahute Mesa. These will be in the form of mass flux versus time at either: (a) the working point of the tests or (b) the intersection of aquifers with the cavity/chimney systems associated with the tests. For a summary description, see [Section 2.0](#) of this document. For more details, see the unclassified hydrologic source term and radionuclide data report.

Transport Parameters

Parameters needed to simulate the radionuclide transport processes at work in the PM-OV flow system include: effective porosity, dispersivity, radioactive decay constants, distribution coefficients, matrix diffusion coefficients, matrix porosity, description of the fracture geometry, and colloid-facilitated transport parameters. The various transport parameters are described in [Section 4.0](#).

Observed Radionuclide Data

Measurements of radionuclide concentrations in groundwater samples may be useful in evaluating the CAU-model predictions. These data may be used to calibrate the transport model and/or provide further confidence in the simulations. Evidence of radionuclide migration away from test locations, such as was observed near the TYBO test, could be compared with simulated results of the CAU model. Additionally, time series of radionuclide concentrations from cavity samples may be of sufficient quality to compare with simulated concentration declines at the same locations.

4.0 Data Analysis Approach

Data analysis is the process of assessing and interpreting available data in preparation for transport modeling. Data come in a wide variety of types, from a wide variety of sources, and represent a wide variety of scales. The process of analyzing the data can be summarized in the following six steps which are explained in the subsequent text: (1) compilation of existing data in the study area, (2) transfer of applicable data from outside the PM-OV area, (3) assignment of data quality indicators, (4) calculation of the average value and range of uncertainty for the model parameters, (5) assessment of data scale and likely impacts to the CAU model, and (6) discussion of data limitations and the possible impacts to the model.

4.1 Data Compilation

The compilation of existing data is a multiple step process of identifying existing data, acquiring the data, and compiling the data into structured databases. Data types of interest and data sources are discussed in the following sections.

4.1.1 Data Types

A general description of the various types of information needed is provided in the following sections. The descriptions are followed by definitions of the transport parameters of interest to the CAU models.

4.1.1.1 General Description

Major data types of interest to this report are contaminant transport parameters and supporting information.

As stated previously, contaminant transport parameters include effective porosity, dispersivity, matrix porosity, matrix diffusion, sorption coefficients, and colloid-facilitated transport parameters. Descriptions of these parameters are provided in [Section 4.1.1.2](#).

Supporting information includes the following types of information will be recorded, when applicable and available:

- Site or core information

- Chemical constituent
- Method of data collection or type of test
- Date of data collection
- Stratigraphic unit
- Lithology
- Alteration
- Hydrostratigraphic unit
- Method of data analysis
- Observed parameter value
- Uncertainties
- Any references relating to the data records
- Any noted deficiencies

References to the specific sources of information are provided along with the data. A general description of the data sources is provided in [Section 4.1.2](#).

4.1.1.2 Description of Contaminant Transport Parameters

As stated previously, contaminant transport parameters of interest to the CAU models include porosity (effective porosity and matrix porosity), dispersivity, matrix diffusion, sorption coefficients, and colloid-facilitated transport parameters. Descriptions of these parameters are provided in this section.

4.1.1.2.1 Porosity

As stated previously, effective porosity and matrix porosity are required parameters in the CAU models. Porosity, however, can be defined in several different ways depending on the application (Freeze and Cherry, 1979; de Marsily, 1986).

Total Porosity

The total volume of void space divided by the total volume of rock. No other porosity measure can exceed the total porosity.

Bulk Porosity

The bulk porosity is a total porosity measurement and for the purposes of the CAU model can be treated as total porosity. In fractured units, for example, bulk porosity is a sum of matrix and fracture porosity. Bulk porosity measurements are provided in numerous reports.

Drainable Porosity

Also called the specific yield, drainable porosity represents the volume of water that drains from an initially saturated sample under the influence of gravity over a period of time. The drainable porosity is a function of the time the sample is allowed to drain.

Effective Porosity

Also called kinematic porosity by de Marsily (1986), effective porosity is the volume of the rock through which water moves. From the perspective of transport, adhesive water, dead-end pores, isolated pores, or any other water that does not actively move needs to be excluded from the effective porosity. As a result, the effective porosity is always smaller than the total porosity. As noted above, effective porosity is a key parameter governing the velocity of water, and associated radionuclide migration in the groundwater system.

Fracture Porosity

In fractured geologic units, faults, fissures, cracks, joints, and bedding planes form a complicated network of interconnected planar features through which groundwater flows. Often, the majority of groundwater flow is through the fracture network and not through the matrix material separating the fractures. At the scale of the CAU models, this network of planar features will be modeled as an equivalent porous media characterized by an effective porosity. As will be discussed later in this section, the fracture porosity appears to be a lower bound estimate of the effective porosity in fractured media.

Matrix Porosity

The matrix material between fractures is usually porous. In many cases, the porosity of the matrix is several orders of magnitude larger than the fracture porosity. Although the flow through the matrix is often much smaller than through the fractures, the vast majority of the water volume is in the matrix. Matrix porosity becomes very important if diffusion of solutes occurs between fractures and matrix. In many instances, the total porosity is a good approximation of the matrix porosity.

4.1.1.2.2 Dispersivity

The hydrodynamic dispersion of solutes (or particles) in groundwater describes the spreading phenomenon at a macroscopic level by the combined action of mechanical dispersion and molecular diffusion. Dispersion results in transport distances that are greater than those caused by advection alone. The effect of dispersion is quantified and measured in terms of dispersion coefficient or dispersivity. The dispersion coefficient is defined as $D_{ij} = v A_{ij}$, where D is the dispersion coefficient, A is the macrodispersivity, and i, j represent coordinate directions. In the general case, the dispersivity and the dispersion coefficient are second-rank tensors. In most applications, however, only the diagonal terms of the tensor are used.

4.1.1.2.3 Matrix Diffusion Coefficient

In fractured rock systems where the primary pathway for groundwater flow is through the fractures, the matrix material is saturated with groundwater that is considered immobile for the purposes of modeling. The amount of immobile

water in the matrix is governed primarily by the matrix porosity. In many fractured aquifers, the matrix porosity may be 10 or more times larger than the fracture porosity. Thus, although the bulk of the water travels through the fractures, a very large reservoir of water in the matrix can act to store contaminants temporarily via a process called matrix diffusion. If a contaminant diffuses into the matrix for a period of time, it effectively stops moving relative to the water in the fracture. Therefore, matrix porosity and the matrix diffusion process are very important to the successful modeling of contaminant transport in fractured aquifers.

As noted above, matrix diffusion is an important process governing the transport of contaminants in fractured aquifer systems. The matrix diffusion coefficient describes the rate at which a particular contaminant will diffuse into the nearby rock matrix. If there are no physical barriers to diffusion, the diffusion coefficient is a function of the diffusion coefficient of the molecule in free water which is primarily related to the size of the molecule. In real aquifer systems, the diffusion coefficient definition is complicated by physical and chemical factors at the fracture matrix interface such as fracture coatings which can inhibit the diffusion process.

4.1.1.2.4 Matrix and Fracture Sorption Parameters

Contaminant sorption is a general term describing a variety of chemical processes that bind (temporarily or permanently) contaminants to rock material. The rock material may be the matrix or fracture minerals. Often this chemical binding is treated mathematically via a linear equilibrium approach where the amount of contaminant stored on the rock is a function of the concentration in the water. The transfer from the water to the rock is assumed to occur instantaneously and is completely reversible. Therefore, sorption acts to temporarily store contaminants and slows the migration of the contaminants with respect to the groundwater.

In the equilibrium approach, the sorption is represented by a distribution coefficient, K_d , defined by the relationship:

$$S = K_d C^b \quad (4-1)$$

where:

- S = The mass of the contaminant adsorbed on the solids per unit bulk dry mass
- C = The contaminant concentration as mass per volume of water
- K_d = The distribution coefficient

In many cases, the exponent b is set to 1, which leads to a linear adsorption isotherm. Sorption may also be accounted for using retardation factors (R parameters) in the solute transport equation.

4.1.1.2.5 Colloid-Facilitated Transport Parameters

Colloids are defined as small particles (less than 1 micrometer) comprised of either organic material or inorganic mineral fragments and secondary minerals of the host rock. Oxides and hydroxides of actinide elements (e.g., plutonium) can also form as colloids (Kersting et al., 1998). Migration of a given nuclide sorbed onto colloids is more rapid than that of the same nuclide in solution. Parameters needed to represent colloid-facilitated transport include colloid types, concentrations, and size distribution; radionuclide sorption/desorption rates onto colloids, and colloid filtration rate constants.

4.1.2 Data Sources

A great many sources for the data have been identified. In many cases, existing databases developed as part of the Regional Groundwater Flow and Transport Modeling (OECD/NEA, 1998) were used as starting points. These data were supplemented with new data collected as part of ongoing UGTA field investigations and existing data not previously identified. [Plate 4](#) shows the locations of sites on the NTS and vicinity for which transport data are available.

Data for the Pahute Mesa area come from numerous organizations including BN, LLNL, LANL, DRI, USGS, Shaw, and the University of Nevada, Las Vegas-Harry Reid Center for Environmental Studies.

Historic data are available in many publications. Typically, much of the data has been compiled during the preparation of the CAIP, but these data need to be supplemented with new data and newly-identified existing data.

Site-Specific Data

Site-specific data refers to data collected within, or near, the boundaries of the CAU study area which is defined as the PM-OV area ([Figure 1-2](#)). These are directly applicable to the HSUs within the study area, and require little justification of their relevance to the study area.

Yucca Mountain Data

Yucca Mountain is the proposed geologic storage location for commercial high-level waste in the United States. During investigations of the Yucca Mountain site, a great amount of high-quality data have been collected and analyzed. The Yucca Mountain Project (YMP) is located adjacent to the southern edge of the study area. The geology in the YMP region is similar, but not identical, to Pahute Mesa. A process was developed to assess the transferability of YMP data for use in the Pahute Mesa Model. This process is described in [Appendix B](#).

Other Data

In some cases, the data from the much more distant sites may be used to estimate parameter values. Data from distinct sites will only be used in cases where the data from the study area or the YMP site are very limited. As with the YMP data,

the transferability of all data will be assessed prior to using it for the Pahute Mesa Model.

4.2 Data Transfer Methodology

It has been proposed that using data from other sites to reduce flow and transport parameter uncertainty is an appropriate approach when developing models in a sparse data environment (Freeze et al., 1990), such as that of the PM-OV area. This type of approach incorporates flow and transport parameter data from investigations of similar environments for parameters to be used in modeling of the study area. Utilization of such existing data can be both a cost-effective and necessary step for a modeling effort in a sparse data environment. Nearby sites considered as sources of additional data for the Pahute Mesa CAUs are other UGTA CAUs and the YMP (which constitutes the most important source). Factors influencing flow and transport, the general transfer methodology, and the case of YMP data transfer are described in this section.

4.2.1 Factors Influencing Flow and Transport

Numerous factors may influence the flow and transport of groundwater in the subsurface environment in a variety of ways. These factors can include the overall geologic history of the area, lithology, alteration, stress history, and groundwater chemical composition.

Geologic History

The geologic history of an area has a significant impact on the flow and transport of groundwater. For example, the depositional environment of a rock can influence things such as the primary porosity of sedimentary rocks or the texture of volcanic rocks. In addition, subsequent structural episodes may increase faulting in a given area that could lead to an increase in groundwater flow.

Lithology

The specific rock type of a study area has an important impact on the flow and transport of groundwater. Alluvial materials ranging in texture from fine sand to coarse gravels that are well sorted would obviously have different hydraulic properties than an indurated, nonfractured carbonate rock.

Alteration

The alteration of a given rock can play a large factor in the flow and transport of groundwater in the subsurface environment. For example, the formation of zeolitic minerals in volcanic tuffs can greatly decrease the permeability of a given formation by directly affecting the fracture geometry.

Stress History

The stress history of a given area has a large impact on the flow and transport of groundwater in the subsurface environment. Stress can influence a variety of

things such as fracture orientation, aperture distribution, and fracture connectivity. For example, regions of extensional stress tend to form fractures that are open to flow and would tend to increase groundwater movement.

Groundwater Chemical Composition

Groundwater chemistry can play an important role in the flow and transport of groundwater. It can have a large impact on everything from mineral dissolution and precipitation reactions to fracture geometry. For example, mineral precipitation or dissolution reactions within fractures can cause a reduction in permeability from filling fractures with minerals, or it can cause an enhancement of permeability due to dissolution of flow channels.

4.2.2 General Transfer Methodology

The use of flow and transport data from other study areas to develop parameter distributions for flow and transport modeling of UGTA CAUs can be justified by examining specific similarities that may exist between various investigation areas. It must be shown that there is a sufficient similarity that exists between the two areas, taking into account the various factors mentioned previously. A general approach for the transfer of data from one area to another may be accomplished using the following strategy:

- For each parameter of interest, sites need to be identified that may contain data of the same type. In the best-case scenario, sites could be found in the same general area that have roughly the same geologic setting. Sometimes, however, sites will be identified that are located much farther away but have similar types of rocks. In the worst-case scenario, data may have to be transferred from locations that have no similarities at all to the original study area other than data were collected there for the specific parameter of interest.
- Once the source of the flow and transport parameter data is identified, the factors effecting the specific parameter need to be clarified. If it can be shown that only one factor influences a given parameter, it may make the transfer of data easier to justify. For example, if it can be shown that a parameter is only influenced by a specific type of lithology, then it should be easier to justify the transfer of data from one investigation area to another.
- Comparisons of the donor and recipient geologic units are then made with respect to the factors influencing the parameter under consideration.
- Finally, if sufficient data are available for the recipient geologic unit, a comparison of the two datasets can be made to see if they are comparable. Such comparisons may be done using statistical tests such as the T-test and the F-test. If it can be shown that the two datasets have comparable values, it would provide further justification for the incorporation of the data into the existing dataset.

For a more in-depth examination of the justification for a given parameter, see the data analysis section for each transport parameter.

4.2.3 YMP Data Transfer

The Yucca Mountain Site Characterization Project has implemented one of the largest hydrologic and geologic characterization studies of volcanic rocks ever conducted. The proximity and similar hydrogeologic environment of the Yucca Mountain site to Pahute Mesa make it particularly attractive as a source of potential data for the UGTA modeling effort. A detailed rationale for the transfer of data from the YMP is provided in [Appendix B](#); however, a brief summary is presented here:

- Both areas are located in the SWNVF.
- Volcanic rocks in both areas are the result of similar depositional processes.
- Both areas contain similar lithologic units and even lithologic units from the same source area.
- Both areas have experienced similar types of alteration including devitrification and zeolitization of volcanic material.
- Both areas have undergone similar types of regional tectonic stresses resulting in a similarity in the two areas' regional fracture orientations.
- Both have similar groundwater chemistry.

As a result of the two areas similarities, the use of flow and transport parameter data from the Yucca Mountain area can be partially justified in helping to develop parameter distributions for the PM-OV modeling effort.

4.3 Data Documentation Evaluation

The data documentation evaluation provides information on the traceability (or pedigree) of the data. Typically, data collected in the recent past has much better documentation than data collected and reported many years ago. The qualification of the documentation of the data makes it easier to investigate and evaluate the quality of the data that are being compiled in the model.

Each data record of a given dataset was assigned a DDE_F designed to indicate the level of documentation available for that data record. This process of data qualification ensures that the pedigree of the data is retained for data users. However, it is important to note the data qualification does not indicate the usefulness of data for Pahute Mesa transport modeling. Historic data, while often

poorly documented by today's standards, are often of high quality and extremely useful in the CAU investigations.

The five levels of data documentation evaluation flags are as follows:

Level 1

Data are collected in accordance with NNSA/NSO ERP quality assurance project plans, approved State of Nevada procedures, and/or participant-specific procedures. This ranking indicates that all supporting documentation for the data is on file and available for review by data users.

Level 2

Data are collected in accordance with approved plans and procedures as required for Level 1 with the exception that one or more documentation requirements may be deficient in some way. Examples of data documentation deficiencies may include lost or destroyed field-data collection forms or data acquired using interim or procedures.

Level 3

Data are collected using accepted scientific methodology (e.g., American Society for Testing and Materials [ASTM], EPA methods, USGS procedures) and accompanied by supporting and corroborative documentation such as testing apparatus diagrams, field or laboratory notes, and procedures.

Level 4

Data are collected by a participating NNSA/NSO ERP organization or another organization not associated with the NNSA/NSO ERP prior to the issuance and implementation of project-approved standard policies, procedures, or practices governing data acquisition and qualification. The methods of data collection are documented and traceable; however, the validity of data use or compliance with reference procedures is indeterminate. Supporting documentation may or may not exist.

Level 5

Data are obtained under unknown, undesirable, or uncertain conditions. When data documentation is unknown, any available supporting or helpful descriptions of the intended use and conditions of data capture should be described.

4.4 Data Quality Evaluation

The data assessment process varies depending on the parameter. In general, the process includes an evaluation of the quality of the data. The criteria used to evaluate the different types of required data are dependent on the type and the intended use of the data. Thus, various criteria are used to evaluate data quality. The general procedure consists of assigning one or more flags, termed Data Quality Evaluation Flag (DQE_F), to a given record or group of similar records compiled in the database, indicating the data quality or suitability of the record(s)

for the intended usage. Data-type specific quality evaluation procedures are described in the corresponding section of this document.

4.5 Development of Transport Parameter Distributions

With very few exceptions, the parameters in the transport model represent heterogeneous properties that must be averaged in some way to be used. The data collection process also generates uncertainty in parameter values because of the spatial variability and errors in the data collection and analysis processes. Each parameter will be described by a central tendency and uncertainty about that central tendency as represented by a probability density function (PDF) or a cumulative distribution function (CDF).

The process of describing variable data with a probability distribution begins with the compilation and examination of the data. Histograms are used to examine datasets. The data are grouped into bins, the width of which is a function of the number of data points and the level of detail that is desired. The histogram plot is one way to portray the distribution of parameter values. From the histogram, much can be learned about the nature of the variability.

A decision point occurs after the initial examination of the histogram. If the number of data samples is small, the limits of possible values are assessed based on the data or on physical/chemical laws. For example, most aquifer parameters are non-negative. In some cases, the best that can be done is to assign lower and upper bounds to the data. The approach to defining these bounds depends on the amount of data available. If a lot of data are available, then the range of measured values could be used to define the bounds. However, if we invoke scaling considerations, then the range of mean values should always fall within the range of measured values. If the parameter distribution is properly scaled, then the measured value endpoints would clearly serve as bounds. Otherwise, it may be necessary to examine data from other locations outside the study area; therefore, the range of uncertainty will be quite large.

As more information becomes available, more detail about the distribution can be assigned. Any number of distributions may be assigned. We use an approach based on the commercially available software, BestFit (Palisade, 2002). BestFit can fit as many as 28 distributions to the sample datasets using the method of “least squares” ([Appendix C](#)). The fitted distributions are ranked using one or more fit statistics: Chi-Square, Anderson-Darling, or Kolmogorov-Smirnov.

4.6 Scaling Philosophy

Scaling of parameters for use in numerical models is an issue of concern (OECD/NEA, 1998). In most modeling of groundwater flow and solute transport situations, the data required are never measured at the scale required for the models. In most cases, data are measured at scales smaller than the model grid size.

The international group of scientists that have attended Nuclear Energy Agency workshops agree that scaling methods for transport parameters are developing (OECD/NEA, 1998). According to these scientists (OECD/NEA 1998, p. 26), *“The present state of the art in methods for up-scaling has proved most successful in deriving permeabilities and transmissivities for the modelling of groundwater flow. The methods are less well founded in the case of transport processes, and are still in the infancy stage in the case of chemical processes. In all cases, the range of uncertainty in the appropriate values for effective parameters may be high.”*

Additional discussion in OECD/NEA (1999) indicates that, as a general rule, participants felt it was better to model processes in detail than to use up-scaled parameters. This “best case” statement does not acknowledge the reality of limitations in data collection, analysis, and modeling that are inherent in any real-world study. The workshop participants recognize that when scaled parameters are necessary, the scaling needs to be analytically or numerically justified.

Recent work by researchers at LLNL uses the numerical modeling approach to address scaling. Pawloski et al. (2001), model the migration of selected radionuclides from the CHESHIRE cavity on Pahute Mesa using detailed process models that include spatially variable parameters, temperature effects, and reactive transport. Zavarin et al. (2002) built upon the process model results to derive up-scaled retardation coefficients that were justified on the basis of detailed simulations of surface complexation and ion exchange mechanism approaches.

Shapiro (2001) addresses up-scaled matrix diffusion in fractured rock. Shapiro (2001) used one-dimensional simulation along pathlines to derive scaled matrix diffusion coefficients at the kilometer scale and compared those with measured diffusion at the laboratory scale. The conclusion reached is that the effective large-scale diffusion coefficient may be several orders of magnitude larger than the laboratory-scale values.

The up-scaling process leads to averaged parameters that are typically less variable than the underlying small-scale values. The scaling is dependent on the individual parameters. As such, a more detailed discussion of scaling will be presented for each parameter. The reader should be aware that the scaling is dependent on the scale of the model as well as that of the data. Also, the scaling issue may be reevaluated in the future if new information becomes available.

4.7 Data Analysis Limitations

Data limitations that may affect confidence in the data need to be identified. These limitations may be related to density of spatial coverage, data collection method, number of data points, or other factors that may limit confidence in the values. Data limitations will be noted within the discussion of each dataset.

5.0 *Matrix Porosity*

As explained in [Section 4.0](#), there are several types of porosity. Of particular interest are matrix and effective porosities. For fractured geologic units these two types of porosity are distinct, while for porous geologic units the two overlap. In fact, matrix porosity measurements may be used to approximate the effective porosity of porous geologic units. Thus, following a discussion of the role of matrix porosity in radionuclide transport in groundwater, this section includes descriptions of the evaluation of the matrix porosity data available for both porous and fractured rocks, and the development of probability distributions for the fractured HSUs of the PM-OV area. The probability distributions developed for porous geologic units are reported in [Section 6.0](#). Scaling considerations and limitations are also discussed.

5.1 *Role of Matrix Porosity in Contaminant Transport*

The role of matrix porosity depends on whether the host geologic media are porous or fractured.

In porous geologic media, water movement occurs through the rock matrix. As stated in [Section 4.0](#), water actually flows through the connected pores measured as effective porosity, which in the case of porous media, is only slightly smaller than the total porosity. This will be further discussed in [Section 6.0](#).

In fractured rock material, the portion of the rock that is not fractured is considered the matrix. It is generally accepted that water movement is primarily through the fractures in the rock, but not all fractures transmit measurable quantities of water. Therefore, the volume of rock through which the majority of water flows is a small percentage of the total rock volume. The matrix represents the majority of the rock volume. In fractured saturated geologic units, the volume of water in the matrix porosity may be up to 100 times greater than the volume in the fractures. This large reservoir of water in the matrix may be extremely important to the simulation of radionuclide migration. If radionuclides migrate from the fracture into the matrix, via a process called matrix diffusion, the radionuclides will slow down relative to the water flowing in the fractures. The matrix porosity, coupled with the matrix diffusion coefficient, govern the movement of the radionuclides into and out of the matrix. Thus, matrix porosity is expected to be an important parameter in the simulation of radionuclide migration in the groundwater system of Pahute Mesa.

5.2 Data Compilation

Matrix porosity data are widely available from many of the boreholes in the NTS and vicinity. The porosity data are described and presented in this section.

5.2.1 Data Types

Most of the available porosity data were derived from interpretations of geophysical logs. A small subset of the data was derived from core measurements. Such data provide little information about fracture porosity or the effective porosity of fractured media, but are a good source of information for matrix porosity. They also provide useful information about the effective porosity of porous HSUs such as the Alluvial Aquifer or the tuff confining units.

The geophysical log-derived measurements are described in Burkhard (1989). In many of the studies, the porosity is calculated from the grain density, the wet bulk density, and the water content. The grain density is measured on samples of cuttings pulled from the discharge line or, in some cases, from sidewall core samples. The wet bulk density, measured *in situ*, is determined from a density log. The water content is measured using a downhole epithermal neutron log. The porosity is calculated from the relation:

$$n = (1 - \rho_b / \rho_p) \quad (5-1)$$

where:

ρ_p = is the particle density and the dry bulk density
 ρ_b = is determined from the relationship

$$\rho_b = \rho_{bw} / (1 + \theta) \quad (5-2)$$

where:

ρ_{bw} = the wet bulk density measured *in situ*
 θ = the volumetric water content.

Another method of calculating porosity from geophysical logs is through cross plots as described by Muller (1981). In this approach, the porosity is calculated using a direct algebraic expression of the log value. Serra (1984) discusses the application of geophysical logging methods for determining porosity, and notes that the area of investigation extends out to a meter or so depending on the type of log.

A third approach uses conventional core. In this method, the dry bulk density and grain density are measured in the laboratory. The porosity is calculated using [Equation 5-1](#).

A large portion of the data used to determine matrix porosity is in fact total porosity. In most fractured rock aquifers, the total porosity is the sum of matrix porosity and effective or fracture porosity. Fracture porosities are typically less than 1 percent, whereas matrix porosity may be 25 percent or more. The total porosity is, therefore, a good estimator of the matrix porosity of fractured rocks in

most cases. In the case of porous rocks, matrix porosity is equivalent to total porosity.

5.2.2 Data Sources

The porosity dataset is built upon the porosity database compiled during the data analysis phase of the regional groundwater model (IT, 1996e). The database of porosity values was updated to include the most recent geologic information, and any additional data not available in 1996. The new dataset includes additional data from the YMP and the ERP. For each discrete depth in each well, an accompanying hydrostratigraphic unit designation, lithology, and alteration were assigned by geologists from Bechtel Nevada (BN, 2002).

5.2.3 Data Documentation Evaluation

Data types prioritized for documentation and quality evaluation are the porosity values. The level of documentation for each data record was assessed to provide the users with some basis for traceability of the reported values. The levels were assigned to each record to assess the documentation available for each porosity value. The levels assigned do not reflect the accuracy or reliability of the reported data, only the level of documentation. The data documentation levels were presented in [Section 4.0](#).

5.3 Data Description and Evaluation

The matrix porosity dataset is described in [Appendix D](#) and [Appendix E](#). Two data assessments were performed prior to the development of parameter distributions. First, a comparison was made between porosity data collected from core samples versus porosity data derived from geophysical logs. There was an expectation that the core-derived data were likely to be more accurate; therefore, it is important to assess errors or bias that the geophysical log-derived values might introduce into the analysis. Second, the possible depth dependence of the porosity was investigated. A qualitative comparison of the depth dependence of porosity values derived from the saturated zone and that of porosity values derived from the unsaturated zone was made where possible.

5.3.1 Comparison of Core- and Geophysical Log-Derived Porosity

In most cases, matrix porosity values were derived from both cores and geophysical logs. In some cases, conventional core was collected from which particle density and dry bulk density were determined. Porosity was then calculated using [Equation 5-1](#). In many other cases, for which no conventional core was available, the particle density was determined from cutting samples, or sidewall core, and the bulk density was determined from an *in situ* bulk density corrected for water content, both estimated from geophysical logs. Another

method of determining porosity from geophysical logs is through cross plots and direct relationships. It is possible that the errors associated with the geophysical log-derived porosity values may be larger than those from the core-derived porosity values. Additionally, any potential bias between core- and geophysical log-derived porosity values were assessed.

Five boreholes were identified with both core- and geophysical log-derived porosity values: UE-20ae, UE-20ad, UE-18t, UE-19t/U-19t, and WW-8. A crossplot (Figure 5-1) was constructed to illustrate the relationship between the core-derived and the geophysical log-derived porosity using data from the five boreholes. Inspection of Figure 5-1 reveals that for each of the five boreholes, the data points tend to plot along the bisecting line. The bisecting line is the line at

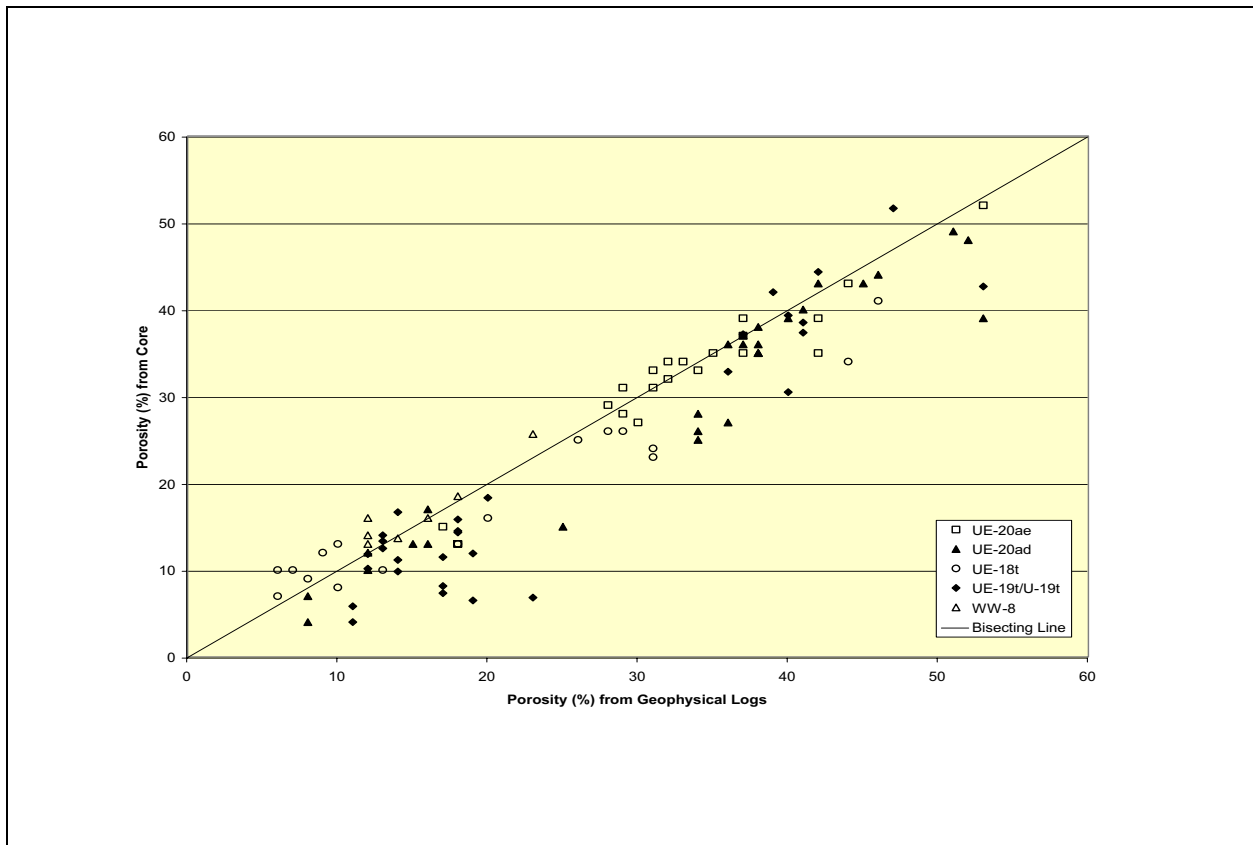


Figure 5-1
Crossplots of Geophysical Log-Derived and Core-Derived Porosity Values

which equal porosity measurements from the two measurement methods would plot. If the data tend to plot below the bisecting line, then one would expect that the core-derived porosity measurement would be lower than the geophysical log-derived measurement. If the data tend to plot above the bisecting line, then one would expect that the geophysical log-derived porosity is lower than the core-derived porosity. The data illustrated in Figure 5-1 also suggest that there is no significant bias in one measurement method over the other. Some variations in the data, however, can be seen in the figure. For example, Figure 5-1 shows that

the data for borehole UE-19t/U-19t are more variable than data for the other four boreholes. In addition, Figure 5-1 shows that the data for UE-20ad tend to plot mostly below the bisecting line. This suggests that the core-derived porosity values for UE-20ad would be lower than the geophysical log-derived porosity values. However, Figure 5-1 shows that overall, there is no significant difference between the core-derived and geophysical log-derived porosity.

To further assess potential differences between core- and geophysical log-derived porosity values, additional comparisons were made on a borehole by borehole basis.

For each of the borehole locations, the core-derived porosity and the geophysical log-derived porosity were plotted as a function of depth. Figure 5-2 is the porosity-depth plot for borehole UE-20ae. For depths with both measurements, the two sets of data plot together, suggesting no bias in one method versus the other for determining porosity. In addition, there does not appear to be greater variability in measurements using one technique or the other.

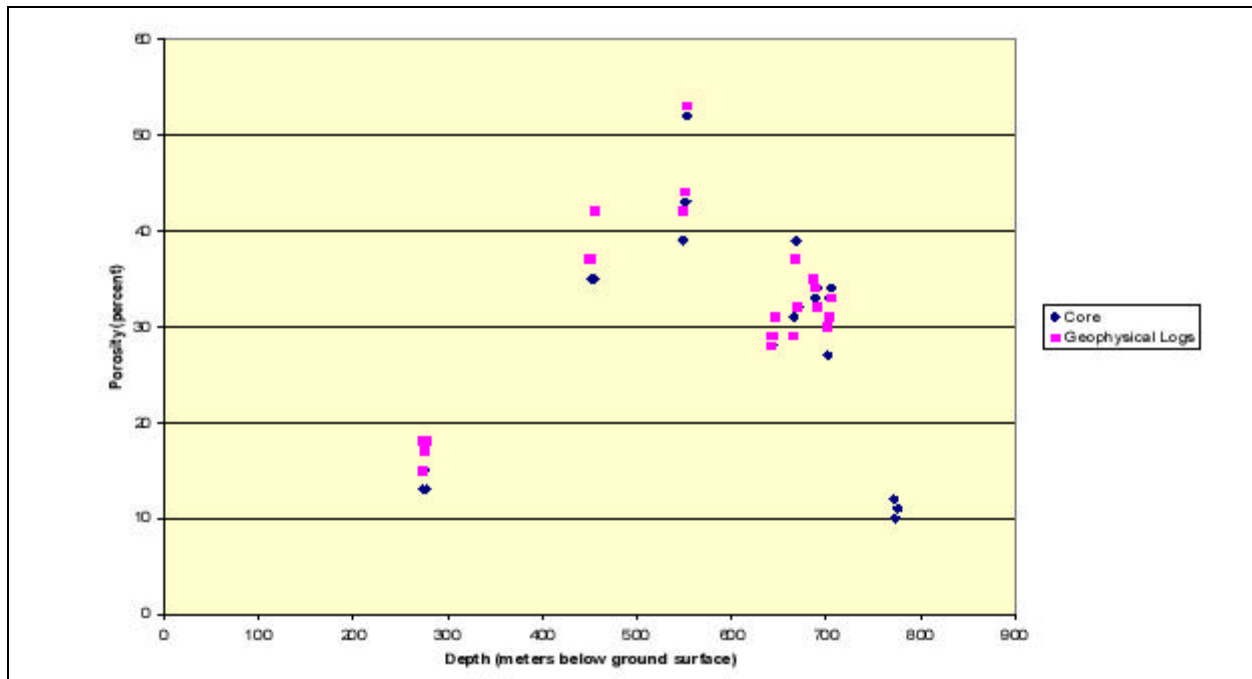


Figure 5-2
Comparison of Core-Derived and Geophysical Log-Derived Porosity Values for UE-20ae

For borehole UE-20ad (Figure 5-3), the two sets of measurements are generally similar, but there may be some differences. There is a large difference between one of the core measurements at 90 m depth and the rest of the values in the 90- to 170-m depth range. Additionally, there appears to be a tendency for the core-derived values to be slightly lower than the geophysical log-derived values by as few to as much as 10 percent.

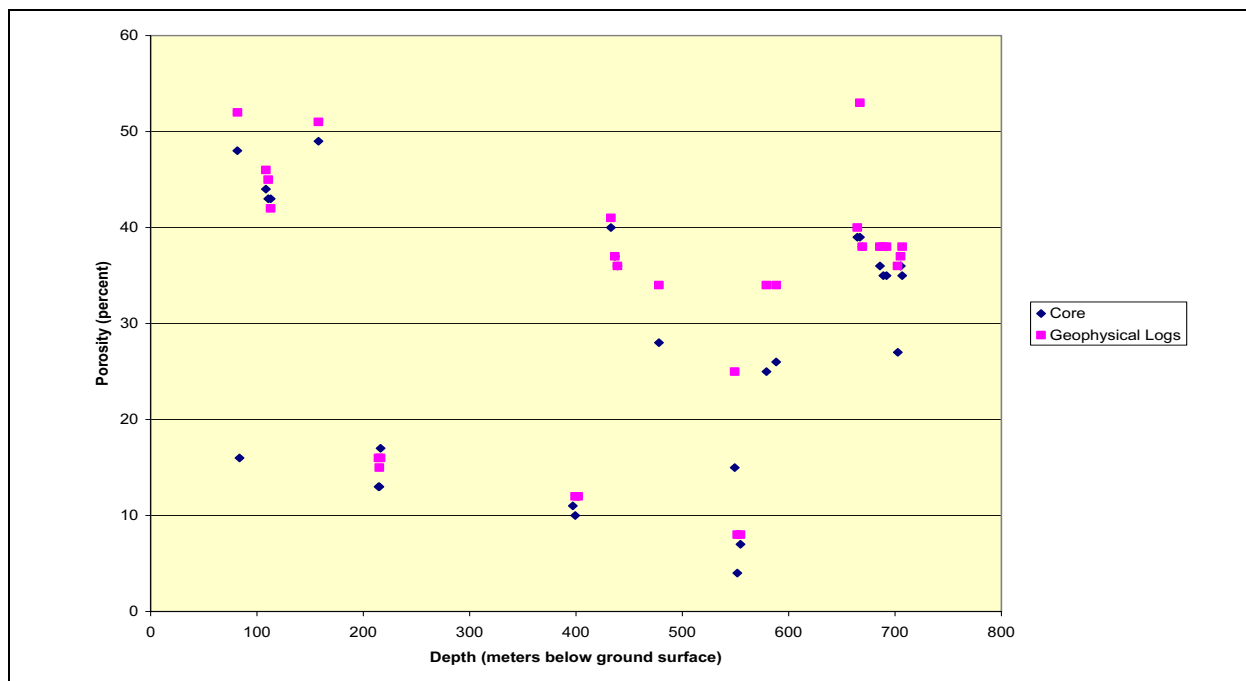


Figure 5-3
Comparison of Core-Derived and Geophysical Log-Derived
Porosity Values for UE-20ad

In borehole UE-18t (Figure 5-4), there are fewer core-derived porosity values than geophysical log-derived values. In general, there does not appear to be a bias in one method over the other. Byers and Hawkins (1981) provide more information regarding the samples from this borehole.

For boreholes UE-19t and U-19t (Figure 5-5), the data from each have been combined for ease of analysis. The two boreholes are at the same general location and are only about 30 m apart. For this location, there are more core-derived porosity values than geophysical log-derived values. There does not appear to be a bias between the two methods. The core values were determined from multiple subsamples of a larger core. It can be seen that the range of porosity values at any depth spans a range of values of about 10 to 15 percent. It is not clear from the data if the variability at any one depth is due to measurement error, or if it represents natural variability that was observed via the subsampling procedure. The larger variability in the core-derived data may be an artifact of the larger dataset and the method used to subsample the core.

The data from WW-8 (Figure 5-6) are similar to the other boreholes. The two methods yield similar porosity estimates. There is no bias in one method or the other, nor does one method appear more variable than the other.

On the basis of this comparative analysis, the porosity data derived from core and geophysical logs have been combined for the remainder of the analysis. It is also clear from these data that porosity can be quite variable even within small depth intervals. For example, the data in Figure 5-2 from borehole UE-20ae plot in five distinct groups. Within four of the groups, the porosity values span a range of

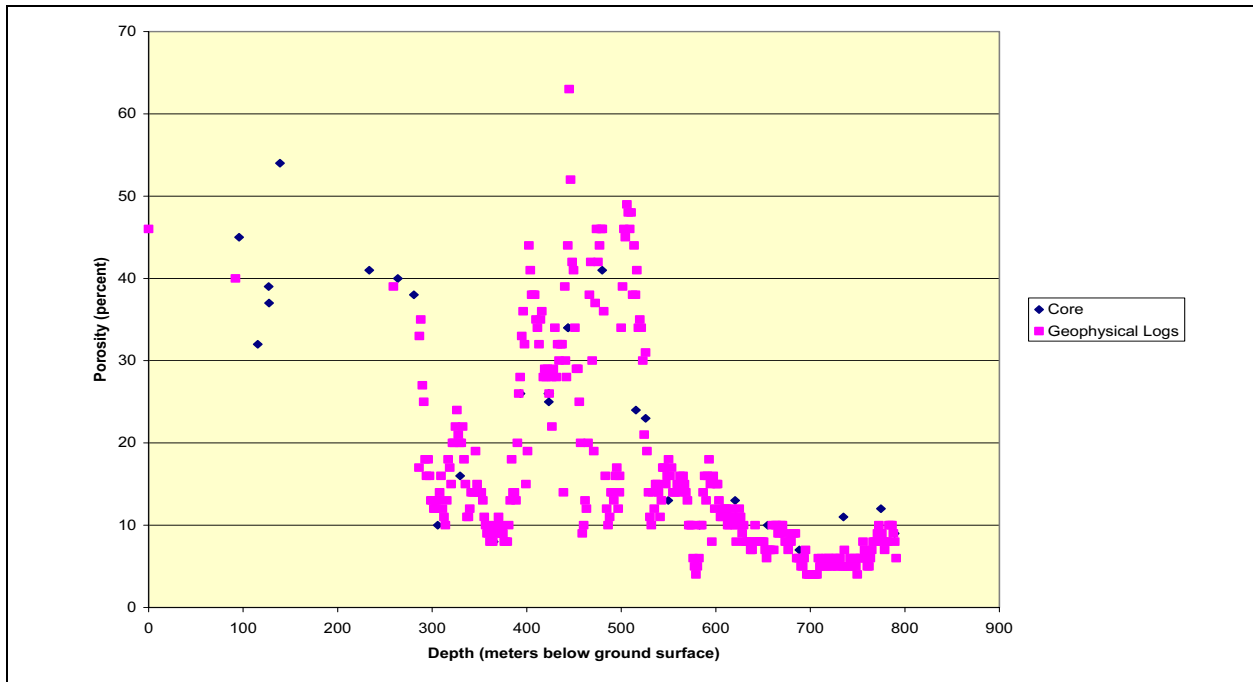


Figure 5-4
Comparison of Core-Derived and Geophysical Log-Derived Porosity Values for UE-18t

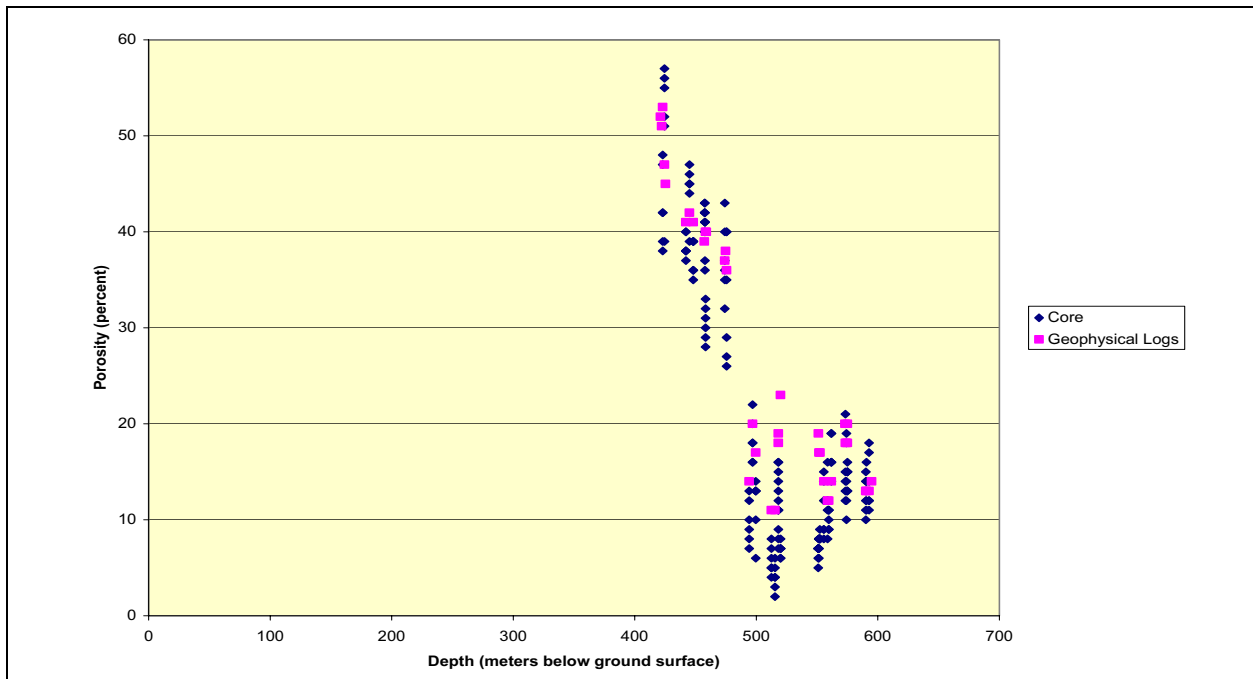


Figure 5-5
Comparison of Core-Derived and Geophysical Log-Derived Porosity Values for UE-19t and U-19t

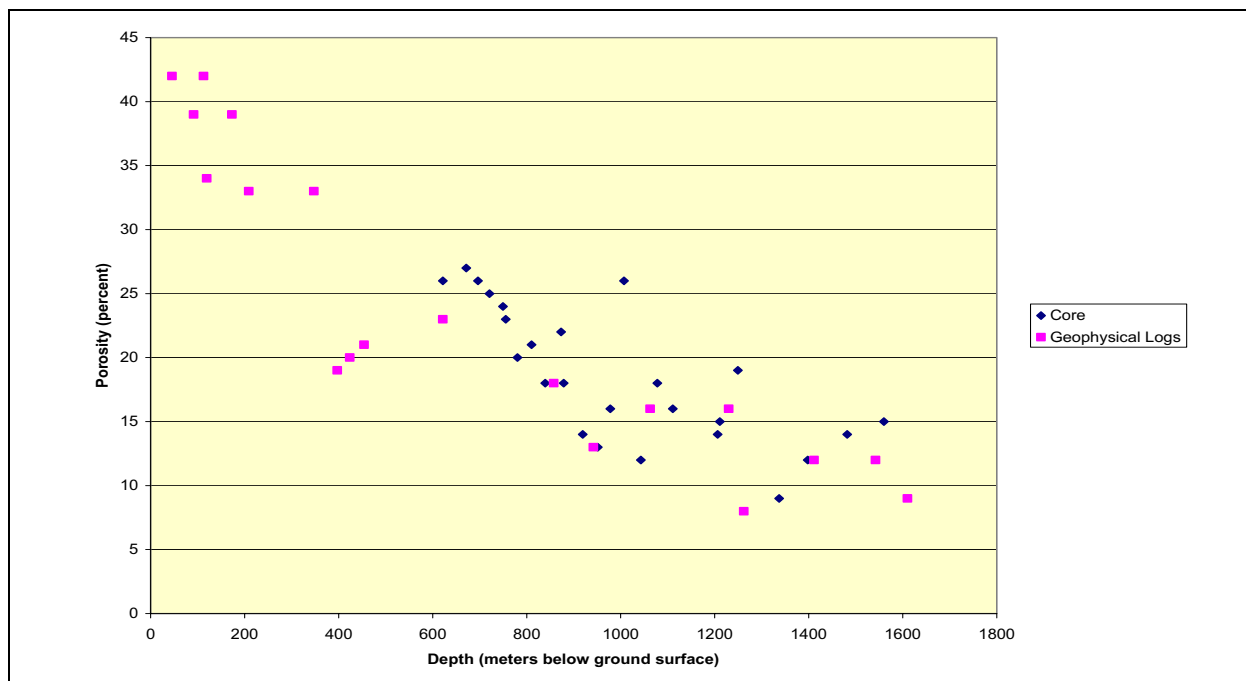


Figure 5-6
Comparison of Core-Derived and Geophysical Log-Derived
Porosity Values for WW-8

about 10 percent (for example, at the 600 to 700 m depths, the porosity values range from about 37 to 49 percent). The other figures showed similar, or larger, variability in some depth intervals.

5.3.2 Assessment of Porosity Changes with Depth

The previous figures (Figure 5-2 through Figure 5-6) presented matrix porosity values for five borehole locations on and around Pahute Mesa as a function of depth, using two measurement methods. There was no reason to expect consistent trends in the porosity values with depth in any particular location because of changing geologic units with depth. Geologic reasoning, however, suggests that if matrix porosity data are grouped by lithology, the porosity within a group may decrease with depth. The grouping of porosity data by lithology would also reveal the effect the degree of saturation would have on the depth dependence of porosity, if any exists.

Figure 5-7 is a plot of porosity values with depth for measurements that were classified as either bedded tuff or nonwelded tuff. Both lithologies can be described as porous units that may be loosely packed when initially deposited. As these units become buried, one would expect the clasts to be more closely packed, leading to a decrease in porosity. As expected, there is a clear decrease in porosity with depth. At very shallow depths, the mean porosity is greater than 50 percent, but at depths near 500 m, the mean porosity is closer to 40 percent. At greater depths, the number of data points decreases, but available data follow a

consistent pattern of decrease with depth. A linear trend fit to the data is presented in Figure 5-7. The trend line is shown continuing to a great depth, but there must be a depth where the decrease in porosity nearly stops and a constant porosity remains. The available data do not allow an assessment of porosity at greater depths, but it is not expected that porosity will decrease below 10 percent even at great depths. A visual inspection of the graph (Figure 5-7) reveals that a similar decreasing trend exists in both the saturated and unsaturated zones.

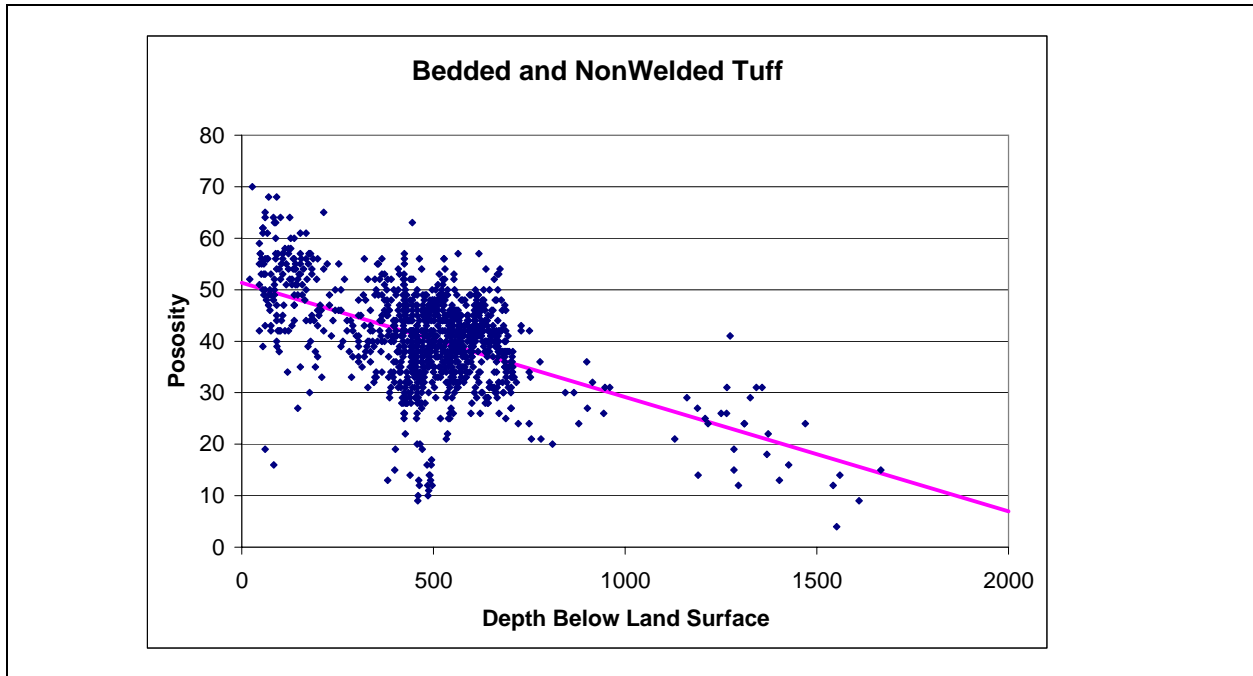


Figure 5-7
Porosity vs. Depth Trend: Bedded and Nonwelded Tuff (Depth in Meters)

Another grouping of porosity values is based on units that are welded to varying degrees or began as solidified glassy units. This second group contains porosity values from lava flows, moderately welded tuffs, densely welded tuffs, and vitrophyres. Figure 5-8 is a plot of porosity with depth for glassy and welded units. There is a tendency for larger porosity values to be located at shallower depths. However, even at shallow depths, the majority of values are smaller, generally between 10 and 20 percent. This tendency for the majority of porosity values to be small does not appear to change with depth. Therefore, no depth dependency of matrix porosity for glassy or welded units will be assumed. This also implies that there appears to be no distinction between the saturated and unsaturated zones as far as the porosity variations with depth are concerned.

Two other groups of lithologies were examined. These were flow breccias and tuff breccias as one group (Figure 5-9) and pumaceous lava and partially-welded tuff as the other (Figure 5-10). In Figure 5-9, it is clear that there are insufficient data with which to judge whether a trend is present with respect to depth. Of the handful of values at depths greater than 800 m, the values tend to be lower, but it would be inappropriate to extrapolate a trend with the data. It would, therefore,

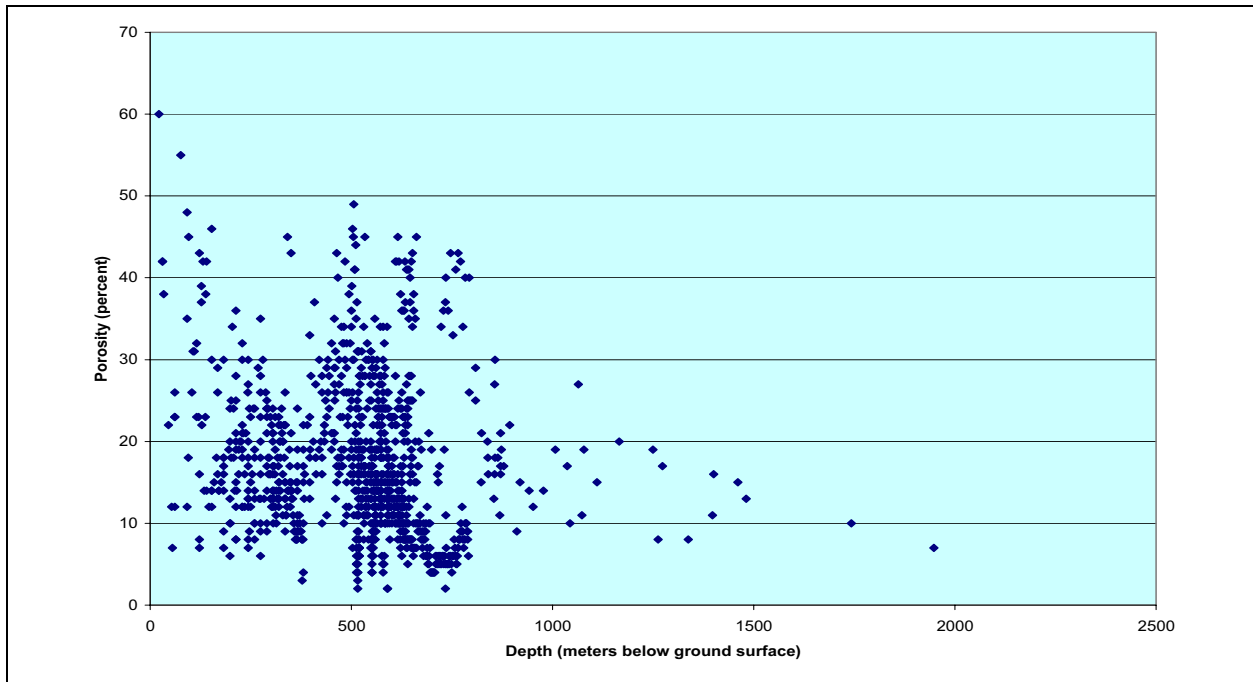


Figure 5-8
Porosity vs. Depth: Lava Flow, Moderately Welded Tuff, and Densely Welded Tuff

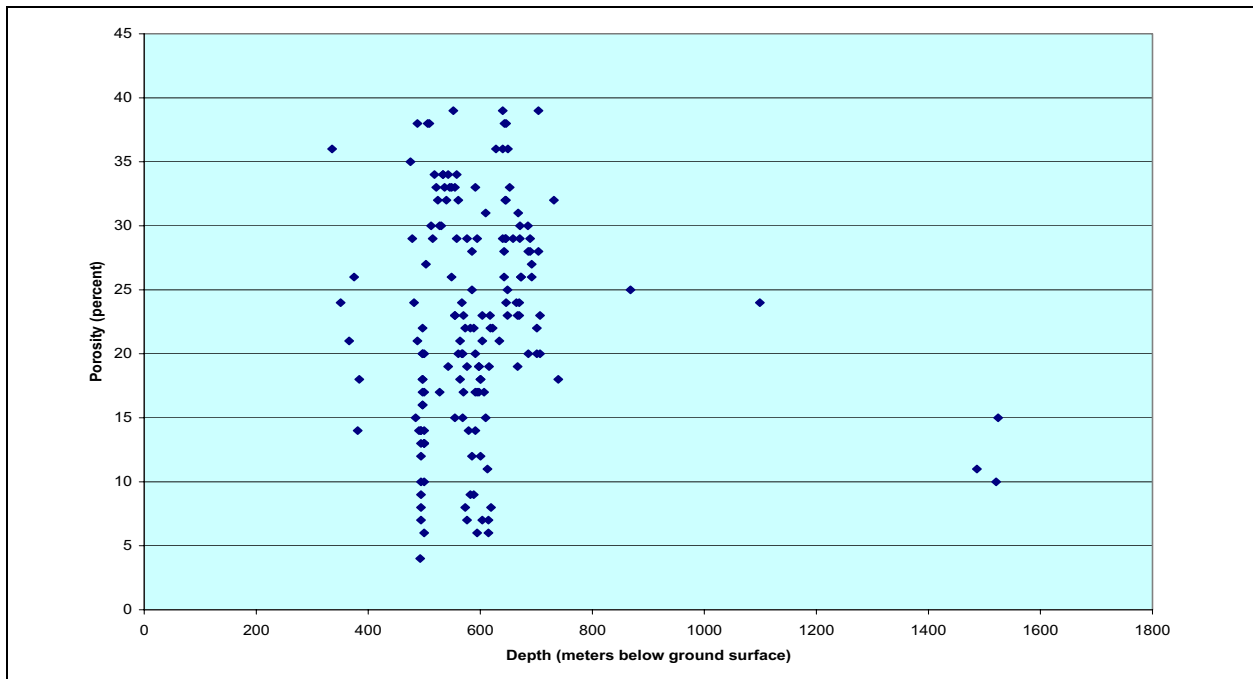


Figure 5-9
Porosity vs. Depth: Flow Breccia and Tuff Breccia

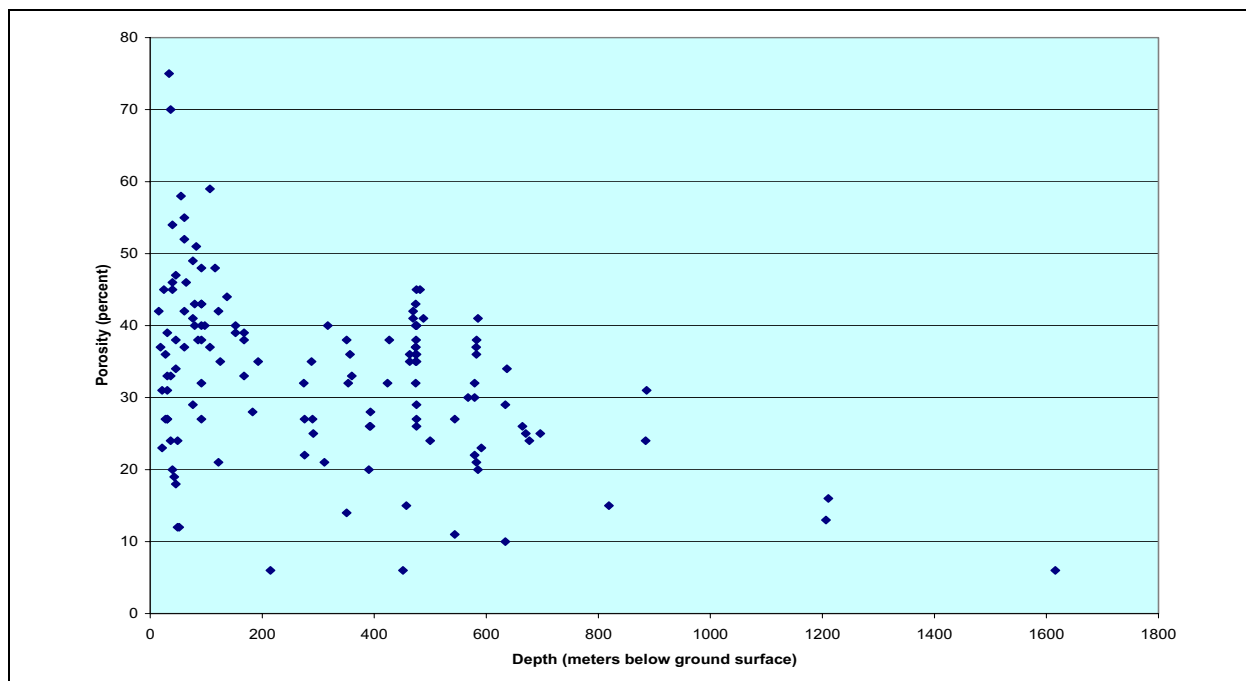


Figure 5-10
Porosity vs. Depth: Pumiceous Lava and Partially Welded Tuff

also be inappropriate to attempt a comparison between trends in the saturated and unsaturated zone data. In [Figure 5-10](#), there appears to be a trend of decreasing porosity with depth. The values are about 40 percent at shallow depths, but decrease substantially to less than 20 percent at depths below 1,000 m. A visual inspection of the graph ([Figure 5-10](#)) reveals that a similar decreasing trend exists in both the saturated and unsaturated zones. The scatter is, however, greater in the unsaturated-zone data subset.

5.4 Development of Parameter Distributions

As with all the parameters in the models, measured porosities are not available for all HSUs. One of the goals of the data analysis is to identify a method for assigning matrix porosity values to each HSU. An approach was developed to understand the data, and ultimately place the data into categories that allow for prediction and classification of the porosity for all of the HSUs in the model.

5.4.1 Approach

The porosity data come from a wide range of hydrostratigraphic units, alterations, and lithologies. Thus, matrix porosity was investigated by grouping the porosity based on three different classifications. The first classification was based on hydrostratigraphic unit, the second on alteration, and the third on lithology.

The dataset of all porosity values available for the PM-OV area was sorted into groups according to HSU, alteration, and lithology. This was done so that an evaluation of the data could be made to determine the appropriate divisions of data. PFDs were used to compare various possible groups of data. A PFD is a plot of the frequency of occurrence, or the number of values per bin, divided by the total number of values. Once it was decided how to divide the data into subsets, the Palisade (2002) BestFit data analysis software package was used to analyze the PFDs and cumulative frequency distributions (CFDs) for the curves that best fit the data. A PDF is the theoretical model (i.e., function) that describes the frequency distribution, and a CDF is the theoretical model that describes the cumulative frequency distribution.

The process begins by extracting the porosity values from the database for each class. Only data with unique identifiers were used. For example, if a sample interval crossed multiple HSUs, that sample was excluded from HSU classification. After the data subset was compiled, the BestFit software was used to construct the parameter distributions.

The data were then used to generate a PFD plot. This is similar to a histogram, but rather than grouping values into bins, each porosity value is treated individually because the porosity values had been rounded to the nearest whole number, when expressed as a percent. The frequency of occurrence is normalized by the total number of values. In addition, the data are also plotted in the form of a CFD, normalized in the range of zero to one.

The BestFit software then uses the method of least squares to fit up to 28 PDFs or CDFs to the sample PFD or CFD. The Bestfit software ranks the fitted distributions using one of a variety of fit statistics, including Chi-squared, Anderson-Darling, and Kolmogorov-Smirnov. One PDF (or CDF) is chosen to represent the data. The selected PDF may not necessarily be the top-ranked distribution. For example, if two fitted PDFs have nearly identical goodness-of-fit results, one distribution may be chosen over another on the basis of physical arguments, historic information, or similar studies in the literature.

5.4.2 Distribution of Porosity Values Based on HSUs

The easiest approach to providing porosity data for the Pahute Mesa CAU transport model is to assess the parameter distributions per HSU and use that data directly. Categorization by HSU should follow a logical pattern to make it useful for assigning porosity. The HSUs fall into seven classes: volcanic aquifers, volcanic confining units, volcanic composite units, alluvial aquifers, Paleozoic carbonate aquifers, Paleozoic clastic confining units, and intrusives. The primary goal for the Pahute Mesa CAU model was to assess the classification of volcanic units; however, a brief discussion is presented for the Paleozoic and the intrusive HSUs. Of the volcanic HSUs represented in the dataset, 11 are aquifers, 6 are composite units, and 5 are confining units. The confining units are treated as porous units and are discussed under the topic of effective porosity in [Section 6.0](#).

It should be noted for the volcanic units that porosity data from Rainier Mesa, which are outside of the PM-OV CAU, were incorporated into this analysis when

appropriate. Specifically, the Rainier Mesa dataset contains porosity data for volcanic aquifers and composite units that were determined to be equivalent to the Belted Range Aquifer (BRA), Paintbrush Volcanic Tuft Aquifer (PVTA), and Pre-Belted Range Composite Unit (PBRCM) HSUs of the PM-OV CAU. For these HSUs, a statistical comparison of the Rainier Mesa and PM-OV data was conducted to quantitatively support the use of data from Rainier Mesa in the PM-OV HSUs. The results of the tests can be seen in [Table 5-1](#). For a brief discussion of t-Tests and F-Tests, the reader is referred to the book by Davis (1973). The results of the statistical tests showed that there was no evidence for concluding that the means and variances are different between the two datasets for the BRA and PVTA HSUs. The statistical tests showed, however, that there was evidence for concluding that the mean value was different between the two datasets for the PBRCM HSU. As a result, the Rainier Mesa porosity data were combined with existing data for the BRA and PVTA HSUs, but not for the PBRCM HSU.

Table 5-1
Test Statistics for the Comparison of Rainier Mesa
and PM-OV Porosity Data as a Function of HSU

	BRA HSU	PVTA HSU	PBRCM HSU
t Statistic	-0.10801	-0.19755	-22.26581
t Critical two-tail	2.01289	1.96733	1.973157
F Statistic	1.105248	1.89911	1.297084
F Critical one-tail	2.028318	253.9163	1.498667

Volcanic Aquifers

Of the HSUs for which porosity data were available, 11 are categorized as aquifers. Of those, seven have more than 25 porosity values and were considered in this analysis. It can be seen in the following seven figures that the PFDs of porosity values from HSUs classified as aquifers do not have consistent matrix porosity distributions. For example, the Timber Mountain Aquifer (TMA) ([Figure 5-11](#)) and BA ([Figure 5-12](#)) HSUs have a large portion of values in the range of 10 to 30 percent. The TMA also has a second peak near 40 percent porosity that the Benham Aquifer (BA) results do not contain. Different still, the PVTA ([Figure 5-13](#)) and Calico Hills Vitric Tuff Aquifer (CHVTA) ([Figure 5-14](#)) HSUs have well-defined distributions that range from 30 to 50 percent. The Paintbrush Lava Flow Aquifer (PLFA) ([Figure 5-15](#)), Thirsty Canyon Volcanic Aquifer (TCVA) ([Figure 5-16](#)), and BRA HSUs ([Figure 5-17](#)) have distributions that do not follow any of the others. There does not appear to be a way to extrapolate matrix porosity data simply on the basis of identifying an HSU as an aquifer.

Volcanic Composite Units

Of the six HSUs with porosity data that were classified as composite units, 4 have more than 25 samples. The distributions for the volcanic composite units can be seen in the following four figures. Two of the four, CHZCM ([Figure 5-18](#)) and TCM ([Figure 5-19](#)), have similar distributions, with most of the matrix porosity

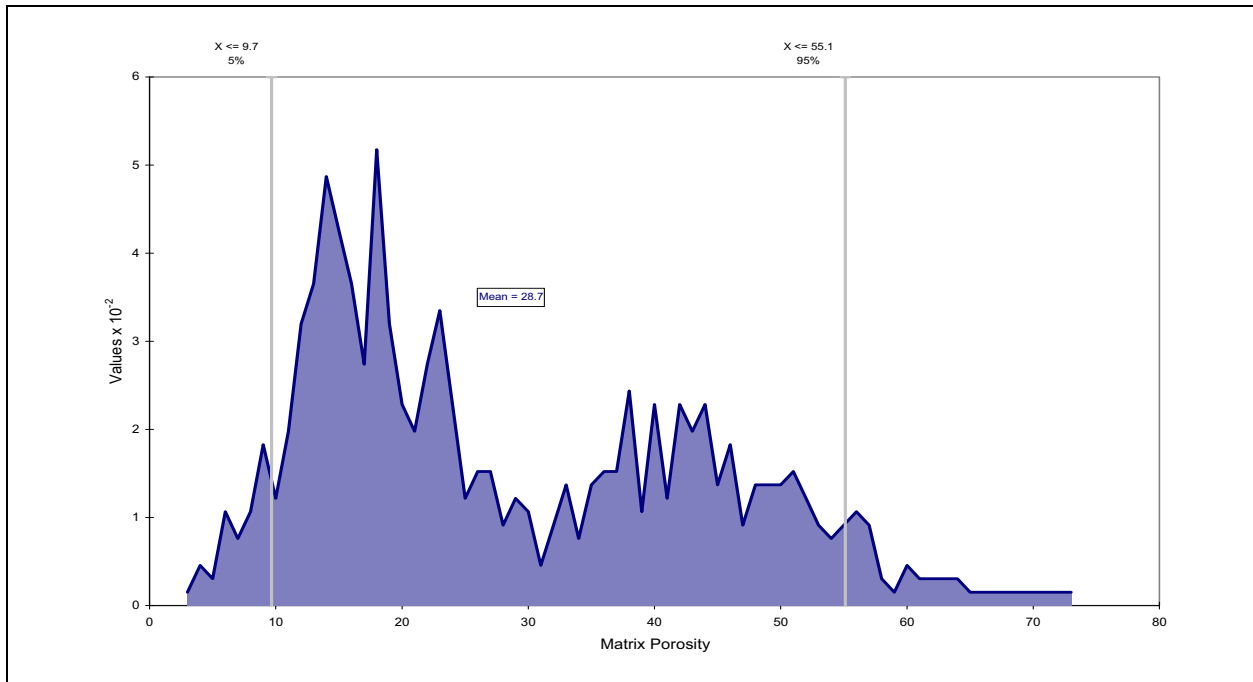


Figure 5-11
PFD of Porosity Data (in Percent): Timber Mountain Aquifer HSU (648 Samples)

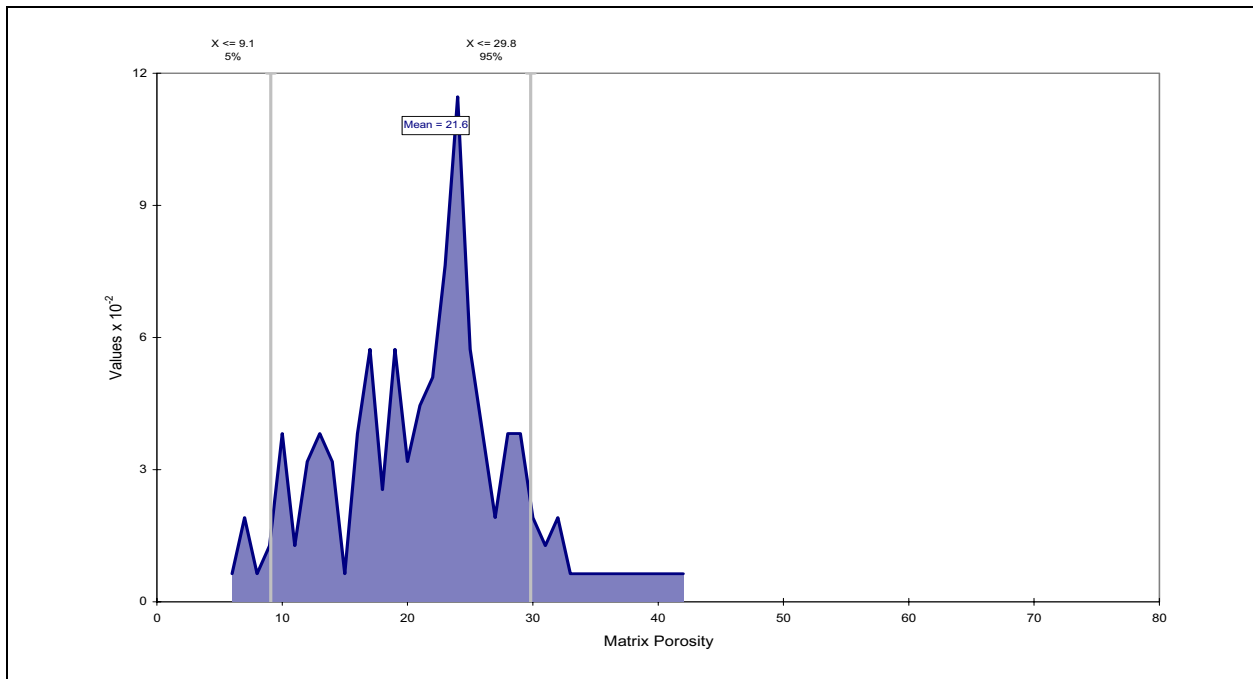


Figure 5-12
PFD of Porosity Data (in Percent): Benham Aquifer HSU (154 Samples)

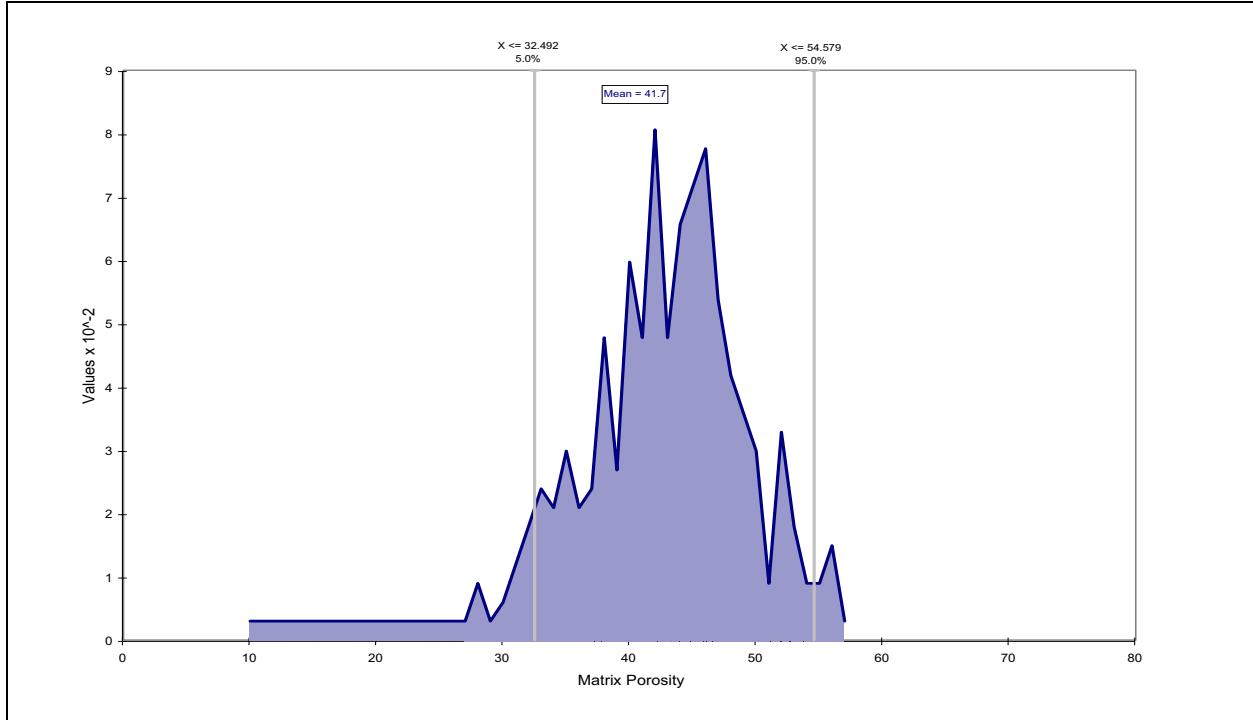


Figure 5-13
PFD of Porosity Data (in Percent): Paintbrush Vitric Tuff Aquifer HSU (325 Samples)

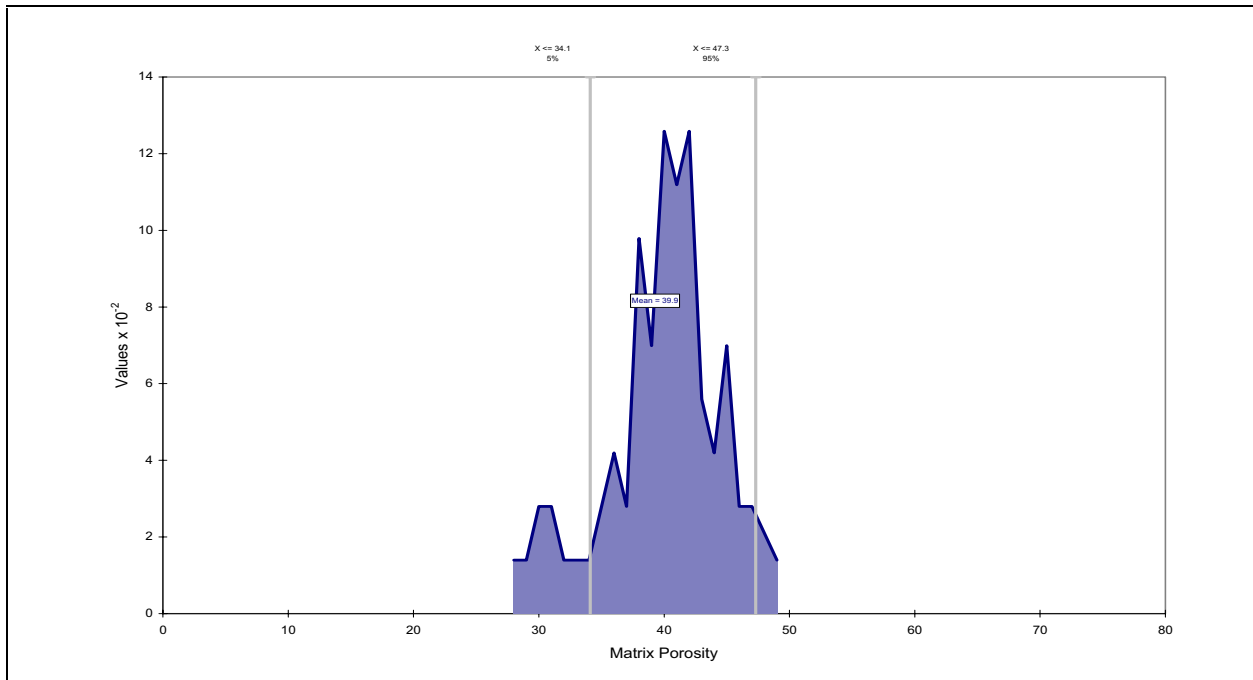


Figure 5-14
PFD of Porosity Data (in Percent): Calico Hills Vitric Tuff Aquifer HSU (71 Samples)

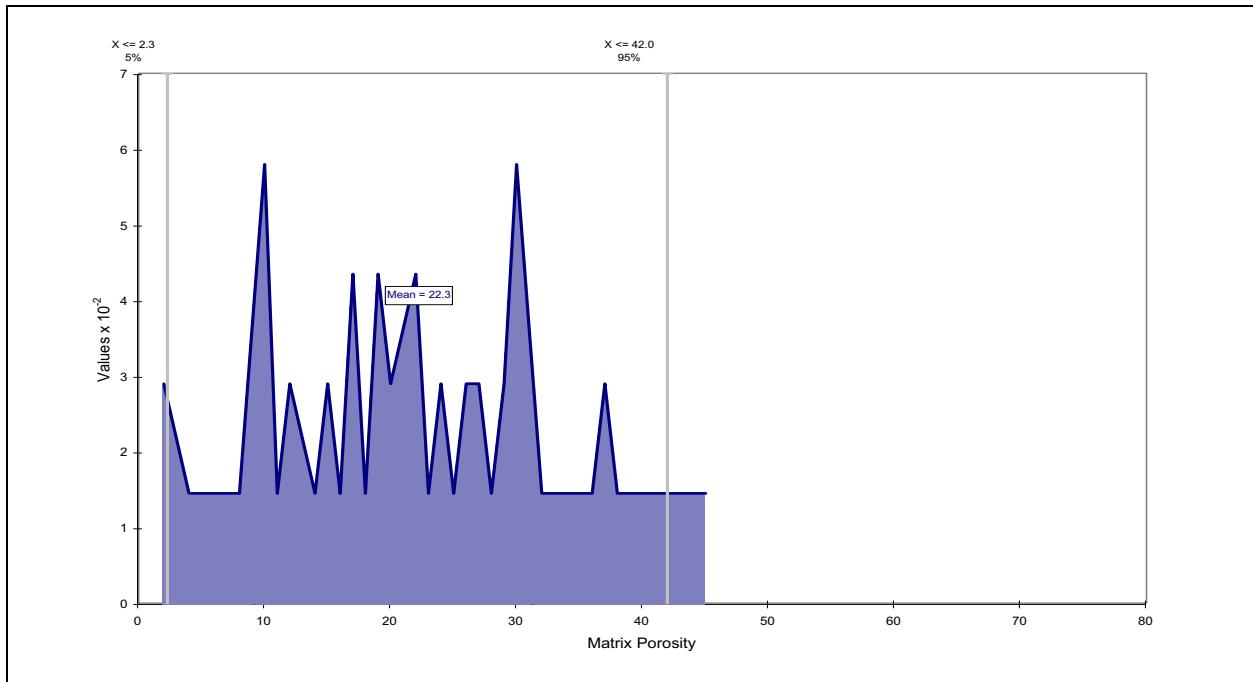


Figure 5-15
PFD of Porosity Data (in Percent): Paintbrush Lava-Flow Aquifer HSU (54 Samples)

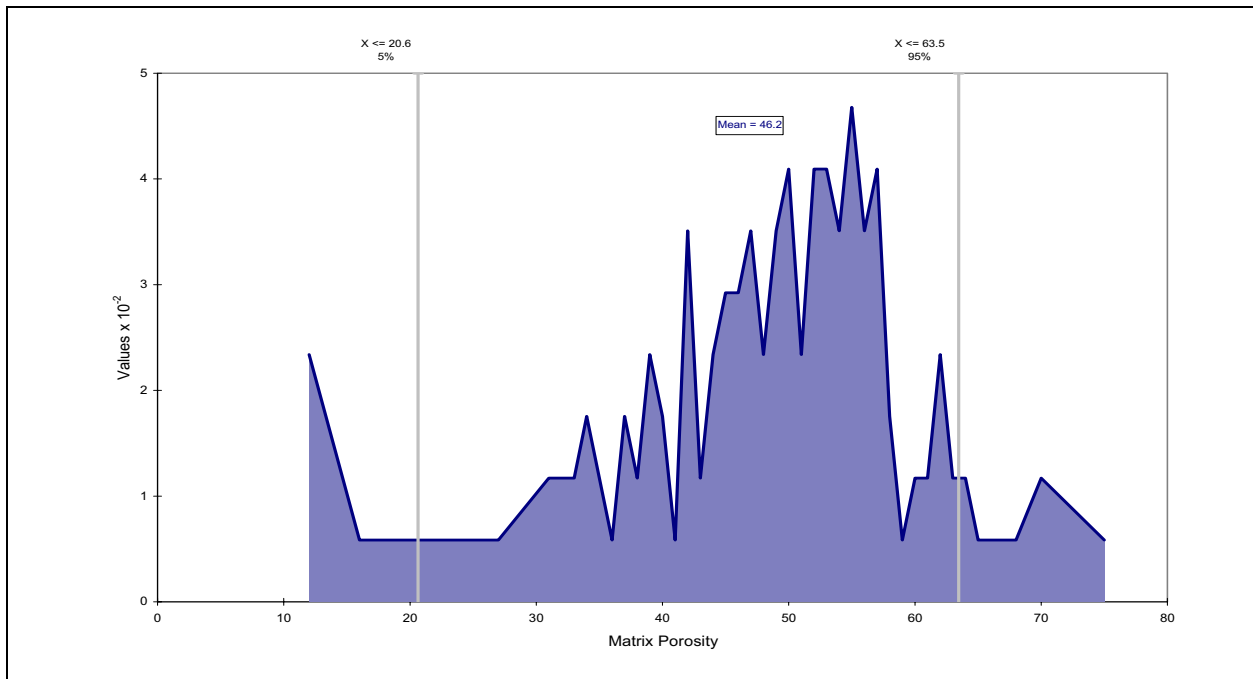


Figure 5-16
PFD of Porosity Data (in Percent): Thirsty Canyon Volcanic Aquifer HSU (146 Samples)

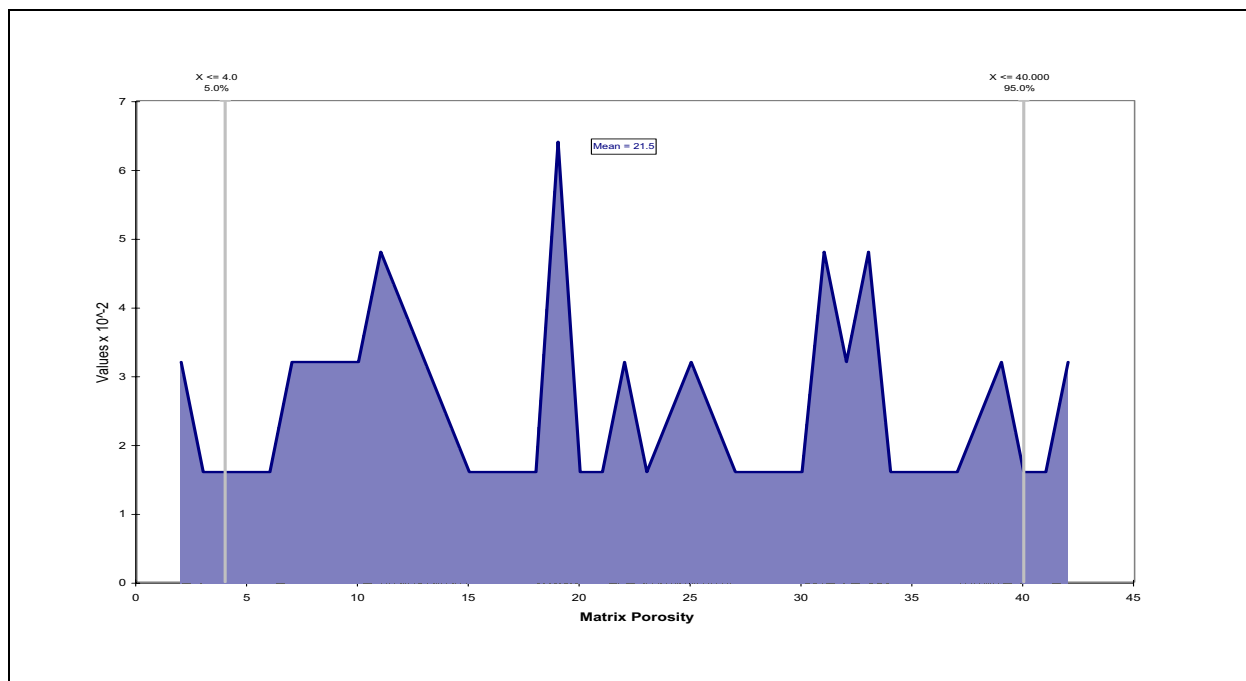


Figure 5-17
PFD of Porosity Data (in Percent): Belted Range Aquifer HSU (48 Samples)

values less than 20 percent. The other two composite units, Calico Hills Vitric Composite Unit (Figure 5-20) and Pre-Belted Range Composite Unit (Figure 5-21), have higher matrix porosity values, as large as 40 percent. As stated earlier, simply identifying an HSU as a composite unit does not provide a way to estimate the most appropriate range of matrix porosity values to be expected.

Paleozoic Units

Of the paleozoic units in the PM-OV CAU, only one contains site-specific matrix porosity data. The PFD for the LCA can be seen in Figure 5-22. The LCA has a unique matrix porosity distribution that can be based on the available data, although it has less than 25 measurements. It can be seen from the figure that the data from the LCA have a mean value of 3.2 percent.

There are no site-specific matrix porosity data available, however, for the paleozoic clastic confining units. As a result, data were obtained for this HSU from the regional groundwater flow and tritium transport model (DOE/NV, 1997). This was deemed appropriate because the LCCU of the PM-OV CAU can be directly correlated back to the regional groundwater flow and transport model. As a result, the LCCU HSU will have a mean value of 3.3 percent.

Intrusives

Of the seven intrusive HSUs found in the PM-OV CAU, none of them have matrix porosity data. As a result, data from the Climax stock were used to create a PFD for the intrusive HSUs. It was felt that this was justifiable given the fact that no

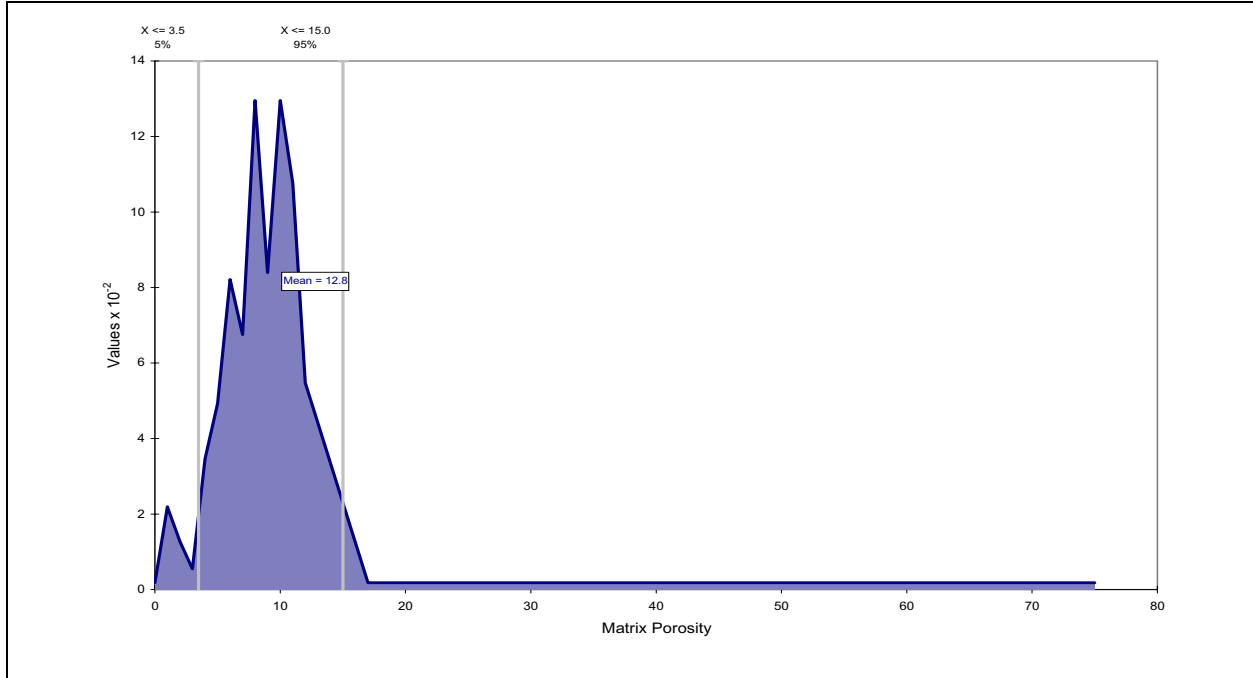


Figure 5-18
PFD of Porosity Data (in Percent): Calico Hills Zeolitized Composite Unit HSU (430 Samples)

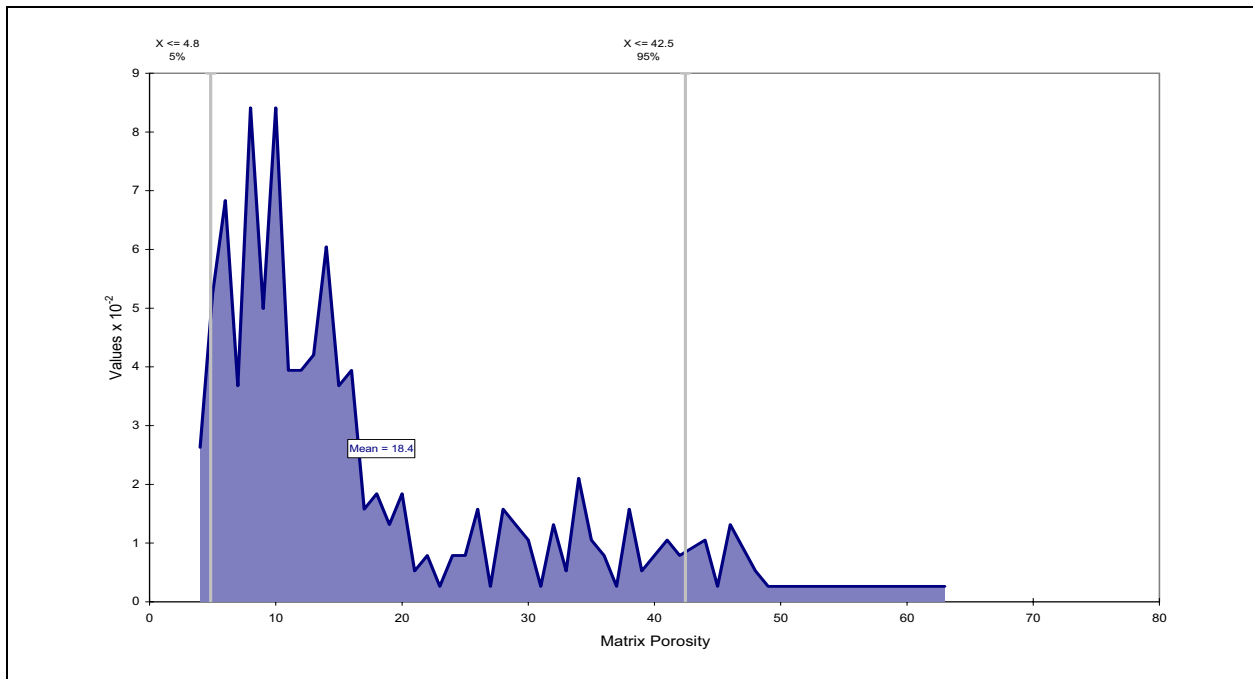


Figure 5-19
PFD of Porosity Data (in Percent): Timber Mountain Composite Unit HSU (364 Samples)

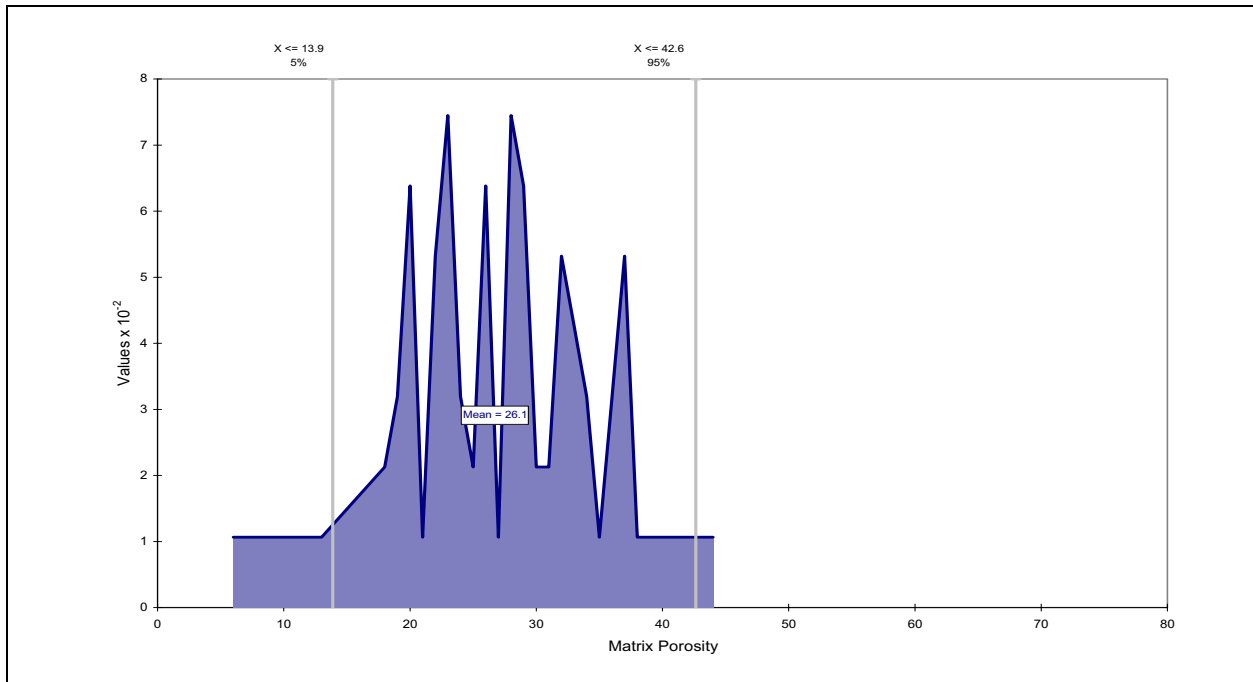


Figure 5-20
PFD of Porosity Data (in Percent): Calico Hills Vitric Composite Unit HSU (83 Samples)

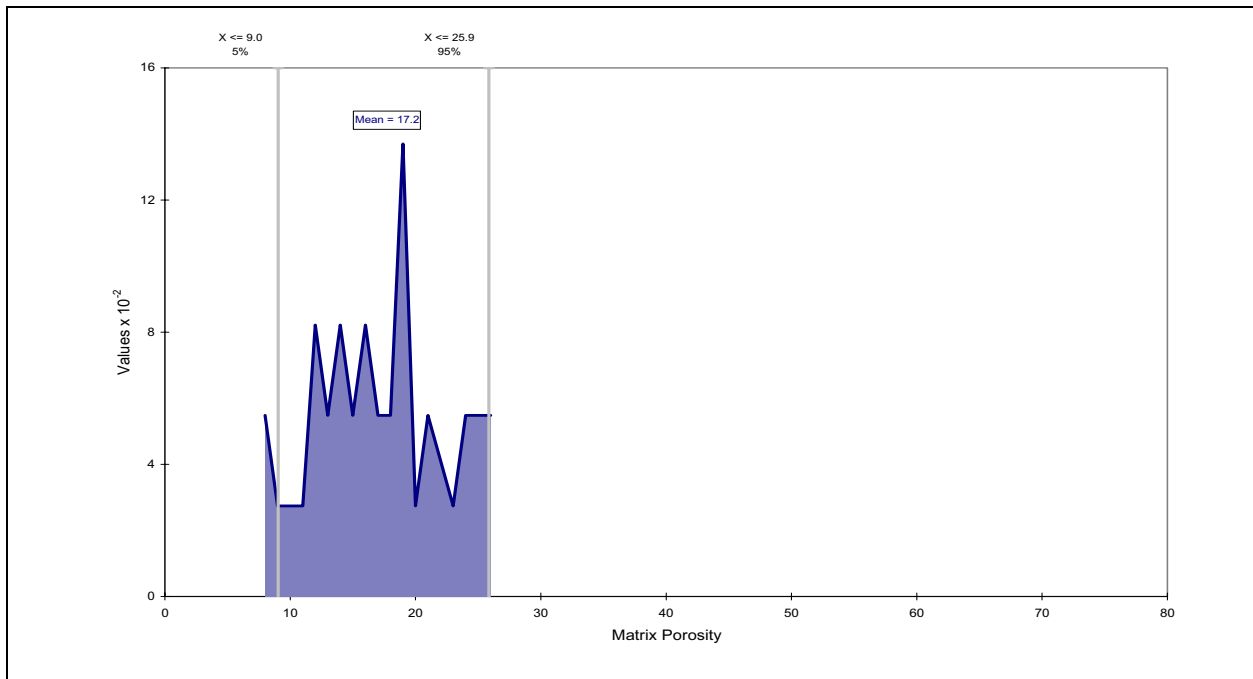


Figure 5-21
PFD of Porosity Data (in Percent): Pre-Belted Range Composite Unit HSU (37 Samples)

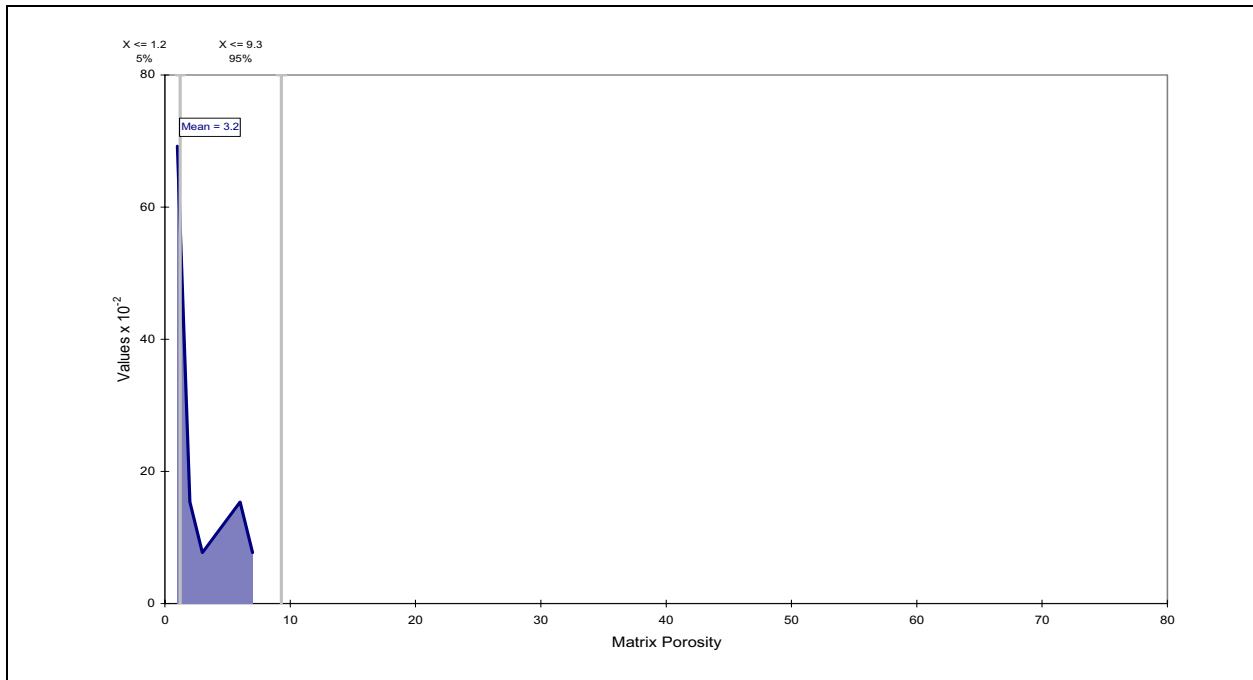


Figure 5-22
PFD of Porosity Data (in Percent): Lower Carbonate Aquifer HSU (15 Samples)

site-specific data were available and that the Climax stock data was for similar lithologic units. In addition, no statistical comparison could be made due to the lack of data in the study area. The PFD for the intrusives can be seen in [Figure 5-23](#). It can be seen from the figure that most of the matrix porosity values are less than 2 percent with a mean value of 1.8 percent.

Summary of Classification per HSU

After reviewing the matrix porosity data for units classified by HSU type, it was not possible to determine a clear relationship between HSU type and matrix porosity. Thus, it does not appear likely that a method can be developed to predict matrix porosity values for the HSUs which have less than 25 data points based solely on the HSU type.

5.4.3 Distribution of Porosity Values Based on Alteration

An additional assessment of the matrix porosity data, classified on the basis of the alteration, was undertaken. This assessment is applicable to volcanic units only. Alteration refers to post-deposition mineralogic changes to the volcanic units. Alteration may have a large impact on some parameters and may influence matrix or fracture porosity, particularly if there is significant precipitation of mineral phases that decreases porosity. Alteration categories are presented by Bechtel Nevada (2002) as part of the presentation of the HSU models. Several examples of plots of porosity data classified by alteration are presented in this section for discussion.

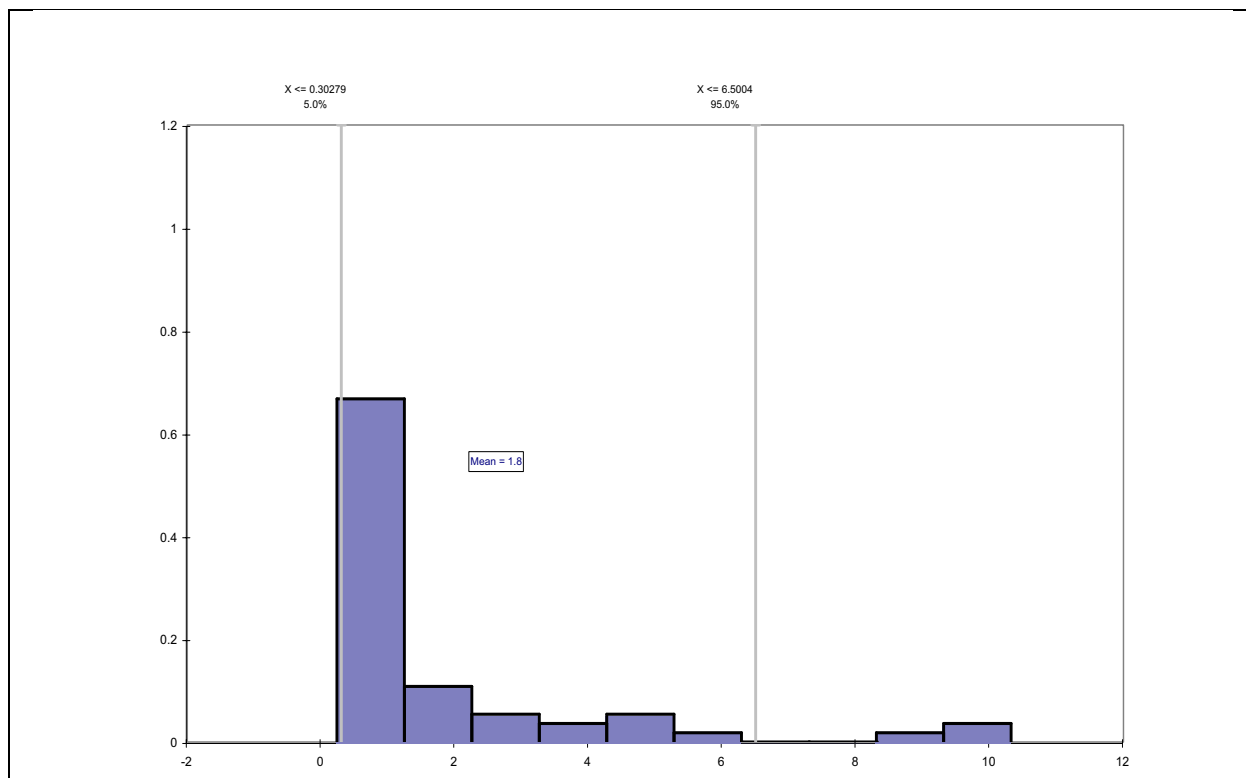


Figure 5-23
PFD of Porosity Data (in Percent): Intrusive Confining Unit HSUs (55 Samples)

Two major classifications for volcanic unit alteration are vitric or devitrified. A vitric tuff can be thought of as a primarily bedded unit that is composed mainly of glass shards that have not been altered to a great extent. Figure 5-24 is the porosity distribution of units listed as vitric. These show a generally well-defined peak near 45 percent, but a secondary peak appears near 10 percent. This likely represents different states of welding, with the welded units having the smaller porosity. The devitrified alteration (Figure 5-25) represents alteration from the unstructured glass to the structure of a mineral. These units show a very clear reduced porosity with a peak near 10 percent. Other altered units, such as those with zeolites (clinoptilolite, analcime), tend to have higher porosities similar to the vitric tuff.

There appears to be correlation between alteration and matrix porosity, especially the degree of devitrification. The extent to which this can be extrapolated to the volcanic units without porosity data is not clear. Even within the existing drill hole dataset, the degree of alteration is not always presented. Extrapolating this to other units seems problematic.

5.4.4 Distribution of Matrix Porosity Values Based on Lithology

Lithology was the last classification of porosity used to develop a method to estimate matrix porosity values for all the HSUs. As noted in the geologic model

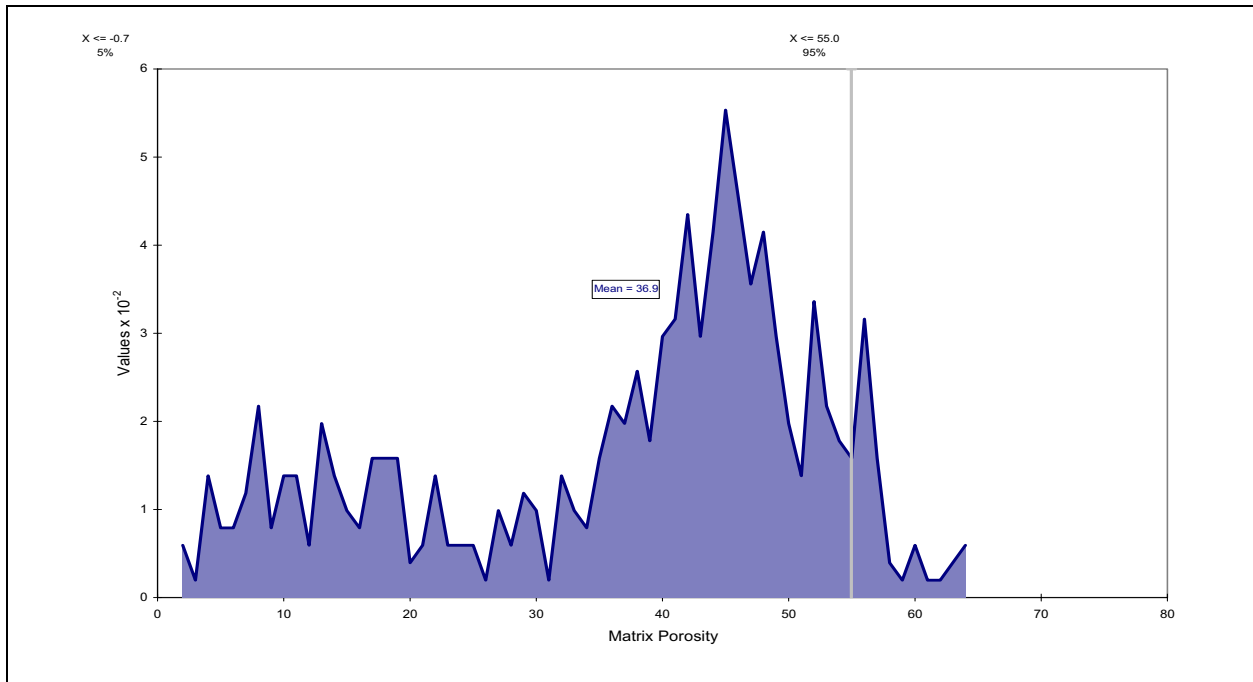


Figure 5-24
PFD of Porosity Data (in Percent): Vitric Alteration (509 Samples)

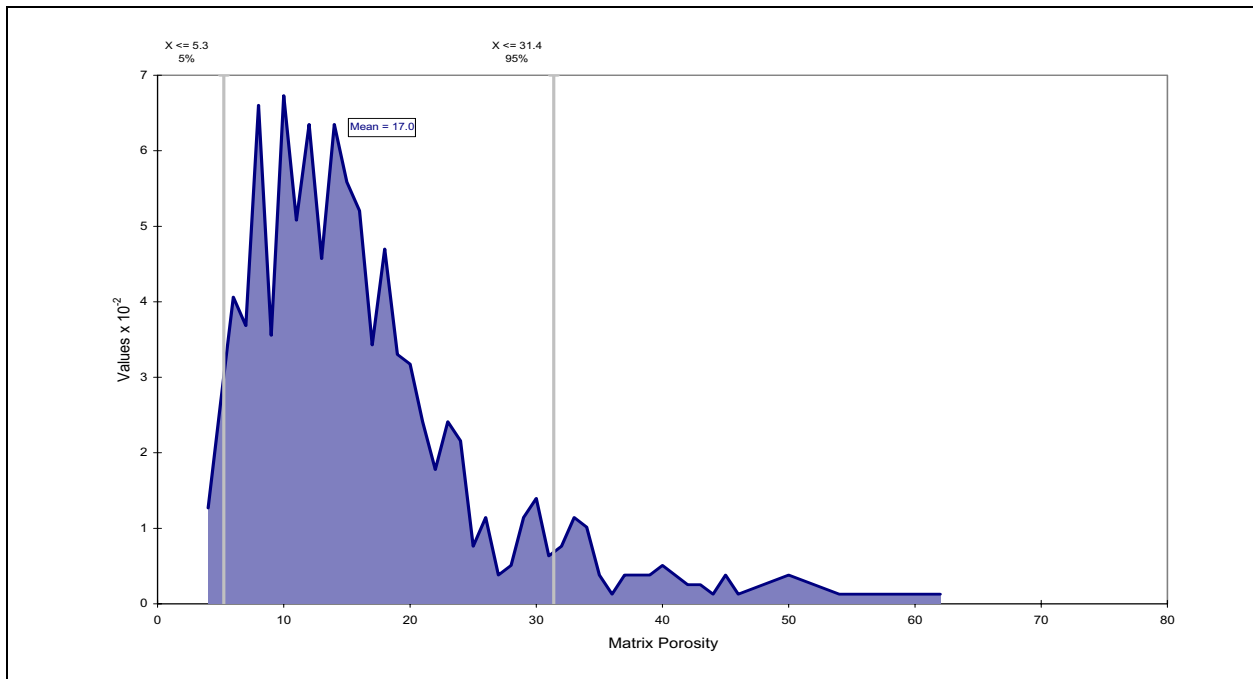


Figure 5-25
PFD of Porosity Data (in Percent): Devitrified Alteration (771 Samples)

documentation (BN, 2002), 20 different lithologies were identified. Of these 20, 15 refer directly to the volcanic units. The remaining five lithologies represent alluvium, dolomite, intrusives, siltstone, and argillite.

In assessment of the lithologies, it became clear that degree of welding is expected to play a major factor in differentiating matrix porosity. Further, degree of welding is an indicator of the extent to which pores in the material are filled or healed. Thus, it seems likely that lithology aspects that refer to the amount of solidification of the pore space can be expected to be effective for estimating matrix porosity.

The matrix porosity data was plotted as a function of the lithology. Based on these plots and geologic reasoning, the matrix porosity data for volcanic rocks were grouped into four groups based on the lithology of the unit. These groups are:

Group 1. Welded Tuff, Densely Welded Tuff, Moderately Welded Tuff, Lava, and Vitrophyre

Group 2. Bedded Tuff and Nonwelded Tuff

Group 3. Partially Welded Tuff and Pumaceous Lava

Group 4. Flow Breccia and Tuff Breccia

Analysis results for these four groups are discussed in the remainder of this section. Analysis results for the LCA, clastic confining units, and intrusive confining units are also discussed.

It should be noted that an attempt was made to incorporate porosity data from Rainier Mesa into this analysis. The porosity data from Rainier Mesa included numerous measurements that were collected from various welded tuffs and bedded tuffs. As a result, the Rainier Mesa porosity data can be subdivided into both Groups 1 and 2. The results of statistical tests showed, however, that there was evidence for concluding that the mean value for the Group 1 data and the variance value for the Group 2 data were different if the datasets were combined. The results of the tests can be seen in [Table 5-2](#). As a result, the Rainier Mesa porosity data were not combined with the existing PM-OV data for either of the two Groups.

Table 5-2
Test Statistics for the Comparison of Rainier Mesa and
PM-OV Porosity Data Based on Lithology

	Group 1 Lithologies	Group 2 Lithologies
t Statistic	-2.5587	12.58216
t Critical two-tail	1.9619	1.961707
F Statistic	1.5338	1.79138
F Critical one-tail	1.5509	1.18846

Group 1 - Welded Tuff, Densely Welded Tuff, Moderately Welded Tuff, Lava, and Vitrophyre

Figure 5-26 is a plot of the combined welded tuff, densely welded tuff, moderately welded tuff, lava, and vitrophyre matrix porosity values, along with the fitted lognormal PDF and CDF. These lithologies produce a mean porosity value of about 17.5 percent, with a clearly asymmetric distribution. Nineteen probability distributions were fit to the data, then ranked by goodness-of-fit. The distributions, their parameters, and their RMS-error are summarized in Table 5-3. Figure 5-26 showed the lognormal distribution fit, which according to Table 5-3 is the 3rd ranked distribution. Figure 5-27 shows the RMS (root-mean squared)-error for each distribution relative to the #1 ranked distribution, the Pearson V. It is clear that the top three ranked distributions are indistinguishable from each other. The lognormal distribution is chosen because of its widespread acceptance in the subsurface flow and transport literature. When used in the CAU-scale modeling, this distribution will be truncated at the lower end to prevent negative numbers.

From the plot of matrix porosity with depth, Figure 5-8, it is hypothesized that the matrix porosity of the material does not decrease substantially with depth for the welded units. Outlier values, particularly large porosity values, disappear at depth. For the purposes of the CAU model, the matrix porosity of the welded units will not be treated as depth dependent; but, the values that represent the tails of the distribution will be restricted when applied to the model grid. It would be inconsistent with the data to allow large matrix porosity values (larger than 45 percent) to occur in the saturated zone.

Group 2 - Bedded Tuff and Nonwelded Tuff

The second group of lithologies represented the non-welded and bedded tuffs. Figure 5-28 is a plot of the porosity data with the fitted normal PDF and CDF. The fit of 19 PDFs is presented in Table 5-4. The normal distribution is not the top-ranked distribution, rather it was second ranked. Figure 5-29 shows the relative root-mean squared (RMS)-error for each of the distributions. Unlike group one, the second ranked distribution is distinguishable from the first ranked, logistic distribution (Figure 5-30). The mean is essentially the same, but the standard deviation is slightly smaller for the normal distribution.

Even with the reduced standard deviation of the normal distribution, the range of values as presented by this distribution is too large because of the depth dependence shown in Figure 5-7. The straight line in Figure 5-7 is an equation that describes the mean matrix porosity as a function of depth, and it is given by the equation

$$\text{Mean porosity} = -0.022 * \text{Depth(meters)} + 51.35 \quad (5-3)$$

This equation indicates that the expected mean porosity is 51.35 percent at the land surface, and decreases at the rate of 0.022 percent per meter depth. At any particular depth, the mean porosity is given by Equation 5-3, but the variance is smaller than that shown in Table 5-4. The assumption will be made that the variance of the distribution will not change as a function of depth such that the range of values is the same at all depths. Additionally, there is no reason to expect the trend of decreasing porosity with depth to continue beyond the range of the

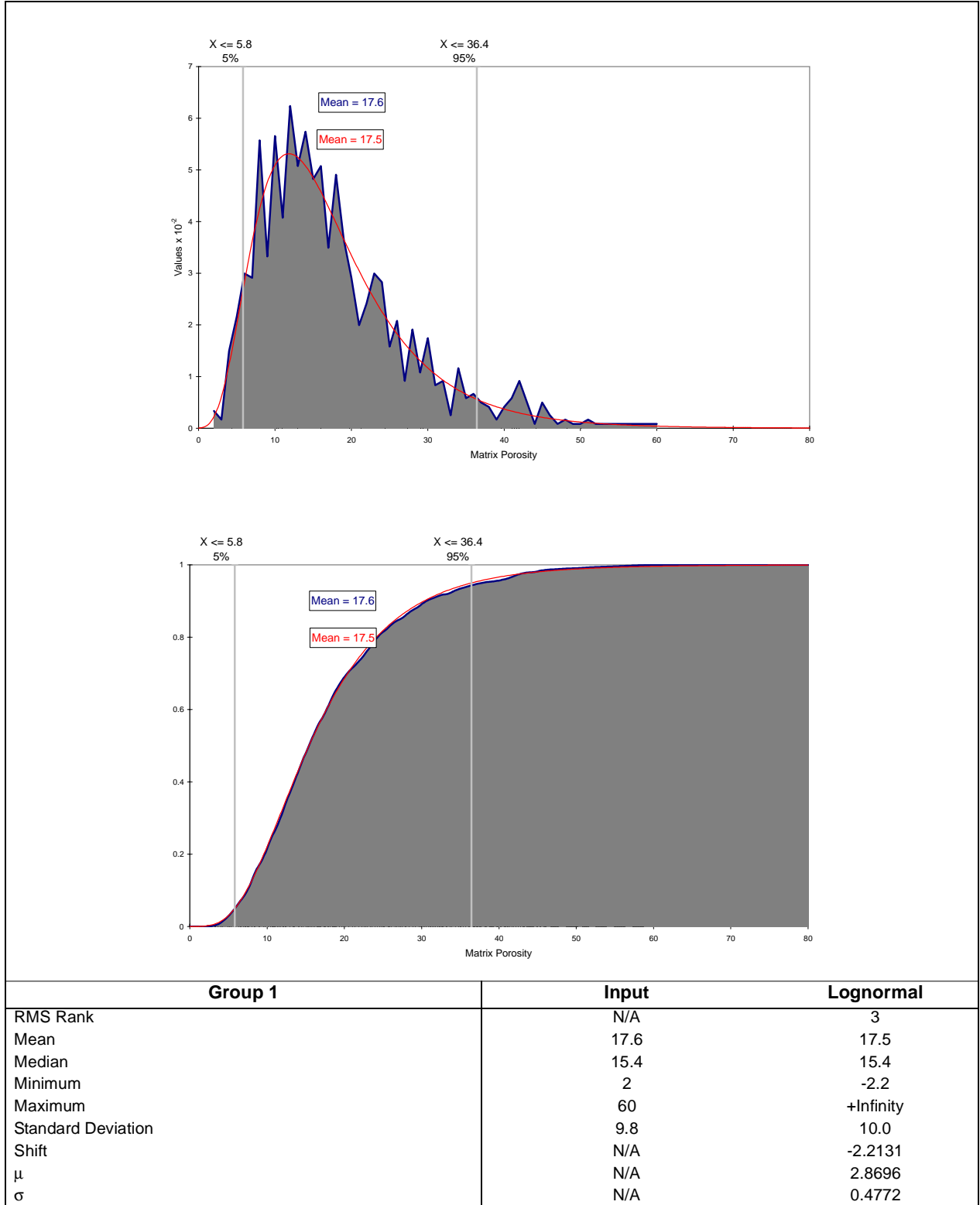
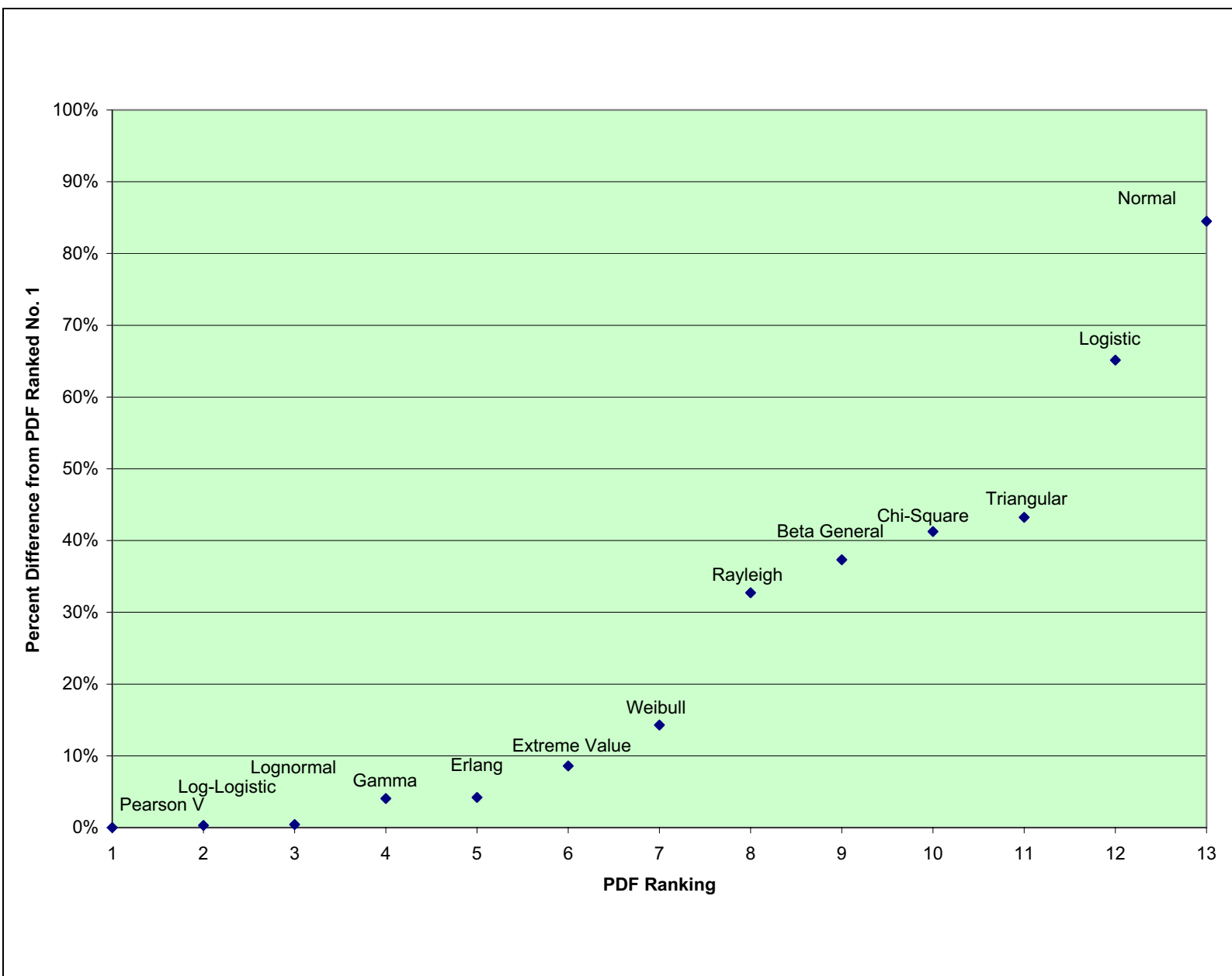


Figure 5-26
 PDF and CDF Curve Fits for Group 1: Lognormal (Format 2) Distribution
 (Matrix Porosity in Percent)

**Table 5-3
Group 1 Summary Statistics**

Group 1	Input	Pearson V	Log-Logistic	Lognormal	Gamma	Erlang
RMS Rank		1	2	3	4	5
RMS Error		2.6E-05	2.6E-05	2.6E-05	2.7E-05	2.7E-05
RPD from RMS Rank 1		0%	0.3%	0.4%	4.1%	4.2%
Mean	17.6	17.7	19.0	17.5	17.2	17.0
Mode	12	11.9	12.2	11.8	11.8	11.9
Median	15.4	15.4	15.5	15.4	15.4	15.4
Minimum	2	-7.2	0.3	-2.2	2.1	1.6
Maximum	60	+Infinity	+Infinity	+Infinity	+Infinity	+Infinity
Standard Deviation	9.8	10.6	16.1	10.0	9.0	8.9
Variance	9.5E+01	1.1E+02	2.6E+02	1.0E+02	8.2E+01	7.9E+01
Skewness	1.2	2.1	N/A	1.6	1.2	1.2
Kurtosis	4.7	13.0	N/A	8.2	5.1	5
Group 1	Input	Extreme Value	Weibull	Rayleigh	Beta General	Chi-Square
RMS Rank		6	7	8	9	10
RMS Error		2.8E-05	3.0E-05	3.4E-05	3.6E-05	3.7E-05
RPD from RMS Rank 1		9%	14%	33%	37%	41%
Mean	17.6	16.5	16.9	16.0	16.3	15.3
Mode	12	12.6	11.9	13.1	11.8	13.3
Median	15.4	15.1	15.4	15.2	15.3	14.7
Minimum	2	-Infinity	3.5	1.6	3.5	-14.7
Maximum	60	+Infinity	+Infinity	+Infinity	43.675	+Infinity
Standard Deviation	9.8	8.8	8.4	7.6	7.5	7.7
Variance	9.5E+01	7.7E+01	7.0E+01	5.7E+01	5.6E+01	6.0E+01
Skewness	1.2	1.1	0.9 [estimated]	0.6	0.5	0.5
Kurtosis	4.7	5.4	3.5 [estimated]	3.2	2.7	3.4
Group 1	Input	Triangular	Logistic	Normal	Exponential	Uniform
RMS Rank		11	12	13	14	15
RMS Error		3.7E-05	4.3E-05	4.8E-05	9.2E-05	1.2E-04
RPD from RMS Rank 1		43%	65%	85%	254%	379%
Mean	17.6	16.2	13.9	14.1	22.2	15.5
Mode	12	10.2	13.9	14.1	7.2	N/A
Median	15.4	15.2	13.9	14.1	17.6	15.5
Minimum	2	1.7	-Infinity	-Infinity	7.2	4.0
Maximum	60	36.8	+Infinity	+Infinity	+Infinity	27.0
Standard Deviation	9.8	7.5	8.7	7.8	15.0	6.6
Variance	9.5E+01	5.6E+01	7.5E+01	6.1E+01	2.2E+02	4.4E+01
Skewness	1.2	0.4	0	0	2	0
Kurtosis	4.7	2.4	4.2	3	9	1.8
Group 1	Input	Pareto	Error Function	Inverse Gaussian	Student's t	
RMS Rank		16	17	18	19	
RMS Error		1.6E-04	2.9E-04	6.6E-04	6.9E-04	
RPD from RMS Rank 1		528%	1031%	2450%	2567%	
Mean	17.6	N/A	0	18.7	0	
Mode	12	8.0	0	2.0	0	
Median	15.4	24.9	0	2.0	0	
Minimum	2	8.0	-Infinity	2.0	-Infinity	
Maximum	60	+Infinity	+Infinity	+Infinity	+Infinity	
Standard Deviation	9.8	N/A	17.0	8.9E+02	+Infinity	
Variance	9.5E+01	N/A	2.9E+02	8.0E+05	+Infinity	
Skewness	1.2	N/A	0	1.6E+02	+Infinity	
Kurtosis	4.7	N/A	3	4.3E+04	+Infinity	

Figure 5-27
Comparison of Group 1 PDF Root Mean Squared Errors



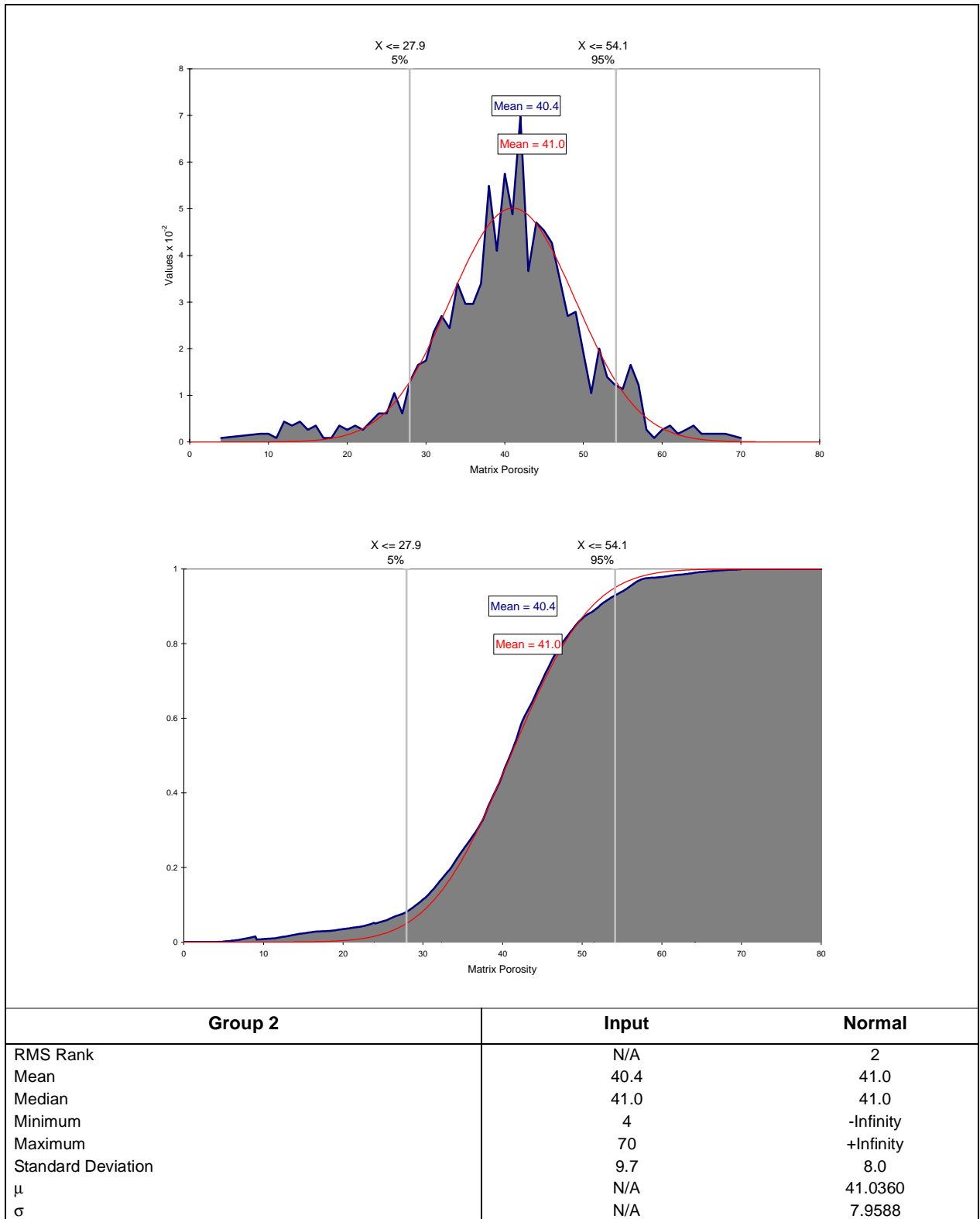


Figure 5-28
PDF and CDF Curve Fits for Group 2: Normal Distribution
(Matrix Porosity in Percent)

**Table 5-4
Group 2 Summary Statistics**

Group 2	Input	Logistic	Normal	Beta General	Lognormal	Erlang
RMS Rank		1	2	3	4	5
RMS Error		2.3E-05	2.7E-05	2.7E-05	2.7E-05	2.8E-05
RPD from RMS Rank 1		0%	17.6%	17.8%	19.5%	20.8%
Mean	40.4	41.1	41.0	40.7	41.4	41.5
Mode	42	41.1	41.0	41.2	40.8	40.7
Median	41.0	41.1	41.0	40.9	41.2	41.2
Minimum	4	-Infinity	-Infinity	-3.3E+02	-1.3E+02	-42.2
Maximum	70	+Infinity	+Infinity	1.4E+02	+Infinity	+Infinity
Standard Deviation	9.7	8.8	8.0	8.0	8.0	8.0
Variance	9.4E+01	7.8E+01	6.3E+01	6.4E+01	6.3E+01	6.4E+01
Skewness	-0.4	0	0	-0.1	0.1	0.2
Kurtosis	4.3	4.2	3	3.0	3.0	3.1
Group 2	Input	Gamma	Triangular	Log-Logistic	Chi-Square	Pearson V
RMS Rank		6	7	8	9	10
RMS Error		2.8E-05	2.8E-05	2.8E-05	3.0E-05	3.5E-05
RPD from RMS Rank 1		21%	22%	23%	34%	55%
Mean	40.4	41.5	41.1	43.2	42.2	43.2
Mode	42	40.7	41.5	40.3	40.2	39.7
Median	41.0	41.2	41.2	41.9	41.5	41.9
Minimum	4	-42.4	22.5	10.5	8.2	4.0
Maximum	70	+Infinity	59.2	+Infinity	+Infinity	+Infinity
Standard Deviation	9.7	8.1	7.5	10.0	8.2	8.9
Variance	9.4E+01	6.5E+01	5.6E+01	1.0E+02	6.8E+01	7.9E+01
Skewness	-0.4	0.2	0	1.7	0.5	1.0
Kurtosis	4.3	3.1	2.4	13.2	3.4	4.8
Group 2	Input	Extreme Value	Rayleigh	Uniform	Exponential	Pareto
RMS Rank		11	12	13	14	15
RMS Error		3.8E-05	4.0E-05	1.3E-04	1.4E-04	1.7E-04
RPD from RMS Rank 1		66%	76%	488%	499%	637%
Mean	40.4	43.7	42.7	41.5	51.1	81.3
Mode	42	39.4	39.5	N/A	33.2	32.0
Median	41.0	42.1	41.7	41.5	45.6	48.7
Minimum	4	-Infinity	26.8	26.0	33.2	32.0
Maximum	70	+Infinity	+Infinity	57	+Infinity	+Infinity
Standard Deviation	9.7	9.6	8.3	8.9	17.9	N/A
Variance	9.4E+01	9.3E+01	6.9E+01	8.0E+01	3.2E+02	N/A
Skewness	-0.4	1.1	0.6	0	2	N/A
Kurtosis	4.3	5.4	3.2	1.8	9	N/A
Group 2	Input	Error Function	Weibull	Inverse Gaussian	Student's t	
RMS Rank		16	17	18	19	
RMS Error		4.2E-04	5.1E-04	5.6E-04	5.8E-04	
RPD from RMS Rank 1		1763%	2147%	2345%	2438%	
Mean	40.4	0	62.8	40.9	0	
Mode	42	0	4.0	4.1	0	
Median	41.0	0	8.5	4.8	0	
Minimum	4	-Infinity	4.0	4.0	-Infinity	
Maximum	70	+Infinity	+Infinity	+Infinity	+Infinity	
Standard Deviation	9.7	45.9	2.2E+02	3.6E+02	+Infinity	
Variance	9.4E+01	2.1E+03	5.0E+04	1.3E+05	+Infinity	
Skewness	-0.4	0	5.6 [est]	29.2	+Infinity	
Kurtosis	4.3	3	40.1 [est]	1.4E+03	+Infinity	

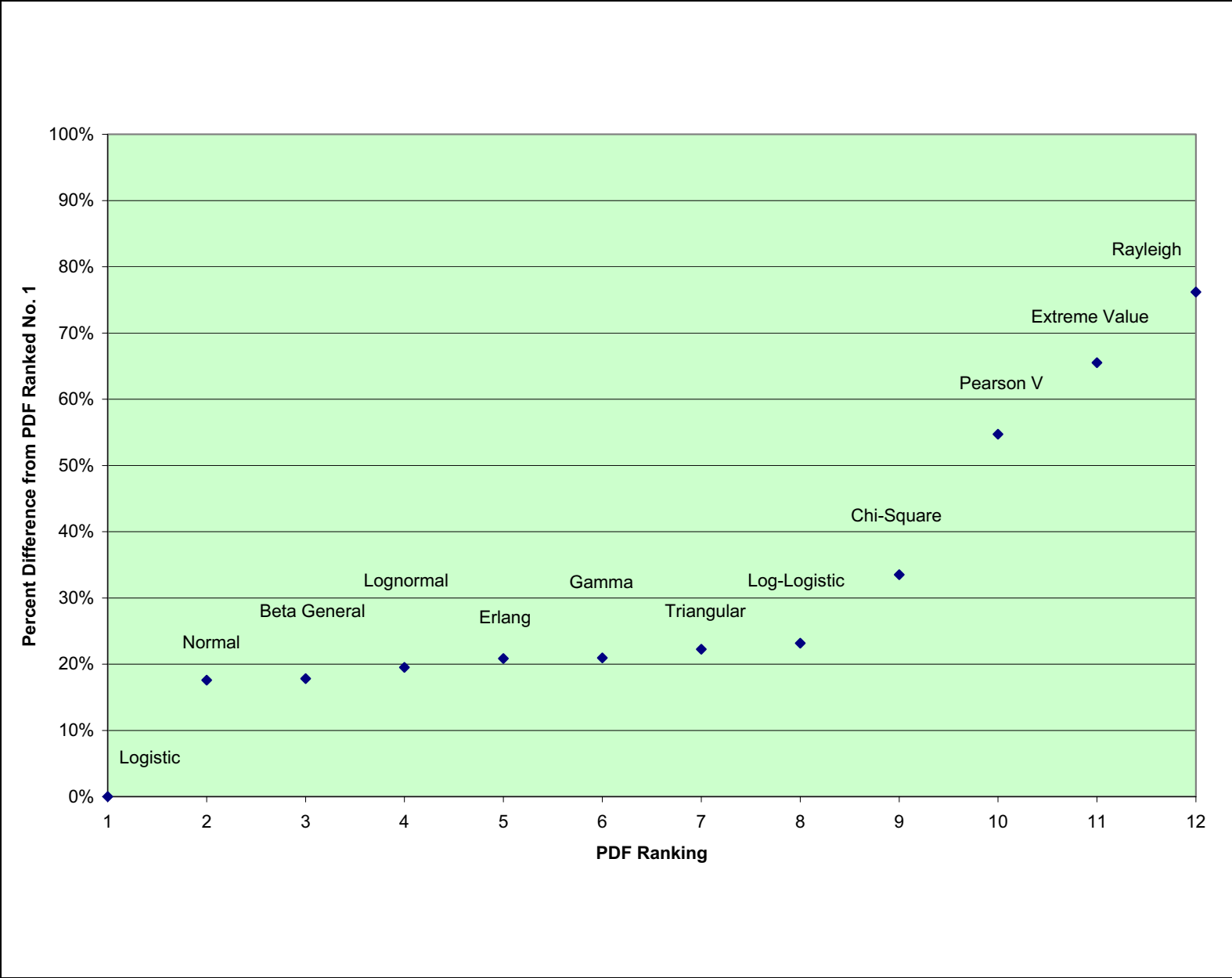


Figure 5-29
Comparison of Group 2 PDF Root Mean Squared Errors

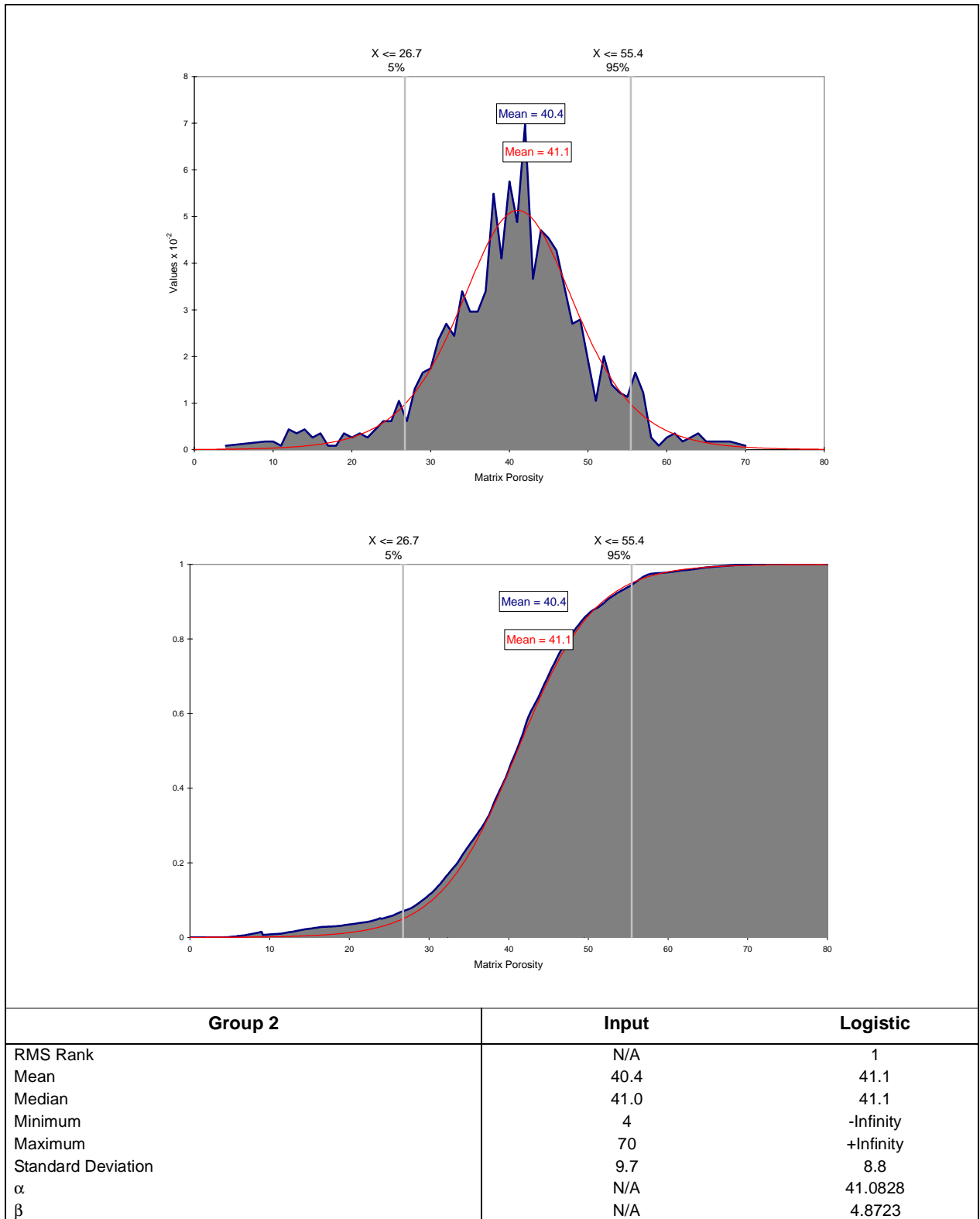


Figure 5-30
PDF and CDF Curve Fits for Group 2: Logistic Distribution
(Matrix Porosity in Percent)

measured data. If it did, that would lead to zero or negative porosities, which are physically impossible. For the CAU-scale modeling, the assumption will be made that mean porosity of the bedded and nonwelded units does not decrease below 15 percent at any depth. The variation in porosity, evident at shallower depths, should decrease at larger depths. To accommodate this expectation, the somewhat arbitrary assumption is made that for depths greater than 1,500 m, porosity must remain within the range of 10 to 20 percent.

Group 3 - Partially Welded Tuff and Pumaceous Lava

[Figure 5-31](#) is the normal PDF fitted to the porosity CFD of the partially welded tuff and the pumaceous lavas. These two lithologies have a mean porosity of about 7 percent less than the nonwelded tuffs, but have a much broader range of values. This is expected because the nature of these lithologies is quite variable. [Table 5-5](#) contains the parameters of the fitted distributions for the Group 3 data. The relative RMS-error for the fitted distributions is presented in [Figure 5-32](#). The normal distribution presented in [Figure 5-31](#) is the 6th ranked distribution. This was chosen for several reasons: (1) the distribution is common, and (2) the fit to the CFD was better for the normal than the top three ranked distributions. The distribution will need to be truncated to avoid unusually large or negative porosity values. The reader should also be aware that the apparent depth dependence of the data ([Figure 5-10](#)) indicates that the largest porosity values are associated with only the shallowest depths, and these are not relevant for saturated zone simulations. For saturated zone simulations, where the depths are generally greater than 600 m, a smaller mean porosity of 30 percent should be used. Ignoring data shallower than 200 m, there is no clear depth dependence of porosity data in [Figure 5-10](#). Too few data are available for depths greater than 700 m to make any projections of depth-dependent changes. The parameters of the normal distribution presented in [Table 5-5](#) are not correct because the mean and variance are too large. Nonetheless, this distribution of data is distinct from the welded units with low porosity and the non-welded units with larger porosity. The distribution will be used as it is, but the upper bound may need to be reduced during the transport simulations.

Group 4 - Flow Breccia and Tuff Breccia

[Figure 5-33](#) is the normal PDF fitted to the PFD data for the breccia units. The parameters of the 19 distributions fit to this data are presented in [Table 5-6](#). As with the other cases, the normal distribution is not the top-ranked distribution. As seen in [Figure 5-34](#), the top nine or so distributions have similar statistics. In most of the cases, the fit of the PDF and the corresponding CDF, do not fit the data well, especially at the tails. The data show a generally symmetric distribution, with a mean value between the welded units and the pumaceous units. This is expected because this lithology is made up of broken welded units, which are expected to have relatively small matrix porosity values. The variances are quite large for these small-scale measurements.

No depth dependence could be determined from these data as shown in [Figure 5-9](#). The range of depths is too small to estimate any trend with depth. Therefore, the range of values is assumed to apply over all depths. The distribution will need to be truncated before using it in the CAU modeling to avoid negative values.

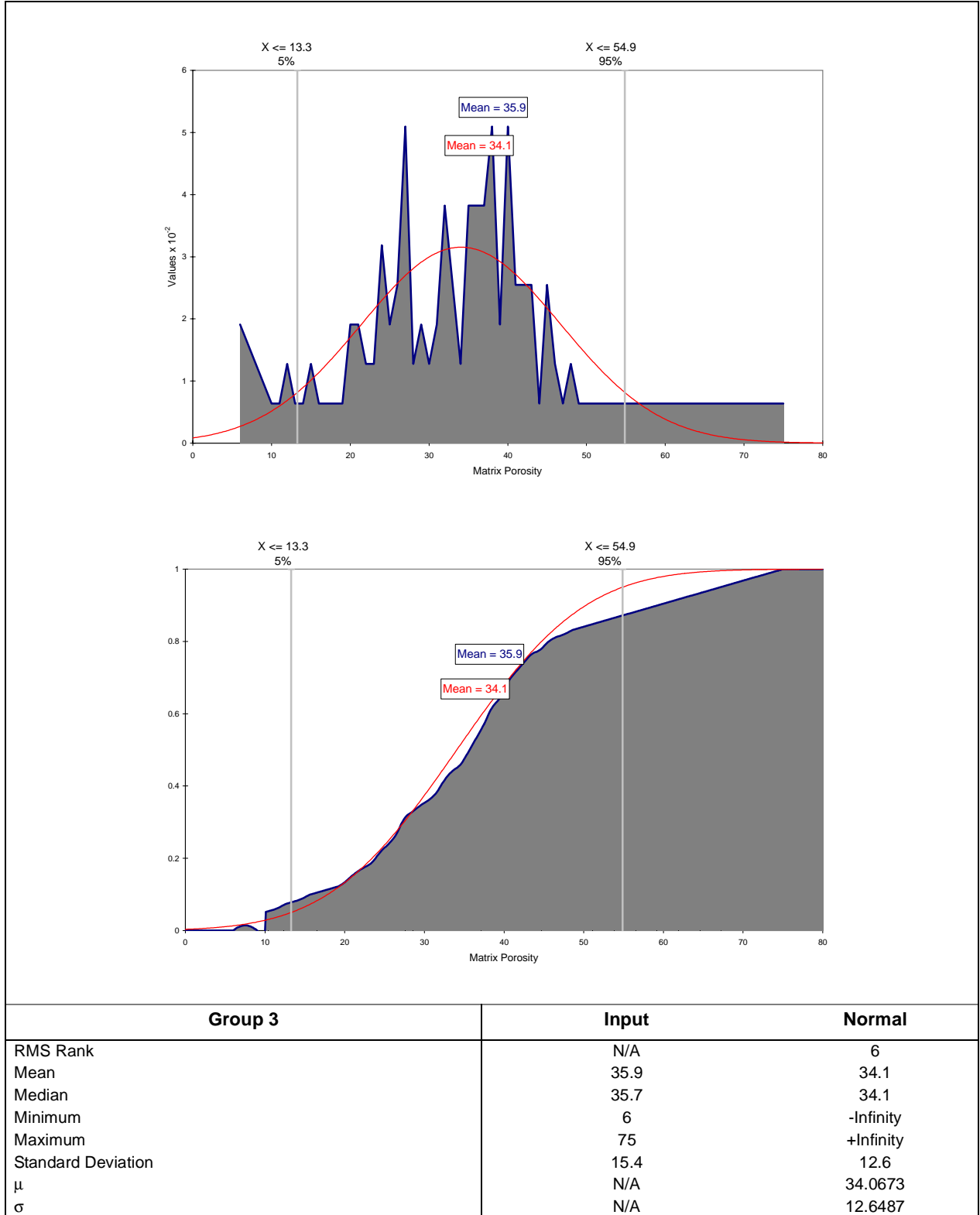
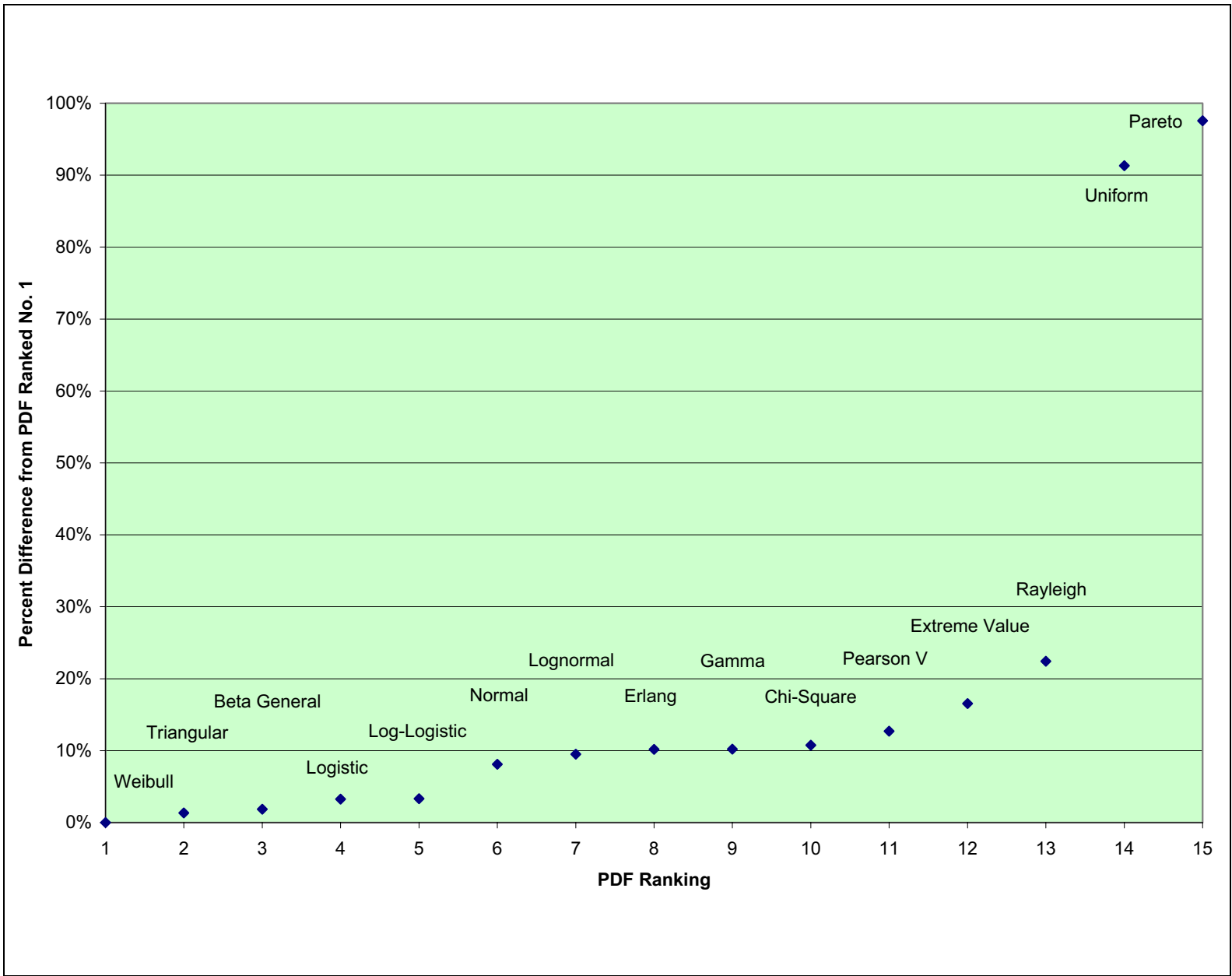


Figure 5-31
PDF and CDF Curve Fits for Group 3: Normal Distribution
(Matrix Porosity in Percent)

**Table 5-5
Group 3 Summary Statistics**

Group 3	Input	Weibull	Triangular	Beta General	Logistic	Log-Logistic
RMS Rank		1	2	3	4	5
RMS Error		8.7E-05	8.8E-05	8.8E-05	8.9E-05	8.9E-05
RPD from RMS Rank 1		0%	1.3%	1.9%	3.2%	3.3%
Mean	35.9	29.6	30.4	26.3	34.3	34.3
Mode	N/A	35.9	38.0	37.4	34.3	34.3
Median	35.7	31.9	31.9	29.9	34.3	34.3
Minimum	6	-1.1E+03	-2.5	-1.1E+04	-Infinity	-10624.7
Maximum	75	+Infinity	55.8	49.5	+Infinity	+Infinity
Standard Deviation	15.4	14.5	12.2	16.1	14.2	14.0
Variance	2.4E+02	2.1E+02	1.5E+02	2.6E+02	2.0E+02	2.0E+02
Skewness	0.4	-1.0 [est]	-0.3	-1.4	0	0.0
Kurtosis	3.0	4.2 [est]	2.4	5.8	4.2	4.2
Group 3	Input	Normal	Lognormal	Erlang	Gamma	Chi-Square
RMS Rank		6	7	8	9	10
RMS Error		9.4E-05	9.5E-05	9.5E-05	9.5E-05	9.6E-05
RPD from RMS Rank 1		8%	9%	10%	10%	11%
Mean	35.9	34.1	34.9	35.1	35.1	35.5
Mode	N/A	34.1	33.8	33.5	33.5	33.5
Median	35.7	34.1	34.6	34.5	34.6	34.9
Minimum	6	-Infinity	-1.9E+02	-72.1	-72.6	-52.5
Maximum	75	+Infinity	+Infinity	+Infinity	+Infinity	+Infinity
Standard Deviation	15.4	12.6	12.9	13.1	13.2	13.3
Variance	2.4E+02	1.6E+02	1.7E+02	1.7E+02	1.7E+02	1.8E+02
Skewness	0.4	0	0.2	0.2	0.2	0.3
Kurtosis	3.0	3	3.1	3.1	3.1	3.1
Group 3	Input	Pearson V	Extreme Value	Rayleigh	Uniform	Pareto
RMS Rank		11	12	13	14	15
RMS Error		9.7E-05	1.0E-04	1.1E-04	1.7E-04	1.7E-04
RPD from RMS Rank 1		13%	17%	22%	91%	98%
Mean	35.9	36.4	39.2	37.5	39.6	N/A
Mode	N/A	32.7	32.1	32.1	N/A	24.0
Median	35.7	35.2	36.6	35.8	39.6	49.2
Minimum	6	-60.4	-Infinity	10.7	14.1	24.0
Maximum	75	+Infinity	+Infinity	+Infinity	65.1	+Infinity
Standard Deviation	15.4	13.9	15.8	14.0	14.7	N/A
Variance	2.4E+02	1.9E+02	2.5E+02	2.0E+02	2.2E+02	N/A
Skewness	0.4	0.6	1.1	0.6	0	N/A
Kurtosis	3.0	3.7	5.4	3.2	1.8	N/A
Group 3	Input	Exponential	Error Function	Inverse Gaussian	Student's t	
RMS Rank		16	17	18	19	
RMS Error		2.2E-04	2.9E-04	4.3E-04	4.7E-04	
RPD from RMS Rank 1		150%	231%	393%	438%	
Mean	35.9	51.5	0	36.6	0	
Mode	N/A	6.0	0	6.1	0	
Median	35.7	37.5	0	7.0	0	
Minimum	6	6.0	-Infinity	6.0	-Infinity	
Maximum	75	+Infinity	+Infinity	+Infinity	+Infinity	
Standard Deviation	15.4	45.5	35.6	2.5E+02	+Infinity	
Variance	2.4E+02	2.1E+03	1.3E+03	6.2E+04	+Infinity	
Skewness	0.4	2	0	24.3	+Infinity	
Kurtosis	3.0	9	3	9.9E+02	+Infinity	

Figure 5-32
Comparison of Group 3 PDF Root Mean Squared Errors



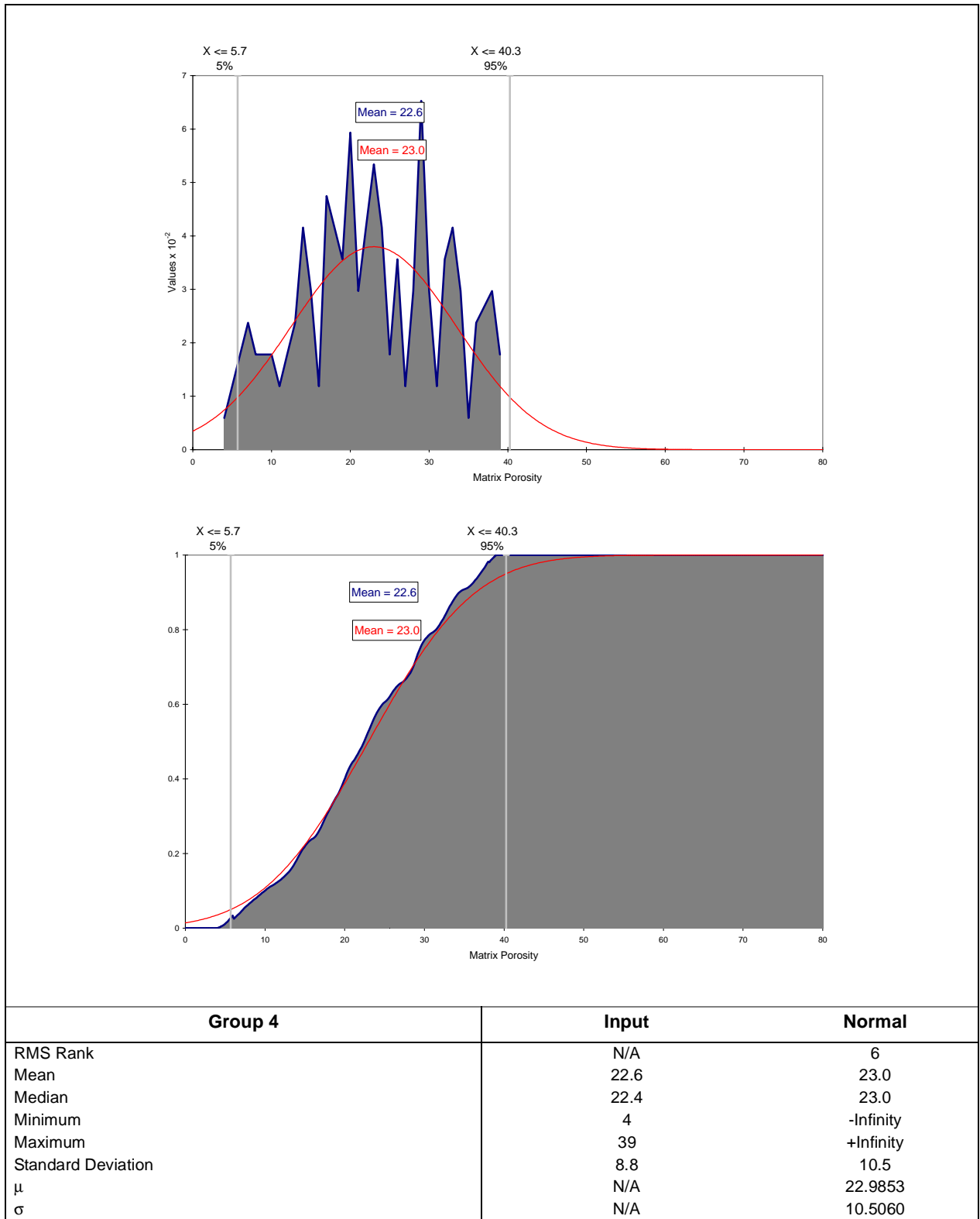
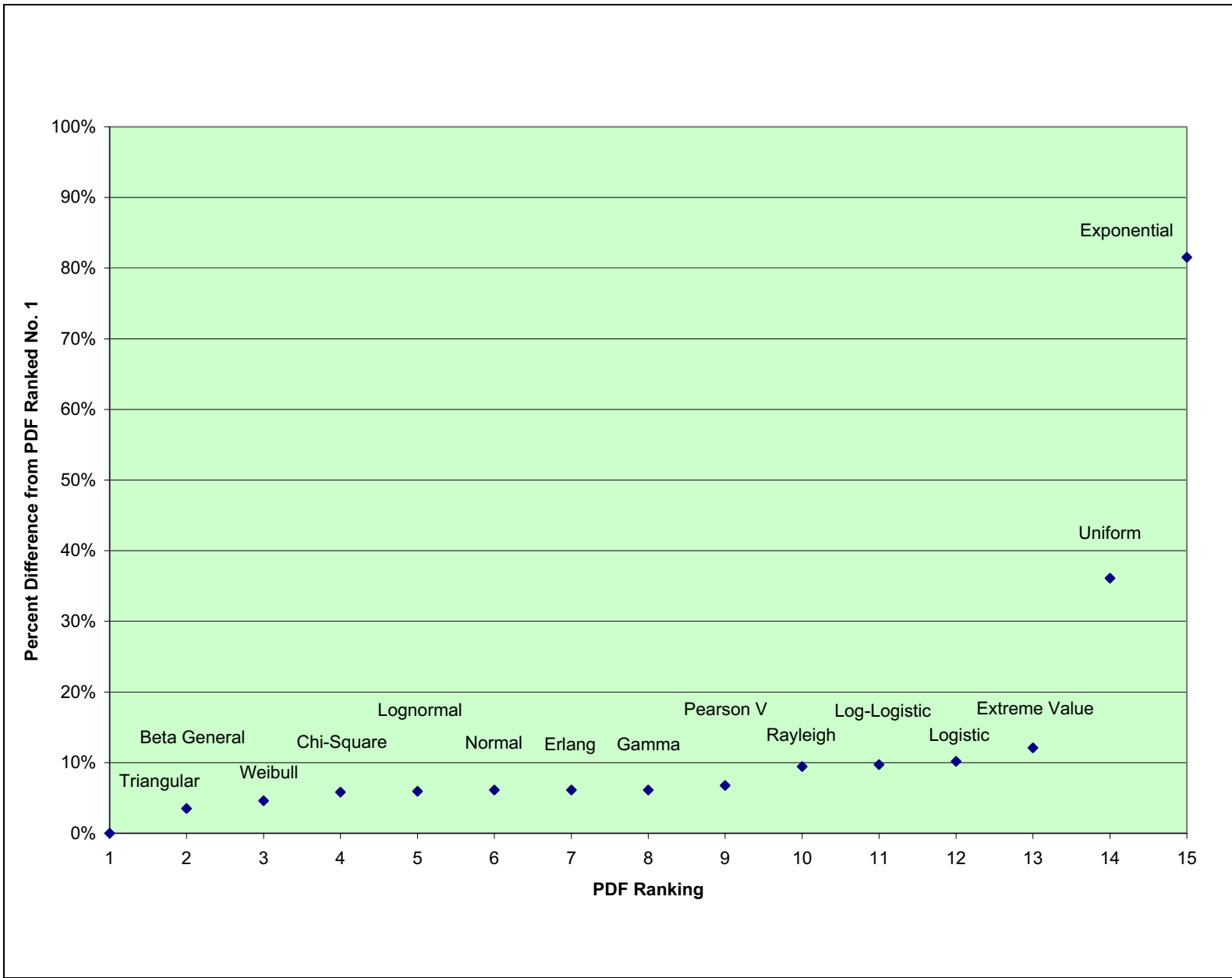


Figure 5-33
PDF and CDF Curve Fits for Group 4: Normal Distribution
(Matrix Porosity in Percent)

Table 5-6
Group 4 Summary Statistics

Group 4	Input	Triangular	Beta General	Weibull	Chi-Square	Lognormal
RMS Rank		1	2	3	4	5
RMS Error		1.5E-04	1.5E-04	1.5E-04	1.6E-04	1.6E-04
RPD from RMS Rank 1		0%	3.5%	4.6%	5.9%	5.9%
Mean	22.6	23.7	23.0	23.8	24.1	24.0
Mode	29.0	20.0	23.4	22.5	22.1	22.3
Median	22.4	23.0	23.1	23.3	23.4	23.4
Minimum	4	1.9	2.5	-1.7	-31.9	-70.8
Maximum	39	49.2	42.6	+Infinity	+Infinity	+Infinity
Standard Deviation	8.8	9.7	9.1	10.1	10.6	10.6
Variance	7.8E+01	9.5E+01	8.3E+01	1.0E+02	1.1E+02	1.1E+02
Skewness	-0.1	0.2	0	0.2 [est]	0.4	0.3
Kurtosis	2.1	2.4	2.1	2.7 [est]	3.2	3.2
Group 4	Input	Normal	Erlang	Gamma	Pearson V	Rayleigh
RMS Rank		6	7	8	9	10
RMS Error		1.6E-04	1.6E-04	1.6E-04	1.6E-04	1.6E-04
RPD from RMS Rank 1		6%	6%	6%	7%	9%
Mean	22.6	23.0	24.2	24.3	24.5	25.1
Mode	29.0	23.0	21.9	22.0	21.7	20.9
Median	22.4	23.0	23.5	23.6	23.5	23.9
Minimum	4	-Infinity	-24.5	-24.4	-56.8	4.4
Maximum	39	+Infinity	+Infinity	+Infinity	+Infinity	+Infinity
Standard Deviation	8.8	10.5	10.6	10.7	10.9	10.9
Variance	7.8E+01	1.1E+02	1.1E+02	1.1E+02	1.2E+02	1.2E+02
Skewness	-0.1	0	0.4	0.4	0.5	0.6
Kurtosis	2.1	3	3.3	3.3	3.6	3.2
Group 4	Input	Log-Logistic	Logistic	Extreme Value	Uniform	Exponential
RMS Rank		11	12	13	14	15
RMS Error		1.6E-04	1.6E-04	1.6E-04	2.0E-04	2.7E-04
RPD from RMS Rank 1		10%	10%	12%	36%	82%
Mean	22.6	23.9	22.9	26.2	22.6	35.6
Mode	29.0	22.4	22.9	20.6	N/A	14.0
Median	22.4	23.2	22.9	24.2	22.6	29.0
Minimum	4	-74.9	-Infinity	-Infinity	5.6	14.0
Maximum	39	+Infinity	+Infinity	+Infinity	39.6	+Infinity
Standard Deviation	8.8	11.9	11.7	12.4	9.8	21.6
Variance	7.8E+01	1.4E+02	1.4E+02	1.5E+02	9.7E+01	4.7E+02
Skewness	-0.1	0.6	0	1.1	0	2
Kurtosis	2.1	5.1	4.2	5.4	1.8	9
Group 4	Input	Pareto	Error Function	Inverse Gaussian	Student's t	
RMS Rank		16	17	18	19	
RMS Error		3.3E-04	5.6E-04	9.1E-04	9.8E-04	
RPD from RMS Rank 1		128%	281%	519%	564%	
Mean	22.6	5.5E+02	0	23.6	0	
Mode	29.0	17.0	0	4.0	0	
Median	22.4	33.3	0	4.3	0	
Minimum	4	17.0	-Infinity	4.0	-Infinity	
Maximum	39	+Infinity	+Infinity	+Infinity	+Infinity	
Standard Deviation	8.8	N/A	23.9	2.3E+02	+Infinity	
Variance	7.8E+01	N/A	5.7E+02	5.1E+04	+Infinity	
Skewness	-0.1	N/A	0	34.6	+Infinity	
Kurtosis	2.1	N/A	3	2.0E+03	+Infinity	

Figure 5-34
Comparison of Group 4 PDF Root Mean Squared Errors



Lower Carbonate Aquifer

The matrix porosity of the carbonate aquifers is based on a very small number of samples. The distribution from the Regional Tritium Transport model (DOE/NV, 1997) is used because no new data were available. In that report, the matrix porosity of the carbonates was assumed to be uniformly distributed with a range of 1 to 15 percent.

Clastic Confining Units and Intrusive Confining Units

The Paleozoic clastic confining units and the intrusive confining units are assumed to be fracture flow dominated with crystalline matrix material. For the Pahute Mesa CAU model, these units are assumed to have negligible matrix porosity.

5.5 Data Limitations

Most of the data were derived from geophysical logging of boreholes that penetrated only a short distance into the saturated zone. The vadose zone porosity estimates are almost always calculated via a correction for water content. Some of the data appear to have a trend of decreasing values of porosity with depth, but the amount of data below the water table is small. The distributions of porosity values developed from all the data will be biased toward values that are too large for the saturated zone. The modelers need to be aware that smaller matrix porosity values are most likely the norm at depth. In addition, the variances calculated using the dataset without depth correction will be overestimated. The variance contains elements of the trend. Thus, when applied to the CAU model, the variances will need to be reduced.

5.6 Scaling Considerations

Scaling of matrix porosity will consider the following issues. The porosity data are clearly very small-scale measurements. As noted by McKenna and Rautman (1996), porosity can be quite effectively scaled by the volume-variance technique, which is also presented in several textbooks including Journel and Huijbregts (1978), and Vanmarcke (1983). In both of these publications, the variance reduction due to spatial averaging is a function of the ratio of the correlation length of the point process to the averaging interval. As the point process correlation length is unknown, this method will be difficult to apply.

Additional complications related to heterogeneity are the result of widely different lithologies in one HSU. Consider for example, a package of welded tuffs sandwiched between non-welded tuffs in a single Composite Unit HSU. Because the welded unit is likely to transmit most of the flow, the scaled matrix porosity should reflect the welded unit, rather than a simple numerical average of all lithologies. This adds uncertainty to the scaling process that cautions against a simple volume-averaging approach, at least at smaller scales.

In all cases, the scaling process is not expected to change the mean value of the matrix porosity. However, the scaling, which amounts to spatial averaging, will reduce the variance in the parameter values. This variance reduction will limit the

acceptable range of values for each of the HSUs. The amount of variance reduction cannot be calculated at this time. Therefore the approach for incorporating scaling of matrix porosity in the CAU model has two components. First, the mean value is unchanged by scaling and will be used as presented in [Table 5-7](#). The variance is reduced by scaling, but it is not possible at this time to determine the amount of reduction. Initially, during the uncertainty and sensitivity analyses, the full “point process” variance will be used. If the model results are sensitive to matrix porosity, and in particular the range of uncertainty, that will be noted for future consideration.

5.7 Summary of Matrix Porosity by Hydrostratigraphic Unit

[Table 5-7](#) is a summary of the matrix porosity distributions assigned to each of the HSUs expected in the Pahute Mesa CAU model. If a unit is primarily non-fractured such as alluvium, bedded tuff, or non-welded tuff, the matrix porosity distributions will not be presented in this table. For the HSUs that had matrix porosity data available, the reported lower bound, upper bound, and mean values were obtained from the statistical distribution that best fit the data. For the remaining HSUs, matrix porosity distributions were obtained in two different ways. Specifically, for HSUs that had dominant lithologies that corresponded to the groupings defined in [Section 5.4.4](#), the lower bound, upper bound, and mean values were obtained from the statistical distribution that best fit the data for that lithologic group. As a result, numerous HSUs have the same lower bound, upper bound, and mean values because they are composed of similar lithologic units. For the remaining HSUs, the lower bound, upper bound, and mean values were obtained from the regional groundwater flow and tritium transport model (DOE/NV, 1997).

Table 5-7
Pahute Mesa - Matrix Porosity - Dominant Lithology for Each HSU
 (Page 1 of 2)

Layer Number	Symbol	Name	Dominant HGU	Continuous Lithology	Lower Bound	Mean	Upper Bound	Distribution	Group Number
45	YVCM	Younger Volcanic Composite Unit	LFA, WTA, VTA	PWT	6	34.1	75	Normal	3
44	TCVA	Thirsty Canyon Volcanic Aquifer	WTA, LFA, lesser VTA	WT	14.3	46.4	70.9	Triangular	N/A
43	DVCM	Detached Volcanics Composite Unit	WTA, LFA, TCU	PWT	6	34.1	75	Normal	3
42	DVA	Detached Volcanics Aquifer	WTA, LFA	WT	2	17.5	60	Lognorm2	1
41	FCCM	Fortymile Canyon Composite Unit	LFA, TCU, lesser WTA	PWT	6	34.1	75	Normal	3
40	FCA	Fortymile Canyon Aquifer	WTA, LFA	WT	2	17.5	60	Lognorm2	1
39	TMCM	Timber Mountain Composite Unit	TCU, unaltered WTA, lesser LFA	DWT	2.4	17.4	63	Lognorm2	N/A
38	THLFA	Tannenbaum Hill Lava-flow Aquifer	LFA	LA	2	17.5	60	Lognorm2	1
37	THCM	Tannenbaum Hill Composite Unit	TCU, lesser WTA	NWT	4	41.0	70	Normal	2
36	TMA	Timber Mountain Aquifer	WTA, minor VTA	WT	4.4	28.6	68.4	Triangular	N/A
33	WWA	Windy Wash Aquifer	LFA	LA	2	17.5	60	Lognorm2	1
32	PCM	Paintbrush Composite Unit	WTA, LFA, TCU	MWT	2	17.5	60	Lognorm2	1
31	PVTA	Paintbrush Vitric-tuff Aquifer	VTA	BED	10	43.5	57	Logistic	N/A
30	BA	Benham Aquifer	LFA	LA	3.5	20.4	33.6	Triangular	N/A
28	TCA	Tiva Canyon Aquifer	WTA	WT	2	17.5	60	Lognorm2	1
27	PLFA	Paintbrush Lava-flow Aquifer	LFA	LA	2.0	23.6	45.1	Uniform	N/A
25	TSA	Topopah Spring Aquifer	WTA	WT	2	17.5	60	Lognorm2	1
24	YMCFCM	Yucca Mountain Crater Flat Composite Unit	LFA, WTA, TCU	PWT	6	34.1	75	Normal	3
23	CHVTA	Calico Hills Vitric-tuff Aquifer	VTA	NWT	28	40.7	49	Logistic	N/A
22	CHVCM	Calico Hills Vitric Composite Unit	VTA, LFA	NWT	0	26.5	44	Normal	N/A

Table 5-7
Pahute Mesa - Matrix Porosity - Dominant Lithology for Each HSU
 (Page 2 of 2)

Layer Number	Symbol	Name	Dominant HGU	Continuous Lithology	Lower Bound	Mean	Upper Bound	Distribution	Group Number
21	CHZCM	Calico Hills Zeolitic Composite Unit	LFA, TCU	NWT	0	9.2	75	Normal	N/A
20	CHCU	Calico Hills Confining Unit	TCU, minor LFA	NWT	4	41.0	70	Normal	2
19	IA	Inlet Aquifer	LFA	LA	2	17.5	60	Lognorm2	1
18	CFCM	Crater Flat Composite Unit	LFA, intercalated TCU	WT	2	17.5	60	Lognorm2	1
16	KA	Kearsarge Aquifer	LFA	LA	2	17.5	60	Lognorm2	1
14	BRA	Belted Range Aquifer	LFA, WTA, lesser TCU	WT	2.0	22.0	42.0	Uniform	N/A
13	PBRCM	Pre-belted Range Composite Unit	TCU, WTA, LFA	PWT	3.2	17.2	29.5	Triangular	N/A
12	BMICU	Black Mountain Intrusive Confining Unit	IICU	IN	0.24	1.82	10.3	InvGauss	N/A
11	ATICU	Ammonia Tanks Intrusive Confining Unit	IICU	IN	0.24	1.82	10.3	InvGauss	N/A
10	RMICU	Rainier Mesa Intrusive Confining Unit	IICU	IN	0.24	1.82	10.3	InvGauss	N/A
9	CCICU	Claim Canyon Intrusive Confining Unit	IICU	IN	0.24	1.82	10.3	InvGauss	N/A
8	CHICU	Calico Hills Intrusive Confining Unit	IICU	IN	0.24	1.82	10.3	InvGauss	N/A
7	SCICU	Silent Canyon Intrusive Confining Unit	IICU	IN	0.24	1.82	10.3	InvGauss	N/A
6	MGCU	Mesozoic Granite Confining Unit	GCU	IN	0.24	1.82	10.3	InvGauss	N/A
5	LCA3	Lower Carbonate Aquifer - Thrust Plate	CA	DM	1.0	5.0	9.7	Beta General	N/A
4	LCCU1	Lower Clastic Confining Unit - Thrust Plate	CCU	Quartzite	0.2	3.3	10	Uniform	N/A
2	LCA	Lower Carbonate Aquifer	CA	DM	1.0	5.0	9.7	Beta General	N/A
1	LCCU	Lower Clastic Confining Unit	CCU	Quartzite	0.2	3.3	10	Uniform	N/A

6.0 Effective Porosity

This section includes descriptions of the role of effective porosity in radionuclide transport in groundwater, the available effective porosity data, and the analysis of the data and associated results. The effective porosity data are first examined on the basis of the hydrogeologic unit type. Then, to accommodate the Pahute Mesa CAU model which is subdivided on the basis of HSUs, the HGU effective porosity is converted for application to HSUs. The alluvial aquifer which is a minor HGU in the PM-OV area except in the southern portion near Oasis Valley, is discussed first. The fractured volcanic aquifers which are expected to be the primary transport units within the volcanic caldera areas, are discussed second. The remaining HGUs: carbonate aquifers, vitric tuff aquifers, tuff confining units, and intrusive volcanic confining units are then discussed together. The process of converting HGU effective porosity for application to HSUs is described last.

6.1 Role of Effective Porosity in Contaminant Transport

Effective porosity affects the movement of contaminants in groundwater because it is an important factor in determining the magnitudes of groundwater velocity and matrix diffusion. The velocity of groundwater is calculated as the volumetric flow rate per cross-sectional open area. The area open to flow is the interconnected pore space through which water flows and is generally characterized by the effective porosity. Effective porosity can be related to the groundwater velocity via the equation:

$$v = q/n_e \quad (6-1)$$

where:

- v = Mean groundwater velocity length/time [L/T]
- q = Groundwater-specific discharge [L/T], which is the volumetric flow rate divided by the cross-sectional area
- n_e = Effective porosity [dimensionless]

In silt-size and larger granular materials such as alluvium, the effective porosity is often only slightly smaller than the total porosity. For example, Blout et al. (1995) provides porosity data for Frenchman Flat alluvium in the vicinity of the Radioactive Waste Management Site (RWMS). The average total porosity for six boreholes ranged from 33.9 to 38.4 percent. Burbey and Wheatcraft (1986) simulated breakthrough of tritium and chlorine-36 from the CAMBRIC tracer experiment, conducted in Frenchman Flat alluvium south of the RWMS, and determined the effective porosity to be between 31 and 36 percent. These data

from Frenchman Flat are evidence that the total porosity is an acceptable estimate for effective porosity.

In fractured media, as previously noted, two components of the porosity can be identified: a fracture porosity and a matrix porosity. Water primarily flows through the more permeable fracture openings. Thus, the fracture porosity generally controls the velocity of groundwater. The range of effective porosity in porous media (typically 15 to 40 percent) can result in a factor of 2 or 3 variation in groundwater velocity; but for fractured systems, the effective porosity variation (<0.01 to 10 percent [Freeze and Cherry, 1979]) can produce several orders of magnitude variation in pore velocity.

As discussed in [Section 5.0](#), in fractured media, permeable fractures are separated by blocks of unfractured rock material that constitute the matrix rock. Contaminants can diffuse into, and sorb onto the rock matrix. The diffusion and adsorption processes are governed, in part, by the magnitude and distribution of matrix porosity which was discussed in [Section 5.0](#).

6.2 Effective Porosity for the Alluvial Aquifer

This section includes descriptions of the available effective porosity data for the Alluvial Aquifer, and the associated data analysis and results.

6.2.1 Data Compilation

The alluvial aquifer designation applies to a variety of sediments including older Tertiary gravels, tuffaceous sediments, and nonwelded tuffs (BN, 2002). Although alluvial deposits are present in several portions of the study area, the alluvium is saturated only in the southwest corner of the model area, near Oasis Valley. The distance from the edge of the NTS boundary to the saturated alluvium is approximately 24 kilometers (km).

6.2.1.1 Data Types

The bulk porosity for an alluvial unit provides a good estimate for the effective porosity. The types of data used to determine porosity include bulk density, grain density, and water content. These parameters may be determined from laboratory measurements on cores and through the interpretation of geophysical logs. The alluvial porosity averages provided in this report were typically calculated using the water content and grain density information from cores, while bulk density was determined from geophysical logs. Water content was typically measured on cores using the weight loss at 105 degrees centigrade (°C) method. Grain densities were determined using core samples by gas volumetry, and bulk densities were determined using geophysical techniques including compensated density logs and gravimeter data. Typically, the bulk density measurements are reported with an estimated 5 percent error.

6.2.1.2 Data Sources

The alluvial aquifer in the Pahute Mesa study area is typically thin with a significant presence occurring near the margins of the study area. Therefore, there is a general lack of alluvial porosity data from this region. There is, however, an abundance of alluvial porosity data from the nearby Yucca Flat region of the NTS.

The porosity of alluvial materials is largely controlled by the lithologic properties of the alluvium. Therefore, porosity data from regions of similar lithologic composition may be used as a surrogate for the alluvial materials present within the PM-OV area. Table 6-1 shows a comparison of the lithologic descriptions for wells in the PM-OV and Yucca Flat regions. The comparison is limited to the saturated alluvium in the PM-OV model area near Oasis Valley. As shown in the table, the lithologies of the two regions are quite similar and, therefore, the porosities from Yucca Flat may be used to represent the alluvial aquifer in the PM-OV study area.

Table 6-1
Pahute Mesa-Oasis Valley and Yucca Flat Lithologic Comparison

	General ER-OV Well Lithologic Description (Robledo et al., 1998)	ER-3-2 Lithologic Description (Prothro et al., 1999)
Location	Pahute Mesa-Oasis Valley	Yucca Flat
Size	Gravel and gravelly sands	Gravel and gravelly sands
Parent Material	Tuffaceous	Tuffaceous
Consolidation	Unconsolidated to weakly consolidated	Unconsolidated
Sorting	Poorly sorted	Poorly to moderately sorted
Rounding	Angular to rounded	Subangular to subrounded

Porosity information for Yucca Flat has been synthesized in the report titled *Physical Properties in LLNL Yucca Flat Areas: The ROCK PILE Concept* (Burkhard, 1989). The porosities in this report represent single well zonal averages for each stratigraphic unit. Corresponding depth information for the zonal averages were obtained from the LLNL site characteristic summary memoranda.

6.2.1.3 Data Documentation Evaluation

The level of documentation of the available data was assessed to provide the user with some basis for traceability of the reported values. The levels were assigned to each record to assess the documentation available for each data point. The levels assigned do not reflect the accuracy or reliability of the reported data, only the level of documentation.

Nearly all of the alluvial porosity data were obtained from an LLNL report. These data were collected by LLNL during the containment testing period before the initiation of the ERP. Therefore, these data were not collected under Nevada ERP project-approved standard policies, procedures, or practices. As a result, all of the porosity data for alluvium have been assigned a DDE_F of 4.

6.2.1.4 Dataset Description

Based on the data analysis needs and the existing methods of porosity measurement, the following data types were compiled to build the alluvial porosity dataset presented in [Appendix E](#):

- Well_name- name of the well
- Top_depth (meters below ground surface [mbgs])- upper depth associated with the interval sampled
- Bottom_depth (mbgs)- bottom depth associated with the interval sampled
- Aver_poro(%)- average porosity for the given interval
- Porosity_type- bulk, matrix, fracture
- HSU
- Stratigraphic unit
- Reference
- Source
- DDE_F

6.2.2 Data Evaluation

Porosity was calculated by LLNL personnel using bulk density, grain density, and water content measurements. The data for alluvial porosity come almost exclusively from wells in Yucca Flat and represent values from the vadose zone. The equation to calculate porosity from the measured parameters by Burkhard (1989) is given by:

$$n_b = 1 - \rho_b / \rho_g (1 - Z) \quad (6-2)$$

where:

- n_b = Bulk porosity or in the case of alluvium effective porosity
- ρ_b = The bulk density [total mass/total volume]
- ρ_g = The grain density [mass of solids/volume of solids]
- Z = The water content [mass of water/total mass of sample]

The porosity values obtained were then averaged over the stratigraphic zone for each well. Inhomogeneities in the stratigraphic units as well as differences in the measurement techniques should be eliminated by using averaged values (Burkhard, 1989).

6.2.3 Development of Parameter Distributions

The alluvial porosity data are averaged over lithologic intervals. The total number of values per lithologic interval per well was not recorded by Burkhard (1989). The average porosity data from Burkhard (1989) were first rounded to the nearest whole value as a percentage. So 34.3 percent porosity became 34 percent and 34.7 percent porosity became 35 percent. These rounded porosity values were plotted in the form of a PFD, where the frequency of each whole porosity value was plotted individually (Figure 6-1).

The alluvial porosity values range from 26 to 49 percent, a span of about a factor of two. The mean value, 34.9 percent, is within the range of values reported by Blout et al. (1995) and by Burbey and Wheatcraft (1986) for Frenchman Flat Alluvium. Interpolating between integer values of porosity, 5 percent of the porosity values are less than 26.2 percent, 50 percent of the values are less than 34.2 percent, and 95 percent of the porosity values are less than 43.6 percent.

The sample mean and standard deviation of the data are 34.8 and 4.9 percent, respectively. Applying an assumption of a normal distribution, the calculated 5 percent mean, and 95 percent values are: 26.8, 34.8, and 42.8 percent. Rounding the mean and standard deviation to 35 and 5 percent, respectively, the calculated 5 and 95 percent porosity values are 26.8 and 43.2 percent, respectively. The latter values will be used to define the mean and ranges of uncertainty for the effective porosity of the alluvium.

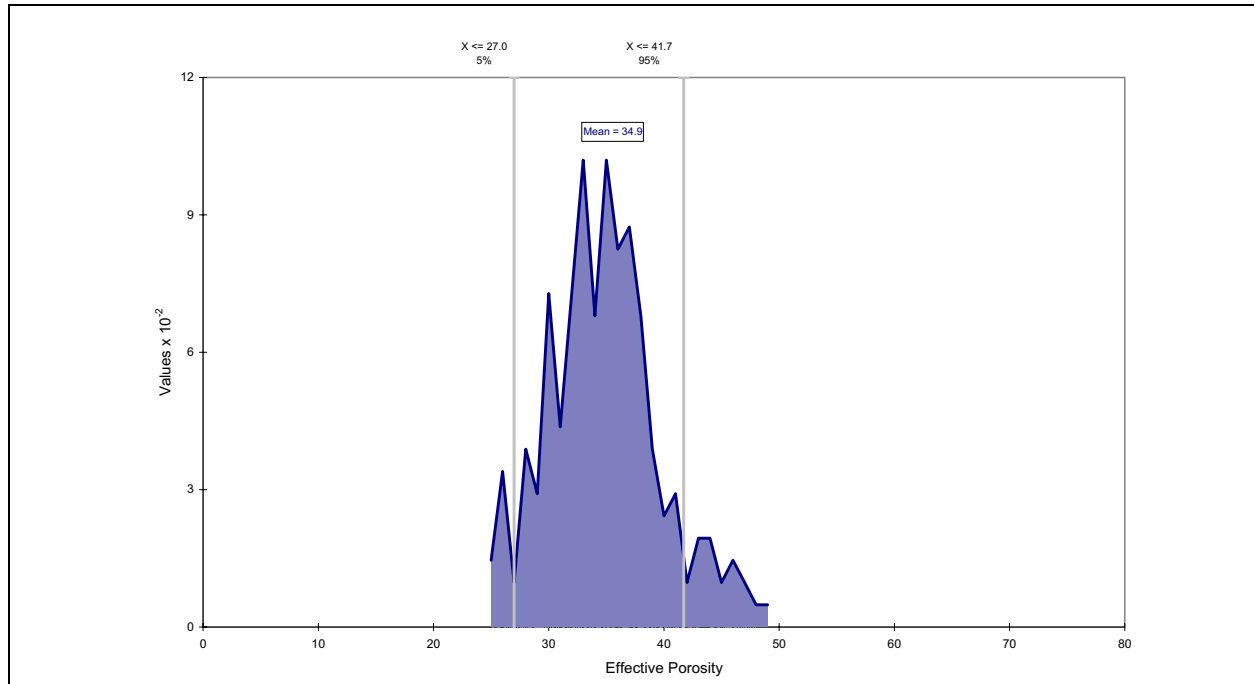


Figure 6-1
PFD of Porosity Data: Alluvium HSU (208 Samples)

The analysis to date has examined total porosity; but, as noted earlier, it is expected that effective porosity of the alluvium should be less than the total porosity. To estimate the amount of reduction to obtain effective porosity from total porosity consider two sets of data from the alluvium of Frenchman Flat. Blout et al. (1995) present porosity data from the shallow boreholes in Frenchman Flat. The average porosity of 269 samples was 36.9 percent. Burbey and Wheatcraft (1986) summarize other porosity data from borehole UE-5n and showed that total porosity was 37 percent above the water table and 33 percent below the water table. Calibration of tracer breakthrough at the CAMBRIC tracer experiment (Burbey and Wheatcraft, 1986) produced effective porosity values that ranged from 31 to 36 percent. These data suggest that the effective porosity may be about 3 percent less than the total porosity based on the data from alluvial porosity measurements in Frenchman Flat (Blout et al., 1995; Burbey and Wheatcraft, 1986). An appropriate mean effective porosity of the alluvium in the PM-OV study area should be 32 percent, or about 3 percent less than the mean total porosity. The range of values for effective porosity should shift 3 percent lower as well, producing 5 and 95 percent bounds on the porosity population of 23.8 and 40.2 percent, respectively.

6.2.4 Data Limitations

Limitations associated with the alluvial porosity dataset include the lack of alluvial porosity data within the Pahute Mesa study area as well as the method by which the effective porosity was determined.

The alluvial porosity dataset only contains one value from the Pahute Mesa study area. This value was determined from Well UE-18t. The rest of the data was transferred from the Yucca Flat region of the NTS. While we believe this transfer is justified because of the similar source environment and lithologic descriptions, it is possible that localized differences in the alluvium from the two regions may result in differences in porosity values.

Another limitation is the indirect method by which the porosity values were obtained. Many of the porosity values in the dataset were calculated from measurements of bulk density, grain density, and water content. There is an associated error with each of these measurements. In fact, the bulk density measured by geophysical techniques usually contains a stated potential error of 5 percent. Another source of uncertainty is that this method calculates the total porosity and not the effective porosity. For alluvial materials, this should be very similar but is still another potential limitation.

Overall, these limitations are not expected to add significant uncertainty to the estimate of effective porosity for the alluvium.

6.2.5 Scaling Considerations

For effective porosity, the simplest approach is to calculate the arithmetic mean of all values, which is about 32 percent. The 95 percent confidence interval about the mean value, using a sample size of 208 values, ranges from 31.3 to 32.7 percent (using classical statistics, an assumption of normality, and large sample size). This range of uncertainty is very small, suggesting that for all practical purposes the effective porosity of the alluvium could be treated as a constant. However, this analysis fails to address the issue of spatial variability.

McKenna and Rautman (1996) discuss scaling of parameters for numerical simulations associated with the Yucca Mountain Project. They assessed scaling of porosity and hydraulic conductivity with respect to reproducing both global flux and first arrival times. They indicate that the arithmetic mean is an appropriate measure of the scaled mean porosity. Using numerical experiments with random fields to verify relationships presented by Clark (1979), McKenna and Rautman (1996) verified the reduction in porosity variance as a result of integrating over larger volumes. Unfortunately, there is insufficient data for porosity in the saturated alluvium of the study area to define correlation scales, which are necessary to apply the relationships in Clark (1979).

The vertical interval over which Burkhard (1989) averaged alluvial porosity values ranged from just a few meters to as much as 500 m. The average length is less than 200 m for 85 percent of the locations in Burkhard's dataset. The thickness of the alluvium in the southwest corner of the Pahute Mesa CAU model area is up to 500 m thick (BN, 2002). There does not appear to be a significant increase in average thickness from the data to the model area. This similarity of the vertical average distance means that vertical averaging is likely to have a small influence on the parameter uncertainty.

The horizontal dimension of the data in Burkhard (1989) is small (immediate vicinity of the borehole) compared with the size of the model cells (which are expected to be as large as 1,000 m on a side). Burkhard (1989) does not provide an estimate of the horizontal correlation length of the alluvial porosity. Istok et al. (1994) analyzed the spatial variability of alluvium properties in Frenchman Flat. They do not address porosity directly, but consider dry bulk density, which can be used to assess porosity via [Equation 6-2](#) if the grain density is assumed to be constant. Blout et al. (1995) show that the grain density varies only a small amount (standard deviation of about 0.04 grams per cubic centimeter [g/cm^3]) compared with the dry bulk density standard deviation of between 0.1 and 0.2 g/cm^3 . Istok et al. (1994) found bulk density horizontal correlation scales to range from less than 1.5 to 46 m. For large model cells, the horizontal averaging at the scale of the model cell is likely to be significant. For example, if the porosity samples are taken to represent a horizontal distance equal to a correlation length of 50 m, the thickness of the averaged data and model cells are the same, and the model cell size is 500 x 500 m, then according to McKenna and Rautman (1996), the standard deviation of upscaled porosity would be 30 percent of the value from the Burkhard (1989) data. In this case, it reduces the standard deviation from 5 percent porosity to 1.5 percent. This produces 5 and 95 percent

limits of 29.5 and 34.5 percent. These narrower limits will be applied to the alluvium in the PM CAU model.

6.3 Effective Porosity for the Fractured Volcanic Aquifers

This section includes descriptions of the available effective porosity data for the fractured volcanic aquifers, and the associated data analysis and results.

6.3.1 Data Compilation

The effective porosity of the fractured volcanic aquifers plays a more crucial role than that of the alluvium because the transport of radionuclides is expected to mostly occur in volcanic aquifers.

6.3.1.1 Data Types

Porosity types discussed in this section are fracture porosity and effective porosity. As stated before, fracture porosity is the volume of fracture void spaces divided by the total volume of the rock. Effective porosity is the volume of void spaces through which water can travel in a rock divided by the total volume of the rock.

In a fracture flow system, where the matrix material is crystalline (such as in granite), it is generally assumed that the fracture porosity may be a good initial measure of the effective porosity. For aquifers where the matrix material is porous and permeable, this relationship may not hold. In addition, even in fractured areas, not all fractures conduct water. In this case, only a small percent of the fracture porosity would be the effective porosity.

Although direct measurement of fracture porosity at the field scale is not feasible, an indirect approach can be used to provide estimates of this parameter. This approach estimates fracture porosity through representation of the fracture network as a parallel plate model.

The "cubic law" is commonly used to describe flow in a single fracture. The fracture is represented as two parallel plates separated by a constant aperture. Observed fracture geometries can be approximated by sets of parallel plates and intersecting parallel plates. The parallel plate model can be used to estimate the fracture porosity of rock given the following assumptions:

- The geometry of the fracture system can be represented by sets of parallel plates characterized by frequency, orientation, and aperture equivalent to those measured by core logs and borehole logs
- Core and borehole logs are representative of the system
- Flowing fractures are sampled (CRWMS M&O, 2000a)

These estimates require information about fracture location, fracture orientation, and hydraulic conductivity of the unit. Fracture location and orientation are obtained from interpretation of geophysical logging of boreholes, and hydraulic conductivity is estimated from pumping tests. Several geophysical tools can provide information required for fracture analysis and stratigraphic correlation. Fracture data described in [Appendix E](#) were collected using a borehole televiewer (BHTV) (ultrasonic borehole imager [UBI]), formation microimager (FMI) or micro-resistivity electronic scanner (FMS) tools (IT, 2001b).

Fracture porosity can also be estimated in the absence of hydraulic test data using aperture, density, orientation, and percent open area data obtained from studies of core.

Estimates of effective porosity based on estimates of specific yield were used by the YMP for cases where the aquifer was a deep, unconfined saturated unit. These estimates were considered to provide an upper bound on the uncertainty in effective porosity given that the thickness of the transmissive unit was known or conservatively estimated (CRWMS M&O, 2000a). In addition, estimates of effective porosity were developed by YMP from unsaturated zone gas tracer tests and seepage tests (DOE, 2001).

Estimates of effective porosity can also be obtained from tracer tests. This is done by adjusting parameters such as the effective porosity in a transport model to reproduce tracer breakthrough behavior measured in a field tracer test. Effective porosity was estimated in this manner from the BULLION Forced-Gradient Experiment (FGE), a tracer test conducted on Pahute Mesa, and from tracers tests at the C-wells complex near Yucca Mountain.

6.3.1.2 Data Sources

Specific data sources for data required to estimate fracture porosity of the volcanic aquifers are listed in [Table 6-2](#). For each parameter, a data tracking number (DTN) from the ERP Common Data Repository and any related reports are listed, if applicable.

Specific data sources for data required to estimate effective porosity of the volcanic aquifers are listed in [Table 6-3](#). For each parameter, a DTN and any related reports are listed, if applicable.

6.3.1.3 Data Documentation Evaluation

The five levels of data documentation flags are explained in detail in [Section 4.0](#). Data documentation flags for the parameters fracture location/fracture orientation, HGU/HSU classification, and hydraulic conductivity used to estimate fracture porosity are shown by well in [Table 6-4](#). Data documentation flags for effective porosity estimates obtained from interpretation of the BULLION FGE and for the effective porosity distribution developed by YMP are shown in [Table 6-5](#).

Table 6-2
Sources for Data Required for Estimation of Fracture Porosity of Volcanic Aquifers

Parameter	Data Tracking Number (DTN)	Report Reference
Hydrostratigraphic/Hydrogeologic Classification	NA	BN (2002)
Fracture Location	1161, 1180, 1181, 1257	IT, 2001b; Drellack et al., 1997; IT, 1999
Fracture Orientation	1161, 1180, 1181, 1257	IT, 2001b; Drellack et al., 1997; IT, 1999
Fracture Aperture	NA	Drellack et al., 1997; IT, 1999
Hydraulic Conductivity	843, 974	IT, 1998a, 2002 a through h; Blankennagel and Weir, 1973

NA = Not applicable

Table 6-3
Sources for Data for Estimation of Effective Porosity of Volcanic Aquifers

Parameter	Data Tracking Number (DTN)	Report Reference
Effective Porosity (NTS)	843	IT, 1998a
Effective Porosity (NTS)	843	Reimus and Haga, 1999
Effective Porosity (YMP)	NA	CRWMS M&O, 2000a; DOE, 2001

NA = Not applicable

Table 6-4
Data Documentation Evaluation Flags for Parameters Required to Estimate Fracture Porosity of Volcanic Aquifers

Well	Fracture Location/ Fracture Orientation	HGU/HSU Classification	Hydraulic Conductivity
ER-EC-1	1	1	1
ER-EC-2a	1	1	1
ER-EC-4	1	1	1
ER-EC-5	1	1	1
ER-EC-6	1	1	1
ER-EC-7	1	1	1
ER-EC-8	1	1	1
ER-18-2	1	1	1
UE-18r	1	3	4
ER-20-6 #1	1	1	1
ER-20-6#2	1	1	1

Table 6-5
Data Documentation Flags for Tracer Migration Experiments

Source	Data Documentation Flag
BULLION FGE Interpretation	1
YMP Uncertainty Distribution	3

6.3.2 Dataset Description and Data Evaluation

Estimates of fracture porosity were obtained from two sources: (1) parallel plate models of fracture networks and (2) calculations based on fracture property measurements made on core samples. Estimates of effective porosity were obtained from two sources: (1) interpretation of tracer behavior from the BULLION FGE and (2) uncertainty distributions for effective porosity developed for the Yucca Mountain Site. Data obtained from each source are described and evaluated in the following sections.

6.3.2.1 Dataset Description

Values of fracture porosity estimated using parallel plate models are shown in [Table 6-6](#). Hydraulic conductivity values required to estimate apertures are listed in the table. Fracture spacing is calculated from fracture frequency data described in [Appendix E](#). Data sources are given in [Table 6-2](#). In this method, it is assumed that all fractures in an interval have the same aperture. In reality, some of the fractures may be closed. Porosity values derived using this method are, thus, likely to be higher than reality.

A study of core from seven wells from Pahute Mesa (Drellack et al., 1997) was conducted to characterize fractures in the volcanic units. A range of fracture porosities, calculated from aperture, density, orientation, and percent open area data (IT, 1999) are presented in [Table 6-7](#).

Three methods were used to estimate effective porosity from the observed breakthrough of tracers in the BULLION FGE (IT, 1998a; Reimus and Haga, 1999; Shaw, 2003). These modeling efforts estimated effective porosity considering multiple conceptual models for flow geometry and using observations from multiple transport pathways. Ranges of values of effective porosity derived from interpretations of the BULLION FGE are shown in [Table 6-8](#). The effective porosity derived from the calibrated discrete fracture network (DFN) model used by Shaw (2003) was three orders of magnitude smaller than the porosity estimated by IT (1998a) using MODFLOWT. Estimates of effective porosity were also made using the cubic law based on fracture frequency and orientation data from ER-20-6 #1. The calculated average was 2.6×10^{-4} (Shaw, 2003) which is one order of magnitude higher than that obtained using the DFN model.

6.3.2.2 Data Evaluation

The evaluation of the fracture data is described in this section. It includes fracture porosity evaluations from the hydraulic data as well as effective porosity values from a limited number of tracer test experiments.

**Table 6-6
Fracture Porosity of Volcanic Aquifers Estimated Using Parallel Plate Models**

Well	Interval Name	Top of Interval (m)	Bottom of Interval (m)	Hydraulic Conductivity Minimum (m/s)	Hydraulic Conductivity Maximum (m/s)	Fracture Spacing (m)	Aperture Minimum (m)	Aperture Maximum (m)	Fracture Porosity Minimum	Fracture Porosity Maximum	Hydrogeologic Unit	Hydrostratigraphic Unit ^b
ER-20-6#1 ^a		701.0	898.0	2.40E-05		0.62	2.63E-04		4.26E-04		LFA	CHZCM
ER-20-6#2 ^a		777.0	887.0	1.49E-05		3.37	3.95E-04		1.17E-04		LFA	CHZCM
ER-EC-1	Screen Joint 1	691.9	715.7	1.26E-04	5.41E-04	1.68	6.39E-04	1.04E-03	3.80E-04	6.17E-04	LFA	BA
ER-EC-1	Screen Joint 2	715.7	737.3	2.27E-05	1.23E-04	1.68	3.60E-04	6.34E-04	2.14E-04	3.77E-04	LFA	BA
ER-EC-1	Screen Joint 3	737.3	758.6	8.26E-05	2.71E-04	1.68	5.55E-04	8.24E-04	3.30E-04	4.90E-04	LFA	BA
ER-EC-1	Screen Joint 4	758.6	780.0	3.50E-06	3.70E-05	1.68	1.93E-04	4.24E-04	1.15E-04	2.52E-04	LFA	BA
ER-EC-4	Screen 1	293.2	326.9	1.95E-04	4.76E-04	8.67	1.28E-03	1.72E-03	1.47E-04	1.98E-04	LFA	TCVA
ER-EC-4	Screen 2	326.9	348.5	1.66E-04	7.38E-04	8.67	1.21E-03	1.99E-03	1.40E-04	2.29E-04	LFA	TCVA
ER-EC-4	Screen 3-1	348.5	357.0	1.27E-04	6.90E-03	8.67	1.11E-03	4.19E-03	1.28E-04	4.83E-04	LFA	TCVA
ER-EC-6	Screen 1	489.5	511.7	8.09E-06	2.60E-05	7.02	4.12E-04	6.08E-04	5.86E-05	8.66E-05	LFA	BA
ER-EC-6	Screen 2	511.7	533.2	6.91E-07	2.78E-06	7.02	1.81E-04	2.88E-04	2.58E-05	4.11E-05	LFA	BA
ER-EC-7	Screen 1	278.0	312.1	3.90E-06	2.60E-05	3.21	2.49E-04	4.68E-04	7.75E-05	1.46E-04	LFA	FCCM
ER-EC-7	Screen 2	360.9	399.3	5.84E-05	1.22E-04	2.38	5.55E-04	7.09E-04	2.33E-04	2.98E-04	LFA	FCCM
UE-18-r ^a		1,083.3	1,184.5	3.24E-06		1.64	1.87E-04		1.14E-04		LFA	TMCM
UE-18-r ^a		897.6	1,027.2	3.24E-06		0.82	1.48E-04		1.81E-04		VTA	TMCM
UE-18-r ^a		1,184.5	1,367.0	3.24E-06		0.66	1.38E-04		2.09E-04		VTA	TMCM
ER-18-2		411.9	758.0	7.31E-09	1.53E-08	2.65	2.88E-05	3.68E-05	1.09E-05	1.39E-05	WTA	TMCM
ER-EC-5	Screen Joint 1	361.8	389.5	4.61E-06	5.13E-05	2.37	2.38E-04	5.31E-04	1.00E-04	2.24E-04	WTA	TMCM
ER-EC-5	Screen Joint 2	389.5	410.9	7.83E-06	1.06E-04	2.37	2.84E-04	6.76E-04	1.20E-04	2.85E-04	WTA	TMCM
ER-EC-5	Screen Joint 3	410.9	439.8	7.95E-08	8.59E-06	2.37	6.14E-05	2.92E-04	2.59E-05	1.23E-04	WTA	TMCM
ER-EC-5	Screen Joint 4	565.4	601.4	5.58E-05	1.85E-04	2.37	5.45E-04	8.13E-04	2.30E-04	3.43E-04	WTA	TMCM
ER-EC-5	Screen Joint 5	601.4	623.0	7.92E-05	6.52E-04	2.37	6.13E-04	1.24E-03	2.59E-04	5.22E-04	WTA	TMCM
ER-EC-5	Screen Joint 6	623.0	654.1	3.89E-07	2.44E-04	2.37	1.04E-04	8.92E-04	4.40E-05	3.76E-04	WTA	TMCM
ER-EC-5	Screen Joint 7	677.6	699.8	1.09E-05	1.92E-04	2.37	3.17E-04	8.23E-04	1.34E-04	3.47E-04	WTA	TMCM
ER-EC-5	Screen Joint 8	699.8	721.5	1.11E-05	1.57E-04	2.37	3.19E-04	7.71E-04	1.34E-04	3.25E-04	WTA	TMCM
ER-EC-5	Screen Joint 9	721.5	755.9	6.29E-06	1.71E-04	2.37	2.64E-04	7.92E-04	1.11E-04	3.34E-04	WTA	TMCM
ER-EC-8	Screen Joint 9	544.6	566.2	9.14E-07	1.14E-05	2.50	1.41E-04	3.27E-04	5.64E-05	1.31E-04	WTA	TMCM
ER-EC-8	Screen Joint 10	566.2	606.6	2.63E-07	9.15E-06	2.50	9.31E-05	3.04E-04	3.72E-05	1.22E-04	WTA	TMCM
UE-18-r ^a		485.0	897.6	3.24E-06		0.72	1.42E-04		1.97E-04		WTA	TMCM
UE-18-r ^a		1,027.2	1,083.3	3.24E-06		1.19	1.68E-04		1.41E-04		WTA	TMCM
UE-18-r ^a		1,367.0	1,504.0	3.24E-06		0.62	1.35E-04		2.17E-04		WTA	TMCM

^aOnly single values of K were available for these wells; only single values of aperture and porosity were calculated

^bSee Table A.1-1 for definitions.

Data Sources: See Table 6-2.

Table 6-7
Fracture Porosity Obtained from the Study of Volcanic Core

Hydrostratigraphic Unit	Fracture Porosity Range
Uppermost Welded Tuffs	2.2×10^{-5} to 1.9×10^{-4}
Tuff Cones	2.6×10^{-6} to 4.6×10^{-4}
Welded Tuffs Above Basal Confining Unit	1.2×10^{-5} to 4.4×10^{-5}
Basal Aquifer	6.1×10^{-6} to 2.3×10^{-4}

Table 6-8
Effective Porosity for Volcanic Aquifers Obtained from the BULLION Forced-Gradient Experiment

Transport Path	Effective Porosity Minimum (Reimus and Haga, 1999)	Effective Porosity Maximum (Reimus and Haga, 1999)	Effective Porosity (IT, 1998a)	Effective Porosity (Shaw, 2003)
Well #1 to Well #3	0.0066	0.008	0.018	2.4×10^{-5}
Well #1 to Well #2	0.00036	0.0023	0.018	
Well #2 to Well #3	0.011	0.021	0.023	

6.3.2.2.1 Parallel Plate Model

Given the assumptions listed in Section 6.3.1.1, the effective porosity, n_f , of fractured rock is given by:

$$n_f = e/b \quad (6-3)$$

where:

- e = Fracture aperture
- b = Mean distance between fractures

Fracture aperture is estimated from the cubic law:

$$e = [(12 \mu b K)/g \rho]^{1/3} \quad (6-4)$$

where:

- μ = Viscosity of water: 1.002×10^{-3} pascal-second (Pa-s) (20°C)
- g = Acceleration due to gravity: 9.80665 meters per square second (m/s^2)
- K = Hydraulic conductivity of a fracture
- ρ = Density of water: 998.2 kilogram per cubic meter (kg/m^3) (20°C)

Hydraulic conductivity (K) is obtained from pumping tests, and fracture spacing is estimated from an analysis of fracture location and orientation measurements.

To obtain fracture spacing, calculations were required to obtain values for four types of quantities. These were:

- Fracture Frequency [meters⁻¹]
- Average Dip [degrees]
- Corrected Frequency [meters⁻¹]
- Total Corrected Frequency [meters⁻¹]

To calculate the fracture frequency, fractures in an HSU interval were grouped according to dip. Categories were:

- 0 <= dip <= 30
- 30 < dip <= 60
- 60 < dip <= 90

The average fracture frequency, N_r , was then calculated by dividing the number of fractures counted in a category by the interval depth in meters. The average dip in degrees for each of the three categories was calculated.

Fracture frequencies derived from data collected from a vertical borehole which intersects nonhorizontal fractures are biased. The true fracture spacing (distance between two parallel fractures measured perpendicular to the fracture plane) is not the same as the fracture spacing observed in the borehole. To account for this orientation bias, it is necessary to correct the fracture frequency (NRC, 1996) using the following equation:

$$\langle N_c \rangle = \langle N_r \rangle / \cos (f) \quad (6-5)$$

where:

- $\langle N_c \rangle$ = Corrected average fracture frequency
- $\langle N_r \rangle$ = Average fracture frequency
- f = Average dip angle for that category measured from the horizontal

The total corrected frequency is then obtained by summing corrected frequencies for each category. Values of fracture spacing are calculated from total corrected frequency and used with the estimated apertures to provide estimates of fracture porosity.

6.3.2.2 BULLION FGE

Three wells were installed downgradient from the location of the BULLION test. The well furthest from the test was pumped to produce a hydraulic gradient while tracers were injected into the other two wells. Tracer breakthrough curves were obtained for three different flow path segments. Three estimates of effective porosity were obtained (IT, 1998a) by calibrating the transport model to the observed breakthrough curves. Ten estimates of effective porosity were obtained from the LANL analysis (Reimus and Haga, 1999) by considering three flow paths, linear and radial flow models, and a range for the lumped matrix diffusion

parameter. As noted in [Table 6-8](#), the effective porosity estimates from the BULLION FGE range from 3.6×10^{-4} to 2.3×10^{-2} (IT, 1998a; Reimus and Haga, 1999, Shaw, 2003).

The smallest value comes from interpretation of tracer movement between the two injection wells located close together. It is likely that these two wells are located along, or near, the strike of a fracture or fracture zone. Thus, this low porosity can be viewed as applicable to discrete fractures. The larger porosity values measured at the BULLION FGE represent flow over a longer interval from the injection wells to the discharge well. In this case, the range of effective porosity values is from 6.6×10^{-3} to 2.3×10^{-2} .

6.3.2.2.3 Simulation of Plutonium Migration from the BENHAM Test

Researchers at the LANL (Wolfsberg et al., 2002) simulated the migration of radionuclides from the BENHAM cavity. Radionuclides have been observed at wells near the TYBO test approximately 1 mile away. Investigations indicated that the BENHAM cavity was the source of the plutonium. The primary aquifers for radionuclide migration identified in the model are the TSA and the lava unit of the CHZCM. Wolfsberg et al. (2002) estimated fracture porosity from geometric relationships of fracture apertures and spacing for the TSA and used values derived from the BULLION FGE for the lava unit of the CHZCM. Fracture porosity values for TSA units other than lava were estimated by Wolfsberg et al. (2002) from geometric relationships of fracture apertures and spacing ([Table 6-9](#)). For lava, Wolfsberg et al. (2002) used the range of values derived from the BULLION FGE (IT, 1998a). The model, which included colloid-facilitated transport, was able to simulate travel times and radionuclide concentrations that are consistent with the field observations in the ER-20-5 observation wells. Later, Wolfsberg and Boryta (2002) extended the work of Wolfsberg et al. (2002) to incorporate new information. In the extension report, Wolfsberg and Boryta (2002) used the low values of fracture porosity shown in [Table 6-9](#) in their base-case model. This allowed the model to match the observed arrival times of radionuclides migrating from the BENHAM test to the ER-20-5 observation wells. Radionuclides suspected to originate from the BENHAM test were first observed at the ER-20-5 observation wells 28 years after the BENHAM test was detonated. This suggests that the effective porosity values used by Wolfsberg et al. (2002), including the ones derived from the BULLION FGE analysis, may be appropriate for CAU-scale simulations.

Table 6-9
Fracture Porosities Used by Wolfsberg et al. (2002)

	Welded	Lava	Altered/Nonwelded
Base	4.98E-4	2.09E-3	1.06E-4
Low	7.00E-5	2.19E-4	1.13E-5
High	3.54E-3	2.00E-2	1.00E-3

6.3.2.2.4 YMP Estimates of Fracture and Effective Porosity

An initial uncertainty distribution was developed based on a parallel plate model and interpretations of pumping and tracer tests (CRWMS M&O, 2000a). The lower bound for the distribution was obtained from a parallel plate model. Using $n = Ne$ where n is porosity, N is the number of fractures per unit distance and e is aperture or $n_f = 3Ne$ in three dimensions, fracture porosities based on core from USW-G1, USW-GU3, USW-G4 and UE25a#1 were estimated to range from 8.0×10^{-5} to 1.0×10^{-3} .

The upper bound of the distribution was obtained from pumping and tracer tests. Specific yields were derived from pump test data collected at the C wells using analytical solutions (assuming porous media). These specific yields range from 0.01 to 0.20 (Geldon et al., 1998). Tracer test results at the C-well complex provided estimates of effective porosity ranging from 0.004 to 0.125. Re-interpretation of the C-well pumping tests by Winterle and La Femina (1999) resulted in estimates of specific yields ranging from 0.004 to 0.03.

A reinterpretation of conservative tracer tests at the C-wells complex submitted in June of 2001 (DOE, 2001) provided estimates of effective porosity from tracer tests in the Bullfrog tuff ranging from 0.0037 to 0.12, and estimates from testing in a second interval in the Prow Pass tuff ranging from 0.0027 to 0.0062.

Results from unsaturated zone (UZ) gas tracer tests and seepage tests conducted in the Exploratory Studies Facility (ESF) and saturated zone (SZ) cross-hole tracer tests conducted at the C-wells complex led to a reevaluation of the distribution for effective porosity (DOE, 2001).

Gas tracer tests were conducted in Topopah Spring middle nonlithophysal welded tuff to provide estimates of effective porosity (CRWMS M&O, 2000b). Assumptions required for this analysis were that the diffusion of gas into the matrix is negligible compared to flow-through fractures, the fracture network is well connected, and the geometry of the network is known. Porosities for this unit ranged from 0.006 to 0.02 with a mean of 0.01.

A seepage test was conducted by injecting water into three boreholes located above Niche 3650 (Niche 2) in the ESF (CRWMS M&O, 2000b). Assuming one-dimensional flow and negligible sorption by the matrix, the following mass balance relation is used:

$$z_p(\theta_{av} - \theta_r) = q_s t \quad (6-6)$$

where:

- z_p = The depth from the water supply source to the wetting front
- $\theta_{av} - \theta_r$ = The difference between the average volumetric water content between the source and the wetting front and the residual volumetric water content
- q_s = The constant flux of water at the source
- t = Time required for the wetting front to reach depth z_p .

The estimated water content differentials correspond to effective porosities given the assumptions.

Based on results from gas tracer tests, seepage tests in the ESF, and cross-hole tracer tests at the C-wells complex, the uncertainty distribution has been revised to a log-triangular distribution with a lower bound of -5.0, a most likely value of -3.0, and an upper bound of -1.0 (DOE, 2001). The midpoint value represents the smallest values of the effective porosity estimated from the new data.

6.3.3 Development of Parameter Distributions

Based on early information from the C-well complex at Yucca Mountain, the conclusion in CRWMS M&O (2000a) is that the uncertainty in effective porosity in fractured volcanic aquifers was best represented by a log-uniform distribution from 0.00001 to 0.10.

Upon later analysis, an uncertainty distribution for effective porosity was developed by the YMP based on parallel plate models, pumping tests, tracer tests, and a seepage test. A log-triangular distribution was proposed with a lower bound of -5.0, a most likely value of -3.0, and an upper bound of -1.0 (DOE, 2001). This revised distribution has the same lower and upper bounds as the previous distribution, but provides for a central tendency.

The fracture porosities, as presented [Table 6-6](#) and [Table 6-7](#), range between 2×10^{-6} and 6×10^{-4} . This range is consistent with other measurements of fracture porosity (Lee and Farmer, 1993). The tracer experiments at the BULLION site and the C-well complex both yield effective porosity values much larger than the calculated fracture porosity values. In part, this disparity led the YMP to propose very large ranges of effective porosity values (spanning four orders of magnitude from 10^{-5} to 10^{-1}).

The lower bound value from the YMP studies appears to be too low to be realistic for simulations associated with the Pahute Mesa CAU. To investigate this, an estimate of the minimum effective porosity can be determined from available information in the PM-OV flow system. From the definition in [Equation 6-1](#), the effective porosity can be calculated as the specific discharge divided by the groundwater velocity. The specific discharge is estimated from the following information:

Total discharge at Oasis Valley is assumed to be the ET loss presented by Reiner et al. (2002). Figure 18 of their report gives the range of discharge as 4,000 to 8,500 acre-feet per year (ac-ft/yr) (4,933,920 to 10,484,580 cubic meters per year [m^3/yr]), with a mean value of 6,200 ac-ft/yr (7,647,576 m^3/yr). All of this water is assumed to come from the Pahute Mesa testing area. The cross-sectional area of flow is the product of the width times the thickness. The width is assumed to be as small as 5 km to as large as 24 km. The lower bound is the width of the trough in the potentiometric surface west of Timber Mountain, and the upper bound is the width of the testing area parallel to the direction of flow. The thickness ranges from a minimum of 500 m to a maximum of 1,000 m.

The minimum is not well constrained, but the maximum is the distance between the water table to the deepest underground nuclear test.

The velocity is estimated on the basis of lack of detected radionuclides in Oasis Valley at the present time. Taking the time since tests were conducted on Pahute Mesa, which ranges from 1965 to 1991, the travel time ranges from 11 to 27 years. The distance of travel ranges from the closest of 24 km to as large as 40 km. These parameters, including the ranges of uncertainty, were simulated with a Monte Carlo method using GoldSim (Golder Associates, 2002a and b). With 1,000 realizations, the calculated range of minimum effective porosity values is 1×10^{-4} to 2.5×10^{-3} .

This simple analysis ignores the effects of dispersion and matrix diffusion. Dispersion will cause earlier breakthrough than the center of mass; thus, if dispersion were included, the minimum effective porosity would be larger than calculated in this analysis. Conversely, if matrix diffusion is considered, the opposite result occurs. Matrix diffusion will slow all radionuclides relative to the water. In that case, smaller effective porosity values could be used, yet radionuclide breakthrough would be delayed at Oasis Valley. It is our intention to include matrix diffusion in the PM-OV CAU model. Therefore, the range of values assumed for the YMP of 10^{-5} to 10^{-1} will be adopted here as well. It is recognized that, if matrix diffusion is not modeled, the lower bound of the effective porosity must be increased to at least 10^{-4} .

Assessment of Fracture Porosity per HSU and per HGU

Table 6-13 contains estimates of fracture porosity for the tuff confining unit discussed later in Section 6.4. Fracture porosity estimates for the tuff confining unit are included in this assessment for convenience. The minimum and maximum fracture porosity values from Table 6-6 and Table 6-13 were combined and plotted as cumulative frequency as a function of porosity. The minimum fracture porosity values were ordered from smallest to largest. The points were then labeled in two different ways. First, by HGU, then HSU. Some of the values listed as minimum are in fact a single value and may not represent the minimum. These will be discussed, as appropriate, in the paragraphs below. The first plots, Figures 6-2 and 6-3, are the minimum and maximum fracture porosity, respectively, labeled per HGU.

In Figure 6-2, four HGUs are represented, TCU (6 values), LFA (14 values), WTA (14 values), and VTA (2 values). It is not possible to identify a trend in the data. The TCU minimum fracture porosity values are concentrated on the small porosity end of the plot, but this is not surprising because hydraulic conductivity is used to estimate porosity and confining units have lower hydraulic conductivity. The LFA and WTA have a similar number and range of values and do not appear to have distinctly different fracture porosity estimates. The VTA values tend to be toward the larger porosity values, but with only two data points, no conclusions can be drawn. Additionally, the two VTA values are not true minimum values, so skewing toward the high end is expected. Finally, and most importantly, Bechtel Nevada (2002) described the vitric tuff aquifers as having limited fracture flow. Therefore, the VTA will be treated as a porous aquifer. The removal of three

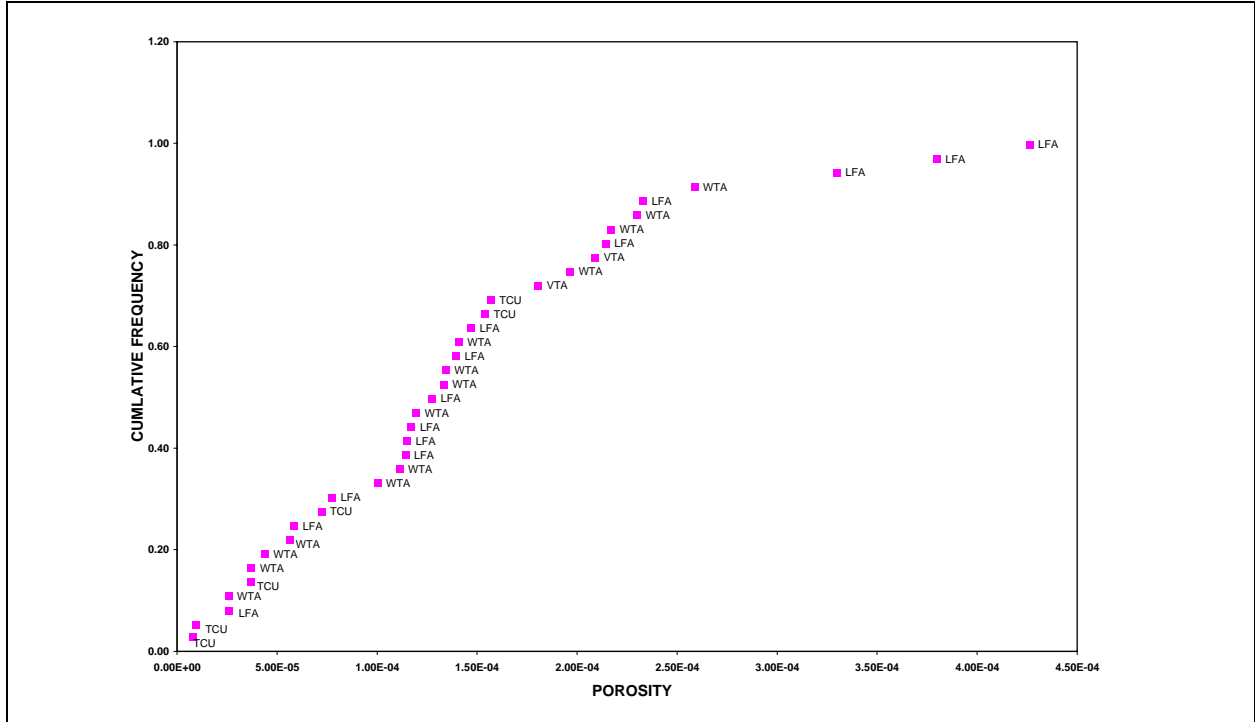


Figure 6-2
Minimum Fracture Porosity (HGU)

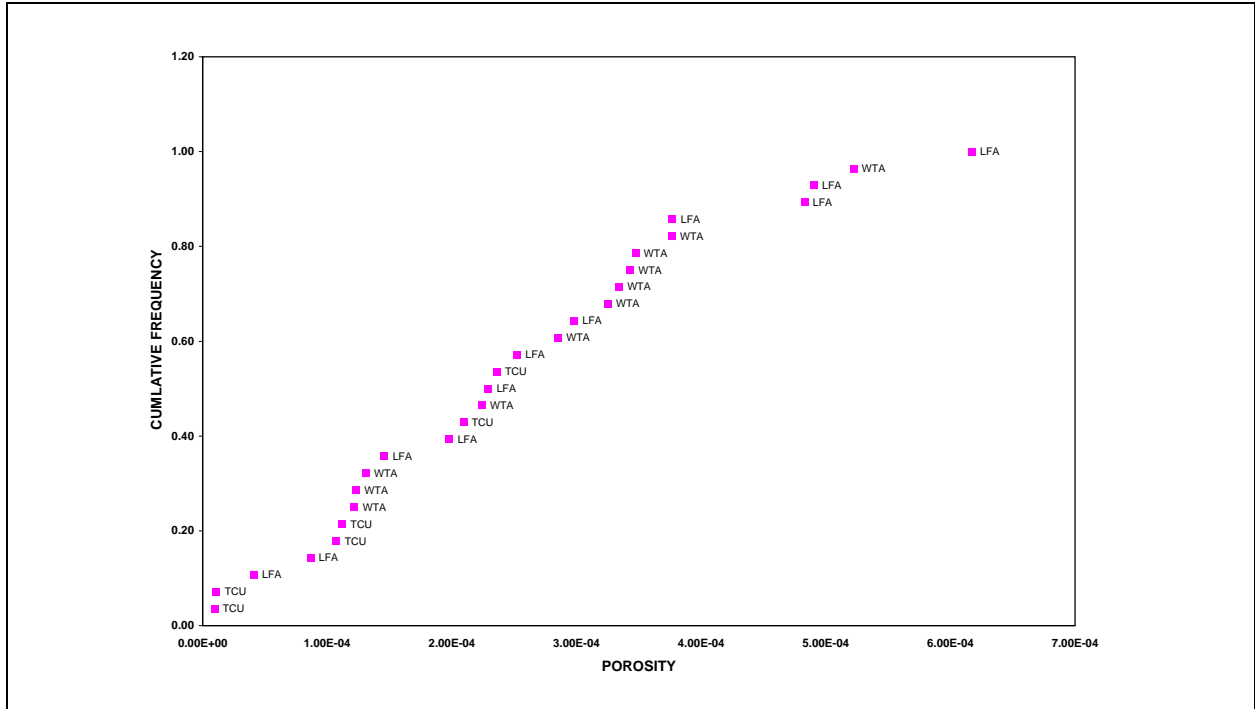


Figure 6-3
Maximum Fracture Porosity (HGU)

LFA, three WTA, and two VTA values because they are not true minimums does not change the conclusions already drawn.

In [Figure 6-3](#), the maximum porosity labeled by HGU is presented for three HGUs. The WTA and LFA both span nearly the full range of values. The TCU tends toward smaller values, but this is consistent with the method of estimating the fracture porosity and the expected smaller hydraulic conductivity of the confining units.

[Figure 6-4](#) and [Figure 6-5](#) present the porosity data shown in [Figures 6-2](#) and [6-3](#), but labeled by HSU. [Figure 6-4](#) is the minimum fracture porosity, labeled by HSU, plotted as a cumulative frequency. Five HSUs are represented in the dataset; Fortymile Canyon Composite Unit (FCCM) (7 values), Timber Mountain Composite Unit (TMC) (18 values), BA (6 values), CHZCM (2 values), and TCVA (3 values). Of those, the values for the BA, TMC, and FCCM appear to span the full range of values with no noticeable grouping of values. The CHZCM values tend toward larger values, but with only two values, it cannot be determined with certainty. The TCVA data are concentrated over a narrow range in the middle of the distribution, but again, with too few data points to draw conclusions. From these data, it would appear that the range of fracture porosity values is not a function of the HSU.

If data for which only one value was determined are removed, two observations can be made. First, the CHZCM values are both removed, so their location toward the high end of the range may be due to the fact that those values represent a central tendency, not a lower bound. Secondly, 6 of 11 highest porosity values for the TMC are also eliminated if single values are not plotted. However, in this case, the overall conclusion is not changed.

In [Figure 6-5](#), the maximum fracture porosity cumulative frequency, labeled by HSU, is presented. The BA and TMC span the full range of values and do not appear to be distinguishable from one another. The other two HSUs, TCVA, and FCCM tend to be slightly skewed toward the high end and low end of values, respectively. The three TCVA values are probably not significant because of the small number of data points. The FCCM tend toward lower values.

Some of these results run counter to expectations regarding confining unit HGUs and composite HSUs, where the bedded and nonwelded units are expected to exhibit limited fracture flow and be dominated by slower matrix flow. The completion intervals in the ER-EC wells were placed to intercept the most permeable zones. This means the results will under represent the least permeable intervals. The fractured portions of the tuff confining units may act like aquifers over small intervals, but this behavior is not expected to be representative of the tuff confining unit HGU as a whole.

6.3.4 Data Limitations

There are two types of limitations for these data, those due to sparse data and those due to uncertainties in the methods used to estimate porosity. The Pahute Mesa

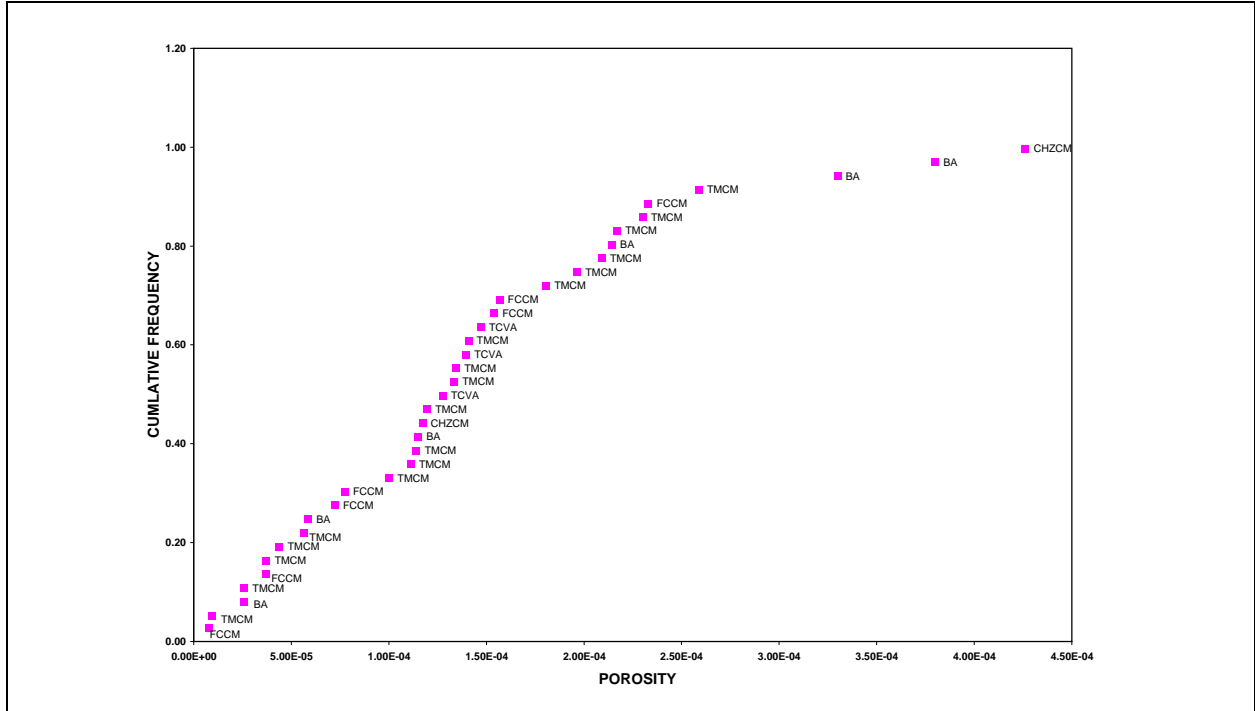


Figure 6-4
Minimum Fracture Porosity (HSU)

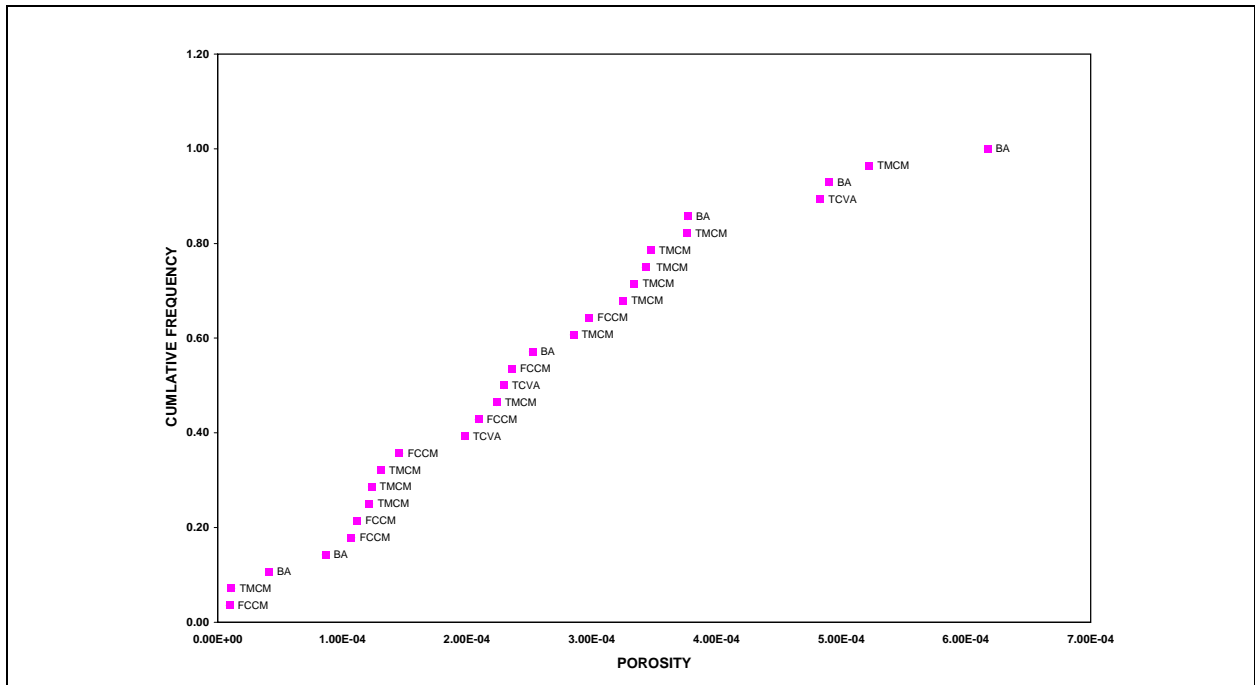


Figure 6-5
Maximum Fracture Porosity (HSU)

CAU model will require prediction of contaminant movement through deep aquifers in a large system (tens of kilometers on a side). Data for estimating effective porosity have been collected at few locations, representing only a subset of the hydrogeologic units found in the PM-OV region. While some data specific to the NTS are available, uncertainty distributions for effective porosity must rely heavily on the use of data from other sites and expert judgement.

Effective porosity cannot be measured directly but must be estimated from fracture data or tracer migration experiments. Fracture porosity was estimated using parallel plate models. Drawbacks to the parallel plate approach include assumptions that fractures are infinite and have the same properties everywhere. Parallel plate models are believed to provide at best a lower bound for effective porosity (CRWMS M&O, 2000a).

6.3.5 Scaling Considerations

The Committee on Fracture Characterization and Fluid Flow from the National Research Council reported that while estimates of effective porosity can in principle be obtained from tracer tests, techniques for determining effective porosity are poorly developed (NRC, 1996). In addition, the Committee pointed out that in fractured rock systems, it is not apparent how observations of tracer migration at small scales can be extrapolated to larger scales (NRC, 1996).

The modeling approach for simulation of radionuclide migration in the Pahute Mesa CAU will utilize a porous media equivalent approach to simulate transport. Several reports from the YMP site assessment investigations recommend using an arithmetic average to scale porosity values (McKenna and Rautman, 1996; CRWMS M&O, 2000b). The variability in fracture effective porosity, as observed in fracture porosity and tracer test-derived effective porosity represents the population of values. At larger scales of interest, one might expect that the mean value would remain unchanged; but the uncertainty, as represented by the variance, would decrease. The scaling should take into account the scale of variation of the fracture effective porosity, as given by the correlation scale. Unfortunately, there is no information regarding the horizontal or vertical correlation scale of the effective porosity, so the amount of variance reduction cannot be readily determined. Defensible upscaling is difficult to define in this case. Therefore the full range of uncertainty will be used in the CAU model simulations. The inability to establish a scaling relationship at this time leads to larger parameter uncertainty. For the Pahute Mesa CAU model, the range of values given by the available data, 10^{-5} to 10^{-1} , will be used in the model.

6.4 Effective Porosity for Carbonate Aquifers and Confining Units

This section includes descriptions of the available effective porosity data for carbonate aquifers, vitric tuff aquifers, and confining units.

6.4.1 Data Compilation

The types, sources, and documentation of the data available for effective porosity of carbonate aquifers and confining units are discussed in this section.

6.4.1.1 Data Types

This set of data includes effective porosity for carbonate aquifers, vitric tuff aquifers, and volcanic and clastic confining units (tuff confining unit, intrusive confining units, and the clastic Paleozoic rocks).

The carbonate aquifer is present outside the caldera boundaries and may be a significant pathway for transport if radionuclides leave the caldera region. Flow in the carbonate is fractured and/or dissolution-channel dominated and the effective porosity is expected to reflect that.

The porosity for vitric tuff units comes primarily from total porosity measurements because these units are expected to be dominated by porous flow rather than fracture flow.

Confining units include the tuff confining unit, intra-caldera intrusive confining units, granite confining units, and clastic confining units. The tuff confining units, when viewed as HSUs, are considered to be relatively impermeable and without significant fracture porosity. These confining units are treated as porous units for the purposes of effective porosity. However, for the sake of completeness, the fracture porosity for the tuff confining unit (HGU) has been calculated for two wells on Pahute Mesa using a parallel plate model. As noted earlier, the effective porosity of the TCU is in a similar range as for the volcanic aquifers. These measurements are believed to represent anomalous values for the confining units as a whole.

6.4.1.2 Data Sources

Specific sources for data required to estimate fracture porosity of the tuff confining unit are listed in [Table 6-10](#) below. For each parameter, a DTN from the ERP Common Data Repository and any related reports are listed, if applicable. In the more general case where flow through the vitric tuff aquifers and tuff confining units is expected to be primarily via porous flow, the porosity data are built upon the porosity database compiled during the data analysis phase of the regional groundwater model (IT, 1996e), as discussed in [Section 5.0](#).

Specific data sources for effective porosity of the carbonate aquifer include laboratory core measurements, and estimates derived from geophysical logs and tracer tests. Tracer tests conducted in the vicinity of Pahute Mesa include the USGS Amargosa Tracer Calibration Site, and a tracer test at Water Wells C and C-1 on the NTS. The sources of data are listed in [Table 6-11](#) including test locations and related reports.

Table 6-10
Sources for Data Required to Estimate
Fracture Porosity of Tuff Confining Unit

Parameter	Data Tracking Number (DTN)	Report Reference
Hydrostratigraphic/ Hydrogeologic Classification	NA	BN, 2002
Fracture Location	1180, 1181	IT, 2001b
Fracture Orientation	1180, 1181	IT, 2001b
Hydraulic Conductivity	974	IT, 2002 and g

NA = Not applicable

Table 6-11
Data Sources for the Effective Porosity of the Carbonate Aquifer

Source	Data Collection Method	Location
Winograd and Thordarson, 1975	Laboratory core experiment	Nevada Test Site and Vicinity
Berger, 1992	Geophysical logging	Coyote Springs, Nevada
Leap and Belmonte, 1992	Field tracer test	USGS Amargosa Valley Tracer Calibration Site
Winograd and West, 1962	Field tracer test	Water Wells C and C-1, Nevada Test Site

A compilation of fracture porosity values for clastic, metavolcanic, and crystalline rocks is available in a publication by Lee and Farmer (1993). Effective porosity values from cores were reported by Winograd and Thordarson (1975) for the Lower Clastic Confining unit. Effective porosity values for granitic intrusive rocks are available for northern Yucca Flat in a report by Walker (1962) and for the Stripa site, in Sweden, in a report by Neretnieks et al. (1989).

6.4.1.3 Data Documentation Evaluation

The five levels of data documentation flags are explained in detail in [Section 4.0](#). Data documentation flags for the parameters fracture location/fracture orientation, HGU/HSU classification, and hydraulic conductivity used to estimate fracture porosity are shown by the well in [Table 6-4](#). Data documentation flags for porosity estimates for the LCA are shown in [Table 6-12](#).

Sources of effective porosity data for the intrusive and clastic confining units were assigned a level of documentation of 4.

Table 6-12
Data Documentation Flags for Tracer Migration Experiments

Source	Location	Data Documentation Flag
Winograd and Thordarson, 1975	Nevada Test Site and Vicinity	5
Berger, 1992	Coyote Springs, Nevada	5
Leap and Belmonte, 1992	Amargosa Valley Tracer Tests	4
Winograd and West, 1962	Water Wells C and C-1 Tracer Tests	4

6.4.2 Data Evaluation

The evaluation of data follows approaches already provided with respect to the alluvial aquifer or volcanic units. The analysis of the porosity data of the porous units includes a comparison of core versus geophysically derived values, an assessment of depth dependence, and presentation of statistics as described in [Section 5.0](#).

6.4.2.1 Dataset Description

Estimates of fracture porosity of the tuff confining unit were obtained from calculations based on parallel plate models of fracture networks. Values of effective porosity estimated using parallel plate models are shown in [Table 6-13](#). Hydraulic conductivity values required to estimate apertures are listed in the table. Fracture spacing is calculated from fracture frequency data described in [Appendix E](#). These data are classified as confining units on the basis of the hydrogeologic unit, but are composite units when classified per the hydrostratigraphic unit. In any case, the fractured portions of the confining units are not expected to be a dominant component of the unit. Therefore, these data will not be used to define the effective porosity ranges for the confining units.

Two studies of tracer movement within or near the NTS have yielded estimates of effective porosity for the carbonate aquifer and are summarized in [Table 6-14](#).

The remainder of the confining units are separated into two groups. First are the deep intrusive bodies which are expected to have very small amounts of flow, but any flow that does occur will be through the fracture network. Second are the bedded or nonwelded confining units which are represented by porous flow and which were described in [Section 5.0](#).

**Table 6-13
Estimate of Fracture Porosity for the Tuff Confining Unit**

Well	Interval Name	Top of Interval (m)	Bottom of Interval (m)	Hydraulic Conductivity Minimum (m/s)	Hydraulic Conductivity Maximum (m/s)	Fracture Spacing (m)	Aperture Minimum (m)	Aperture Maximum (m)	Fracture Porosity Minimum	Fracture Porosity Maximum	Hydrogeologic Unit	Hydrostratigraphic Unit
ER-EC-2A	Screen 1	504.7	681.5	1.12E-07	1.85E-07	16.40	1.31E-04	1.55E-04	8.00E-06	9.46E-06	TCU	FCCM
ER-EC-2A	Screen 2-2	1,003.2	1,066.8	7.32E-08	1.19E-07	10.50	9.81E-05	1.15E-04	9.34E-06	1.10E-05	TCU	TMCM
ER-EC-8	Screen Joint 1	199.3	249.4	5.53E-05	1.31E-04	4.20	6.58E-04	8.78E-04	1.57E-04	2.09E-04	TCU	FCCM
ER-EC-8	Screen Joint 2	231.0	267.8	5.25E-05	1.89E-04	4.20	6.47E-04	9.91E-04	1.54E-04	2.36E-04	TCU	FCCM
ER-EC-8	Screen Joint 3	249.4	286.1	5.43E-06	2.01E-05	4.20	3.04E-04	4.70E-04	7.23E-05	1.12E-04	TCU	FCCM
ER-EC-8	Screen Joint 5	286.1	320.0	7.26E-07	1.78E-05	4.20	1.55E-04	4.51E-04	3.70E-05	1.07E-04	TCU	FCCM

**Table 6-14
Effective Porosity of the Carbonate Aquifer**

Source	Test	Effective Porosity Average	Effective Porosity Range	Hydrostratigraphic Unit
Winograd and Thordarson, 1975	Core studies	0.023	0 - 0.09	Carbonate Aquifer
Berger, 1992	Geophysical log analyses	-	0.006 - 0.096	Carbonate Aquifer
Leap and Belmonte, 1992	USGS Amargosa Valley Tracer Calibration Site	0.10	-	Carbonate Aquifer
Winograd and West, 1962	Water Wells C and C-1, Nevada Test Site	-	0.00064 to 0.005	Carbonate Aquifer

6.4.2.2 Data Generation

Effective Porosity of Tuff Confining Units

Fracture porosity for the tuff confining unit HGU was estimated using the parallel plate model method described in [Section 6.3.2.2](#). The results were plotted on [Figures 6-2 and 6-3](#). In those plots, the porosity of the confining units did not differ significantly from the aquifer units because the hydraulic conductivity values are in the same range as the aquifer units. However, as noted earlier, the intervals screened in the wells were placed across what was expected to be the more permeable zones. Therefore, these fractured zones in the tuff confining unit are not considered representative of that HGU.

The more general situation is for the confining units to be bedded and nonwelded volcanic tuffs. The bedded and nonwelded tuffs are considered confining units because they are generally zeolitized below the water table. The groundwater flow through these bedded confining units is very slow and primarily through the porous material, not through a fracture network. The effective porosity of the bedded confining units will be developed in the same manner as the alluvium. Hence, the effective porosity will be assumed to be slightly smaller than the total porosity.

[Figure 6-6](#) and [Figure 6-7](#) are probability frequency distribution plots for the bedded and nonwelded tuff lithologies, respectively. Both have a strong central tendency value near 40 percent with values that range approximately from 10 to 70 percent. These two data categories were combined into a single group and analyzed statistically. Probability density functions were fit to the probability frequency distributions using the program BestFit. The fitted distributions were ranked by the root mean squared error. A normal distribution was one of the best fits to the data with a mean value of 41 percent, and a standard deviation of 8 percent.

Further examination of the data as a function of depth ([Figure 5-3](#)) help explain some of the features of the probability frequency distribution (PFD) plots. The very high porosity values are associated with the shallowest measurements. Measurements near the water table (depth of 650 to 700 m) have a central value of about 40 percent and span a range of 30 to 50 percent, with some values outside that range. At greater depths, the number of values decrease substantially. However, there appears to be a trend of decreasing porosity at depths between 650 to 700 m. This apparent depth dependence of the effective porosity of the bedded and nonwelded units needs to be taken into consideration when the parameter distributions are presented.

Vitric Tuff Aquifers

The porosity data for the vitric tuff aquifers is summarized in [Figure 6-8](#). The dataset for the vitric tuff aquifers is limited, but does show that the porosity can span a wide range of values from about 4 percent up to 46 percent. The

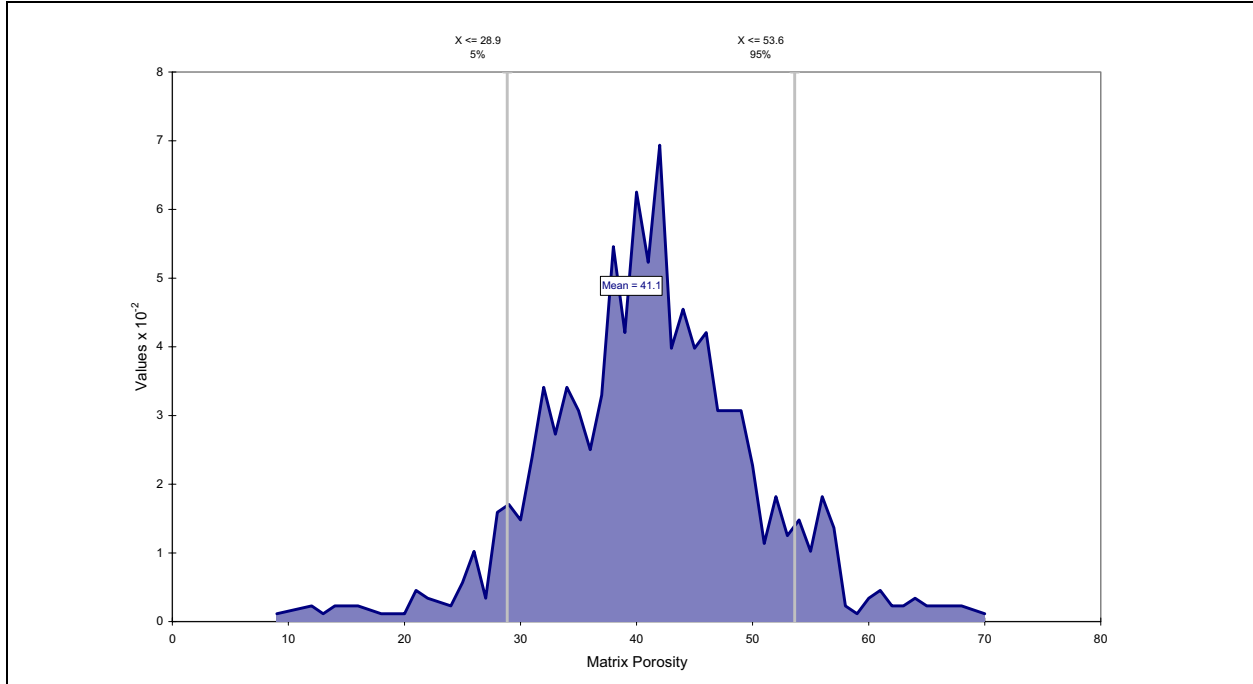


Figure 6-6
PFD of Porosity Data: Bedded Tuff Lithology (868 Samples)

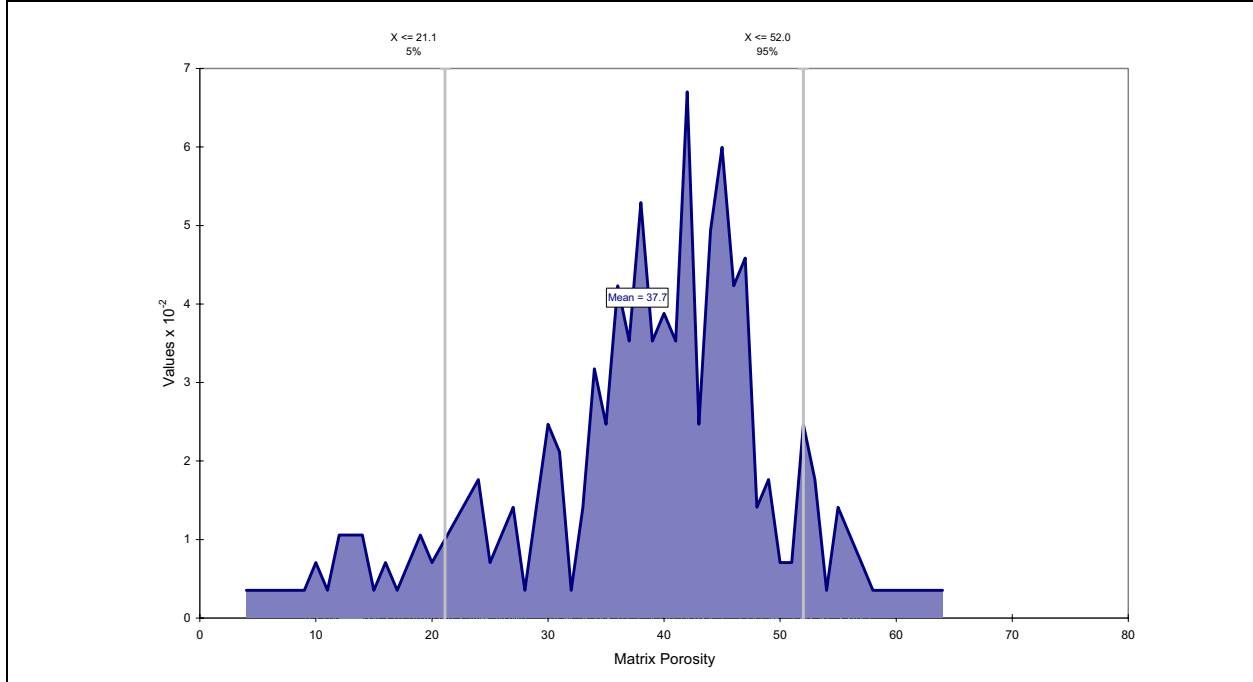


Figure 6-7
PFD of Porosity Data: Nonwelded Tuff Lithology (264 Samples)

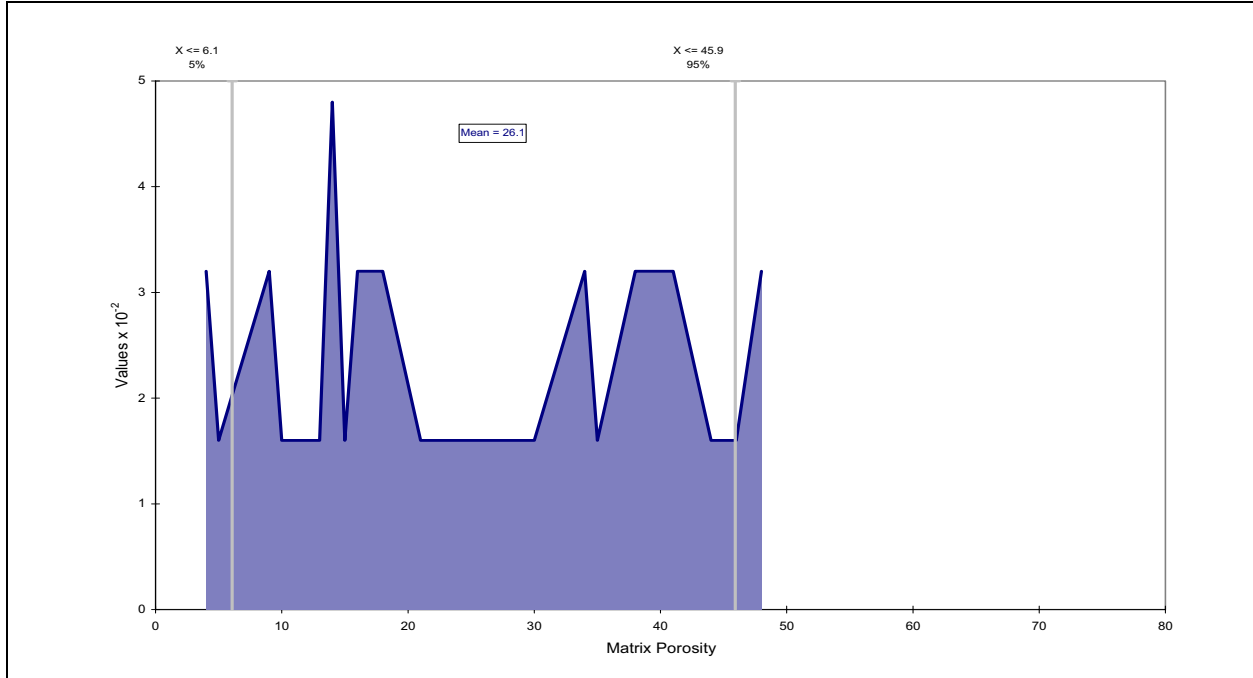


Figure 6-8
PFD of Porosity Data: Vitric Tuff Lithology (20 Samples)

distribution of values shows no central tendency, so a uniform distribution will be used.

Intrusive Confining Units and the Clastic Confining Units

Deep volcanic intrusives are believed to underlie the calderas. The intrusive confining units, which are represented by intrusive rocks in the HSU model (BN, 2002), are assumed to be fractured rocks, but the majority of the fractures are expected to be healed due to mineral precipitation or simply overburden pressure. There are no data regarding the porosity of these intrusive units on Pahute Mesa. However, Lee and Farmer (1993) summarize a large amount of information on fluid flow in fractured rock. They showed that fracture porosity typically ranges from 5×10^{-6} to 5×10^{-4} for clastic, metavolcanic, and crystalline rocks. At the Stripa site, in Sweden, the flow porosity is in the range of 1×10^{-5} to 2×10^{-4} (Neretnieks et al., 1989). In the Climax Stock, a granitic intrusive in northern Yucca Flat, the porosity of core samples averaged 9×10^{-3} (Walker, 1962). An appropriate range of effective porosity for the fractured intrusive confining units is taken to be 5×10^{-6} to 9×10^{-3} . With no other data, a log-uniform distribution will be assumed.

The clastic confining units are the Paleozoic clastics rocks, the Eleana/Chainman formation, and the Lower Clastic Confining Unit. Winograd and Thordarson (1975) reported estimates of effective porosity for the LCCU from core studies. Estimates of effective porosity were calculated using the mercury-injection method on 20 core samples. The estimates ranged from 0.006 to 0.05, with a median of 0.019 and a mean of 0.019. This range is higher than that of 5×10^{-6} to 5×10^{-4} reported by Lee and Farmer (1993) for various fractured rocks including

clastics. The core-derived range is probably not representative of the formation as the open fractures in the core samples are probably not part of the connected fracture network in the formation. Thus, the distributions for effective porosity of the LCCU and similar units will be taken from publication by Lee and Farmer (1993).

Lower Carbonate Aquifer

Effective porosity for the LCA reported by Winograd and Thordarson, 1975; Berger, 1992; Leap and Belmonte, 1992; and Winograd and West, 1962, are presented.

Winograd and Thordarson (1975) reported estimates of effective porosity for the LCA from core studies. Estimates of effective porosity were calculated using the mercury-injection method. The estimates ranged from 0.00 to 0.09, with a median of 0.011 and a mean of 0.023. Except for the lower end of the range, the core-derived values most probably represent higher than actual values because the open and vuggy fractures tested are not necessarily connected to other open fractures in the formation. In addition, effective porosity measurements in cores may be lower than actual values when the fractures present in the core samples are all closed. Effective porosity measurements derived from cores are, therefore, assigned a “low” level of quality for the intended use.

Berger (1992) analyzed geophysical data to derive porosity for several carbonate wells located in Coyote Springs Valley, east of the NTS. Their analysis resulted mostly in total porosity values. They also generated M-N plots to detect secondary porosity and provide additional information on the mineral composition of the rocks. The magnitude of the secondary porosity was estimated from the M-N plots for Well CE-DT. The range was estimated to be between 0.006 and 0.096 Berger (1992). The data were, however, obtained from zones interpreted to be composed almost completely of silica. Secondary porosity measurements derived from geophysical logs are assigned a “low” level of quality for the intended use because they represent limited areas around the borehole.

Leap and Belmonte (1992) examined data from the USGS’ Amargosa Tracer Calibration Site, located 24 km southwest of Mercury, Nevada. They reported that the tracer test was conducted within a fractured section of the Bonanza King dolomite of the carbonate aquifer. The thickness of the tested interval ranged between 3.1 to 14.6 m. The average tested interval thickness was 8.5 m. Leap and Belmonte (1992) calculated an effective porosity of 0.10 for this interval.

A preliminary assessment of the Winograd and West (1962) tracer experiment at Water Wells C and C-1, located on the NTS, was conducted by IT (1999). This assessment yielded an effective porosity between 0.00064 and 0.005 for the carbonate aquifer. The derivation of the porosity range from IT (1999) is presented here in detail. The effective porosity can be estimated from tracer tests conducted by Winograd and West (1962) at the Water Well C and C-1 site in Yucca Flat. This tracer test was conducted at the southern end of the Yucca Flat in Area 6 of the NTS to determine the rate of movement of groundwater between two wells 30.5 m apart. The objective of the test was to understand whether the drilling mud used at Water Well C-1 might be carried by groundwater to

production Well C. The unconfined aquifer tapped by these wells is fractured limestone of Paleozoic age which, as shown by cores from Water Well C, transmits water primarily through fractures. The total depth of Water Well C is 518.5 m with 32.9 m of screen at the depth of 478.2 m to 511.1 m. The submersible pump delivered 1,200 m³/d, creating less than 0.15 m of drawdown. Water Well C-1 was drilled to a depth of 520.3 m. The opening (uncased hole) begins at the depth of 281.6 m to the bottom of the well. The actual distance between the two wells is 29.3 m at the water table. Fluorescein, used as a tracer, was injected into Water Well C-1. The tracer was clearly seen in a sample collected 252 minutes after discharge began. Samples of water were collected periodically for 17 hours after the first appearance of the dye. The concentration of the tracer gradually increased to a maximum in another 3 to 4 hours (432 to 492 minutes after discharge began) and then slowly decreased until, in another 4 to 5 hours ($t_e = 672$ to 792 minutes after discharge began), it was no longer visually detectable.

To estimate the effective porosity, the radial flow tracer experiment case of Welty and Gelhar (1989) was used to relate the time to the peak concentration to the pumping rate and porosity-thickness product through the relation:

$$t_m = R^2 \pi n b / Q \quad (6-7)$$

where:

- t_m = Time to the peak concentration (assuming a Gaussian breakthrough)
- R = The distance between wells
- Q = The discharge rate
- n = Effective porosity
- b = Tested interval thickness

Rearranging the equation and using $Q = 0.83$ cubic meters per minute (m³/min), $R = 29.3$ m, and $t_m = 496$ min, the nb product is found to be 0.04 m. Using the thickness of 32.9 m from Water Well C, the effective porosity is 0.005. If the greater thickness from Water Well C-1 of 239 m is used, then the effective porosity is 0.00064.

The simplistic radial flow solution was used because the sparsity of the data collected during the experiment did not allow the use of a more sophisticated solution. In the radial flow solution, the transport of the tracer is assumed to be caused by advection only. Other transport processes such as matrix diffusion are not accounted for in this method. The derived values of effective porosity may, therefore, be larger than the actual values.

Tracer tests provide the best estimates of effective porosity for modeling at the CAU scale. Effective porosity values derived from tracer tests data are, therefore, assigned a "high" level of quality.

Although the range of possible effective porosity values derived from the two tracer tests for the carbonate aquifer is very wide (0.00064 to 0.1), it is the most representative for the intended use. Ranges estimated from cores (0.00 - 0.09 [Winograd and Thordarson, 1975]) and geophysical logs (0.006 - 0.096 [Berger, 1992]) are comparable to those derived from tracers tests only at the high end. The low end of effective porosity ranges obtained from cores and geophysical logs are not representative of the larger scales needed for the model. As no new tracer tests have been recently conducted in the carbonates, the distributions for effective porosity of the LCA will be taken from the regional tritium transport model (DOE/NV, 1997).

6.4.3 Development of Parameter Distributions

The parameter distributions for the vitric tuff aquifers and tuff confining units were developed from the PFDs of the porosity data. The PDFs of the other units, summarized in [Section 6.5](#), were taken from the NTS regional model.

6.4.4 Data Limitations

The same data limitations apply as were discussed for volcanic aquifers in [Section 6.3.4](#). Radionuclides are not expected to migrate through any of the intrusive confining units, so the lack of site-specific data is not considered to be a major shortcoming.

6.4.5 Scaling Considerations

As noted for porosity data for the other units, it is expected that as the porosity data are averaged into larger volumes, such as the model grid cells, the variability will reduce. Unfortunately, the basic statistical description of the small-scale values is lacking. In the absence of quantitative measures of spatial variability, no credit is taken for the variance reduction.

A second, and more important issue, related to scaling is the apportionment of effective porosity in a model layer made up of widely different lithologies, such as in a composite unit. Consider a model layer 100 meters thick, with a 25 meter thick fractured unit (effective porosity = 0.01) surrounded by bedded tuff (effective porosity = 25 percent). The appropriate effective porosity is not thickness weighted arithmetic average, which is 19 percent in this case. The geometric mean, as presented in [Table 6-15](#), yields an effective porosity of 11 percent. If the fractured layer is continuous through the entire model cell, then even the geometric mean will produce an inappropriate parameter. In many cases, however, there is no way to know if the fractured unit is continuous. If it were, it would most likely have been mapped as a continuous unit. Nonetheless, this points out factors that will need to be taken into account if the effective porosity values are to be scaled for the CAU model.

6.5 Summary of Effective Porosity by Hydrostratigraphic Unit

Some of the HSUs contain multiple HGUs. As presented in the preceding sections, the effective porosity can vary significantly depending on the dominance of fracture flow in the unit. The approach for estimating the mean effective porosity for an HSU with multiple HGUs is presented in this section.

Table 6-15 is a summary of the effective porosity distributions assigned to each of the HSUs expected in the Pahute Mesa CAU model. In some cases, the distribution derived for a specific HSU is the same as the corresponding HGU such as the Alluvial Aquifer, the Intrusive Volcanic Confining Units, and the Lower Carbonate Aquifer. The fractured volcanic aquifer units were given the same effective porosity distribution because the limited amount of HSU-specific fracture porosity data did not suggest any differences between fracture porosity values of the aquifer HSUs.

The effective porosity values of the vitric tuff aquifers and the volcanic confining units are based on the total porosity, with a correction for the apparent decrease in total porosity with depth for the bedded and nonwelded lithologies. The same relationship will be used for all the bedded and welded volcanic confining units, but the depth dependence will produce different effective porosities in different units. The vitric tuff units were assigned one porosity distribution based on the limited available data.

Any volcanic HSU composed of multiple HGUs, especially the composite units, are a more difficult problem. A few of the volcanic aquifers are composed of fractured flow-dominated HGUs and porous flow-dominated vitric tuff. The composite units are, by definition, complex units with a wide range of lithologies from densely welded tuffs to nonwelded and bedded units. These units are generally expected to have a wide range of lithologies. If the composite unit can be described as having continuous interconnected welded units, then the effective porosity of the unit should reflect fracture flow as dominant. On the other hand, if the welded units are not continuous, then the bedded and nonwelded effective porosities should dominate. However, in most cases, it is not possible to definitively state the dominant continuous lithology - otherwise, the unit would have been subdivided in the first place.

An approach is proposed for assigning effective porosity on the basis of percentage of each lithology in each HSU composed of multiple HGUs. A weighted geometric mean of the porosities will be calculated. For example, if the composite unit is made up of two lithologies (welded and bedded), with porosities of 0.0001 and 0.3, respectively. And if the composite unit is 75 percent welded, suggesting fracture dominated flow, the geometric mean is 0.0007. Or if the composite unit is 25 percent welded suggesting porous dominated flow, the geometric mean effective porosity is 0.04. The weighted geometric mean of the reported lithologies appears to provide a reasonable estimate of the appropriate mean effective porosity. The range of effective porosity will be taken to the range provided by the respective HGUs. In the example, the range in both cases would be 0.00001 to 0.55. The distribution is assumed to be log triangular. This will emphasize the mean porosity yet maintain the full range of values.

Table 6-15
Pahute Mesa - Effective Porosity - Dominant Lithology for Each HSU
 (Page 1 of 3)

Layer Number	Symbol	Name	Dominant HGU	Continuous Lithology	Transport Parameter Category	Lower Bound	Mean	Upper Bound	Distribution	Fractured	Vitric	Porous	Geometric Mean
46	AA	Alluvial Aquifer	AA	AI	Alluvium	23.8	32	40.2	Normal			1	
45	YVCM	Younger Volcanic Composite Unit	LFA, WTA, VTA	PWT	WTA 75% VTA 25%	0.00001	0.00402	0.46	Log Triangular	0.75	0.25		0.00402
44	TCVA	Thirsty Canyon Volcanic Aquifer	WTA, LFA, lesser VTA	WT	WTA 75% LFA 25%	0.00001	0.001	0.1	Log Triangular	1			0.001
43	DVCM	Detached Volcanics Composite Unit	WTA, LFA, TCU	PWT	WTA 85% TCU 15%	0.00001	0.00246	0.55	Log Triangular	0.85		0.15	0.00246
42	DVA	Detached Volcanics Aquifer	WTA, LFA	WT	WTA	0.00001	0.001	0.1	Log Triangular	1			0.001
41	FCCM	Fortymile Canyon Composite Unit	LFA, TCU, lesser WTA	PWT	LFA 60% TCU 30% WTA 10%	0.00001	0.00603	0.55	Log Triangular	0.7		0.3	0.00603
40	FCA	Fortymile Canyon Aquifer	WTA, LFA	WT	WTA 80% LFA 20%	0.00001	0.001	0.1	Log Triangular	1			0.001
39	TMCM	Timber Mountain Composite Unit	TCU, unaltered WTA, lesser LFA	DWT	TCU 75% WTA 25%	0.00001	0.08944	0.55	Log Triangular	0.25		0.75	0.08944
38	THLFA	Tannenbaum Hill Lava-flow Aquifer	LFA	LA	LFA	0.00001	0.001	0.1	Log Triangular	1			0.001
37	THCM	Tannenbaum Hill Composite Unit	TCU, lesser WTA	NWT	TCU 75% WTA 25%	0.00001	0.08944	0.55	Log Triangular	0.25		0.75	0.08944
36	TMA	Timber Mountain Aquifer	WTA, minor VTA	WT	WTA 80% VTA 20%	0.00001	0.00304	0.46	Log Triangular	0.8	0.2		0.00304
35	SCVCU	Subcaldera Volcanic Confining Unit	TCU	NWT	TCU	0.1	0.4	0.55	Normal			1	0.4
34	FCCU	Fluorspar Canyon Confining Unit	TCU	NWT	TCU	0.1	0.4	0.55	Normal			1	0.4
33	WWA	Windy Wash Aquifer	LFA	LA	LFA	0.00001	0.001	0.1	Log Triangular	1			0.001
32	PCM	Paintbrush Composite Unit	WTA, LFA, TCU	MWT	WTA 75% TCU 25%	0.00001	0.00447	0.55	Log Triangular	0.75		0.25	0.00447
31	PVTA	Paintbrush Vitric-tuff Aquifer	VTA	BED	VTA	0.05	0.26	0.46	Uniform		1		0.26
30	BA	Benham Aquifer	LFA	LA	LFA	0.00001	0.001	0.1	Log Triangular	1			0.001
29	UPCU	Upper Paintbrush Confining Unit	TCU	BED	TCU	0.1	0.4	0.55	Normal			1	0.4

Table 6-15
Pahute Mesa - Effective Porosity - Dominant Lithology for Each HSU
 (Page 2 of 3)

Layer Number	Symbol	Name	Dominant HGU	Continuous Lithology	Transport Parameter Category	Lower Bound	Mean	Upper Bound	Distribution	Fractured	Vitric	Porous	Geometric Mean
28	TCA	Tiva Canyon Aquifer	WTA	WT	WTA 70% VTA 30%	0.00001	0.0053	0.46	Log Triangular	0.7	0.3		0.0053
27	PLFA	Paintbrush Lava-flow Aquifer	LFA	LA	LFA	0.00001	0.001	0.1	Log Triangular	1			0.001
26	LPCU	Lower Paintbrush Confining Unit	TCU	NWT	TCU	0.1	0.4	0.55	Normal			1	0.4
25	TSA	Topopah Spring Aquifer	WTA	WT	WTA	0.00001	0.001	0.1	Log Triangular	1			0.001
24	YMFCM	Yucca Mountain Crater Flat Composite Unit	LFA, WTA, TCU	PWT	WTA 75% TCU 25%	0.00001	0.00447	0.55	Log Triangular	0.75		0.25	0.00447
23	CHVTA	Calico Hills Vitric-tuff Aquifer	VTA	NWT	VTA	0.05	0.26	0.46	Uniform		1		0.26
22	CHVCM	Calico Hills Vitric Composite Unit	VTA, LFA	NWT	VTA 75% LFA 25%	0.00001	0.06475	0.46	Log Triangular	0.25	0.75		0.06475
21	CHZCM	Calico Hills Zeolitic Composite Unit	LFA, TCU	NWT	TCU 75% LFA 25%	0.00001	0.08944	0.55	Log Triangular	0.25		0.75	0.08944
20	CHCU	Calico Hills Confining Unit	TCU, minor LFA	NWT	TCU 90% LFA 10%	0.00001	0.21971	0.55	Log Triangular	0.1		0.9	0.21971
19	IA	Inlet Aquifer	LFA	LA	LFA	0.00001	0.001	0.1	Log Triangular	1			0.001
18	CFCM	Crater Flat Composite Unit	LFA, intercalated TCU	WT	LFA 75% TCU 25%	0.00001	0.00447	0.55	Log Triangular	0.75		0.25	0.00447
17	CFCU	Crater Flat Confining Unit	TCU	NWT	TCU	0.1	0.4	0.55	Normal			1	0.4
16	KA	Kearsarge Aquifer	LFA	LA	LFA	0.00001	0.001	0.1	Log Triangular	1			0.001
15	BCU	Bullfrog Confining Unit	TCU	NWT	TCU	0.1	0.4	0.55	Normal			1	0.4
14	BRA	Belted Range Aquifer	LFA, WTA, lesser TCU	WT	WTA 50% LFA 50%	0.00001	0.001	0.1	Log Triangular	1			0.001
13	PBRCM	Pre-belted Range Composite Unit	TCU, WTA, LFA	PWT	TCU 75% WTA 25%	0.00001	0.08944	0.55	Log Triangular	0.25		.75	0.08944
12	BMICU	Black Mountain Intrusive Confining Unit	IICU	IN	Intrusive	5E-06	0.00005	0.009	Log Uniform	1			0.00005
11	ATICU	Ammonia Tanks Intrusive Confining Unit	IICU	IN	Intrusive	5E-06	0.00005	0.009	Log Uniform	1			0.00005

Table 6-15
Pahute Mesa - Effective Porosity - Dominant Lithology for Each HSU
 (Page 3 of 3)

Layer Number	Symbol	Name	Dominant HGU	Continuous Lithology	Transport Parameter Category	Lower Bound	Mean	Upper Bound	Distribution	Fractured	Vitric	Porous	Geometric Mean
10	RMICU	Rainier Mesa Intrusive Confining Unit	IICU	IN	Intrusive	5E-06	0.00005	0.009	Log Uniform	1			0.00005
9	CCICU	Claim Canyon Intrusive Confining Unit	IICU	IN	Intrusive	5E-06	0.00005	0.009	Log Uniform	1			0.00005
8	CHICU	Calico Hills Intrusive Confining Unit	IICU	IN	Intrusive	5E-06	0.00005	0.009	Log Uniform	1			0.00005
7	SCICU	Silent Canyon Intrusive Confining Unit	IICU	IN	Intrusive	5E-06	0.00005	0.009	Log Uniform	1			0.00005
6	MGCU	Mesozoic Granite Confining Unit	GCU	IN	Intrusive	5E-06	0.00005	0.009	Log Uniform	1			0.00005
5	LCA3	Lower Carbonate Aquifer - Thrust Plate	CA	DM	carbonate	0.001	0.004	0.01	Log Normal	1			0.004
4	LCCU1	Lower Clastic Confining Unit - Thrust Plate	CCU	Quartzite	clastic	5E-06	0.00003	0.0005	Log Normal	1			0.00003
3	UCCU	Upper Clastic Confining Unit	CCU	SLT	clastic	5E-06	0.00003	0.0005	Log Normal			1	NA
2	LCA	Lower Carbonate Aquifer	CA	DM	carbonate	0.001	0.004	0.01	Log Normal	1			0.004
1	LCCU	Lower Clastic Confining Unit	CCU	Quartzite	clastic	5E-06	0.00003	0.0005	Log Normal	1			0.00003

7.0 *Dispersivity*

This section includes descriptions of the role of dispersion in contaminant transport in groundwater, the available dispersivity data, and the data analysis and associated results.

7.1 *Role of Dispersion in Contaminant Transport*

The hydrodynamic dispersion of solutes in groundwater describes the spreading phenomenon at a macroscopic level by the combined action of mechanical dispersion and molecular diffusion (EPA, 1988). At typical scales of observation, dispersion is a mixing process, the result of which causes dilution of the solute (Freeze and Cherry, 1979). The effect of dispersion is commonly quantified and measured in terms of longitudinal and transverse dispersivities. Assessment of aquifer dispersivity is essential for predicting contaminant concentrations in groundwater. The dispersivities, both the longitudinal and transverse, are key input parameters to the governing transport equation used to estimate the concentration distribution of a solute in groundwater over time and space.

Dispersivity values are derived from data collected during tracer experiments or other observations of plume migration. Based on the existing data, dispersivity appears to be scale-dependent (Gelhar et al., 1992; Neuman, 1990), but the exact dispersivity value at any site and any scale is not discernable from the available data. Field-scale dispersion of plumes is generally accepted to be the result of the heterogeneous velocity field at scales smaller than the scale of the plume. Heterogeneity at scales larger than the plume cause changes in the mean position of the plume, but do not contribute to dispersion. The nature of heterogeneity likely differs from site to site; therefore, dispersivity values may differ from site to site, sometimes by orders of magnitude.

For small-scale sites, it is a common practice to conduct field-scale tracer tests to obtain dispersivity values suitable for modeling that given site. However, with a site as large and as varied as the Pahute Mesa CAU, it is not practical to conduct tracer tests in enough locations to accurately measure dispersivity. Additionally, tracer tests conducted at scales of a few hundred meters may not yield dispersivity values appropriate at the CAU scale because of the apparent trends in dispersivity with scale. Time and budget constraints make it nearly impossible to perform a tracer test at the CAU scale. Thus, the appropriate dispersivity to use for the CAU scale modeling will depend on the size of the plume and expected distance of travel. The treatment of dispersion in the CAU model will be documented as part of the model report. This report is intended to document the available data.

7.2 Data Compilation

The dispersivity data types, the sources of data, and the data quality evaluation process are described in this section.

7.2.1 Data Types

As stated above, dispersivity values are derived from information collected during tracer tests. Thus, data types needed to document the dispersivity data include site and test information, data analysis method and results, and the sources of information.

7.2.2 Data Sources

The available dispersivity measurements conducted at or near the NTS were derived from six tracer transport experiments. Five of these experiments were conducted at the following sites:

- BULLION Test, Pahute Mesa, Nevada
- C-Well Complex, Yucca Mountain, Nevada
- Amargosa Tracer Calibration Site, Amargosa Desert, Nevada
- C-Well Site, Yucca Flat, Nevada
- CAMBRIC Site, Frenchman Flat, Nevada

The sixth experiment (CHESHIRE site) was terminated prior to completion and dispersivity values were not determined. Additional data available for non-NTS sites were obtained from the literature. An important source of non-NTS dispersivity data is the dispersivity review paper of Gelhar et al. (1992). Tracer test data for the NTS and vicinity will be used to supplement the data available from the literature to derive a range of dispersivity values for use in the Pahute Mesa CAU model.

7.2.3 Data Documentation Evaluation

DDE_Fs were assigned to all information of a given tracer test based on the level of documentation available as described in [Section 4.0](#). The BULLION FGE is the only tracer test conducted under the ERP and was assigned a DDE_F of 1 as adequate documentation is available. Documentation of the tracer tests conducted at the CAMBRIC and C-well complex of Yucca Mountain were assigned a level of 3 as these two tests were conducted outside of the ERP but are well documented. Documentation on the tracer tests conducted in Yucca Flat and Amargosa Desert was assigned a level 4. All other data were assigned a DDE_F of 5 as sufficient documentation on the procedures and their application during field data collection and analysis are not readily available.

7.3 Data Evaluation

The approach is to summarize the existing NTS tracer experiments including the range of values obtained by different investigators, and incorporate data from the compilation of dispersivity available from the literature to determine a range of values appropriate for the transport modeling effort. Descriptions of the available data are presented followed by the results of the data analysis.

7.3.1 Dataset Description

The dispersivity data derived from the available tracer tests were compiled into a comprehensive dataset described in [Appendix E](#). The dataset contains 148 records containing NTS and non-NTS data. Summary descriptions of the available NTS-related and non-NTS dispersivity data are provided in this section. Dispersivity values derived from modeling are also presented and discussed. They were, however, not included in the dataset because the modeling studies do not constitute data.

7.3.1.1 NTS Data

This section describes the six tracer tests conducted to date at the NTS and vicinity. Results derived from the tracer test data using different technical approaches are included in the descriptions. The data for five of the tests are summarized in [Table 7-1](#) and are described with regard to the aquifer type and geology, test method, tracer type, analytical method, and the derived dispersivities. In two of the cases, the tracer breakthrough data were analyzed by a new method and presented for comparison with published values, if available. The CHESHIRE tracer test is not listed in [Table 7-1](#) because it was terminated prior to completion, and dispersivity values could not be derived from the test.

7.3.1.1.1 BULLION Site

The field portion of the BULLION FGE was performed from June to August 1997 at the BULLION underground nuclear test site on Pahute Mesa, Area 20, of the NTS. Three characterization wells (ER-20-6 #1, #2, and #3) were completed in a fractured lava-flow aquifer, approximately downgradient of the BULLION cavity, aligned with the dominant fracture system. The most downgradient well (#3) was pumped to induce groundwater movement from the BULLION cavity and from Wells #1 and #2 to Well #3. The distance between wells (i.e., straight line length) ranged from 42 to 132 m (IT, 1998a). The shortest distance is between Wells #1 and #2 and the largest distance is between Wells #1 and #3. Pentafluorobenzoic acid and yellow polystyrene microsphere tracers were injected into Well #2 and sodium iodide, difluorobenzoic acid, and red polystyrene microspheres were injected into Well #1. Tracer concentrations were monitored to produce decline and/or breakthrough curves for each well. Hydraulic data were also collected during the FGE. Groundwater flow and tracer transport were evaluated by

**Table 7-1
Dispersivity Information Summary from the Nevada Test Site and Vicinity**

Site Location	Test Site Geology	Scale of Test (meters)	Test Method	Tracers	Analysis Method	Longitudinal Dispersivity (meters)	References
BULLION Test, Pahute Mesa, Nevada	Fractured lava-flow aquifer, Calico Hills Formation	42.3 to 131.5	Radial converging with monitoring at an intermediate well and the pumped well	Pentafluorobenzoic acid; difluorobenzoic acid; sodium iodide; carboxylate-modified latex polystyrene microspheres	Calibration of numerical 3-D transport model and 2-D analytic	10 (horiz. trans. 3) (vert. trans. 2)	IT, 1998a; Reimus and Haga, 1999
C-Well Complex, Yucca Mountain, Nevada	Bull Frog and Tram Tuffs	90	Radial conversion with two injection wells	Iodide; difluorobenzoic acid; pyridone; pentafluorobenzoic acid; lithium bromide; polystyrene microspheres	1-D and 2-D analytical models	3.3 to 59	Winterle and La Femina, 1999
Amargosa Tracer Calibration Site, Amargosa Desert, Nevada	Cambrian Bonanza King Dolomite (fractured)	122.8	Doublet recirculation (tritium, sulfur-35, bromide)	Tritium (pulse)	1-D quasi-uniform Fitting of Grove's curves	15 to 30.5	Leap and Belmonte, 1992
C-Well Site, Yucca Flat, Nevada	Fractured Limestone	29.3	Radial converging (fluorescein) test at Well C and C-1	Fluorescein dye	2-D analytical Welty and Gelhar (1994)	0.6 to 1.4	Winograd and West, 1962 (calculation not included)
CAMBRIC Test, Frenchman Flat, Nevada	Tuffaceous Alluvium	91.0	Radial converging with monitoring the elutions of tritium and chlorine-36 at pumping Well RNM-2S	Nuclear test radionuclides: H3	1. Welty and Gelhar, 1994	9.6	Thompson, 1991 (calculation not included)
				Nuclear test radionuclides: H3	2. Sauty's Method	2.0	Burbey and Wheatcraft, 1986
				Nuclear test radionuclides: H3	3. Sauty's Method	9.1	Travis et al., 1983
				Nuclear test radionuclides: H3, Cl-36	4. Sauty's Method	15.1	Thompson, 1988; Ogard et al., 1988

^aDFBA = Difluorobenzoic acid

^bPFBA = Pentafluorobenzoic acid

analytical (Reimus and Haga, 1999) and numerical modeling (IT, 1998a). Based on calibration of the BULLION numerical transport model, the following dispersivities were determined (Table 7-1):

- Longitudinal: 5, 10, or 25 m (alternative calibrations)
- Horizontal transverse: 1, 3, or 7.5 m (alternative calibrations)
- Vertical transverse: 1, 2, or 5 m (alternative calibrations) (IT, 1998a).

The semianalytical solutions of Reimus and Haga (1999) yielded the following dispersivity values:

- Longitudinal: 9 to 30 (alternative calibrations)
- Horizontal transverse: not applicable
- Vertical transverse: not applicable

The longitudinal and horizontal transverse dispersivities are in the range of measured values summarized by Gelhar et al. (1992) for tests at scales of about 100 m. Both the numerical and semi-analytic models simulated matrix diffusion as a separate process. Therefore, the longitudinal dispersivities are representative of mechanical dispersion and are not biased upward by lumping matrix diffusion effects. There is not much confidence in the horizontal transverse dispersivity because the radial flow configuration of the FGE is not sensitive to transverse dispersion due to averaging at the pumped well. The vertical dispersivity is also unreliable because the tracer was vertically mixed within the model layer. Therefore, the vertical dispersivity in the model was irrelevant.

The longitudinal dispersivity for the shorter flow path, 42 m (Well #1 to #2), may be too large, based on a sensitivity analysis of dispersivity where it appeared that a relatively large dispersive flux was causing tracer migration upgradient against the direction of groundwater flow. This situation is physically unrealistic (IT, 1998a). Another explanation for the large spreading predicted by the model, including upgradient, may be numerical dispersion. If this is a numerical dispersion effect, then part of the dispersive flux is generated by the numerical dispersion and the calibrated longitudinal dispersivity may be too small. The similarity between the numerical and semi-analytical derived longitudinal dispersivity suggests that the impact of numerical dispersion is not too large.

7.3.1.1.2 C-Well Complex Site

The C-well complex is located at Yucca Mountain, Nevada, less than 16 km (10 miles) south of the Pahute Mesa-Oasis Valley area. The flow and transport experiments were conducted to determine the properties of the Bullfrog volcanic tuff beneath Yucca Mountain in the saturated zone.

The estimated transmissivity of the aquifer determined from pump tests vary from 640 to 3,500 square meters per day (m^2/day), with much of the variance due to a significantly higher transmissivity for Well C#2, which may not be indicative of the large-scale aquifer properties. Composite analysis of the aquifer tests using the Theis method yielded 2,200 m^2/day , and considering horizontal anisotropy, the Papadopulos method gave 1,300 m^2/day . The horizontal anisotropy analysis indicates a directional transmissivity of 2,900 m^2/day oriented N 33° E, and a minimum of 580 m^2/day at N 123° E. It is believed that the fracture network is primarily responsible for the anisotropy.

The tracer tests consisted of two pilot tests using pentafluorobenzoate (PFBA) and iodide, and a long-term multiple-tracer test using PFBA and lithium bromide. Colloidal transport was also performed using 360-nanometer (nm) microspheres.

The method used to estimate the aquifer parameters is described in Appendix A of Reimus et al. (1999). The method applies to one-dimensional, steady-state, advective-dispersive flow through parallel-plate fractures in a homogenous, dual-porosity aquifer. The longitudinal dispersivity from the single successful pilot test is reported to be 1.1 m. The longitudinal dispersivity from the long-term test yielded a range from 3.3 to 59 m (Winterle and La Femina, 1999). The test provided important information about the relative role of matrix diffusion as a result of normalized peak concentrations between bromide and the PFBA. Although the matrix diffusion was not specifically determined, it was apparent that it played an important role as an effective attenuation mechanism for dissolved species in the volcanic aquifer. This relative aspect of the dispersion/matrix diffusion is discussed in the summary for this section.

7.3.1.1.3 Amargosa Tracer Calibration Site

Tracer tests were conducted at the Amargosa Tracer Calibration Site located in the Amargosa Desert in southern Nevada, approximately 24 kilometers southwest of Mercury, Nevada (Leap and Belmonte, 1992). The objectives of the tracer tests were to:

- Determine the apparent longitudinal dispersivity of a fissured and fractured aquifer within the Cambrian Bonanza King dolomite draining the NTS.
- Determine the effective porosity of the carbonate aquifer.
- Study the usefulness of tritium, sulfur-35, and bromide as tracers in this aquifer.

The tests were performed under different recirculating rates and pore pressures. Two fully penetrating wells, aligned parallel with the direction of regional flow (northeast to southwest), were used for tracer recirculating tests. The injection well was located 122.8 m upgradient of the pumping well, and they were connected together by a polyvinyl chloride (PVC) pipe. Measurements of the transmissivity of the aquifer ranged from 4,800 to 10,900 m²/day. The storage coefficient was approximately 5×10^{-4} and the regional hydraulic gradient was between 10^{-4} and 10^{-5} . Two other fully penetrating wells in the vicinity were used to collect water samples.

Breakthrough curves were constructed from analysis of effluent samples collected from the pumping well. These curves were matched and compared to synthetic curves constructed from various combinations of porosity and longitudinal dispersivity using the Grove method (Grove and Beteem, 1971), which provides a solution to the Fickian dispersion model. Apparent dispersivities of the aquifer were then taken to be those of the best-fit synthetic curves, within an accuracy of ± 3.0 m.

The results of these tests are as follows:

- Test 1 (tritium as tracer) yielded a best-fit apparent dispersivity of 15 m and a porosity of 10 percent.
- Test 2 (sulfur-35 in the form of sodium sulfate as tracer) yielded a best-fit dispersivity of 22.9 m and a porosity of 10 percent.
- In Test 3 (tritium and bromide as tracers), the tritium curve fit yielded an apparent dispersivity of 27.4 m and a porosity of 10 percent; the bromide curve fit yielded an apparent dispersivity of 30.5 m and a porosity of 10 percent. The tests were run at a recirculation rate of 31 percent less than that of Test 1.

The relatively large difference in apparent dispersivity between the sulfur-35 and tritium tests is likely caused by greater adsorption and/or retardation of the more active sulfate ion than that of either the bromide or tritiated water. The 10-percent difference in computed apparent dispersivity between the two tracers (tritium and bromide) for the same recirculation rate (Test 3) was attributed to the adsorption or retardation difference between tritium and bromide. The difference between Tests 1 and 3 is more difficult to explain. Leap and Belmonte (1992) postulated that the differences were due to changes in fracture openings caused by the increased pressure for the higher flow test. The variation between Tests 1 and 3 emphasizes the typical range in dispersivity values at a single site.

7.3.1.1.4 C-Well Site, Yucca Flat

The tracer test was conducted at the southern end of Yucca Flat in Area 6 of the NTS to determine the rate of movement of groundwater between two wells (Water Wells C and C-1) 30.5 m apart (Winograd and West, 1962). The objective of the test was to understand whether the drilling mud used at Water Well C-1 might be carried by groundwater to the production Well C.

The unconfined aquifer tapped by these wells is fractured limestone of Paleozoic age which, as shown by cores from Water Well C, transmits water primarily through fractures. The total depth of Water Well C is 518.5 m with 32.9 m of screen at the depth of 478.2 to 511.1 m. The submersible pump delivered 1,200 cubic meters per day (m^3/day) creating less than 0.15 m of drawdown. Well C-1 was drilled to a depth of 520.3 m. The opening (uncased hole) begins at the depth of 281.6 m to the bottom of the well. The actual distance between the two wells is 29.3 m at the water table.

Fluorescein, used as a tracer, was injected in Water Well C-1. The tracer was clearly seen in a sample collected 252 minutes (t_0) after discharge began. Samples of water were collected periodically for 17 hours after the first appearance of the dye. The concentration of the tracer gradually increased to a maximum in 3 to 4 hours (432 to 492 minutes) after discharge began, and then slowly decreased until, in another 4 to 5 hours ($t_e = 672$ to 792 minutes) after discharge began, it was no longer detectable with the naked eye.

The velocity of the first arrival was estimated to be 0.12 meters per minute. However, the peak concentration was not included in the report.

An equation developed by Welty and Gelhar (1989) to estimate the longitudinal dispersivity is as follows:

$$\Delta t = t_2 - t_1 = t_m \left[\frac{16\alpha}{3R} \right]^{1/2} \left[\left[1 - \left(1 - \frac{t_2}{t_m} \right) \left| 1 - \frac{t_2}{t_m} \right|^{1/2} \right]^{1/2} + \left[1 - \left(1 - \frac{t_1}{t_m} \right) \left| 1 - \frac{t_1}{t_m} \right|^{1/2} \right]^{1/2} \right] \quad (7-1)$$

where:

- t_1 and t_2 = The times corresponding to the breakthrough concentration at the $C_m e^{-1}$ level, respectively, on both sides of the curve (Figure 7-1)
- t_m = The time when peak concentration occurs
- α = The longitudinal dispersivity
- R = The distance between the injection well and the pumping well

Since the peak concentration (C_m) is not available, t_1 and t_2 were estimated assuming that the breakthrough curve is a triangular distribution (Figure 7-2), meaning that the following proportionality holds:

$$\frac{t_1 - t_0}{t_m - t_0} = \frac{C_m}{C_m} = \frac{1}{e} \quad (7-2)$$

Where t_m is the average of the time interval (432 to 492 minutes) during which the peak concentration was reported. This implies that t_1 is not a function of C_m . In other words, t_1 and t_2 can be estimated regardless of C_m . Using Equation 7-2, t_1 was calculated to be 329 minutes. Likewise, t_2 was estimated to be 632 minutes. Therefore, using Equation 7-1, $\alpha = 0.6$ m. If t_0 is taken as t_1 and t_e as t_2 (where $t_0 = 252$ minutes and $t_e = 732$ minutes), then $\alpha = 1.4$ m.

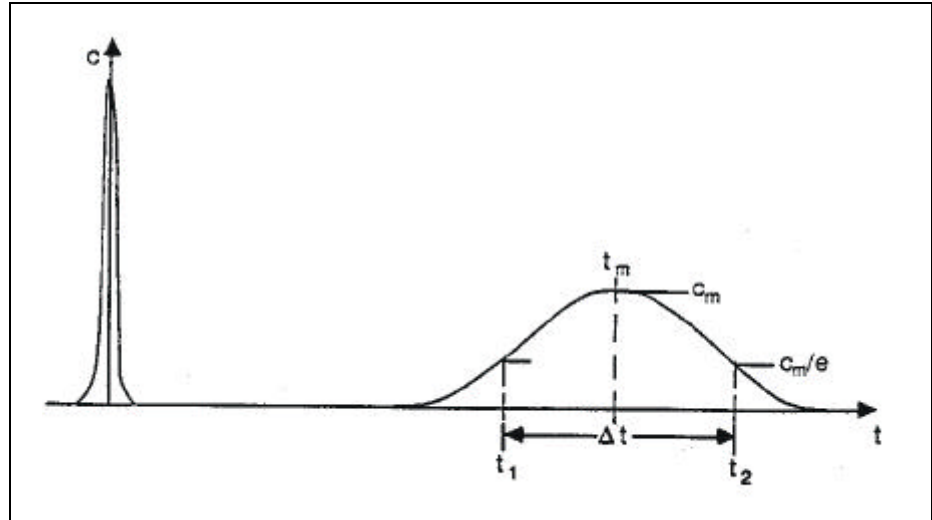


Figure 7-1
Illustration of the Breakthrough-Curve, Pulse-Width Method of Analysis
 (Welty and Gelhar, 1989)

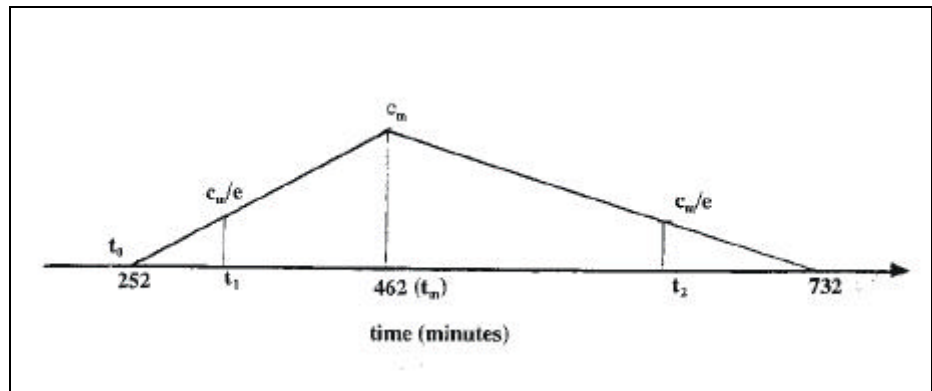


Figure 7-2
Conceptualized Breakthrough Curve

7.3.1.1.5 CAMBRIC Site Test

The CAMBRIC nuclear test was detonated in the subsurface at the NTS in May 1965. Beginning in 1974, the site was studied under the Hydrology/Radionuclide Migration Project (HRMP) for the DOE. The nuclear test took place at a depth of 294 m below land surface and below the water table in the tuffaceous alluvium of Frenchman Flat. There is very slow ambient groundwater movement at the location, and the radionuclides resulting from the test remained in the cavity region. The RNM-1 hole was drilled into the cavity in 1974. An auxiliary well, RNM-2S, was drilled 91 m away to a depth of 350 m. It was pumped continuously at a rate of about 1.0 m³/min from October 1975 until October 1977, and then at a rate of 2.3 m³/min until August 1991.

The concentrations of radionuclides were monitored. Analyses of water samples showed that the migration velocities of tritium, chlorine-36 (Cl-36), krypton-85 (Kr-85), technetium-99 (Tc-99), ruthenium-106 (Ru)-106, and iodine-129 (I-129) were nearly the same as that of the moving water, from the explosion site to the pumped well (Bryant, 1992). The concentration of Pu-239 at the pumping well was below the detection limit of 10^6 atoms per milliliter in water collected at the time of peak tritium concentration. As of 1990, the last samples collected from the cavity showed that the levels of activity of both tritium and Kr-85 had fallen almost beyond the limits of detection capability (Thompson, 1991). As water was pumped from Well RNM-2S, Kr-85 and tritium have moved away from the cavity at approximately the same rate, with Kr-85 lagging slightly behind. Other radionuclides such as Sr-90 and Cs-137 have decreased considerably in the cavity region during the period of pumping at Well RNM-2S. Less than 0.5 percent of the total strontium-90 (Sr-90) and 0.0003 percent of the total Cs-137 accompanied the tritium to the pumped well, although both isotopes appear to have migrated away from the source zone to some extent.

In 1977, two years after initiation of groundwater pumping from Well RNM-2S, tritium began to appear in the water collected from Well RNM-2S. The tritium concentration peaked in 1981 and has been declining since. Although almost 91 percent of the CAMBRIC tritium source term had been pumped out of Well RNM-2S by September 1990, continued pumping allowed the definition of the tail of the elution curve (Thompson, 1991). The concentrations of tritium and Kr-85 (in picocuries per liter [pCi/L]) versus the cumulative volume of water pumped (i.e., the elution curves) are shown in [Figure 7-3](#) and [Figure 7-4](#), respectively.

With the above information, the longitudinal dispersivity (α) of the porous aquifer can be estimated by two different approaches. The estimates are presented below.

Welty and Gelhar Method

Using the data shown in [Figure 7-3](#) for tritium:

- Peak concentration $C_m = 7.0 \times 10^6$ pCi/L
- Cumulative volume of water pumped corresponding to the time at peak concentration, $V_m = 5 \times 10^6$ cubic meters (m^3)

The time variables t_1 and t_2 in [Equation 7-1](#) can be derived by the following procedures:

- The value for C_m/e is $7.0 \times 10^6 / 2.7183 = 2.6 \times 10^6$ pCi/L.
- The cumulative volume corresponds to C_m/e is $2.95 \times 10^6 m^3$ (V_1) on the rising limb and $12.5 \times 10^6 m^3$ (V_2) on the falling limb (illustrated as t_1 and t_2 , respectively, in [Figure 7-1](#)).

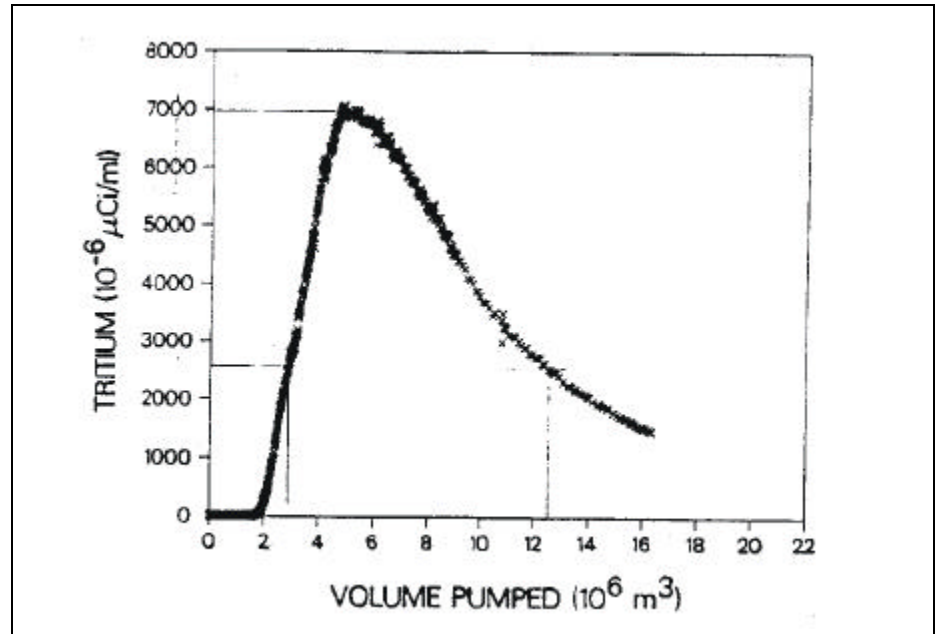


Figure 7-3
Tritium Concentration in Water Pumped from Well RNM-2S versus Volume Pumped (Thompson, 1991; activity concentrations corrected to CAMBRIC zero time)

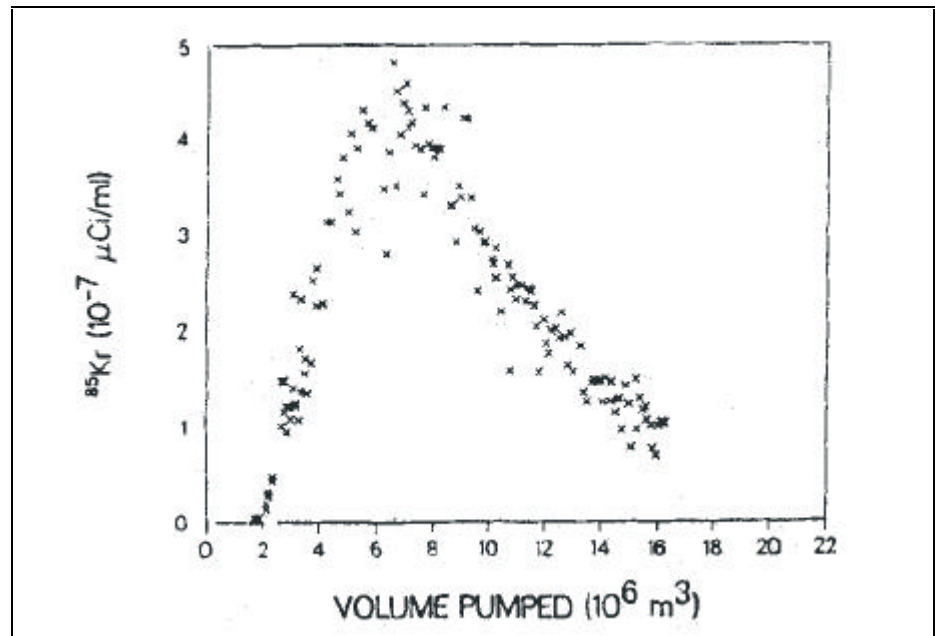


Figure 7-4
The ⁸⁵Kr Concentration in Water Pumped from Well RNM-2S versus Volume Pumped (Thompson, 1991; activity concentrations corrected to CAMBRIC zero time)

- Assuming continuous pumping at Well RNM-2S with a rate of 2.3 m³/min (Q), the time at V₁, V₂, and V_m is calculated by t = V/Q:
 - t₁ = 891 days
 - t₂ = 3,774 days
 - t_m = 1,510 days

Using Equation 7-1 with R = 91 m, t₁ = 891 days, t₂ = 3774 days; and t_m = 1,510 days, the longitudinal dispersivity (α) calculated for the CAMBRIC experiment is 9.6 m.

Sauty Model

The transport of tritiated water from the source to the satellite well was compared with Sauty's (1980) two-dimensional (2-D) calculation for instantaneous tracer injection in a radial, converging flow field that is similar to the RNM well tracer tests (Daniels, 1981; Daniels et al., 1983; Daniels and Thompson, 1984). Sauty provided a series of calculated "type curves" with dimensionless time T_r and dimensionless concentration C_r for different Peclet numbers (Figure 7-5). The shape of the elution curve depends on the Peclet number, which is inversely proportional to the dispersivity. The smaller the Peclet number, the larger the dispersivity; hence, the broader and more skewed the elution peak. A Peclet number is defined as (Zheng, 1990):

$$P_e = \frac{|v|L}{D} \quad (7-3)$$

where:

- v = The magnitude of the seepage velocity
- L = A characteristic length, commonly taken as the distance from the source to the point of observation
- D = The dispersion coefficient
- Because D = αv when ignoring the molecular diffusivity, Equation 7-3 can be reduced to:

$$P_e \approx \frac{L}{\alpha} \quad (7-4)$$

To compare the experimental data with the calibrated type curves, the time of experiment has to be converted to a dimensionless T_r and, similarly, the observed concentration has to be converted to a dimensionless C_r. A dimensionless time T_r = 1 corresponds to the time required to pump the volume of water contained in a cylinder whose radius is the distance from the satellite well to the source. The dimensionless concentration, C_r, is calculated relative to the maximum concentration.

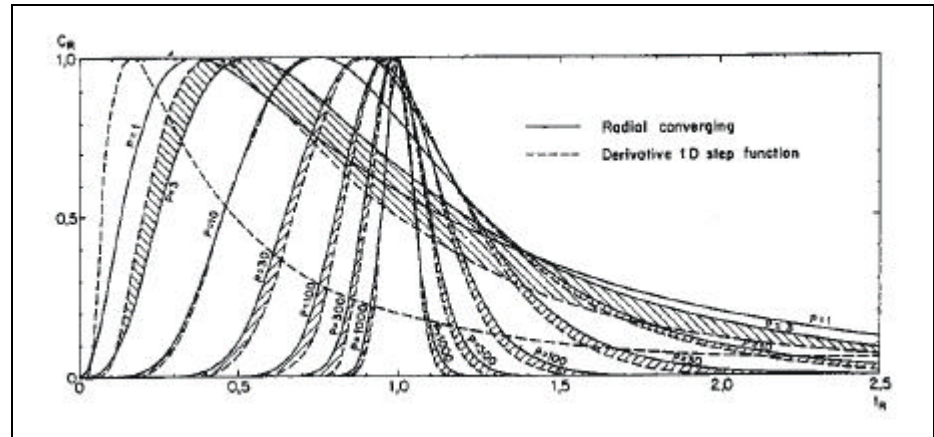


Figure 7-5
Type Curves for Instantaneous Tracer Injection in Radial Converging
Flow Field: Comparison with Derivative of Imposed Step Function
(Sauty, 1980)

The Sauty model has been applied to the CAMBRIC site data several times. Three applications were performed by the following authors:

Burbey and Wheatcraft (1986)

In the case of CAMBRIC site, the time to pump water from the 91-m radius cylinder from Well RNM-2S was estimated to be 2,100 days. From this point, the initial tracer breakthrough and the time to peak can be related to T_r . Sauty's type curve fitting those two points corresponds to a Peclet number of 45. The corresponding dispersivity is estimated at 2 m ($91/45$), which can be derived from [Equation 7-4](#).

Burbey and Wheatcraft (1986) used this longitudinal dispersivity as an input parameter to a 3-D, transient, finite difference, transport model called the "Deep Well Disposal Model." In the model, the longitudinal dispersivity was not calibrated (i.e., fixed at 2 m), only the transverse dispersivity was calibrated. They used $\alpha_L/\alpha_T = 1.3$, $\alpha_L/\alpha_T = 0.67$, and $\alpha_L/\alpha_T = 10.0$ to produce the tritium concentration hydrograph. They concluded that the transverse dispersivity, $\alpha_T = 1.5$ m would produce the most accurate peak concentration in relation to the field data.

Travis et al. (1983)

Travis and others employed a 3-D numerical code "TRACR3D" to the overall transport problem at the CAMBRIC site (Daniels et al., 1983). They also used Sauty's type curves to fit the field elution data for tritium. A good fit was found for data up to a cumulative volume of water pumped from Well RNM-2S using a Peclet number of 10 ([Figure 7-6](#)), but the tritium source had to be adjusted downward to 70 percent of the original estimated value. With $P_e = 10$, the longitudinal dispersivity was estimated to be 9.1 m. The need to use a reduced initial concentration makes this result less reliable than the others.

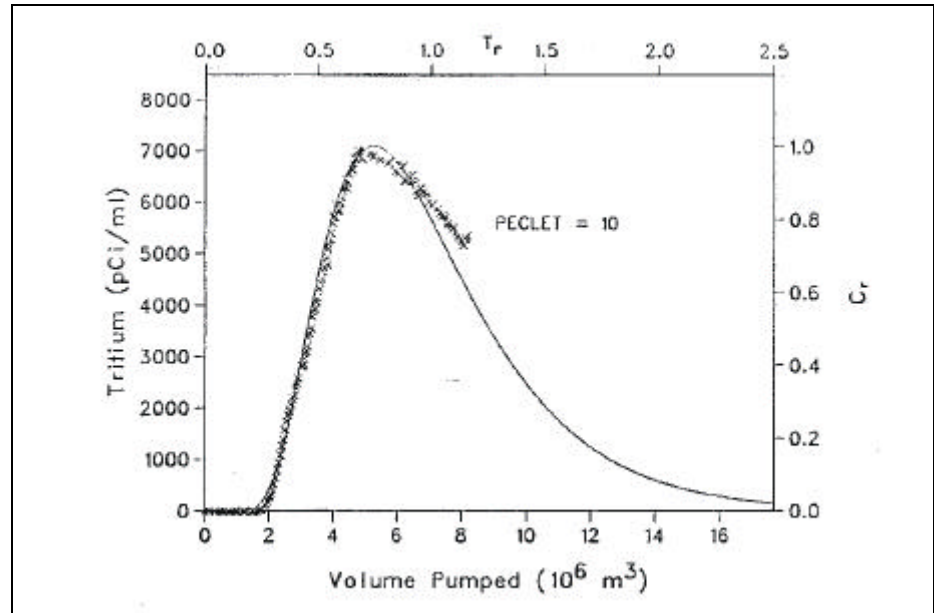


Figure 7-6
Tritium Concentration Data (X) for Well RNM-2S Water and Calculated
Elution of Tracer after Instantaneous Tracer Injection in a Radial
Converging Flow Field for Peclet Number 10
(Daniels and Thompson, 1984)

Thompson, 1988 and Ogard et al., 1988

In the migration study of tritium and Cl-36, it was found previously that the Cl-36 elution at Well RNM-2S preceded the tritium elution by a significant volume (Thompson, 1988) (Figure 7-7). Researchers at LANL attributed this phenomenon to the “anion exclusion” effect, that is, anions such as chloride were eluted before cations or neutral species such as tritiated water. Anions, being of the same charge as the clays and zeolites in the soil, are repelled and effectively prevented from entering into the intragranular porosity of the soil particles. Though a Sauty-type curve with $P_e = 10$ fits the tritium data through the maximum, a better fit to the tailing portion of the data up to $12 \times 10^6 \text{ m}^3$ of the water pumped can be made using a type curve with a Peclet number of 6 (Figure 7-8). A Peclet number of 6 corresponds to a dispersivity of 15.1 m. A similar fit to the Cl-36 data is shown on Figure 7-9. The difference in slope between data and the Sauty curve at a longer pumping time is evident (especially for Cl-36), which indicates that a curve with a still lower Peclet number, hence a higher dispersivity (Equation 7-4), may be expected to fit the subsequent data. The alluvium of Frenchman Flat is heterogeneous with interbedded fine- and coarse-grained material. If the observed dispersion includes a dead-end pore or mobile/immobile effects, then the observed dispersivities may be an over-estimate of the mechanical dispersion. On the other hand, the excellent fit between observed and theoretical breakthrough curves suggests that using the derived dispersivities will be adequate for simulation of transport in Frenchman Flat alluvium with a single porosity model.

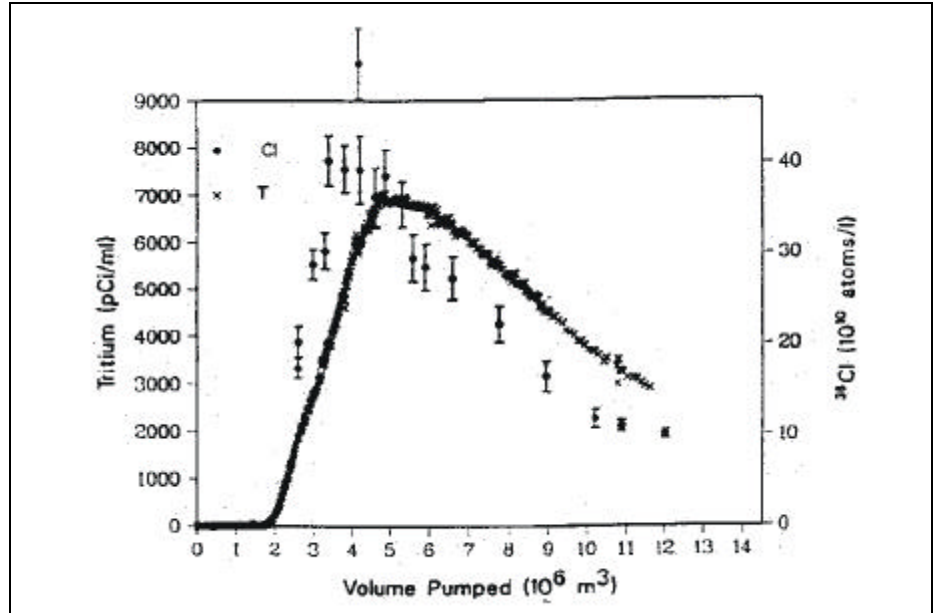


Figure 7-7
Elution of Tritium and Cl-36 from Well RNM-2S (Thompson, 1988)

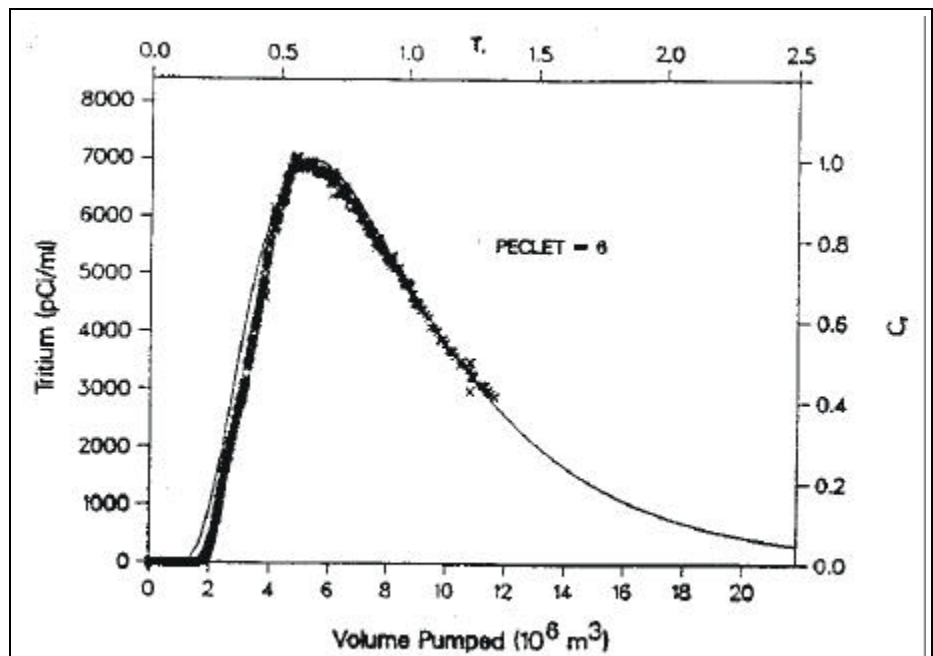


Figure 7-8
Elution of Tritium Compared with Sauty Model (Thompson, 1988)

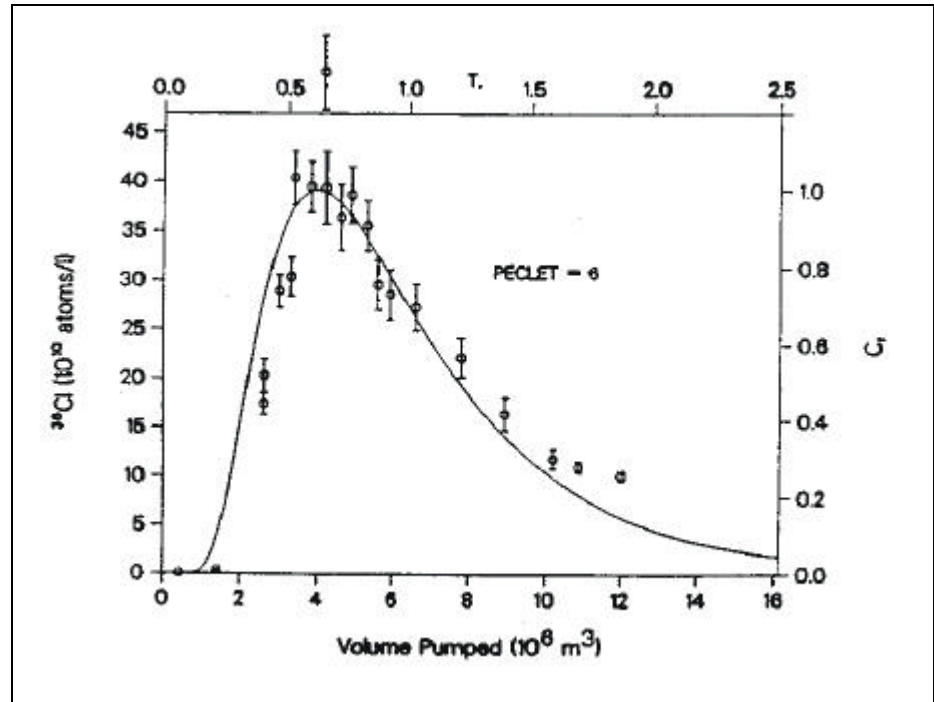


Figure 7-9
Elution of Cl-36 Compared with Sauty Model (Thompson, 1988)

7.3.2 Non-NTS Dispersion Studies

Most of the dispersivity data available for locations outside the NTS were obtained from the review paper prepared by Gelhar et al. (1992). Twenty-three additional data records were also derived from the literature published after Gelhar et al. (1992).

Gelhar et al. (1992) reviewed dispersivity observations from 59 different field sites, domestic and abroad. The review included extensive tabulations of information on site location, description of aquifer material, average aquifer saturated thickness, hydraulic properties, effective porosity, mean pore velocity, flow configuration, dimensionality of monitoring network, tracer type, method of data interpretation, overall scale of observation, and longitudinal and transverse dispersivities from original sources (Gelhar et al., 1992).

Gelhar et al. (1992) classified the dispersivity data into three reliability classes corresponding to the data quality evaluation flags described in Section 7.4.1. The analysis indicated a trend of systematic increase of the longitudinal dispersivity with observation scale, but the trend is much less clear when the reliability of the data is considered. The longitudinal dispersivities reported by Gelhar et al. (1992) ranged from 10^{-2} to 10^4 m for travel distances ranging from 10^{-1} to 10^5 m; however, the largest distance with high-reliability data was only 250 m, and the longitudinal dispersivity was only 4 m. Gelhar et al. (1992) also concluded from the data that,

overall, dispersivity values did not appear to vary with lithology (porous versus fractured media).

Gelhar et al. (1992) reported that, based on two high-reliability data points, horizontal transverse dispersivity is one order of magnitude less than longitudinal dispersivity. Gelhar et al. (1992) found that in all cases where both horizontal and vertical transverse dispersivities were measured, the values of vertical transverse dispersivity were one to two orders of magnitude less than those of the horizontal transverse dispersivity.

7.3.3 Dispersivity Estimation Through Modeling

Borg et al. (1976) and Neuman (1990) reported longitudinal dispersivity obtained from the calibration of numerical solute transport models against hydraulic and concentration data. More recently, Hu (1998) derived dispersivity values from contaminant transport simulations in heterogeneous porous material in Frenchman Flat using a random field approach.

The longitudinal dispersivities reported by Borg et al. (1976) ranged from 11.6 to 91 m for a wide variety of lithologies, ranging from glacial outwash sand and gravel, basalt lava, to dolomite and limestone. The value was 21.3 m for a sand or gravel deposit, which is a lithology that most closely resembles the tuffaceous alluvium at the CAMBRIC site (Daniels and Thompson, 1984). The dispersivity for the Bonanza King Formation near the NTS was estimated to be 15 m (Borg et al., 1976).

Neuman (1990) reported that most of the calibrated dispersivities used in his paper were associated with large-scale plumes. The scales were in excess of 100 m and lay below the defined lower confidence limit line and were, therefore, inconsistent with theoretical results. However, the calibrated dispersivities were found to vary more slowly with the scale of the study than did dispersivities determined by other means. This appears to be because calibration often provides information about the spatial variation of hydraulic conductivities on scales exceeding the dimensions of model subregions (called “zones”) within which they are kept constant or allowed to vary at a relatively slow rate. The calibrated dispersivities are associated with a reduced length scale L_r that depends on the dimensions of the zones rather than on the mean travel distance L_s of the plume. A regression analysis showed that L_r increased with the mean travel distance at an average rate proportional to $L_s^{0.5}$. This, in turn, explains that groundwater modelers tended to design the zones of their computational grids in a manner roughly proportional to $L_s^{0.5}$. Neuman (1990) concluded that the scale parameter not only controls dispersivities in a given transport model, but that the scale parameter diminished as the density of information about hydraulic heterogeneity increases.

The DRI performed 50 transport simulations of a hypothetical nonreactive contaminant in heterogeneous Frenchman Flat HSUs (Hu, 1998) using a random field approach. Effective dispersivities were derived from each of the simulations. Based on the locations of underground nuclear tests, two separate areas of Frenchman Flat were selected for modeling: a northern test area (tests conducted

near the border of Areas 5 and 11) and a southern test area (tests conducted near the center of Frenchman Flat). Input data for the simulations included randomly generated hydraulic conductivity fields from Shirley et al. (1996) and hydraulic head data from the regional model (DOE/NV, 1997) at the simulation boundaries. Table 7-2 presents the mean dispersivities derived from the transport simulations. For the northern test area, the mean groundwater flow was mainly downward, and for the southern test area primarily horizontal (Hu, 1998).

Table 7-2
Dispersivity from Hypothetical Transport Simulations for
Frenchman Flat Underground Test Areas

Test Area	Transport Distance (meters)	Flow and Transport Direction	Mean Longitudinal Dispersivity (meters)	Mean Horizontal Transverse Dispersivity (meters)	Mean Vertical Transverse Dispersivity (meters)
Northern	1,280	Downward	9 ^c < 74 < 394 ^d	ND ^a	ND
Northern	400	Downward	7 < 45 < 286	0.5 < 2.1 < 14	0.7 < 6.0 < 88 ^b
Southern	3,000	Horizontal	72 < 320 < 1,421	6 < 21 < 24	2 < 6.3 < 42
Southern	1,200	Horizontal	42 < 176 < 882	4 < 10 < 38	1 < 4.2 < 19

^aNo data

^bNot a vertical dispersivity; both transverse dispersivities are horizontal, because flow direction is downward

^cThe smallest dispersivity of the simulations

^dThe largest dispersivity of the simulations

Table 7-2 also contains the smallest and largest dispersivity determined from any of the realizations. The reader will notice that the ranges are quite large, typically spanning between 1 and 2 orders of magnitude. Additionally, for flow perpendicular to the layering (northern test area), the range of values is typically larger than for flow parallel to layering (southern test area). The longitudinal dispersivity values fall in the range of values as presented by Gelhar et al. (1992). The same is true for the horizontal transverse dispersivity (for the northern test model of 400 m, both transverse dispersivities are horizontal). The vertical dispersivities from the modeling of Hu (1998) tend to be much larger than observed data. The comparison is tenuous, however, because of the lack of vertical dispersivity measurements at scales greater than 300 m.

The values determined from the work of Hu (1998) are derived and cannot be treated as data. However, it illustrates one method to estimate large-scale dispersivity values. If the characteristics of the heterogeneity can be quantified and represented by a covariance function, then multiple realizations of the random field can be created. These random fields are generated on a model grid that is much smaller than the scale of interest (i.e., plume scale or maximum distance of travel). Simulating flow in the random field explicitly models the small-scale velocity variations that lead to dispersion. The simulated contaminant distributions are summarized by spatial moments or averaged over a breakthrough plane to yield apparent dispersion. These apparent dispersivities are applicable to the larger scale transport simulations using the advection-dispersion-equation

(ADE) approach. The uncertainty in this method is the scarcity of data with which to define the heterogeneity.

7.4 Data Evaluation

Data assessment includes an evaluation of data quality and an evaluation of the variability of dispersivity values and the factors influencing them.

7.4.1 Data Quality Evaluation

Data Quality Evaluation Flags were used to rank the level of quality of the data. The quality levels defined correspond to the levels of reliability defined by Gelhar et al. (1992). They are as follows:

- Level 1: Corresponds to "High Reliability" Level I data of Gelhar et al. (1992). The tracer study meets the following criteria: (1) Tracer test was either ambient flow, radial diverging flow, or two-well instantaneous pulse test without recirculation, (2) Tracer input was well defined, (3) Tracer was conservative, (4) Spatial dimensionality of the tracer concentration measurements was appropriate, and (5) Analysis of the tracer concentration data was appropriate and consistent with the measurements (Gelhar et al., 1992).
- Level 2: Corresponds to "Intermediate Reliability," Level II, of Gelhar et al. (1992). Tracer study does not meet the criteria for high or low reliability (Gelhar et al., 1992).
- Level 3: Corresponds to Gelhar et al.'s (1992) "Low Reliability," Level III. Tracer study meets the following criteria: (1) Two-well recirculating test with step input was used; (2) Single-well, injection-withdrawal test with tracer monitoring at the single well was used; (3) Tracer input was not clearly defined; (4) Tracer breakthrough curve was assumed to be the superposition of breakthrough curves in separate layers; (5) Measurement of tracer concentration in space was inadequate; and (6) Equation used to obtain dispersivity was not appropriate for the data collected (Gelhar et al., 1992).

7.4.2 Evaluation of Scale Dependency

A preliminary examination of the updated dispersivity dataset ([Appendix E](#)) confirms Gelhar et al.'s (1992) conclusion that dispersivity values do not appear to be differentiated with respect to lithology (porous versus fractured media). The evaluation was, therefore, limited to examining the scale-dependency. Log-log plots were prepared using the dataset ([Appendix E](#)) to analyze the variations in longitudinal and transverse dispersivity with the scale of the tracer test ([Figure 7-10](#), [Figure 7-11](#), and [Figure 7-12](#)). In each figure, if multiple

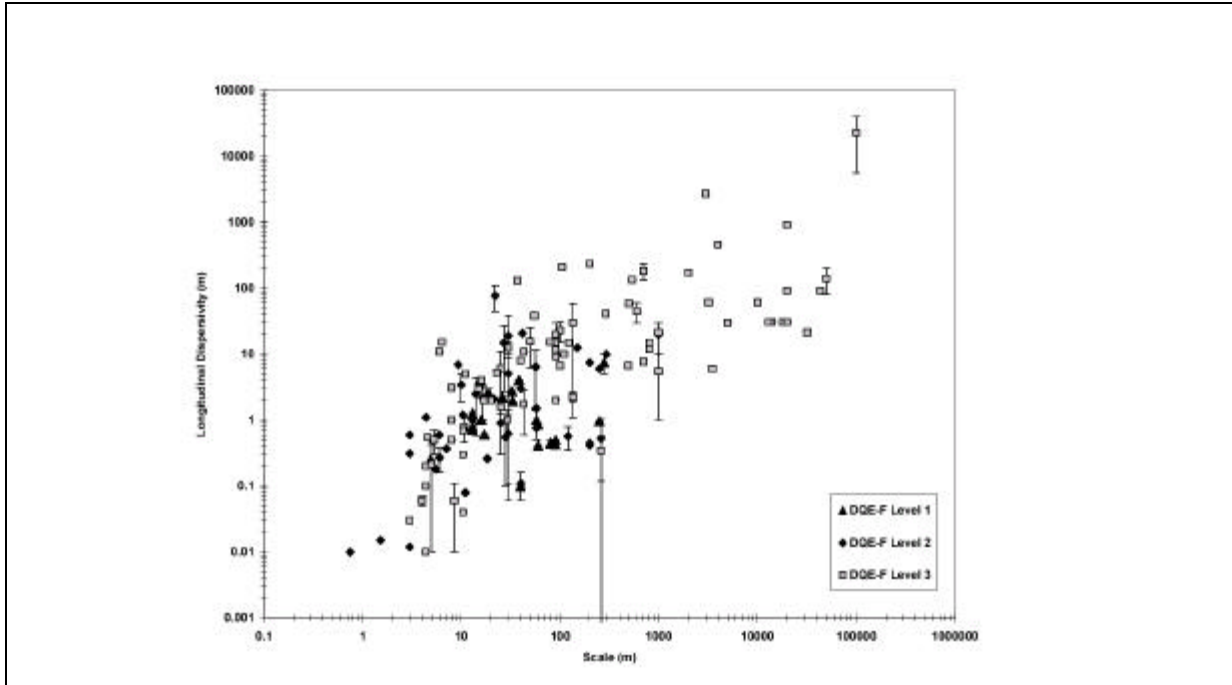


Figure 7-10
Longitudinal Dispersivity Versus Tracer Test Scale

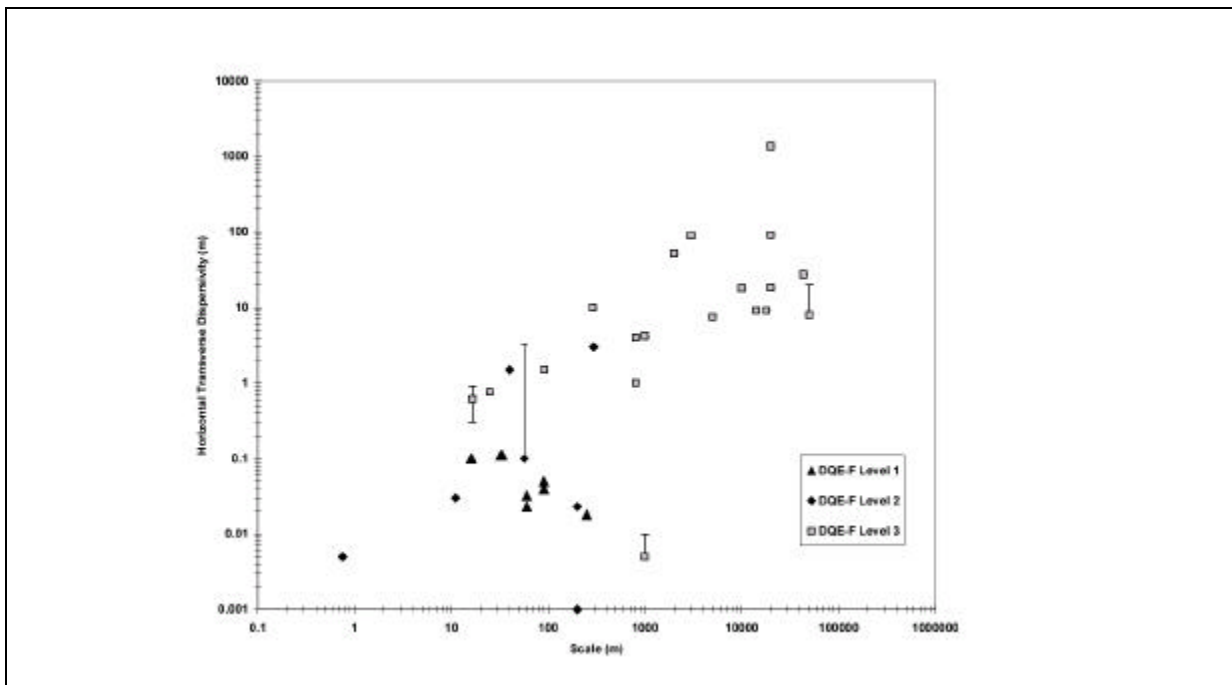


Figure 7-11
Transverse Horizontal Dispersivity Versus Tracer Test Scale

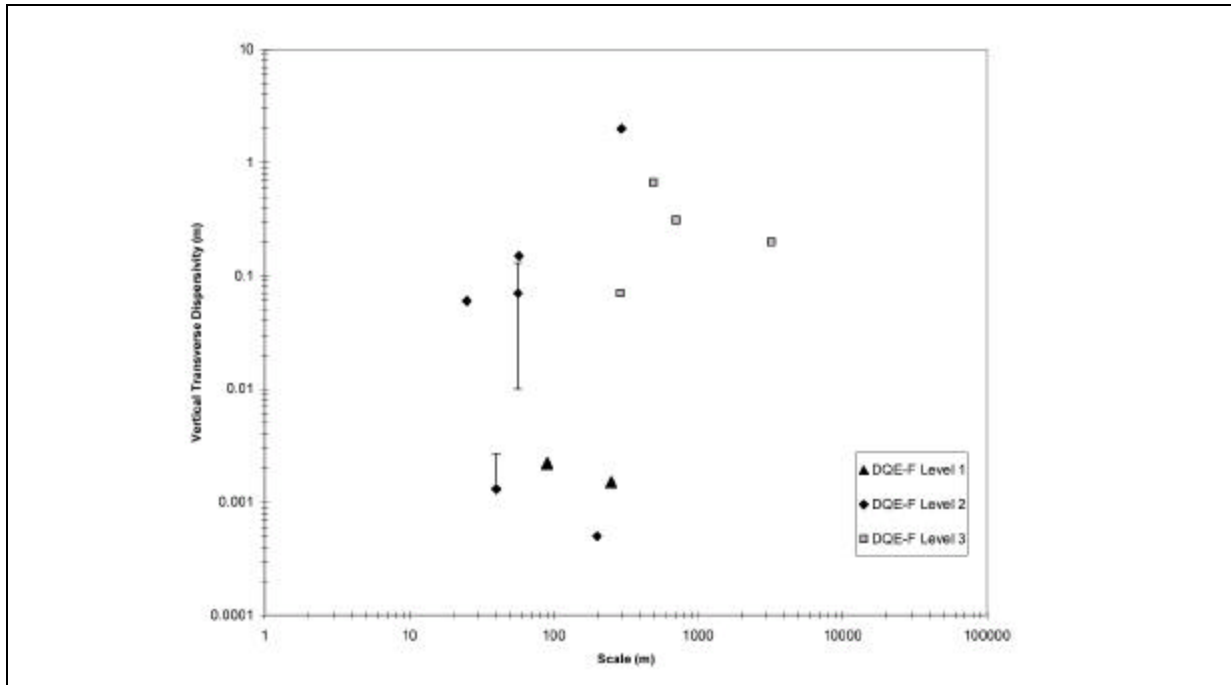


Figure 7-12
Transverse Vertical Dispersivity Versus Tracer Test Scale

interpretations of a dataset were reported, the range of values is indicated by the “whiskers.”

The analysis indicated a trend of systematic increase of the longitudinal dispersivity with observation scale, as shown in Figure 7-10. The longitudinal dispersivities ranged from 1.37×10^{-7} to 4×10^5 m for travel distances up to 10^5 m. However, the trend is much less clear when the quality of the data is considered: the largest distance with high-reliability data (DQE_F=1) was only 280 m, and the longitudinal dispersivity was only 10 m. The high-reliability data tends to be smaller in magnitude than other data at any particular scale. As displayed by the data (Figure 7-10), dispersivity appears to be scale-dependent, but the reliability of values at large scales is low. These findings are consistent with those of Gelhar et al. (1992) and Neuman (1990) and indicate that, in general, larger dispersivity values are associated with larger scale problems.

The scale dependency is, however, still somewhat debated. The data presented in this document should not be interpreted to suggest that dispersivity simply increases with distance for any particular plume. At two sites, Borden and Otis Air Force Base, the dispersivity was observed to increase for a limited distance and then reach an asymptote. In Neuman’s model (1990), universal scaling is operative over large distances and dispersivity may increase significantly as plumes migrate downgradient. However, many examples exist of long plumes that retain relatively modest dispersion, such as the Cape Cod sewage lagoon plume of LeBlanc (1982). An additional interpretation is for the plume-scale dispersivity to reach an asymptote, while the plume remains within a geologic unit with a stationary covariance function describing variability. As the plume crosses

into other geologic units (with presumably different correlation structure), the plume may again begin to spread. This dispersivity may, in fact, be represented by a series of increasing plateaus. For the Pahute Mesa CAU model, the assumption is made that dispersivity will not continue to increase as the length of transport increases, but, rather, will reach an asymptotic value that will apply over a large travel distance.

The data available for horizontal transverse dispersivity, or the spreading of the tracer at right angles to the direction of groundwater flow horizontally, is shown in [Figure 7-11](#). Transverse horizontal dispersivities up to 1,370 m have been observed. Although not as numerous as in the longitudinal case, the data also exhibit the same pattern as longitudinal dispersivity of increasing value with distance. However, the appropriate value at large scale is not at all clear. Although the low- and intermediate-reliability data show an increasing trend, the high-reliability data show a trend of decreasing horizontal dispersivity values with scale. The horizontal transverse dispersivity is, in general, about one order of magnitude less than the longitudinal dispersivity, but is much smaller if only high-reliability data are included.

[Figure 7-12](#) depicts the sparse data for transverse vertical dispersivity or the vertical spreading of the tracer. Transverse vertical dispersivities up to 2 m have been observed. A possible trend of increasing values is indicated by the low- and intermediate-reliability data, but no trend appears with the high-reliability data. The only significant observation is that the transverse vertical dispersivity is much less than either longitudinal or horizontal transverse dispersivity. This reduction in spreading is thought to be controlled mainly by the layering of the geologic materials themselves, where less permeable layers will significantly reduce the ability of the tracer to disperse upward or downward.

The trends of high reliability dispersivity values with scale are generally consistent with predictions presented in Gelhar (1993) and Dagan (1989) for steady uniform flow in mildly heterogeneous aquifers describable by stationary random fields. Unfortunately, the high-reliability data do not exist at scales of interest in the CAU model. As a result, it is not clear if the predictive tools of Gelhar (1993) and Dagan (1989) will be adequate at larger scales. All of the predictive tools require quantification of the autocovariance of natural log hydraulic conductivity at large scales. This is no easy task. Two compromise approaches are proposed. First, the covariance is defined on the scale of an HSU (a less onerous task) and a stochastic random field approach is used to model groundwater velocity heterogeneity at the scale of the model grid (up to a few 100 meters). Multiple realizations are used to define the spreading. A second approach uses an ADE with effective parameters defined over regions as large as an HSU. The effective dispersivities would correspond to the values presented in [Figure 7-10](#), [Figure 7-11](#), and [Figure 7-12](#). These values are uncertain, as noted above. Initial modeling will use the second approach.

The measured longitudinal dispersivity values for the NTS region are shown in [Figure 7-13](#). It can be clearly seen in [Figure 7-13](#) that the values of dispersivity from tracer tests conducted at the NTS and vicinity are consistent with those derived from tracer tests conducted elsewhere.

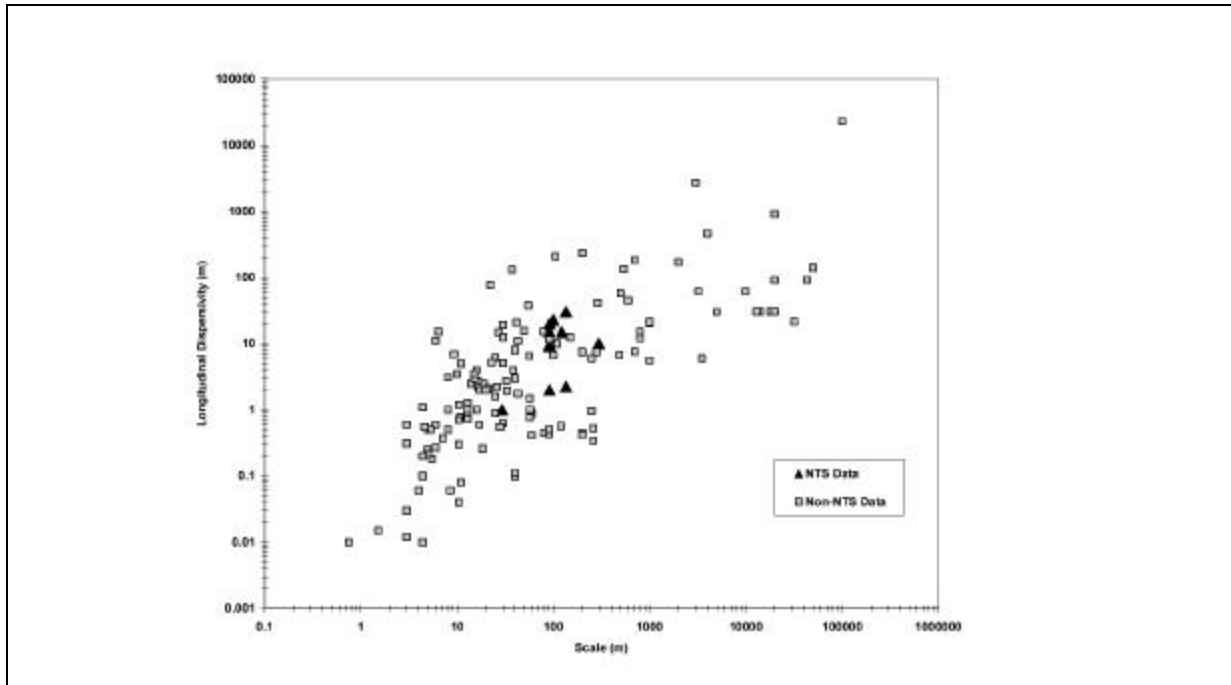


Figure 7-13
NTS Data as Compared to Non-NTS Data for Longitudinal Dispersivity

In summary, several important conclusions related to the selection of dispersivity and solute transport modeling for the NTS can be drawn based on the available information. They are as follows:

- The longitudinal dispersivity apparently increases with scale (distance from the contaminant source or the spacing between the injection well and the monitoring well). However, it is not clear how increases occur for an individual plume. Data suggest that if dispersivity increases, it is not a smooth monotonic function of travel distance.
- The ratio longitudinal dispersivity/transverse dispersivity is in the range of 3 to 50, and the ratio of longitudinal dispersivity/vertical dispersivity is in the range of 10 to 700. The vertical dispersivity is also about 10 to 100 times smaller than the horizontal transverse dispersivity.
- As the density of information about hydraulic conductivity increases, the effect of the scale parameter may be reduced. Dispersivity accounts for unmeasured variability. As more of the variability is modeled explicitly, the dispersivity does not need to increase.
- The lithology, porous or fractured media, has no significant effect on the dispersivity. In other words, dispersivities used for porous media can also be used in fractured media. This conclusion may be invalid at small

scales, but it is considered valid at the scale of the Pahute Mesa CAU model.

- The longitudinal dispersivity data from the NTS fall within the data summarized by Gelhar et al. (1992).

7.5 Scaling Considerations

As presented in [Section 7.4.2](#), the dispersivity values appear to be scale-dependent. This means that longitudinal dispersivities in the range of 0.6 to 30 m obtained at the scale of the NTS tracer tests, 30 to 120 m, may not be appropriate for the scale of the Pahute Mesa CAU flow model, which will be on the order of several 10s of kilometers. It is generally expected that larger longitudinal dispersivities will be appropriate based on the data presented in this section ([Figure 7-10](#)). The exact nature of the scaling is uncertain; therefore, a range of longitudinal dispersivities will be defined to account for this uncertainty. The sensitivity of the assigned ranges will be tested in the modeling via sensitivity and uncertainty analyses.

The transverse and vertical dispersivity are also scale-dependent parameters, but the trends with increasing scale are more uncertain than was the case with longitudinal dispersivity. High-reliability data suggest the transverse and vertical dispersivities will always be small, regardless of scale. However, there is no consensus among researchers defining the large-scale behavior of the non-longitudinal dispersivities. We must, therefore, leave open the possibility that larger transverse and vertical dispersivity values are possible at large scales.

7.6 Probability Distributions

During the uncertainty phase of the modeling, probability distributions will be required to represent uncertainty in dispersivity values. The probability plots for the longitudinal, transverse, and vertical dispersivities are presented in [Figure 7-14](#). Based primarily on [Figure 7-10](#), [Figure 7-11](#), and [Figure 7-12](#), the following rules will be applied to the uncertainty in dispersivity. In the longitudinal direction, at scales greater than 1,000 m, the dispersivity varies between 5 and 500 m. A few outliers of even larger values have been presented in the literature, but these are considered to have a low likelihood of occurrence. The distribution will be represented by a log-triangular distribution with a lower bound of 3 m, an upper bound of 2,000 m, and a most likely value of 40 m. This simple distribution will represent the observed range of values.

In the horizontal transverse direction, the log triangular distribution will be defined with a lower bound of 0.01 m, a most likely value of 1 m and an upper bound value of 200. As indicated by the high-reliability data, horizontal dispersivity would be much smaller than the longitudinal value. An additional constraint will be placed on the ratio of longitudinal to transverse dispersivity. That ratio will be maintained between 3 and 50 for all realizations.

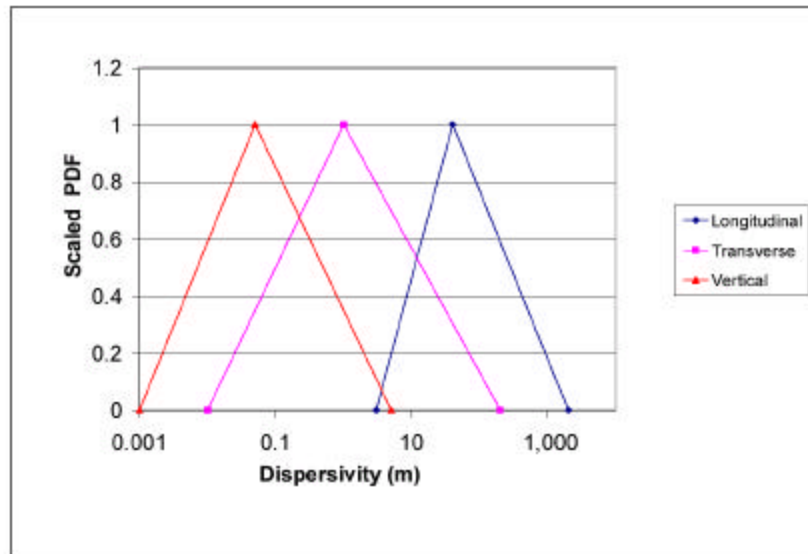


Figure 7-14
Probability Density Functions for Dispersivity

The vertical transverse dispersivity is more difficult to define. Few values are available for scales greater than 500 m. With very little to constrain it, the vertical transverse dispersivity will be assumed to be defined by the log-triangular distribution with a range between 0.001 and 5.0 m and a most likely value of 0.05 m. The most reliable values are very small; therefore, the distribution will be biased toward smaller values. Constraints of the ratio of longitudinal/vertical (10 to 700) and transverse to vertical (10 to 100) will be imposed.

It is expected that longitudinal and horizontal transverse dispersion will be the most important, with vertical dispersivity relatively unimportant. These assumptions will be tested as part of the modeling activities.

7.7 Data Limitations

Dispersivity is not an intrinsic property of the medium in the way that porosity and hydraulic conductivity are thought to be. Dispersivity is dependent on the scale of the measurement, and on the type of test and method of analysis. The data available from the NTS region come from only six tracer experiments, five of which yielded quantitative values of longitudinal dispersivity. None of the NTS tracers tests produced good estimates of transverse dispersivities. The trends in dispersivity with travel distance come from a compilation of data from around the world. As a result, the appropriate longitudinal dispersivity to apply at large scales for the Pahute Mesa CAU model has an uncertainty of about two orders of magnitude. The importance of this uncertainty will be assessed during sensitivity and uncertainty analyses during the modeling.

8.0 Matrix Diffusion Parameters

This section includes descriptions of the role of matrix diffusion in contaminant transport in groundwater, the data available for matrix diffusion parameters, and the data analysis and associated results.

8.1 Role of Matrix Diffusion in Contaminant Transport

Matrix diffusion has the effect of attenuating both the concentration and travel time of solute contaminants moving through saturated, fractured rock. The matrix diffusion process involves the diffusion of contaminants out of flowing fractures and into the relatively stagnant water in the pores of the surrounding matrix (and vice-versa).

8.2 Data Compilation

The matrix diffusion data types, sources of data, and the data quality evaluation process are described in this section.

8.2.1 Data Types

The matrix diffusion mass transfer coefficient (MTC) is the lumped parameter that governs the rate at which solutes diffuse out of fractures and into the matrix. The MTC may be expressed as follows:

$$\text{MTC} = n \frac{\sqrt{D_m}}{b} \quad (8-1)$$

where:

- D_m = Matrix diffusion coefficient
- n = Matrix porosity
- b = Fracture half-aperture

The MTC can be estimated directly in tracer transport tests, or the individual parameters that make up the MTC can be measured independently in laboratory tests.

8.2.2 Data Sources

Diffusion cell tests have been employed to measure matrix diffusion coefficients (D_m values) for various radionuclides and anions in a large number of volcanic rocks from beneath Pahute Mesa and from the saturated zone near Yucca Mountain in Area 25 of the NTS (Reimus et al., 2002a; Reimus et al., 1999). [Table 8-1](#) summarizes all the diffusion cell experiments used to obtain matrix diffusion coefficient estimates for this report. Generally, both matrix porosity and matrix permeability of rock samples are measured in conjunction with diffusion cell experiments.

Matrix diffusion mass transfer coefficients have been measured directly in several tracer transport experiments in fractured cores in the laboratory (Reimus et al., 2002a; Reimus et al., 1999). [Table 8-2](#) summarizes all of the fracture transport experiments used to obtain estimates of the MTC for this report. As with diffusion cell experiments, matrix porosity and matrix permeability are generally measured in conjunction with fracture transport experiments.

8.2.3 Data Documentation Evaluation

Matrix diffusion coefficients and the product of matrix porosity and matrix diffusion coefficients from both diffusion cell and fracture transport experiments were estimated from model interpretations of the datasets from these tests (Reimus et al., 2002a; Reimus et al., 1999). The data were checked by LANL personnel prior to tabulation, and they were also checked for consistency after tabulation.

8.3 Data Evaluation

This discussion of the evaluation of matrix diffusion data includes descriptions of the dataset and the parameter generation process.

8.3.1 Dataset Description

Matrix diffusion coefficients and the products of matrix porosity and matrix diffusion coefficients from both diffusion cell and fracture transport tests are tabulated along with matrix porosities and matrix permeabilities in [Appendix G](#).

8.3.2 Parameter Generation

Matrix diffusion coefficients and the product of matrix porosity and matrix diffusion coefficients from both diffusion cell and fracture transport experiments were estimated from model interpretations of the datasets from these tests (Reimus et al., 2002a; Reimus et al., 1999). A one-dimensional numerical

Table 8-1
Summary of Diffusion Cell Experiments, Including Rocks Samples, Matrix Porosities and
Permeabilities, and Solutes for Which Diffusion Coefficients Were Measured
 (Page 1 of 2)

Borehole / Depth (ft)	Porosity (Fraction)	Permeability m ²	Solutes
UE20c / 2856D	0.21	5.6E-17	³ H ₂ O, H ¹⁴ CO ₃ ⁻ , ⁹⁹ TcO ₄ ⁻
UE20c / 2856E	0.21	3.0E-17	³ H ₂ O, H ¹⁴ CO ₃ ⁻ , ⁹⁹ TcO ₄ ⁻
UE20c / 2856F	0.21	2.4E-17	³ H ₂ O, H ¹⁴ CO ₃ ⁻ , ⁹⁹ TcO ₄ ⁻
UE20c / 2858A	0.17	9.6E-18	³ H ₂ O, H ¹⁴ CO ₃ ⁻ , ⁹⁹ TcO ₄ ⁻
UE20c / 2809A	0.16	NM	³ H ₂ O, H ¹⁴ CO ₃ ⁻ , ⁹⁹ TcO ₄ ⁻
UE20c / 2809B ^a	0.16	NM	³ H ₂ O, H ¹⁴ CO ₃ ⁻ , ⁹⁹ TcO ₄ ⁻
UE20c / 2751A	0.20	2.8E-17	³ H ₂ O, H ¹⁴ CO ₃ ⁻ , ⁹⁹ TcO ₄ ⁻
UE20c / 2751B ^a	0.20	3.8E-17	³ H ₂ O, H ¹⁴ CO ₃ ⁻ , ⁹⁹ TcO ₄ ⁻
UE20c / 2908A	0.31	NM	³ H ₂ O, H ¹⁴ CO ₃ ⁻ , ⁹⁹ TcO ₄ ⁻
UE20c / 2908D ^a	0.31	NM	³ H ₂ O, H ¹⁴ CO ₃ ⁻ , ⁹⁹ TcO ₄ ⁻
UE20f / 2842	0.30	4.1E-18	³ H ₂ O, H ¹⁴ CO ₃ ⁻ , ⁹⁹ TcO ₄ ⁻
UE18t / 1003A	0.10	NM	³ H ₂ O, H ¹⁴ CO ₃ ⁻ , ⁹⁹ TcO ₄ ⁻
UE18t / 1003A ^a	0.10	NM	³ H ₂ O, H ¹⁴ CO ₃ ⁻ , ⁹⁹ TcO ₄ ⁻
UE18t / 1387.5A	0.26	6.00E-18	³ H ₂ O, H ¹⁴ CO ₃ ⁻ , ⁹⁹ TcO ₄ ⁻
UE18t / 1387.5B	0.26	2.40E-17	³ H ₂ O, H ¹⁴ CO ₃ ⁻ , ⁹⁹ TcO ₄ ⁻
UE18t / 1390	0.26	6.40E-18	³ H ₂ O, H ¹⁴ CO ₃ ⁻ , ⁹⁹ TcO ₄ ⁻
UE18r / 2228A	0.057	NM	³ H ₂ O, H ¹⁴ CO ₃ ⁻ , ⁹⁹ TcO ₄ ⁻
UE18r / 2228B	0.057	3.40E-17	³ H ₂ O, H ¹⁴ CO ₃ ⁻ , ⁹⁹ TcO ₄ ⁻
PM1 / 4823A	0.24	3.00E-17	³ H ₂ O, H ¹⁴ CO ₃ ⁻ , ⁹⁹ TcO ₄ ⁻
PM1 / 4823B	0.24	4.20E-17	³ H ₂ O, H ¹⁴ CO ₃ ⁻ , ⁹⁹ TcO ₄ ⁻
PM2 / 4177A	0.17	1.2E-18	³ H ₂ O, H ¹⁴ CO ₃ ⁻ , ⁹⁹ TcO ₄ ⁻
PM2 / 4177B	0.17	1.1E-18	³ H ₂ O, H ¹⁴ CO ₃ ⁻ , ⁹⁹ TcO ₄ ⁻
PM2 / 4177C ^a	0.17	2.1E-18	³ H ₂ O, H ¹⁴ CO ₃ ⁻ , ⁹⁹ TcO ₄ ⁻
ER-20-6#1 / 2236.3C	0.297	3.9E-18	I, PFBA
ER-20-6#1 / 2236.3D	0.297	4.9E-18	I, PFBA
ER-20-6#1 / 2236.3Z	0.297	2.0E-18	I, PFBA
ER-20-6#1 / 2406A1	0.369	3.4E-17	I, PFBA
ER-20-6#1 / 2406A2	0.369	3.1E-17	I, PFBA
ER-20-6#1 / 2406C	0.369	2.8E-17	I, PFBA
ER-20-6#1 / 2406D	0.369	3.1E-17	I, PFBA
ER-20-6#1 / 2602A1	0.259	8.6E-16	I, PFBA

Table 8-1
Summary of Diffusion Cell Experiments, Including Rocks Samples, Matrix Porosities and
Permeabilities, and Solutes for Which Diffusion Coefficients Were Measured
 (Page 2 of 2)

Borehole / Depth (ft)	Porosity (Fraction)	Permeability m ²	Solutes
ER-20-6#1 / 2602A2	0.259	2.7E-16	I ⁻ , PFBA ⁻
ER-20-6#1 / 2602B3	0.259	2.4E-16	I ⁻ , PFBA ⁻
ER-20-6#1 / 2811E1	0.303	7.1E-15	I ⁻ , PFBA ⁻
ER-20-6#1 / 2811F1	0.303	3.3E-15	I ⁻ , PFBA ⁻
ER-20-6#1 / 2811G	0.303	8.3E-15	I ⁻ , PFBA ⁻
ER-20-6#1 / 2834C	0.179	6.0E-18	I ⁻ , PFBA ⁻
ER-20-6#1 / 2834F	0.179	1.8E-16	I ⁻ , PFBA ⁻
ER-20-6#1 / 2834G	0.179	8.9E-15	I ⁻ , PFBA ⁻
ER-20-6#1 / 2851C1	0.111	2.4E-17	I ⁻ , PFBA ⁻
ER-20-6#1 / 2851C2	0.111	4.0E-18	I ⁻ , PFBA ⁻
UE25c#1 / 2346	0.094	1.1E-18	Br ⁻ , PFBA ⁻
UE25c#1 / 2608	0.298	9.5E-17	Br ⁻ , PFBA ⁻
UE25c#2 / 1749	0.272	4.7E-15	Br ⁻ , PFBA ⁻
UE25c#2 / 1814	0.138	7.8E-19	Br ⁻ , PFBA ⁻
UE25c#1 / 1880A	0.288	4.5E-16	Br ⁻ , PFBA ⁻
UE25c#1 / 1880B	0.288	4.5E-16	Br ⁻ , PFBA ⁻

^aDenotes diffusion cell with a mineralized fracture surface

NM – Not measured

Letters after depths indicate subsamples (replicate measurements)

³HHO - Tritiated water

H¹⁴CO₃⁻ - Bicarbonate

⁹⁹TcO₄⁻ - Pertechnetate

I⁻ - Iodide

PFBA - Pentafluorobenzoate

Br⁻ - Bromide

Table 8-2
Fracture Transport Experiment Rock Samples, Solutes Tested, and
Number of Experiments In Each Fracture

Borehole / Depth (ft)	Matrix Porosity (Fraction)	Solutes	Number of Tests ^a
UE20f / 2,838	0.30	³ HHO, H ¹⁴ CO ₃ ⁻ , ⁹⁹ TcO ₄ ⁻	5
UE18r / 2,228	0.057	³ HHO, H ¹⁴ CO ₃ ⁻ , ⁹⁹ TcO ₄ ⁻	5
UE18t / 1,384	0.26	³ HHO, H ¹⁴ CO ₃ ⁻ , ⁹⁹ TcO ₄ ⁻	5
UE18t / 996	0.11	³ HHO, H ¹⁴ CO ₃ ⁻ , ⁹⁹ TcO ₄ ⁻	5
UE18t / 1,235	0.10 ^b	³ HHO, H ¹⁴ CO ₃ ⁻ , ⁹⁹ TcO ₄ ⁻	5
UE20c / 2,851	0.21	³ HHO, H ¹⁴ CO ₃ ⁻ , ⁹⁹ TcO ₄ ⁻	4
UE20c / 2,858	0.17	³ HHO, H ¹⁴ CO ₃ ⁻ , ⁹⁹ TcO ₄ ⁻	4
ER-20-6#1 / 2,236	0.297	I ⁻ , PFBA ⁻	2
ER-20-6#1 / 2,406	0.369	I ⁻ , PFBA ⁻	2
ER-20-6#1 / 2,811	0.303	I ⁻ , PFBA ⁻	1
ER-20-6#1 / 2,851	0.111	I ⁻ , PFBA ⁻	3
UE25c#2 / 1,749	0.272	I ⁻ , Br ⁻ , PFBA ⁻	8
UE25c#2 / 1,814	0.138	I ⁻ , Br ⁻ , PFBA ⁻	5
UE25c#1 / 1,880	0.288	Br ⁻ , PFBA ⁻	2
UE25c#1 / 2,608	0.298	Br ⁻ , PFBA ⁻	2

^aTests were typically conducted at different flow rates.

^bEstimated porosity

³HHO - Tritiated water

H¹⁴CO₃⁻ - Bicarbonate

⁹⁹TcO₄⁻ - Pertechnetate

I⁻ - Iodide

PFBA - Pentafluorobenzoate

Br⁻ - Bromide

diffusion model (DIFFCELL) was used to interpret the diffusion cell tests, and a semi-analytical, dual-porosity transport model (RELAP) was used to interpret the fracture transport experiments. In DIFFCELL, all input parameters were known or measured prior to data analysis, with the exception of the matrix diffusion coefficient which was used as the only adjustable parameter to “fit” the dataset. In RELAP, the responses of different tracers in a given test or of the same tracer in different tests (conducted at different flow rates) in a given fracture were simultaneously analyzed to obtain estimates of the following parameters:

- The mean tracer residence time, τ (hr)
- The Peclet number, $Pe = L/\alpha$, where L = fracture length (cm) and α = dispersivity (cm)

- The MTC, $n \frac{\sqrt{D_m}}{b}$ ($\text{hr}^{-1/2}$)

Fracture half-apertures were estimated in fracture transport tests from the mean residence time of tracers in the fractures, the known flow rate through the fractures, and the area (length times width) of the fracture surfaces, as follows:

$$b = \frac{Q\tau}{2LW} \quad (8-2)$$

where:

- Q = Flow rate through fracture, cm^3/hr
- τ = Tracer mean residence time in fracture determined from test interpretation, hr
- W = Width of fracture, cm
- L = Length of fracture, cm

Once half-apertures were estimated, and assuming that matrix porosities were known, matrix diffusion coefficient (D_m) values could be estimated directly from the MTCs. Details of the analysis procedures for both diffusion cell tests and fracture transport tests can be found in Reimus et al. (1999 and 2002a).

8.4 Development of Parameter Distributions

Matrix diffusion parameters derived for tritiated water (^3HHO) were combined in this report with matrix diffusion parameters for the simple halides bromide (Br^-) and iodide (I^-) to form a large dataset considered to be representative of both ^3HHO and simple anionic radionuclides (e.g., Cl^- , I^-). The free diffusion coefficient of ^3HHO has been reported to be 2.4×10^{-5} square centimeters per second (cm^2/s) (Skagius and Neretnieks, 1986), whereas Br^- and I^- have free diffusion coefficients at infinite dilution of approximately 2.08 and 2.04×10^{-5} cm^2/s , respectively (Newman, 1973). Thus, the diffusion coefficients of these free species are within approximately 15 to 20 percent of each other, which is well within the variability that can be expected in experimental measurements on different samples of the same rock type (Reimus et al., 2002a). The anions could experience some exclusion from small pores as a result of having the same charge as the rock surfaces (at $\text{pH} > 5$ to 6), which would tend to lower their diffusion coefficients in low-porosity, low-permeability rocks relative to tritiated water. However, to a first approximation, the diffusion coefficients of ^3HHO , Br^- , and I^- were all considered to be representative of ^3HHO and simple anionic radionuclides. Reimus et al. (2002a) also measured diffusion coefficients of Tc-99 (as pertechnetate [TcO_4^-]) and carbon-14 (C-14) (as bicarbonate [HCO_3^-]) in the same rocks as the ^3HHO measurements. They found that TcO_4^- had a significantly smaller effective matrix diffusion coefficient than ^3HHO in most rocks, while HCO_3^- had a highly variable diffusion coefficient that was larger than ^3HHO in some rocks and smaller in other rocks. The diffusion coefficients measured for these species could have been affected by reactions such as the reduction of TcO_4^- to TcO_2 (which would have then sorbed or precipitated),

exchange of C-14 with carbonate minerals, or biological uptake of C-14, so the values obtained for these species were not used to develop distributions in this report.

The following sections describe three different approaches to obtain a representative stochastic value of the matrix diffusion coefficient for ^3HHO or a simple anion. In the first approach, it is assumed that data are available for both the matrix porosity and the matrix permeability of the HSU in which fracture transport is assumed to occur. In the second approach, it is assumed that there is information only on the matrix porosity. In the third approach, it is assumed that there is no information on either matrix porosity or permeability.

8.4.1 Matrix Diffusion Coefficients as a Function of Matrix Porosity and Permeability

Most of the diffusion cell and fracture transport experiments were accompanied by measurements of matrix porosity and matrix permeability of the rocks. Reimus et al. (2002a) found that matrix diffusion coefficients obtained from diffusion cell tests were correlated with both of these parameters according to the following multiple linear regression equation:

$$\text{Log}(D_m) = -3.38 + 1.48(n) + 0.174(\text{Log}(k)) \quad (8-3)$$

where:

- D_m = Matrix diffusion coefficient (cm^2/s)
- n = Matrix porosity (fraction)
- k = Permeability (m^2)

The R^2 value for this regression is 0.44 indicated significant scatter in the data, which is reflected in the large confidence intervals presented below. Clearly, this simple regression equation is an approximate method to estimate the diffusion coefficient.

The 95 percent confidence intervals of the regression parameters are calculated using equations from Draper and Smith (1981):

$$\begin{aligned} \text{Intercept} &= -3.38 \pm 1.55 \\ \text{Coefficient for porosity} &= 1.48 \pm 1.27 \\ \text{Coefficient for log perm.} &= 0.174 \pm 0.084. \end{aligned}$$

The larger 95 percent confidence interval (relative to the mean) for the porosity coefficient compared with the log permeability coefficient is consistent with an F-test result that log permeability is a better predictor variable than matrix porosity. However, stepwise F tests indicated that both matrix porosity and log permeability make significant contributions to the regression equation at the 95 percent confidence level (i.e., the predictive ability of the equation is improved significantly when adding either variable to the equation after the other is already in the equation).

The diffusion coefficient data considered in obtaining the parameters of Equation 8-3 by multiple linear regression are plotted in Figure 8-1 as a function of matrix porosity (n) and log permeability (k). Note that Equation 8-3 has slightly different coefficients for porosity and log permeability and a slightly different intercept from equation (2.5) in Reimus et al. (2002a) because a few of the data points of Figure 8-1 were inadvertently weighted by a factor of 2 in Reimus et al. (2002a).

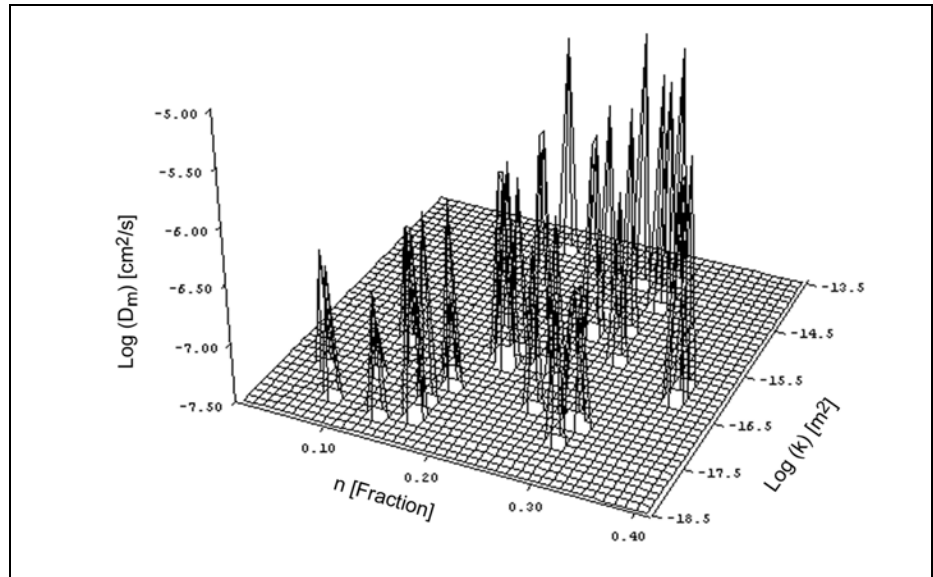


Figure 8-1

Log Matrix Diffusion Coefficients as a Function of Both Matrix Porosity and Log Matrix Permeability for ^3HHO in Pahute Mesa Rocks (Reimus et al., 2002a), for Bromide in Rocks From the UE25 C-Wells (Reimus et al., 1999), and for Iodide in Rocks From ER-20-6 #1 (Reimus et al., 2000).

Confidence intervals for the predicted values of $\text{Log}(D_m)$ from Equation 8-3 can be calculated using standard methods (Draper and Smith, 1981). The 95 percent confidence intervals vary over the n - $\text{Log}(k)$ parameter space from approximately $\text{Log}(D_m) \pm 0.57$ to $\text{Log}(D_m) \pm 0.62$, with the smallest confidence interval occurring when n and $\text{Log}(k)$ are at their mean values and larger intervals occurring as n and $\text{Log}(k)$ approach the ends of their respective ranges. It is recommended that, for any given values of n and $\text{Log}(k)$, the value of $\text{Log}(D_m)$ obtained from Equation 8-3 be used as the mean of a normal distribution with a standard deviation of 0.285 to 0.31 (again with the smallest value when n and $\text{Log}(k)$ are at their mean values). This distribution should then be randomly sampled to obtain a stochastic value of $\text{Log}(D_m)$ that correspond to the specified values of n and $\text{Log}(k)$.

8.4.2 Matrix Diffusion Coefficients as a Function of Matrix Porosity

Diffusion coefficients derived from fracture transport experiments were not used in the multiple linear regression (Equation 8-3) and are not plotted in Figure 8-1 because matrix permeabilities in these experiments could not be readily measured. Furthermore, the permeabilities of representative matrix samples often varied considerably from sample to sample, so it was unreliable to assign a matrix permeability to a fracture experiment using these measurements.

However, porosities of multiple matrix samples were generally in very good agreement and were, therefore, considered to be good representations of matrix porosities in the fracture experiments.

An estimate of the matrix diffusion coefficient in fracture transport experiments can be obtained by dividing the MTC by the matrix porosity and multiplying by the fracture half-aperture and then squaring the result. Estimates of the half-aperture in the fracture experiments can be determined from Equation 8-2.

Equation 8-2 yields a lower-bound estimate of the half-aperture because it assumes that the entire fracture is a parallel-plate channel that is the length and width of the fractured core. Any channeling of flow through the fracture will result in half-apertures that are locally larger in the channels because the same flow rate will be channeled through a smaller effective fracture width. Thus, the use of Equation 8-2 to obtain a fracture half-aperture estimate will ultimately yield a lower-bound estimate for the D_m .

Figure 8-2 shows the D_m from both diffusion cell (direct measurements) and fracture transport experiments (deduced from MTC using the method described in the previous paragraph) as a function of matrix porosity in all of the tests listed in Table 8-1 and Table 8-2. It is apparent from Figure 8-2 that (1) the matrix diffusion coefficients from the fracture experiments tend to be more scattered, and (2) the diffusion coefficients from the fracture experiments tend to be larger than those from the diffusion cell experiments. The first result is very likely due to the additional uncertainty associated with the half-aperture estimates required to obtain diffusion coefficients from fracture experiments; this source of uncertainty does not exist for diffusion cell measurements. The second result could be due to the fact that some of the diffusion in fracture transport experiments is very likely occurring in free water in the fractures rather than entirely in the matrix, as in diffusion cell experiments. In this case, larger apparent diffusion coefficients in the fracture experiments would be expected because diffusion coefficients in free water are always higher than in a tortuous matrix. Linear regression fits to the diffusion cell, and fracture data are also shown in Figure 8-2. The R^2 values for these fits clearly indicate poor regressions, especially for the fracture data. A combined fit of all the data is not shown.

From a modeling perspective, the product of the matrix porosity and matrix diffusion coefficient (in numerical models) or of the matrix porosity and the square root of the matrix diffusion coefficient (in many analytical or semi-analytical models) effectively serves as a lumped parameter to account for matrix diffusion. Figure 8-3 shows how the product of matrix porosity and

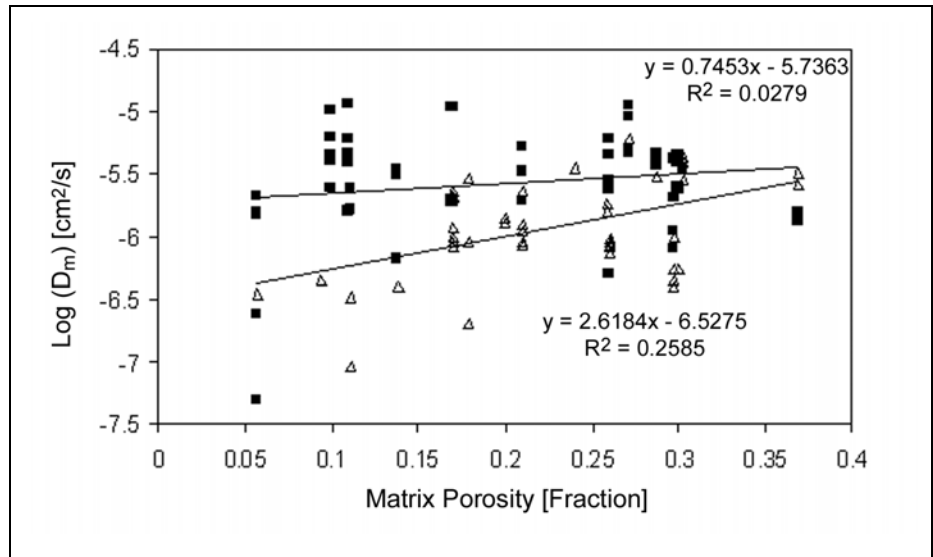


Figure 8-2
Log Matrix Diffusion Coefficients as a Function of Matrix Porosity (Fraction) Determined From Diffusion Cell Tests (Triangles) and Fracture Transport Tests (Squares). The Least-Squares Linear Regressions Indicate Relatively Poor Fits to the Individual Datasets

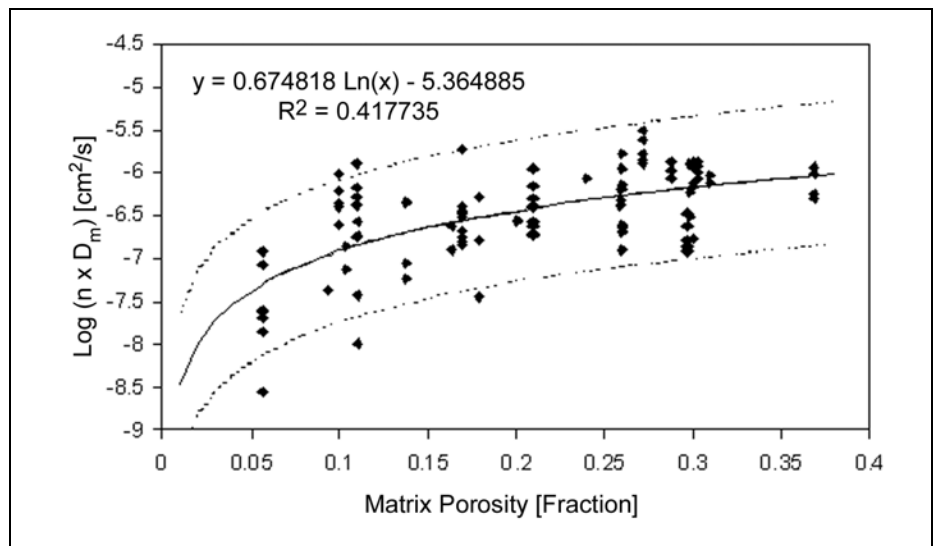


Figure 8-3
Log (nD_m) Values as a Function of Matrix Porosity (Fraction), and a Logarithmic Fit to the Data. The Dashed Lines Represent 95 Percent Confidence Intervals

diffusion coefficient (using all the data shown in [Figure 8-2](#)) depends on matrix porosity. Obviously, there is a correlation between $n D_m$ and n because the former is a lumped parameter that includes the latter. [Figure 8-3](#) also shows a logarithmic fit to the data and 95 percent confidence bounds associated with this fit. The regression equation using \log_{10} instead of natural log is as follows:

$$\text{Log}(nD_m) = 1.5538 \text{Log}(n) - 5.3649 \quad (8-4)$$

Using the properties of logarithms, the relationship for D_m as a function of n becomes:

$$\text{Log}(D_m) = 0.5538\text{Log}(n) - 5.3649 \quad (8-5)$$

[Equation 8-4](#) could be used to obtain an estimate of the mean value of $\text{Log}(n D_m)$ for any known value of n , and then a normal distribution of $\text{Log}(n D_m)$ values with this mean and a standard deviation of 0.41 to 0.42 could be randomly sampled to obtain a stochastic estimate of $\text{Log}(n D_m)$ for that porosity. The standard deviation of $\text{Log}(n D_m)$ varies slightly over the full range of porosities, with the value being 0.41 at the mean experimental porosity (0.21) and increasing to 0.42 at porosities of 0.015 and 0.405. It is recommended that [Equation 8-4](#) be used rather than the linear regressions shown in [Figure 8-2](#) to obtain matrix diffusion coefficients (or, more specifically, the product of porosity and matrix diffusion coefficient) as a function of matrix porosity.

8.4.3 Cumulative Distribution of Matrix Diffusion Coefficients with No Dependence on Matrix Porosity or Permeability

[Figure 8-4](#) shows a cumulative probability distribution of all the $\text{Log}(n D_m)$ values in [Figure 8-3](#) with no regard to matrix porosity. The parameters derived from diffusion cell and fracture transport tests were equally weighted. The line in [Figure 8-4](#) is a fit of a normal distribution to these data (the fitted distribution is actually a lognormal distribution when one considers that the $n D_m$ values are log transformed). This distribution has a mean of -6.48 and a standard deviation of 0.49 . In the absence of any data on matrix porosity, random sampling of this normal distribution would provide a representative stochastic value of $\text{Log}(n D_m)$ for use in transport models.

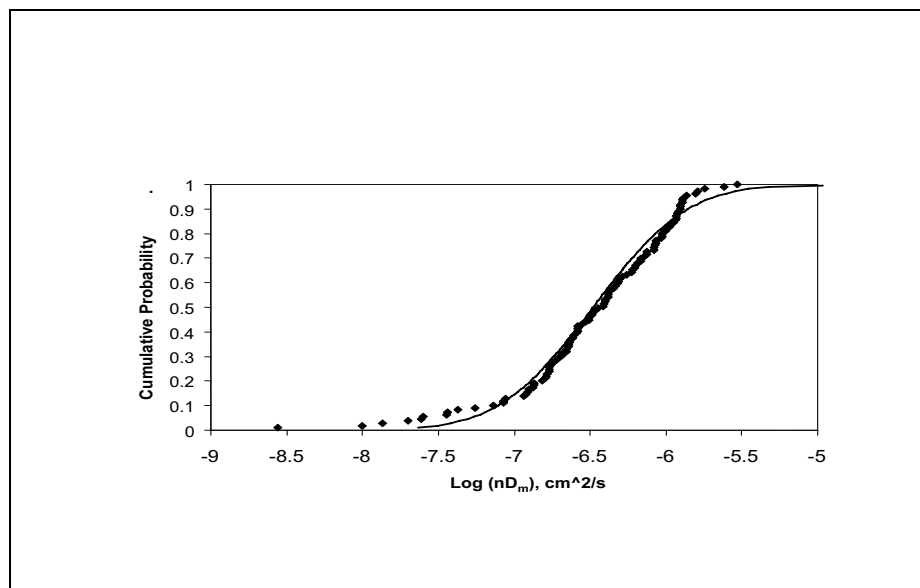


Figure 8-4
Cumulative Probability Distribution of Matrix Diffusion Coefficients from
Figure 8-3 with No Regard to Matrix Porosity or Matrix Permeability.
The Line Represents a Normal Distribution with a Mean of -6.48 and a
Standard Deviation of 0.49

8.4.4 Adjusting Matrix Diffusions Coefficient for Different Species, Temperature, and Ionic Strength

The different methods of estimating diffusion coefficients described in the previous sections will provide values for ^3HHO or simple anions in volcanic rock matrices at approximately 20 to 25°C in waters with an ionic strength of about 0.0035 Molar (M) (typical of Pahute Mesa ground waters). For more complex anions and cations, different temperatures, or different ionic strengths, it will be necessary to adjust these diffusion coefficient estimates. However, in general, the variability in matrix diffusion coefficients due to variability in rock properties should be much greater than the variability due to species properties, temperature, and ionic strength.

Empirical correlations exist in the literature to adjust free diffusion coefficients for species size and charge, but, for matrix diffusion coefficients, we find it more convenient to simply provide guidance for such adjustments. As a general rule, cations have smaller diffusion coefficients than anions because they tend to be more hydrated (i.e., more water molecules move with them, giving them a larger effective radius). Most simple monovalent cations (e.g., potassium $[\text{K}^+]$, ammonium $[\text{NH}_4^+]$, cesium $[\text{Cs}^+]$) have diffusion coefficients only 5 to 10 percent smaller than simple monovalent anions such as Br and I (Newman, 1973). Plutonium dioxide (PuO_2^+) and Neptunium dioxide (NpO_2^+) probably have diffusion coefficients of this magnitude because they both have relatively low charge-to-mass ratios and should not be highly hydrated. However, cations with high charge to mass ratios have much smaller diffusion coefficients. For instance,

sodium (Na^+) has a diffusion coefficient about 0.65 times that of Br^- and I^- , and lithium (Li^+) has a diffusion coefficient about 0.5 times that of these anions (Newman, 1973). Multivalent cations also tend to have small diffusion coefficients, ranging from 0.3 to 0.4 times that of Br^- and I^- (Newman, 1973). Cations with charges of +3 or more typically hydrolyze or form complexes in solution to become species of lower charge (e.g., hydroxyl or carbonate complexes). Large monovalent anions, such as pentafluorobenzoate, have diffusion coefficients about 0.33 times that of Br^- and I^- (Callahan et al., 2000). The diffusion coefficients of such organic bases can be considered reasonable lower bounds for diffusion coefficients of large anionic radionuclide complexes. Multivalent anions (which are generally multi-atom species) tend to have diffusion coefficients of 0.4 to 0.6 times that of Br^- and I^- (Newman, 1973).

The Stokes-Einstein equation predicts that diffusion coefficients will be directly proportional to absolute temperature and inversely proportional to fluid viscosity (which decreases as temperature increases, but not linearly). Table 8-3 summarizes the factor by which diffusion coefficients should increase (relative to 20°C in pure water) as a function of temperature (Weast and Astle, 1982). The higher temperatures in Table 8-3 will be relevant to near-cavity conditions for some time after resaturation.

Table 8-3
Factor by Which Diffusion Coefficients Change
as a Function of Temperature In Water

Temperature (°C)	Relative Diffusion Coefficient
20	1.0
25	1.14
30	1.30
40	1.64
50	2.14
60	2.58
70	3.07
80	3.59
90	4.15
100	4.76

Diffusion coefficients are a relatively weak function of ionic strength until ionic strengths become greater than about 1 M (Newman, 1973). From infinite dilution to 1 M ionic strength, diffusion coefficients should change no more than ± 10 percent. If ionic strengths exceed 1 M, diffusion coefficients may increase or decrease by as much as 25 percent from their values at infinite dilution. However, ionic strengths greater than 1 M are unlikely to occur at NTS, even in cavities, so the effect of ionic strength on diffusion coefficients is considered to be relatively minor compared to the effect of rock properties and temperature.

8.5 Diffusion Coefficients Estimated per HSU

The relationships provided by [Equations 8-3](#) and [8-5](#) are used with matrix porosity data from [Section 5.0](#) and matrix permeability data from the Pahute Mesa hydrologic data report (Rehfeldt et al., 2003) to estimate the effective diffusion coefficient for each HSU. The matrix porosity data have been presented in [Section 5.0](#). For each HSU, the lower bound, most likely (mean), and upper bound matrix porosity were obtained from [Table 5-7](#). The matrix permeability is measured on core and is reported in Rehfeldt et al. (2003, Table 5-1). In that report, the core permeability data are reported on the basis of regional hydrostratigraphic units, LCA, LCCU, and volcanic aquifers (VAs). For the calculation of diffusion coefficients, the same range of matrix permeability was used for each volcanic unit, except the intrusive units. To estimate a range of diffusion coefficients corresponding to the range of input parameters, the lower bound matrix porosity from [Table 5-7](#) and the lower bound matrix permeability (mean - 2 standard deviations) was used in [Equation 8-3](#). As noted in [Section 8.4.1](#), log diffusion coefficient from [Equation 8-3](#) has an error associated with it of 0.62 log units. Therefore, the low bound was reduced by 0.62 log units before converting to diffusion coefficient in units of cm²/s. This provides as small a lower bound as is reasonable. For the most likely value, the mean porosity from [Table 5-7](#) and the mean permeability from Rehfeldt et al. (2003) were used. The upper bound was calculated in the same manner as the lower bound was, with the upper bound porosity, upper bound permeability, and 0.62 log units added to the result for regression equation uncertainty.

For the intrusive volcanic units, there is no matrix permeability data available. [Section 8.4.2](#) provides [Equation 8-5](#) to estimate log diffusion coefficient from log porosity directly. The porosity data was obtained directly from [Table 5-7](#).

[Table 8-4](#) provides the most likely value, lower, and upper bound estimates of the diffusion coefficient calculated from [Equations 8-3](#) and [8-5](#), as appropriate. The distribution of each parameter is taken to be log-triangular because only upper and lower bounds were used along with a most likely value. The significance of these assumptions will be tested during the transport simulations.

8.6 Data Limitations

The data used to generate matrix diffusion parameter distributions do not necessarily represent all of the HSUs on Pahute Mesa. This limitation was addressed by presenting the matrix diffusion parameters as a function of volcanic rock properties (matrix porosity and permeability) rather than as HSU-specific parameters. However, there is uncertainty associated with not having all of the HSUs represented in the datasets because some HSUs may be outliers in the correlations of matrix diffusion parameters with matrix porosity and permeability.

From a CAU-scale modeling perspective, the most uncertain of the three parameters that make up the MTC is the fracture half-aperture, as it is not possible to directly translate aperture measurements made in the laboratory (on core samples) to apertures of flowing fractures in the field. Matrix porosities, matrix

Table 8-4
Pahute Mesa - Matrix Diffusion Coefficient (cm²/s) - Dominant Lithology for Each HSU
 (Page 1 of 3)

Layer Number	Symbol	Name	Continuous Lithology	Matrix Permeability Data Used	Lower Bound	Mean	Upper Bound	Distribution	Equation Used
45	YVCM	Younger Volcanic Composite Unit	PWT	VA	3.9e-08	2.5e-06	2.4e-04	Log-triangular	8-3
44	TCVA	Thirsty Canyon Volcanic Aquifer	WT	VA	5.2e-08	3.8e-06	2.1e-04	Log-triangular	8-3
43	DVCM	Detached Volcanics Composite Unit	PWT	VA	3.9e-08	2.5e-06	2.4e-04	Log-triangular	8-3
42	DVA	Detached Volcanics Aquifer	WT	VA	3.4e-08	1.4e-06	1.5e-04	Log-triangular	8-3
41	FCCM	Fortymile Canyon Composite Unit	PWT	VA	3.9e-08	2.5e-06	2.4e-04	Log-triangular	8-3
40	FCA	Fortymile Canyon Aquifer	WT	VA	3.4e-08	1.4e-06	1.5e-04	Log-triangular	8-3
39	TMCM	Timber Mountain Composite Unit	DWT	VA	3.5e-08	1.4e-06	1.6e-04	Log-triangular	8-3
38	THLFA	Tannenbaum Hill Lava-flow Aquifer	LA	VA	3.4e-08	1.4e-06	1.5e-04	Log-triangular	8-3
37	THCM	Tannenbaum Hill Composite Unit	NWT	VA	3.6e-08	3.1e-06	2.0e-04	Log-triangular	8-3
36	TMA	Timber Mountain Aquifer	WT	VA	3.7e-08	2.0e-06	1.9e-04	Log-triangular	8-3
33	WWA	Windy Wash Aquifer	LA	VA	3.4e-08	1.4e-06	1.5e-04	Log-triangular	8-3
32	PCM	Paintbrush Composite Unit	MWT	VA	3.4e-08	1.4e-06	1.5e-04	Log-triangular	8-3
31	PVTA	Paintbrush Vitric-tuff Aquifer	BED	VA	4.5e-08	3.4e-06	1.3e-04	Log-triangular	8-3
30	BA	Benham Aquifer	LA	VA	3.6e-08	1.5e-06	5.9e-05	Log-triangular	8-3
28	TCA	Tiva Canyon Aquifer	WT	VA	3.4e-08	1.4e-06	1.5e-04	Log-triangular	8-3
27	PLFA	Paintbrush Lava-flow Aquifer	LA	VA	3.4e-08	1.7e-06	8.7e-05	Log-triangular	8-3

Table 8-4
Pahute Mesa - Matrix Diffusion Coefficient (cm²/s) - Dominant Lithology for Each HSU
 (Page 2 of 3)

Layer Number	Symbol	Name	Continuous Lithology	Matrix Permeability Data Used	Lower Bound	Mean	Upper Bound	Distribution	Equation Used
25	TSA	Topopah Spring Aquifer	WT	VA	3.4e-08	1.4e-06	1.5e-04	Log-triangular	8-3
24	YMCFCM	Yucca Mountain Crater Flat Composite Unit	PWT	VA	3.9e-08	2.5e-06	2.4e-04	Log-triangular	8-3
23	CHVTA	Calico Hills Vitric-tuff Aquifer	NWT	VA	8.3e-08	3.1e-06	1.0e-04	Log-triangular	8-3
22	CHVCM	Calico Hills Vitric Composite Unit	NWT	VA	3.3e-08	1.9e-06	8.4e-05	Log-triangular	8-3
21	CHZCM	Calico Hills Zeolitic Composite Unit	NWT	VA	3.3e-08	1.1e-06	2.4e-04	Log-triangular	8-3
20	CHCU	Calico Hills Confining Unit	NWT	VA	3.6e-08	3.1e-06	2.0e-04	Log-triangular	8-3
19	IA	Inlet Aquifer	LA	VA	3.4e-08	1.4e-06	1.5e-04	Log-triangular	8-3
18	CFCM	Crater Flat Composite Unit	WT	VA	3.4e-08	1.4e-06	1.5e-04	Log-triangular	8-3
16	KA	Kearsarge Aquifer	LA	VA	3.4e-08	1.4e-06	1.5e-04	Log-triangular	8-3
14	BRA	Belted Range Aquifer	WT	VA	3.4e-08	1.6e-06	7.9e-05	Log-triangular	8-3
13	PBRCM	Pre-belted Range Composite Unit	PWT	VA	3.5e-08	1.4e-06	5.1e-05	Log-triangular	8-3
12	BMICU	Black Mountain Intrusive Confining Unit	IN	Not Applicable	2.2e-08	4.7e-07	8.5e-06	Log-triangular	8-5
11	ATICU	Ammonia Tanks Intrusive Confining Unit	IN	Not Applicable	2.2e-08	4.7e-07	8.5e-06	Log-triangular	8-5
10	RMICU	Rainier Mesa Intrusive Confining Unit	IN	Not Applicable	2.2e-08	4.7e-07	8.5e-06	Log-triangular	8-5

Table 8-4
Pahute Mesa - Matrix Diffusion Coefficient (cm²/s) - Dominant Lithology for Each HSU
 (Page 3 of 3)

Layer Number	Symbol	Name	Continuous Lithology	Matrix Permeability Data Used	Lower Bound	Mean	Upper Bound	Distribution	Equation Used
9	CCICU	Claim Canyon Intrusive Confining Unit	IN	Not Applicable	2.2e-08	4.7e-07	8.5e-06	Log-triangular	8-5
8	CHICU	Calico Hills Intrusive Confining Unit	IN	Not Applicable	2.2e-08	4.7e-07	8.5e-06	Log-triangular	8-5
7	SCICU	Silent Canyon Intrusive Confining Unit	IN	Not Applicable	2.2e-08	4.7e-07	8.5e-06	Log-triangular	8-5
6	MGCU	Mesozoic Granite Confining Unit	IN	Not Applicable	2.2e-08	4.7e-07	8.5e-06	Log-triangular	8-5
5	LCA3	Lower Carbonate Aquifer - Thrust Plate	DM	LCA	4.5e-08	7.8e-07	1.4e-05	Log-triangular	8-3
4	LCCU1	Lower Clastic Confining Unit - Thrust Plate	Quartzite	LCCU	3.5e-08	2.8e-07	2.6e-06	Log-triangular	8-3
2	LCA	Lower Carbonate Aquifer	DM	LCA	4.5e-08	7.8e-07	1.4e-05	Log-triangular	8-3
1	LCCU	Lower Clastic Confining Unit	Quartzite	LCCU	3.5e-08	2.8e-07	2.6e-06	Log-triangular	8-3

permeabilities, and matrix diffusion coefficients, on the other hand, should be relatively transferable from laboratory to field scales. Once the matrix porosity and D_m values are estimated for a given HSU, it is assumed that fracture apertures will be sampled from distributions for that HSU in CAU-scale models to yield MTC estimates (or ranges) for that HSU.

8.7 Scaling Considerations

One of the most important scaling considerations (and uncertainties) associated with the MTC is the manner in which fracture apertures scale with distance. MTCs that have been deduced from field tracer tests have generally been significantly smaller than MTCs derived from laboratory tracer tests, even when the tests at each scale were nominally conducted in the same HSU. [Figure 8-5](#) shows MTC values from a large number of laboratory and field tracer tests in volcanic rocks as a function of test time scale. The smaller MTC values in field tests are probably the result of larger effective fracture apertures in the field than in the laboratory. Fracture surfaces in the laboratory are generally well aligned and held together under pressure in flow apparatuses, whereas fracture surfaces in the field may be offset by shear. Effective apertures would be expected to increase with length scale, at least up to some limit, because as control volumes increase, a greater multiplicity of potential flow pathways can be expected; therefore, there will be greater likelihood of larger aperture flow pathways for groundwater to follow.

An additional matrix diffusion scaling consideration is the effective distance into the matrix that solutes can diffuse from fractures before encountering either another flowing fracture or some sort of diffusion boundary. The distance to another fracture or to a diffusion boundary can be used to calculate an upper limit of the volume of matrix pore water that is accessible to solutes in a large-scale fracture flow system. The matrix pore water volume plus the flowing porosity divided by the flowing porosity in a system effectively constitutes a maximum retardation factor for solutes moving through the system over long time and length scales (independent of the MTC). Field-scale tracer tests generally do not provide estimates of the available volume of matrix pore water in a system because these tests cannot be conducted for long enough time periods to allow tracers to diffuse throughout the entire accessible pore water volume (unless the volume is very small). Flowing fracture spacings, which can be considered upper-bound estimates of distances that solutes will diffuse into the matrix before encountering another flow fracture or a diffusion boundary could be estimated from borehole flow surveys. However, these estimates will be biased toward subhorizontal fractures and will not provide a good estimate of spacing between subvertical fractures, so such estimates are not provided for this report. Fracture flow porosities must also be estimated in the flow systems to fully address the scaling of matrix diffusion. For now, scaling of matrix diffusion will have to be addressed through model sensitivity analyses using current knowledge of matrix porosities and MTC values, and treating fracture flow porosity, fracture apertures, and fracture spacing as stochastic parameters with relatively large uncertainties.

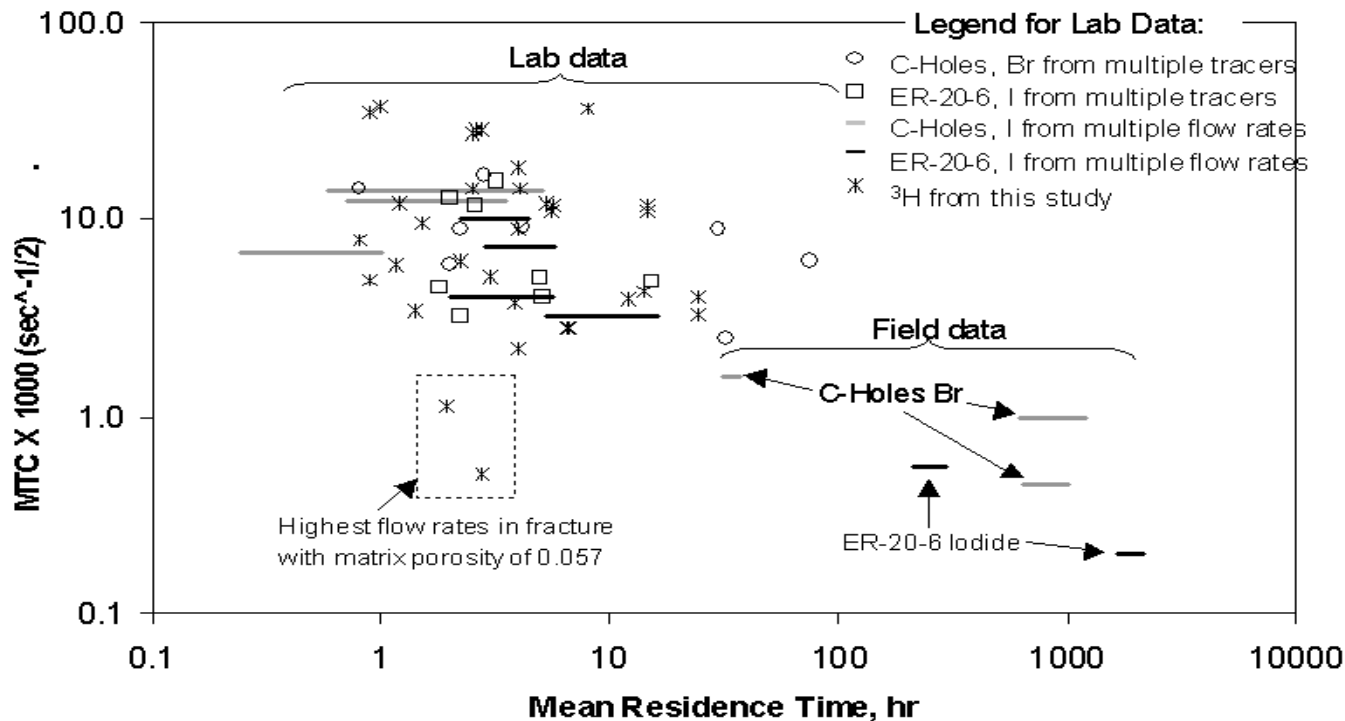


Figure 8-5
Matrix Diffusion Mass Transfer Coefficients for Halides and Tritium Obtained in Laboratory Fracture Transport Experiments and Field Tracer Tests in Volcanic Rocks From the Nevada Test Site. There is a Tendency for Smaller Mass Transfer Coefficients as Time Scales Increase. Laboratory and Field Data for C-hole Rocks are from Reimus et al. (1999); Laboratory Data for ER-20-6 Rocks are from Reimus and Haga (1999). The Horizontal Lines for the Field Data Reflect the Range of Uncertainty in Mean Residence Times in These Tests.

9.0 Matrix Sorption Parameters

This section includes a description of the matrix sorption process, a review of the available data, and analyses of the data that provide distribution functions. In order to enhance the readability of this section, all figures and tables called out in the text have been grouped in [Section 9.8](#) and [Section 9.9](#), respectively.

9.1 The Role of Matrix Sorption in Contaminant Transport Models

Matrix sorption is the physiochemical process at mineral-water interfaces that controls solute mobility and, hence, solute retardation within the pore spaces of the immobile rock matrix. Similar physiochemical processes may occur on minerals coating fractures. These are treated separately in [Section 10.0](#) because the conceptual and numerical models differentiate between the sorption process within the matrix pore space and along fracture walls. There are multiple methods for mathematically representing the matrix sorption process in parameterized groundwater transport models. These methods include, but are not limited to: (a) mechanistic pore-scale models that represent the sorption process on each immobile mineral grain with thermodynamic relationships for each type of reactive surface, (b) mechanistic complexation and exchange models representing average processes on integrated volumes represented with discretized continuum models, and (c) isotherms that seek to describe or abstract on a large scale the integrated behavior of the smaller scale mechanistic processes. One such isotherm is the linear distribution coefficient, K_d . Modeling solute transport using K_d s is attractive due to the simplicity with which they are implemented and because the K_d s represent an average behavior over the large volumes likely to be represented in the CAU-scale transport model. For the purposes of this document, it is assumed that the matrix sorption parameter for use in the CAU transport model is the K_d .

The distribution coefficient K_d provides a relatively simple method for simulating retardation due to equilibrium sorption with immobile minerals. The K_d value is simply defined as:

$$K_d = \frac{\text{Moles of solute per gram of solid phase}}{\text{Moles of solute per milliliter of solution}} \quad (9-1)$$

Thus, an assumption of instantaneous equilibrium between aqueous and sorbed phase is inherent in the use of this parameter.

The K_d parameter may be developed either by direct measurement on aquifer material samples or it can be computed by upscaling mechanistic processes. Both approaches are discussed in the next sections.

9.1.1 The K_d Parameter

Grid cells in the Pahute Mesa CAU transport model may be as large as 1 km x 1 km x 250 m. Within such a large volume, it is likely that sub-block heterogeneities will affect where water and solutes flow and what minerals the solutes come into contact with. Thus, averaging of the specific processes that occur at each mineral reaction site is necessary and appropriate for such large-scale simulations. Although measured on a small sample, the K_d begins to provide such averaging. Additionally, modeling transport of sorbing solutes at the CAU scale presents a computational challenge for more mechanistic transport models. K_d s, however, are easy to include in large-scale transport models.

9.1.2 Limitations of the K_d Parameter

Use of the K_d parameter requires the assumption of local equilibrium. Reactions that are actually kinetic in nature must be assumed to occur fast enough that the K_d captures the process either adequately or conservatively in field-scale simulations. Further, the K_d parameter does not allow for changing sorption behavior due to changes in water chemistry or mineral surfaces. It can vary spatially, but is not capable of representing dynamic system changes during the course of a simulation.

9.2 Matrix K_d Data Compilation

Matrix K_d s are needed for source term radionuclides that enter the natural hydrologic systems and react with immobile minerals. Pawloski et al. (2001) provide a list of 37 source term radionuclides, of which 21 are classified as reactive. Those 21 include multiple isotopes of only 12 different elements. Further, of the 15 source term radionuclides, Pawloski et al.; (2001) list as non-reactive tracers, isotopes of nickel (Ni), zirconium (Zr), niobium (Nb), and tin (Sn) are implicated as being nonconservative species in other studies; therefore, they are considered here as well. Thus, the 16 reactive elements (and their isotopes) of interest for Pahute Mesa CAU transport modeling include calcium (Ca), strontium (Sr), cesium (Cs), samarium (Sm), europium (Eu), holmium (Ho), curium (Cm), uranium (U), neptunium (Np), plutonium (Pu), americium (Am), Ni, Zr, Nb, and Sn. Although not in the list of Pawloski et al. (2001), thorium (Th) may also be of interest due to its presence in the source term list of Smith (2001), and lead (Pb) may be of interest due to its abundance in emplacement materials. Of these elements, we are unaware of K_d measurements or estimates only for Ho and Cm. Pawloski et al. (2001) group these two elements with Eu, suggesting they have similar transport characteristics. Sorption data on representative material are available for Pu, Np, U, Sr, Cs, and Pb. K_d values for

the remaining elements are estimated based on data collected for other materials, elemental properties of the radionuclides, or mechanistic simulation estimates.

9.2.1 Data Types

Data types include K_d values derived from upscaled mechanistic sorption models and directly-measured K_d values.

9.2.1.1 K_d Derived From Upscaled Mechanistic Sorption Models

Reactions of solutes with immobile minerals involve a host of processes. Triay et al. (1997) and Zavarin and Bruton (2000a and b) provide descriptions of the reactive processes and controls affecting solute sorption to immobile minerals associated with the volcanic systems of the NTS. Mechanistic modeling approaches seek to represent the fundamental reactions between the solutes and the specific surfaces with which they come into contact. Using thermodynamic reaction-constant databases, mechanistic approaches represent processes including surface complexation, ion exchange, and precipitation. Additionally, the mechanistic modeling approach seeks to incorporate all aqueous-aqueous and aqueous-solid reactions. These include speciation reactions such as those involving carbonate complexes, oxidation/reduction reactions, and rock water reactions that may control the concentration of surface sites with which radionuclides come into contact. $K_{d,s}$ can be developed from mechanistic models by simulating the effective distribution of a solute between its aqueous phase and sorbed phase by considering all relevant reactions listed above for a sample of aquifer material and specified geochemical conditions.

A benefit of the mechanistic modeling approach is its ability to specifically represent the reactions that control and affect a radionuclide's mobility. Due to the complete representation of all reactions, the mechanistic modeling approach describes how groundwater chemistry changes (e.g., pH), affect sorption reactions, as well as how sorption reactions may affect groundwater chemistry.

A limitation of the mechanistic modeling approach is that, although a detailed set of reactions may be simulated, parameters for those reactions may not be available, particularly at the CAU scale. For example, a mechanistic transport model requires the concentration of available reactive surface sites (often represented as percent mass of various minerals for which total reactive surface sites are known) be specified. Characterization of surfaces that a solute may come in contact with is generally not known and must be inferred. Further, coatings of reactive mineral sites with other compounds may serve to modify the available reactive surface sites for a given mineral. Another limitation of mechanistic models is that they require large amounts of computer resources due to the complexity and nonlinearity of the processes that they attempt to capture.

Although mechanistic models are faced with some limitations in their application for large-scale systems, they remain attractive due to their ability to capture

significant processes. By doing so, they present both a capability to provide technical credibility to scaled or abstracted methods as well as providing a process with which to develop such scaled parameters.

Until recently, mechanistic sorption modeling has been primarily focused on small-scale systems where detailed characterization of mineral composition is available. Recognizing the need to extend such models for utility to CAU-scale problems, Zavarin et al. (2002) has begun to develop a methodology that upscales mechanistic sorption models to prescribe K_d values. This approach formalizes concepts for Pahute Mesa presented by Pawloski et al. (2001) and Wolfsberg et al. (2002, Appendix B), as well as by Davis et al. (1998) and others too numerous to fully review for other hydrogeologic systems. Only a brief summary of the method, results, and limitations of the mechanistic scaling approach are presented here. Zavarin et al. (2002) provide detail on the methods and results.

In upscaling the mechanistic transport modeling approach (Zavarin and Bruton, 2000a and b); Zavarin et al. (2002) seek to represent all processes governing retardation of each radionuclide of interest. These include aqueous speciation, surface complexation, ion exchange, and precipitation reactions. Further, such processes for one radionuclide may be codependent upon the similar reactions associated with other radionuclides, thus leading to a large set of coupled reactions that must be considered simultaneously. The methods for solving such systems of equations are well documented. However, Zavarin et al. (2002) recognize that such methods are well suited for small or well-constrained problems, but that simplification is necessary for applicability at larger scales (e.g., CAU scale). Thus, following a set of assumptions, K_{ds} are developed based upon the mechanistic modeling approach. The assumptions include (a) time-invariant solution groundwater chemistry, (b) time-invariant sorbing mineral abundances, (c) far greater abundance of available sorption sites than sorbing radionuclides in solution, and (d) conditions in which precipitation of minerals with the radionuclides can be neglected. Wolfsberg et al. (2002) made similar assumptions to justify simplifications in mechanistic models of fracture sorption K_{ds} .

Following the assumptions listed above, a set of numerical experiments can be performed to compute K_{ds} for a material. The information needed for such calculations include (a) initial radionuclide concentrations in solution, (b) groundwater chemistry (assumed to be unchanging), (c) thermodynamic reactions for all aqueous speciation and sorption reactions (e.g., Zavarin and Bruton, 2000 a and b), and (d) most importantly, available reactive surface site concentrations of the surface complexation and ion-exchange sites at which sorption reactions will occur.

Zavarin et al. (2002) estimate matrix K_{ds} for Ca, Sr, Cs, Am, Eu, Sm, Np, Pu, and U for multiple Pahute Mesa HSUs, as summarized in [Section 9.4](#). It is also applied to estimate K_{ds} in alluvial material in Frenchman Flat. If radionuclide migration in alluvial material in the Pahute Mesa CAU transport model becomes a process for consideration, then the analyses of Zavarin et al. (2002) will be relevant there as well. The K_{ds} estimated by Zavarin et al. (2002) for alluvium match measured values much better than the tuff estimates.

9.2.1.2 Directly Measured K_d

As described in the previous section, K_d may be computed from mechanistic processes. K_d can also be measured directly during sorption experiments. The experiments are generally designed with knowledge of the mechanistic processes that affect K_d , but with the goal of simply measuring it given some set of environmental controls. Measurements of K_d values for several radionuclides on multiple types of minerals and rock material have been collected in support of UGTA and YMP transport studies. Such studies generally provide information on the rock type and the experimental conditions under which the experiment was performed. Such conditions include:

- Water chemical composition
- Temperature
- pH
- Eh (and/or other indicators of oxidation/reduction state such as oxygen fugacity)
- Solute concentration
- Rock characteristics
- Experimental atmospheric conditions (e.g., air or carbon dioxide to control pH)

Thus, each K_d measured is for a specific set of environmental conditions, albeit generally designed to represent *in situ* conditions to some degree. The information that would be necessary to scale mechanistic studies to reproduce measured K_d values is generally not available. Namely, the detailed trace mineral characterizations of the samples on which K_d s are measured do not exist. Thus, through analysis of large numbers of K_d measurements, variation and uncertainty are integrated through the use of probability distribution functions.

Although the experiments used to obtain K_d parameters are fast, easy, and inexpensive, there are important limitations associated with the use of such parameters in transport models. Whereas transport processes are dynamic, the measurements with which the parameters are obtained are static. Experimentally determined K_d values that are very small or very large contain the greatest uncertainties, even for the static conditions in which they are measured, due to the subtraction of two large numbers necessary for the calculation. K_d values do not seek to describe the behavior of any particular species. Rather, they simply represent the total mass of the element of interest. However, if more detailed mechanistic understanding is desired, it is possible to derive the speciation given the environmental conditions describing the experiment. Finally, although the K_d parameter represents an integrated response of a sample brought in contact with the aqueous solute of interest, the sample size is still far smaller than the volumes

in the CAU-scale model that will be parameterized with flow and transport parameters.

9.2.2 Sources of K_d Data

Sources of K_d data including values derived from upscaled mechanistic sorption models and measured values are described in this section.

9.2.2.1 K_d s Derived From Mechanistic Modeling Studies

Section 9.2.1.1 describes the scaled mechanistic modeling method of Zavarin et al. (2002) for estimating K_d s theoretically. In addition to six regional volcanic HSUs, Zavarin et al. (2002) also estimate K_d s for alluvial material in Frenchman Flat. Those analyses will be relevant if radionuclide migration in alluvial material within the Pahute Mesa CAU transport model becomes significant. We are unaware at this time of other studies that seek to derive K_d values for representative NTS aquifer materials using mechanistic modeling studies. Davis et al. (1998) and Davis (2001) provide detailed analyses comparing measured and mechanistically computed K_d s for Uranium, but not for material representative of NTS material.

9.2.2.2 Measured K_d Values

The YMP has studied sorption of radionuclides on minerals and volcanic rocks for over two decades. These studies, discussed in the next section, provide the majority of data and analyses relevant to radionuclide sorption on matrix material in Pahute Mesa aquifers. The data are discussed by Triay et al. (1997) and Conca (2000) and stored in the YMP Technical Data Management System (TDMS). The NTS-UGTA Project has conducted a limited number of studies at DRI, primarily involving sorption of lead, strontium, and cesium on a select number of rocks from Pahute Mesa boreholes (Papelis and Um, 2002; Um and Papelis, 2001a and b). The results of these studies are compared with the data distributions developed from YMP databases.

Although most of the Pahute Mesa aquifers are comprised of volcanic tuff, there are some carbonate aquifer and aquitards within the CAU system as well as some granite. Sorption data for radionuclides on carbonate material elsewhere, primarily in support of the Waste Isolation Pilot Plant (WIPP) Project, have been reported and summarized by Dosch and Lynch (1980), Stout and Carroll (1992), and Perkins et al. (1998). These studies provide primarily qualitative insight into the affinity of radionuclides for carbonate material; they do not represent specific NTS material or water chemistry. Pohll et al. (1998) report sorption studies on granite in support of the Project Shoal investigation.

9.2.3 Data Documentation Evaluation

The documentation of the K_d is generally good and is dependent on the four primary sources of data:

- The mechanistic scaling study of Zavarin et al. (2002) is a modeling study dependent upon multiple other data sources. The modeling is conducted in accordance with LLNL procedures. The information used as model input to predict the K_d values are available in LLNL reports.
- YMP-published K_d distributions are based upon expert elicitation (Triay et al., 1997; Conca, 2000). Although the experts are intimately familiar with the published K_d data, documentation describing the process for developing the distributions is not available. (Note: YMP scientists are currently documenting and revising the K_d distributions.)
- A database of K_d measurements is maintained in the YMP TDMS. These data were collected under a stringent QA environment and are fully traceable with laboratory notebooks and data-tracking numbers. These data are utilized in the present study to create new estimates of K_d distributions for Pu, Np, U, Sr, and Cs.
- Sorption studies for Pb, Cs, and Sr were conducted by Papelis and Um (2002) using several samples from Pahute Mesa. These studies are documented in a UGTA report, and the experiments were conducted and documented under DRI QA protocol. Other DRI studies involving Pb and Sr sorption on zeolitized tuff are reported in manuscripts submitted to journals for publication and in university M.S. theses.
- The carbonate K_d data referenced in [Section 9.2.2.2](#) provides a qualitative assessment of sorption onto carbonate material, but do not represent NTS rock material or water chemistry.

9.3 Data Evaluation

Descriptions of the K_d datasets are provided, followed by the process and results of manipulations used to generate matrix sorption parameters from K_d measurements in the YMP TDMS.

Sorption data described in this section are classified by alteration, stratigraphy, and hydrogeologic units. [Table 9-1](#) provides a description of the stratigraphy, alteration, hydrogeologic units, lithology, and hydrostratigraphic units used in this chapter.

9.3.1 Dataset Descriptions

A description of the available K_d data is provided in this section. The K_d data have been organized into four datasets as follows:

- K_d derived from scaled mechanistic models
- Measured K_d values for Pahute Mesa samples
- Measured K_d values for alluvium
- Measured K_d distributions derived from YMP databases

9.3.1.1 K_d Derived From Scaled Mechanistic Models

Using component additivity, Zavarin et al. (2002) compute effective K_d for a radionuclide for given bulk material as follows:

$$K_d = \sum_{i=1}^n K_{d,i} \phi_{m,i} \quad (9-2)$$

where:

- $K_{d,i}$ = is the specific K_d for individual mineral i
 $\phi_{\mu,i}$ = mass fraction of mineral i with respect to the total bulk medium

Using mineralogic characterization by Warren et al. (2000b) on multiple samples from multiple NTS wells, Zavarin et al. (2002) predict bulk K_d values for each sample. The data listed by Zavarin et al. (2002) are sorted by stratigraphy and statistical distributions of K_d are fit to each stratigraphic classification. These are listed in [Table 9-2](#) and are used later to assign K_d distributions to PM-OV CAU HSUs.

[Table 9-3](#) lists the matrix K_d values reported in Zavarin et al. (2002) for HSUs as labeled in the regional NTS model (DOE/NV, 1997). Thus, these represent data from multiple PM-OV HSUs in some cases. The minimum and maximum values represent only variations due to differences in mineral composition. Water chemistry, surface site density on individual minerals, and mineral densities are assumed constant.

Zavarin et al. (2002) also estimate K_d values for several radionuclides for Frenchman Flat alluvium. Those values are provided in [Table 9-4](#). The minimum and maximum values are based on one standard deviation or the lower-limit sorption constant for all minerals in the representative sample description.

9.3.1.2 Measured K_d Values for Pahute Mesa Samples

Papelis and Um (2002) conducted sorption experiments for Pb, Cs, and Sr on tuff and devitrified lava samples from Pahute Mesa. First, uptake experiments were conducted at various pH and solute concentration conditions. Then, K_d s were determined at pH 8.3 from batch sorption and desorption experiments and from analysis of diffusion studies. The batch sorption experiments were conducted on crushed rock and the diffusion/sorption experiments were conducted on intact core. Both Cs and Pb showed very strong affinity for sorption with K_d s greater than 100 milliliters per gram (mL/g) in nearly all batch sorption experiments. Strontium, however, did not show much affinity for sorption in any experiments. One explanation provided by Papelis and Um (2002) is that naturally occurring Sr was already heavily sorbed onto the material used in the sorption experiments.

Cesium

Cs sorption shows minor pH dependence at high solute concentrations, decreasing as the solute concentration decreases. As the solute concentration decreases, there is less competition to occupy sorption sites, allowing access to ion exchange sites on smectites and pH independent behavior. Such behavior is more likely for trace solute concentration in the CAU domain away from sources. [Table 9-5](#) summarizes the Cs sorption experiments. Desorption K_d s are higher than sorption K_d s, indicating some irreversible behavior in the Cs sorption process. The range in values for sorption K_d s is relatively small, indicating that differences in smectite content have only small impacts in the measured sorption K_d s. The largest desorption K_d is associated with a sample with somewhat lower smectite content, indicating the difficulty in correlating material reactivity with mineral content, an important issue when evaluating the applicability of mechanistic scaling models. The K_d s derived from the diffusion study highlight the reduced reactive surface area in intact cores compared to crushed tuff. The solutes come into contact with fewer sorption sites, leading to lower measured K_d s.

Strontium

Negligible Sr sorption was attributed to high initial concentrations of Sr in the solid material. However, the experiments were not conducted in a manner in which it could be determined whether the ambient Sr was exchanged with the new Sr added to the system. Using isotopic tagging of Sr could facilitate making such a determination in future studies.

Lead

Of the divalent cations, Pb showed greater sorption affinity than Cs or Sr. As pH increases, negative surface charge increases, leading to increased sorption. Increasing the aqueous Pb concentration did not reduce the sorption affinity as it did for Cs. [Table 9-6](#) summarizes the Pb sorption experiments. Desorption K_d s are only slightly higher than sorption K_d s, indicating less irreversible behavior than for Cs. However, the K_d s are so large, little mobility is expected for Pb in contact with these solids. The K_d s derived from the diffusion study are large, but smaller than for the crushed-tuff batch experiments, highlighting the reduced reactive surface area in intact cores compared to crushed tuff. The solutes come into contact with fewer sorption sites, leading to lower measured K_d s.

Additional DRI Sorption Studies

Researchers at DRI have conducted several other relevant studies involving primarily lead and strontium sorption on various rock types. Bernot (1999) investigated various mechanisms for Pb and Sr sorption on zeolitized tuff from Rainier Mesa. Although her research primarily focuses on specific mechanisms affecting the sorption rates of these two metals, she found that Pb has a much greater affinity for zeolitized tuff than Sr, but that both are much greater than 100 mL/g. Um and Papelis (2001a and b) have also investigated sorption and desorption behavior of Pb and Sr on NTS zeolitized tuffs using batch and column experiments. Again, Pb sorption is found to be stronger than Sr, and showed a greater pH dependence. For typical NTS groundwater compositions, both Sr and Pb are expected to sorb nearly irreversibly on zeolitized tuff, consistent with the large K_d s measured by YMP (Table 9-7). Sloop (1998) also investigated the equilibrium sorption of Pb and Sr on zeolitized tuff from Rainier Mesa. He investigated ionic uptake of these elements for varying pH and ionic strength conditions. As with the other DRI studies, Pb(II) is found to have a greater affinity for zeolitized tuff from Rainier Mesa than Sr(II) for all geochemical conditions considered, and that both have a very large affinity for zeolitized tuff. Linear sorption K_d s consistent with standard solute transport models are provided by Sloop (1998), with the caveat that the non-linear Freundlich isotherm is actually a more accurate descriptor of solute uptake for this system. Sloop (1998) reports sorption K_d s for Pb with a background electrolyte concentration of 1.0 M sodium nitrate (NaNO_3), and for Sr with background electrolyte concentrations of 0.1 and 0.01 M NaNO_3 . Table 9-8 summarizes the Pb and Sr K_d s for zeolitic tuff reported by Sloop (1998, Tables 9, 12, and 14).

9.3.1.3 Measured K_d Values for Alluvium

Zavarin et al. (2002) summarize batch sorption experiments Wolfsberg (1978) performed using Frenchman Flat alluvium. K_d s for Sr, Cs, and Eu were reported to be 217 \pm 45; 7,000 \pm 1,600; and >20,000 milliliters per gram (mL/g) for those elements, respectively. An average alluvial K_d for uranium of 29 mL/g was also reported. Uranium and neptunium sorption to alluvium, as measured by the Yucca Mountain Project, are also discussed in Section 9.3.2.

Papelis and Um (2002) measured K_d s for Sr, Cs, and Pb on Frenchman Flat alluvium samples. For Sr, they measured the K_d range of 80 to 225,000 mL/g; for Cs, they measured K_d s between 700 and 3,000 mL/g; and for Pb, they measured K_d s between 5,500 and 570,000 mL/g.

9.3.1.4 Measured K_d Distributions Derived From YMP Databases

The largest set of K_d values applicable to this study for radionuclides on volcanic rock is found in the Yucca Mountain sorption database, summarized primarily by Thomas (1987), Wilson et al. (1994), Triay et al. (1997), and Conca (2000). These reports summarize more than two decades of studies examining radionuclide sorption to a variety of materials. All of these reports provide reviews of the

mechanistic processes governing sorption of radionuclides and describes the experiments that were conducted by YMP. As more data became available, one finds an evolving understanding and interpretation of sorption of radionuclides on minerals and volcanic rocks. Thus, Conca (2000) provides the most current data and interpretations. However, Triay et al. (1997) provide greater detail for some experiments and background material not found in Conca (2000). Thus, the two reports provide complimentary sets of information and analyses.

Whereas the Yucca Mountain reports provide detailed descriptions of experiments and mechanisms associated with the radionuclide sorption studies, the distributions presented do not capture the detail that is available in the datasets. The K_d distributions presented by Conca (2000, Table 2b) are meant to provide input to the Yucca Mountain performance assessment, a process that does not explicitly seek to differentiate between stratigraphic units and water chemistry. Therefore, a significant difference between Conca (2000) and the present study is that the data have been reevaluated in this study and new distributions relevant to stratigraphic classification on Pahute Mesa have been developed. Comparisons between the present data analyses and the distributions developed by Conca (2000) are presented in the next sections.

The validity of YMP data for Western Pahute Mesa is described in [Appendix B](#) of this report. Summarizing the YMP database, [Table 9-10](#) lists the radionuclides and rock types on which K_d experiments were conducted and distributions were assessed. Of those, the current YMP TDMS contains QA databases for plutonium, neptunium, selenium, uranium, cesium, strontium, and barium.

9.3.1.4.1 Radionuclides Considered

Sorption coefficient distributions on devitrified, vitric, zeolitic, iron oxide, and sometimes alluvium have been developed by the Yucca Mountain Project for the following radionuclides: americium, actinium, thorium, samarium, zirconium, niobium, plutonium, uranium, neptunium, radium, cesium, strontium, nickel, lead, tin, protactinium, selenium, carbon, chlorine, technetium, and iodine (Triay et al., 1997; Conca, 2000). The sorption coefficient distributions provided in these documents are based on expert elicitation. Of this list, the current YMP TDMS contains QA databases for plutonium, neptunium, selenium, uranium, cesium, strontium, and barium. Sorption coefficients for the remaining radionuclides in the list above are derived from Thomas (1987), Meijer (1992), and Conca (2000).

In this document, we present the sorption coefficient distributions developed by YMP and, using data available, rederive sorption coefficient distributions to more precisely represent the most current datasets described in [Appendix H](#). A table providing a matrix of QA sorption available in the YMP TDMS for analysis is described in [Appendix K](#). Included in this table, but not considered in the present study, are the sorption data for various pure minerals. Whereas the objective of the present study is to provide sorption parameters for the specific rock types in the Pahute Mesa CAU domain, the individual mineral data may be of use for

future modeling studies seeking to develop scaled parameters starting with detailed mechanistic considerations (see [Section 9.2.1.1](#)).

9.3.1.4.2 Rock Types

The HGUs of the Pahute Mesa CAU modeling domain are primarily defined based upon physical hydrologic significance (e.g., hydraulic conductivity). Sorption studies, on the other hand, classify rocks used in the experiments by their mineralogy. Specifically, a substantial portion of the available sorption data using field samples are for vitric tuff, devitrified tuff, zeolitized tuff, and alluvium. This grouping is based on the fact that sorption of radionuclides is the result of chemical reactions between radionuclides in groundwater and the minerals in the immobile material. Thomas (1987) provided a classification of the different mineralogies for Pahute Mesa volcanic rocks. An additional classification appropriate for this study is the alluvium. Descriptions of the various classes are as follows:

Vitric Tuff

High percentage of original glass in samples (not devitrified or altered to zeolites)

> 40% glass; < 10% clay; < 10% zeolite

Devitrified Tuff

Composed primarily of quartz and feldspar

< 10% clay; < 10% zeolite

Zeolitized Tuff

Dominated by alteration assemblages of zeolites

> 20% zeolite; < 10% clay; < 10% glass

Alluvium

Alluvium represents the complex material associated with windblown and water-transported material weathered from former primary rock structures. The specific mineralogy of alluvium varies and classifications are not provided here.

The mineralogic composition of the various HGUs is provided in the lithologic descriptions. There generally is not a one-to-one correspondence between mineralogic classification and lithologic compositions for any specific HGU. For example, the WTA HGU is described with a vitric to devitrified lithology ([Table 2-1](#)). Thus, to assign a single sorption coefficient to a WTA HGU, or to develop a spatial distribution of sorption coefficients within a WTA HGU, will require development of a weighted sampling scheme that draws from distributions for vitric and devitrified tuff. Similar considerations apply to most other HGUs, which are comprised of multiple mineralogic lithologies. Exceptions include VTA, LFA, and specific TCUs known to be entirely altered.

9.3.1.4.3 Water Types Used in YMP Sorption Experiments

Nearly all of the YMP K_d experiments involving rock samples taken from the field were conducted with water from, or similar in composition to that from, either Well J-13 or Well UE25p#1 (p#1). Well J-13 samples the Topopah Spring aquifer, a hydrologic unit also present in parts of Pahute Mesa. Well p#1 samples the carbonate aquifer below the volcanic tuffs at Yucca Mountain. The groundwater compositions of these two wells are listed in [Table 9-9](#). With the exception of pH, these two different groundwater types reasonably bound the compositions expected in Pahute Mesa groundwater (two examples are also given in [Table 9-9](#)), with Well J-13 generally providing a closer match. The pH of both J-13 and p#1 groundwater is lower than those found in many Pahute Mesa, and fortunately Yucca Mountain, groundwater samples. Therefore, YMP sorption experiments using water with J-13 and p#1 compositions were conducted with atmospheric conditions (generally labeled as “air” or “bench” conditions) to obtain pH values between 8.5 and 9, and with carbon dioxide (CO₂) overpressure inside of glove boxes to obtain pH values of about 7.

Because only a fraction of the citations in the database list the pH but all citations list the experimental atmosphere, the atmosphere is used to delimit high (~8 to 9) and low (~7) pH experiments in the proceeding analyses.

9.3.1.4.4 YMP Laboratory Sorption Data Obtained Prior to 1993

In 1993, the Yucca Mountain Project conducted an expert elicitation regarding K_d values and distributions for various radionuclides and rock types (Wilson et al., 1994). The distributions developed in the elicitation are due substantially to a summary report by Thomas (1987). Thomas (1987) summarizes sorption experiment results performed by the Yucca Mountain Project prior to the QA procedures that were required for the analysis and model report by Conca (2000). The sections that follow describe K_d distributions developed in the present study; references are made for comparison with the distributions developed by Thomas (1987). However, the distributions developed in Wilson et al. (1994) are improved upon in Conca (2000) by the same researchers. Thus, only the distributions of Conca (2000) are listed in the present report.

9.3.1.4.5 YMP Laboratory Sorption Data Obtained After 1993

With new data collected after 1993, Triay et al. (1997) developed improved K_d distributions for multiple radionuclides on devitrified, vitric, zeolitic, and iron oxide rock types (iron oxides are important to YMP for assessing sorption in the vicinity of waste packages). These distributions were modified somewhat again by Conca (2000), whose distributions are listed in [Table 9-10](#). Ideally, the sorption coefficient distributions developed by YMP would be directly transferable to UGTA due to the similarity in rock types within the two study areas. However, examination of the radionuclide K_d distributions presented by Conca (2000, Table 2b), the text of that report (Section 6.4.4) and the YMP QA

sorption database (YMP [1996] DTN: LAIT831341AQ96.001) indicate some discrepancies that require further consideration in the present study. For example, the YMP distribution for plutonium sorption to vitric tuff uses a K_d range between 50 and 300 mL/g. However, the data range between 20 and 2,000 mL/g.

The discrepancies may be due to the fact that Triay et al. (1997) and Conca (2000) developed distributions in support of performance assessment modeling at Yucca Mountain, where the entire volcanic rock section was parameterized with a single K_d in any realization of the Monte Carlo analyses (TRW, 2000). For Western Pahute Mesa, sorption parameters are needed for individual stratigraphic units, thus warranting the additional analyses presented here.

The data cited in Conca (2000) are available in the YMP TDMS, with appropriate data-tracking numbers and QA pedigrees linking to raw data and laboratory notebooks. These data provide the input to the distribution developed in the next sections.

9.3.1.5 Measured K_d Values for Carbonate Rock Material

Although K_d s for radionuclides and carbonate rock material have not been measured for NTS or YMP projects, three studies provide insight into these sorption reactions. Dosch and Lynch report dolomite K_d s for Cs, Sr, Eu, Pu, and Am, examining differences in initial solute concentration and groundwater composition. Stout and Carroll (1992) summarize several studies from the literature up to 1992, and Perkins et al. (1998) provide K_d estimates for Pu and Am determined from a flowing column experiment. [Table 9-11](#) summarizes the measured carbonate K_d s from these studies.

9.3.1.6 Measured K_d Values for Granite

Pohll et al. (1998) report K_d values for Pb and Cs on granite as part of the Project Shoal investigation. The K_d ranges are listed below in mL/g units:

- Pb: Range (1E1, 1E5)
- Cs: Range (3.1E1, 5.5E1)
- Sr: Nonsorbing

9.3.2 Parameter Generation

Manipulations to develop or improve matrix sorption parameters (and their distributions) are conducted for K_d measurements in the YMP TDMS. The values estimated with mechanistic models, including estimated ranges, are reported in a previous section. Similarly, K_d measurements conducted for the UGTA Project are reported in the previous section, but the dataset is too sparse to attempt to develop a probability distribution. The results from the UGTA Project studies, the

mechanistic modeling, and the manipulations described in this section are compared at the end of this chapter.

In the next several subsections, measured K_d data collected by YMP are evaluated. Distributions are developed using only the data in the YMP TDMS. Further, whereas previous distributions have been developed for YMP using the process of expert elicitation (Table 9-5), here we focus on fitting K_d distributions to the data in the database. Probability distribution functions and cumulative distribution functions are developed for K_d values in the YMP TDMS for Pu, Np, U, Sr, and Cs. For each of the radionuclides, sorption measurements were conducted on multiple pure-phase minerals as well as on tuffs classified as vitric, devitrified, and zeolitic. Whereas the pure-phase mineral studies could serve to inform future mechanistic modeling studies, in this analysis, only the tuffs are considered because they can be correlated with Pahute Mesa HSUs. On the different tuff samples, experiments were conducted with J-13 water and often with the higher ionic strength p#1 water (see Table 9-4). Additionally, pH was often controlled by either conducting experiments with an air environment to achieve pH between 8 and 9, or with CO_2 over pressure to force the pH closer to 7. Finally, most experiments were conducted at 20 to 25°C, but many were conducted at temperatures up to 90°C. These different environmental conditions may or may not affect distributions developed from the data. Therefore, in the analyses that follow, the roles of the different environmental conditions are highlighted and specific distributions are developed, as appropriate.

9.4 Development of K_d Distributions: YMP Database

As part of the present evaluation, K_d distribution functions were derived from the YMP data for several nuclides: Pu, Np, Sr, Cs, and U. The results are discussed in this section.

9.4.1 Plutonium

The plutonium sorption data discussed and referenced by Conca (2000) are reevaluated for this report in order to develop distribution functions from which K_d values can be drawn for different rock types and groundwater compositions.

9.4.1.1 Review of YMP Studies

Triay et al. (1997) provide a detailed discussion of the physiochemical processes affecting plutonium speciation and sorption. The exact nature of plutonium sorption is not well understood. Most importantly, sorption and desorption of plutonium on the volcanic rocks considered is clearly not an equilibrium process. A possible explanation provided by Conca (2000) is that Pu(V) must undergo reduction prior to sorbing as Pu(IV). A result of this conclusion is that laboratory experiments conducted under oxidizing conditions should lead to smaller K_d s than exist in less oxidizing field conditions. Kersting et al. (2002b) have recently

addressed the question of Pu(V) reduction to Pu(IV) during sorption (see [Section 11.3.2.2](#)). Further, Conca (2000) concludes that K_d s derived from laboratory batch experiments would likely lead to conservative transport predictions (due to the short time scales associated with the laboratory Pu K_d measurements – longer contact with immobile minerals leads to increased sorption).

Thomas (1987) found that sorption of plutonium onto zeolitic rock samples had lower K_d values than vitric and devitrified tuffs due possibly to the lack of reduction sites. In that study, the largest K_d values were measured for samples with calcite and clays. Thomas (1987) also observed the strong dependence of K_d values on water composition, but not on pH. She observed that the high bicarbonate concentration in p#1 water might actually lead to coprecipitation of plutonium rather than surface complexation or ion exchange.

For plutonium sorption on various rock and mineral types, Conca (2000) discusses results for both J-13 and p#1 water. Modifying the conclusions of Thomas (1987) and Wilson et al. (1994), Conca's analysis indicates that the most important factors controlling plutonium sorption in oxidizing water are the abundance of montmorillonite clays, zeolite minerals, and possibly calcite. Thus, zeolitic tuffs should sorb plutonium strongest, followed closely by vitric tuffs. Devitrified tuffs sorb plutonium less strongly for both types of water, but the values are non-negligible. The data discussion provided by Conca (2000, Section 6.4.4) is not consistent with the distribution of K_d values provided in that report (e.g., compare Table 2b and Table 4 in that report). Therefore, the data in the YMP TDMS have been reevaluated for the present study. The distributions from Conca (2000, Table 2b) are plotted in [Figure 9-1](#) for comparison with the distributions developed in the remainder of this section.

9.4.1.2 Plutonium K_d Distributions Fit to YMP Data

The Pu sorption data in the YMP TDMS (YMP [1996] DTN: LAIT831341AQ96.001) are initially used to develop K_d distributions for comparison with the distributions reported by Conca (2000, shown in [Table 9-10](#) here). The distributions, plotted in [Figure 9-2](#), provide an interesting comparison with those in [Figure 9-1](#). For all rock types, the ranges of Pu K_d parameters are substantially larger in the present study. Therefore, the subsequent analyses focus on interpretation of the data in the YMP TDMS, rather than upon previously developed distributions.

Thomas (1987) and Conca (2000) note that water composition has a significant impact on plutonium K_d distributions. That conclusion is supported in the following analyses. Therefore, all samples are divided between those conducted with J-13 water and p#1 water (see [Section 9.3.1.4.3](#)). Additionally, the atmospheric conditions affecting pH in the experiments are also included in this analysis. Conca (2000) points out that the pH of J-13 and p#1 groundwater in contact with atmospheric carbon dioxide levels is generally in the range of 8.2 to 8.5. Therefore, in some experiments the pH was adjusted down to near 7.0 by

imposing an overpressure of CO₂ to address lower pH values observed among some saturated zone waters in the Yucca Mountain flow system.

Distributions are developed for Pu on each different rock type separately for J-13 and p#1 water. Initially, separate distributions are not developed for different pH values (governed by imposed experimental atmospheric conditions). However, when the analysis indicates significant pH dependence, separate distributions are provided for air or CO₂ overpressure measurements.

All data used to fit new distributions in this analysis are found in the YMP TDMS system. The specific YMP [1996] DTN is LAIT831341AQ96.001. [Table 9-12](#) provides a summary of the Pu sorption distributions developed in this section.

Pu Sorption to Vitric Tuff – J-13 Water

Twenty-seven YMP sorption experiments were conducted with Pu, J-13 water, and vitric tuff material. Of those, three were conducted with CO₂ over pressure to reduce the pH to near 7.0. [Figure 9-3](#) shows the distributions for Pu K_d on vitric tuff in J-13 water. A clear relationship between pH and K_d is evident for this sorption reaction. Although only three values are reported for the lower pH conditions, they are associated with the three lowest K_d values in the distribution. However, the next set of K_d values in the distribution are only a factor of two larger and they were obtained with pH values of 8.4 (YMP [1996] DTN: LAIT831341AQ96.001). Therefore, it is not clear whether a separate distribution is required that excludes the lower pH measurements. [Figure 9-4](#) shows the CDF and parameters for the distribution when the CO₂ overpressure experiments are excluded. In this case, the range and the mean increase slightly for the refinement.

Pu Sorption to Vitric Tuff – p#1 Water

Of the 56 K_d parameters measured for Pu on vitric tuff in p#1 water, only 2 were conducted with CO₂ overpressure to reduce pH ([Figure 9-5](#)). With the high carbonate content in the p#1 water, the Pu K_d distribution on vitric tuff shifts substantially toward smaller values as compared to those for J-13 water. Also, reducing the pH with CO₂ overpressure has the opposite effect on K_d when compared to J-13 water experiments. However, it is not necessary to create a K_d distribution excluding the few samples measured with CO₂ overpressure because the air environment K_ds extend to values nearly as large as them.

Pu Sorption to Devitrified Tuff – J-13 Water

In measuring Pu K_d on devitrified tuff in J-13 water, there is a tendency toward lower K_ds for the measurements conducted with CO₂ overpressure, as shown in [Figure 9-6](#). However, there is an overlap between the air and CO₂ experiments and, more importantly, the values are strongly correlated to the duration of the experiments, so separate distributions are not established. [Figure 9-7](#) shows the relationship between the experiment duration and K_d for air atmosphere experiments. This disequilibrium behavior for Pu sorption highlights the need for special care in parameter assignment and interpretation of results. Because more data are collected for small duration experiments, the distribution is skewed to lower K_ds, which will lead to conservative Pu mobility estimates. Finally, the

single high K_d value for CO₂ conditions should be discarded as its duplicate companion experiment yielded a much smaller K_d value.

Pu Sorption to Devitrified Tuff – p#1 Water

The range of K_d s for Pu on devitrified tuff in p#1 water, shown in [Figure 9-8](#), is close to the range cited by Conca (2000). However, the few lower pH experiments clearly yielded the high values of the distribution. Therefore, a new distribution is created for the air-only experiments. There are not enough data to create a distribution for pH 7 conditions, but a value of about 300 mL/g is indicated by the two experiments.

Pu Sorption to Zeolitic Tuff – J-13 Water

The relative affinities for Pu on specific minerals for plutonium are, in decreasing order, hematite > montmorillonite > clinoptilolite > calcite > gibbsite > albite > quartz (Conca, 2000). Although this generalization does not take into account water chemistry, it is expected that rocks containing large abundances of zeolite should also show relatively strong affinities for Pu. Sorption of Pu to zeolitic tuff in J-13 is strong, as shown in [Figure 9-9](#). However, the large values in the data range are not as large as those for Pu sorption to vitric tuff, indicating that such sorption reactions may be dominated by the presence or absence of a few key minerals such as clay, which may determine the overall sorption capacity of a particular rock. Likewise, the mean is substantially smaller. There does not appear to be a strong correlation between pH and K_d values for Pu sorption to zeolitic tuffs.

Pu Sorption to Zeolitic Tuff – p#1 Water

Two of the three sorption experiments for Pu and zeolitic tuff in p#1 water conducted with CO₂ overpressure produced K_d values near the upper end of the range ([Figure 9-10](#)). With an air environment, more than 25 percent of the K_d values fall below 20 mL/g in the distribution with a mean of 300.

Pu Sorption To Alluvium

Due to the lack of Pu sorption data on alluvial material and the detail with which Pu migration in Frenchman Flat has been studied, it is recommended that the values of Zavarin et al. (2002) be considered, if needed, for the Pahute Mesa CAU transport model.

9.4.2 Neptunium

Neptunium has been one the most studied radionuclides by the Yucca Mountain Project. It is important due to its abundance in nuclear waste packages, its long half-life, and its relative low affinity for sorption to immobile minerals. Yet, the exact mechanisms controlling Np sorption, particularly to zeolitic tuff, are still only partially understood. Triay et al. (1997) and Conca (2000) describe in detail the history and results of Np sorption studies for YMP. The sorption behavior of Np on apparently similar rock types varies between samples, indicating that minor primary or secondary phases such as calcite, hematite, or trace quantities of

ferrous iron may govern the exact sorption process. Thus, mechanistic predictions of Np adsorption would require detailed knowledge of the surface areas of these trace minerals in the various hydrologic units.

An unexpected result of the YMP sorption studies involving Np is the relatively low K_d associated with zeolitic tuff. Whereas a strong cation exchange reaction was expected, the low values indicate that perhaps the neptunyl cation is too large relative to the zeolite cage sizes to come into contact with the exchange sites.

The complexities of Np sorption observations still present multiple challenges to decipher the precise governing mechanisms. However, the large number of K_d data collected by YMP provides input to the present process of developing distributions of the parameter expected to be used in CAU-scale transport simulations. Thus, it is expected that variability in K_d values represents variability in controlling factors such as trace mineral quantities.

Using the distribution parameters developed by YMP (Table 9-10), Figure 9-11 plots the K_d distributions for Np on four different rock types. The remainder of this section re-examines the QA data from YMP and provides new K_d distributions.

9.4.2.1 Neptunium K_d Distributions Fit to YMP Data

In the present study, Np sorption data from the YMP TDMS are reevaluated in the development of K_d distribution functions for Np on various rock types. Figure 9-12 plots the Np K_d distributions for different rock types using all data for different water compositions. Clearly, the distributions supported by this dataset are somewhat different than those presented by Conca (2000) and shown in Figure 9-11. Therefore, this section reexamines that YMP TDMS dataset for Np sorption and produces new distributions.

Np Sorption on Vitric Tuff

Changes in pH values between 7 and 9 do not have a marked impact on the minimal sorption of Np to vitric tuff in J-13 water. Also, the groundwater composition has only a minor impact on the K_d distribution. Both Figure 9-13 and Figure 9-14 are quite similar to the overall distribution for Np on vitric tuff shown in Figure 9-12, indicating no specific controls associated with pH or ion concentration.

Np Sorption on Devitrified Tuff

As with vitric tuff, Np sorption to devitrified tuff is generally characterized with low K_d s. Figure 9-15 and Figure 9-16 show the Np K_d distributions on devitrified tuffs in J-13 and p#1 water. Also labeled in those figures are the contributing data points collected at high temperatures. For the J-13 water experiments, pH and temperature do not appear to exert specific influence on the K_d values. For the p#1 water experiments, the low pH results tend to be reflected by lower K_d values. However, once the high temperature and outlying high K_d values are removed

from the distribution (Figure 9-17), the distribution range drops to values below 2 and there are no clear differences associated with pH.

Np Sorption on Zeolitic Tuff

Np sorption on zeolitic tuff is considered with respect to water composition and temperature. Figure 9-18 through Figure 9-23 show that as data from higher temperature experiments are included in the distribution, the mean and range increase only slightly toward higher values. When only the highest temperature data are considered (Figure 9-21), then the distribution shifts clearly towards larger values, as expected. Similarly, including high temperature experiment results in the K_d distribution of Np on zeolitic tuff in p#1 water only shifts the distribution marginally toward larger values. Otherwise, the K_d s in p#1 water are slightly smaller than those in J-13, but both distributions are reasonably well captured with the overall distribution shown in Figure 9-12.

Np Sorption on Alluvium

The Yucca Mountain Project has collected some sorption data for Np on alluvial material (YMP [2001] DTN: LA0109MD831341.001). Figure 9-24 shows the PDF fit using the YMP data and compares it with the distribution of Conca (2000) listed in Table 9-10. Although slightly different, the new and previous distributions are quite similar, capturing the same range of uncertainty in the data. Thus, either are suitable for this parameter in the absence of new studies using Pahute Mesa CAU alluvial material. These can also be compared with values developed by Zavarin et al. (2002) in Table 9-4, or with the results of ongoing mechanistic studies at LLNL.

9.4.3 Strontium and Cesium

These two elements are grouped together, as in Triay et al. (1997) and Conca (2000), because they show fairly simple solution behavior in typical groundwaters. Just as they are not subject to oxidation-state changes in the groundwater compositions of Yucca Mountain, we expect the same simplicity in Pahute Mesa groundwaters. Their sorption is primarily controlled by ion-exchange reactions, where the selectivity of most clays and zeolites for these elements should be larger than for major cations in solutions. Sorption coefficients should be lower in higher ionic strength water (e.g., p#1) and should decrease with increasing solution concentrations. Sorption of these two elements has been extensively studied and reviewed by Daniels et al. (1983), Thomas (1987), and Meijer (1990), and summarized by Triay et al. (1997) and Conca (2000). Table 9-13 and Table 9-14 summarize the K_d distributions developed for Sr and Cs in the remainder of this section.

9.4.3.1 Strontium

The data collected by YMP since 1993 (in the TDMS) is used in the present analysis of sorption coefficients. One limitation of this dataset is that only sorption measurements with J-13 water are documented. Plotted in Figure 9-25

through [Figure 9-27](#) are the data, distributions fit in the present study, and the YMP distributions of Conca (2000) for strontium. Clearly, the ranges between the YMP distributions and the present study are quite different. One difference is that Conca (2000) considers previously collected data for Sr sorption in higher ionic strength water (e.g., from p#1). All of the data in the YMP TDMS are for experiments involving J-13 water only. Whereas this may explain the smaller range obtained in the present study for devitrified tuff, it does not explain the differences for vitric and zeolitic tuff. Additionally, all of the data used in the present study were obtained for pH 8.3 to 8.6 experiments. However, temperatures were varied. [Figure 9-28](#) shows the relationship between strontium sorption and temperature for the three different rock types. Although in each case there may be a positive relationship, it would not completely explain the differences in the distributions. Other factors affecting the distributions that are not considered in the fitting of these distributions are solute concentration variations between experiments and duration of experiments.

Comparing the Sr K_d values determined from YMP data with those developed for NTS-UGTA, we note that for devitrified tuff, the results of Papelis and Um (2002) identify either no Sr sorption or they are inconclusive. The YMP data do not imply negligible sorption. For zeolitized tuff, both the YMP data and the DRI studies conducted by Bernot (1999) and Um and Papelis (2001a and b) ([Table 9-7](#)) indicate very strong affinity between Sr and the matrix minerals.

Sr sorption to alluvium has not been measured by YMP, but NTS measurements and mechanistic modeling studies are discussed in previous sections.

9.4.3.2 Cesium

For vitric tuff, the previous YMP studies suggest that Cs has a greater range in K_d than Sr, extending both to smaller and larger values. For devitrified tuff, the YMP Cs distribution extends to larger values, and for zeolitic tuff the low values are smaller than those for Sr. [Figure 9-29](#) through [Figure 9-31](#) compare the distributions fit to the Cs sorption data in the YMP TDMS and the previous YMP distributions reported by Conca (2000). As with the Sr data, only sorption experiments conducted in J-13 water are considered here ([Table 9-15](#)); whereas, Conca (2000) likely considered higher ionic strength and solute concentration effects as well, but only in a qualitative assessment. The data used to develop the distributions here were conducted with essentially the same initial concentrations. If field concentrations are greater than those used in the experiments supporting these distributions, then Cs K_d s will likely be lower, favoring the lower end of the distribution, particularly for devitrified and vitric tuffs.

The Cs K_d values measured for devitrified tuff by Papelis and Um (2002) in [Table 9-7](#) are very similar to those fit here for YMP data. To date, we are unaware of Cs sorption experiments conducted for zeolitic tuff from locations other than Yucca Mountain.

Cs sorption to alluvium has not been measured by YMP, but NTS measurements and mechanistic modeling studies are discussed in previous sections.

9.4.4 Uranium

A summary of the evaluation of YMP uranium sorption data (Triay et al., 1997; and Conca, 2000) is presented, followed by results of the current analyses of the same dataset.

9.4.4.1 Summary of Former YMP Evaluation

Triay et al. (1997) summarize uranium sorption analyses indicating that it will likely be affected by pH, carbonate content, and concentrations of calcium and manganese. Carbonate concentration and pH may be, but are not necessarily, dependent upon each other. Complexation with carbonate species in solution will likely reduce the sorption coefficients for uranium. Thus, if pH decreases with carbonate concentration, one would expect reduced sorption coefficients. However, in the presence of zeolite minerals, decreasing pH would lead to an increase in uranyl ion concentrations and an increase in sorption coefficients. Data supporting this conclusion are cited in Conca (2000) in which sorption to zeolites in pH 9 water is near zero, but increases to approximately 25 mL/g at pH of 6 in J-13 water. In p#1 water, K_d s are generally smaller than in J-13 water due to increased complexes with carbonate.

9.4.4.2 Analyses of YMP TDMS Database For Uranium Sorption

Table 9-16 summarizes the distribution fit in the present study for uranium sorption using only the data in the YMP TDMS (YMP [1996] DTN: LAIT831341AQ96.001). The distributions are separated by water types used in the experiments (J-13 and p#1). For all rock types, uranium sorption is less when p#1 water is used, likely due to increased carbonate complexation. Figure 9-32 through Figure 9-37 show the distributions derived for this study and compare them with the YMP distributions of Conca (2000). For devitrified and vitric tuff, there is little change over the YMP distributions other than the exponential form that places even more weight on the low values. The ranges are similar and the values are generally low. By separating p#1 water results from J-13 results, the distributions highlight the reduced sorption expected under higher carbonate concentration groundwater. For zeolite sorption, the new distributions fit here show a significantly different range compared to those of Conca (2000). For J-13 experiments, a much larger range in K_d is demonstrated with the current data. For p#1 experiments, sorption coefficients substantially smaller than those in the former YMP distribution are expected. This refinement provides additional guidance for CAU simulations, where water composition of different aquifers may be known.

Refinement of the distributions by pH was not specifically conducted for uranium sorption. Both Triay et al. (1997) and Conca (2000) indicate that pH may play an important role in controlling uranyl species formation. However, for the specific groundwater types used in these experiments, we do not see a clear trend in pH dependence. Figure 9-38 through Figure 9-40 show the K_d s plotted against pH for

uranium sorption in both p#1 and J-13 water. From these figures, the water composition is shown to be a much clearer delineator for K_d distributions on any of the tuff material. The YMP uranium sorption distribution for alluvium is tabulated in [Table 9-10](#).

9.5 Data Limitations

The YMP TDMS dataset of sorption K_d s of Pu, Np, Cs, Sr, and U contains an extensive set of experimentally-determined K_d values with which probability distribution functions can be developed. However, the uncertainty in the measured K_d values and the uncertainty in field K_d values may not be governed by the same processes. Multiple rock samples are associated with the K_d distributions for Pu, Np, and U, providing some insight into spatial variability within a given HGU. The variability represented in the Cs and Sr datasets clearly indicates only variability due to experimental conditions and replication as all measurements for a specific rock type are conducted on the same core sample. Additionally, all K_d values determined from experimental sorption studies are specific to the small sample of aquifer material and the experimental conditions. Thus, applying the measured K_d values to field simulations involves the assumptions that groundwater conditions in the field are similar to those in the experiments and unchanging, or at least that the probability distribution represents variability that may exist in the field. The K_d s used in this analysis are not correlated with such physical parameters as hydraulic conductivity. Thus, although other studies (e.g., Tompson et al., 1996) have suggested correlation between physical and chemical parameters for porous media systems, correlations for physical and chemical properties of matrix material in fractured rock have not been developed. Finally, the K_d s have not been correlated with mineral composition of the samples in greater detail than the rock classification as vitric, devitrified, or zeolitic. Improving such correlation for development of spatial parameter distributions could be accomplished if samples, with which mineralogic characterization is conducted, were also used to assess radionuclide sorption affinity for both mechanistic and abstracted K_d model parameters.

9.6 Summary: K_d s by HSU

The K_d data described previously in this chapter are developed from both direct measurements and mechanistic model predictions. Comparing the two for HSUs in the PM-OV CAU domain is difficult because the measured data are classified by alteration and the mechanistic data are classified by stratigraphy. Thus, two summary tables are presented to support uncertainty sensitivity analyses in the CAU transport model. In each case, the data are correlated to HSU characteristics, as described in the HSU model report (BN, 2002). [Table 9-17](#) lists the HSUs and corresponding HGUs, alteration, lithology, and stratigraphy. [Table 9-18](#) lists the K_d distributions developed from direct measurements relevant to each HSU based upon alteration of material. Often, more than one distribution is listed due to the presence of multiple alteration phases found within a given HSU. The results shown represent distributions described previously for J-13 water in the YMP

experiments. Although distributions were also developed for experiments conducted with carbonate aquifer conditions (p#1 water), such conditions are not widely encountered in the PM-OV system, so they are not considered in the summary distributions.

Table 9-19 summarizes K_d distributions listed in Table 9-2 by HSU. These theoretically-derived K_d s provide substantial ranges for sensitivity analyses when compared with Table 9-18.

9.7 Scaling Considerations

Pahute Mesa CAU transport simulations for contaminant boundary assessment will be conducted over multi-kilometer spatial scales. Volumes in the computational model represented with a single set of transport parameters could be larger than one million cubic meters in some portions of the model domain and often on the order of twenty-five thousand cubic meters. Thus, a scaling consideration regards how well measurements conducted on less than one cubic meter of aquifer material represents the integrated sorptive behavior of a much larger volume in the CAU-scale model. One method for addressing this consideration is to use the data presented in this documentation report in a scaling component of the analysis and evaluation study. Scaling simulations could be designed to identify the effective K_d of a CAU-scale model block using multiple realizations of spatially distributed values from this study. It is likely that such an analysis will produce tighter distributions, filtering out both the small and large values in the lab-scale distributions.

9.8 Figures

All figures relating to matrix sorption are included in this section.

9.9 Tables

All tables relating to matrix sorption are included in this section.

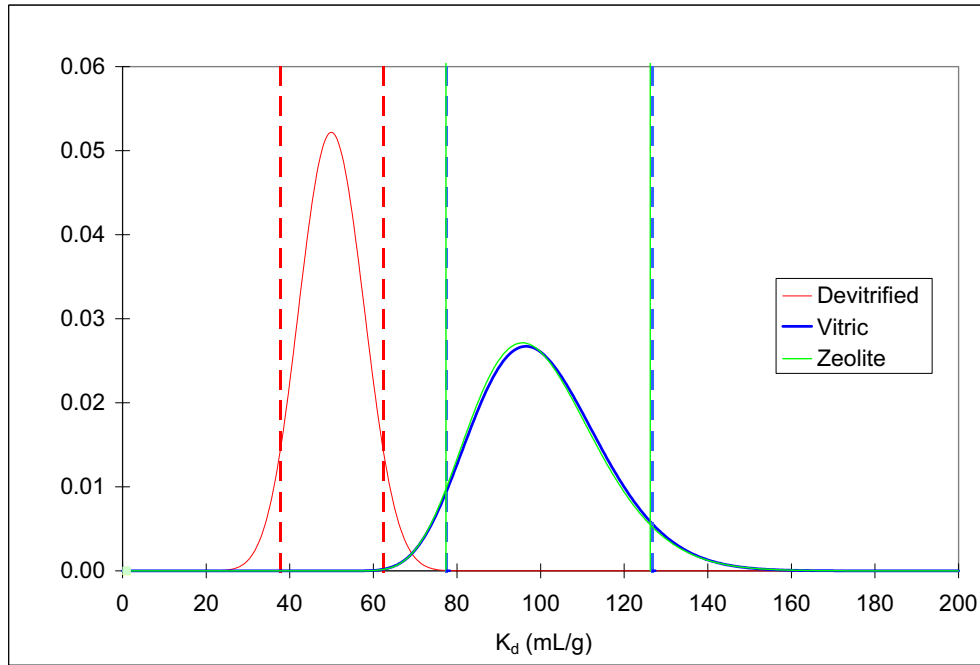


Figure 9-1
YMP PDF Distributions for Pu Sorption on Volcanic Tuff (Conca, 2000, Table 2b; Table 9-10 this Report); Vertical Lines Indicate the 95 Percent Confidence Intervals

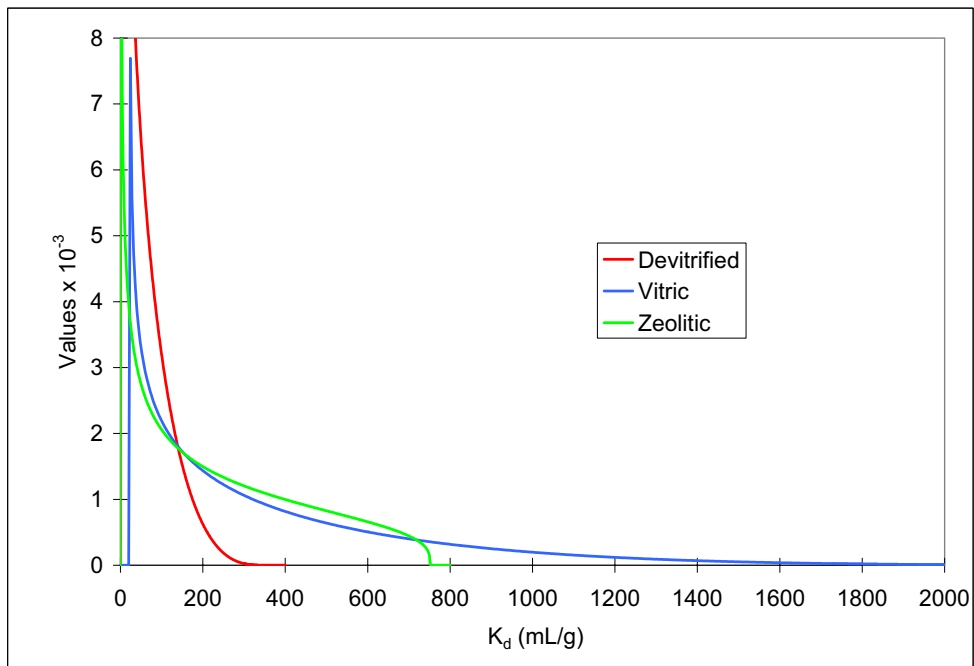


Figure 9-2
Distributions Fit to All Pu Sorption Data for Three Different Rock Types Using YMP Data in YMP (1996) DTN: LAIT831341AQ96.001

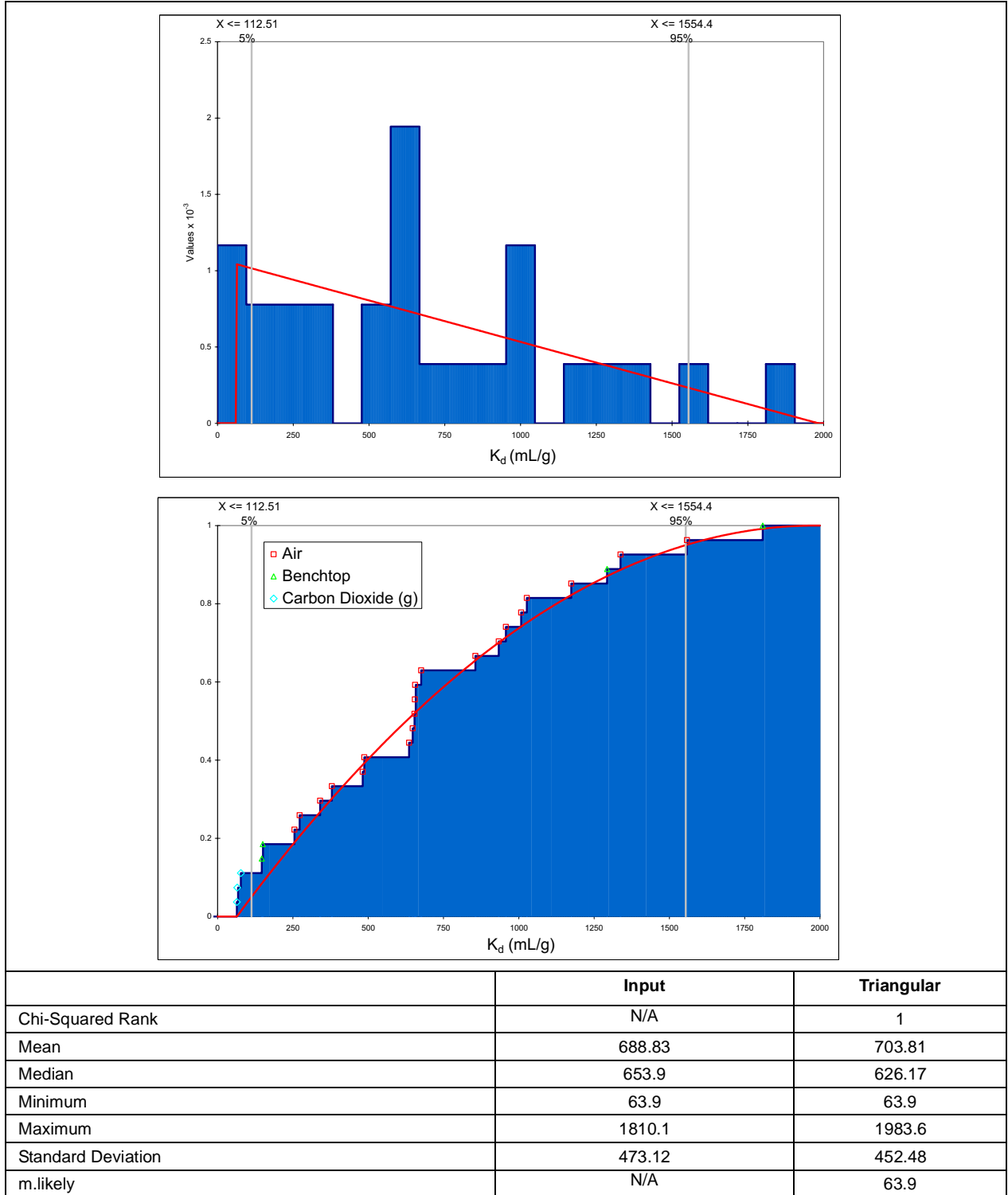


Figure 9-3

PDF and CDF of Pu K_d on Vitric Tuff in J-13 Water at 20°C: Triangular Distribution Shown with Red Line; Symbols Indicate Experimental Atmosphere for Individual Data Points in Distribution (Note: Benchtop Conditions are Atmospheric with pH Approximately 8.4)

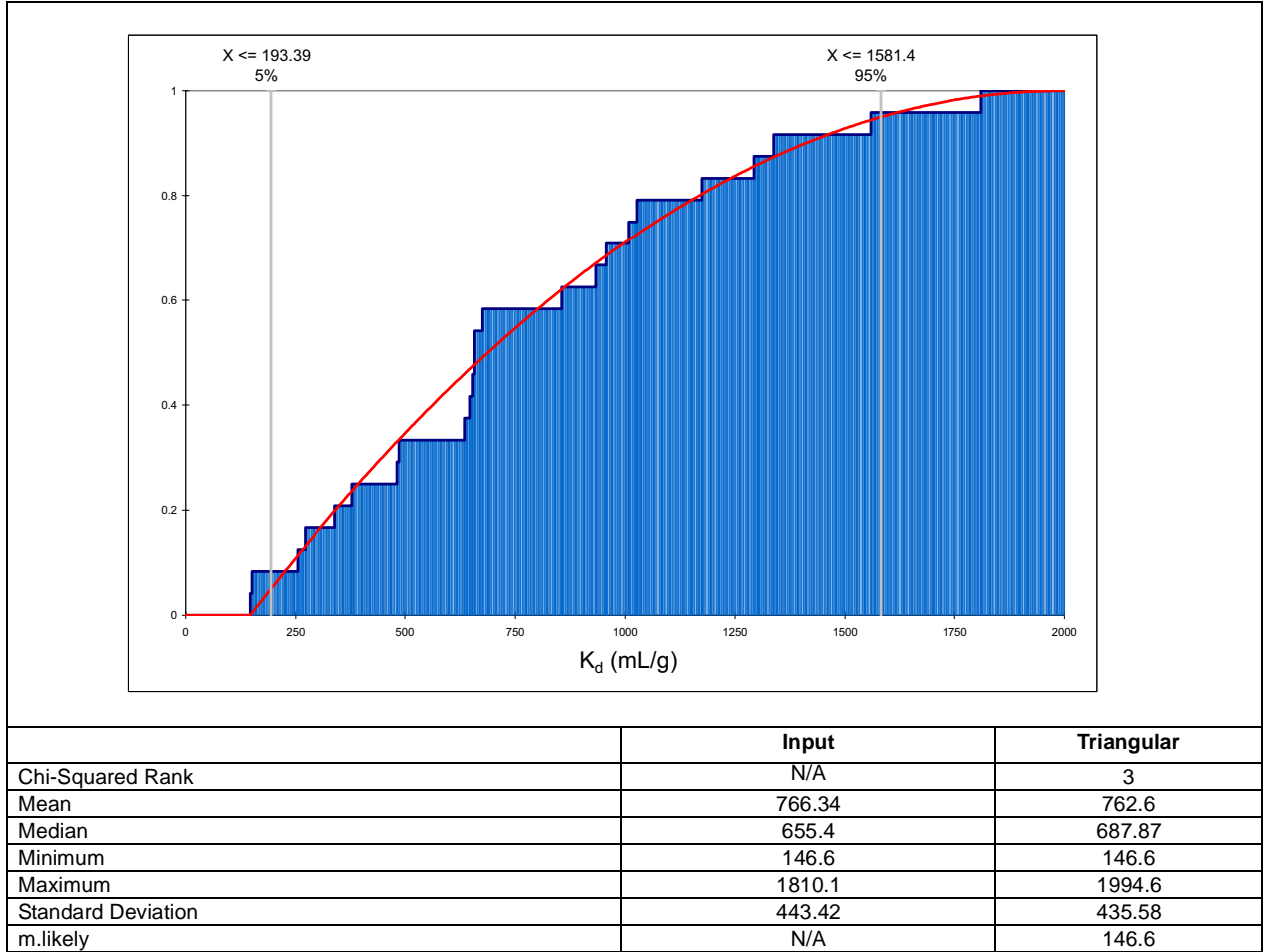
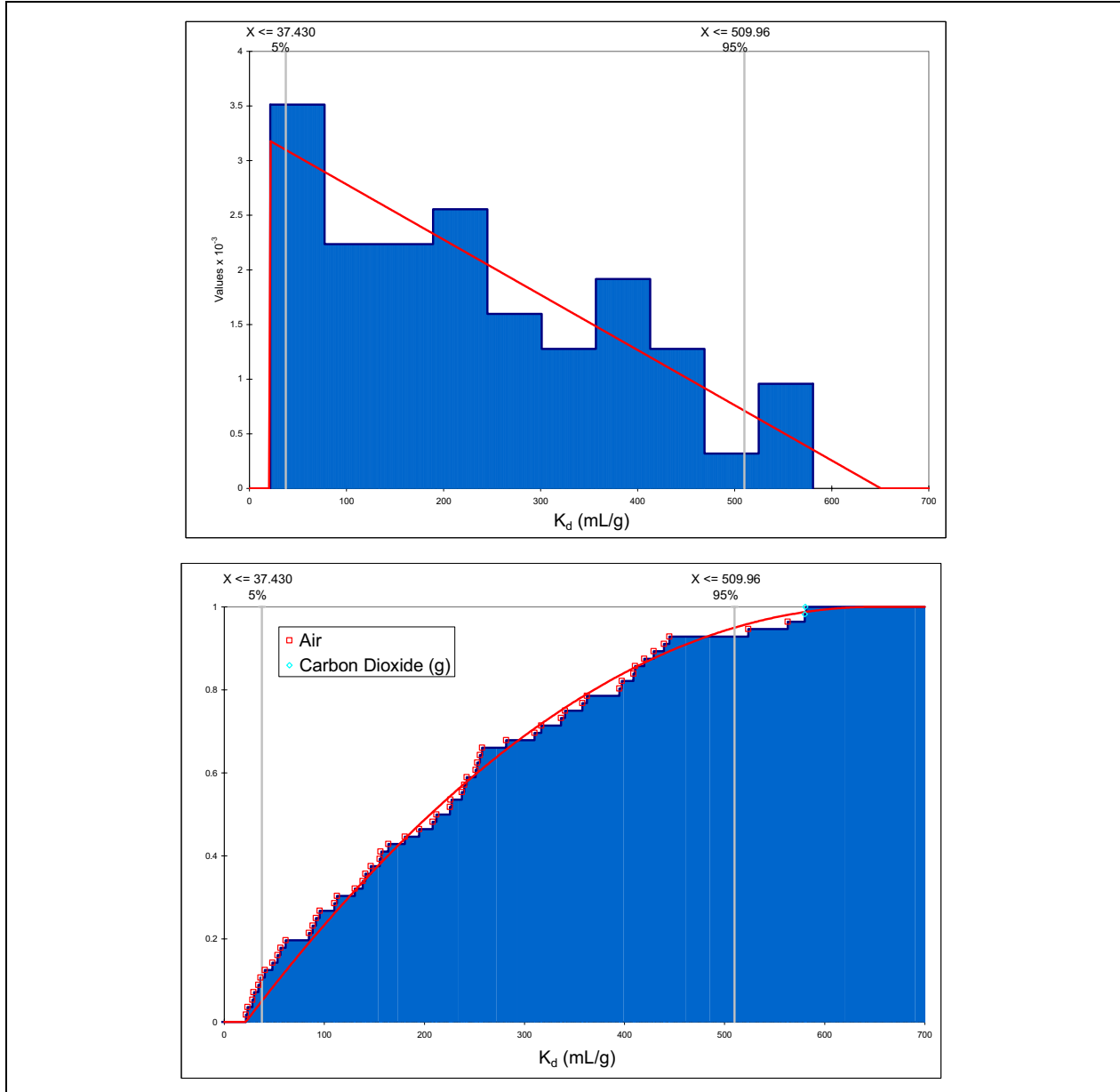


Figure 9-4
CDF of Pu K_d on Vitric Tuff in J-13 Water at 20°C: Triangular Distribution Shown with Red Line; Distribution Only for Air Environment (pH >8) Experiments



	Input	Triangular
Chi-Squared Rank	N/A	1
Mean	230.83	231.21
Median	218.8	205.77
Minimum	21.5	21.5
Maximum	580.7	650.64
Standard Deviation	157.65	148.29
m.Likely	N/A	21.5

Figure 9-5
PDF and CDF of Pu K_d on Vitric Tuff in p#1 Water at 20°C: Triangular Distribution Shown with Red Line; Symbols Indicate Experimental Atmosphere for Individual Data Points in Distribution

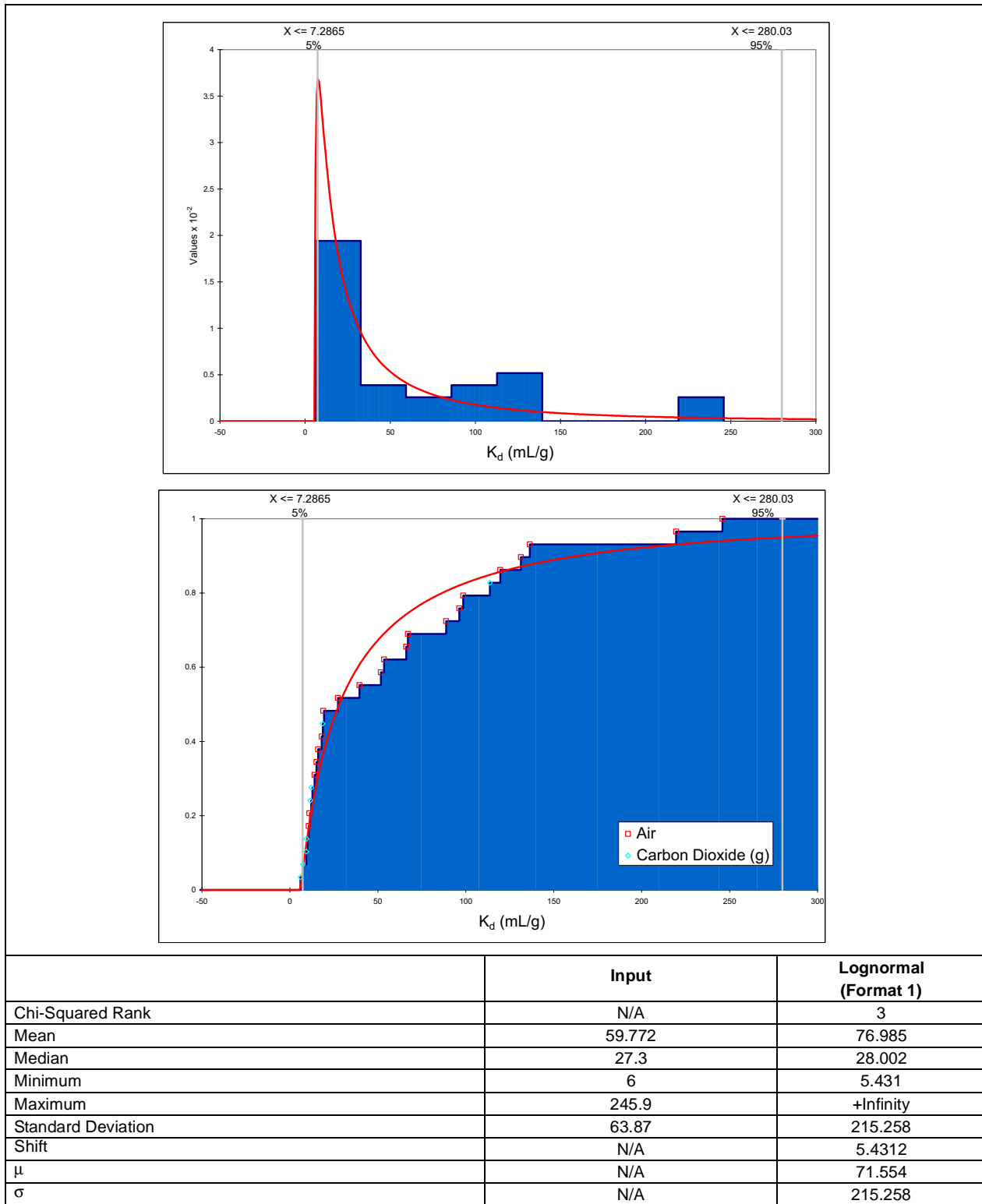


Figure 9-6

PDF and CDF of Pu K_d on Devitrified Tuff in J-13 Water at 20°C: Lognormal Distribution Shown with Red Line; Symbols Indicate Experimental Atmosphere for Individual Data Points in Distribution

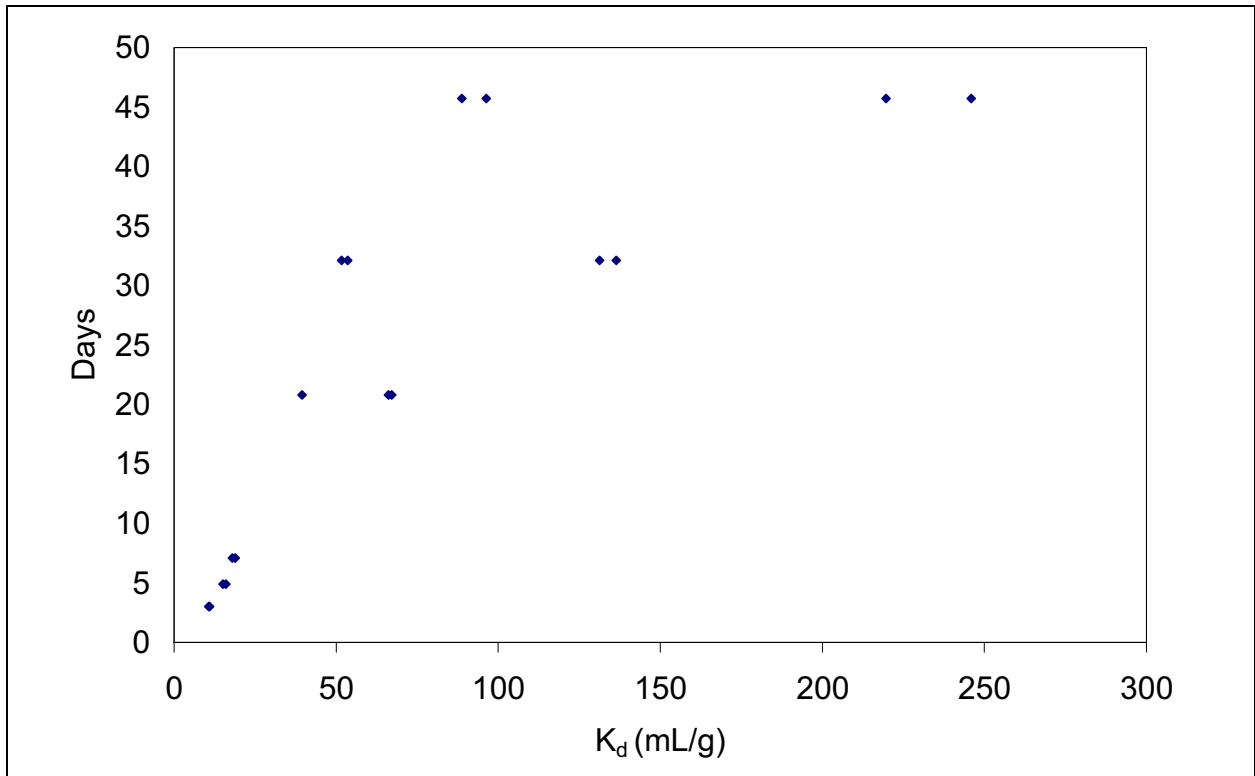


Figure 9-7
Relationship Between Duration of Experiment and K_d Value for Pu on Devitrified Tuff in J-13 Water

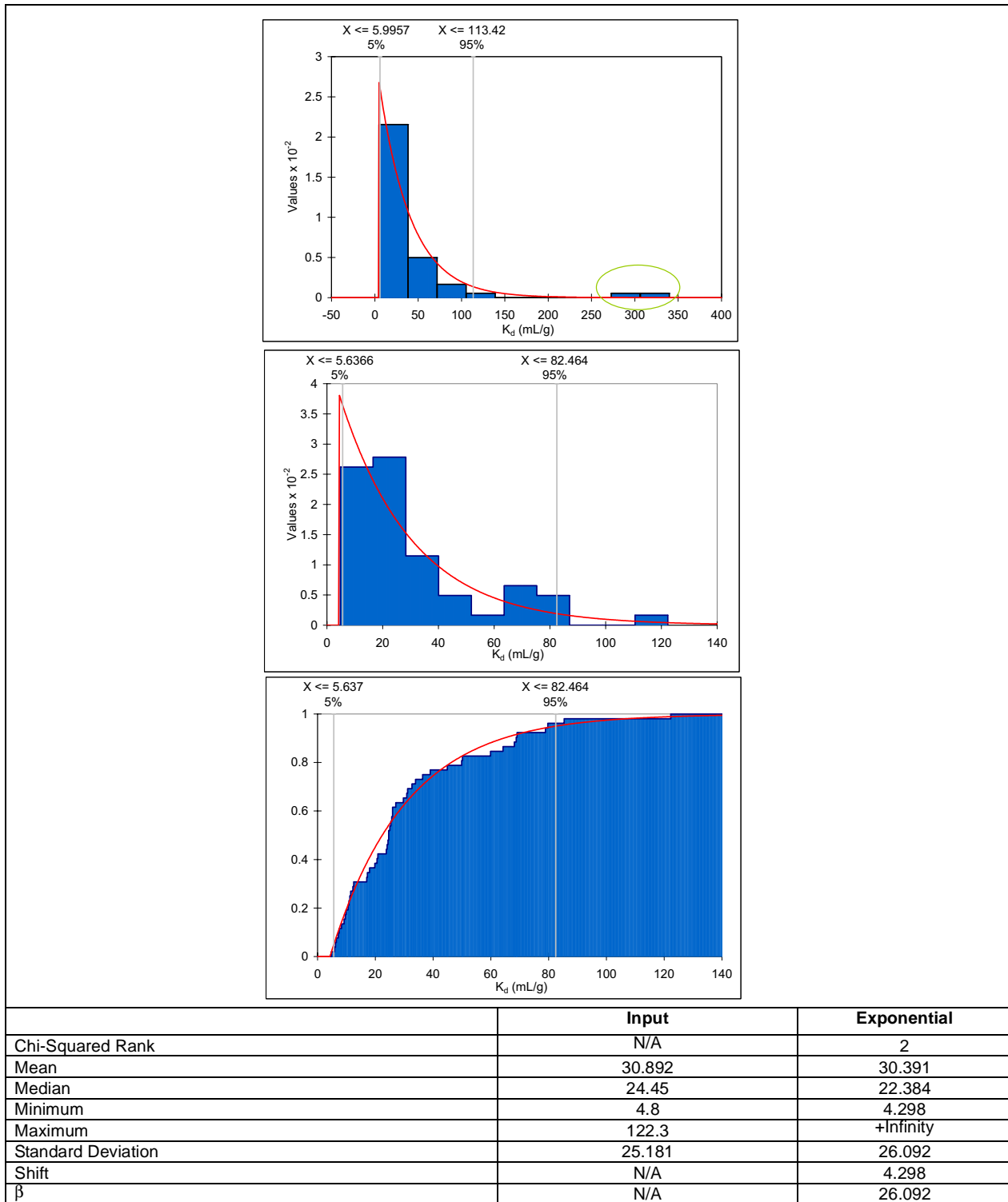
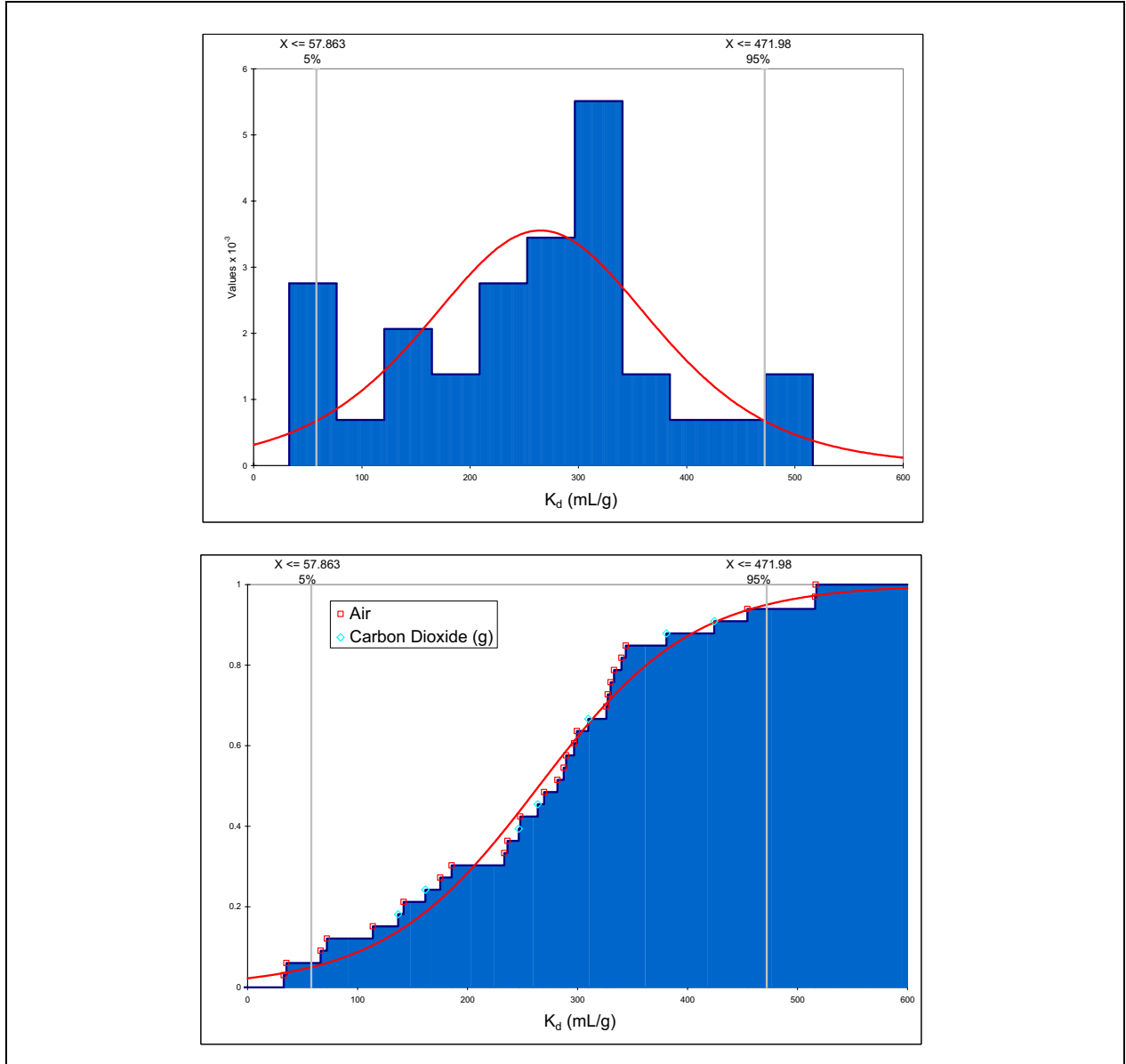


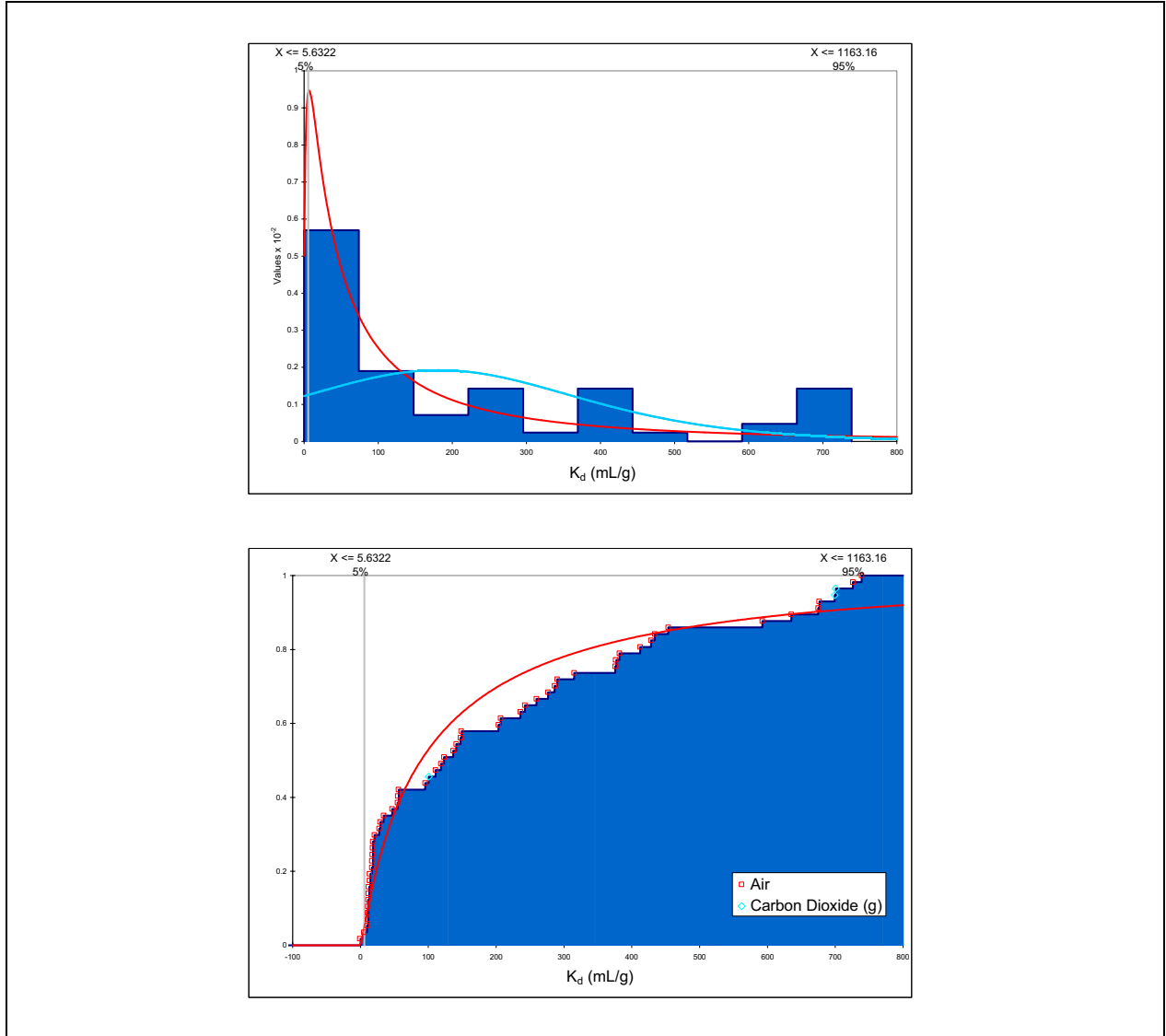
Figure 9-8

PDF and CDF of Pu K_d on Devitrified Tuff in p#1 Water at 20-25°C: Exponential Distribution Shown with Red Line; Components of Distribution Associated with CO₂ Atmosphere Circled in Green in Upper Plot; Middle and Lower Plot are for Air Atmosphere Experiments Only



	Input	Logistic
Chi-Squared Rank	N/A	1
Mean	262.93	264.924
Median	281.7	264.924
Minimum	32.8	-Infinity
Maximum	516.5	+Infinity
Standard Deviation	125.01	127.551
α	N/A	264.924
β	N/A	70.323

Figure 9-9
PDF and CDF of Pu K_d on Zeolitic Tuff in J-13 Water at 20-25°C: Logistic Distribution Shown with Red Line; Symbols Indicate Experimental Atmosphere for Individual Data Points in Distribution



	Input	Lognormal (Format 1)
Chi-Squared Rank	N/A	1
Mean	215.12	300.94
Median	123.2	89.114
Minimum	0	-1.403
Maximum	738.9	+Infinity
Standard Deviation	232.46	963.540
Shift	N/A	-1.403
μ	N/A	302.340
σ	N/A	963.539

Figure 9-10
PDF and CDF of Pu K_d on Zeolitic Tuff in p#1 Water at 20-25°C: Lognormal Distribution Shown with Red Line (Logistic Distribution Shown with Blue Line for Comparison with Figure 9-9); Symbols Indicate Experimental Atmosphere for Individual Data Points in Distribution

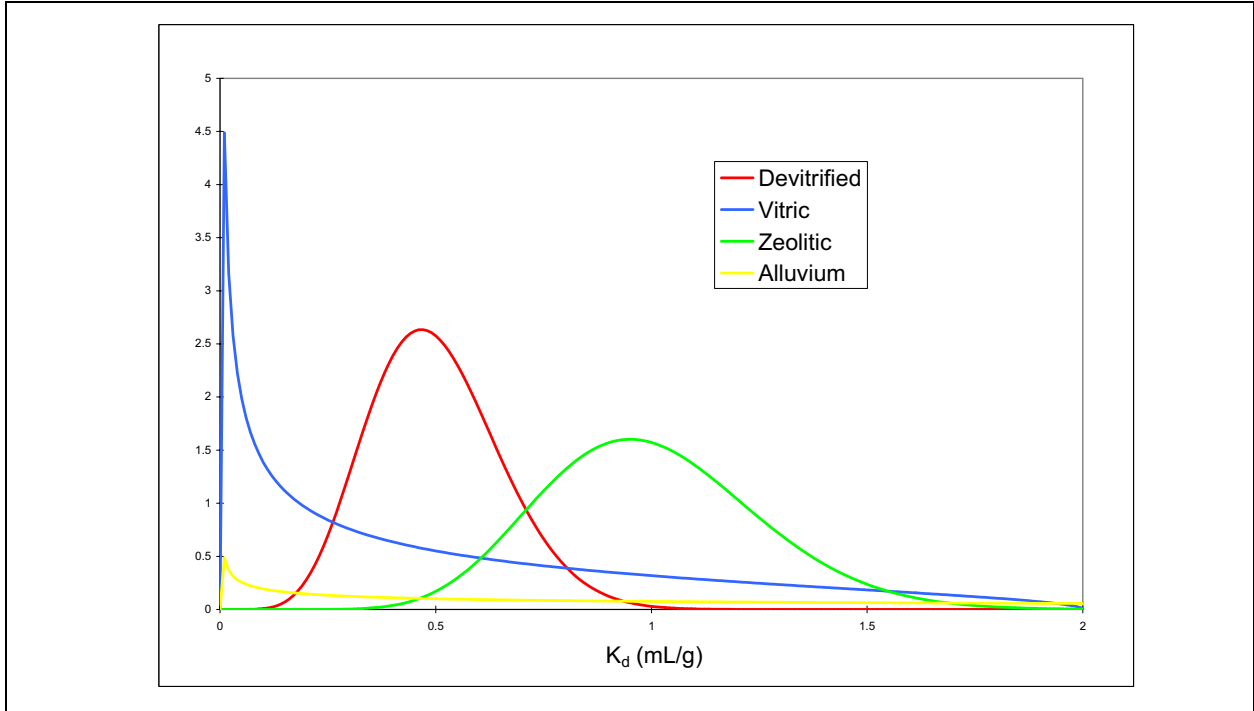


Figure 9-11
YMP PDF Distributions for Np Sorption on Volcanic Tuff (Conca, 2000, Table 2b)

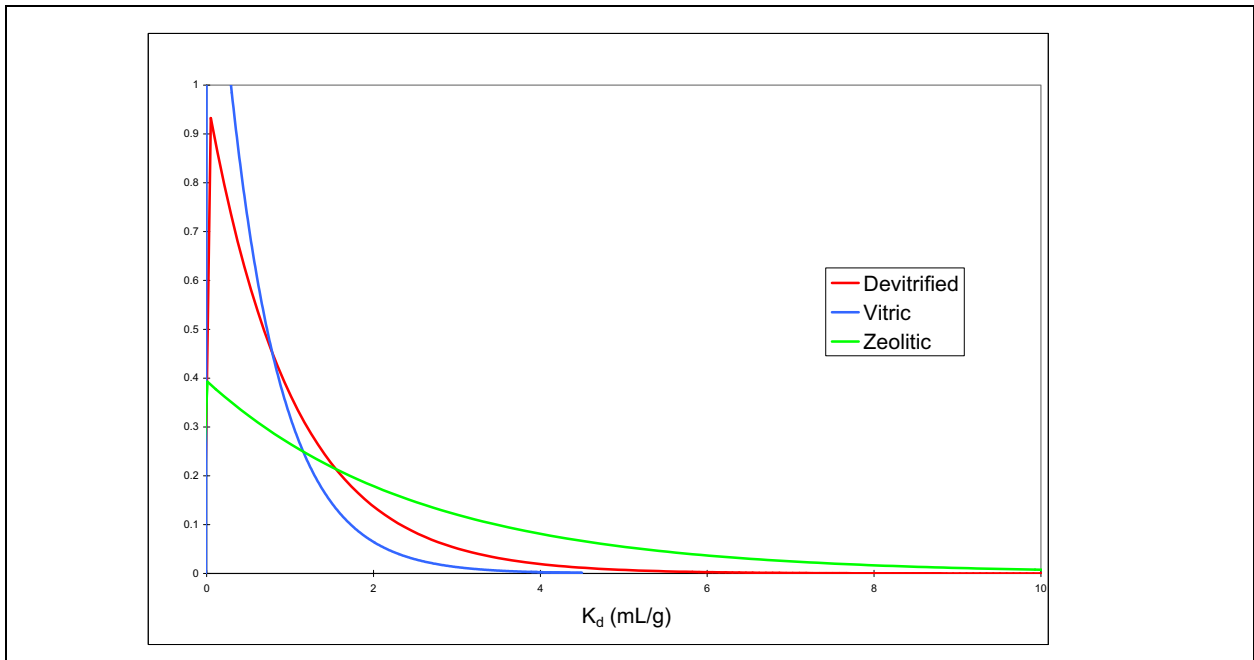
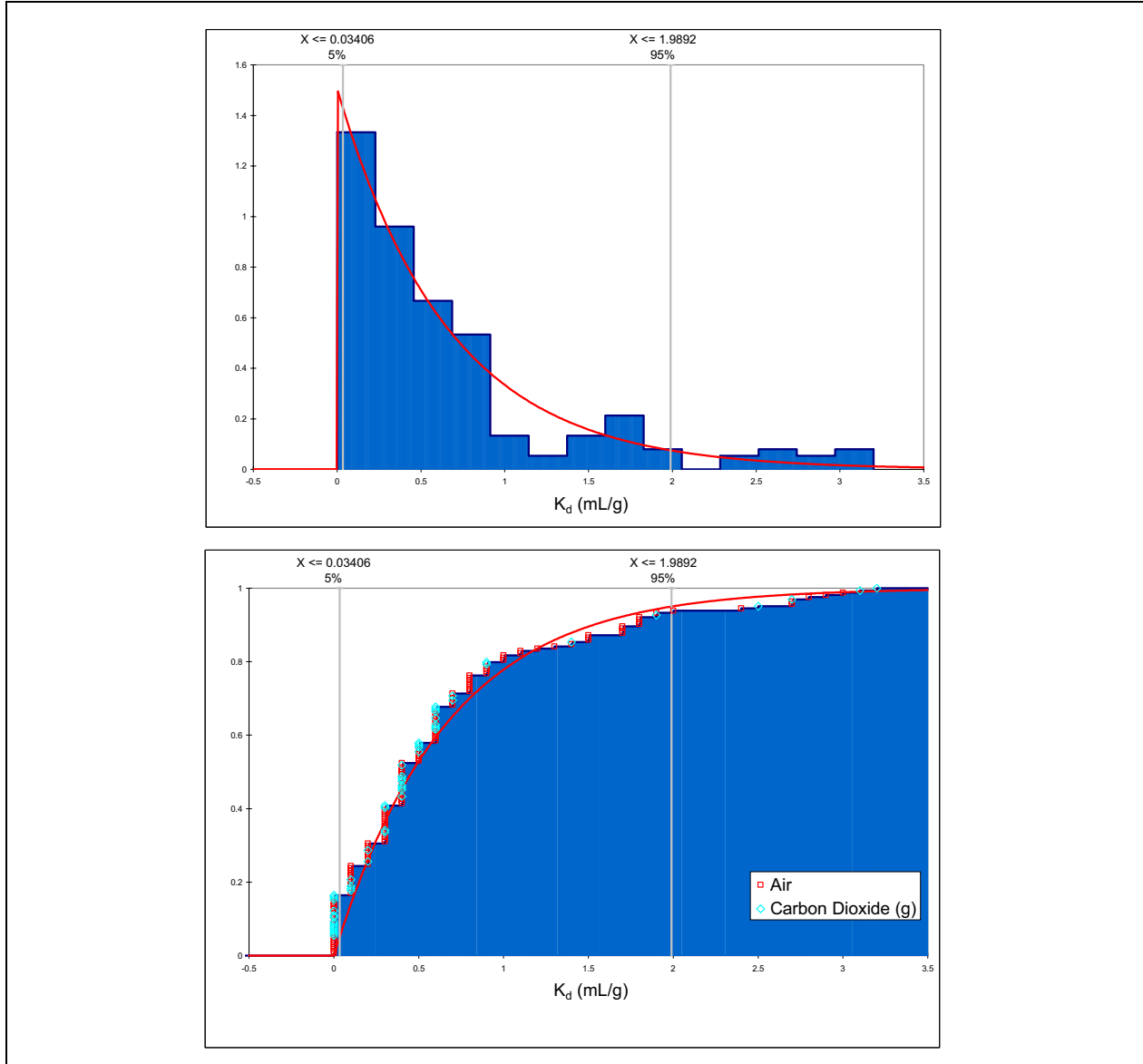


Figure 9-12
Np K_d Distributions Fit to YMP TDMS Data for All Experimental Conditions
Included in YMP (1996) DTN: LAIT831341AQ96.001



	Input	Exponential
Chi-Squared Rank	N/A	1
Mean	0.66402	0.66402
Median	0.4	0.46027
Minimum	0	0
Maximum	3.2	+Infinity
Standard Deviation	0.73333	0.66402
Shift	N/A	0
β	N/A	0.66402

Figure 9-13
PDF and CDF of Np K_d on Vitric Tuff in J-13 Water at All Temperatures (20-90°C): Symbols Indicate Experimental Atmosphere for Individual Data Points in Distribution
(Note: All But 4 Experiments Conducted at 20-25°C)

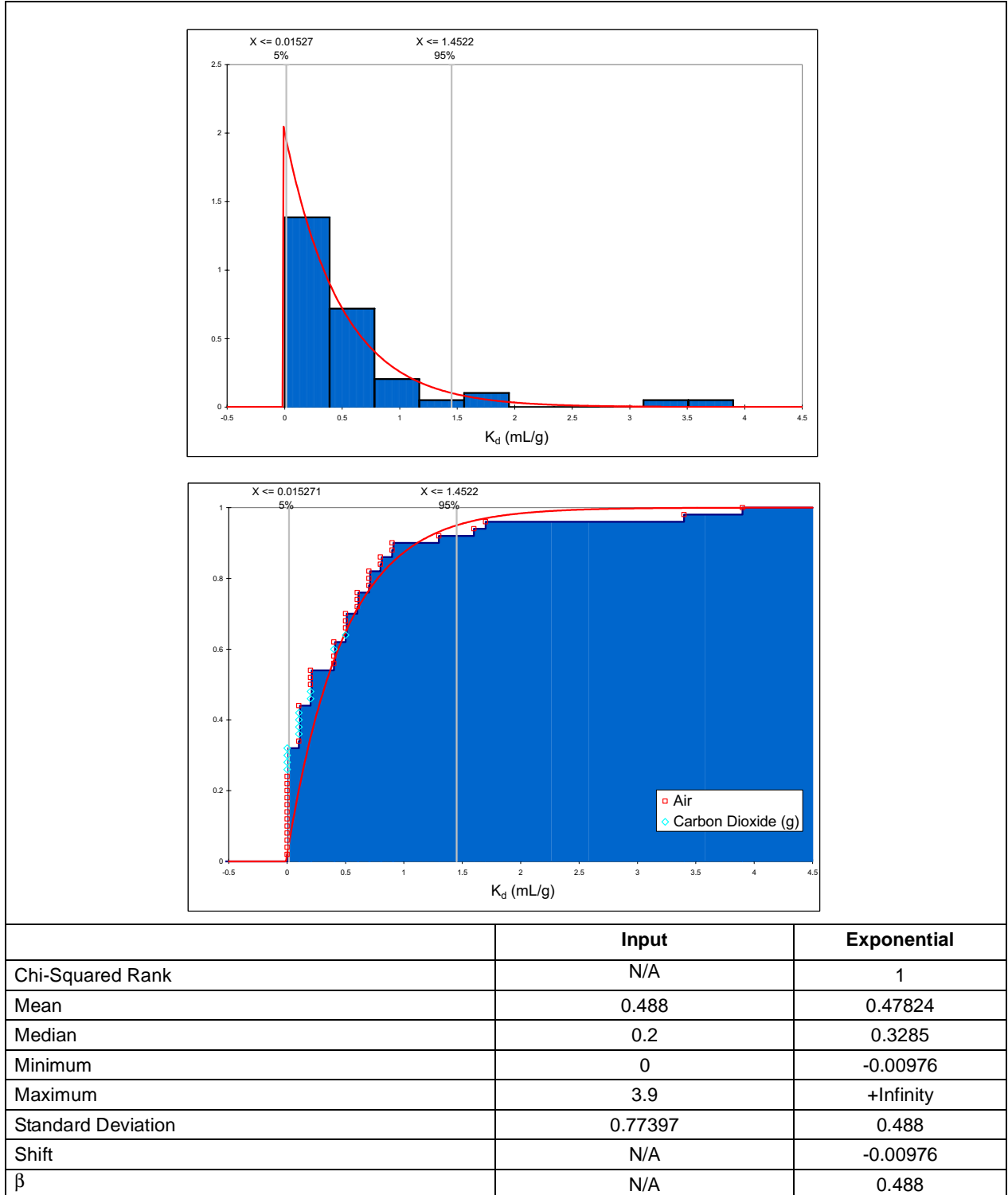


Figure 9-14
PDF and CDF of Np K_d on Vitric Tuff in p#1 Water at All Temperatures (20-60°C): Symbols Indicate Experimental Atmosphere for Individual Data Points in Distribution
(Note: All But 1 Experiment Conducted at 20-25°C)

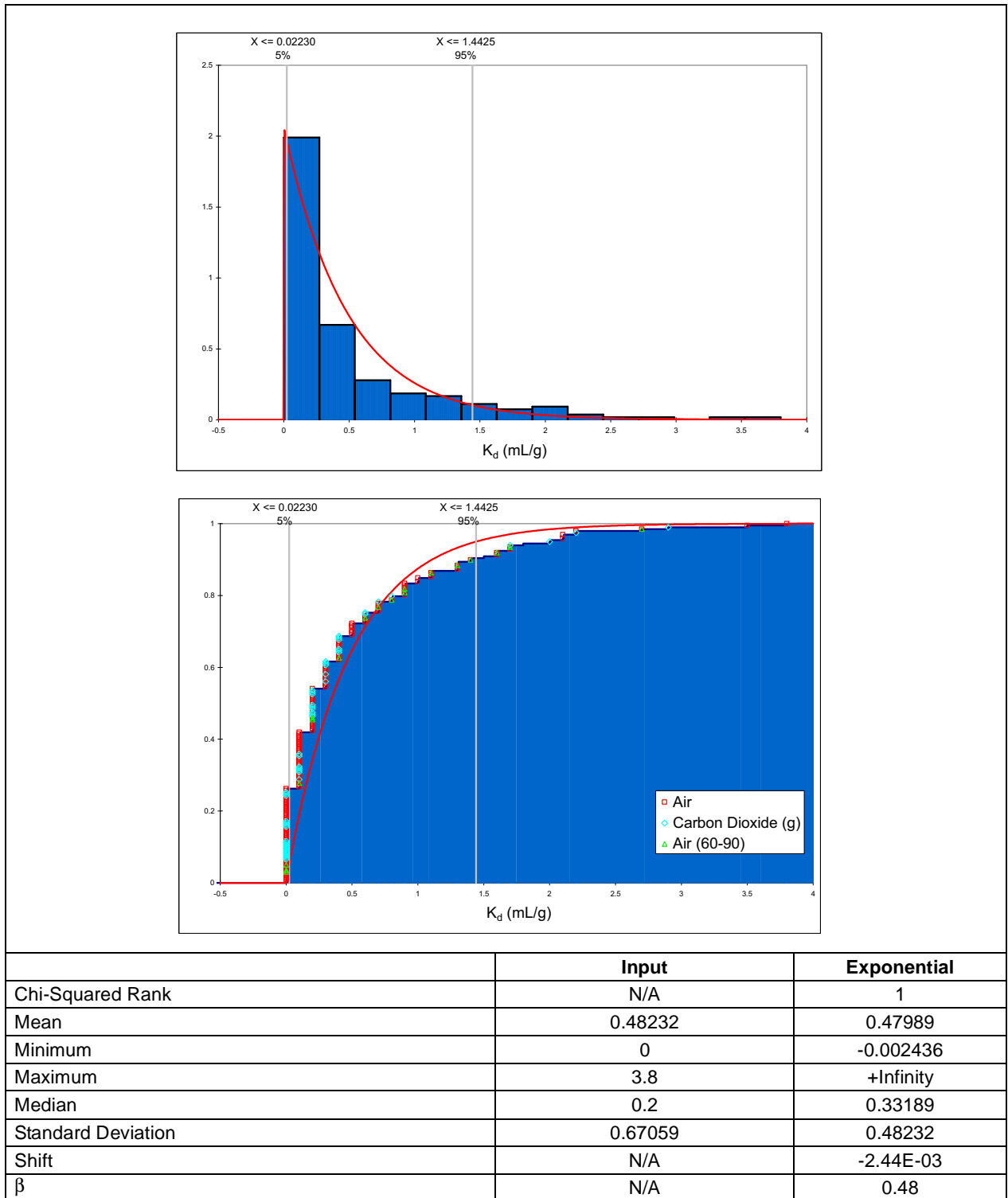
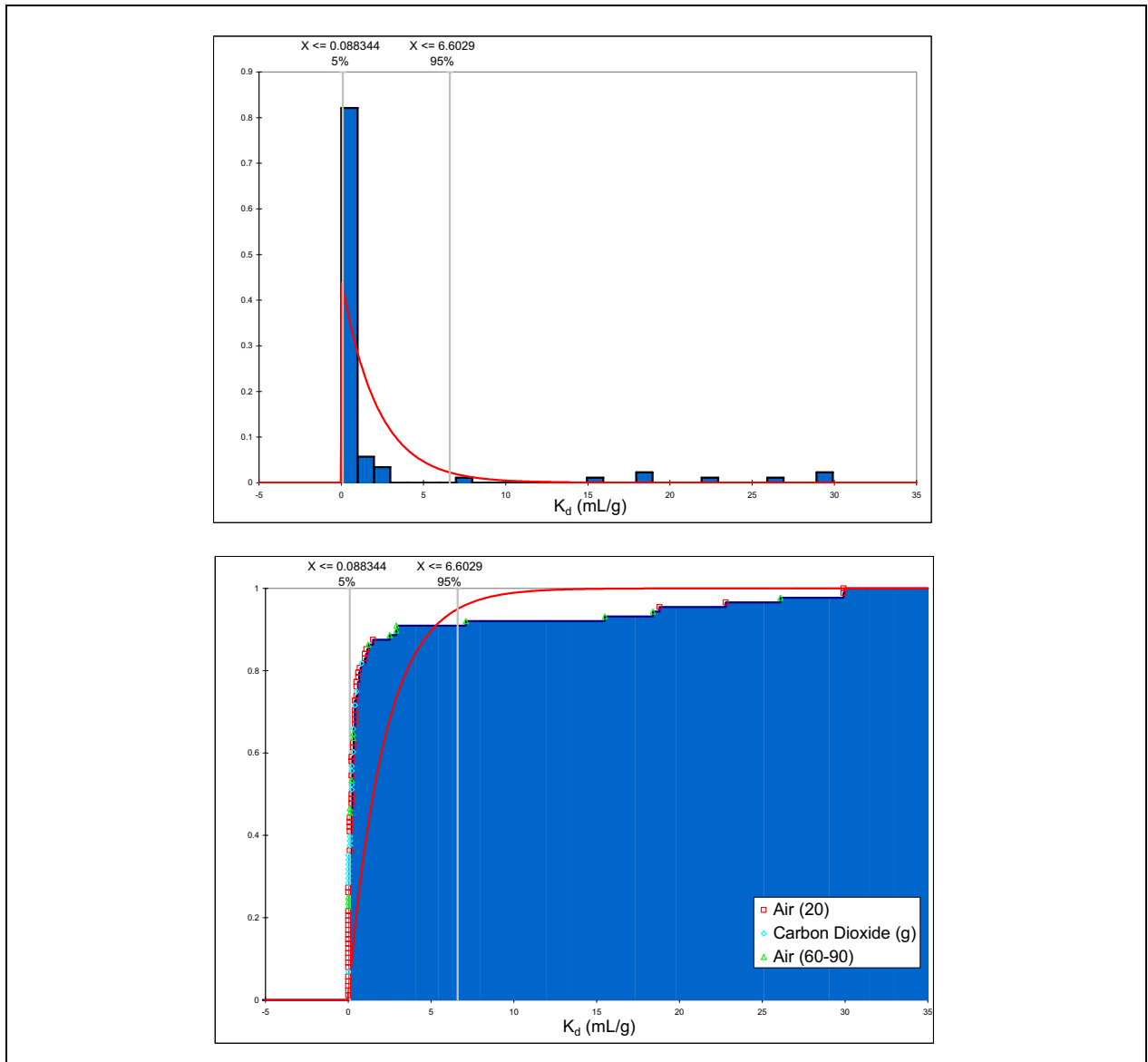


Figure 9-15
PDF and CDF of Np K_d on Devitrified Tuff in J-13 Water; Symbols Indicate Experimental Atmosphere and Temperature (for Experiments Conducted at High Temperature) for Individual Data Points in Distribution



	Input	Exponential
Chi-Squared Rank	N/A	1
Mean	2.2125	2.1874
Median	0.2	1.5084
Minimum	0	-0.025142
Maximum	29.9	+Infinity
Standard Deviation	6.411	2.2125
Shift	N/A	-2.51E-02
β	N/A	2.2125

Figure 9-16
PDF and CDF of Np K_d on Devitrified Tuff in p#1 Water; Symbols Indicate Experimental Atmosphere and Temperature for Individual Data Points in Distribution

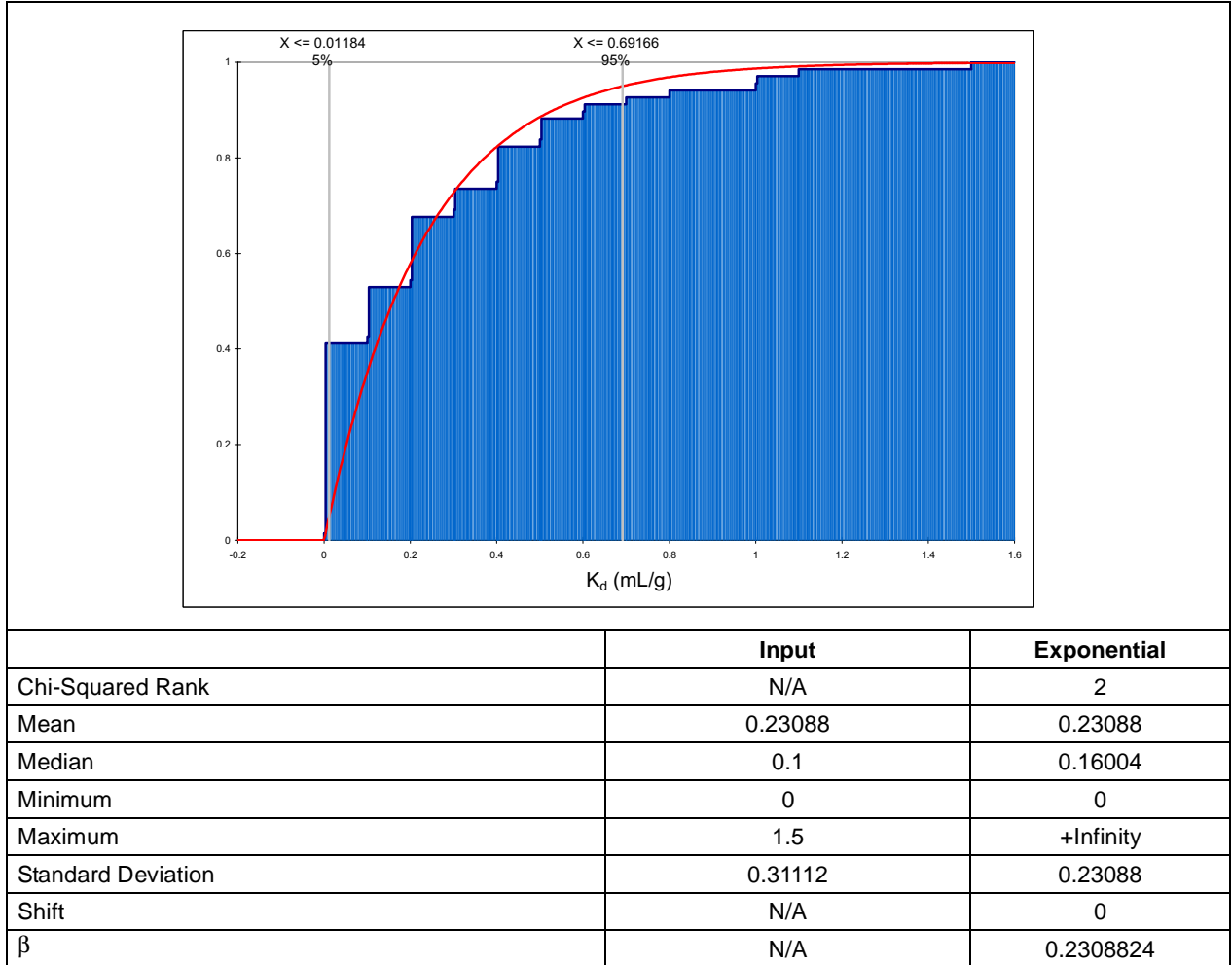


Figure 9-17
CDF of Np K_d on Devitrified Tuff in p#1 Water; Distribution for 20-25°C Only,
and Upper 4 K_d Values (> 18) are Rejected

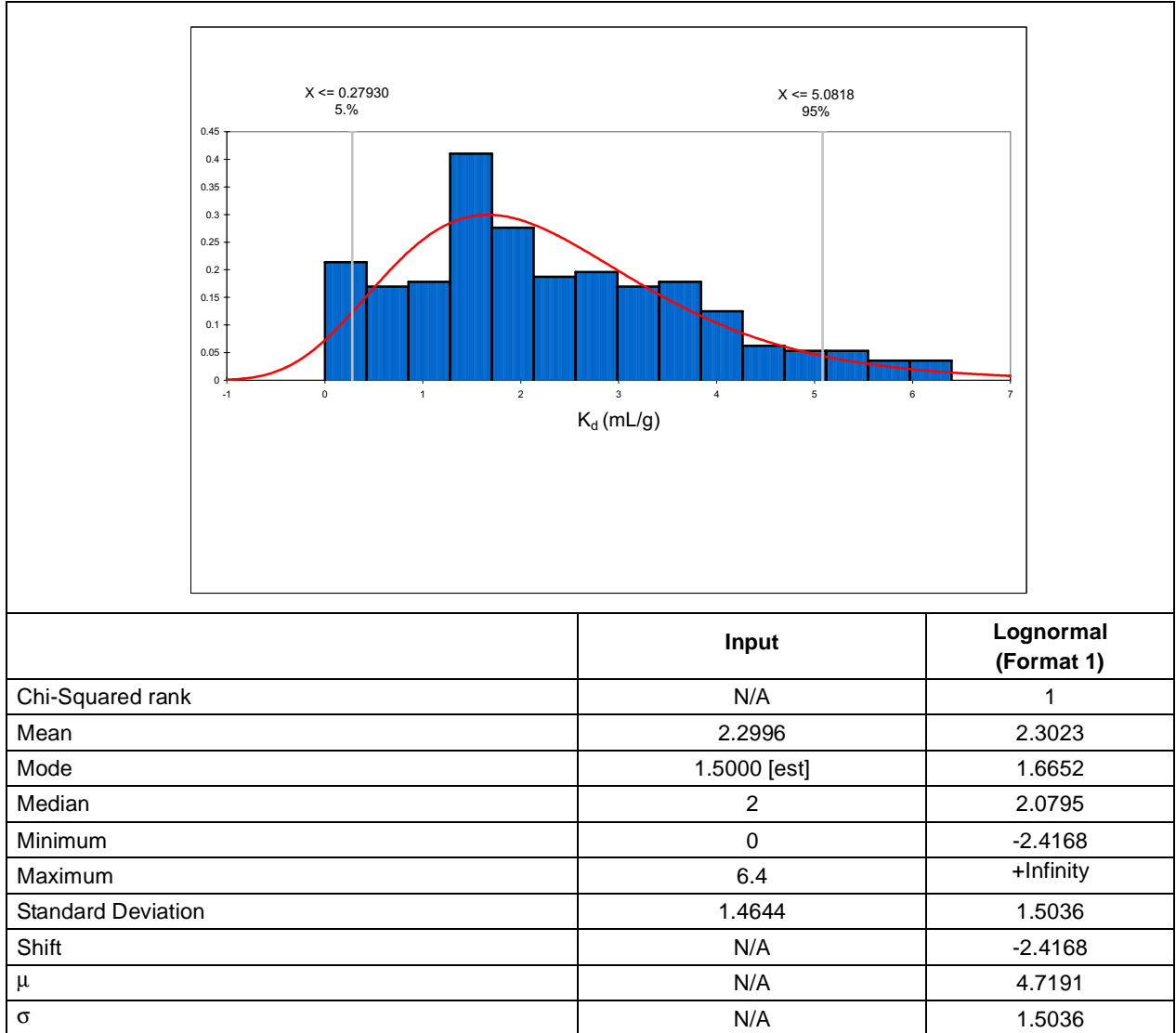


Figure 9-18
Np K_d on Zeolitic Tuff in J-13 Water at 20-25°C

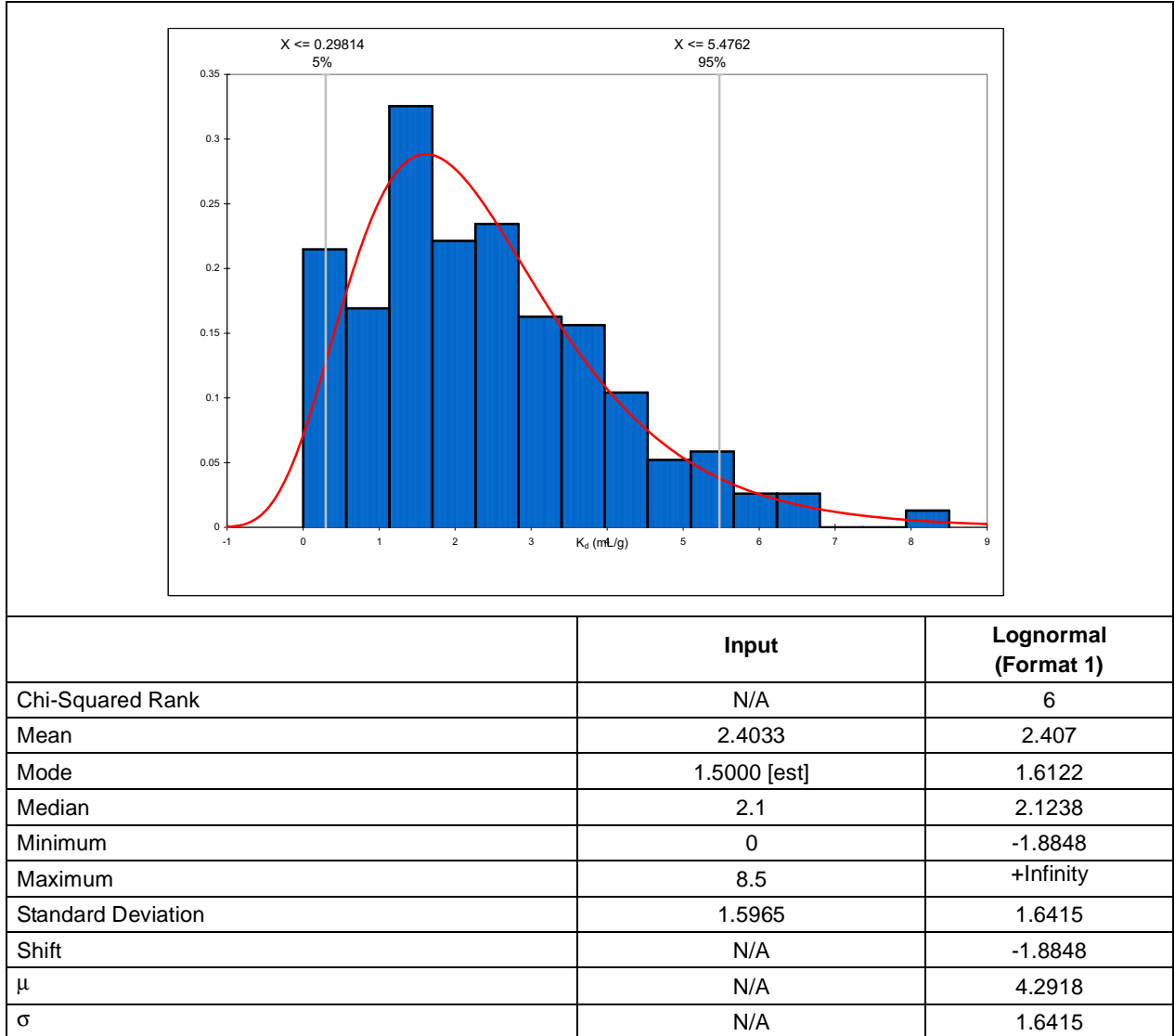


Figure 9-19
Np K_d on Zeolitic Tuff in J-13 Water at 20-60°C

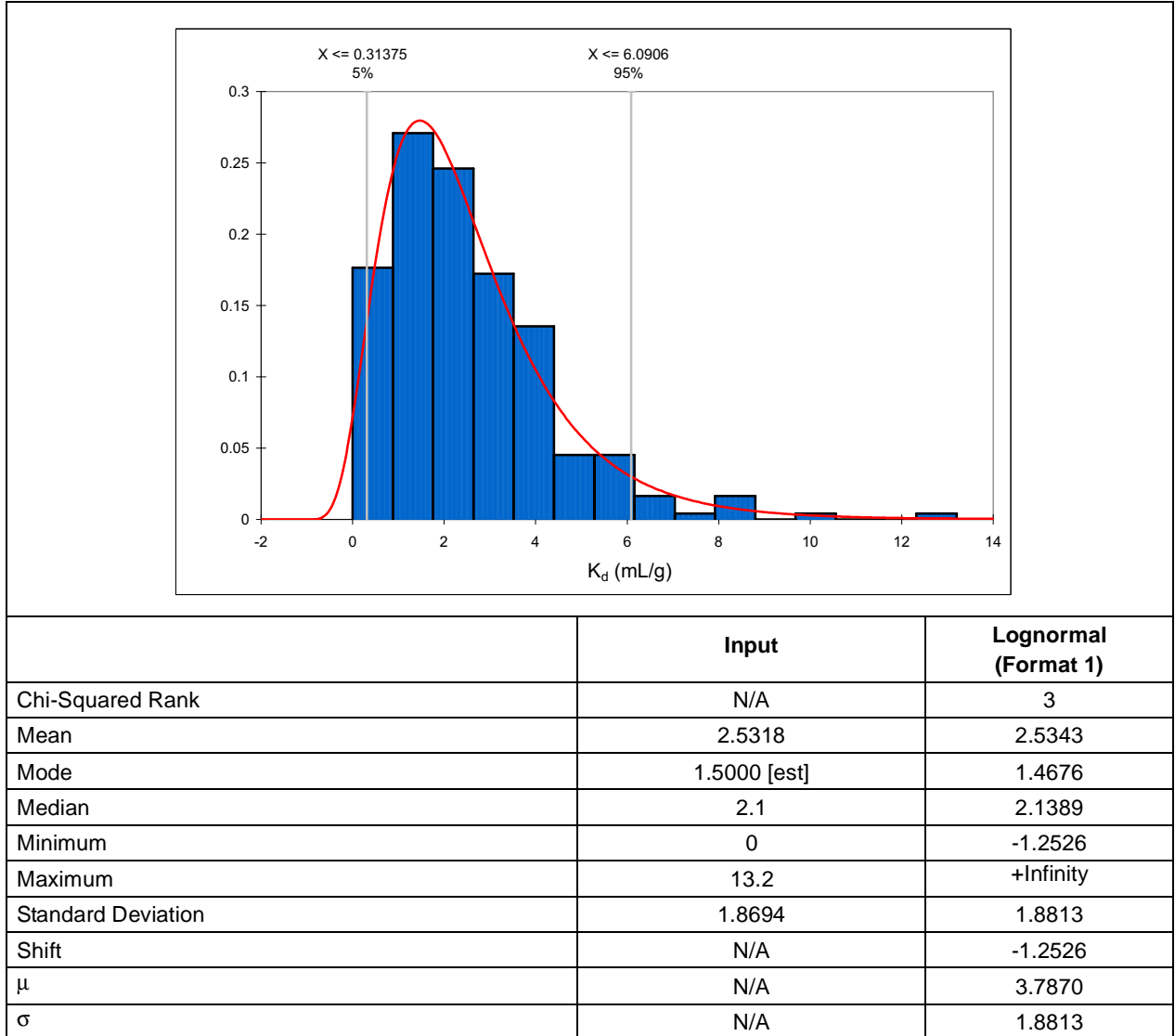


Figure 9-20
Np K_d on Zeolitic Tuff in J-13 Water at 20-90°C

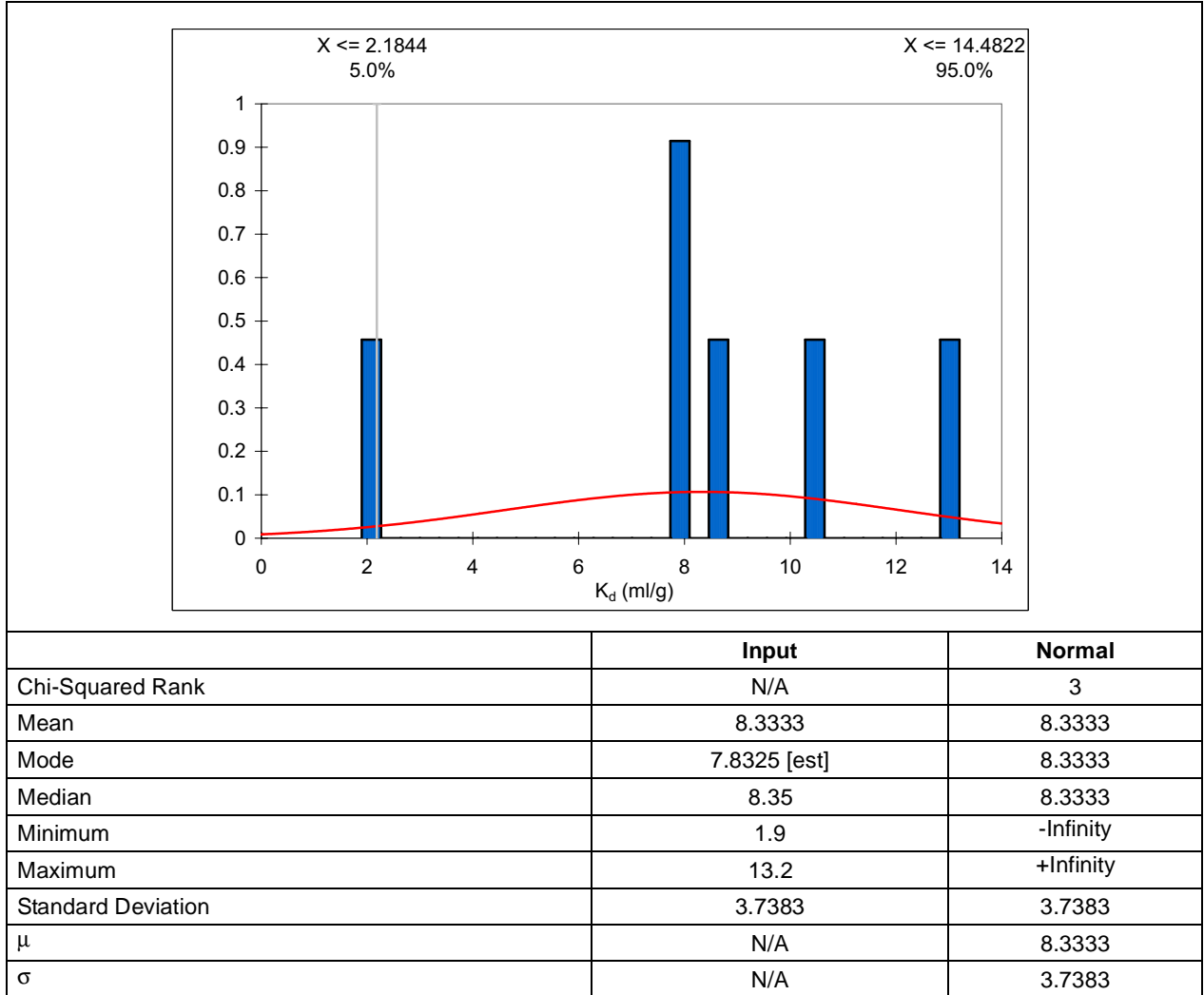
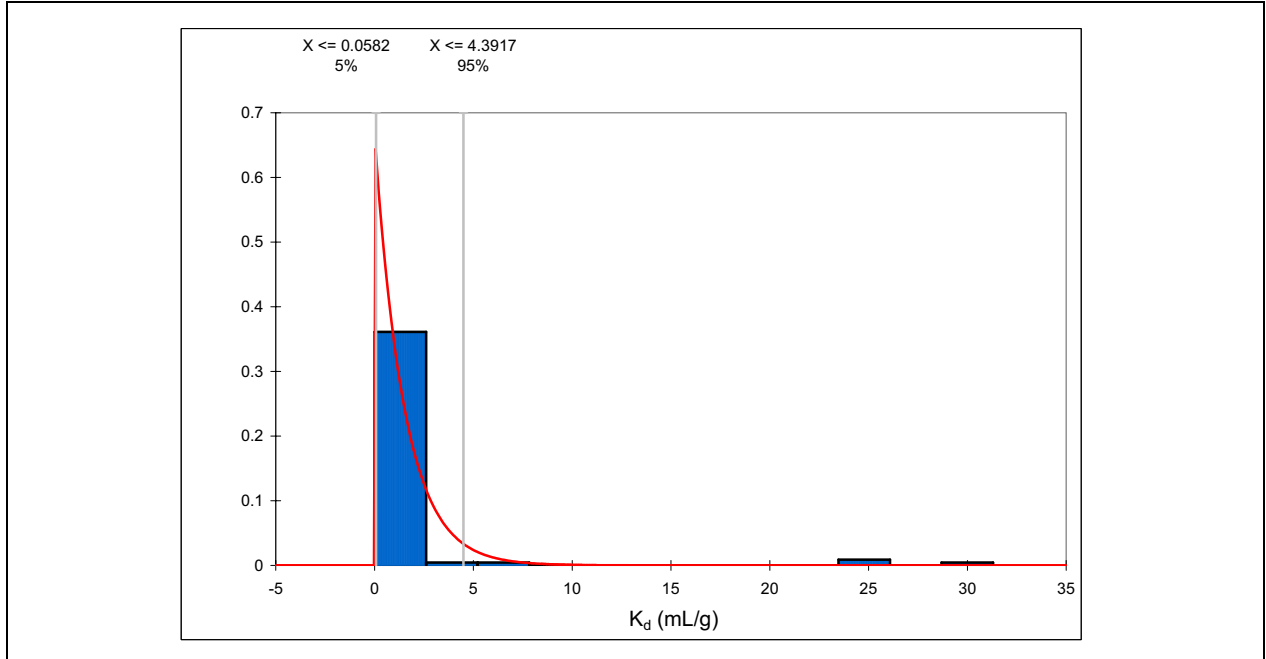
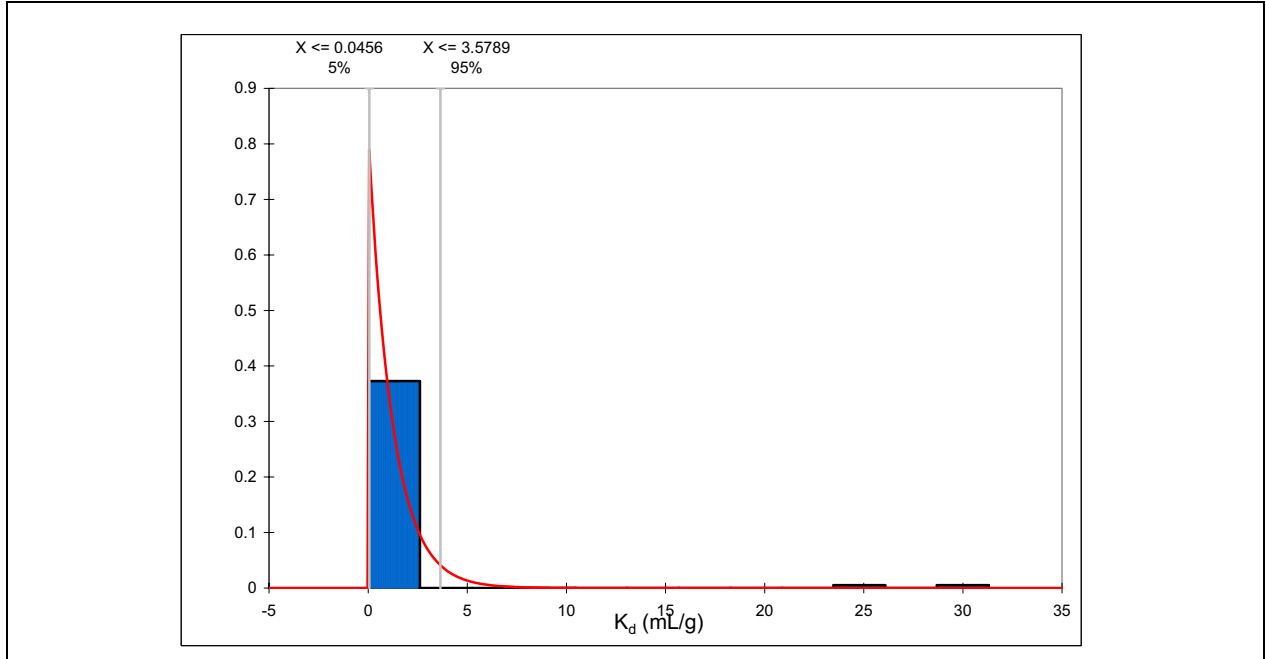


Figure 9-21
Np K_d on Zeolitic Tuff in J-13 Water at 90°C



	Input	Exponential
Chi-Squared Rank	N/A	2
Mean	1.4718	1.4544
Mode	0.0000 [est]	-0.0173
Median	0.4	1.0028
Minimum	0	-0.0173
Maximum	31.3	+Infinity
Standard Deviation	4.9478	1.4718
Shift	N/A	-1.73E-02
β	N/A	1.4718

Figure 9-22
Np K_d on Zeolitic Tuff in p#1 Water at 20-90°C



	Input	Exponential
Chi-Squared Rank	N/A	2
Mean	1.2	1.184
Mode	0.0000 [est]	-0.016
Median	0.4	0.8158
Minimum	0	-0.016
Maximum	31.3	+Infinity
Standard Deviation	4.5292	1.2
Shift	N/A	-0.016
β	N/A	1.2

Figure 9-23
Np K_d on Zeolitic Tuff in p#1 Water at 20-25°C

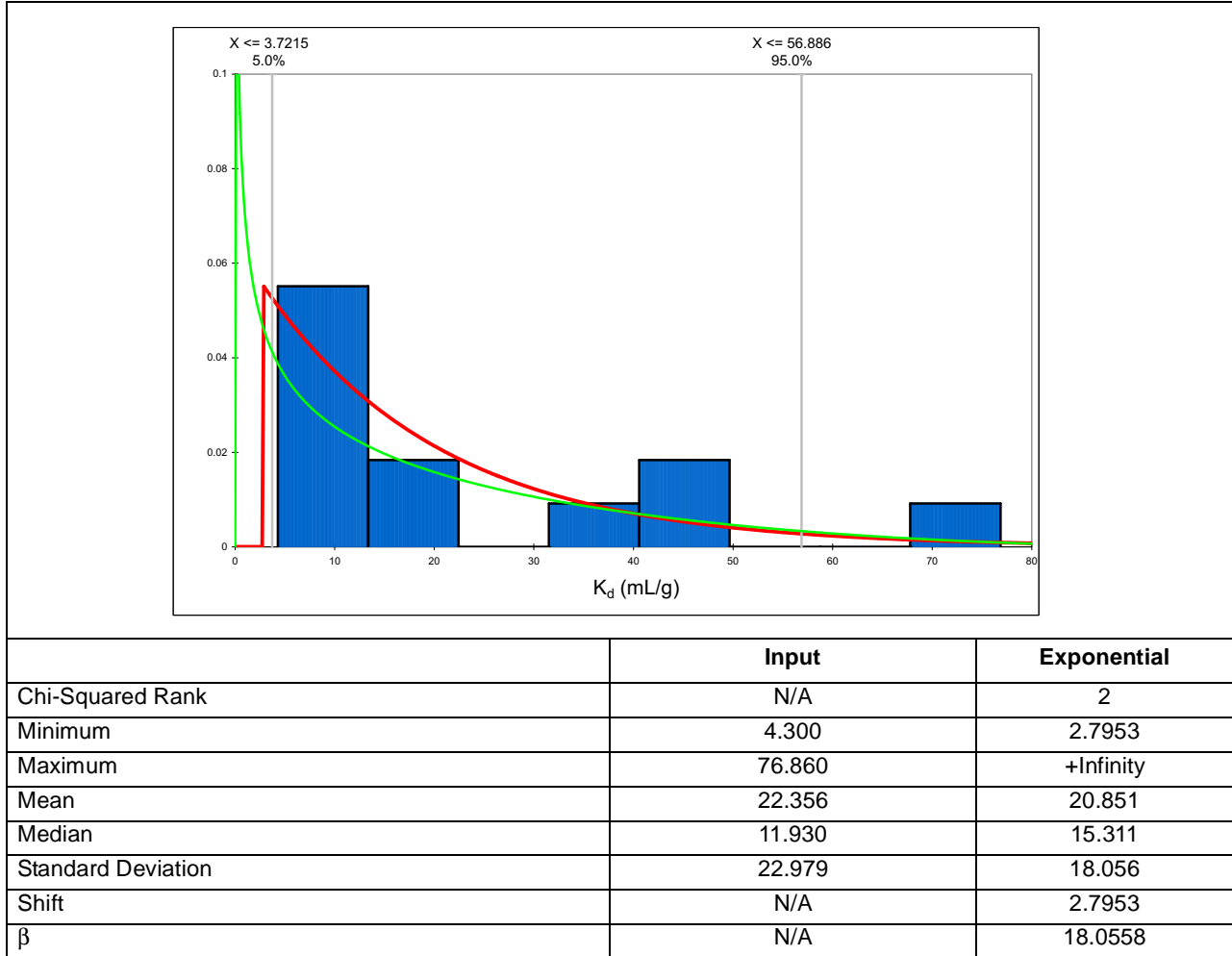


Figure 9-24
CDF of Np K_d Alluvium

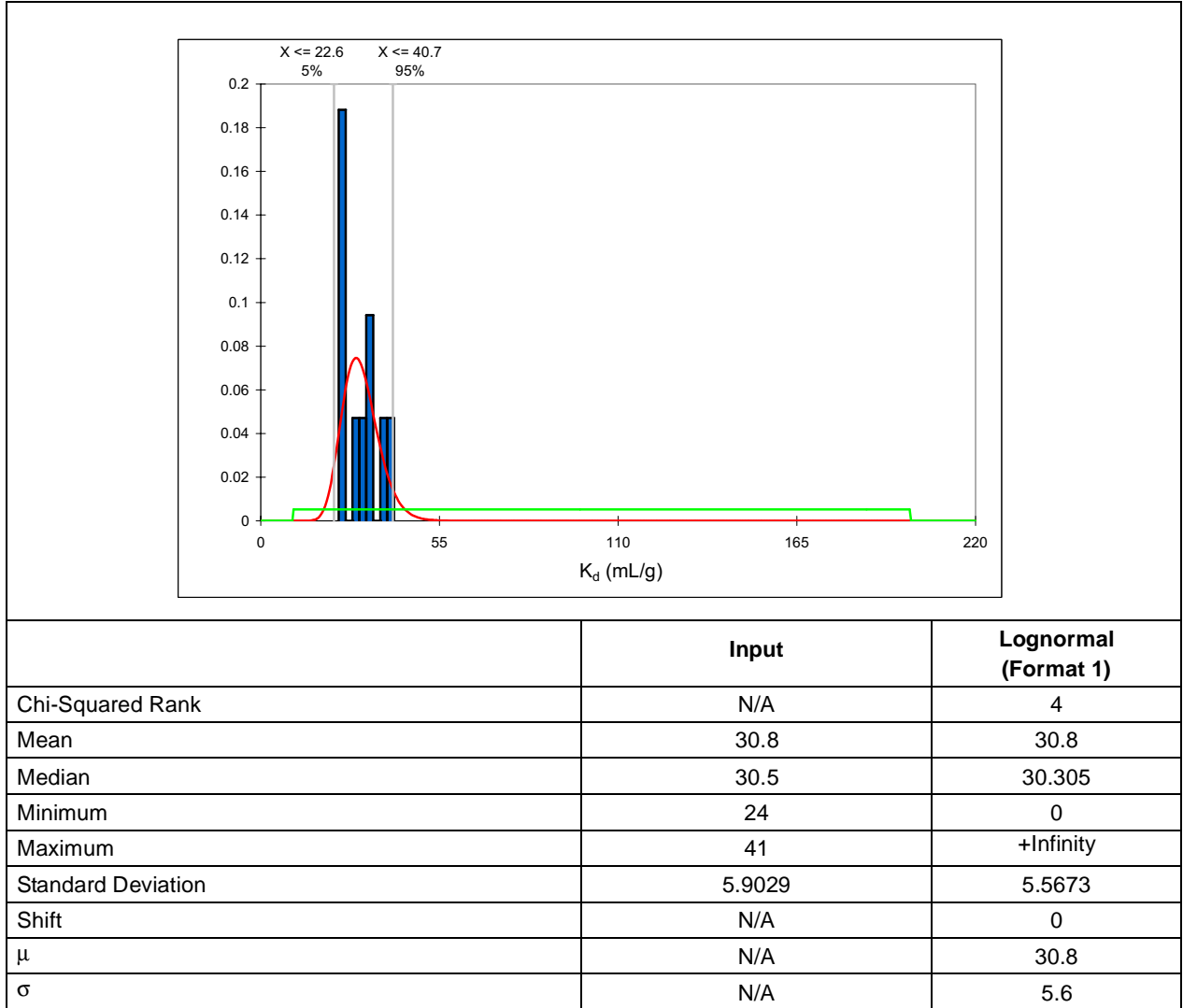


Figure 9-25
Strontium Sorption on Devitrified Tuff in J-13 Water; Red Line Shows Lognormal Distribution to YMP TDMS Data (YMP [1996] DTN: LAIT831341AQ96.001); Green Line Shows YMP Distribution (Table 9-10)

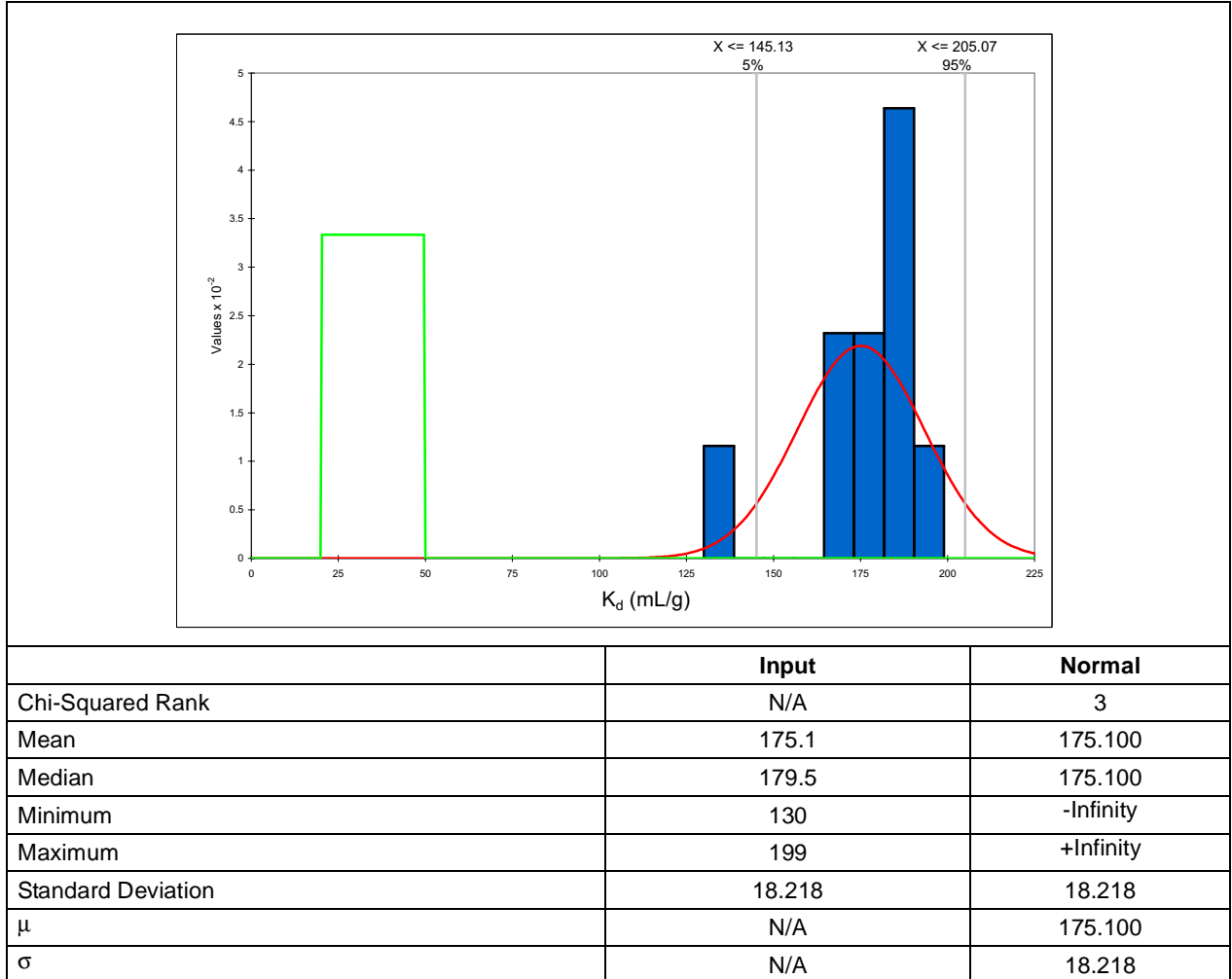


Figure 9-26
Strontium Sorption on Vitric Tuff in J-13 Water; Red Line Shows Normal Distribution to YMP TDMS Data (YMP [1996] DTN: LAIT831341AQ96.001); Green Line Shows YMP Distribution (Table 9-10)

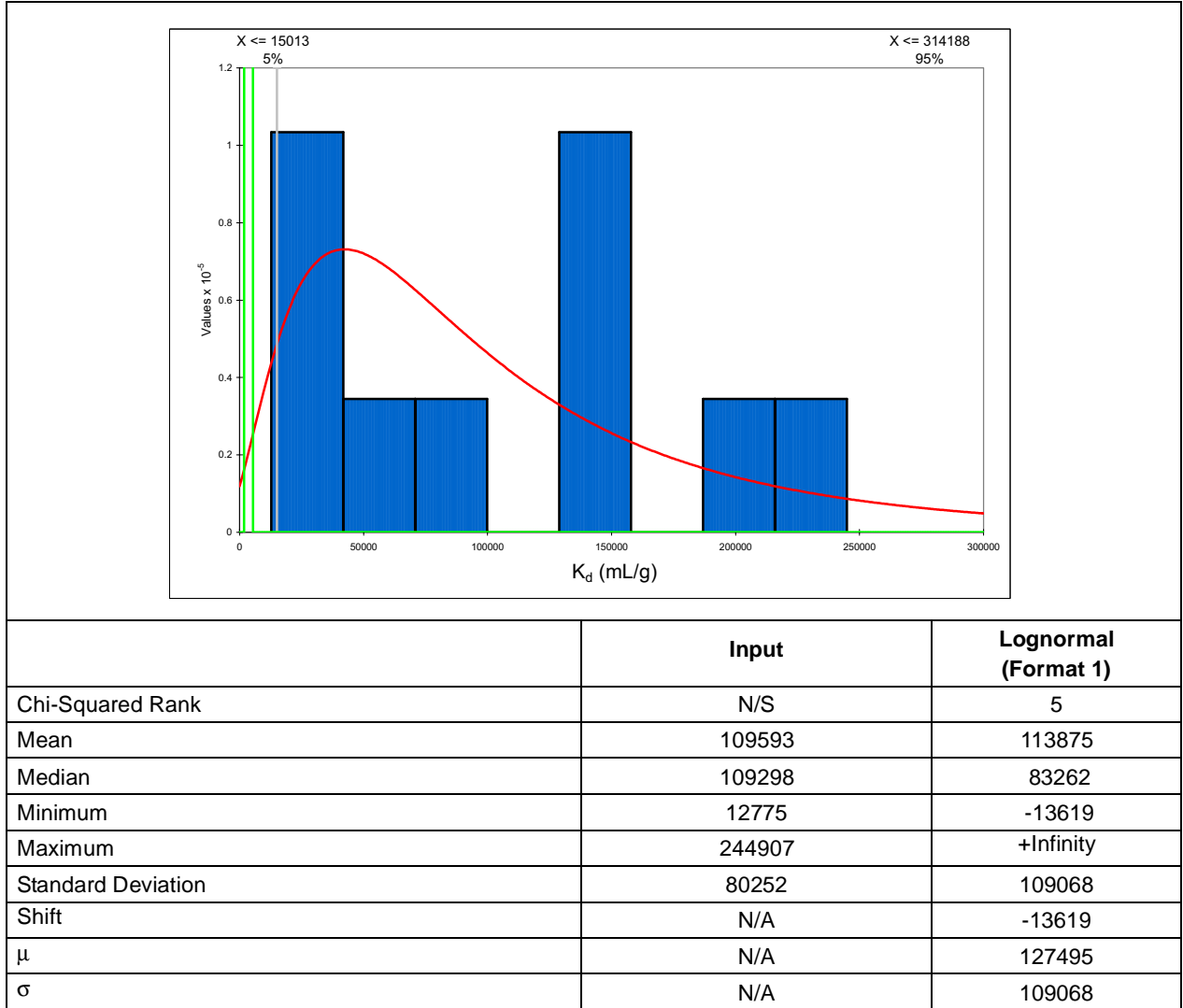


Figure 9-27

Strontium Sorption on Zeolitic Tuff in J-13 Water; Red Line Shows Lognormal Distribution to YMP TDMS Data (YMP [1996] DTN: LAIT831341AQ96.001); Green Line Shows YMP Distribution (Table 9-10)

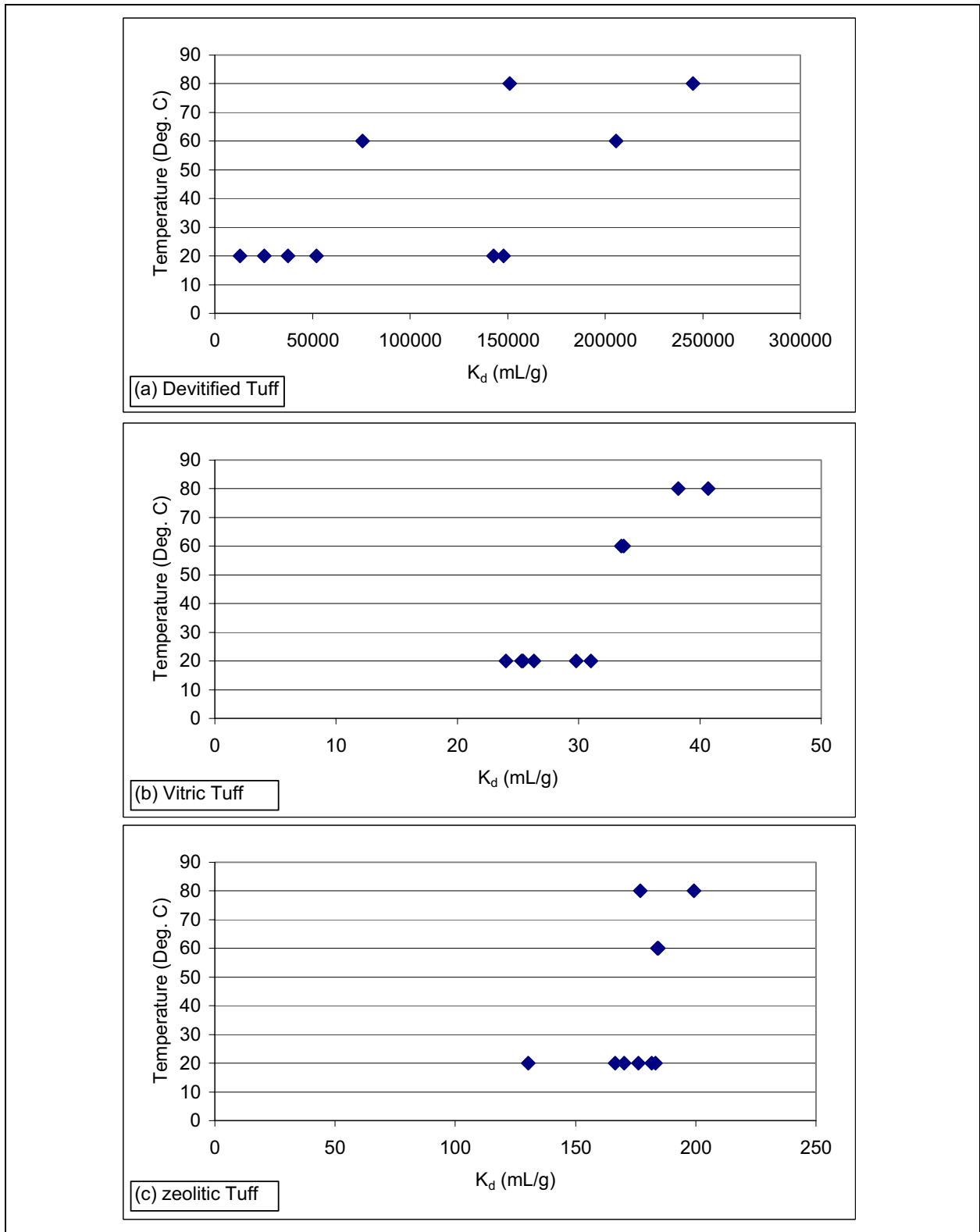
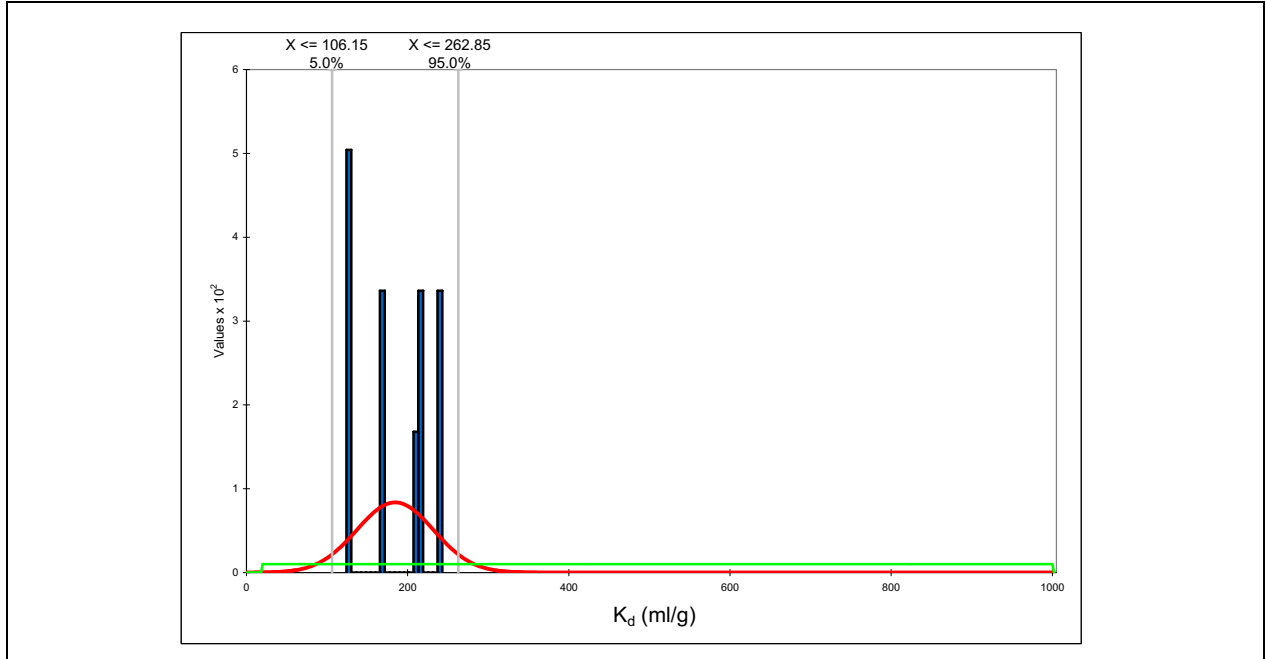


Figure 9-28
 Temperature Dependence of Sr K_d for (a) Devitrified Tuff, (b) Vitric Tuff, and (c) Zeolitic Tuff



	Input	Normal
Chi-Squared Rank	N/A	3
Mean	184.5	184.5
Mode	126.98 [est]	184.5
Median	191.5	184.5
Minimum	124	-Infinity
Maximum	243	+Infinity
Standard Deviation	47.636	47.636
μ	N/A	184.5
σ	N/A	47.636

Figure 9-29
Cesium Sorption on Devitrified Tuff in J-13 Water; Red Line Shows Normal Distribution to YMP TDMS Data (YMP [1996] DTN: LAIT831341AQ96.001); Green Line Shows YMP Distribution (Table 9-10)

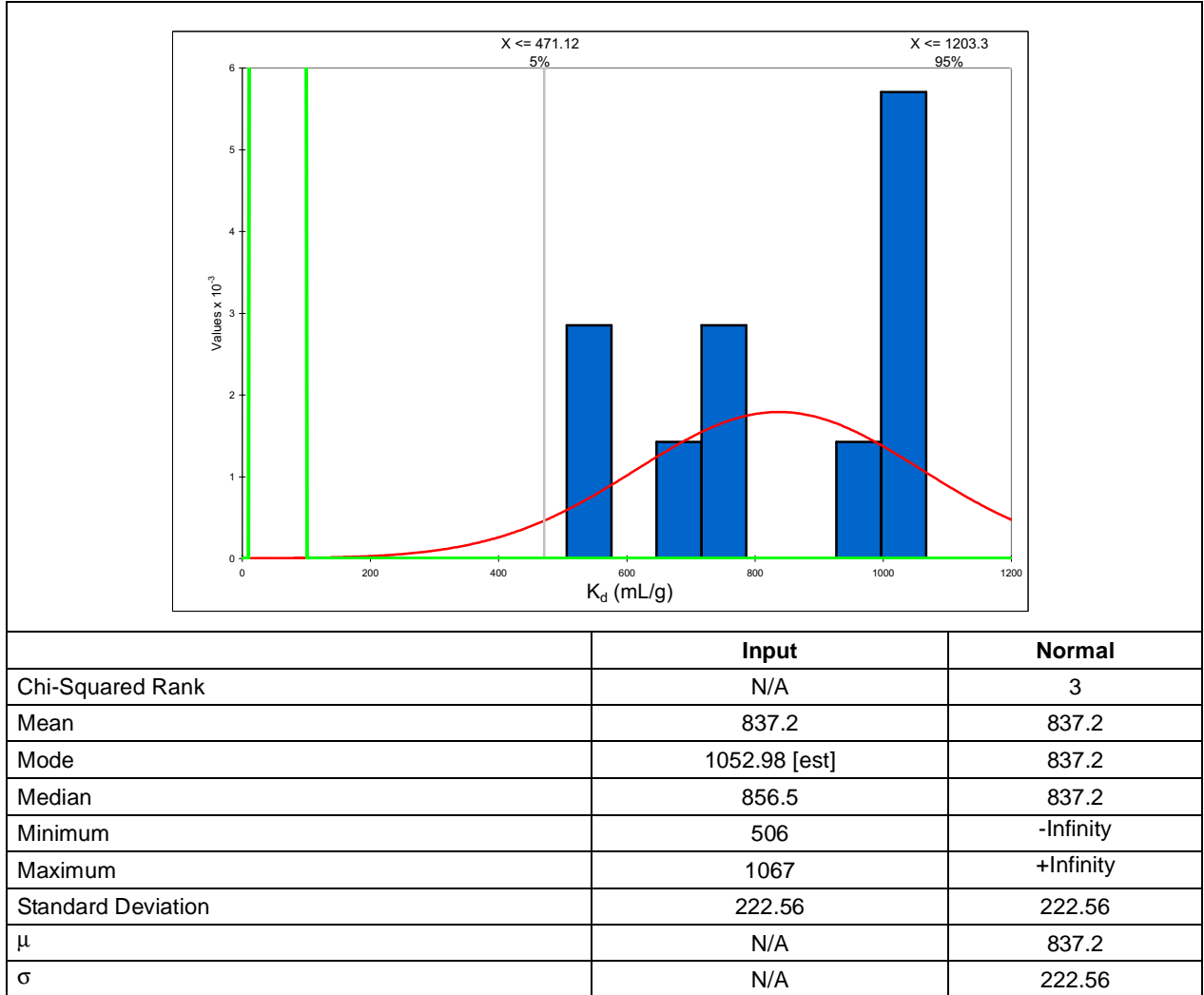
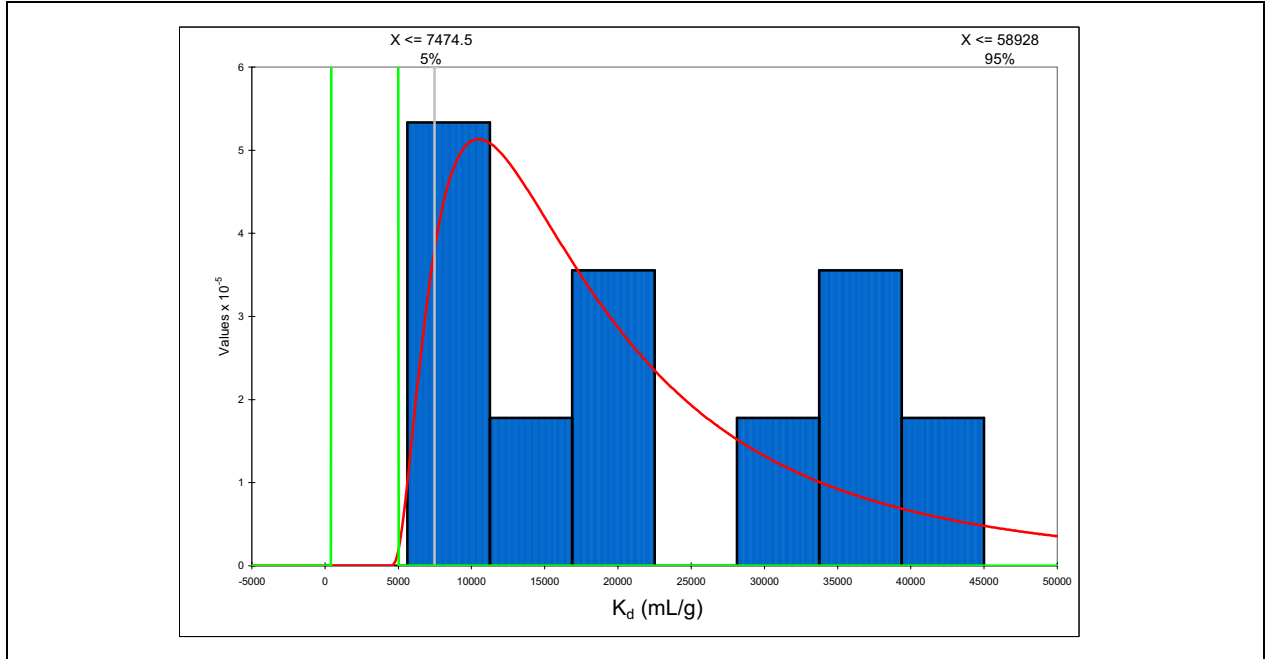


Figure 9-30

Cesium Sorption on Vitric Tuff in J-13 Water; Red Line Shows Normal Distribution to YMP TDMS Data (YMP [1996] DTN: LAIT831341AQ96.001); Green Line Shows YMP Distribution (Table 9-10)



	Input	Lognormal (Format 1)
Chi-Squared Rank	N/A	7
Chi-Squared Rank	N/A	7
Mean	22223	23402
Mode	16924 [est]	10474
Median	18424	17400
Minimum	7353	4357.1
Maximum	42158	+Infinity
Standard Deviation	12733	20265
Shift	N/A	4357
μ	N/A	19045
σ	N/A	20265

Figure 9-31
Cesium Sorption on Zeolitic Tuff in J-13 Water; Red Line Shows Lognormal Distribution to YMP TDMS Data (YMP [1996] DTN: LAIT831341AQ96.001); Green Line Shows YMP Distribution (Table 9-10)

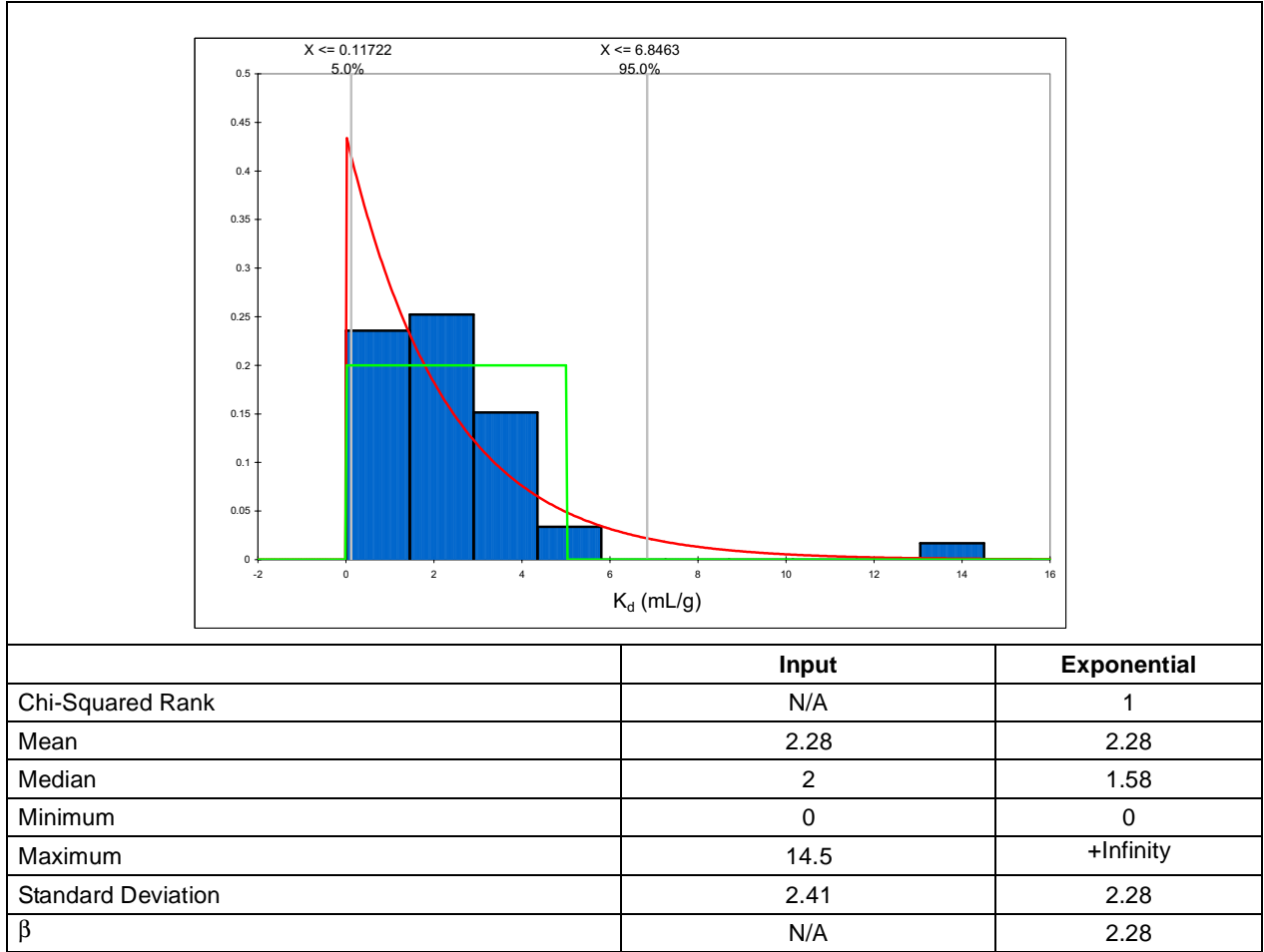


Figure 9-32
Uranium Sorption on Devitrified Tuff in J-13 Water; Red Line Shows Exponential Distribution to YMP TDMS Data (YMP [1996] DTN: LAIT831341AQ96.001); Green Line Shows YMP Distribution (Table 9-10)

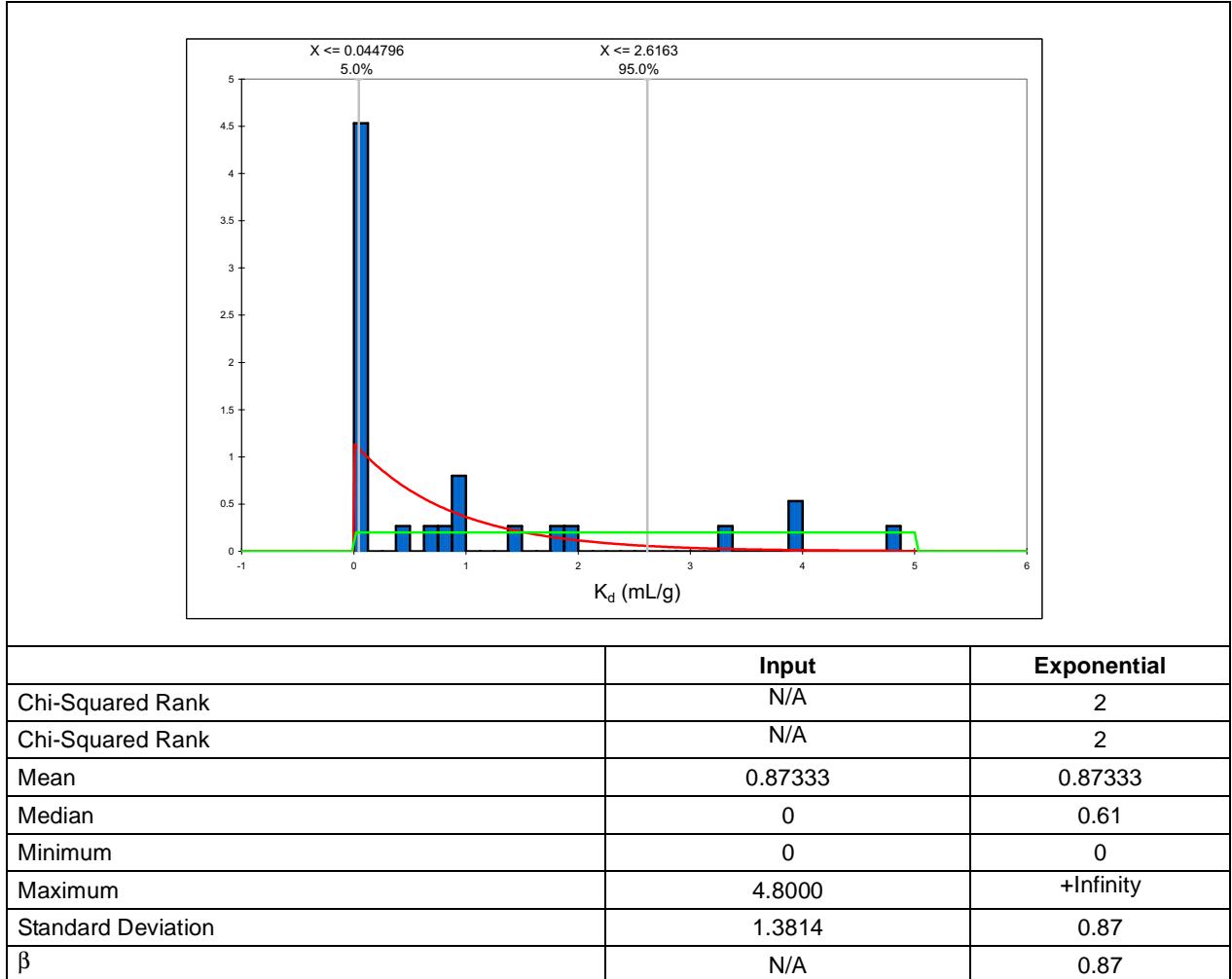


Figure 9-33
Uranium Sorption on Devitrified Tuff in p#1 Water; Red Line Shows Exponential Distribution to YMP TDMS Data (YMP [1996] DTN: LAIT831341AQ96.001); Green Line Shows YMP Distribution (Table 9-10)

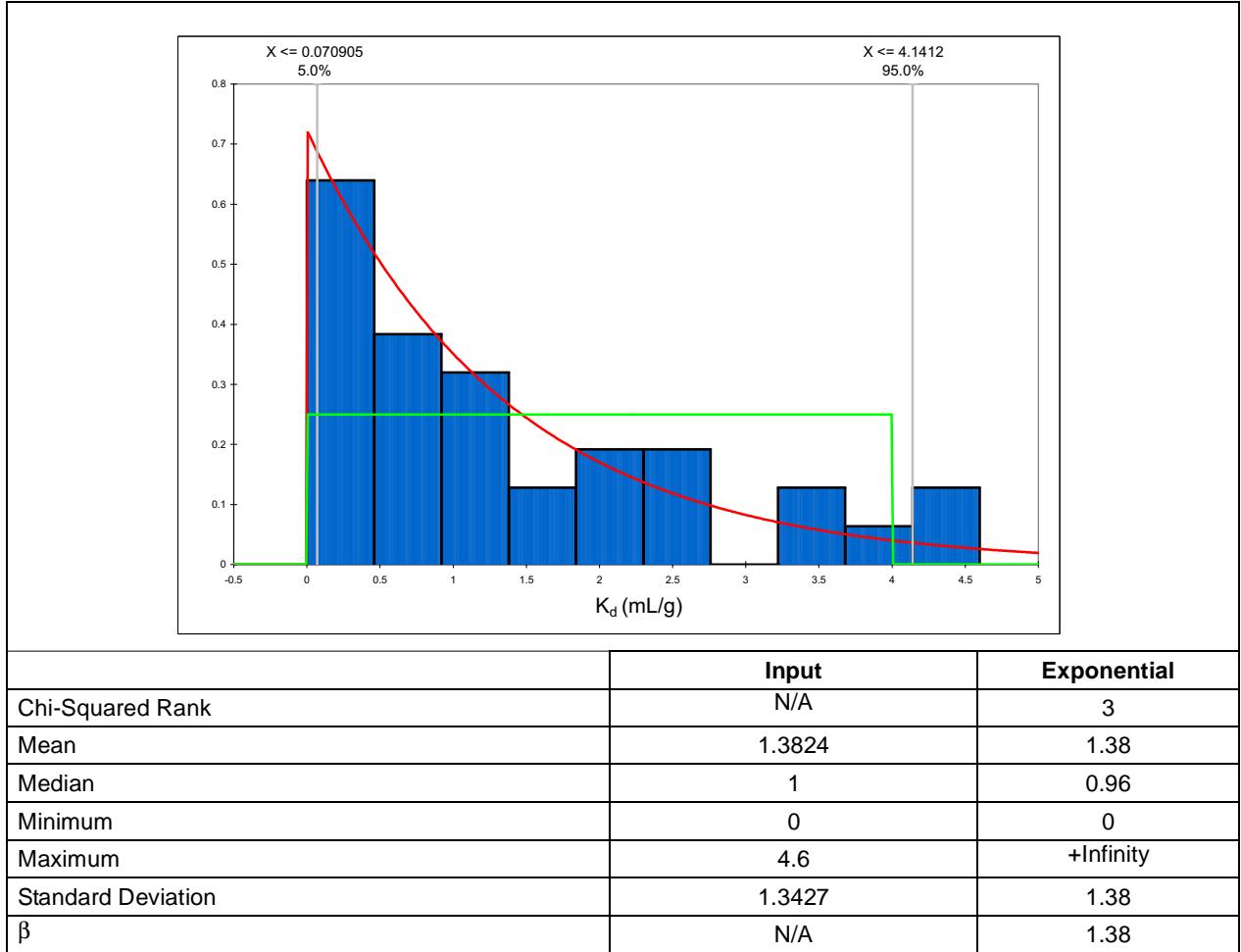


Figure 9-34
Uranium Sorption on Vitric Tuff in J-13 Water; Red Line Shows Exponential Distribution to YMP
TDMS Data (YMP [1996] DTN: LAIT831341AQ96.001); Green Line Shows YMP Distribution
(Table 9-10)

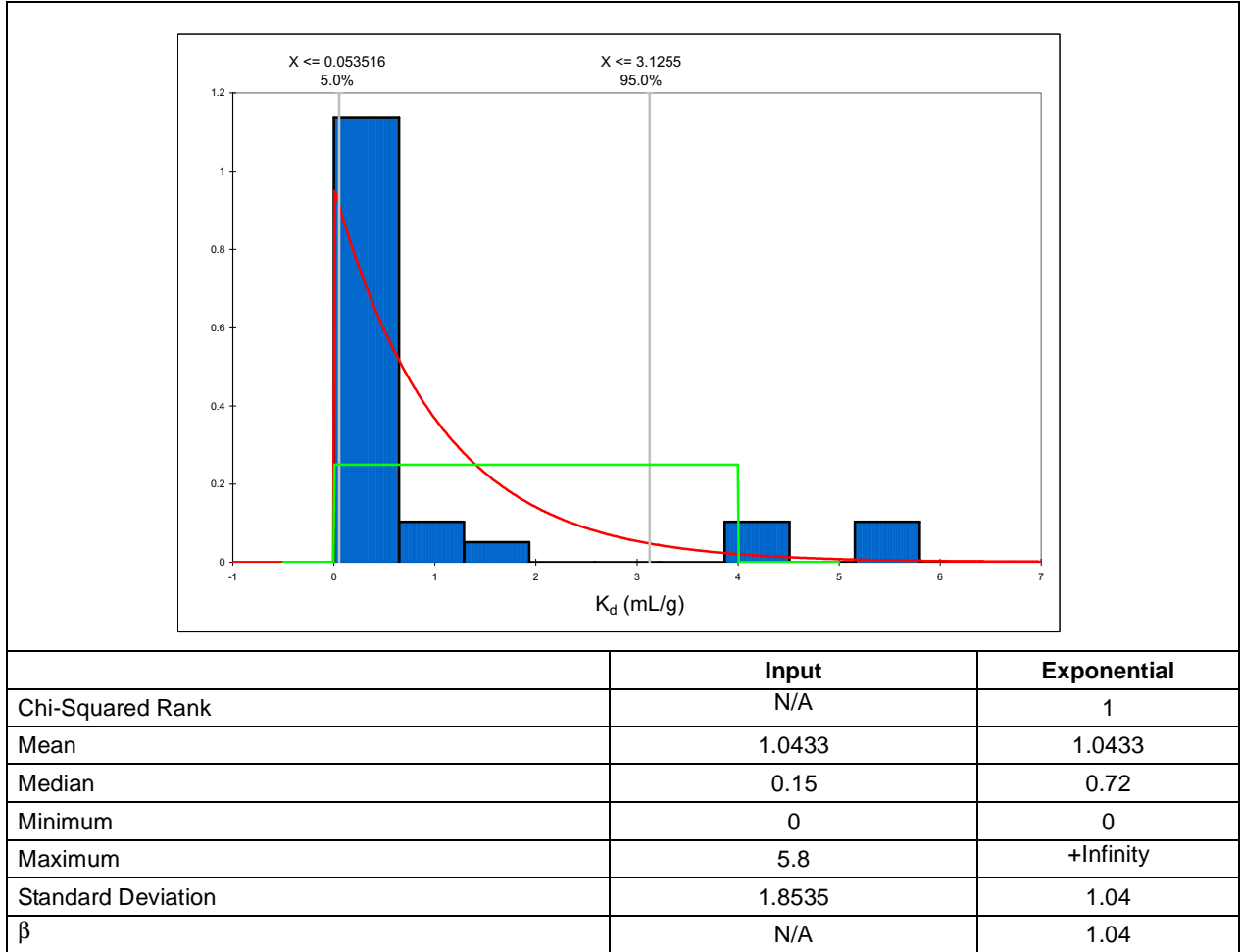


Figure 9-35
Uranium Sorption on Vitric Tuff in p#1 Water; Red Line Shows Exponential Distribution to YMP
TDMS Data (YMP [1996] DTN: LAIT831341AQ96.001); Green Line Shows YMP Distribution
(Table 9-10)

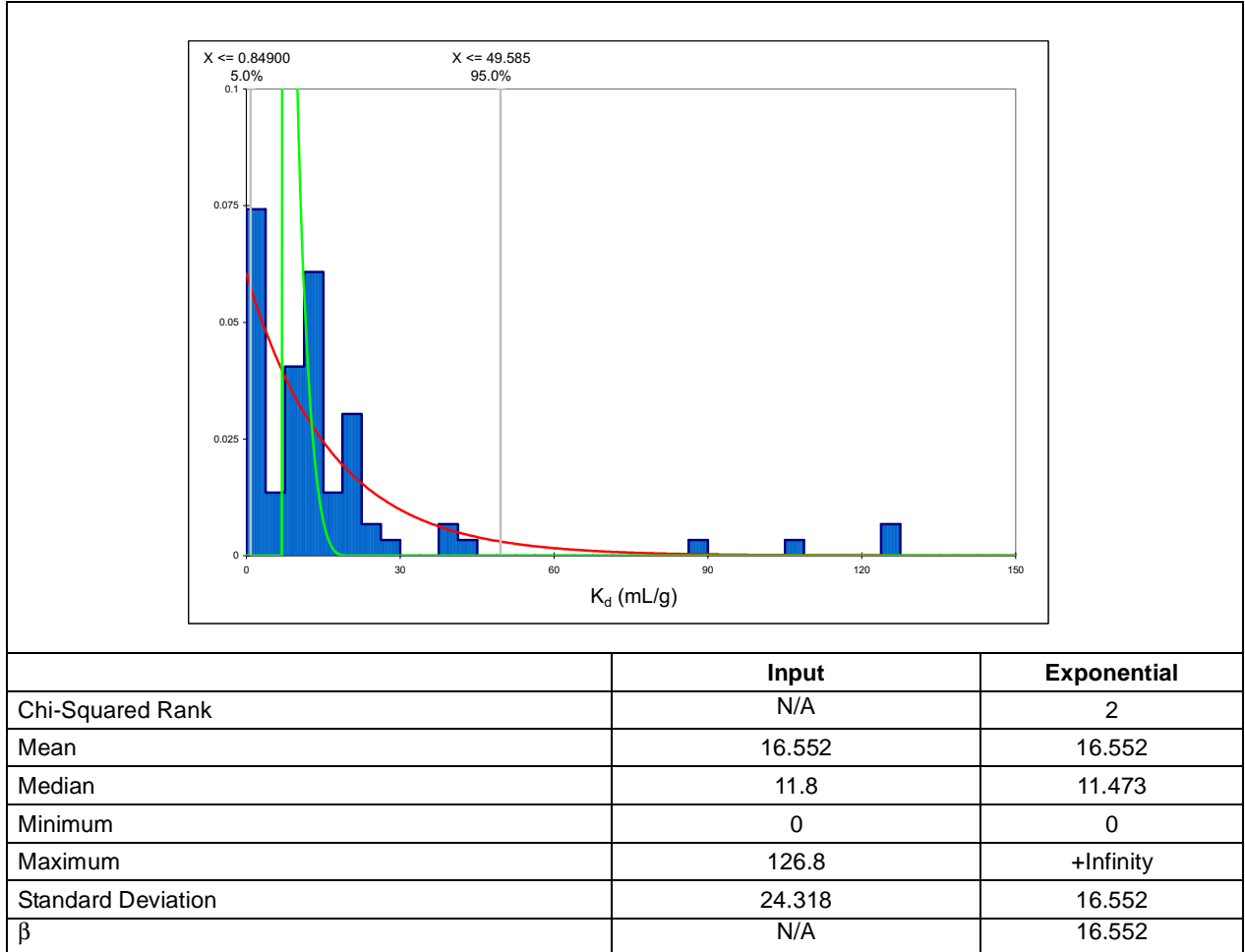


Figure 9-36
Uranium Sorption on Zeolitic Tuff in J-13 Water; Red Line Shows Exponential Distribution to YMP TDMS Data (YMP [1996] DTN: LAIT831341AQ96.001); Green Line Shows YMP Distribution (Table 9-10)

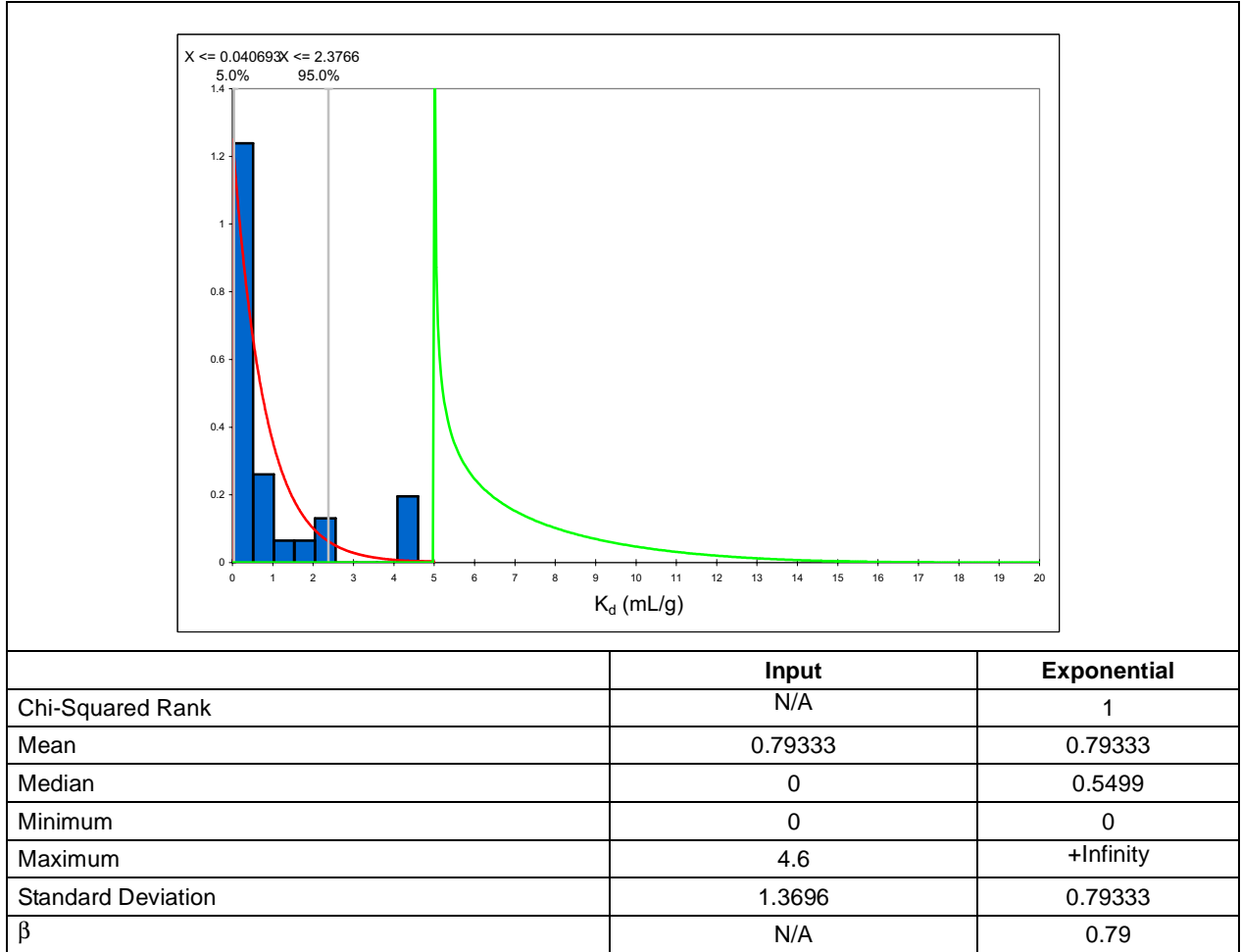


Figure 9-37
Uranium Sorption on Zeolitic Tuff in p#1 Water; Red Line Shows Exponential Distribution to YMP TDMS Data (YMP [1996] DTN: LAIT831341AQ96.001); Green Line Shows YMP Distribution (Table 9-10)

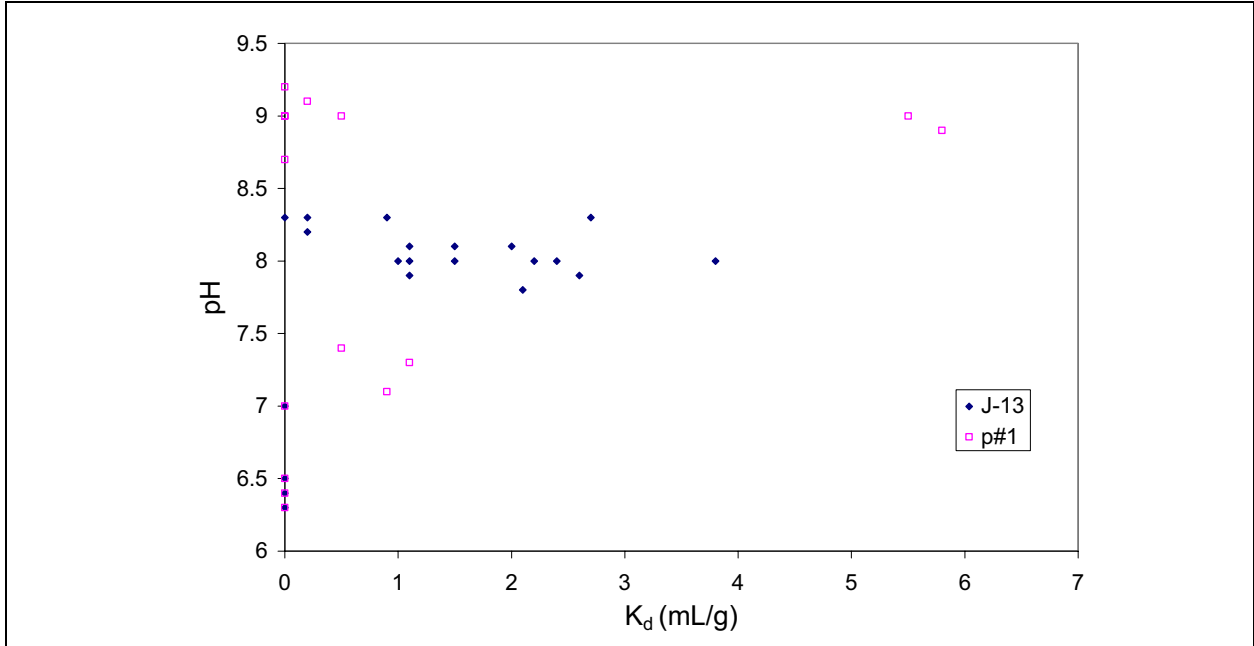


Figure 9-38
pH and K_d Relationships for U Sorption on Vitric Tuff in p#1 and J-13 Water

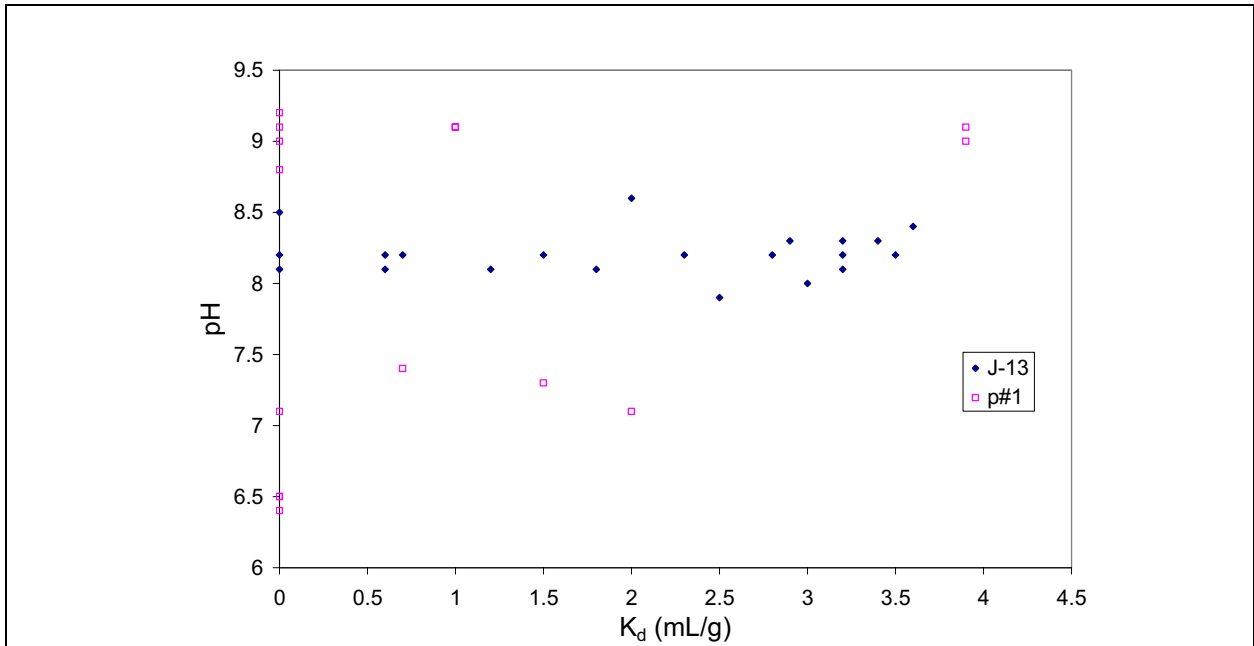


Figure 9-39
pH and K_d Relationships for U Sorption on Devitrified Tuff in p#1 and J-13 Water

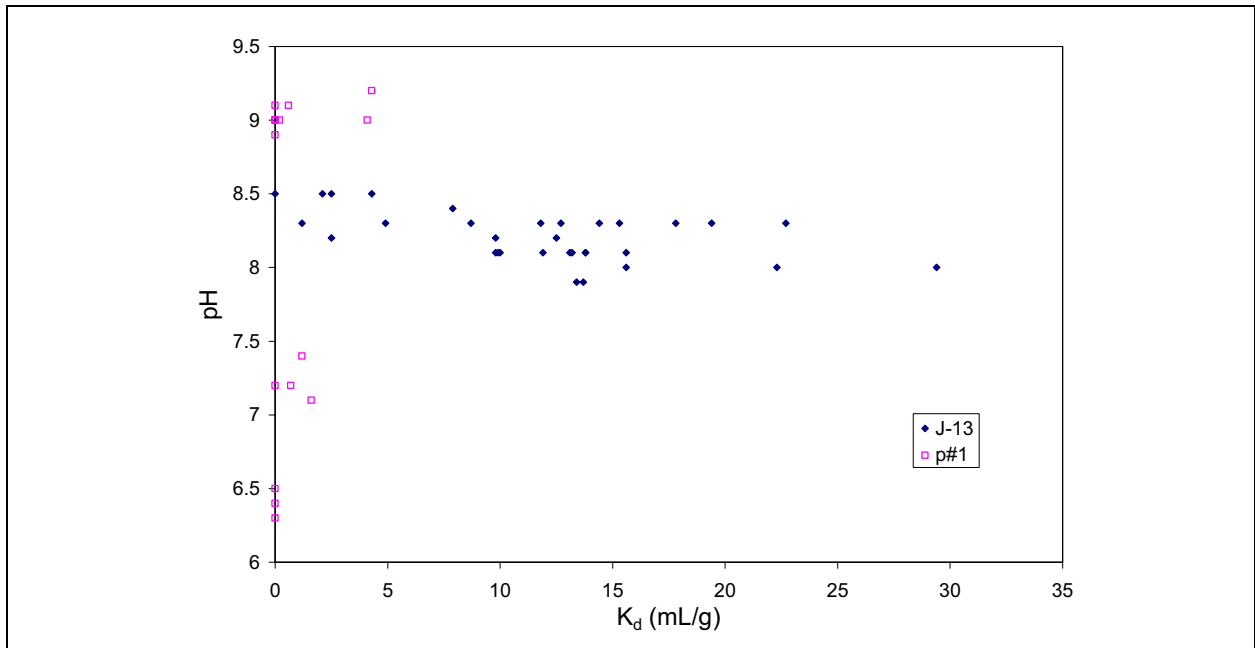


Figure 9-40
pH and K_d Relationships for U Sorption on Zeolitic Tuff in p#1 and J-13 Water

Table 9-1
Descriptions of Stratigraphy, Hydrogeologic Units (HGUs), Lithology,
and Alteration Considered in This Section
 (Page 1 of 2)

Stratigraphy	Hydrogeologic Units	Lithology/Rock type
unk = unknown	AA = Alluvial aquifer	AL = alluvium
Tgs = Tertiary sediments	WTA = Welded tuff aquifer	BD = basaltic dike
Tt = Thirsty Canyon Group	VTA = Vitric Tuff aquifer	BS = basalt
Ttt = Trail Ridge Tuff	LFA = Lava flow aquifer	BED = bedded tuff
Ttp = Pahute Mesa and Rocket Wash Tuffs	TCU = Tuff confining unit	DM = dolomite
Tf = Volcanics of Fortymile Canyon	CCU = Clastic confining unit	DWT = densely welded tuff
Tfb = Beatty Wash Formation		FB = flow breccia
Tm = Timber Mountain Group	Major Alteration	IN = intrusive
Tma = Ammonia Tanks Tuff	KA = kaolinitic	ITL = intermediate to trachytic lava
Tmr = Rainier Mesa Tuff	KF = potassic	LA = lava
Tmrf = Rhyolite of Fluorspar Canyon	MP = microporphyritic (holocrystalline)	MWT = moderately welded tuff
Tmt = Basalt of Tierra	OP = opalline	NWT = nonwelded tuff
Tmat = Rhyolite of Tannebaum Hill	PI = pilotaxitic (holocrystalline)	PL = pumiceous (frothy) lava
Tmrx = Landslide or eruptive breccia	PY = pyritic	PWT = partially welded tuff
Tmaw = Tuff of Buttonhook Wash	QC = silicic (chalcedony)	QTZ = quartzite or sandstone
Tp = Paintbrush Group	QF = quartzo-feldspathic	RWT = reworked tuff
Tpb = Rhyolite of Benham	QZ = silicic	SLT = siltstone
Tpc = Tiva Canyon Tuff	SE = seriate (holocrystalline)	TS = tuffaceous sandstone
Tpd = Rhyolite of Delirium Canyon	unk = unknown	TUF = tuff
Tpe = Rhyolite of Echo Peak	VP = devitrified (vapor phase)	TB = tuff breccia
Tpr = Rhyolite of Silent Canyon	ZA = zeolitic (analcime)	unk = unknown
Tpt = Topopah Spring Tuff	ZC = zeolitic (clinoptilolite)	VT = vitrophyric tuff
Th = Calico Hills Formation	ZE = zeolitic	WBE = welded bedded tuff
Tc = Crater Flat Group	ZM = zeolitic (mordenite)	WT = welded tuff
Tcp = Prow Pass Tuff		
Tci = Rhyolite of Inlet		
Tcj = Andesite of Grimy Gulch		
Tcpc = Rhyolite of Kearsarge		
Tcb = Bullfrog Tuff		
Tct = Tram Tuff		
Tb = Belted Range Group		

Table 9-1
Descriptions of Stratigraphy, Hydrogeologic Units (HGUs), Lithology,
and Alteration Considered in This Section
 (Page 2 of 2)

Stratigraphy	Hydrogeologic Units	Lithology/Rock type
Tbd = Deadhorse Flat Formation		
Tq = Volcanics of Quartz Mountain		
To = Volcanics of Oak Spring Butte		
Ton = Older tunnel beds		
Tor = Redrock Valley Tuff		
Tot = Tuff of Twin Peaks		

Table 9-2
Theoretically Computed Matrix K_d Distributions by Stratigraphy
(Data from Zavarin et al. 2002)
 (Page 1 of 2)

Stratigraphy	N	Am	Ca	Cs	Eu	Np	-
Tcb	2	Range(16712.3,16712.3)	Range(2612,2612)	Range(2112.2,2112.2)	Range(5662.8,5662.8)	Range(3.2,3.2)	-
Tcbp	2	Range(954.9,954.9)	Range(1529.5,2637.8)	Range(5725.6,12101.7)	Range(323.5,323.5)	Range(0.1,0.1)	-
Tcby	47	Exp(2964.2)	Lognorm(1484.5,25636)	Lognorm(7252.8,13979)	Exp(1040.4)	Exp(1.5)	-
Tcl	1	Range(9549.9)	Range(178.4)	Range(9233.6)	Range(3235.9)	Range(1.8)	-
Tcp	32	Exp(4329.6)	Lognorm(2107.7,27364)	Exp(2249.3)	Exp(1475.5)	Exp(0.9)	-
Tct	55	Exp(9234.2)	Lognorm(365.6,1310.4)	Exp(9469.2)	Exp(3207.6)	Exp(2.3)	-
Tp	3	Range(0,0)	Range(2707.1,3383.9)	Range(2150.3,27882)	Range(0,0)	Range(0,0)	-
Tpb	7	Exp(3001.4)	Exp(2376.1)	Exp(32993)	Exp(1017)	Exp(0.6)	-
Tpcp	12	Exp(1037.7)	Exp(26.5)	Exp(325.7)	Exp(354.3)	Exp(0.3)	-
Tpcr	4	Range(0,50.2)	Range(0,22.6)	Range(0,25415.4)	Range(0,60.3)	Range(0,1.2)	-
Tpd	11	Exp(1917)	Lognorm(3178.5,3666.6)	Exp(5843.8)	Exp(652.5)	Exp(0.4)	-
Tpe	2	Range(2965.4,6684.9)	Range(1139.1,2796.4)	Range(2236.3,4539.5)	Range(1091.5,2265.1)	Range(1.3,3.1)	-
Tpg	7	Exp(8639.1)	Lognorm(358.4,866.6)	Exp(1147.4)	Exp(2945.8)	Exp(1.8)	-
Tpp	22	Exp(8333.3)	Lognorm(1385.2,7192.2)	Lognorm(7177.5,2785.4)	Exp(3084.1)	Exp(3)	-
Tptb	2	Range(0,0)	Range(279.9,3543.1)	Range(1673.6,2814.4)	Range(0,0)	Range(0,0)	-
Tptbp	1	Range(4774.9)	Range(3140.6)	Range(2505.3)	Range(1617.9)	Range(0.9)	-
Tptbr	6	Exp(27257)	Exp(1143.7)	Exp(4596.5)	Exp(9453.8)	Exp(6.4)	-
Tptp	82	Exp(3508.9)	Exp(494.5)	Exp(1451)	Exp(1288.9)	Exp(1.3)	-
Tptq	1	Range(16488)	Range(106.4)	Range(116.4)	Range(6494.8)	Range(7.6)	-
Tptr	12	Lognorm(3129.4,27456)	Lognorm(59.4,170.3)	Lognorm(14116,68310)	Lognorm(665.1,2087.3)	Lognorm(0.7,0.6)	-
Tpy	4	Range(0,47749.6)	Range(0,353.9)	Range(0,388.1)	Range(0,16179.6)	Range(0,17)	-

Table 9-2
Theoretically Computed Matrix K_d Distributions by Stratigraphy
(Data from Zavarin et al. 2002)
 (Page 2 of 2)

Stratigraphy	N	Pu (10^{-5}) ^a	Pu (10^{-10}) ^a	Pu (10^{-15}) ^a	Sm	Sr	U
Tcb	2	Range(14.8,14.8)	Range(32.5,32.5)	Range(159.6,159.6)	Range(8185.3,8185.3)	Range(1514.4,1514.4)	Range(7.4,7.4)
Tcbp	2	Range(0.8,0.8)	Range(1.8,1.8)	Range(9.1,9.1)	Range(467.7,467.7)	Range(903.3,1553.2)	Range(0.4,0.4)
Tcby	47	Exp(4.4)	Exp(11)	Exp(61.1)	Exp(1509.3)	Lognorm(852,14243)	Exp(7.7)
Tcl	1	Range(8.5)	Range(18.6)	Range(91.2)	Range(4677.3)	Range(94.8)	Range(4.2)
Tcp	32	Exp(4)	Exp(8.9)	Exp(44.1)	Exp(2138.8)	Lognorm(1229,17375)	Exp(2.4)
Tct	55	Exp(8.7)	Exp(19.5)	Exp(97.6)	Exp(4707.9)	Lognorm(189.8,669.7)	Exp(5.5)
Tp	3	Range(0,0)	Range(0,0)	Range(0,0)	Range(0,0)	Range(1594,1992.5)	Range(0,0)
Tpb	7	Exp(2.7)	Exp(5.9)	Exp(28.7)	Exp(1470)	Exp(1406.3)	Exp(1.3)
Tpcp	12	Exp(1.1)	Exp(2.5)	Exp(12.8)	Exp(512.2)	Exp(14.3)	Exp(1)
Tpcr	4	Range(0,2.5)	Range(0,7.4)	Range(0,46.8)	Range(0,87.3)	Range(0,22.6)	Range(0,9.1)
Tpd	11	Exp(1.7)	Exp(3.8)	Exp(18.4)	Exp(946.1)	Lognorm(2008.6,2747.9)	Exp(0.9)
Tpe	2	Range(5.9,7.5)	Range(13,20.4)	Range(63.8,121.1)	Range(1577.8,3274.1)	Range(668.1,1637.2)	Range(2.9,19.5)
Tpg	7	Exp(7.7)	Exp(16.9)	Exp(83.1)	Exp(4276.4)	Lognorm(189,556.9)	Exp(3.8)
Tpp	22	Exp(8)	Exp(18)	Exp(90.4)	Exp(4714.2)	Lognorm(825.4,4794.2)	Exp(4)
Tptb	2	Range(0,0)	Range(0,0)	Range(0,0)	Range(0,0)	Range(165.3,2086.3)	Range(0,0)
Tptbp	1	Range(4.2)	Range(9.3)	Range(45.6)	Range(2338.6)	Range(1842.5)	Range(2.1)
Tptbr	6	Exp(24.8)	Exp(54.5)	Exp(269.1)	Exp(13880)	Exp(637)	Exp(12.3)
Tptp	82	Exp(3.7)	Exp(8.4)	Exp(43.1)	Exp(1956.2)	Exp(286.9)	Exp(2.8)
Tptq	1	Range(16.3)	Range(36.7)	Range(186.3)	Range(10290.1)	Range(42.2)	Range(6.3)
Tptr	12	Exp(2)	Lognorm(5.3,5.1)	Exp(27.6)	Lognorm(993.3,3098.4)	Lognorm(31.3,70.5)	Exp(3.3)
Tpy	4	Range(0,42.5)	Range(0,93.1)	Range(0,456)	Range(0,23386.7)	Range(0,140.9)	Range(0,21.3)

^a - For Pu, oxygen fugacities of 1E-5, 1E-10, and 1E-15 are considered as they affect the speciation and valence of Pu

Table 9-3
Predicted Average Log K_d for Selected Regional Hydrostratigraphic Units
from Zavarin et al. (2002)^{a, b}

	TMA			TC			TCB			TBA			BCU			BAQ		
	E(x)	Min	Max	E(x)	Min	Max	E(x)	Min	Max	E(x)	Min	Max	E(x)	Min	Max	E(x)	Min	Max
Ca	2.7	2.7	2.7	2.6	2.6	2.6	2.8	2.8	2.8	2.2	2.2	2.2	2.3	2.3	2.3	2.7	2.7	2.7
Cs	3.4	2.5	3.4	3.5	2.5	3.5	3.6	2.6	3.6	3.6	2.6	3.6	3.6	2.7	3.6	3.6	2.7	3.6
Sr	2.4	2.4	2.4	2.3	2.3	2.3	2.5	2.5	2.5	1.9	1.9	1.9	2.1	2.1	2.1	2.4	2.4	2.4
Am	3.3	3.0	3.6	3.4	3.1	3.7	2.6	2.4	3.0	3.8	3.6	4.2	4.0	3.8	4.4	4.0	3.8	4.4
Eu	2.8	2.4	3.3	2.9	2.5	3.4	2.2	1.7	2.7	3.4	2.9	3.9	3.6	3.1	4.1	3.6	3.1	4.1
Sm	3.0	2.5	3.5	3.1	2.7	3.6	2.4	1.9	2.9	3.6	3.2	4.1	3.8	3.3	4.3	3.8	3.4	4.3
Np	-0.1	-0.3	0.3	0.0	-0.3	0.3	-0.3	-0.5	0.1	0.4	0.1	0.8	0.6	0.2	0.9	0.6	0.3	1.0
U	0.4	0.0	0.8	0.4	0.1	0.9	0.3	-0.1	0.7	0.6	0.3	1.1	0.8	0.4	1.2	0.8	0.4	1.2
Pu-5	0.4	-0.1	0.8	0.4	0.0	0.9	0.0	-0.4	0.5	0.8	0.4	1.3	1.0	0.5	1.5	1.0	0.6	1.5
Pu-10	0.7	0.2	1.2	0.8	0.3	1.3	0.4	-0.1	0.9	1.2	0.7	1.7	1.4	0.9	1.9	1.4	0.9	1.9
Pu-15	1.4	0.9	1.9	1.5	1.0	2.0	1.1	0.7	1.6	1.9	1.4	2.4	2.1	1.6	2.5	2.1	1.6	2.6

^aMin and Max based solely on variations in mineral abundances.

^bSee Table 2-2 for description of regional HSUs.

Table 9-4
Predicted Radionuclide K_d s (mL/g) for Frenchman Flat Alluvium
by Zavarin et al. (2002)

Radionuclide	Frenchman Flat Alluvium Log (K_d)		
	E(x) ^a	Minimum	Maximum
Am	3.7	3.4	4.1
Ca	2.4	2.4	2.4
Cs	3.7	2.7	3.7
Eu	3.1	2.7	3.6
Np	0.7	0.3	1.1
Pu ($O_2 = 10^{-5}$) ^b	0.9	0.4	1.4
Pu ($O_2 = 10^{-10}$) ^c	1.3	0.8	1.8
Pu ($O_2 = 10^{-15}$) ^d	1.9	1.4	2.3
Sm	3.4	2.9	3.8
Sr	2.18	2.18	2.18
U	0.4	-0.3	0.8

^aExpected value of variable x

^b K_d computed using an $O_2(g)$ fugacity of 10^{-05} bars where Pu(V) dominates

^c K_d computed using an $O_2(g)$ fugacity of 10^{-10} bars where Pu(V) dominates

^d K_d computed using an $O_2(g)$ fugacity of 10^{-15} bars where Pu(V) dominates

Table 9-5
Cs K_d s Reported by Papelis and Um (2002) for Crushed Pahute Mesa Material
and for Intact Plugs Used in Diffusion Experiments

Sample	Lithology ^a	Major Alteration ^a	HGU ^a	HSU ^a	Batch Sorption (mL/g)	Batch Desorption (mL/g)	Ratio	From Diffusion Study (mL/g)	Notes
UE18R 2228 F	MWT	DV	WTA	TMCM	144.0	1050.0	7.3		
UE18R 2228 M	MWT	DV	WTA	TMCM	66.7	637.0	9.6	1.1	
UE20C 2908	PWT	DV	WTA	TSA	172.0	871.0	5.1	1.4	Hi smectite
UE20C 2855 M	MWT	DV	WTA	TSA	117.0	287.0	2.5	0.5	
UE20C 2855 F	MWT	DV	WTA	TSA	162.0	448.0	2.8	1.6	
PM-1 4823 M	NWT	AB	TCU	BFCU	71.1	144.0	2.0	0.7	Hi smectite
PM-1 4823 F	NWT	AB	TCU	BFCU	266.0	320.0	1.2		Hi smectite
PM-2 4177	Lava	unk	LFA	PBRCM	220.0	240.0	1.1		Hi smectite

^aSee Table 9-1 for definitions.

pH = 8.3, other experimental conditions not reported

All solids were crushed prior to experimentation

F indicates a sample that included a fracture and matrix material

M indicates samples with matrix material only

Table 9-6
Pb K_d s Reported by Papelis and Um (2002) for Crushed Pahute Mesa Material
and for Intact Plugs Used in Diffusion Experiments

Sample	Lithology ^a	Major Alteration ^a	HGU ^a	HSU ^a	Batch Sorp (mL/g)	Batch Desorp (mL/g)	Ratio	From Diffusion Study (mL/g)	Notes
UE18R 2228 F	MWT	DV	WTA	TMCM	3160.0	4120.0	1.3	868.0	
UE18R 2228 M	MWT	DV	WTA	TMCM	1320.0	3280.0	2.5	671.0	
UE20C 2908	PWT	DV	WTA	TSA	3220.0	5380.0	1.7	2880.0	Hi smectite
UE20C 2855 M	MWT	DV	WTA	TSA	854.0	2250.0	2.6	724.0	
UE20C 2855 F	MWT	DV	WTA	TSA	1320.0	2570.0	1.9	1170.0	
PM-1 4823 M	NWT	AB	TCU	BFCU	4740.0	5700.0	1.2	3910.0	Hi smectite
PM-1 4823 F	NWT	AB	TCU	BFCU	4270.0	3580.0	0.8	3290.0	Hi smectite
PM-2 4177	Lava	Unk	LFA	PBRCM	5090.0	10600.0	2.1	3520.0	Hi smectite

^aSee Table 9-1 for definitions.

pH = 8.3, other experimental conditions not reported

All solids were crushed prior to experimentation

F indicates a sample that included a fracture and matrix material

M indicates samples with matrix material only

Table 9-7
Sr and Pb K_d s Reported by Um and Papelis (2001b) for
Zeolitized Tuff from Rainier Mesa

Metal	Ionic Strength (Molar)	K_d (Sorption) (mL/g)	K_d (Desorption) (mL/g)
Sr	0.01	3,900	4,900
Sr	0.1	420	810
Pb	0.01	94,000	640,000
Pb	0.1	87,000	320,000
Pb	1	1,600	4,700
Pb	1	260	710

Table 9-8
Sr and Pb K_d s Reported by Sloop (1998) for Zeolitized Tuff from Rainier Mesa

Metal	Ionic Strength (Molar)	pH	K_d (Sorption) (mL/g)
Pb	1	7	1.24e3
Pb	1	8	3.87e3
Pb	1	9	8.06e3
Sr	0.1	7, 8, 9	1.92e2
Sr	0.01	7, 8, 9	2.5e3

Table 9-9
Chemical Composition (mg/L) of Water in J-13, p#1,
and Two Locations on Pahute Mesa

Constituent	J-13 Water ^{a, b}	p#1 Water ^{a, b}	PMa ^c	PMb ^d
Sodium	45	171	65	72
Potassium	5.3	13.4	3.4	4
Magnesium	1.8	31.9	0.5	0.2
Calcium	11.5	87.8	10.4	3.1
Silicon	30	30	56	60.5
Fluoride	2.1	3.5	NR	3.14
Chloride	6.4	37	12	16.8
Sulfate	18.1	129	35	34
Bicarbonate	143	698	107	89.5
pH	6.9	6.7	8.2	8.8

^aYMP (1997) DTN: LAIT831361AQ95.003 (SEP Table S98491.002)

^bOgard and Kerrisk (1984) (In Meijer, 1992)

^cPahute Mesa water composition – example 1: Pawloski et al. (2001; Table 6.10), Zavarin et al. (2002)

^dPahute Mesa water composition – example 2: Well ER-20-5 #3 (IT, 2001a).

Table 9-10
YMP Sorption Coefficient Distributions for Saturated Zone Units (Conca, 2000; Table 2b)

Element	Rock type	Min K_d (mL/g)	Max K_d (mL/g)	$E[x]^a$	Covariance ^b	Distribution Type
Americium Actinium Samarium, Zirconium, Niobium, Thorium	Devitrified	100	2,000	—	—	Uniform
	Vitric	100	1,000	400	0.2	Beta
	Zeolitic	100	1,000	—	—	Uniform
	Iron Oxide	1,000	5,000	—	—	Uniform
Pu ^b	Devitrified	5	100	50	0.15	Beta
	Vitric	50	300	100	0.15	Beta
	Zeolitic	50	400	100	0.15	Beta
	Iron Oxide	1,000	5,000	—	—	Uniform
U ^b	Devitrified	0	5	N/A	N/A	Uniform
	Vitric	0	4	N/A	N/A	Uniform
	Zeolitic	5	20	7	0.3	Beta
	Iron Oxide	100	1,000	N/A	N/A	Uniform
	Alluvium	0	8	N/A	N/A	Uniform
Np ^b	Devitrified	0	2	0.5	0.3	Beta
	Vitric	0	2	0.5	1	Beta (exp)
	Zeolitic	0	5	1	0.25	Beta
	Iron Oxide	500	1,000	—	—	Uniform
	Alluvium	0	100	18	1	Beta
Ra	Devitrified	100	500	—	—	Uniform
	Vitric	100	500	—	—	Uniform
	Zeolitic	1,000	5,000	—	—	Uniform
	Iron Oxide	0	1,500	30	1	Beta (exp)
Cs ^{b, c}	Devitrified	20	1,000	—	—	Uniform
	Vitric	10	100	—	—	Uniform
	Zeolitic	500	5,000	—	—	Uniform
	Iron Oxide	0	500	30	1	Beta (exp)
Sr ^{b, c}	Devitrified	10	200	—	—	Uniform
	Vitric	20	50	—	—	Uniform
	Zeolitic	2,000	5,000	—	—	Log uniform
	Iron Oxide	0	30	10	0.25	Beta
Ni	Devitrified	0	200	—	—	Uniform
	Vitric	0	50	—	—	Uniform
	Zeolitic	0	200	—	—	Uniform
	Iron Oxide	0	1,000	—	—	Uniform
Pb ^c	Devitrified	100	500	—	—	Uniform
	Vitric	100	500	—	—	Uniform
	Zeolitic	100	500	—	—	Uniform
	Iron Oxide	100	1,000	—	—	Uniform
Sn	Devitrified	20	200	—	—	Uniform
	Vitric	20	200	—	—	Uniform
	Zeolitic	100	300	—	—	Uniform
	Iron Oxide	0	5,000	—	—	Uniform
Protactinium	Devitrified	0	100	—	—	Uniform
	Vitric	0	100	—	—	Uniform
	Zeolitic	0	100	—	—	Uniform
	Iron Oxide	500	1,000	—	—	Uniform
Selenium ^b	Devitrified	0	1	0.1	1	Beta (exp)
	Vitric	0	1	0.1	1	Beta (exp)
	Zeolitic	0	1	0.2	1	Beta (exp)
	Iron Oxide	0	500	30	1	Beta (exp)

Source: YMP [2000] DTN: LA0003AM831341.001

Sources of Input: Thomas, 1987; Triay et al., 1997; YMP (1996) DTN: LAIT831341AQ96.001, SEP TABLE S97026.009

^aExpected value of variable X

^bQA data available in YMP TDMS (YMP [1996] DTN: LAIT831341AQ96.001) – reevaluated in this study

^cConsidered by Papeis and Um (2002) for some Pahute Mesa rocks

Note: Iron Oxide results presented only for comparison. This report seeks to represent sorption to bulk rock material, not individual phases.

Table 9-11
Carbonate Sorption K_d Ranges

Radionuclide	Dosch and Lynch (1980)	Stout and Carroll (1992)	Perkins et al. (1998)	Total Range
Cs	Range(4,101)	-	-	Range(4,101)
Sr	Range(5,16)	-	-	Range(5,16)
Eu	Range(1E4,4E5)	-	-	Range(1E4,4e5)
Pu	Range(2E3,7E3)	Range(1E2, 1E4)	275	Range(1E2, 1E4)
Am	Range(2E3,2E4)	Range(2E3,3E5)	Range(150,350)	Range(2E3,3E5)
U	Range(2,132)	Range(1E-5, 0.3)	-	Range(0,132)
Np	-	Range(<1E2, 5E3)	-	Range(<1E2, 5E3)

Table 9-12
Summary of Distributions Fit for Pu Sorption Using YMP Data -
Minimum and Maximum of Dataset Listed in Parentheses When Different from Distribution

Rock Type	Water	Exp. Atmos.	Min	Max	Mean	Std Dev	Parameters	Distribution ^a
Vitric	all	all	214	3085	360	362	$\alpha_1 = 0.6$ $\alpha_2 = 5.4$	Beta
Devit	all	all	0	350	55	54	$\alpha_1 = 0.7$ $\alpha_2 = 3.8$	Beta
Zeo	all	all	0	750	240	205	$\alpha_1 = 0.6$ $\alpha_2 = 1.3$	Beta
Vitric	J-13	Air & CO ₂	64	1984 (1810)	704	453	-	Triangular
Vitric	J-13	Air	147	1995 (1810)	763	535	-	Triangular
Vitric	P#1	Air & CO ₂	21	651 (580)	231	148	-	Triangular
Devit	J-13	Air & CO ₂	5.4 (6)	N/A (246)	77	215	$\mu = 72$ $\sigma = 215$	Lognormal
Devit	p#1	Air	4.3 (4.8)	N/A (122)	30	26	b = 26	Exponential
Devit	p#1	CO ₂	-	-	300	-	-	2 Data Points
Zeolitic	J-13	Air & CO ₂	N/A (32)	N/A (516)	265	127	$\alpha = 265$ $\beta = 70$	Logistic
Zeolitic	p#1	Air & CO ₂	0	N/A(739)	89	963	$\mu = 302$ $\sigma = 963$	Lognormal

^aSee Appendix C for distribution definitions.

All data fit for these distributions from YMP [1996] DTN: LAIT831341AQ96.001

Table 9-13
Summary of Distributions Fit for Np Sorption Using YMP Data

Rock Type	Water	Exp. Atmos.	Min	Max	Mean	Std Dev	Parameters	Distribution ^a	Comments
Devit	all	all	0	Inf ^b (30)	1	1	Shift = -3.3	Exponential	
Vitric	all	all	0	Inf (4)	0.62	0.62	Shift = -2.8	Exponential	
Zeolite	all	all	0	Inf (41)	2.5	2.5	Shift = -6.7	Exponential	
Vitric	J-13	Air & CO ₂	0	Inf (3.5)	0.66	0.66	$\beta = 0.66$	Exponential	
Vitric	P#1	Air & CO ₂	0	Inf (4)	0.48	0.49	$\beta = 0.49$	Exponential	
Devit	J-13	Air & CO ₂	0	Inf (3.5)	0.48	0.48	$\beta = 0.48$	Exponential	
Devit	p#1	Air & CO ₂	0	Inf (30)	2.2	2.2	$\beta = 2.2$	Exponential	Temperatures 20-90°C
Devit	p#1	Air & CO ₂	0	Inf (30)	0.23	0.23	$\beta = 0.23$	Exponential	Temperatures 20-25°C, Upper 4 valued (>18) rejected.
Zeolitic	J-13	Air & CO ₂	-2.4 (0)	Inf (6.5)	2.3	1.5	$\mu = 4.7$ $\sigma = 1.5$	Lognormal	T = 20-25°C
Zeolitic	J-13	Air & CO ₂	-1.8 (0)	Inf (8.5)	2.4	1.6	$\mu = 4.3$ $\sigma = 1.6$	Lognormal	T = 20-60°C
Zeolitic	J-13	Air & CO ₂	-1.2 (0)	Inf (13.2)	2.5	1.9	$\mu = 3.8$ $\sigma = 1.9$	Lognormal	T = 20-90°C
Zeolitic	J-13	Air & CO ₂	-Inf (2)	Inf (13.2)	8.3	3.7	$\mu = 8.3$ $\sigma = 3.7$	Normal	T = 90°C
Zeolitic	p#1	Air & CO ₂	0	Inf (32)	1.45	1.47	$\beta = 1.47$	Exponential	T=25-90°C

^aSee Appendix C for distribution definitions.

^bInfinity

Source data for distributions: YMP [1996] DTN: LAIT831341AQ96.001

Table 9-14
Summary of Distributions Fit for Sr Using YMP Data

Rock Type	Water	Exp. Atmos.	Min	Max	Mean	Std Dev	Distribution ^a	Comments
Devit	J-13	Air & CO ₂	0 (24)	Inf (41)	30.8	5.6	Lognormal	T = 20-80 °C
Vitric	J-13	Air & CO ₂	0 (130)	Inf (199)	175	18	Lognormal	T = 20-80 °C
Zeolitic	J-13	Air & CO ₂	Inf (2.4e5)	0 (1.2e4)	1.2e5	1.4e5	Lognormal	T = 20-80 °C

^aSee [Appendix C](#) for distribution definitions.

Source data for distributions: YMP [1996] DTN: LAIT831341AQ96.001

Compare with [Table 9-10](#) for distributions of Conca (2000)

Table 9-15
Summary of Distributions Fit for Cs Using YMP Data

Rock Type	Water	Exp. Atmos.	Min	Max	Mean	Std Dev	Distribution ^a	Comments
Devit	J-13	Air & CO ₂	0 (124)	Inf (243)	185	46	Lognormal	T = 20-80 °C
Vitric	J-13	Air & CO ₂	0 (506)	Inf (1067)	837	223	Lognormal	T = 20-80 °C
Zeolitic	J-13	Air & CO ₂	4357 (7353)	Inf (4.2e4)	17400	20265	Lognormal	T = 20-80 °C

^aSee [Appendix C](#) for distribution definitions.

Source data for distributions: YMP [1996] DTN: LAIT831341AQ96.001

Compare with [Table 9-10](#) for distributions of Conca (2000)

Table 9-16
Summary of Distributions Fit for U Using YMP Data

Rock Type	Water	Exp. Atmos.	Min	Max	Mean	Std Dev	Distribution ^a	Comments
Devit	J-13	Air & CO ₂	0	Inf (14.5)	2.28	2.28	Exponential	T = 20-80 °C
Devit	p#1	Air & CO ₂	0	Inf (4.8)	0.87	0.87	Exponential	T = 20-80 °C
Vitric	J-13	Air & CO ₂	0	Inf (4.6)	1.38	1.38	Exponential	T = 20-80 °C
Vitric	p#1	Air & CO ₂	0	Inf (5.8)	1.04	1.04	Exponential	T = 20-80 °C
Zeolitic	J-13	Air & CO ₂	0	Inf (126)	16.5	16.5	Exponential	T = 20-80 °C
Zeolitic	p#1	Air & CO ₂	0	Inf (4.6)	0.79	0.79	Exponential	T = 20-80 °C

^aSee [Appendix C](#) for probability distribution definitions.

Source data for distributions: YMP [1996] DTN: LAIT831341AQ96.001

Compare with [Table 9-10](#) for distributions of Conca (2000)

Table 9-17
HSUs and Corresponding HGUs, Alteration, Lithology, and Stratigraphy^a
 (Page 1 of 3)

HSU Number	HSU Name ^b	HGUs ^c	Representative Alteration	Lithologies Encountered	Stratigraphy	Summary of Alterations Contributing K _d Distributions
1	LCCU	CCU		SLT/QTZ/SS		Carbonate/Clay
2	LCA	CA		DM		Carbonate
3	UCCU	CCU/SCU		SLT	MDc	Carbonate/Clay
4	LCCU1	CCU/SCU		SLT/QTZ/SS	CZw	Carbonate/Clay
5	LCA3	CA		DM	DSsi	Carbonate
6	MGCU	GCU				Granite
7-12	SCICU, CHICU, CCICU, RMICU, ATICU, BMICU	IICU				
13	PBRM	TCU, WTA, LFA	ZE, DV, QC, AR, AB	NWT, BED, PWT, MWT, DWT, TB, FB, LA, IN	bgb, Tbq, Tln, Tn, Tn3D, Tn4AF, Tn4J, Tn4K, To, Toa, Toh, Ton2, Tor, Tot, Toy, Tq, Tqh, Tqj, Tqm, Tqu, Trg, Trl, Trpd, Trr, Tub, unk	Zeolitic tuff, Devitrified tuff Lava
14	BRA	LFA, WTA, TCU, VTA,	DV, ZC, ZE, AB, PY, QC, KF	LA, FB, BED, NWT, MWT, PWT, DWT, PL	QTa, Tbd, Tbdb, Tdbc, Tbdk, Tbdl, Tbds, Tbg, Tbgb, Tbgm, Tbgp, Tbgr, Tbgs, Tbq, Tcl, Tn4JK, Trl, Trr, unk	Lava, Devitrified tuff Zeolitic tuff
15	BFCU	TCU	ZE, ZC, DV	BED, NWT, LA	Tbdl, Tcblp, Tcblr, Tcbp, Tcbr, Tcbs, Tcbx, Tct	Zeolitic tuff Lava
16	KA	LFA, TCU	DV, GL, ZE, ZC	LA, FB, PL	Tcg, Tcpk	Lava Zeolitic tuff
17	CFCU	TCU, LFA, VTA	ZC, ZE, DV, GL	LA, NWT, BED	Tcg, Tci, Tcj, Tcpc, Tcps, Tcu, unk	Zeolitic tuff Lava Vitric tuff
18	CFCM	Mostly LFA , some TCU	DV, QF, AR, PY, CH, ZA, ZC	LA, FB, BED, NWT	Tcbs, Tcf, Tci, Tcj, Tcpe, Tcpc, Tcps, Tcu, unk	Lava Zeolitic tuff
19	IA	LA	DV, GL, ZC	LA, MWT, FB	Tci	Lava
20	CHCU	TCU, LFA	ZC	NWT, BED, PL	Tcg, Tci, Thp, Thr, Tpe, Tpr, Tptb	Zeolitic tuff Lava
21	CHZCM	LFA, TCU, VTA	ZC, ZE, ZA, DV, GL	LA, FB, PL, BED	Tcj, Tcu, Th, Thp, Thr, Tmw, Tpr, Tpt, Tptm, unk	Zeolitic tuff Lava
22	CHVCM	VTA, LFA, TCU	GL, DV, ZC, ZA	LA, FB, NWT, BED	Tcj, Tcps, Tcu, Thp, Tpt, unk	Vitric tuff Lava
23	CHVTA	VTA, TCU	GL, ZC	NWT, BED, PL	Tcj, Tcpc, Tcps, Tcu, Th, Thp, Tmt, Tpe, Tpr, Tptb, unk	Vitric zeolitic tuff
24	YMCFCM	TCU, LFA, WTA, unk	ZE, ZM, ZC, ZA, AR, QC, AB, CC, KF, DV	NWT, BED, MWT, PWT, LA	Tcby, Tcp, Tct, Thp, Thr	Zeolitic tuff Lava

Table 9-17
HSUs and Corresponding HGUs, Alteration, Lithology, and Stratigraphy^a
 (Page 2 of 3)

HSU Number	HSU Name ^b	HGUs ^c	Representative Alteration	Lithologies Encountered	Stratigraphy	Summary of Alterations Contributing K _d Distributions
25	TSA	WTA, TCU, unk	DV, QF, GL, ZE, unk	NWT, PWT, TUF, MWT, VT	Tptm	Devitrified tuff
26	LPCU	TCU, unk	ZE, ZC, ZA, QZ, QF, PY, CH, unk	NWT, BED, TB, WBE	Thr, Tp, Tpcm, Tpd, Tpe, Tpr, Tptb, Tptm, Tptx	Zeolitic tuff
27	PLFA	LFA, WTA, TCU, VTA, unk	DV, GL, ZC, ZE, VP, AR, unk	LA, FB, PL, NWT, BED, MWT, DWT, VT, PWT, unk	Tpe, Tpr, Tptb, unk	Lava, Devitrified tuff, Zeolitic tuff, Vitric tuff
28	TCA	WTA	DV, QF, VP, QC, QZ, ZE, unk	MWT, PWT, DWT, VT, unk, TUF	Tpcm, Tpcr	Devitrified tuff
29	UPCU	TCU, VTA, LFA, unk	ZC, ZE, GL, QF, KF, unk, OP	NWT, BED, unk, TUF, RWT, FB, BS, TB	Tm, Tmrf, Tmrh, Tmt, Tmw, Tp, Tpb, Tpc, Tpcm, Tpcr, Tpcx, Tpcy, Tpcyp, Tpd, Tpe, unk	Zeolitic tuff, Vitric tuff, Basalt, Lava
30	BA	LFA, TCU, unk	GL, DV, ZE, QZ, unk, QF, OP	LA, PL, FB, VL	Tpb	Lava Devitrified tuff, Zeolitic tuff
31	PVTA	VTA, WTA, LFA, TCU, unk	GL, DV, ZE, ZC, unk, VP, AR	MWT, PWT, DWT, VT, NWT, BED, TUF, unk, RWT, BS, PL	Tm, Tmra, Tmrd, Tmrf, Tmrh, Tmt, Tp, Tpb, Tpcm, Tpd, Tpe, Tpr, Tptb, unk	Vitric tuff Devitrified tuff Zeolitic tuff, Lava
32	PCM	WTA, VTA, TCU, LFA, unk, AA	DV, VP, GL, ZC, ZE, unk, AR, CC, QC, OP	DWT, MWT, VT, PWT, NWT, BED, LA, AL	QTa, Tpcp, Tpg, Tpp, Tptbr, Tptp, Tptr, Tpv, Tpy	Devitrified tuff Vitric tuff, Zeolitic tuff, Lava, Alluvium
33	WWA	LFA, unk	GL, DV, unk, ZE, ZC	LA, FB, PL, WT	Tmw	Lava
34	FCCU	TCU	ZE	NWT, BED	Tmrf	Zeolitic tuff
35	SCVCU	NA	NA	NA		NA
36	TMA	WTA, VTA, unk, TCU, LFA, ICU, AA	unk, GL, DV, VP, ZE, ZC, QF, QZ, CC, OP, AR, KF	MWT, PWT, DWT, VT, unk, TUF, WT, NWT, BED, RWT, AL, BD, LA	Tfbr, Tfbw, Tg, Tm, Tma, Tmab, Tmap, Tmar, Tmay, Tmr, Tmra, Tmrh, Tmrb, Tmrp, Tmrr, Tt, Ttl, Ttp, Ttt, Tyb, unk	Devitrified tuff Vitric tuff Zeolitic tuff, Lava, Alluvium
37	THCM	TCU, WTA, VTA	ZE, GL, DV, QZ	BED, MWT	Tmat	Zeolitic tuff Vitric tuff Devitrified tuff
38	THLFA	LFA, AA	DV, QZ, GL, ZE, unk	LA, VL, PL, AL	Tmat, Qay	Lava Alluvium

Table 9-17
HSUs and Corresponding HGUs, Alteration, Lithology, and Stratigraphy^a
 (Page 3 of 3)

HSU Number	HSU Name ^b	HGUs ^c	Representative Alteration	Lithologies Encountered	Stratigraphy	Summary of Alterations Contributing K _d Distributions
39	TMCM	TCU, WTA , VTA, LFA, AA	QF, DV, ZE , QZ, VP, GL, ZA, QZ, QC, AB, AR, KF, KA, CC, CH, PY	MWT, PWT, DWT, LB, VT, NWT, BED, LA, RWT, TB, TG, TS, TSS, FB	Tma, Tmab, Tmac, Tmap, Tmar, Tmat, Tmaw, Tmawp, Tmawr, Tmay, Tmr, Tmr _b , Tmrr, Tmrx, Tmx	Zeolitic tuff Devitrified tuff , Lava, Vitric tuff, Alluvium
40	FCA	NA	NA	NA		NA
41	FCCM	LFA, TCU, WTA , VTA, AA	ZE, DV, GL, QZ , QF, QC, CC, AB, PI, MP, CH, PY, unk, AR	MWT, PWT, NWT, TB, unk, RWT, BED, TSS, PL, LA, FB, VL, BS, TSLT, WT, AL	Qay, Tf, Tfb , Tfb _b , Tfb _c , Tfbr, Tfbw , Tfdb, Tff, Tfl, Tfu, Tg, Tgc , unk	Zeolitic tuff Lava Devitrified tuff, Vitric tuff, Basalt, Alluvium
42	DVA	NA	NA	NA	NA	NA
43	DVCM	TCU, WTA	DV , AR, QF	NWT, MWT, PWT	Tf, Tma	Devitrified tuff
44	TCVA	WTA, VTA , LFA, TCU, AA	unk, DV, GL , VP, ZE, CC, QF	MWT, PWT, DWT, NWT, BED, RWT, WT, TUF, ITL, LA, AL, CL k	QTa, Tfb, Tfbr, Tfbw, Tfr, Tmap, Tt, Ttc, Ttcl, Ttcm, Ttg, Ttp, Ttr, Ttt, un	Devitrified tuff Vitric tuff Lava, Zeolitic tuff, Alluvium
45	YVCM	LFA, WTA , AA	unk, DV , VP	AL, BS, PWT	QTa, Tg, Ts, Tsc, Typ	Devitrified tuff Basalt Alluvium
46	AA	AA , VTA, WTA, LFA, TCU	unk, GL, VP , AR, CC, ZE, ZC	AL, TS, RWT, BS, NWT, BED, PWT, MWT, PWT	Qa, QTa, Tg , Tgc, Tgs , Tt, Tte, Ttp, Ttt, Tyo	Alluvium Devitrified tuff Vitric tuff Zeolitic tuff, Basalt

^a See Table 9-1 for definitions of material descriptions.

^b See Table A.1-1 for descriptions of HSUs.

^c See Table 2-1 and Table 2-5 for descriptions of HGUs.

Note: Bold text mean prominent material type encountered - basis for consideration

Table 9-18
K_d Distributions Based on Laboratory Experiments Characterized by Material Alteration
 (Page 1 of 3)

HSU #	HSU Name	Summary of Contributing K _d Distributions	Ca	Sr ^c	Cs	Am, Sm, Eu ^a	U	Np	Pu
1 ^e	LCCU	Carbonate/Clay	-	-	-	-	-	-	-
2 ^e	LCA	Carbonate	-	-	-	-	-	-	-
3 ^e	UCCU	Carbonate/Clay	-	-	-	-	-	-	-
4 ^e	LCCU1	Carbonate/Clay	-	-	-	-	-	-	-
5 ^e	LCA3	Carbonate	-	-	-	-	-	-	-
6	MGCU	Granite	-	-	-	-	-	-	-
7-12	SCICU, CHICU, CCICU, RMICU, ATICU, BMICU		-	-	-	-	-	-	-
13	PBRM	Zeolitic tuff, Devitrified tuff Lava		Lognorm(1.2E5, 1.1E5, -1.3E4) Lognorm(31, 5.6) NDA	Lognorm(1.74E4, 2.03E4) Lognorm(185, 46) ^b NDA	Range(100,1000) Range(100,2000) NDA	Exp(16.5) Exp(2.28) NDA	Lognorm(4.3, 1.6, -1.9) Exp(0.48) NDA	Logistic(265, 70) Lognormal(72, 215) NDA
14	BRA	Lava, Devitrified tuff Zeolitic tuff		NDA Lognorm(31, 5.6) Lognorm(1.2E5, 1.1E5, -1.3E4)	NDA Lognorm(185, 46) Lognorm(1.74E4, 2.03E4)	NDA Range(100,2000) Range(100,1000)	NDA Exp(2.28) Exp(16.5)	NDA Exp(0.48) Lognorm(4.3, 1.6, -1.9)	NDA Lognormal(72, 215) Logistic(265, 70)
15	BFCU	Zeolitic tuff Lava		Lognorm(1.2E5, 1.1E5, -1.3E4) NDA	Lognorm(1.74E4, 2.03E4) ^b NDA	Range(100,1000) NDA	Exp(16.5) NDA	Lognorm(4.3, 1.6, -1.9) NDA	Logistic(265, 70) NDA
16	KA	Lava Zeolitic tuff		NDA	NDA	NDA	NDA	NDA	NDA
17	CFCU	Zeolitic tuff Lava Vitric tuff		Lognorm(1.2E5, 1.1E5, -1.3E4) NDA Norm(175.1, 18,2)	Lognorm(1.74E4, 2.03E4) NDA Lognorm(837, 223)	Range(100,1000) NDA Beta(400,0.2)	Exp(16.5) NDA Exp(1.38)	Lognorm(4.3, 1.6, -1.9) NDA Exp(0.66)	Logistic(265, 70) NDA Traing(63, 1983)
18	CFCM	Lava Zeolitic tuff		NDA	NDA	NDA	NDA	NDA Lognorm(4.3, 1.6, -1.9)	NDA Logistic(265, 70)
19	IA	Lava		NDA	NDA	NDA	NDA	NDA	
20	CHCU	Zeolitic tuff Lava		Lognorm(1.2E5, 1.1E5, -1.3E4)	Lognorm(1.74E4, 2.03E4) NDA	Range(100,1000)	Exp(16.5) NDA	Lognorm(4.3, 1.6, -1.9)	Logistic(265, 70)
21	CHZCM	Zeolitic tuff Lava		Lognorm(1.2E5, 1.1E5, -1.3E4) NDA	Lognorm(1.74E4, 2.03E4) NDA	Range(100,1000) NDA	Exp(16.5) NDA	Lognorm(4.3, 1.6, -1.9) NDA	Logistic(265, 70) NDA
22	CHVCM	Vitric tuff Lava		Normal(175.1, 18,2) NDA	Lognorm(837, 223) NDA	Beta(400,0.2) NDA	Exp(1.38) NDA	Exp(0.66) NDA	Triang(63, 1983) NDA

Table 9-18
K_d Distributions Based on Laboratory Experiments Characterized by Material Alteration
 (Page 2 of 3)

HSU #	HSU Name	Summary of Contributing K _d Distributions	Ca	Sr ^c	Cs	Am, Sm, Eu ^a	U	Np	Pu
23	CHVTA	Vitric zeolitic tuff		Normal(175.1, 18,2)	Lognorm(837, 223)	Beta(400,0.2)	Exp(1.38)	Exp(0.66)	Triang(63, 1983)
24	YMCFCM	Zeolitic tuff Lava		Lognorm(1.2E5, 1.1E5, -1.3E4)	Lognorm(1.74E4, 2.03E4) NDA	Range(100,1000) NDA	Exp(16.5) NDA	Lognorm(4.3, 1.6, -1.9) NDA	Logistic(265, 70)
25	TSA	Devitrified tuff		Lognorm(31, 5.6)	Lognorm(185, 46) ^b	Range(100,2000)	Exp(2.28)	Exp(0.48)	Lognormal(72, 215)
26	LPCU	Zeolitic tuff		Lognorm(1.2E5, 1.1E5, -1.3E4)	Lognorm(1.74E4, 2.03E4)	Range(100,1000)	Exp(16.5)	Lognorm(4.3, 1.6, -1.9)	Logistic(265, 70)
27	PLFA	Lava, Devitrified tuff, Zeolitic tuff, Vitric tuff		NDA Lognorm(31, 5.6)	NDA Lognorm(185, 46)	NDA Range(100,2000)	NDA Exp(2.28)	NDA Exp(0.48)	NDA Lognormal(72, 215)
28	TCA	Devitrified tuff		Lognorm(31, 5.6)	Lognorm(185, 46)	Range(100,2000)	Exp(2.28)	Exp(0.48)	Lognormal(72, 215)
29	UPCU	Zeolitic tuff Vitric tuff, Basalt, Lava		Lognorm(1.2E5, 1.1E5, -1.3E4)	Lognorm(1.74E4, 2.03E4)	Range(100,1000) ND	Exp(16.5)	Lognorm(4.3, 1.6, -1.9)	Logistic(265, 70)
30	BA	Lava Devitrified tuff, Zeolitic tuff		NDA	NDA	NDA	NDA	NDA	NDA
31	PVTA	Vitric tuff Devitrified tuff Zeolitic tuff, Lava		Normal(175.1, 18,2) Lognorm(31, 5.6)	Lognorm(837, 223) Lognorm(185, 46)	Beta(400,0.2) Range(100,2000)	Exp(1.38) Exp(2.28)	Exp(0.66) Exp(0.48)	Triang(63, 1983) Lognormal(72, 215)
32	PCM	Devitrified tuff Vitric tuff, Zeolitic tuff, Lava, Alluvium		Lognorm(31, 5.6) Normal(175.1, 18,2)	Lognorm(185, 46) Lognorm(837, 223)	Range(100,2000) Beta(400,0.2)	Exp(2.28) Exp(1.38)	Exp(0.48) Exp(0.66)	Lognormal(72, 215) Triang(63, 1983)
33	WWA	Lava		NDA	NDA	NDA	NDA	NDA	NDA
34	FCCU	Zeolitic tuff		Lognorm(1.2E5, 1.1E5, -1.3E4)	Lognorm(1.74E4, 2.03E4)	Range(100,1000) NDA	Exp(16.5)	Lognorm(4.3, 1.6, -1.9)	Logistic(265, 70)
35	SCVCU	NA							
36	TMA	Devitrified tuff Vitric tuff Zeolitic tuff, Lava, Alluvium		Lognorm(31, 5.6) Normal(175.1, 18,2)	Lognorm(185, 46) Lognorm(837, 223)	Range(100,2000) Beta(400,0.2)	Exp(2.28) Exp(1.38)	Exp(0.48) Exp(0.66)	Lognormal(72, 215) Triang(63, 1983)
37	THCM	Zeolitic tuff Vitric tuff Devitrified tuff		Lognorm(1.2E5, 1.1E5, -1.3E4) Norm(175.1, 18,2)	Lognorm(1.74E4, 2.03E4) Lognorm(837, 223)	Range(100,1000) Beta(400,0.2)	Exp(16.5) Exp(1.38)	Lognorm(4.3, 1.6, -1.9) Exp(0.66)	Logistic(265, 70) Triang(63, 1983)

Table 9-18
K_d Distributions Based on Laboratory Experiments Characterized by Material Alteration
 (Page 3 of 3)

HSU #	HSU Name	Summary of Contributing K _d Distributions	Ca	Sr ^c	Cs	Am, Sm, Eu ^a	U	Np	Pu
38	THLFA	Lava Alluvium		NDA	NDA	NDA	NDA	NDA	NDA
39	TMCM	Zeolitic tuff Devitrified tuff Lava, Vitric tuff, Alluvium		Lognorm(1.2E5, 1.1E5, -1.3E4) Lognorm(31, 5.6)	Lognorm(1.74E4, 2.03E4) Lognorm(185, 46) ^b	Range(100,1000) Range(100,2000)	Exp(16.5) Exp(2.28)	Lognorm(4.3, 1.6, -1.9) Exp(0.48)	Logistic(265, 70) Lognormal(72, 215)
40	FCA	NA							
41	FCCM	Zeolitic tuff Lava Devitrified tuff, Vitric tuff, Basalt, Alluvium		Lognorm(1.2E5, 1.1E5, -1.3E4) NDA	Lognorm(1.74E4, 2.03E4) NDA	Range(100,1000) NDA	Exp(16.5) NDA	Lognorm(4.3, 1.6, -1.9) NDA	Logistic(265, 70) NDA
42	DVA	NA							
43	DVCM	Devitrified tuff		Lognorm(31, 5.6)	Lognorm(185, 46)	Range(100,2000)	Exp(2.28)	Exp(0.48)	Lognormal(72, 215)
44	TCVA	Devitrified tuff Vitric tuff Lava, Zeolitic tuff, Alluvium		Lognorm(31, 5.6) Normal(175.1, 18,2)	Lognorm(185, 46) Lognorm(837, 223)	Range(100,2000) Beta(400,0.2)	Exp(2.28) Exp(1.38)	Exp(0.48) Exp(0.66)	Lognormal(72, 215) Triang(63, 1983)
45	YVCM	Devitrified tuff Basalt Alluvium		Lognorm(31, 5.6) NDA	Lognorm(185, 46) NDA	Range(100,2000) NDA	Exp(2.28) NDA	Exp(0.48) NDA	Lognormal(72, 215) NDA
46	AA	Alluvium Devitrified tuff Vitric tuff Zeolitic tuff, Basalt		Range (80,22500) ^d	Range (700,3000) ^d				

^aBased on Table 9-8 from Conca (2000)

^bSee Table 9-3 for individual UGTA sample values

^cFor zeolite only, see Table 9-5 and Table 9-6 for UGTA measurements on individual samples

^dUGTA samples reported in Papelis and Um (2002, Table 3-1)

^eCarbonate K_d values from Table 9-11

Note: Ca, Sr estimated to have no sorption on granite; Am, Eu, Sm, Pu, Np estimated to be strongly sorbing, analogous to Pb (Pohll, 1998)

Table 9-19
Summary of K_d s Estimated by Stratigraphy with Mechanistic Model,
Correlated to HSUs (Data in Zavarin et al., 2002)
 (Page 1 of 4)

HSU #	HSU Name	Stratigraphy	Stratigraphy in Mechanistic Model Dataset	Ca	Sr	Cs	Sm	Eu	U	Np	Pu (10^{-5})	Pu (10^{-10})	Pu (10^{-15})	Am
1	LCCU													
2	LCA													
3	UCCU													
4	LCCU1													
5	LCA3													
6	MGCU													
7-12	SCICU, CHICU, CCICU, RMICU, ATICU, BMICU													
13	PBRCM ^b			Range (1139.1,2796.4) Range (279.9,3543.1)	Range (668.1,1637.2) Range (165.3,2086.3)	Range (2236.3,4539.5) Range (1673.6,2814.4)	Range (1577.8,3274.1) Range (0,0)	Range (1091.5,2265.1) Rang (0,0)	Range (2.9,19.5) Range (0,0)	Range (1.3,3.1) Range (0,0)	Range (5.9,7.5) Range (0,0)	Range (13,20.4) Range (0,0)	Range (63.8,121.1) Range (0,0)	Range(2965.4,6684.9) Range (0,0)
14	BRA	QTa, Tbd, Tbdb, Tdbc, Tbdk, Tbdl, Tbds, Tbg, Tbgb, Tbgm, Tbgp, Tbgr, Tbgs, Tbg, Tci, Tn4JK, Tri, Trr, unk	Tcl (N=1)	Range(178.4)	Range(94.8)	Range(9233.6)	Range(4677.3)	Range(3235.9)	Range(4.2)	Range(1.8)	Range(8.5)	Range(18.6)	Range(91.2)	Range(9549.9)
15	BFCU	Tbdl, Tcbip, Tcbir, Tcbp, Tcbr, Tcbs, Tcbx, Tct	Tcbp (N=2) Tct (N=55)	Range (1529.5,2637.8) Lognorm (365.6,1310.4)	Range (903.3,1553.2) Lognorm (189.8,669.7)	Range (5725.6,12101.7) Exp (9469.2)	Range (467.7,467.7) Exp (4707.9)	Range (323.5,323.5) Exp (3207.6)	Range (0.4,0.4) Exp (5.5)	Range (0.1,0.1) Exp (2.3)	Range (0.8,0.8) Exp (8.7)	Range (1.8,1.8) Exp (19.5)	Range (9.1,9.1) Ex p(97.6)	Range (954.9,954.9) Exp (9234.2)
16	KA ^c	Tcg, Tcpg		Exp(2376.1)	Exp(1406.3)	Exp(32993)	Exp(1470)	Exp(1017)	Exp(1.3)	Exp(0.6)	Exp(2.7)	Exp(5.9)	Exp(28.7)	Exp(3001.4)
17	CFCU ^b	Tcg, Tci, Tcj, Tcpg, Tcps, Tcu, unk		Range (1139.1,2796.4) Range (279.9,3543.1)	Range (668.1,1637.2) Range (165.3,2086.3)	Range (2236.3,4539.5) Range (1673.6,2814.4)	Range (1577.8,3274.1) Range (0,0)	Range (1091.5,2265.1) Range (0,0)	Range (2.9,19.5) Range (0,0)	Range (1.3,3.1) Range (0,0)	Range (5.9,7.5) Range (0,0)	Range (13,20.4) Range (0,0)	Range (63.8,121.1) Range (0,0)	Range (2965.4,6684.9) Range (0,0)
18	CFCM ^b	Tcbs, Tcf, Tci, Tcj, Tcpe, Tcpg, Tcps, Tcu, unk		Range (1139.1,2796.4) Range (279.9,3543.1)	Range (668.1,1637.2) Range (165.3,2086.3)	Range (2236.3,4539.5) Range (1673.6,2814.4)	Range (1577.8,3274.1) Range (0,0)	Range (1091.5,2265.1) Range (0,0)	Range (2.9,19.5) Range (0,0)	Range (1.3,3.1) Range (0,0)	Range (5.9,7.5) Range (0,0)	Range (13,20.4) Range (0,0)	Range (63.8,121.1) Range (0,0)	Range (2965.4,6684.9) Range (0,0)

Table 9-19
Summary of K_d s Estimated by Stratigraphy with Mechanistic Model,
Correlated to HSUs (Data in Zavarin et al., 2002)
 (Page 2 of 4)

HSU #	HSU Name	Stratigraphy	Stratigraphy in Mechanistic Model Dataset	Ca	Sr	Cs	Sm	Eu	U	Np	Pu (10^{-5})	Pu (10^{-10})	Pu (10^{-15})	Am
19	IA ^c	Tci		Exp(2376.1)	Exp(1406.3)	Exp(32993)	Exp(1470)	Exp(1017)	Exp(1.3)	Exp(0.6)	Exp(2.7)	Exp(5.9)	Exp(28.7)	Exp(3001.4)
20	CHCU	Tcg, Tci, Thp, Thr, Tpe, Tpr, Tptb	Tpe (N=2) Tptb (N=2)	Range (1139.1,2796.4) Range (279.9,3543.1)	Range (668.1,1637.2) Range (165.3,2086.3)	Range (2236.3,4539.5) Range (1673.6,2814.4)	Range (1577.8,3274.1) Range (0,0)	Range (1091.5,2265.1) Range (0,0)	Range (2.9,19.5) Range (0,0)	Range (1.3,3.1) Range (0,0)	Range (5.9,7.5) Range (0,0)	Range (13,20.4) Range (0,0)	Range (63.8,121.1) Range (0,0)	Range (2965.4,6684.9) Range (0,0)
21	CHZCM ^b	Tcj, Tcu, Th, Thp, Thr, Tmw, Tpr, Tpt, Tptm, unk		Range (1139.1,2796.4) Range (279.9,3543.1)	Range (668.1,1637.2) Range (165.3,2086.3)	Range (2236.3,4539.5) Range (1673.6,2814.4)	Range (1577.8,3274.1) Range (0,0)	Range (1091.5,2265.1) Range (0,0)	Range (2.9,19.5) Range (0,0)	Range (1.3,3.1) Range (0,0)	Range (5.9,7.5) Range (0,0)	Range (13,20.4) Range (0,0)	Range (63.8,121.1) Range (0,0)	Range (2965.4,6684.9) Range (0,0)
22	CHVCM ^b	Tcj, Tcps, Tcu, Thp, Tpt, unk		Range (1139.1,2796.4) Range (279.9,3543.1)	Range (668.1,1637.2) Range (165.3,2086.3)	Range (2236.3,4539.5) Range (1673.6,2814.4)	Range (1577.8,3274.1) Range (0,0)	Range (1091.5,2265.1) Range (0,0)	Range (2.9,19.5) Range (0,0)	Range (1.3,3.1) Range (0,0)	Range (5.9,7.5) Range (0,0)	Range (13,20.4) Range (0,0)	Range (63.8,121.1) Range (0,0)	Range (2965.4,6684.9) Range (0,0)
23	CHVTA	Tcj, Tcpc, Tcps, Tcu, Th, Thp, Tmt, Tpe, Tpr, Tptb, unk	Tpe (N=2) Tptb (N=2)	Range (1139.1,2796.4) Range (279.9,3543.1)	Range (668.1,1637.2) Range (165.3,2086.3)	Range (2236.3,4539.5) Range (1673.6,2814.4)	Range (1577.8,3274.1) Range (0,0)	Range (1091.5,2265.1) Range (0,0)	Range (2.9,19.5) Range (0,0)	Range (1.3,3.1) Range (0,0)	Range (5.9,7.5) Range (0,0)	Range (13,20.4) Range (0,0)	Range (63.8,121.1) Range (0,0)	Range (2965.4,6684.9) Range (0,0)
24	YMCFCM	Tcby, Tcp, Tct, Thp, Thr	Tcby (N=47) Tcp (N=32) Tct (N=55)	Lognorm (1484.5,25636) Lognorm (2107.7,27364) Lognorm (365.6,1310.4)	Lognorm (852,14243) Lognorm (1229,17375) Lognorm (189.8,669.7)	Lognorm (7252.8,13979) Exp (2249.3) Exp (9469.2)	Exp (1509.3) Exp (2138.8) Exp (4707.9)	Exp (1040.4) Exp (1475.5) Exp (3207.6)	Exp (7.7) Exp (2.4) Exp (5.5)	Exp (1.5) Exp (0.9) Exp (2.3)	Exp (4.4) Exp (4) Exp (8.7)	Exp (11) Exp (8.9) Exp (19.5)	Exp (61.1) Exp (44.1) Exp (97.6)	Exp (2964.2) Exp (4329.6) Exp (9234.2)
25	TSA ^a	Tptm		Range(0,22.6)	Range(0,22.6)	Range(0,25415.4)	Range(0,87.3)	Range(0,60.3)	Range(0,9.1)	Range(0,1.2)	Range(0,2.5)	Range(0,7.4)	Range(0,46.8)	Range(0,50.2)
26	LPCU	Thr, Tp, Tpcm, Tpd, Tpe, Tpr, Tptb, Tptm, Tptx	Tp (N=3) Tpd (N=11) Tpe (N=2) Tptb (N=2)	Range (2707.1,3383.9) Lognorm (3178.5,3666.6) Range (1139.1,2796.4) Range (279.9,3543.1)	Range (1594,1992.5) Lognorm (2008.6,2747.9) Range (668.1,1637.2) Range (165.3,2086.3)	Range (2150.3,27882) Exp (5843.8) Range (2236.3,4539.5) Range (1673.6,2814.4)	Range (0,0) Exp (946.1) Range (1577.8,3274.1) Range (0,0)	Range (0,0) Exp (652.5) Range (1091.5,2265.1) Range (0,0)	Range (0,0) Exp (0.9) Range (2.9,19.5) Range (0,0)	Range (0,0) Exp (0.4) Range (1.3,3.1) Range (0,0)	Range (0,0) Exp (1.7) Range (5.9,7.5) Range (0,0)	Range (0,0) Exp (3.8) Range (13,20.4) Range (0,0)	Range (0,0) Exp (18.4) Range (63.8,121.1) Range (0,0)	Range (0,0) Exp (1917) Range (2965.4,6684.9) Range (0,0)
27	PLFA	Tpe, Tpr, Tptb, unk	Tpe (N=2) Tptb (N=2)	Range (1139.1,2796.4) Range (279.9,3543.1)	Range (668.1,1637.2) Range (165.3,2086.3)	Range (2236.3,4539.5) Range (1673.6,2814.4)	Range (1577.8,3274.1) Range (0,0)	Range (1091.5,2265.1) Range (0,0)	Range (2.9,19.5) Range (0,0)	Range (1.3,3.1) Range (0,0)	Range (5.9,7.5) Range (0,0)	Range (13,20.4) Range (0,0)	Range (63.8,121.1) Range (0,0)	Range (2965.4,6684.9) Range (0,0)
28	TCA	Tpcm, Tpcr	Tpcr (N=4)	Range(0,22.6)	Range(0,22.6)	Range(0,25415.4)	Range(0,87.3)	Range(0,60.3)	Range(0,9.1)	Range(0,1.2)	Range(0,2.5)	Range(0,7.4)	Range(0,46.8)	Range(0,50.2)

Table 9-19
Summary of K_d s Estimated by Stratigraphy with Mechanistic Model,
Correlated to HSUs (Data in Zavarin et al., 2002)
 (Page 3 of 4)

HSU #	HSU Name	Stratigraphy	Stratigraphy in Mechanistic Model Dataset	Ca	Sr	Cs	Sm	Eu	U	Np	Pu (10^{-5})	Pu (10^{-10})	Pu (10^{-15})	Am
29	UPCU	Tm, Tmrf, Tmrh, Tmt, Tmw, Tp, Tpb, Tpc, Tpcm, Tpcr, Tpcx, Tpcy, Tpcyp, Tpd, Tpe, unk	Tp (N=3) Tpb (N=7) Tpcr (N=4) Tpd (N=11) Tpe (N=2)	Range (2707.1,3383.9) Exp (2376.1) Range (0,22.6) Lognorm (3178.5,3666.6) Range (1139.1,2796.4)	Range (1594,1992.5) Exp (1406.3) Range (0,22.6) Lognorm (2008.6,2747.9) Range (668.1,1637.2)	Range (2150.3,27882) Exp (32993) Range (0,25415.4) Exp (5843.8) Range (2236.3,4539.5)	Range (0,0) Exp (1470) Range (0,87.3) Exp (946.1) Range (1577.8,3274.1)	Range (0,0) Exp (1017) Range (0,60.3) Exp (652.5) Range (1091.5,2265.1)	Range (0,0) Exp (1.3) Range (0,9.1) Exp (0.9) Range (2.9,19.5)	Range (0,0) Exp (0.6) Range (0,1.2) Exp (0.4) Range (1.3,3.1)	Range (0,0) Exp (2.7) Range (0,2.5) Exp (1.7) Range (5.9,7.5)	Range (0,0) Exp (5.9) Range (0,7.4) Exp (3.8) Range (13,20.4)	Range (0,0) Exp (28.7) Range (0,46.8) Exp (18.4) Range (63.8,121.1)	Range (0,0) Exp (3001.4) Range (0,50.2) Exp (1917) Range (2965.4,6684.9)
30	BA	Tpb	Tpb (N=7)	Exp(2376.1)	Exp(1406.3)	Exp(32993)	Exp(1470)	Exp(1017)	Exp(1.3)	Exp(0.6)	Exp(2.7)	Exp(5.9)	Exp(28.7)	Exp(3001.4)
31	PVTA	Tm, Tmra, Tmrd, Tmrf, Tmrh, Tmt, Tp, Tpb, Tpcm, Tpd, Tpe, Tpr, Tptb, unk	Tp (N=3) Tpb (N=7) Tpd (N=11) Tpe (N=2) Tptb (N=2)	Range (2707.1,3383.9) Exp (2376.1) Lognorm (3178.5,3666.6) Range (1139.1,2796.4) Range (279.9,3543.1)	Range (1594,1992.5) Exp (1406.3) Lognorm (2008.6,2747.9) Range (668.1,1637.2) Range (165.3,2086.3)	Range (2150.3,27882) Exp (32993) Exp (5843.8) Range (2236.3,4539.5) Range (1673.6,2814.4)	Range (0,0) Exp (1470) Exp (946.1) Range (1577.8,3274.1) Range (0,0)	Range (0,0) Exp (1017) Exp (652.5) Range (1091.5,2265.1) Range (0,0)	Range (0,0) Exp (1.3) Exp (0.9) Range (2.9,19.5) Range (0,0)	Range (0,0) Exp (2.7) Exp (1.7) Range (5.9,7.5) Range (0,0)	Range (0,0) Exp (5.9) Exp (3.8) Range (13,20.4) Range (0,0)	Range (0,0) Exp (28.7) Exp (18.4) Range (63.8,121.1) Range (0,0)	Range (0,0) Exp (3001.4) Exp (1917) Range (2965.4,6684.9) Range (0,0)	
32	PCM	QTa, Tpcp, Tpg, Tpp, Tptbr, Tptp, Tptr, Tpv, Tpy	Tpcp (N=12) Tpg (N=7) Tptbr (N=6) Tptp (N=82) Tptr (N=12) Tpy (N=4)	Exp (26.5) Lognorm (358.4,866.6) Exp (1143.7) Exp (494.5) Lognorm (59.4,170.3) Range (0,353.9)	Exp (14.3) Lognorm (189,556.9) Exp (637) Exp (286.9) Lognorm (31.3,70.5) Range (0,140.9)	Exp (325.7) Exp (1147.4) Exp (4596.5) Exp (1451) Lognorm (14116,68310) Range (0,388.1)	Exp (512.2) Exp (4276.4) Exp (13880) Exp (1956.2) Lognorm (993.3,3098.4) Range (0,23386.7)	Exp (354.3) Exp (2945.8) Exp (9453.8) Exp (1288.9) Lognorm (665.1,2087.3) Range (0,16179.6)	Exp (1) Exp (3.8) Exp (12.3) Exp (2.8) Exp (3.3) Range (0,21.3)	Exp (0.3) Exp (1.8) Exp (6.4) Exp (1.3) Lognorm (0.7,0.6) Range (0,17)	Exp (1.1) Exp (7.7) Exp (24.8) Exp (3.7) Exp (2) Range (0,42.5)	Exp (2.5) Exp (16.9) Exp (54.5) Exp (8.4) Lognorm (5.3,5.1) Range (0,93.1)	Exp (12.8) Exp (83.1) Exp (269.1) Exp (43.1) Exp (27.6) Range (0,456)	Exp (1037.7) Exp (8639.1) Exp (27257) Exp (3508.9) Lognorm (3129.4,27456) Range (0,47749.6)
33	WWA ^a			Range(0,22.6)	Range(0,22.6)	Range(0,25415.4)	Range(0,87.3)	Range(0,60.3)	Range(0,9.1)	Range(0,1.2)	Range(0,2.5)	Range(0,7.4)	Range(0,46.8)	Range(0,50.2)
34	FCCU													
35	SCVCU													
36	TMA ^a			Range(0,22.6)	Range(0,22.6)	Range(0,25415.4)	Range(0,87.3)	Range(0,60.3)	Range(0,9.1)	Range(0,1.2)	Range(0,2.5)	Range(0,7.4)	Range(0,46.8)	Range(0,50.2)
37	THCM ^a			Range(0,22.6)	Range(0,22.6)	Range(0,25415.4)	Range(0,87.3)	Range(0,60.3)	Range(0,9.1)	Range(0,1.2)	Range(0,2.5)	Range(0,7.4)	Range(0,46.8)	Range(0,50.2)
38	THLFA ^a			Range(0,22.6)	Range(0,22.6)	Range(0,25415.4)	Range(0,87.3)	Range(0,60.3)	Range(0,9.1)	Range(0,1.2)	Range(0,2.5)	Range(0,7.4)	Range(0,46.8)	Range(0,50.2)

Table 9-19
Summary of K_d s Estimated by Stratigraphy with Mechanistic Model,
Correlated to HSUs (Data in Zavarin et al., 2002)
 (Page 4 of 4)

HSU #	HSU Name	Stratigraphy	Stratigraphy in Mechanistic Model Dataset	Ca	Sr	Cs	Sm	Eu	U	Np	Pu (10^{-5})	Pu (10^{-10})	Pu (10^{-15})	Am
39	TMCM ^a			Range(0,22.6)	Range(0,22.6)	Range(0,25415.4)	Range(0,87.3)	Range(0,60.3)	Range(0,9.1)	Range(0,1.2)	Range(0,2.5)	Range(0,7.4)	Range(0,46.8)	Range(0,50.2)
40	FCA													
41	FCCM ^a			Range(0,22.6)	Range(0,22.6)	Range(0,25415.4)	Range(0,87.3)	Range(0,60.3)	Range(0,9.1)	Range(0,1.2)	Range(0,2.5)	Range(0,7.4)	Range(0,46.8)	Range(0,50.2)
42	DVA													
43	DVCM ^a			Range(0,22.6)	Range(0,22.6)	Range(0,25415.4)	Range(0,87.3)	Range(0,60.3)	Range(0,9.1)	Range(0,1.2)	Range(0,2.5)	Range(0,7.4)	Range(0,46.8)	Range(0,50.2)
44	TCVA ^a			Range(0,22.6)	Range(0,22.6)	Range(0,25415.4)	Range(0,87.3)	Range(0,60.3)	Range(0,9.1)	Range(0,1.2)	Range(0,2.5)	Range(0,7.4)	Range(0,46.8)	Range(0,50.2)
45	YVCM ^a			Range(0,22.6)	Range(0,22.6)	Range(0,25415.4)	Range(0,87.3)	Range(0,60.3)	Range(0,9.1)	Range(0,1.2)	Range(0,2.5)	Range(0,7.4)	Range(0,46.8)	Range(0,50.2)
46	AA			See Table 9-4	See Table 9-4	See Table 9-4	See Table 9-4	See Table 9-4	See Table 9-4	See Table 9-4	See Table 9-4	See Table 9-4	See Table 9-4	See Table 9-4

^a K_d ranges assigned based on similarity to TCA unit for which estimates based upon stratigraphy were reported by Zavarin et al. (2002)
^b K_d ranges assigned based on similarity to CHCU unit for which estimates based upon stratigraphy were reported by Zavarin et al. (2002)
^c K_d ranges assigned based on similarity to BA unit for which estimates based upon stratigraphy were reported by Zavarin et al. (2002)

Note - For Pu, oxygen fugacities of 1E-5, 1E-10, and 1E-15 are considered as they affect the speciation and valence of Pu.

10.0 Fracture Sorption Parameter

This section includes a description of the fracture sorption process and a discussion of methods for parameterizing it in the CAU models.

10.1 The Role of Fracture Sorption in Contaminant Transport

As with matrix sorption, fracture sorption is the physiochemical process at mineral-water interfaces that control solute mobility and, hence, solute retardation in fractures within flowing groundwater systems. Fracture sorption is treated separately from matrix sorption because it strictly involves the sorption of radionuclides to minerals coating fracture surfaces, prior to diffusion into the matrix material, where matrix sorption may occur. Further, fracture sorption is not considered for matrix material in which fractures are not present and porous media flow controls fluid and solute mass transport. Where fractures are present, the CAU-scale parameter of interest is the solute retardation factor in fractures.

[Section 9.0](#) highlights measurements of radionuclide sorption to matrix material; however, observational data have not been collected to isolate and parameterize the process of radionuclide sorption to fracture minerals. Thus, estimates of this retardation process are based upon mechanistic modeling studies, utilizing the same reaction principals described in the previous chapter for matrix sorption.

Retardation factors (R parameters) for solutes in fractures are the simplest method with which to represent sorption to fracture minerals. Although easily derived from each other, R is preferable to K_d because the K_d is based upon a volumetric sample of material, as appropriate for matrix material. In the fracture, all of the reactive processes leading to solute retardation are represented per unit length of fracture, rather than per unit volume of rock. As with the K_d , R is straightforward to apply in transport models, avoiding the computational challenge for more mechanistic transport models while providing parametric upscaling.

Use of the R parameter requires the assumption of local equilibrium. Reactions that are actually kinetic in nature must be assumed to occur fast enough that R captures the process either adequately or conservatively in field-scale simulations. Further, the R parameter does not allow for changing sorption behavior due to changes in water chemistry or mineral surfaces. It can vary spatially, but is not capable of representing dynamic system changes during the course of a simulation.

10.2 Data Compilation and Evaluation

The fracture sorption data types and sources of data are described in this section.

10.2.1 Data Types

The modeling studies seeking to upscale mechanistic processes to larger scale retardation factors are based upon the same processes as those described for mechanistic models of matrix K_d in the previous section. The key components to estimating reactions with fracture coatings are as follows:

- The effective reactive surface area of fracture-coating minerals available to solutes flowing in the fracture
- The mineralogic composition of the fracture coatings
- The distribution (existence) of fracture-coating minerals in fractures

Once estimated, these three factors can be used to parameterize mechanistic models, which ultimately provide effective fracture retardation factors.

A benefit of the mechanistic modeling approach is that it specifically represents which reactions control and affect sorption to fracture-coating minerals. Due to the complete representation of all reactions, the mechanistic modeling approach can also describe how groundwater chemistry changes such as pH affect sorption reactions, as well as how sorption reactions may affect groundwater chemistry.

A limitation of the mechanistic modeling approach is that, although a detailed set of reactions may be simulated, parameters for those reactions may not be available, particularly at the CAU scale. This is particularly important for estimating fracture retardation factors where spatial variation of fracture-coating materials will have first-order effects on the estimated parameters.

Two recent approaches within the UGTA project have begun to assess fracture retardation. Wolfsberg et al. (2002, Chapter 7 and Appendix F) used estimates of fracture-coating thickness, distribution, mineral content, and availability in conjunction with surface complexation thermodynamic data reported by Pawloski et al. (2001) to predict fracture retardation factors. They find that the primary factor controlling fracture retardation is how much of the fracture coating is accessible to solutes migrating in the fracture. Zavarin et al. (2002) extends upon developments made by Pawloski et al. (2001), with estimates of fracture retardation due to mechanistic processes. In their approach, Zavarin et al. (2002) make an assumption regarding flow in the fracture coatings as well as a portion of the matrix neighboring the fracture. This conceptualization, referred to by Zavarin and Bruton (2000a and b) as the matrix reactive zone, leads to a greater effective porosity than what is calculated from fracture apertures and densities. With this simplification, diffusion between fractures and matrix material is not explicitly modeled. Rather, this method seeks to capture the effect of some diffusion into the matrix near the fracture wall with the increased effective porosity. Thus, the

method also combines the effects of sorption to matrix material and fracture minerals with a single set of parameters. Additional diffusion into the matrix beyond the matrix reactive zone can be simulated, understanding that the first portion of reactive matrix minerals is wrapped up in the fracture effective porosity abstraction with this method.

Using thermodynamic data bases for sorption reactions to specific minerals and measurement of specific mineral compositions in field samples, these theoretical methods provide estimates of retardation resulting from radionuclides sorbing to reactive minerals surrounding flowing fractures.

10.2.2 Data Sources

Wolfsberg et al. (2002) and Zavarin et al. (2002) have provided estimates of fracture retardation factors for various rock types on Pahute Mesa. These modeling studies seek to incorporate information regarding specific reactions and estimates of fracture-coating properties. Coupled with other processes of matrix diffusion, matrix reaction, and colloid-facilitated transport, the expected values of fracture retardation factors were used by Wolfsberg et al. (2002) in predicting radionuclide concentrations in Wells ER-20-5 #1 and ER-20-5 #3. In those simulations, the radionuclides with large R values in fractures were shown to have minimal mobility in the absence of colloids. Zavarin et al. (2002) also demonstrate the increased predicted mobility when colloids are present and compete with immobile reactive minerals for radionuclide sorption.

10.3 Data Evaluation

This section includes a description of the data available for the fracture retardation factor, followed by a discussion covering their limitations and range of values.

10.3.1 Dataset Descriptions

Two recent UGTA Project studies have sought to derive fracture retardation factors using mechanistic modeling approaches.

10.3.1.1 Derivation by Wolfsberg et al. (2002)

Wolfsberg et al. (2002, Chapter 7 and Appendix F) apply a semimechanistic approach for estimating fracture retardation factors. They assume invariant water chemistry representative of Pahute Mesa groundwater and group radionuclides into the classes shown in [Table 10-1](#). Their derivation shows the dependence of the fracture retardation factor on the uncertain fracture-coating properties listed in [Section 10.2.1](#). The method is based on three major assumptions: (1) a fixed percent coverage of fractures with coatings, (2) a fixed coating thickness where they exist, and (3) fixed availability of reactive minerals within the coatings.

Table 10-1
Radionuclide Classes in Wolfsberg et al. (2002)

Class	Radionuclide	Symbol
Class I	Tritium	3H
	Carbon	C-14
	Chloride	Cl-36
	Krypton	Kr-85
	Technetium	Tc-99
	Iodine	I-129
Class II	Samarium	Sm-151
	Americium	Am-241
	Europium	Eu-152
	Europium	Eu-154
Class III	Strontium	Sr-90
	Cesium	Cs-137
Class IV	Uranium (D&S)	U-234
	Uranium (D&S)	U-238
	Neptunium	Np-237
Class V	Plutonium	Pu-239
	Plutonium	Pu-240

Variability in fracture retardation factors associated with variability in mineral content in the coatings calculated using this method are presented in [Table 10-2](#). Wolfsberg et al. (2002, Appendix F) noted that uncertainty in percent fracture-coating coverage and the percent of the coatings available for reactions can add up to three orders of magnitude uncertainty on these values.

Table 10-2
Fracture Retardation Factors from Wolfsberg et al. (2002)
(Class I has R=1)

Radionuclide	Class	Range	Rock Type						
			Bedded	Non-welded	Welded	Lava	Altered	Fractured Non-welded	Bedded-Altered
Class II	low		N/A	N/A	63	163	22	192	N/A
	base		N/A	N/A	195	207	25	223	N/A
	high		N/A	N/A	837	231	129	265	N/A
Class III	low		N/A	N/A	1.01	1.04	1	1.04	N/A
	base		N/A	N/A	1.07	1.05	1	1.05	N/A
	high		N/A	N/A	1.23	1.06	1.01	1.07	N/A
Class IV	low		N/A	N/A	1.13	1.35	1.03	1.43	N/A
	base		N/A	N/A	3.5	2.7	1.43	2.7	N/A
	high		N/A	N/A	13.5	4.9	2.5	5.5	N/A
Class V	low		N/A	N/A	2.7	9.2	1	8.4	N/A
	base		N/A	N/A	13.6	10.3	3.9	9.6	N/A
	high h		N/A	N/A	39	13	6.8	15	N/A

N/A - Not applicable

10.3.1.2 Derivation by Zavarin et al. (2002)

Zavarin et al. (2002) apply a mechanistic model using the thermodynamic reaction databases of Zavarin and Bruton (2000 a and b) to predict fracture retardation factors for several regional model HSUs. [Table 10-3](#) provides the estimated retardation factors from that study. In this study, the range of uncertainty is only related to uncertainty in mineralogic composition of the fracture coatings, not of their abundance or the accessibility of those minerals to solutes in the fracture water.

Table 10-3
Fracture Retardation Factors, Log(R), Estimated for Regional HSUs by Zavarin et al., 2002

Regional HSU ^a	TMA			TC			TBA			BAQ		
	E(x)	Min	Max	E(x)	Min	Max	E(x)	Min	Max	E(x)	Min	Max
Ca	3.3	3.3	3.3	3.0	3.0	3.0	3.2	3.2	3.2	3.4	3.4	3.4
Cs	4.0	3.1	4.0	3.2	2.4	3.2	4.3	3.3	4.3	3.3	2.7	3.3
Sr	3.1	3.1	3.1	2.7	2.7	2.7	3.0	3.0	3.0	3.1	3.1	3.1
Am	4.0	3.8	4.4	3.9	3.6	4.2	4.6	4.4	5.0	4.3	4.2	4.3
Eu	3.6	3.1	4.1	3.5	3.0	4.0	4.2	3.7	4.7	4.1	3.6	4.6
Sm	3.8	3.4	4.3	3.7	3.3	4.2	4.4	3.9	4.9	4.7	4.2	5.2
Np	0.8	0.6	1.1	1.1	0.7	1.5	1.7	1.3	2.2	1.6	1.2	2.1
U	1.2	0.9	1.6	1.8	1.4	2.2	2.5	2.1	2.9	0.2	0.2	0.2
Pu-5	1.2	0.8	1.6	1.4	0.9	1.9	2.1	1.6	2.6	1.5	1.0	2.0
Pu-10	1.5	1.1	2.0	1.8	1.3	2.3	2.5	2.0	3.0	1.9	1.4	2.4
Pu-15	2.2	1.7	2.7	2.6	2.1	3.1	3.3	2.8	3.8	2.6	2.1	3.1

^aCorrelations between the regional HSUs and the PM-OV HSUs are provided in [Table 2-6](#).

10.3.2 Fracture Retardation Factor Summary and Integration

The two studies described in this section present approaches for estimating retardation in fractures due to reactions with fracture-coating minerals. Although they highlight methodologies to account for processes that may affect migration rates and groundwater concentration of reactive radionuclides, these approaches are theoretical. The two methods yield different results due to conceptual model differences and assumptions about the processes that lead to fracture retardation. One of the largest differences is that Zavarin et al. (2002) include reactions with matrix minerals as well as with fracture-coating minerals. This likely leads to substantial increases in the estimated retardation factors. Wolfsberg et al. (2002) only consider reactions with the minerals coating the fracture. Reactions with matrix minerals is considered in conjunction with the matrix diffusion component of their model. However, integrated transport models where Zavarin et al. (2002) lump coating and matrix mineral reactions (and increased effective porosity), and Wolfsberg et al. (2002) consider fracture-coating reactions, matrix mineral reactions, and diffusion as separate, coupled processes that may in fact yield similar results.

Table 10-4 summarizes the results from the two different approaches and correlates the results with HSUs in the CAU model domain. Considering the two different approaches, the range of uncertainty is large due to the strictly theoretical nature of the estimation methods.

Table 10-4
Summary of Fracture Retardation Factors for HSUs^a
 (Page 1 of 3)

HSU #	HSU Name	Regional HSU (Zavarin et al. 2002)	HGUs	Representative Alteration	Lithologies Encountered	Ca	Cs	Sr	Am	Eu	Sm	Np	U	Pu (10 ⁻⁵)	Pu (10 ⁻¹⁰)	Pu (10 ⁻¹⁵)
1	LCCU		CCU		SLT/QTZ/SS											
2	LCA		CA		DM											
3	UCCU		CCU/SCU		SLT											
4	LCCU1		CCU/SCU		SLT/QTZ/SS											
5	LCA3		CA		DM											
6	MGCU		GCU													
7-12	SCICU, CHICU, CCICU, RMICU, ATICU, BMICU		IICU													
13	PBRCM	BAQ	TCU, WTA, LFA	ZE, DV, QC, AR, AB	NWT, BED, PWT, MWT, DWT, TB, FB, LA, IN	Range (2302)	Range (1, 1.23) Range (460, 1862)	Range (1, 1.23) Range (1380)	Range (22, 837) Range(1500, 20000)	Range (22, 837) Range(4345, 43450)	Range (22, 837) Range(45000, 150000)	Range (1, 14) Range(14, 128)	Range (1, 14) Range(1.6)	Range(1,40) Range (11.95)	Range (25,236)	Range (132, 1310)
14	BRA	TBA	LFA, WTA, TCU, VTA	DV, ZC, ZE, AB, PY, QC, KF	LA, FB, BED, NWT, MWT, PWT, DWT, PL	Range (1737)	Range (1, 1.23) Range (2165, 21000)	Range (1, 1.23) Range(989)	Range (22, 837) Range(2000, 100000)	Range (22, 837) Range(5530, 52000)	Range (22, 837) Range(8810, 84200)	Range (1, 14) Range(22,53)	Range (1, 14) Range (100,800)	Range(1,40) Range (39,370)	Range (100,1000)	Range (600,6000)
15	BFCU ^b	TC	TCU	ZE, ZC, DV	BED, NWT, LA	Range(897)	Range (1,1.23) Range (251, 1541)	Range (1,1.23) Range(527)	Range (22,837) Range(4324, 17780)	Range (22,837) Range(1076, 10224)	Range (22,837) Range(1829, 17740)	Range(1,14) Range (6, 32)	Range(1,14) Range (24, 164)	Range(1,40) Range (9, 75)	Range (22, 201)	Range (123, 1193)
16	KA	TC	LFA, TCU	DV, GL, ZE, ZC	LA, FB, PL	Range(897)	Range (1,1.23) Range(251, 1541)	Range (1,1.23) Range(527)	Range (22,837) Range(4324, 17780)	Range (22,837) Range(1076, 10224)	Range (22,837) Range(1829, 17740)	Range(1,14) Range (6, 32)	Range(1,14) Range (24, 164)	Range(1,40) Range (9, 75)	Range (22, 201)	Range (123, 1193)
17	CFCU ^b	TC	TCU, LFA, VTA	ZC, ZE, DV, GL	LA, NWT, BED	Range(897)	Range (1,1.23) Range(251, 1541)	Range (1,1.23) Range(527)	Range (22,837) Range(4324, 17780)	Range (22,837) Range(1076, 10224)	Range (22,837) Range(1829, 17740)	Range(1,14) Range (6, 32)	Range(1,14) Range (24, 164)	Range(1,40) Range (9, 75)	Range (22, 201)	Range (123, 1193)
18	CFCM ^c	TC	Mostly LFA, some TCU	DV, QF, AR, PY, CH, ZA, ZC	LA, FB, BED, NWT	Range(897)	Range (1,1.23) Range(251, 1541)	Range (1,1.23) Range(527)	Range (22,837) Range(4324, 17780)	Range (22,837) Range(1076, 10224)	Range (22,837) Range(1829, 17740)	Range(1,14) Range (6, 32)	Range(1,14) Range (24, 164)	Range(1,40) Range (9, 75)	Range (22, 201)	Range (123, 1193)
19	IA	TC	LA	DV, GL, ZC	LA, MWT, FB	Range(897)	Range (1,1.23) Range(251, 1541)	Range (1,1.23) Range(527)	Range (22,837) Range(4324, 17780)	Range (22,837) Range(1076, 10224)	Range (22,837) Range(1829, 17740)	Range(1,14) Range (6, 32)	Range(1,14) Range (24, 164)	Range(1,40) Range (9, 75)	Range (22, 201)	Range (123, 1193)
20	CHCU	TC	TCU, LFA	ZC	NWT, BED, PL	Range(897)	Range (1,1.23) Range (251, 1541)	Range (1,1.23) Range(527)	Range (22,837) Range(4324, 17780)	Range (22,837) Range(1076, 10224)	Range (22,837) Range(1829, 17740)	Range(1,14) Range (6, 32)	Range(1,14) Range (24, 164)	Range(1,40) Range (9, 75)	Range (22, 201)	Range (123, 1193)
21	CHZCM	TC	LFA, TCU, VTA	ZC, ZE, ZA, DV, GL	LA, FB, PL, BED,	Range(897)	Range (1,1.23) Range(251, 1541)	Range (1,1.23) Range(527)	Range (22,837) Range(4324, 17780)	Range (22,837) Range(1076, 10224)	Range (22,837) Range(1829, 17740)	Range(1,14) Range (6, 32)	Range(1,14) Range (24, 164)	Range(1,40) Range (9, 75)	Range (22, 201)	Range(123, 1193)
22	CHVCM	TC	VTA, LFA, TCU	GL, DV, ZC, ZA	LA, FB, NWT, BED	Range(897)	Range (1,1.23) Range (251, 1541)	Range (1,1.23) Range(527)	Range (22,837) Range(4324, 17780)	Range (22,837) Range(1076, 10224)	Range (22,837) Range(1829, 17740)	Range(1,14) Range (6, 32)	Range(1,14) Range (24, 164)	Range(1,40) Range (9, 75)	Range (22, 201)	Range (123, 1193)

Table 10-4
Summary of Fracture Retardation Factors for HSUs^a
 (Page 2 of 3)

HSU #	HSU Name	Regional HSU (Zavarin et al. 2002)	HGUs	Representative Alteration	Lithologies Encountered	Ca	Cs	Sr	Am	Eu	Sm	Np	U	Pu (10 ⁻⁵)	Pu (10 ⁻¹⁰)	Pu (10 ⁻¹⁵)
23	CHVTA	TC	VTA, TCU	GL, ZC	NWT, BED, PL	Range(897)	Range (1,1.23) Range (251, 1541)	Range (1,1.23) Range(527)	Range (22,837) Range(4324, 17780)	Range (22,837) Range(1076, 10224)	Range (22,837) Range(1829, 17740)	Range(1,14) Range (6, 32)	Range(1,14) Range (24, 164)	Range(1,40) Range (9, 75)	Range (22, 201)	Range (123, 1193)
24	YMCFCM	TC	TCU, LFA, WTA, unk	ZE, ZM, ZC, ZA, AR, QC, AB, CC, KF, DV	NWT, BED, MWT, PWT, LA	Range(897)	Range (1,1.23) Range (251, 1541)	Range (1,1.23) Range(527)	Range (22,837) Range(4324, 17780)	Range (22,837) Range(1076, 10224)	Range (22,837) Range(1829, 17740)	Range(1,14) Range (6, 32)	Range(1,14) Range (24, 164)	Range(1,40) Range (9, 75)	Range (22, 201)	Range (123, 1193)
25	TSA ^c	TMA	WTA, TCU, unk	DV, QF, GL, ZE, unk	NWT, PWT, TUF, MWT, VT	Range (2198)	Range (1,1.23) Range(1339, 10918)	Range (1,1.23) Range (1306)	Range (22,837) Range(5671, 23376)	Range (22,837) Range(1347, 11574)	Range (22,837) Range(2248, 20044)	Range(1,14) Range (4, 14)	Range(1,14) Range (7, 39)	Range(2,40) Range (6, 41)	Range (11, 95)	Range (54, 491)
26	LPCU ^b	TC	TCU, unk	ZE, ZC, ZA, QZ, QF, PY, CH, unk	NWT, BED, TB, WBE	Range(897)	Range (1,1.23) Range (251, 1541)	Range (1,1.23) Range(527)	Range (22,837) Range(4324, 17780)	Range (22,837) Range(1076, 10224)	Range (22,837) Range(1829, 17740)	Range(1,14) Range (6, 32)	Range(1,14) Range (24, 164)	Range(1,40) Range (9, 75)	Range (22, 201)	Range(123, 1193)
27	PLFA	TC	LFA, WTA, TCU, VTA, unk	DV, GL, ZC, ZE, VP, AR, unk	LA, FB, PL, NWT, BED, MWT, DWT, VT, PWT, unk	Range(897)	Range (1,1.23) Range (251, 1541)	Range (1,1.23) Range(527)	Range (22,837) Range(4324, 17780)	Range (22,837) Range(1076, 10224)	Range (22,837) Range(1829, 17740)	Range(1,14) Range (6, 32)	Range(1,14) Range (24, 164)	Range(1,40) Range (9, 75)	Range (22, 201)	Range (123, 1193)
28	TCA	TMA	WTA	DV, QF, VP, QC, ZC, ZE, unk	MWT, PWT, DWT, VT, unk, TUF	Range (2198)	Range (1,1.23) Range(1339, 10918)	Range (1,1.23) Range (1306)	Range (22,837) Range(5671, 23376)	Range (22,837) Range(1347, 11574)	Range (22,837) Range(2248, 20044)	Range(1,14) Range (4, 14)	Range(1,14) Range (7, 39)	Range(2,40) Range (6, 41)	Range (11, 95)	Range (54, 491)
29	UPCU	TC	TCU, VTA, LFA, unk	ZC, ZE, GL, QF, KF, unk, OP	NWT, BED, unk, TUF, RWT, FB, BS, TB	Range(897)	Range (1,1.23) Range (251, 1541)	Range (1,1.23) Range(527)	Range (22,837) Range(4324, 17780)	Range (22,837) Range(1076, 10224)	Range (22,837) Range(1829, 17740)	Range(1,14) Range (6, 32)	Range(1,14) Range (24, 164)	Range(1,40) Range (9, 75)	Range (22, 201)	Range (123, 1193)
30	BA	TC	LFA, TCU, unk	GL, DV, ZE, QZ, unk, QF, OP	LA, PL, FB, VL	Range(897)	Range (1,1.23) Range (251, 1541)	Range (1,1.23) Range(527)	Range (22,837) Range(4324, 17780)	Range (22,837) Range(1076, 10224)	Range (22,837) Range(1829, 17740)	Range(1,14) Range (6, 32)	Range(1,14) Range (24, 164)	Range(1,40) Range (9, 75)	Range (22, 201)	Range (123, 1193)
31	PVTA	TC	VTA, WTA, LFA, TCU, unk	GL, DV, ZE, ZC, unk, VP, AR	MWT, PWT, DWT, VT, NWT, BED, TUF, unk, RWT, BS, PL	Range(897)	Range (1,1.23) Range (251, 1541)	Range (1,1.23) Range(527)	Range (22,837) Range(4324, 17780)	Range (22,837) Range(1076, 10224)	Range (22,837) Range(1829, 17740)	Range(1,14) Range (6, 32)	Range(1,14) Range(24, 164)	Range(1,40) Range (9, 75)	Range (22, 201)	Range (123, 1193)
32	PCM	TC	WTA, VTA, TCU, LFA, unk, AA	DV, VP, GL, ZC, ZE, unk, AR, CC, QC, OP	DWT, MWT, VT, PWT, NWT, BED, LA, AL	Range(897)	Range (1,1.23) Range (251, 1541)	Range (1,1.23) Range(527)	Range (22,837) Range(4324, 17780)	Range (22,837) Range(1076, 10224)	Range (22,837) Range(1829, 17740)	Range(1,14) Range (6, 32)	Range(1,14) Range (24, 164)	Range(1,40) Range (9, 75)	Range (22, 201)	Range (123, 1193)
33	WWA ^c	TMA	LFA, unk	GL, DV, unk, ZE, ZC	LA, FB, PL, WT	Range (2198)	Range (1,1.23) Range(1339, 10918)	Range (1,1.23) Range (1306)	Range (22,837) Range(5671, 23376)	Range (22,837) Range(1347, 11574)	Range (22,837) Range(2248, 20044)	Range(1,14) Range (4, 14)	Range(1,14) Range (7, 39)	Range(2,40) Range (6, 41)	Range (11, 95)	Range (54, 491)
34	FCCU ^b	TC	TCU	ZE	NWT, BED	Range(897)	Range (1,1.23) Range (251, 1541)	Range (1,1.23) Range(527)	Range (22,837) Range(4324, 17780)	Range (22,837) Range(1076, 10224)	Range (22,837) Range(1829, 17740)	Range(1,14) Range (6, 32)	Range(1,14) Range (24, 164)	Range(1,40) Range (9, 75)	Range (22, 201)	Range (123, 1193)
35	SCVCU		NA	NA	NA											

Table 10-4
Summary of Fracture Retardation Factors for HSUs^a
 (Page 3 of 3)

HSU #	HSU Name	Regional HSU (Zavarin et al. 2002)	HGUs	Representative Alteration	Lithologies Encountered	Ca	Cs	Sr	Am	Eu	Sm	Np	U	Pu (10 ⁻⁵)	Pu (10 ⁻¹⁰)	Pu (10 ⁻¹⁵)
36	TMA	TMA	WTA, VTA , unk, TCU, LFA, ICU, AA	unk, GL, DV, VP, ZE, ZC, QF, QZ, CC, OP, AR, KF	MWT, PWT, DWT, VT, unk, TUF, WT, NWT, BED, RWT, AL, BD, LA	Range (2198)	Range (1,1.23) Range(1339, 10918)	Range (1,1.23) Range (1306)	Range (22,837) Range(5671, 23376)	Range (22,837) Range(1347, 11574)	Range (22,837) Range(2248, 20044)	Range(1,14) Range (4, 14)	Range(1,14) Range (7, 39)	Range(2,40) Range (6, 41)	Range (11, 95)	Range (54, 491)
37	THCM	TMA	TCU, WTA, VTA	ZE, GL, DV, QZ	BED, MWT	Range (2198)	Range (1,1.23) Range(1339, 10918)	Range (1,1.23) Range (1306)	Range (22,837) Range(5671, 23376)	Range (22,837) Range(1347, 11574)	Range (22,837) Range(2248, 20044)	Range(1,14) Range (4, 14)	Range(1,14) Range (7, 39)	Range(2,40) Range (6, 41)	Range (11, 95)	Range (54, 491)
38	THLFA	TMA	LFA, AA	DV, QZ, GL, ZE, unk	LA, VL, PL, AL	Range (2198)	Range (1,1.23) Range(1339, 10918)	Range (1,1.23) Range (1306)	Range (22,837) Range(5671, 23376)	Range (22,837) Range(1347, 11574)	Range (22,837) Range(2248, 20044)	Range(1,14) Range (4, 14)	Range(1,14) Range (7, 39)	Range(2,40) Range (6, 41)	Range (11, 95)	Range (54, 491)
39	TMCM	TMA	TCU, WTA, VTA, LFA, AA	QF, DV, ZE, QZ, VP, GL, ZA, QZ, QC, AB, AR, KF, KA, CC, CH, PY	MWT, PWT, DWT, LB, VT, NWT, BED, LA, RWT, TB, TG, TS, TSS, FB	Range (2198)	Range (1,1.23) Range(1339, 10918)	Range (1,1.23) Range (1306)	Range (22,837) Range(5671, 23376)	Range (22,837) Range(1347, 11574)	Range (22,837) Range(2248, 20044)	Range(1,14) Range (4, 14)	Range(1,14) Range (7, 39)	Range(2,40) Range (6, 41)	Range (11, 95)	Range (54, 491)
40	FCA		NA	NA	NA											
41	FCCM	TMA	LFA, TCU, WTA, VTA, AA	ZE, DV, GL, QZ, QF, QC, CC, AB, PI, MP, CH, PY, unk, AR	MWT, PWT, NWT, TB, unk, RWT, BED, TSS, PL, LA, FB, VL, BS, TSLT, WT, AL	Range (2198)	Range (1,1.23) Range(1339, 10918)	Range (1,1.23) Range (1306)	Range (22,837) Range(5671, 23376)	Range (22,837) Range(1347, 11574)	Range (22,837) Range(2248, 20044)	Range(1,14) Range (4, 14)	Range(1,14) Range (7, 39)	Range(2,40) Range (6, 41)	Range (11, 95)	Range (54, 491)
42	DVA		NA	NA	NA											
43	DVCM ^c	TMA	TCU, WTA	DV, AR, QF	NWT, MWT, PWT	Range (2198)	Range (1,1.23) Range(1339, 10918)	Range (1,1.23) Range (1306)	Range (22,837) Range(5671, 23376)	Range (22,837) Range(1347, 11574)	Range (22,837) Range(2248, 20044)	Range(1,14) Range (4, 14)	Range(1,14) Range (7, 39)	Range(2,40) Range (6, 41)	Range (11, 95)	Range (54, 491)
44	TCVA	TMA	WTA, VTA, LFA, TCU, AA	unk, DV, GL, VP, ZE, CC, QF	MWT, PWT, DWT, NWT, BED, RWT, WT, TUF, ITL, LA, AL, CL	Range (2198)	Range (1,1.23) Range(1339, 10918)	Range (1,1.23) Range (1306)	Range (22,837) Range(5671, 23376)	Range (22,837) Range(1347, 11574)	Range (22,837) Range(2248, 20044)	Range(1,14) Range (4, 14)	Range(1,14) Range (7, 39)	Range(2,40) Range (6, 41)	Range (11, 95)	Range (54, 491)
45	YVCM ^c	TMA	LFA, WTA, AA	unk, DV, VP	AL, BS, PWT	Range (2198)	Range (1,1.23) Range(1339, 10918)	Range (1,1.23) Range (1306)	Range (22,837) Range(5671, 23376)	Range (22,837) Range(1347, 11574)	Range (22,837) Range(2248, 20044)	Range(1,14) Range (4, 14)	Range(1,14) Range (7, 39)	Range(2,40) Range (6, 41)	Range (11, 95)	Range (54, 491)
46	AA		AA, VTA, WTA, LFA, TCU	unk, GL, VP, AR, CC, ZE, ZC	AL, TS, RWT, BS, NWT, BED, PWT, MWT, PWT	NA	NA	NA	NA	NA	NA	NA	NA	NA	NA	NA

^a Upper value in each cell represents retardation to fracture minerals only from Table 10-2 (Wolfsberg et al., 2002)

^b Lower value in each cell represents retardation due to sorption to fracture minerals and matrix minerals from Table 10-3 (Zavarin et al. 2002)

^c Retardation factors extrapolated from TC regional HSU parameters in Table 10-3

^d Retardation factors extrapolated from TMA regional HSU parameters in Table 10-3

Bold Font = Prominent material type encountered-basis for consideration
 Italic Font = Estimated using other HSU as a surrogate

11.0 Colloid-Facilitated Transport Parameters

This section includes descriptions of the role of colloids in contaminant transport in groundwater, the available data, and the data evaluation and associated results.

11.1 Role of Colloids in Contaminant Transport

Colloids can facilitate the transport of strongly sorbing contaminants in groundwater systems by providing mobile surface area onto which the contaminants can sorb. Colloid-facilitated transport of radionuclides depends on the colloid types, concentrations and size distributions, the actinide distribution coefficients, and the colloid filtration and retardation parameters.

Colloid types are important because contaminant sorption and colloid mobility are strong functions of colloid surface mineralogy. Colloid concentrations and size distributions are important because these parameters determine the available surface area and ultimately the contaminant sorption capacity offered by mobile colloids. Colloid size distributions are also important in determining the mobility of colloids.

Actinide distribution coefficients and sorption/desorption rates onto colloids are important because these parameters govern how strongly and reversibly actinides adsorb to colloids. Strong, irreversible sorption will tend to increase the probability of significant colloid-facilitated transport in a groundwater system.

Colloid filtration and retardation parameters are important because colloid-facilitated contaminant transport can occur to a significant degree only if colloids remain mobile over relatively long distance and time scales.

11.2 Colloid Types, Concentrations, and Size Distributions

This section includes descriptions of the data available on colloid types, concentrations, and size distributions. The associated data analysis and results are also described including a discussion on the limitations of the data and scaling considerations.

11.2.1 Data Compilation and Evaluation

Colloid types, concentrations, and size distributions were obtained the NTS, either for the UGTA Program or the Yucca Mountain Project. Colloid types were determined from mineralogic analyses of colloid samples by XRD at LLNL. Colloid concentrations and size distributions were measured using high-sensitivity liquid *in situ* particle spectrometry (HSLIS) at LANL. Colloid types, concentrations, and size distribution data are described in [Appendix J](#).

Colloid types, concentrations, and size distribution data were checked by LANL personnel prior to tabulation. They were also checked for consistency after tabulation.

11.2.2 Development of Parameter Distributions

The information available on colloid types (mineralogy) and colloid concentrations and size distributions was evaluated and probability distributions were developed.

11.2.2.1 Colloid Types (Mineralogy)

Natural colloids have not been analyzed routinely for their mineralogy at the NTS. However, Brachmann and Kersting (2002) conducted significant mineralogical analysis on colloid samples collected from ER-20-5 #1 and #3 and from U20n PS1 DDH (in and near the CHESHIRE cavity) in Area 20 at the NTS. Among their conclusions were:

- The colloids in the NTS groundwater samples are mineralogically similar, although the actual abundances of each mineral may vary from aquifer to aquifer.
- The colloidal material is composed primarily of clays (smectite and illite) and zeolites (mordenite and clinoptilolite/heulandite). Cristobalite (SiO₂) was also identified in x-ray diffraction spectra of colloids from ER-20-5 #1. These results suggest that potentially important radionuclide-sorbing minerals are clays and zeolites for groundwater hosted in silicic volcanic units. This does not rule out the importance of minor colloidal minerals (i.e., those present at less than 10 percent). Note that relative percentages of the different minerals in the different colloid samples were not reported.
- The same clays and zeolites identified in the groundwater samples are also present in the host rock aquifers at ER-20-5. The colloid minerals mimic the host rock from which they originated.

For the purposes of radionuclide transport modeling, it is recommended that natural colloids be considered to consist primarily of clays and zeolites, with some

silica (either amorphous or crystalline). However, refractory colloids generated at the time of nuclear test detonations or resulting from corrosion of the resulting melt glass (probably mostly clays) cannot be ruled out as a potentially significant contributor to colloid-facilitated transport at the NTS.

11.2.2.2 Colloid Concentrations and Size Distributions

Colloid concentrations and size distributions have been measured in groundwater samples taken from Pahute Mesa and from several wells completed in fractured volcanic tuffs near Yucca Mountain in the past several years by Kung (2000 and 2002). We used the concentration and size distribution data from 32 samples collected from 24 different wells (Kung, 2002) to construct distributions for both concentrations and sizes of colloids in fractured volcanic rocks. Table 11-1 lists the wells and the number of samples from each well that were analyzed.

Figure 11-1 shows the cumulative distribution of log colloid concentrations in all of the samples. The solid line in Figure 11-1 represents a normal distribution with a mean of -7.6 and a standard deviation of 1.2. The open circles are results from Area 25 and Area 29 wells near Yucca Mountain, and the open squares are results from the ER-20-5 well.

The line in Figure 11-1 is a fit of a normal distribution to the data (actually a lognormal distribution given that the concentrations are log transformed). The mean and standard deviation of this fitted distribution are 7.6 and 1.2, respectively. This distribution can be randomly sampled to obtain stochastic samples of Log (concentration) values.

Points that correspond to wells in the vicinity of Yucca Mountain in Figure 11-1 are indicated with open circles, and the ER-20-5 wells are indicated with open squares. It is apparent that (1) there is a tendency for Yucca Mountain wells to have somewhat lower concentrations than Pahute Mesa wells (6 of the 11 lowest concentrations are in Yucca Mountain wells), and (2) the ER-20-5 wells have the highest concentrations of any of the wells sampled. There may be some bias in the Yucca Mountain wells tending to be lower in concentration because four of the samples were taken from wells that were pumped extensively for years prior to collecting three samples from Well J-13 and one from UE25c#3. These wells would be expected to be extremely well purged and developed compared to some of the other wells. The fact that the highest colloid concentrations were measured in the ER-20-5 wells in which colloid-facilitated transport of Pu over significant distances was implicated is an interesting result, but it may be just a coincidence. No attempt was made to correlate the colloid concentrations with water chemistry, which was generally quite similar for the different wells (typically sodium bicarbonate waters with a pH of 7 to 8.5 and relatively low concentrations of divalent cations).

Figure 11-2 shows colloid concentrations in wells completed in saturated alluvium south and southwest of Yucca Mountain as a function of divalent cation concentrations in the groundwater (Kung, 2002). In this case, there is significant variability in the divalent cation concentrations, and it is clear that colloid concentrations are correlated with these concentrations. Correlations of colloid

Table 11-1
Wells Sampled for Colloid Concentration and Size Distribution Analyses

Well	Number of Samples
ER-EC-1	1
ER-18-1	1
ER-EC-2a	2
ER-EC-4	2
ER-EC-5	2
ER-EC-6	2
ER-EC-7	2
ER-EC-8	2
ER-20-5 #1	1
ER-20-5 #3	1
U-19q	1
U-20n	1
UE-18r	1
UE-19h	1
UE-20bh1	1
U-8WW	1
U-20WW	1
UE-25 J-13	3
UE-25c#3	1
UE-29a#1	1
UE-29a#2	1
UE-25 WT#3	1
UE-25 WT#17	1
UE-25 SD6	1

concentrations from these wells with total ionic strength and monovalent cation concentrations were not nearly as good as the correlation with divalent cation concentrations. This result is consistent with colloid stability theory and the Schulze-Hardy Rule (Hiemenz, 1986). Although [Figure 11-2](#) does not represent groundwater samples taken from fractured rocks, it suggests that it may be appropriate to adjust colloid concentrations obtained from the lognormal distribution of [Figure 11-1](#) when divalent cation concentrations in Pahute Mesa waters are found to be significantly different from those in the majority of the wells (which have $\text{Log} [\{\text{Ca}\} + \text{Magnesium } \{\mu\text{g}\}]$ values of approximately 1.0).

[Figure 11-3](#) shows normalized size distributions (log diameters) determined from the 32 samples taken from the 24 wells completed in fractured volcanics ([Table 11-1](#)) as determined by a HSLIS-50 and -100 (Kung, 2000). This instrument has lower and upper size (diameter) limits of 50 and 1,000 nm, respectively. However, only diameters up to 200 nm are shown in [Figure 11-3](#)

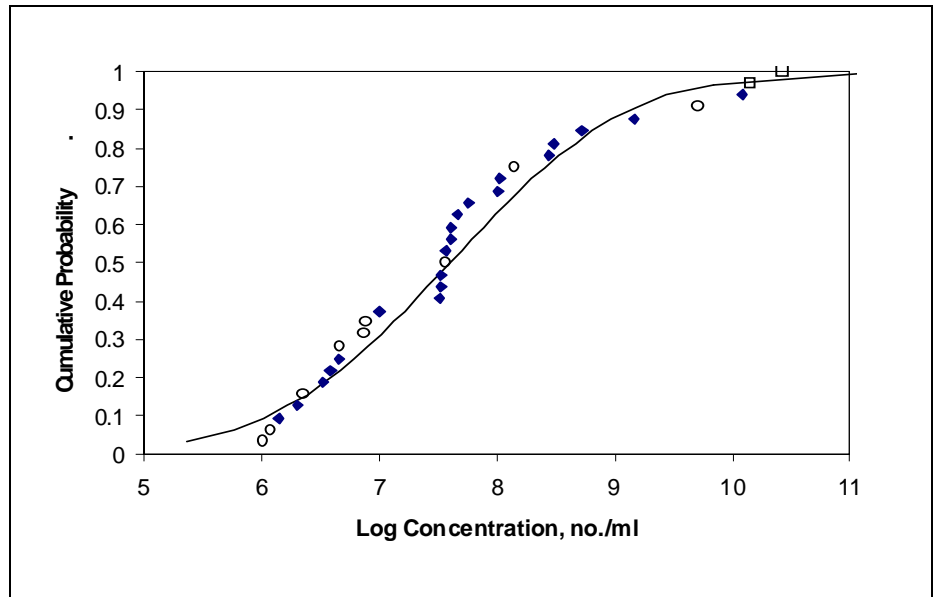


Figure 11-1
Cumulative Probability Distribution of Log Colloid Concentrations
in NTS Fractured Volcanics

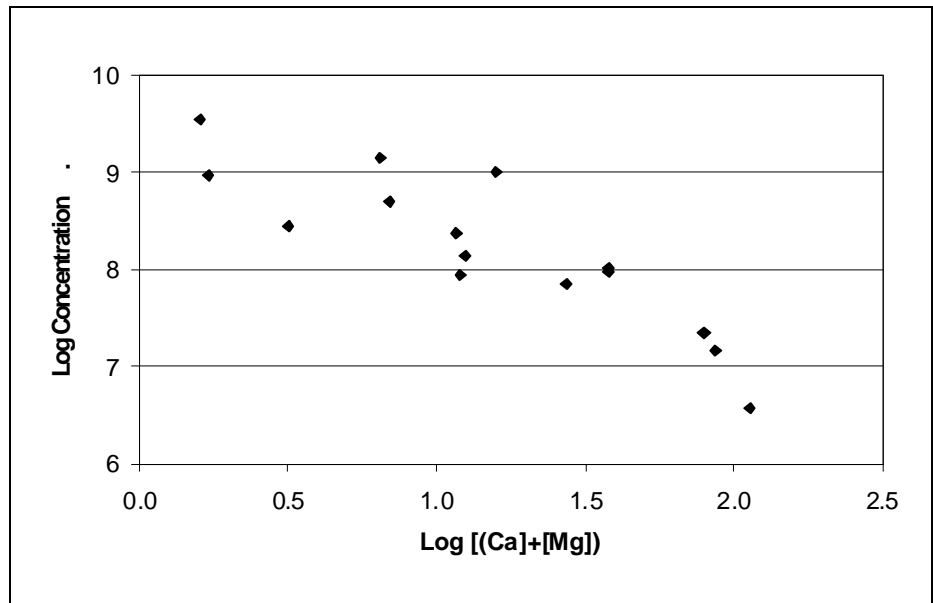


Figure 11-2
Log Colloid Concentrations Versus Log [(Ca)+[Mg)] (M)
in Saturated Alluvium near Yucca Mountain

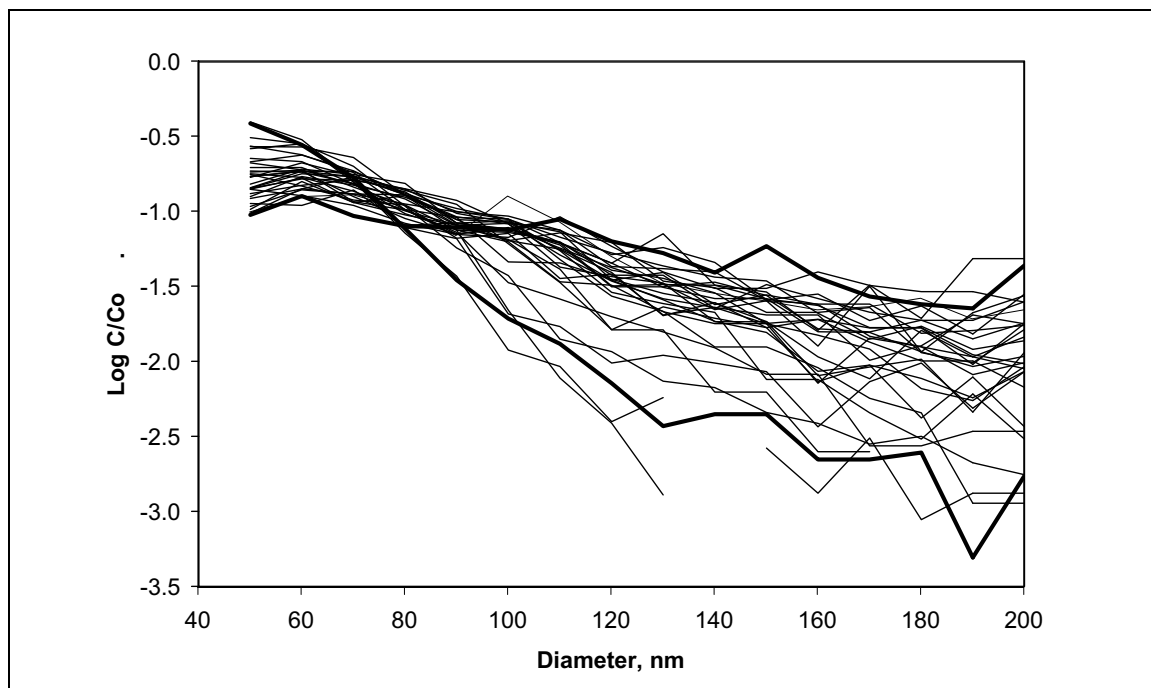


Figure 11-3
Normalized Size Distributions of Colloids in Wells
Located on the Nevada Test Site and Vicinity

because there are very few colloids at larger sizes. The size distributions in [Figure 11-3](#) are normalized by dividing the number of colloids in each size “bin” by the total number of colloids in all bins. This allows the shapes of the distributions to be compared directly. The concentration of colloids in each size bin is represented by “C”, and the total concentration of colloids in all size bins is represented by “Co”.

It is apparent from [Figure 11-3](#) that all of the size distributions are qualitatively similar in shape. However, as indicated by the two bold lines in [Figure 11-3](#), distributions with higher concentrations of larger sizes tend to have lower concentrations of smaller sizes (an expected result of the normalization process). To simplify the parameterization of the size distributions, all of the distributions were lumped together and a mean and standard deviation were calculated for each size bin between 50 and 1,000 nm. The resulting mean normalized size distribution and its 95 percent confidence intervals (with different confidence intervals for each size bin, depending on the standard deviation calculated for each bin) are shown in [Figure 11-4](#). The mean normalized size distribution is represented by diamonds and the 95 percent confidence intervals by dashed lines. A third-order polynomial fit to the mean distribution (solid line) is also shown in [Figure 11-4](#). It is suggested that this equation be used to determine the normalized colloid concentration in each size bin. Then, for any given size x , the normalized colloid concentration, 10^y , should be multiplied by the total colloid concentration determined from the lognormal distribution of [Figure 11-1](#) to obtain the concentration of colloids of that size (bin). This procedure forces all size distributions to have the same shape.

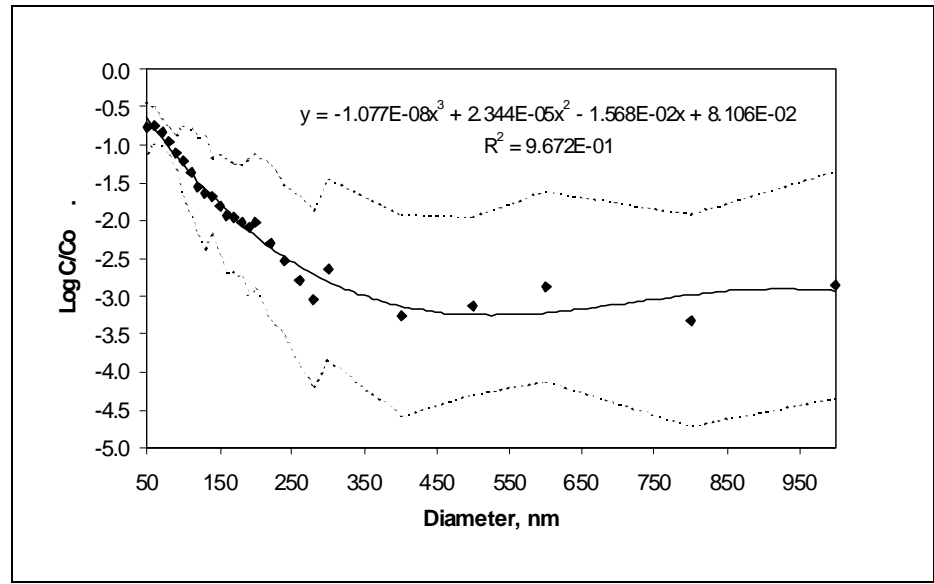


Figure 11-4
Mean Normalized Size Distribution of Colloids in Wells
Located on the Nevada Test Site and Vicinity

If additional sophistication is desired in generating colloid size distributions that have varying shapes that roughly honor the trends shown by the bold lines in Figure 11-3, the following approach is suggested. First, Figure 11-5 shows a fourth-order polynomial fit to the standard deviations of the log concentrations in each size bin from Figure 11-4 as a function of colloid diameter. The solid line shown in Figure 11-5 is a fourth-order polynomial fit to the data (the equation is also shown). For each size bin, a standard deviation could be calculated and used to generate a random number taken from a normal distribution having a mean obtained from the polynomial equation of Figure 11-4. This random number is representative of the log normalized colloid concentration in that bin. However, it is suggested that for one-third of the size distribution “realizations,” the random normal variates (the randomly-generated numbers taken from a normal distribution with a mean of 0 and a standard deviation of 1 which are then multiplied by the actual standard deviation and added to the actual mean) be forced to be positive up to and including the 80-nm bin. The normalized concentration associated with the 90-nm bin could be taken to be the mean determined from the polynomial equation of Figure 11-4, and all size bins greater than 90 nm would have their random normal variates forced to be negative. These actions would result in a size distribution “realization” with sizes greater than the mean below the 90-nm bin and less than the mean above the 90-nm bin. Another one-third of the realizations should have sizes less than the mean below the 90-nm bin and greater than the mean above the 90-nm bin, which would be accomplished by forcing random normal variates to be negative below 90 nm and positive above 90 nm. Finally, the last one-third of the realizations would simply have the mean values obtained from the polynomial equation of Figure 11-4. The end result would be that one-third of the distribution realizations would have larger concentrations at smaller sizes and smaller concentrations at larger sizes, one-third

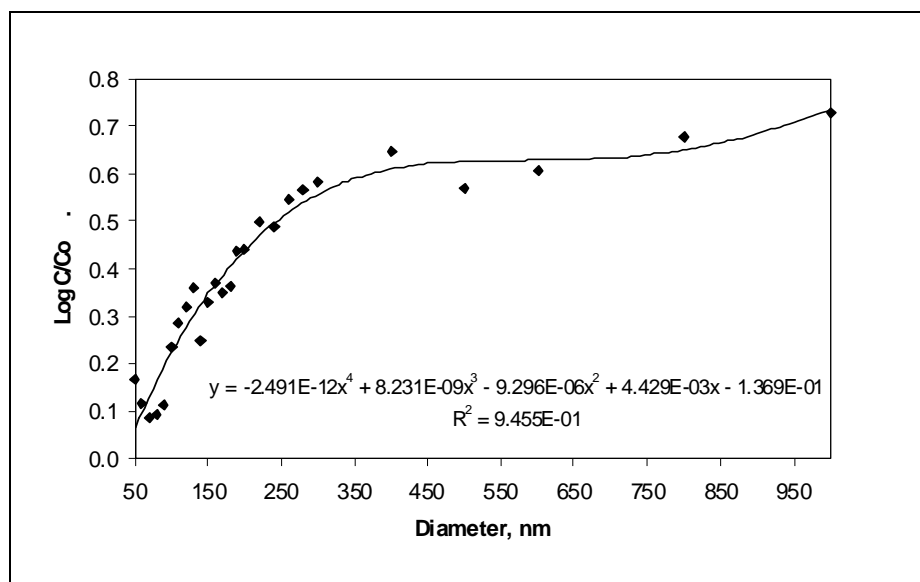


Figure 11-5
Standard Deviations of Normalized Concentrations
Versus Colloid Diameter

would have smaller concentrations at smaller sizes and larger concentrations at larger sizes, and one-third would have mean concentrations in each size bin.

11.2.3 Data Limitations

Colloid samples obtained from pumped wells have potential artifacts resulting from necessary stressing of the aquifer to obtain the samples and also from residual foreign materials that are introduced during drilling (e.g., drilling muds, polymer additives) or from corrosion of well construction materials (e.g., metallic casing, concrete). Colloids that are mobile under stressed conditions may not necessarily be mobile under unstressed conditions.

It is always best to purge a borehole extremely well before sampling for colloids. Unfortunately, well purging was not done in a consistent manner for the samples reported in [Table 11-1](#). Some of the samples came from wells that had been producing large volumes of water at high flow rates for years before they were sampled (e.g., UE-25 J-13 and UE-25c#3), and others could only be bailed or pumped very minimally before sampling. The impact of these sampling inconsistencies on the colloid data cannot be quantified at this time.

In addition, when sampling for colloids, it is best to pump the well at low flow rates to minimize the perturbations to the ambient flow system. High flow rates during sampling may lead to concentrations that are higher in the samples than in the formation. Sampling at the ER wells was conducted at pumping rates that are considered high for representative colloid sampling. The colloid concentrations reported from the ER wells are, therefore, most likely greater than ambient unperturbed concentrations.

11.2.4 Scaling Considerations

Scaling of colloid types, concentrations, and size distributions is probably not an important issue for CAU-scale transport modeling. Scaling of colloid transport behavior and colloid-facilitated contaminant transport are probably far more important.

11.3 Actinide Distribution Coefficients and Sorption Rates onto Colloids

This section includes descriptions of the data available on actinide distribution coefficients and sorption rates (forward and reverse) onto colloids. The associated data analysis and results are also described including a discussion on the limitations of the data and scaling considerations.

11.3.1 Data Compilation and Evaluation

Actinide distribution coefficients and sorption/desorption rates onto colloids were obtained from batch sorption and desorption experiments as well as fracture transport experiments conducted at both LANL and LLNL. All of the YMP experiments and the UGTA fracture transport experiments were conducted at LANL.

Batch sorption/desorption experiments have been conducted for both the UGTA Program (focusing on Pu only) and the Yucca Mountain Project (Pu, Am, Np, and U), and fracture transport experiments have been conducted for the UGTA program (Pu only). Actinide distribution coefficients and sorption/desorption rates onto colloids were checked by LANL personnel prior to tabulation, and they were also checked for consistency after tabulation. Actinide distribution coefficients and sorption/desorption rates onto colloids are described in [Appendix J](#) (distribution coefficients) and in [Table 11-2](#) of this section (rates).

11.3.2 Development of Parameter Distributions

The available data were assessed to derive distribution coefficients (K_d values) and radionuclide desorption rates from colloids.

11.3.2.1 Distribution Coefficients (K_d values)

Between 1997 and 2000, Lu et al. (1998a and b, 2000) conducted several batch sorption and desorption experiments to measure the sorption of Pu(IV), Pu(V), Am(III), Np(V), and U(VI) onto hematite, goethite, montmorillonite, and silica colloids using filtered waters from Well J-13 in Area 25 at the NTS (near Yucca Mountain) and synthetic J-13 water. The Pu(IV) was always introduced as a polymeric colloid (≤ 10 nm diameter) because Pu(IV) is not stable as a solute at

Table 11-2
Ranges of Rate Constants (hr^{-1}) for Sorption and Desorption of Actinides Onto Colloids
(Assuming Only a Single Type of Sorption Site) from UGTA and Yucca Mountain Experiments

Colloids/Actinides	Batch k_f (hr^{-1})	Batch k_b (hr^{-1})	Fracture k_f (hr^{-1})	Fracture k_b (hr^{-1})
Montmorillonite				
Pu(IV)	0.2-0.5	0.0001-0.01		
Pu(V)	0.005-0.04	0.0001-0.01	0.005-0.04	0.1-2
Np(V)	0.02-0.1	ND		
Am(III)	0.04-0.1	ND		
U(VI)	0.02-0.1	ND		
Silica				
Pu(IV)	0.2-0.5	0.01-0.2		
Pu(V)	0.01-0.06	0.01-0.2	0.01-0.06	0.5-1.5
Np(V)	0.02-0.1	ND		
Am(III)	0.04-0.1	ND		
U(VI)	0.02-0.1	ND		
Hematite				
Pu(IV)	1-50	0.00001-0.0001		
Pu(V)	0.04-0.1	0.00001-0.0001		
Np(V)	0.02-0.1	ND		
Am(III)	1-5	ND		
U(VI)	0.02-0.1	ND		
Goethite				
Pu(IV)	1-50	0.00001-0.001		
Pu(V)	0.06-0.1	0.00001-0.001		
Clinoptilolite				
Pu(IV)	1-50	0.001-0.03	1-50	0.001-0.03
Pu(V)	0.001-0.01	ND		
Birnessite				
Pu(V)	1-50	ND		

k_f = Sorption rate constant

k_b = Desorption rate constant.

ND = Not determined

near-neutral pH, except at very low concentrations. The solubility of Pu(IV) at near-neutral pH is less than 10^{-8} M. The measurements of Pu(IV) sorption are, therefore, likely to be valid because the concentrations of Pu in solution were very low after equilibration, even though the kinetics of precipitation, colloid formation, and oxidation are not well known.

The hematite and goethite were selected to represent colloids that could form as a result of the corrosion of iron-containing waste package materials in the potential Yucca Mountain repository. Experiments were conducted at different colloid

concentrations, temperatures, and ionic strengths. The reader is referred to the Lu et al. (1998a and b; 2000) references for details of the experiments.

Figure 11-6 graphically depicts the ranges of radionuclide partition coefficients (K_d values, mL/g) measured for the various radionuclide-colloid combinations at colloid concentrations of 200 mg/L at 20°C in natural J-13 water (ambient Los Alamos temperature of about 20°C) (Lu et al., 1998a, 1998b, 2000; Reimus et al., 2002b, Kersting et al., 2002a and b). UGTA results for Pu(V) distribution coefficients onto silica and montmorillonite colloids in well water from U-20WW (Reimus et al., 2002b) and for Pu(IV) distribution coefficients onto clinoptilolite colloids in a synthetic J-13 well water (Kersting et al., 2002a) are shown as extensions of the bars for the J-13 K_d values in Figure 11-6. Some of the key observations in the J-13 experiments, including the effects of changing the temperature, ionic strength, and colloid concentrations are listed in brief summary fashion for each radionuclide and each colloid below.

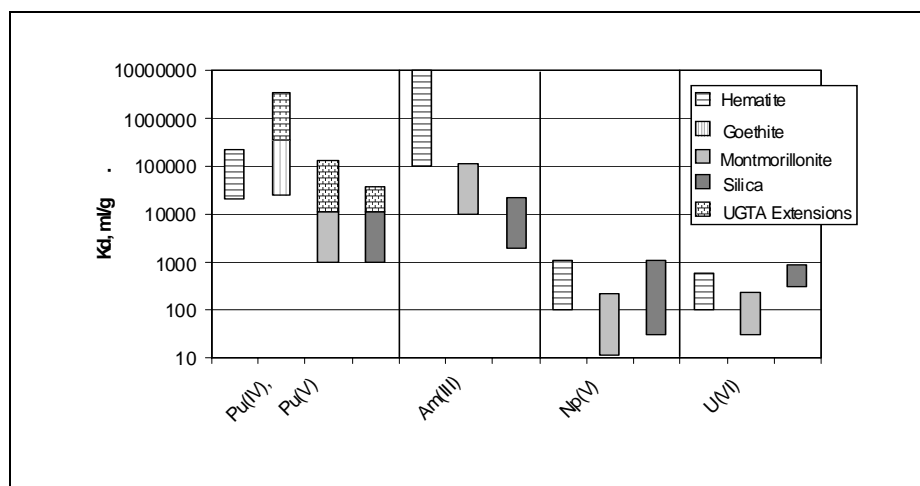


Figure 11-6
Ranges of K_d Values Measured for Actinide Sorption Onto Colloids

Pu(IV) and Pu(V) Sorption to Hematite Colloids:

- Pu(IV) sorption much faster than Pu(V) sorption, although final K_d s were quite similar
- K_d range $2 \times 10^4 - 2 \times 10^5$ mL/g at 20°C, J-13 water, 200 mg/L colloid concentration
- K_d increase to 5×10^6 mL/g as temperature increases to 80°C
- K_d increase to 1×10^7 mL/g as ionic strength increases to 0.07 M or greater
- Slight K_d increase (about a factor of 2) at low colloid concentrations (down to 10 mg/L)

- Desorption K_d comparable to sorption K_d s, so tests appear to indicate reversibility

Pu(IV) and Pu(V) Sorption to Goethite Colloids:

- Pu(IV) sorption much faster than Pu(V) sorption, although final K_d s were quite similar
- No significant effect of ionic strength on K_d values; K_d increase to 3×10^4 mL/g at low colloid concentrations
- Desorption K_d comparable to sorption K_d s, so tests appear to indicate reversibility

Pu(IV) and Pu(V) Sorption to Silica Colloids:

- Pu(IV) sorption much faster than Pu(V) sorption, although final K_d s were quite similar
- K_d range $10^3 - 10^4$ mL/g at 20°C, J-13 water, 200 mg/L colloid concentration
- K_d upper limit of 10^4 mL/g as temperature increases to 80°C
- K_d lower limit of 10^3 mL/g as ionic strength increases to 0.1 M
- K_d increase to 3×10^4 mL/g at low colloid concentrations
- Desorption K_d is comparable to sorption K_d s so tests appear to indicate reversibility

Am(III) Sorption to Hematite Colloids:

- K_d range 10^5 to 10^7 mL/g at 20°C, J-13 water, 200 mg/L colloid concentration
- No significant effect of temperature, although slightly higher K_d s at higher temps
- K_d s approach lower end of K_d range as ionic strength increases to 0.1 M
- Upper end of K_d range is approached at low colloid concentrations
- Desorption K_d is at lower end of range of sorption K_d s, so tests appear to indicate reversibility

Am(III) Sorption to Montmorillonite Colloids:

- K_d range 10^4 to 10^5 mL/g at 20°C, J-13 water, 200 mg/L colloid concentration

- K_d increase to 3×10^5 mL/g as temperature increases to 80°C .
- K_d values approach lower end of K_d range as ionic strength increases to 0.1 M
- K_d increase to 10^6 mL/g at low colloid concentrations (10 mg/L)
- Desorption K_d is within range of sorption K_d s, so tests appear to indicate reversibility

Am(III) Sorption to Silica Colloids:

- K_d range 2×10^3 to 2×10^4 mL/g at 20°C , J-13 water, 200 mg/L colloid concentration
- K_d increase to 6×10^4 mL/g as temperature increases to 80°C .
- K_d values approach lower end of K_d range as ionic strength increases to 0.1 M
- K_d increase to 10^5 mL/g at low colloid concentrations (10 mg/L)
- Desorption K_d is comparable to sorption K_d s, so tests appear to indicate reversibility

Np(V) Sorption to Hematite Colloids:

- K_d range 10^2 to 10^3 mL/g at 20°C , J-13 water, 200 mg/L colloid concentration
- K_d increase to 4×10^3 mL/g as temperature increases to 80°C .
- K_d values approach upper end of K_d range as ionic strength increases to 0.1 M
- Desorption was not measurable, but this is not conclusive because of low amount of sorption

Np(V) Sorption to Montmorillonite Colloids:

- K_d range 10 to 200 mL/g at 20°C , J-13 water, 200 mg/L colloid concentration
- K_d increase to 3×10^3 mL/g as temperature increases to 80°C .
- No significant effect of ionic strength on K_d values
- Desorption was not measurable, but this is not conclusive because of low amount of sorption

Np(V) Sorption to Silica Colloids:

- K_d range 30 to 1,000 mL/g at 20°C, J-13 water, 200 mg/L colloid concentration
- K_d increase to 2×10^3 mL/g as temperature increases to 80°C.
- K_d values approach lower end of K_d range as ionic strength increases to 0.1 M
- Desorption was not measurable, but this is not conclusive because of low amount of sorption

U(VI) Sorption to Hematite Colloids:

- K_d range 100 to 500 mL/g at 20°C, J-13 water, 200 mg/L colloid concentration
- K_d increase to upper end of K_d range as temperature increases to 80°C.
- U precipitated at higher ionic strengths
- Desorption was not measurable, but this is not conclusive because of low amount of sorption

U(VI) Sorption to Montmorillonite Colloids:

- K_d range 30 to 200 mL/g at 20°C, J-13 water, 200 mg/L colloid concentration
- K_d increase to 700 mL/g as temperature increases to 80°C.
- U precipitated at higher ionic strengths
- Desorption was not measurable, but this is not conclusive because of low amount of sorption

U(VI) Sorption to Silica Colloids:

- K_d 300 to 600 mL/g at 20°C, J-13 water, 200 mg/L colloid concentration
- K_d increase to 2×10^3 mL/g as temperature increases to 80°C.
- U precipitated at higher ionic strengths
- Desorption was not measurable, but this is not conclusive because of low amount of sorption

The results of the Pu(IV) and Pu(V) experiments are consistent with at least partial reversibility of sorption, but the results are also consistent with very slow desorption kinetics or irreversible sorption of a fraction of the Pu.

Separate Pu(IV) and Pu(V) sorption experiments onto colloids were recently conducted by Kersting et al. (2002a and b) at LLNL. Pu(IV) sorption onto clinoptilolite colloids was very fast and exhibited K_d values of 15,000 to 25,000 mL/g at 20°C over a pH range of 7 to 9.5 (Kersting et al., 2002a). Pu(V) experiments were conducted using seven different colloids. The resulting K_d values for Mn-oxide, birnessite and pyrolusite; calcite; zeolite, clinoptilolite; Fe-oxide, goethite; clay, montmorillonite; and silica are depicted in Figure 11-7 (Kersting et al., 2002b). The data in Figure 11-7 are in good agreement with the Pu K_d values from LANL experiments shown in Figure 11-6. The K_d values for goethite are slightly higher in the LLNL experiments compared to the range in LANL experiments, although both datasets indicate very strong sorption of Pu(V) to goethite. These are the only types of mineral colloids for which comparisons are possible.

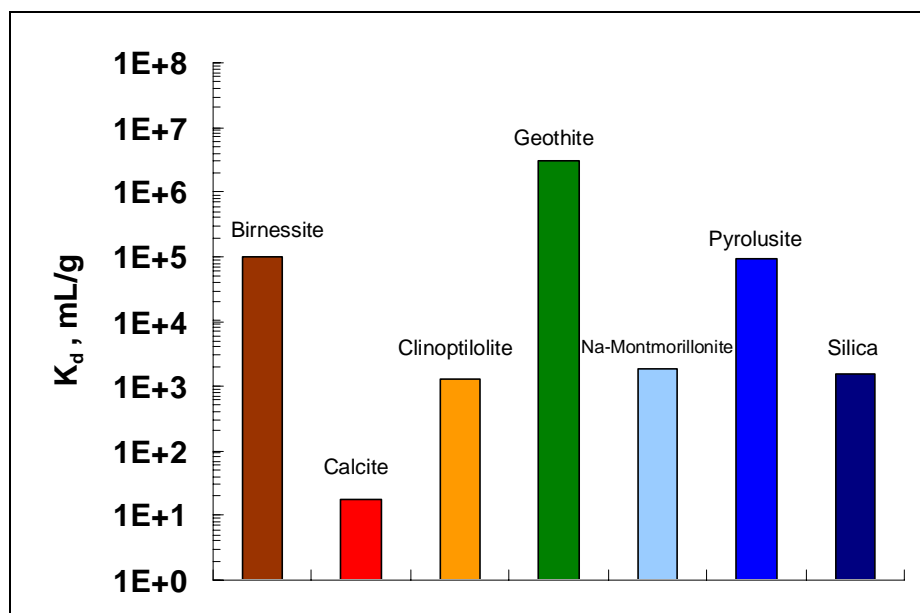


Figure 11-7
Distribution Coefficient (K_d) Calculated for Pu(V) Sorbed
Onto Various Mineral Colloids (Source: Kersting et al., 2002b)

It is recommended that K_d values for actinide sorption onto colloids be sampled from the ranges shown in Figure 11-6 for iron oxide, montmorillonite, and silica colloids. For calcite, birnessite, clinoptilolite, and pyrolusite colloids, the K_d values in Figure 11-7 are the only ones currently available for UGTA modelers to use.

11.3.2.2 Radionuclide Sorption Rates Onto Colloids

Sorption rates of Pu(IV) and Pu(V) onto colloids have been measured in experiments at both LANL and LLNL. Pu(IV) sorption rates onto colloids are typically very rapid, with maximum (or equilibrium) sorption levels being attained within a few hours to at most a day. In experiments conducted at LANL for the UGTA program, Pu(V) sorption rates onto silica colloids were initially faster than rates onto montmorillonite colloids, although final sorption K_d values tended to be somewhat higher on montmorillonite colloids. Maximum sorption levels were attained within a day or so on silica colloids, while they took 5 to 10 days on montmorillonite colloids. In sorption experiments conducted at LLNL, the sorption rates of Pu(V) onto birnessite and goethite colloids were very rapid (on the order of hours), but rates of Pu(V) sorption onto clinoptilolite colloids were extremely slow. In the latter case, it did not appear that equilibrium sorption levels were attained even after 50 days (Kersting et al., 2002b). These experiments were conducted in a synthetic water mimicking J-13 well water from near Yucca Mountain. The results were attributed to the ability of the birnessite and goethite surfaces to reduce Pu(V) to Pu(IV), followed by rapid subsequent sorption of the Pu(IV) onto the colloids. In contrast, Pu(V) reduction to Pu(IV) in the presence of clinoptilolite colloids was interpreted to occur only in the solution phase, a much slower process that was considered to be a necessary precursor to sorption onto the colloids. Spectroscopic methods confirmed that Pu(IV), not Pu(V), was sorbed to the surfaces of all the colloids studied (Kersting et al., 2002a and b).

Sorption rates of U(VI), Np(V), Pu(IV) colloids, Pu(V), and Am(III) onto various types of inorganic colloids have been measured in experiments conducted at LANL for the Yucca Mountain project (Lu et al., 1998a and b; 2000). The results are summarized as follows (all at approximately 20°C, 200 mg/L colloids, and ambient Los Alamos atmosphere):

- Pu(IV) (colloidal) sorbed very quickly (hours) to hematite, goethite, montmorillonite, and silica colloids in J-13 well water.
- Pu(V) sorbed more slowly to all of these colloids, taking 1 to 3 days to reach maximum sorption levels in J-13 water. Sorption tended to be somewhat faster (just a few hours) onto hematite and goethite colloids in a synthetic J-13 water that consisted of only sodium bicarbonate in solution.
- Am(III) sorbed rapidly (within a few hours) and quite strongly onto hematite, montmorillonite, and silica colloids.
- Np(V) sorbed relatively slowly onto hematite, montmorillonite, and silica colloids, taking a day or two to reach maximum sorption levels. Sorption of Np(V) onto these colloids was also much lower (lower K_d values) than for Pu and Am.
- U(VI) sorbed relatively weakly to hematite, montmorillonite, and silica colloids, although maximum sorption levels were reached within a day or so.

Interestingly, Pu(V) sorption rates onto montmorillonite colloids in U-20WW well water seem to be significantly slower (5 to 10 days) than sorption rates onto these same types of colloids in J-13 well water (1 to 3 days). We have no explanation for this result because the two well waters are quite similar in composition. There may be a significant influence of a minor constituent present in one of the waters that is not present in the other, or there could be some differences in the montmorillonite colloids used in the different experiments.

From a practical standpoint, radionuclide sorption rates onto colloids are probably less important for CAU-scale modeling than distribution coefficients (K_d values) and desorption rates. Transport predictions will be relatively insensitive to whether sorption occurs over a matter of hours or a matter of weeks when time scales of interest are many years. However, relative sorption rates onto different colloids may be important from the standpoint of determining which types of colloids radionuclides tend to be associated with. If several different types of colloids are present, radionuclides will, for a while, tend to be preferentially sorbed onto colloids that they sorb onto fastest, even if there are other colloids present that ultimately have larger distribution coefficients (because of slower desorption rates). It is recommended that sensitivity studies be conducted using CAU-scale models to determine how sensitive transport predictions are to relative radionuclide sorption and desorption rates onto colloids.

11.3.2.3 Radionuclide Desorption Rates from Colloids

Far fewer studies have been conducted to determine radionuclide desorption rates from colloids than sorption rates onto colloids. UGTA and Yucca Mountain data exist only for Pu starting as either Pu(IV) or Pu(V). Kersting et al. (2002a and b) report very slow desorption rates of Pu(IV) from clinoptilolite colloids at pHs ranging from 4 to 10. Total desorption over a 7-month period was 2 to 8 percent of the Pu that had sorbed.

In UGTA experiments at LANL, desorption rates were measured for Pu(V) sorbed onto montmorillonite and silica colloids, and also for Pu(IV) sorbed onto clinoptilolite colloids (obtained from LLNL). These experiments were conducted at approximately 20°C in well water from U-20WW. In all cases, desorption rates were slow, although the results were mixed as to exactly how slow for the montmorillonite colloids (Reimus et al., 2002b). In some experiments, approximately 25 percent of the sorbed Pu desorbed in 7 to 11 months, and in other experiments only approximately 1 to 2 percent desorbed in 1 to 4 months. Desorption of Pu from silica colloids ranged from 20 to 30 percent in 7 to 11 months. Desorption of Pu(IV) from clinoptilolite was slow, consistent with the LLNL results, with only 3 to 4 percent of the Pu desorbing in approximately 4 months. The inconsistencies in the montmorillonite results may be the result of using several different batches of montmorillonite colloids that were prepared from two different sources. Some of the differences might also be the result of starting desorption after different time periods of sorption in different experiments. Montmorillonite desorption experiments started after longer sorption time periods tended to have lower amounts and rates of desorption.

Montmorillonite, silica, and clinoptilolite colloids with Pu sorbed onto them were injected into naturally-fractured cores from Pahute Mesa in experiments at LANL between 1999 and 2001 (Reimus et al., 2002b). Interestingly, apparent Pu desorption rates from both montmorillonite and silica colloids were one to two orders of magnitude faster in the fractures than in the batch experiments described in the previous paragraph (the same Pu-colloid solutions were used in both experiments) (Reimus, 2002). Pu desorption from the clinoptilolite colloids, on the other hand, was essentially undetectable, consistent with the batch experimental results. The enhanced desorption rates for the montmorillonite and silica colloids were interpreted as being the result of collisions between the colloids and the fracture surfaces, which offered opportunities for direct transfer of Pu from the colloids to the fracture surfaces, a process that was absent in the batch experiments (Reimus, 2002). The fracture surfaces, which were coated with manganese-oxides in two of the four fractures and had other mineral coatings in the other two, apparently had a greater affinity for the Pu than the montmorillonite and silica colloids. However, in the case of the clinoptilolite colloids, the Pu apparently had a greater affinity for the colloids than the fracture surfaces. These results indicate that results from batch sorption and desorption experiments may not necessarily be directly transferable to modeling of colloid-facilitated transport in real fracture systems.

In YMP project experiments, desorption rates have been measured for Pu(V) and Pu(IV) (colloidal) from hematite, goethite, montmorillonite, and silica colloids over a 268-day period (Lu et al., 1998a). These experiments were conducted at approximately 20°C, with 200 mg/L colloids in J-13 well water, and in ambient Los Alamos atmosphere. The experiments were also conducted with sequential additions of fresh Pu-free water to the colloids at 2, 15, 50, 86, 107, 128, 150, 212, and 268 days (with removal and analyses of the solutions that had been in contact with the colloids at each of these times). This experimental method is in contrast to the methods used for the UGTA batch experiments where fresh solution was never added to the colloids after extracting water for a desorption measurement (i.e., only one desorption step, although measurements were made for several different single-step contact periods). Figure 11-8 presents the results of Yucca Mountain Pu desorption experiments in which Pu(V) was sorbed onto smectite and silica colloids for six days, the Pu was then desorbed in multiple batch steps in which Pu-free water was placed in contact with the colloids. The experiments were conducted at room temperature in J-13 well water (Lu et al., 1998b). The Yucca Mountain results are summarized as follows:

- Less than 0.02 percent of the sorbed Pu(V) and Pu(IV) desorbed from the hematite colloids.
- Less than 1 percent of the sorbed Pu(V) and Pu(IV) desorbed from the goethite colloids.
- Pu(V) desorption from montmorillonite colloids was less than 1 percent after 268 days, but Pu(IV) desorption from these colloids exceeded 10 percent after 150 days.

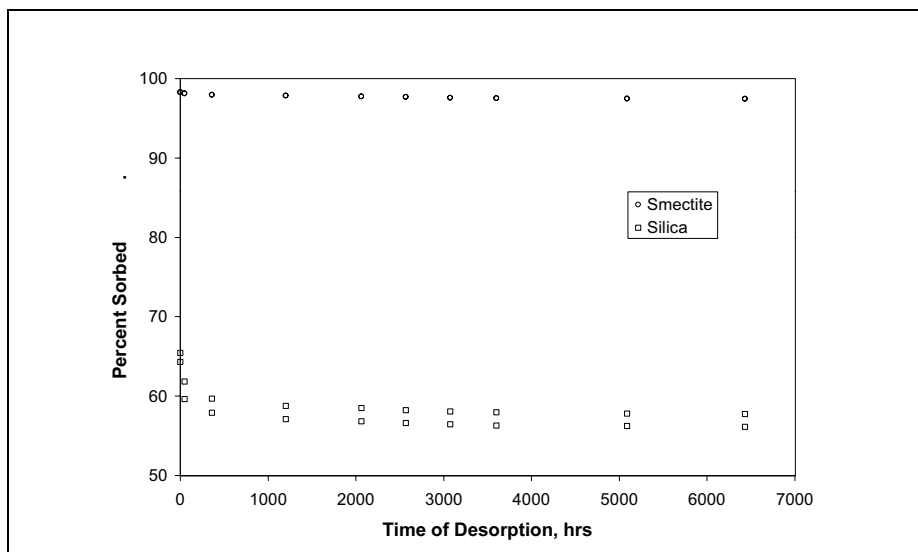


Figure 11-8
Yucca Mountain Pu Desorption Experiments
using Smectite and Silica Colloids (Lu et al., 1998b)

- Pu(V) desorption from silica colloids was about 10 percent after 150 days, and Pu(IV) desorption from these colloids exceeded 20 percent after 150 days.
- Much of the desorption of Pu(V) and Pu(IV) from silica colloids occurred early in the experiments, with a tendency to reach a desorption plateau later in the experiments (see Figure 11-8). Extrapolation of the results could lead one to conclude that some of the Pu sorption may be irreversible, even onto silica colloids that have relatively low measured K_d values.

The last bullet suggests that a multiple sorption site model may be appropriate for Pu sorption onto colloids. Some of the sites appear to be associated with relatively rapid desorption, while others may essentially behave as irreversible or very slowly reversible sites. A two-site sorption model resulted in significantly improved model fits to the sorption and desorption data from the UGTA batch experiments, particularly in the case of the montmorillonite and silica colloids (Reimus, 2002).

The data of Lu et al. (1998a and b) are consistent with at least partial reversibility of actinide sorption onto colloids. However, the data of Figure 11-8 suggest that much of the sorbed Pu may either be irreversibly sorbed or have very slow desorption kinetics. The fracture data are probably more applicable than the batch data because of the presence of minerals that can compete with the colloids for sorption, which is consistent with the real system.

11.3.2.4 Recommendations for Radionuclide Sorption and Desorption Rates From Colloids

In this section, we present ranges of recommended rate constants for actinide sorption onto and desorption from inorganic colloids in NTS waters (either J-13 or U-20WW well waters) at approximately 20°C. Normally, the sorption rate constants, k_p , would be expressed in units of grams water/(g colloid-hr), and the actual rates would then be a function of colloid concentrations and actinide concentrations in solution (a linear dependence on both assuming a first order reaction in each). However, we abandon this convention in favor of presenting rate constants in units of 1/hr so that the reader can gain an immediate appreciation of approximate time scales of sorption ($1-e^{-1}$ of the radionuclide mass should be sorbed after $1/k_p$ hrs). Rate constants can be quickly converted between the two conventions by simply multiplying the conventional rate constant by the colloid mass concentration in solution or dividing the latter rate constant by the colloid concentration.

Table 11-2 provides ranges of actinide sorption and desorption rate constants onto colloids from batch experiments and fracture transport experiments (Pu only) conducted for the UGTA and Yucca Mountain projects. It is apparent that the Pu desorption rate constants for montmorillonite and silica colloids are significantly greater in the fracture experiments than in the batch experiments, as discussed in the previous section.

11.3.3 Data Limitations

It is important to recognize that the data in Figure 11-6 and Table 11-2 reflect only general trends observed in sorption and transport experiments; they do not account for the possibility of multiple types of sorption sites with different sorption strengths on colloids. The desorption rate constants in Table 11-2 should be considered upper bounds because it is possible that some sites may behave as essentially irreversible sites with very low or zero desorption rates. The vast majority of batch experiments conducted to date have not been designed to explicitly investigate this possibility, although the desorption results shown in Figure 11-8 clearly suggest it. A small amount of desorption occurring early in a batch test will tend to skew estimates of desorption rate constants to large values that may apply to only a small percentage of sorption sites.

On the other hand, batch experiments conducted to date also do not account for potential desorption that may occur when other natural mineral surfaces are present to compete with the colloid surfaces for actinides (as in the fracture transport experiments or a real fracture system). We recommend that sensitivity studies using CAU-scale models be conducted using desorption rate constants that extend well beyond the ranges in Table 11-2.

11.3.4 *Scaling Considerations*

An important scaling consideration for actinide distribution coefficients and sorption/desorption rates onto colloids is the question of how desorption rate constants scale with time (or alternatively, how reversible actinide sorption onto colloids is). The experimental results shown in [Figure 11-8](#) suggest that there may be a significant fraction of Pu that desorbs much more slowly from colloids than the initial desorbing mass fraction. In effect, the Pu desorption rates appear to decrease with time, although the observed behavior could also be explained by multiple sorption sites with different sorption strengths or degrees of reversibility. Such desorption behavior could have a profound impact on predictions of colloid-facilitated transport at CAU scales.

Another important “scaling” consideration is actinide sorption and desorption behavior on colloids in the presence of sorbing fracture surfaces (as opposed to being in the presence of only nonreactive test tube walls in batch sorption/desorption experiments). The significant differences between the batch and fracture transport experimental results indicated in [Table 11-2](#) clearly suggest that batch sorption/desorption test results should be very cautiously applied in field-scale fracture transport modeling exercises.

11.4 *Colloid Filtration and Retardation Parameters*

This section includes descriptions of the data available on colloid filtration and retardation parameters. The associated data analysis and results are also described, including a discussion on the limitations of the data and scaling considerations.

11.4.1 *Data Compilation and Evaluation*

Colloid filtration and retardation parameters were obtained primarily from analyses of colloid tracer responses in laboratory and field tracer transport experiments involving inorganic colloids or fluorescent polystyrene microspheres as tracers.

Colloid filtration and retardation parameters were checked by LANL personnel prior to tabulation. They were also checked for consistency after tabulation. Colloid filtration and retardation parameters are described in [Appendix J](#).

11.4.2 *Data Evaluation*

Colloid filtration and detachment rate constants have been derived from colloid responses in tracer tests by using the advection-dispersion equation with appropriate terms for a single reversible first-order reaction to account for mass transfer between mobile water and immobile surfaces (filtration and detachment) to fit the data:

$$\frac{\partial C}{\partial t} + V \frac{\partial C}{\partial x} - D \frac{\partial^2 C}{\partial x^2} + k_{\text{filt}} C - k_{\text{det}} S = 0 \quad (11-1)$$

$$\frac{1}{b} \frac{\partial S}{\partial t} - k_{\text{filt}} C + k_{\text{det}} S = 0 \quad (11-2)$$

where:

- C = Colloid concentration in solution, no./L
- S = Colloid concentration on fracture surfaces, no./cm²
- V = Flow velocity in fractures, cm/wsec
- D = Dispersion coefficient, cm²/sec
- k_{filt} = Filtration rate constant (1/sec) = λV, where λ = filtration coefficient (1/cm)
- k_{det} = Detachment rate constant, 1/cm-sec
- x, t = Independent variables for distance and time, respectively.
- b = Fracture half aperture (cm)

The values for V and D in [Equations \(11-1\) and \(11-2\)](#) were always obtained from interpretations of nonsorbing solute tracer responses; therefore, the filtration and detachment rate constants were the only parameters adjusted to match the colloid responses. Details of the interpretation procedure are provided in Reimus et al. (1999). Note that one plus the filtration rate constant divided by the detachment rate constant is the effective colloid retardation factor.

11.4.3 Development of Parameter Distributions

Colloid filtration rate constants and retardation factors have been estimated in a number of laboratory and field experiments conducted for UGTA and other projects. All of the field measurements have involved fluorescent carboxylate-modified polystyrene latex (CML) microspheres ranging in size from 280 to 640 nm diameter. Laboratory fracture experiments have been conducted using silica, montmorillonite, and clinoptilolite colloids in addition to CML microspheres. In one study, silica colloid transport (approximately 100 nm diameter) was compared directly with CML microsphere transport (330 nm diameter), and it was found that the microspheres transported conservatively relative to the silica colloids (Anghel, 2001). This result suggests that colloid filtration and retardation parameters derived from CML microsphere responses in field tracer tests should be conservative if used to predict natural inorganic colloid transport in fractured systems.

11.4.3.1 Colloid Filtration Rate Constants

[Figure 11-9](#) shows a plot of filtration rate constants obtained from interpretations of several field and laboratory tracer tests conducted in saturated fractured volcanic rocks as a function of the time to reach peak nonsorbing solute concentrations in the tests. The results ([Figure 11-9](#)) are presented as a plot of

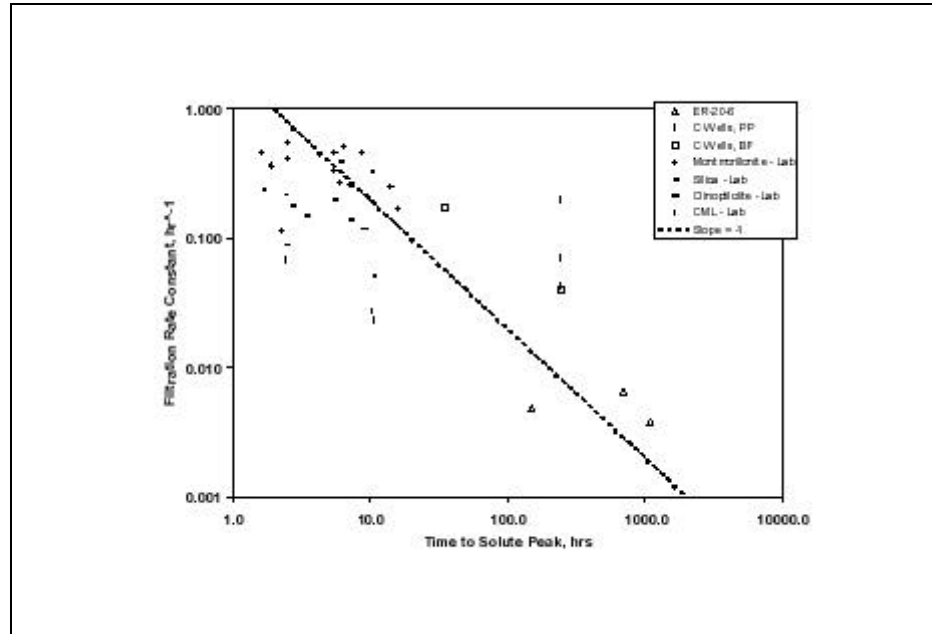


Figure 11-9
CML Microsphere and Inorganic Colloid Filtration Rate Constants as a
Function of Time to Solute Peak Concentration

CML microsphere and inorganic colloid filtration rate constants as a function of time to solute peak concentration. The data were obtained from several field and laboratory tracer tests conducted in saturated, fractured volcanic rocks. These tracer tests include:

- The BULLION Forced-Gradient Experiment (Reimus and Haga, 1999) referred to as “ER-20-6” in [Figure 11-9](#)
- Tracer tests in the Bullfrog Tuff (Member of the Crater Flat Group) at the UE25c Wells at NTS (Reimus et al., 1999) referred to as “C-Wells BF” in [Figure 11-9](#)
- Tracer tests in the Prow Pass Tuff (Members of the Crater Flat Group), at the UE25c Wells at NTS (Reimus et al., 1999) referred to as “C-Wells PP” in [Figure 11-9](#)
- Laboratory experiments conducted at LANL using fractured cores from Pahute Mesa at the NTS

It is important to emphasize that different CML microspheres were used in the different field tests, and also that groundwater chemistry varied slightly from site to site or test to test.

The filtration rate constants reflect the fraction of colloids that were not filtered during the tests (i.e., the rate constant is constrained primarily by the magnitude of the early arrival of colloids). [Figure 11-9](#) shows that, even though different sizes

and types of colloids were used in the different tests, there is an apparent trend of decreasing filtration rate constant with residence time. The line drawn through the data (not a fit) has a slope of -1 , which implies an inverse time dependence of the filtration rate constant. Schijven et al. (1999) observed a similar decrease in filtration rate constants as a function of distance (proportional to time in their system) for bacteriophage transport in a sandy alluvial aquifer.

The trend shown in [Figure 11-9](#) suggests that some fraction of colloids may always transport through a fracture flow system regardless of the time or length scale of the observations. It is tempting to draw the conclusion that filtration rate constants will continually decrease with increasing time scales. However, it may be more appropriate to consider the possibility that, while the majority of colloids might be filtered quite quickly, there is a small fraction of them that are resistant to filtration and, therefore, capable of traveling large distances over long time periods. This statement implies that there may be a distribution of colloid filtration rate constants rather than a fixed rate constant that applies to all colloids. The appearance of a small fraction of colloids at about the same time as nonsorbing solutes in tracer tests, regardless of the overall time scale of the test, forces filtration rate constants to decrease with time when single-rate constants are assumed to apply to all colloids.

Ignoring the possible scale effect for the moment, it is possible to construct a cumulative PDF for the filtration rate constants derived from all of the experiments represented in [Figure 11-9](#). In doing so, we used professional judgement to weight filtration rate constants derived from field tests to be twice that of rate constants from laboratory tests. The rationale for this weighting was that the field tests (10- to 100-m scales) are one- to two-orders of magnitude closer to CAU scales (10000+ m) than the laboratory tests (0.1- to 1-m scales). Also, we added one additional data point that does not come from a tracer test, but rather comes from the observation(s) of colloid-facilitated Pu transport in the ER-20-5 wells that originated from the BENHAM nuclear test cavity. To estimate a filtration rate constant for this observation, several assumptions were made. First, it was assumed that the Pu in the ER-20-5 wells was irreversibly sorbed to colloids, which means that Pu concentrations in the wells reflect colloid transport parameters reasonably well. Second, it was assumed that the concentrations measured in ER-20-5 #1 (on the order of 10^{-13} M Pu) represent a 5 order-of-magnitude decrease from concentrations at the source. Thus, colloid filtration is assumed to result in a 5 order-of-magnitude decrease in colloid concentrations. Third, it was assumed that any colloids that were filtered would never make it to the observation wells (i.e., they were effectively irreversibly filtered). Finally, it was assumed that the travel time from the source to the ER-20-5 wells was approximately 30 years, which represents an upper bound estimate. No assumptions were required about the travel distance. Although these assumptions cannot be verified directly, they allow us to estimate a filtration rate constant using the following expression:

$$1 \times 10^{-5} = \text{Exp} [-(30)(365.25)(24)k_{\text{filt}}] \quad (11-3)$$

where:

$$1 \times 10^{-5} = \text{Fraction of colloids traveling from the source to the ER-20-5 wells} \\ (30)(365.25)(24) = 262,980 = \text{travel time in hours}$$

Solving Equation 11-3 for k_{filt} yields a filtration rate constant of $4.4 \times 10^{-5} \text{ hr}^{-1}$. This estimate is not very sensitive to the fraction of colloids assumed on the left-hand side of Equation 11-3. If the fraction is changed to 1×10^{-8} , the filtration rate constant becomes $7 \times 10^{-5} \text{ hr}^{-1}$. The filtration rate constant is inversely proportional to the assumed travel time, so if the travel time is decreased by a factor of 3 to 10 years, the filtration rate constant increases by a factor of 3 to $1.3 \times 10^{-4} \text{ hr}^{-1}$.

Figure 11-10 shows the resulting cumulative probability distribution of filtration rate constants that includes the data point corresponding to the ER-20-5 observations (which was weighted the same as the field tracer test results). Both axes in Figure 11-10 are logarithmic. Note that data points associated with the two alternative assumptions (shown as two squares) discussed above for the ER-20-5 observations are also shown in Figure 11-10 to illustrate the insensitivity of the overall cumulative distribution to these assumptions.

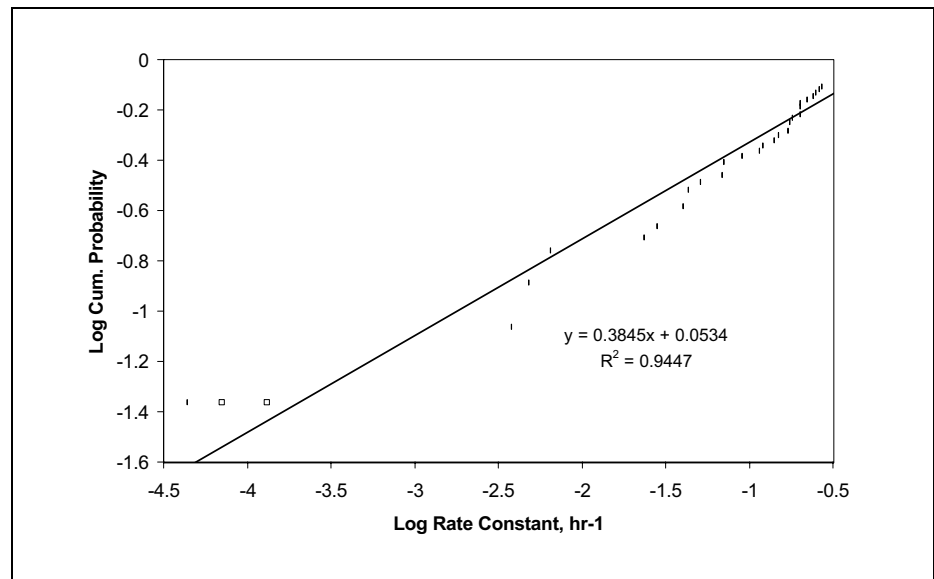


Figure 11-10
Cumulative Probability Distribution
of Log Colloid Filtration Rate Constants

The line fitted to the data in Figure 11-10 can be used to obtain a representative filtration rate constant for use in a transport model given a random number sampled from a uniform distribution that ranges from 0 to 1. The procedure is as follows:

1. Generate the random uniform number.
2. Take the \log_{10} of that number.

3. Insert the result into the regression equation for y and solve for x.
4. Use 10^x as the filtration rate constant in the transport model.

The apparent scale effect of Figure 11-9 is implicitly incorporated into the cumulative probability distribution of Figure 11-10 by weighting the field-derived filtration rate constants twice as much as the laboratory-derived ones. Information is lacking to provide any further recommendations on how the apparent scale effect should be accounted for in CAU-scale modeling. At a minimum, we recommend that transport simulations at the CAU scale include sensitivity analyses to determine the sensitivity of radionuclide transport predictions to assumed values of colloid filtration rate constants.

11.4.3.2 Colloid Retardation Factors

Colloid retardation factors, R_{col} , can be calculated from colloid filtration and detachment rate constants using the expression:

$$R_{col} = 1 + \frac{k_{filt}}{bk_{det}} \quad (11-4)$$

Using the interpretive results from all of the tests represented in Figure 11-9, with the exception of the ER-20-5 observations and two of the three CML microsphere responses from the BULLION FGE, a cumulative probability distribution for R_{col} can be generated. This distribution is shown in Figure 11-11 (log scale on x axis),

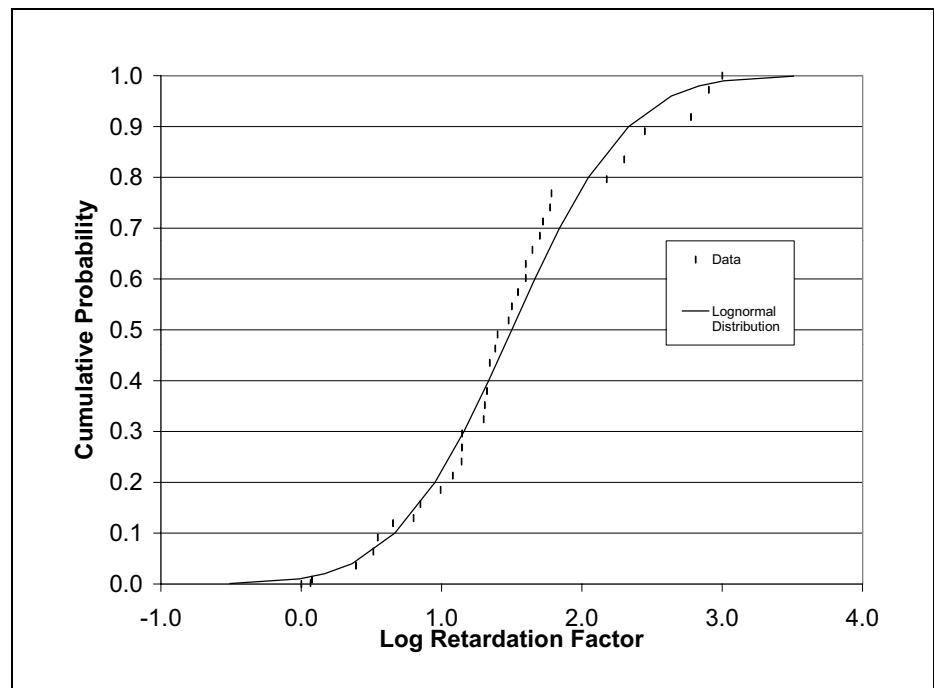


Figure 11-11
Cumulative Probability Distribution of Log Colloid Retardation Factors

which has the field test results weighted a factor of 2 greater than the laboratory test results. Figure 11-11 also shows a fit of a lognormal distribution to the retardation factors. This fit has a mean of 1.5, which corresponds to a mean colloid retardation factor of 31.6, and a standard deviation of 0.65 (log units). The ER-20-5 observations were included in Figure 11-11 by assigning a probability of 0.00001 to a retardation factor of 1.0, which assumes that 0.001 percent of the colloids from the source cavity moved unretarded to the ER-20-5 wells (consistent with the above analysis of filtration rate constants). The results from the two microsphere responses in the BULLION FGE production well were omitted because there was a significant increase in microsphere concentrations in the tails of the responses that apparently resulted from a flow transient in the production well – this increase prevented an unbiased estimate of bk_{det} . The maximum retardation factor assumed for any of the colloid datasets was 1,000. For any of these datasets, the factor of 1,000 could effectively not be distinguished from an infinite retardation factor (because the colloid responses could be fitted equally well assuming no detachment at all). Thus, the distribution of Figure 11-10 is probably conservative at the high end because of this somewhat arbitrary maximum value.

For practical reasons, it may be easier to use the polynomial fit to the log colloid retardation factors shown in Figure 11-12 to randomly sample a colloid retardation factor. The fitted distribution shown in Figure 11-12 has a mean of 1.5 and a standard deviation of 0.65. A representative colloid retardation factor can then be obtained by randomly sampling a uniform distribution ranging from 0 to 1 and substituting the resulting number in for x in the polynomial equation in Figure 11-12 to obtain the \log_{10} of the colloid retardation factor.

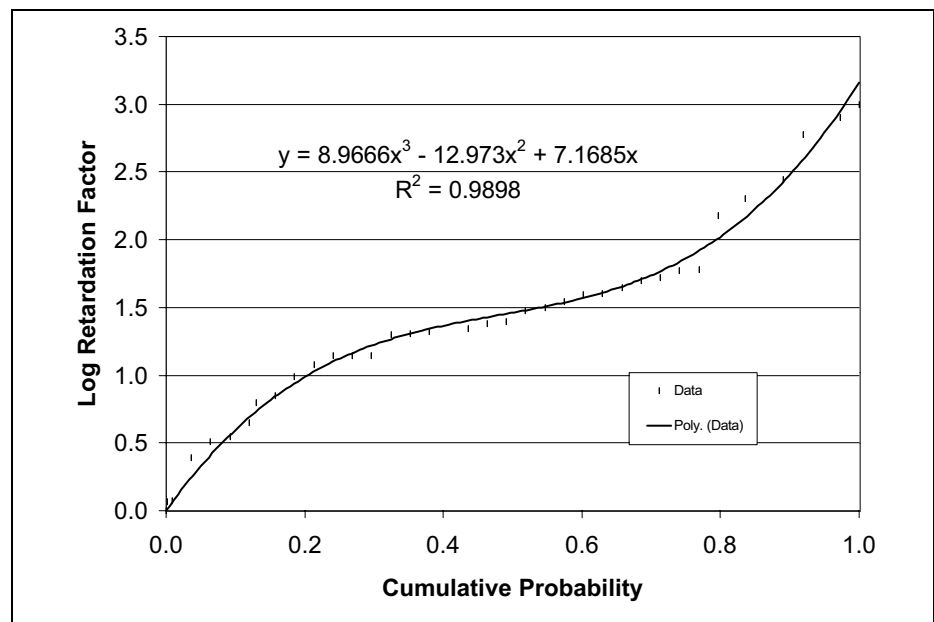


Figure 11-12
Cumulative Probability Distribution of Log Colloid Retardation Factors
and a “fit” of a Lognormal Distribution to the Data

11.4.4 Data Limitations

Colloid filtration rate constants and retardation factors derived from polystyrene microsphere transport data must be used with caution and carefully qualified when applied to colloid-facilitated transport modeling because of the obvious physical and chemical differences between natural colloids and microspheres. Questions about the applicability of microsphere transport data are frequently raised despite the fact the results of Anghel (2001) suggest that polystyrene microspheres transport conservatively through saturated fractures relative to silica spheres (and, by inference, relative to other inorganic colloids as well).

11.4.5 Scaling Considerations

Figure 11-10 and the associated discussion suggest that there may be an important scale dependence of colloid filtration rate constants and retardation factors. However, it is possible that rather than an explicit scale dependence, there may be a wide distribution of colloid filtration rate constants associated with any colloid population and fracture flow system. As a result of this distribution, there may always be a small percentage of colloids that are resistant to filtration and capable of traveling over large distances at essentially the rate of water flow in any given groundwater flow system. This possibility should be seriously considered when modeling colloid-facilitated transport at CAU scales.

11.5 Summary

An approach for modeling colloid transport in groundwater using both colloid filtration rates and colloid retardation factors is presented in this section. This approach is simple and is not HSU-dependent.

The approach is initiated by randomly sampling a retardation factor from Figure 11-12 and inserting it into the advection-dispersion equation to obtain colloid travel times. However, even if retardation factors are large, the ER-20-5 observations suggest that a small fraction of colloid mass may have slow enough filtration rate constants that they can travel large distances effectively unretarded. To allow for this possibility, the following approach is suggested for colloid transport modeling at the CAU scale:

1. Sample a random number, x , from $U(0,1)$ (uniform distribution ranging from 0 to 1).
2. Insert the random number, x , into $y = 8.9666x^3 - 12.973x^2 + 7.1685x$ (from Figure 11-12) to obtain retardation factor $R (= 10^y)$. Apply this retardation factor to all of the colloid mass except for the fraction that travels with an effective retardation factor of 1.0 (steps 3 and 4)
3. Given a mean travel time, τ , to the CAU boundary (possibly calculated from randomly sampled values of specific discharge, effective porosity, and travel distance), calculate a critical filtration rate constant, k_{crit} , as $k_{crit} = 1/\tau$.

4. Calculate the fraction of colloid mass that travels with $R = 1.0$ as $f = 10^{[0.3845 \cdot \text{Log}(k_{\text{crit}}) + 0.0534]}$ (the exponent of 10 is the linear regression fit of the log colloid rates constants in [Figure 11-10](#)).

In steps 3 and 4, the critical filtration rate constant is the rate constant that yields $-k_{\text{crit}} t = -1$, which, when inserted as the argument of the exponent in equation (3), yields a probability of $\exp(-1)$ or ~ 0.37 of a colloid traveling for time t without being filtered. Colloids with this filtration rate constant, or less, will not tend to be filtered over the time scale in question. In contrast, a large fraction of colloids with filtration rates larger than k_{crit} will be filtered (once k_{crit} is exceeded by a factor of 5, less than 1 percent of the colloids will be transported without filtering). Thus, all colloids with filtration rate constants greater than k_{crit} can be assumed to travel with the effective retardation factor sampled from [Figure 11-12](#). A further refinement of this approach could be made by assigning the distribution of [Figure 11-12](#) (or [Figure 11-11](#)) to the entire population of colloids in each CAU-scale model simulation rather than sampling a single retardation factor from the distribution. In this case, a small number of colloids will travel essentially unretarded while the majority of the colloids are retarded. This approach could be expanded further by assigning both the distribution of filtration rate constants from [Figure 11-10](#) and the distribution of retardation factors from [Figure 11-12](#) to the entire population of colloids.

The impact of inconsistencies in the existing data may be accounted for in the uncertainty associated with the data. The text will explain that most methods of colloid sampling would probably tend to result in higher colloid concentrations than are likely to exist in the aquifer under unstressed conditions and far from borehole disturbances.

12.0 References

- Anghel, I. 2001. *Comparison of Polystyrene and Silica Colloids Transport in Saturated Rock Fractures*, M.S. Thesis. Albuquerque, NM: University of New Mexico.
- BN, see Bechtel Nevada.
- Bechtel Nevada. 2002. *A Hydrostratigraphic Model and Alternatives for the Groundwater Flow and Contaminant Transport Model of Corrective Action Units 101 and 102: Central and Western Pahute Mesa, Nye County, Nevada*, DOE/NV/11718-706. Prepared for U.S. Department of Energy, National Nuclear Security Administration Nevada Operations Office. Las Vegas, NV.
- Benedict, F.C., Jr., T.P. Rose, and X. Zhou. 2001. *Mineralogical, Chemical, and Isotopic Characterization of Fracture-Coating Minerals in Borehole Samples from Western Pahute Mesa and Oasis Valley, Nevada*, UCRL-ID-152919. Livermore, CA: Lawrence Livermore National Laboratory.
- Berger, D.L. 1992. *Lithologic Properties of Carbonate-Rock Aquifers at Five Test Wells in the Coyote Spring Valley Area, Southern Nevada, as Determined from Geophysical Logs*. USGS-WRIR-91-4167. Prepared in cooperation with the State of Nevada, the Las Vegas Valley Water District, and the U.S. Bureau of Reclamation. Carson City, NV: U.S. Geological Survey.
- Bernot, P.A. 1999. *Modeling Rates of Lead and Strontium Uptake by Zeolitized Tuff from Rainier Mesa, Nevada Test Site, Nevada*, MS Thesis. Las Vegas, NV: University of Nevada, Las Vegas.
- Blankennagel, R.K., and J.E. Weir, Jr. 1973. *Geohydrology of the Eastern Part of Pahute Mesa, Nevada Test Site, Nye County, Nevada*, USGS-PP-712-B. Denver, CO: U.S. Geological Survey.
- Blout, D.O., W.S. Birchfiel, D.P. Hammermeister, K.A. Zukosky, and K.D. Donnelson. 1995. *Site Characterization Data from the Area 5 Science Boreholes, Nevada Test Site, Nye County, Nevada*, DOE/NV11432-170. Las Vegas, NV: Reynolds Electrical & Engineering Co., Inc.

- Borg, I.Y., R. Stone, H.B. Levy, and L.D. Ramspott. 1976. *Information Pertinent to the Migration of Radionuclides in Ground Water at the Nevada Test Site, Part I: Review and Analysis of Existing Information*, UCRL-52078. Livermore, CA: Lawrence Livermore National Laboratory.
- Bowen, S.M., D.L. Finnegan, J.L. Thompson, C.M. Miller, P.L. Baca, L.F. Olivas, C.G. Geoffrion, D.K. Smith, W. Goishi, B.K. Esser, J.W., Meadows, N.Namboodiri, and J.F. Wild. 2001. *Nevada Test Site Radionuclide Inventory, 1951-1992*, LA-13859-MS. Los Alamos, NM: Los Alamos National Laboratory.
- Brachman, A., and A.B. Kersting. 2002. "Chapter 2 - Characterization of Colloids from NTS Water." *In Colloid-Facilitated Transport of Low-Solubility Radionuclides: A Field, Experimental, and Modeling Investigation*, UCRL-ID-149688. A. B. Kersting and P. W. Reimus, eds. Livermore, CA: Lawrence Livermore National Laboratory; and Los Alamos, NM: Los Alamos National Laboratory.
- Bryant, E.A. 1992. *Colloid Research for the Nevada Test Site*, LA-12301-MS. Los Alamos, NM: Los Alamos National Laboratory.
- Burbey, T.J., and S.W. Wheatcraft. 1986. *Tritium and Chlorine-36 Migration from a Nuclear Explosion Cavity*, Publication No. 45050. Las Vegas, NV: Desert Research Institute.
- Burkhard, N.R. 1989. *Physical Properties in LLNL Yucca Flat Areas: The ROCK Pile Concept*, UCRL-100837. Livermore, CA: Lawrence Livermore National Laboratory.
- Byers, F.M., Jr., and W.L. Hawkins. 1981. *Geology of Drill Hole Ue-18t and Area 18, Timber Mountain Caldera Moat, Nevada Test Site, with a Section on Geophysical Logging by D.C. Muller*, USGS-474-312 (Special Studies I-097). Denver, CO: U.S. Geological Survey.
- CRWMS M&O, see Civilian Radioactive Waste Management System Management and Operating Contractor.
- Callahan, T.J., P.W. Reimus, R.S. Bowman, and M.J. Haga. 2000. "Using Multiple Experimental Methods to Determine Fracture/Matrix Interactions and Dispersion of Nonreactive Solutes in Saturated Volcanic Rock." *In Water Resources Research*, Vol. 36 (12): 3547-3558. Washington, DC: American Geophysical Union.
- Civilian Radioactive Waste Management System Management and Operating Contractor. 1997. *ISM2.0: A 3D Geologic Framework and Integrated Site Model of Yucca Mountain*, B00000000-0717-5700-004, Revision 00. Las Vegas, NV.

- Civilian Radioactive Waste Management System Management and Operating Contractor. 2000a. *Integrated Site Model Process Report*, TDR-NBS-GS-000002 REV 00 ICN 01. Prepared for U.S. Department of Energy, Yucca Mountain Site Characterization Office. Las Vegas, NV: TRW Environmental Safety Systems, Inc.
- Civilian Radioactive Waste Management System Management and Operating Contractor. 2000b. *Fault Displacement Effects on Transport in the Unsaturated Zone*, REV 00, ANL-NBS-HS-000020. Las Vegas, NV.
- Clark, I. 1979. *Practical Geostatistics*. New York, NY: Elsevier Applied Sciences Publishers.
- Conca, J. 2000. *Unsaturated Zone and Saturated Zone Transport Parameters, Yucca Mountain Analysis and Model Report*, ANL-NBS-HS-00019, Rev. 0. Argonne, IL: Argonne National Laboratory.
- DOE, see U.S. Department of Energy.
- DOE/NV, see U.S. Department of Energy, Nevada Operations Office.
- Dagan, G. 1989. *Flow and Transport in Porous Formations*. New York, NY: Springer-Verlag.
- Daniels, W.R., ed. 1981. *Laboratory and Field Studies Related to the Radionuclide Migration Project* (October 1, 1979 - September 30, 1980), LA-8670-PR. Los Alamos, NM: Los Alamos National Laboratory.
- Daniels, J.I., R. Andricevic, R. Anspaugh, and R.L. Jacobson. 1993. *Risk Based Screening Analysis of Ground Water Contaminated by Radionuclides Introduced at the Nevada Test Site (NTS)*, UCRL-LR-112789. Livermore, CA: Lawrence Livermore National Laboratory.
- Daniels, R.R., and J.L. Thompson, comps. and eds. 1984. *Laboratory and Field Studies Related to the Hydrology/Radionuclide Migration Project* (October 1, 1982 - September 30, 1983), LA-10121-PR. Los Alamos, NM: Los Alamos National Laboratory.
- Daniels, W.R., B.R. Erdal, and D.T. Vaniman, eds. 1983. *Research and Development Related to the Nevada Nuclear Waste Storage Investigations*, (July 1 - September 30, 1982), LA-9577-PR. Los Alamos, NM: Los Alamos National Laboratory.
- Dash, Z.V. 2000. *Validation Test Report (VTR) for the FEHM Application Version 2.10*, Yucca Mountain Project Identification Numbers SAN: LANL-1999-046; STN: 10086-2.10-00. Los Alamos, NM: Los Alamos National Laboratory.

- Dash, Z.V. 2001. *Validation Test Report (VTR) for the FEHM Application Version 2.12*, Yucca Mountain Project Identification Numbers SAN: LANL-2001-133; STN: 10086-2.12-00. Los Alamos, NM: Los Alamos National Laboratory.
- Dash, Z.V., B.A. Robinson, and G.A. Zyvoloski. 1997. *Software Requirements, Design, and Verification and Validation for the FEHM Application - A Finite-Element Heat- and Mass-Transfer Code*, LA-13305-MS. Los Alamos, NM: Los Alamos National Laboratory.
- Davis, J.A. 2001. *Surface Complexation Modeling of Uranium (VI) Adsorption on Natural Mineral Assemblages*, NUREG/CR-6708. Washington, DC: U.S. Nuclear Regulatory Commission.
- Davis, J.A., J.A. Coston, D.B. Kent, and C.C. Fuller. 1998. "Application of the Surface Complexation Concept to Complex Mineral Assemblages." In *Environmental Science & Technology*, Vol. 32 (19): 2820-2828. Washington, DC: American Chemical Society.
- Davis, J.C. 1973. *Statistics and Data Analysis in Geology*. New York, NY: John Wiley and Sons.
- de Marsily, G. 1986. *Quantitative Hydrogeology*. Orlando, FL: Academic Press.
- Dosch, R.G., and A.W. Lynch. 1980. "Radionuclide Transport in a Dolomite Aquifer, Scientific Basis for Nuclear Waste Management." In *Proceedings of the International Symposium*, held in Boston, Massachusetts, on November 27-30, 1979. New York, NY: Plenum Press.
- Draper, N.R., and H. Smith. 1981. *Applied Regression Analysis*, Second edition. New York, NY: John Wiley and Sons.
- Drellack, S.L., L.B. Prothro, K.E. Roberson, B.A. Schier, and E.H. Price. 1997. *Analysis of Fractures in Volcanic Cores from Pahute Mesa, Nevada Test Site*, DOE/NV/11718-160. Las Vegas, NV: Bechtel Nevada.
- EPA, see U.S. Environmental Protection Agency.
- FFACO, see *Federal Facility Agreement and Consent Order*.
- Federal Facility Agreement and Consent Order*. 1996 (as amended). Agreed to by the State of Nevada, the U.S. Department of Energy, and the U.S. Department of Defense.
- Ferguson, J.F., A.H. Cogbill, and R.G. Warren. 1994. "A Geophysical-Geological Transect of the Silent Canyon Caldera Complex, Pahute Mesa, Nevada." In *Groundwater*, Vol. 99 (B3): 4323-4339. Columbus: Groundwater Publishing Company.

- Freeze, R.A., and J.A. Cherry. 1979. *Groundwater*. Englewood Cliffs, NJ: Prentice Hall.
- Freeze, R.A., J. Massmann, L. Smith, T. Sperling, and B. James. 1990. "Hydrogeological Decision Analysis: I. A Framework." In *Groundwater*, Vol. 28 (5): 738-766. Columbus, OH: Groundwater Publishing Company.
- Geldon, A.L., A.M.A. Umari, J.D. Earle, M.F. Fahy, J.M. Gemmell, and J.Darnell. 1998. *Analysis of a Multiple-Well Interference Test in Miocene Tuffaceous Rocks at the C-Hole Complex, May-June 1995, Yucca Mountain, Nye County, Nevada*, USGS-WRI-97-4166. Denver, CO: U.S. Geological Survey.
- Gelhar, L.W., C. Welty, and K. Rehfeldt. 1992. "A Critical Review of Data on Field-Scale Dispersions in Aquifers." In *Water Resources Research*. Washington, DC.
- Gelhar, L.W. 1993. *Stochastic Subsurface Hydrology*. Englewood Cliffs, NJ: Prentice-Hall.
- George, D. 1997. *Unstructured 3D Grid Toolbox for Modeling and Simulation*, LA-UR-97-3052. Los Alamos, NM: Los Alamos National Laboratory.
- Golder Associates, Inc. 2002a. *User's Guide: GoldSim Graphical Simulation Environment*, Version 7.40. Redmond, WA.
- Golder Associates, Inc. 2002b. *User's Guide: GoldSim Contaminant Transport Module*, Version 1.30. Redmond, WA.
- Grove, D.B., and W.A. Beetem. 1971. "Porosity and Dispersion Constant Calculations for a Fractured Carbonate Aquifer using the Two Well Tracer Method." In *Water Resources Research*, Vol. 7 (1): 128-134. Washington,DC: American Geophysical Union.
- Hiemenz, P.C. 1986. *Principles of Colloid and Surface Chemistry*. Second edition. New York, NY: Marcel Dekker.
- Houser, F.N., R.E. Davis, and W.L. Emerick. 1961. *Geologic Reconnaissance of Granite Intrusive Masses at Gold Meadows, Tem Piute, and Trappman's Camp, Lincoln and Nye Counties, Nevada, and Comparison with Climax Stock of the Nevada Test Site*, USGS-TEI-793. Denver, CO: U.S. Geological Survey.
- Hu, B. 1998. *Frenchman Flat Contaminant Boundary*, attached to a memorandum from C. Russell (Desert Research Institute) to K. Rehfeldt (HSIGeotrans), 29 May. Las Vegas, NV.

Istok, J.D., D.O. Blout, L. Barker, K.R. Johnejack, and D.P. Hammermeister. 1994. "Spatial Variability in Alluvium Properties at a Low-Level Nuclear Waste Site." In *Soil Science Society of America, Journal*, Vol. 58 (4): 1040-1051. Madison, WI.

IT, see IT Corporation.

IT Corporation. 1996a. *Groundwater Recharge and Discharge Data Documentation Package (Phase I Data Analysis Documentation, Volume III)*, ITLV/10972-181/Vol. III. Prepared for the U.S. Department of Energy, Nevada Operations Office. Las Vegas, NV.

IT Corporation. 1996b. *Hydrologic Parameter Data Documentation Package (Phase I Data Analysis Documentation, Volume IV)*, ITLV/10972-181/Vol. IV. Prepared for the U.S. Department of Energy, Nevada Operations Office. Las Vegas, NV.

IT Corporation. 1996c. *Potentiometric Data Documentation Package (Phase I Data Analysis Documentation, Volume II)*, ITLV/10972-181/Vol. II. Prepared for the U.S. Department of Energy, Nevada Operations Office. Las Vegas, NV.

IT Corporation. 1996d. *Regional Geologic Model Data Documentation Package (Phase I Data Analysis Documentation, Volume I)*, ITLV/10972-181/Vol. I. Prepared for the U.S. Department of Energy, Nevada Operations Office. Las Vegas, NV.

IT Corporation. 1996e. *Transport Parameter and Source Term Data Documentation Package (Phase I Data Analysis Documentation, Volume V)*, ITLV/10972-181/Vol. V. Prepared for the U.S. Department of Energy, Nevada Operations Office. Las Vegas, NV.

IT Corporation. 1996f. *Tritium Transport Model Documentation Package (Phase I Data Analysis Documentation, Volume VII)*, ITLV/10972-181/Vol. VII. Prepared for the U.S. Department of Energy, Nevada Operations Office. Las Vegas, NV.

IT Corporation. 1997a. *Groundwater Flow Model Documentation Package (Phase I Data Analysis Documentation, Volume VI)*, ITLV/10972-181/Vol. VI. Prepared for the U.S. Department of Energy, Nevada Operations Office. Las Vegas, NV.

IT Corporation. 1997b. *Risk Assessment Documentation Package (Phase I Data Analysis Documentation, Volume VIII)*, ITLV/10972-181/Vol. VIII. Prepared for the U.S. Department of Energy, Nevada Operations Office. Las Vegas, NV.

IT Corporation. 1998a. *Report and Analysis of the BULLION Forced-Gradient Experiment*, ITLV/13052-042, DOE/NV-13-52. Las Vegas, NV.

- IT Corporation. 1998b. *Value of Information Analysis for Corrective Action Units Nos. 101 and 102: Central and Western Pahute Mesa, Nevada Test Site, Nevada*, ITLV/13052-041. Prepared for the U.S. Department of Energy, Nevada Operations Office. Las Vegas, NV.
- IT Corporation. 1999. *Underground Test Area Project Corrective Action Unit98: Frenchman Flat, Vol. II Groundwater Data Documentation Package*, Rev.0, DOE/NV/13052-044-V2. Prepared for U.S. Department of Energy, Nevada Operations Office, Las Vegas, NV.
- IT Corporation. 2001a. *A User's Guide to the Comprehensive Chemistry Database for Groundwater at the Nevada Test Site*, Rev. 3, ITLV/13052-070. Las Vegas, NV.
- IT Corporation. 2001b. *Underground Test Area Fracture Analysis Report: Analysis of Fractures in Volcanic Rocks of Western Pahute Mesa-Oasis Valley*, ITLV/13052-150. Prepared for the U.S. Department of Energy, Nevada Operations Office. Las Vegas, NV.
- IT Corporation. 2002a. *Analysis of Well ER-EC-1 Testing, Western Pahute Mesa-Oasis Valley FY 2000 Testing Program*, Rev. 0, ITLV/13052--173, DOE/NV/13052--846. Las Vegas, NV.
- IT Corporation. 2002b. *Analysis of Well ER-EC-2a Testing, Western Pahute Mesa-Oasis Valley FY 2000 Testing Program*, Rev. 0, ITLV/13052--174, DOE/NV/13052--851. Las Vegas, NV.
- IT Corporation. 2002c. *Analysis of Well ER-EC-4 Testing, Western Pahute Mesa-Oasis Valley FY 2000 Testing Program*, Rev. 0, ITLV/13052--175, DOE/NV/13052--850. Las Vegas, NV.
- IT Corporation. 2002d. *Analysis of Well ER-EC-5 Testing, Western Pahute Mesa-Oasis Valley FY 2000 Testing Program*, Rev. 0, ITLV/13052--176, DOE/NV/13052--848. Las Vegas, NV.
- IT Corporation. 2002e. *Analysis of Well ER-EC-6 Testing, Western Pahute Mesa-Oasis Valley FY 2000 Testing Program*, Rev. 0, ITLV/13052--177, DOE/NV/13052--849. Las Vegas, NV.
- IT Corporation. 2002f. *Analysis of Well ER-EC-7 Testing, Western Pahute Mesa-Oasis Valley FY 2000 Testing Program*, Rev.0, ITLV/13052--178, DOE/NV/13052--852. Las Vegas, NV.
- IT Corporation. 2002g. *Analysis of Well ER-EC-8 Testing, Western Pahute Mesa-Oasis Valley FY 2000 Testing Program*, Rev.0, DOE/NV/13052--847, ITLV/13052--179. Las Vegas, NV.
- IT Corporation. 2002h. *Analysis of Well ER-18-2 Testing, Western Pahute Mesa-Oasis Valley FY 2000 Testing Program*, Rev. 0, ITLV/13052--172, DOE/NV/13052--845. Las Vegas, NV.

- IT Corporation. 2002i. *FRACTURE02.mdb* - Fracture characterization database for the Nevada Test Site, September. Las Vegas, NV.
- IT Corporation. 2002j. *GEOCHEM02.mdb* - A comprehensive chemistry database for groundwater at the Nevada Test Site, Rev. 4, September. Las Vegas, NV.
- IT Corporation. 2002k. *Summary of Well Testing and Analysis, Western Pahute Mesa-Oasis Valley FY 2000 Testing Program*, Rev. 0, ITLV/13052--180, DOE/NV/13052--853. Las Vegas, NV.
- Journel, A.G., and Ch. J. Huijbregts. 1978. *Mining Geostatistics*. New York, NY: Academic Press.
- Kane, M.F., M.W. Webring, and B.K. Bhattacharyya. 1981. *A Preliminary Analysis of Gravity and Aeromagnetic Surveys of the Timber Mountain Area, Southern Nevada*. U.S. Geological Survey Open-File Report 81-189. Denver, CO. U.S. Geological Survey.
- Kersting, A.B., D.W. Efurud, D.L. Finnegan, D.J. Rokop, D.K. Smith, and J.L. Thompson. 1998. "Migration of Plutonium in Groundwater at the Nevada Test Site." In *Hydrologic Resources Management Program and Underground Test Area Operable Unit FY 1997 Progress Report*, UCRL-ID-130792. Livermore, CA: Lawrence Livermore National Laboratory.
- Kersting, A.B., and P.W. Reimus. 2003. *Colloid-Facilitated Transport of Low-Solubility Radionuclides: A Field, Experimental, and Modeling Investigation*, UCRL-ID-149688. Livermore, CA: Lawrence Livermore National Laboratory; and Los Alamos, NM: Los Alamos National Laboratory.
- Kersting, A.B., P. Zhao, M. Zavarin, E.R. Sylvester, P.G. Allen, L. Wang, E.J. Nelson, and R.W. Williams. 2002a. "Chapter 4 - Sorption of Pu(IV) on Minerals." In *Colloid-Facilitated Transport of Low-Solubility Radionuclides: A Field, Experimental, and Modeling Investigation*, UCRL-ID-149688. A. B. Kersting and P. W. Reimus, eds. Livermore, CA: Lawrence Livermore National Laboratory; and Los Alamos, NM: Los Alamos National Laboratory.
- Kersting, A.B., P. Zhao, M. Zavarin, E.R. Sylvester, P.G. Allen, and R.W. Williams. 2002b. "Chapter 5 - Sorption of Pu (V) on Mineral Colloids." In *Colloid-Facilitated Transport of Low-Solubility Radionuclides: A Field, Experimental, and Modeling Investigation*, UCRL-ID-149688. A.B. Kersting and P.W. Reimus, eds. Livermore, CA: Lawrence Livermore National Laboratory; and Los Alamos, NM: Los Alamos National Laboratory.

- Kung, K.S. 2000. *Colloid Characterization and Quantification in Groundwater Samples*, LAS-13727-MS. Los Alamos, NM: Los Alamos National Laboratory.
- Kung, S. 2002. Steve's Colloid Site, Los Alamos National Laboratory as accessed on August 20, 2002, at <http://public.lanl.gov/Kung/>.
- Laczniak, R.J., J.L. Smith, P.E. Elliot, G.A. DeMeo, M.A. Chatigny, and G.A. Roemer. 2001. *Ground-Water Discharge Determined from Estimates of Evapotranspiration, Death Valley Regional Flow System, Nevada, and California*. USGS-WRIR-01-4195.
- Laczniak, R.J., J.C. Cole, D.A. Sawyer, and D.A. Trudeau. 1996. *Summary of Hydrogeologic Controls on Ground-Water Flow at the Nevada Test Site, Nye County, Nevada*, USGS-WRIR-96-4109. Denver, CO: U.S. Geological Survey.
- Leap, D.I., and P.M. Belmonte. 1992. "Influence of Pore Pressure on Apparent Dispersivity of a Fissured Mitic Dolomitic Aquifa." In *Groundwater*, Vol.30 (1): 87-95. Columbus, OH: Groundwater Publishing Company.
- LeBlanc, D.R. 1982. *Sewage Plume in a Sand and Gravel Aquifer, Cape Cod, Massachusetts*, USGS-OFR-82-274. Denver, CO: U.S. Geological Survey.
- Lee, C.H., and I. Farmer. 1993. *Fluid Flow in Discontinuous Rocks*. London, UK: Chapman and Hall.
- Lu, N., C.R. Cotter, H.D. Kitten, and J. Bentley. 1998a. "Reversibility of Sorption of Plutonium-239 onto Colloids of Hematite and Goethite." In *Radiochimica Acta*, Vol. 83: 167-173. Munich, Germany: R.Oldenburger.
- Lu, N., I.R. Triay, C.R. Cotter, H.D. Kitten, and J. Bentley. 1998b. *Reversibility of Sorption of Plutonium-239 onto Colloids of Hematite, Goethite, Smectum and Silica*, LA-UR-98-3057. Los Alamos, NM: Los Alamos National Laboratory.
- Lu, N., J. Conca, G.R. Parker, P.A. Leonard, B. Moore, E.A. Strietelmeier, and I.R. Triay. 2000. *Adsorption of Actinides onto Colloids as a Function of Time, Temperature, Ionic Strength and Colloid Concentration*, LA-UR-00-5121. Los Alamos, NM: Los Alamos National Laboratory.
- Maldonado, F. 1977. *Summary of the Geology and Physical Properties of the Climax Stock, Nevada Test Site*, USGS-OFR-77-356. Denver, CO: U.S. Geological Survey.
- Maxey, G.B., and T.E. Eakin. 1949. *Groundwater in White River Valley, White Pine, Nye and Lincoln Counties, Nevada*, Water Resources Bulletin No. 8. Carson City, NV: State of Nevada, Office of the State Engineer.

- McKenna, S.A., and C.A. Rautman. 1996. *Scaling of Material Properties for Yucca Mountain: Literature Review and Numerical Experiments on Saturated Hydraulic Conductivity*, SAND95-1338. Albuquerque, NM: Sandia National Laboratories.
- Meijer, A. 1990. *Yucca Mountain Project Far-Field Sorption Studies and Data Needs*, LA-11671-MS. Los Alamos, NM: Los Alamos National Laboratory.
- Meijer, A. 1992. "A Strategy for the Derivation and Use of Sorption Coefficients in Performance Assessment Calculations for the Yucca Mountain Site." In *Proceedings of the DOE/Yucca Mountain Site Characterization Project Radionuclide Adsorption Workshop*, held at Los Alamos National Laboratory on September 11-12, 1990, LA-12325-C. Los Alamos, NM: Los Alamos National Laboratory.
- Muller, D.C. 1981. "Geophysical Logging." In *Geology of Drill Hole Ue-18t and Area 18, Timber Mountain Caldera Moat, Nevada Test Site*, by Byers, F.M., Jr., and W.L. Hawkins, Special Studies I-097, USGS-474-312. Denver, CO: U.S. Geological Survey.
- NRC, see National Research Council.
- National Research Council. 1996. *Rock Fractures and Fluid Flow*. Washington,DC: National Academy Press.
- Neretnieks, L., H. Abelin, and L. Birgersson. 1989. "Some Recent Observations of Channeling in Fractured Rocks - Its Potential Impact on Radionuclide Migration." In *Proceedings of the Conference on Geostatistical, Sensitivity, and Uncertainty Methods for Ground-Water Flow and Radionuclide Transport Modeling*, held on September 15-17, 1987. CONF-870971: 387-410. SanFrancisco, CA: Battelle Press.
- Neuman, S.P. 1990. "Universal Scaling of Hydraulic Conductivities and Dispersivities in Geologic Media." In *Water Resources Research*, Vol. 26 (8): 1749-1758. Washington, DC: American Geophysical Union.
- Newman, J.L. 1973. *Electrochemical Systems*. Englewood Cliffs, NJ: Prentice-Hall.
- Noble, D.C., and R.L. Christiansen. 1968. "Geologic Map of the Southwest Quarter of the Black Mountain Quadrangle, Nye County, Nevada," U.S. Geological Survey Miscellaneous Geologic Investigations Series Map I-562. Denver, CO: U.S. Geological Survey.
- Noble, D.C., K.A. Sargent, H.H. Mehnert, E.B. Ekren, and F.M. Byers, Jr. 1968. "Silent Canyon Volcanic Center." In *Nevada Test Site*, Geological Society of America Memoir 110, pp. 65-75. Boulder, CO: The Geological Society of America, Inc.

- OECD/DOE, see Organization for Economic Co-Operation and Development/Nuclear Energy Agency.
- Ogard, A.E., and J.F. Kerrisk. 1984. *Groundwater Chemistry Along Flow Paths Between a Proposed Repository Site and the Accessible Environment*, LA-10188-MS. Los Alamos, NM: Los Alamos National Laboratory.
- Ogard, A.E., J.L. Thompson, R.S. Rundberg, K. Wolfsberg, P.W. Kubic, D.Eklmore, and H.W. Bentley. 1988. "Migration of Chlorine-36 and Tritium from an Underground Nuclear Test." In *Radiochim. Acta*, Vol.44/45: 213-217. Munich, Germany: R. Oldenburg.
- Organization for Economic Co-Operation and Development/Nuclear Energy Agency. 1998. "Modeling the Effects of Spatial Variability on Radionuclide Migration." In *Proceedings of a Workshop*, held in Paris, France, on June 9-11, 1997.
- Organization for Economic Co-Operation and Development/Nuclear Energy Agency. 1999. "Water-Conducting Features in Radionuclide Migration." In *Proceedings of Workshop*, held in Barcelona, Spain, on June 10-12, 1998.
- Orkild, P.P., K.A. Sargent, and R.P. Snyder. 1969. "Geologic Map of Pahute Mesa, Nevada Test Site and Vicinity, Nye County, Nevada," U.S. Geological Survey Miscellaneous Geologic Investigations Series Map I-567, scale 1:48,000. Denver, CO: U.S. Geological Survey.
- Palisade Corporation. 2002. *Guide to Using BestFit Distribution Fitting for Windows*, Version 4.5. Newfield, NY: Palisade Corporation.
- Papelis, C., and W. Um, 2002. *Evaluation of Cesium, Strontium, and Lead Sorption, Desorption, and Diffusion in Alluvium from Frenchman Flat, Nevada Test Site: Macroscopic and Spectroscopic Investigations*, DOE/NV/13609-14, DRI Publication No. 45189. Las Vegas, NV: Desert Research Institute.
- Pawloski, G.A., A.F.B. Tompson, and S.F. Carle, eds. 2001. *Evaluation of the Hydrologic Source Term from Underground Nuclear Tests on Pahute Mesa at the Nevada Test Site: CHESHIRE Test*, UCRL-ID-147023. Livermore, CA: Lawrence Livermore National Laboratory.
- Pawloski, G.A., A.F.B. Tompson, and S.F. Carle, eds. 2002. *Evaluation of the Hydrologic Source Term from Underground Nuclear Tests on Pahute Mesa at the Nevada Test Site: CHESHIRE Test*, UCRL-ID-147023. Livermore, CA: Lawrence Livermore National Laboratory.
- Perkins, W.G., D.A. Lucero, and G.O. Brown. 1998. *Column Experiments for Radionuclide Adsorption Studies of Culebra Dolomite: Retardation Parameter Estimation for Non-Eluted Actinide Species*, SAND98-1005. Albuquerque, NM: Sandia National Laboratories.

- Pohll, G., J. Chapman, A. Hassan, L. Papelis, R. Andricevic, and C. Shirley. 1998. *Evaluation of Groundwater Flow and Transport at the Shoal Underground Nuclear Test*, Publication 45162, DOE/NV/11508-35. Las Vegas, NV: Desert Research Institute.
- Prothro, L.B., and S.L. Drellack, Jr. 1997. *Nature and Extent of Lava-Flow Aquifers Beneath Pahute Mesa, Nevada Test Site*, DOE/NV-11718-156. Las Vegas, NV: Bechtel Nevada.
- Prothro, L.B., S.L. Drellack, Jr., and B.M. Allen. 1999. *Lithology and Stratigraphy of Holes Drilled in LANL-Use Areas of the Nevada Test Site*, Volume XIII, 1991-1998, DOE/NV-11718-254. Las Vegas, NV: Bechtel Nevada.
- Rehfeldt, K., W. Drici, B. Lester, D. Sloop, J. Watrus, T. Beard, M. Sully, W. Fryer, and C. Benedict. 2003 (In Production). *Hydrologic Data for the Groundwater Flow and Contaminant Transport Model of Corrective Action Units 101 and 102: Central and Western Pahute Mesa, Nye County, Nevada*, Rev.0, Shaw/13052,-204. Las Vegas, NV: Shaw Environmental, Inc.
- Reimus, P.W. 2002. "Chapter 8 - Quantitative Interpretation of Fracture Transport Experiments and Associated Batch Sorption/Desorption Experiments." In *Colloid-Facilitated Transport of Low-Solubility Radionuclides: A Field, Experimental, and Modeling Investigation*, UCRL-ID-149688. A. B. Kersting and P. W. Reimus, eds. Livermore, CA: Lawrence Livermore National Laboratory; and Los Alamos, NM: Los Alamos National Laboratory.
- Reimus, P.W., and M.J. Haga. 1999. *Preliminary Analysis of Tracer Responses in the BULLION Forced-Gradient Experiment at Pahute Mesa, Nevada*, LA-13615-MS. Los Alamos, NM: Los Alamos National Laboratory.
- Reimus, P.W., A. Adams, M.J. Haga, A. Humphrey, T. Callahan, I. Anghel, and D. Counce. 1999. *Results and Interpretation of Hydraulic and Tracer Testing in the Prow Pass Tuff at the C-Holes, Yucca Mountain Site Characterization Project Milestone Report SP32E7M4*. Los Alamos, NM: Los Alamos National Laboratory.
- Reimus, P.W., M.J. Haga, A.R. Humphrey, D.A. Counce, T.J. Callahan, and S.D. Ware. 2000. *Laboratory Experiments to Support Interpretation of the BULLION Forced-Gradient Experiment: Update Report*, Los Alamos, NM: Los Alamos National Laboratory.
- Reimus, P.W., S.D. Ware, F.C. Benedict, R.G. Warren, A.R. Humphrey, A.I. Adams, B. Wilson, and D. Gonzales. 2002a. *Diffusive and Advective Transport of ³H, ¹⁴C, and ⁹⁹Tc in Saturated Fractured Volcanic Rocks from Pahute Mesa, Nevada*, LA-13891-MS. Los Alamos, NM: Los Alamos National Laboratory.

- Reimus, P.W., S.D. Ware, N. Lu, K.S. Kung, A.I. Abdel-Fattah, I. Anghel, M.P.Neu, and S.D. Reilly. 2002b. "Chapter 7 - Colloid-Facilitated Plutonium Fracture Transport Experiments." In *Colloid-Facilitated Transport of Low-Solubility Radionuclides: A Field, Experimental, and Modeling Investigation*, UCRL-ID-149688. A. B. Kersting and P. W. Reimus, Editors. Livermore, CA: Lawrence Livermore National Laboratory; and LosAlamos,NM: Los Alamos National Laboratory.
- Reiner, S.R., R.J. Laczniaik, G.A. DeMeo, J. L. Smith, P.E. Elliott, W.E.Nylund, and C.J. Fridrich. 2002. *Ground-Water Discharge Determined from Measurements of Evapotranspiration, Other Available Hydrologic Components, and Shallow Water-Level Changes, Oasis Valley, Nye County, Nevada*, USGS-WRI-01-4239. Carson City, NV: U.S.Geological Survey.
- Robledo, A.R., P.L. Ryder, J.M. Fenelon, and F.L. Paillet. 1998. *Geohydrology of Monitoring Wells Drilled in Oasis Valley near Beatty, Nye County, Nevada 1997*, USGS-WRIR-98-4184. Denver, CO: U.S. Geological Survey.
- Rose, T.P., F.C. Benedict, J.M. Thomas, W.S. Sicke, R.L. Hershey, J.B. Paces, I.M. Farnham, and Z.E. Peterman. 2003 (In Production). *Geochemical Data Analysis and Interpretation of the Pahute Mesa - Oasis Valley Groundwater Flow System, Nye County, Nevada*, Livermore, CA: Lawrence Livermore National Laboratory.
- Shaw, see Shaw Environmental, Inc.
- Sauty, J.P. 1980. "An Analysis of Hydrodispersive Transfer in Aquifers." In *Water Resources Research*, Vol. 16 (1): 145-158. Washington, DC: American Geophysical Union.
- Schijven, J.F., W. Hoogenboezem, S.M. Hassanizadeh, and J.H. Peters. 1999. "Modeling Removal of Bacteriophages MS2 and PRD1 by Dune Recharge at Castricum, Netherlands." In *Water Resources Research*, Vol. 35 (4): 1101-1011. Washington, DC: American Geophysical Union.
- Schoff, S.L., and J.E. Moore. 1964. *Chemistry and Movement of Ground Water, Nevada Test Site*. U.S. Geological Survey Report TEI-838. Denver, CO: U.S. Geological Survey.
- Serra, O. 1984. *Fundamentals of Well-Log Interpretation*. New York, NY: Elsevier Publishing Co.
- Shapiro, A.M. 2001. "Effective Matrix Diffusion in Kilometer-Scale Transport in Fractured Crystalline Rock." In *Water Resources Research*, Vol. 37 (3): 507-511. Washington, DC: American Geophysical Union.
- Shaw Environmental, Inc. 2003 (In Production). *Discrete Network and Continuum Approaches for Modeling the BULLION Forced-Gradient Experiment*. Las Vegas, NV.

- Shirley, C., K. Pohlmann, and R. Andricevic. 1996. *Three-Dimensional Mapping of Equiprobable Hydrostratigraphic Units at the Frenchman Flat Correctopm Action Unit, Nevada Test Site*, Publication No. 45152, DOE/NV/112508-20. Las Vegas, NV: Desert Research Institute.
- Skagius, K., and I. Neretnieks. 1986. "Porosities and Diffusivities of Some Nonsorbing Species In Crystalline Rocks." In *Water Resources Research*, Vol.22 (3): 389-398. Washington, DC: American Geophysical Union.
- Slate, J.L., M.E. Berry, P.D. Rowley, C.J. Fridrich, K.S. Morgan, J.B. Workman, O.D. Young, G.L. Dixon, V.S. Williams, E.H. McKee, D.A. Ponce, T.G.Hildenbrand, WC Swadley, S.C. Lundstrom, E.B. Ekren, R.G.Warren,J.C. Cole, R.J. Fleck, M.A. Lanphere, D.A. Sawyer, S.A.Minor, D.J.Grunwald, R.J. Laczniak, C.M. Menges, J.C. Yount, and A.S. Jayko. 1999. *Digital Geologic Map of the Nevada Test Site and Vicinity, Nye, Lincoln, and Clark Counties, Nevada, and Inyo County, California*, USGS-OFR-99-554-A. Denver, CO: U.S. Geological Survey.
- Sloop, D.A. 1998. *Equilibrium Studies of Ion Sorption on Zeolitized Tuff from Rainier Mesa, Nye County, Nevada*, M.S. Thesis. Las Vegas, NV: University of Nevada, Las Vegas.
- Smith, D.K. 2001. *Unclassified Radiologic Source Term for Nevada Test Site Areas 19 and 20*, UCRL-ID-141706. Livermore,CA: Lawrence Livermore National Laboratory.
- Snyder, R.P. 1977. *Geology of the Gold Meadows Stock, Nevada Test Site*, USGS-474-179. Denver, CO: U.S. Geological Survey.
- Stout, D.L., and S.A. Carroll. 1992. *A Literature Review of Actinide-Carbonate Mineral Interaction*, SAND92-7328. Albuquerque, NM: Sandia National Laboratories.
- Thomas, K.W. 1987. *Summary of Sorption Measurements Performed with Yucca Mountain, Nevada, Tuff Samples and Water from Well J-13*, LA-10960-MS. Los Alamos, NM: Los Alamos National Laboratory.
- Thomas, J.M., F.C. Benedict, Jr., T.P. Rose, R.L. Hershey, J.B. Paces, Z.E.Peterman, I.M. Farnham, K.H. Johannesson, A.K. Singh, K.J.Stetzenbach, G.B. Hudson, J.M. Kenneally, G.F. Eaton, and D.K. Smith. 2002. *Geochemical and isotopic interpretations of groundwater flow in the Oasis Valley flow system, southern Nevada*, Publication No. 45190. Las Vegas, NV: Desert Research Institute.
- Thompson, J.L., ed. 1988. *Laboratory and Field Studies Related to the Radionuclide Migration Project (October 1, 1986 - September 30, 1987)*, LA-11223-PR. Los Alamos, NM: Los Alamos National Laboratory.

- Thompson, J.L., ed. 1991. *Laboratory and Field Studies Related to the Hydrology/Radionuclide Migration Project* (October 1, 1989 - September 30, 1990), LA-12100-PR. Los Alamos, NM: Los Alamos National Laboratory.
- Thompson, J.L., ed. 1998. *Laboratory and Field Studies Related to Radionuclide Migration at the Nevada Test Site* (October 1, 1996 - September 30, 1997), LA-13419-PR. Los Alamos, NM: Los Alamos National Laboratory.
- Thompson, F.B., M. Zavarin, C.J. Bruton, and G.A. Pawloski. 2002 (In Production). *Simplified Hydrologic Source Term for Frenchman Flat Sensitivity Studies*. Livermore, CA: Lawrence Livermore National Laboratory.
- Tompson, A.F.B., A.L. Schafer, and R.W. Smith. 1996. "Impacts at Physical and Chemical Heterogeneity on Co-Contaminant Transport in a Sandy Porous Medium." In *Water Resources Research*, 32(4), 801-818. Washington, DC: American Geophysical Union.
- Tompson, A.F.B., C.J. Bruton, and G.A. Pawloski, eds. 1999. *Evaluation of the Hydrologic Source Term from the Underground Nuclear Tests in Frenchman Flat and the Nevada Test Site: The CAMBRIC Test*, UCRL-ID-132300. Livermore, CA: Lawrence Livermore National Laboratory.
- Travis, B.J., H.E. Nuttall, S.W. Hodson, and R.S. Rundberg. 1983. "Section B: Transport of Tritium the Cambic Cavity Region to RNM-2S: Modeling." In *Laboratory and Field Studies Related to the Hydrology/Radionuclide Migration Project* (October 1, 1981 - September 30, 1982), LA-9691-PR. Los Alamos, NM: Los Alamos National Laboratory.
- Triay, I.R., A. Meijer, J.L. Conca, K.S. Kung, R.S. Rundberg, E.A. Strietelmeier, C.D. Tait, D.L. Clark, M.P. Neu, and D.E. Hobart. 1997. *Summary and Synthesis Report on Radionuclide Retardation for the Yucca Mountain Site Characterization Project, Yucca Mountain Site Characterization Program Milestone 3784M*, LA-13262-MS, UC903, and UC-940. Los Alamos, NM: Los Alamos National Laboratory.
- TRW. 2000. *Saturated Zone Flow and Transport Process Model Report*, TDR-NBS-HS-000001, Rev. 00 ICN 02. Prepared for the Yucca Mountain Site Characterization Office. Las Vegas, NV.
- U.S. Department of Energy. 2001. *FY01 Supplemental Science and Performance Analyses, Volume 1: Scientific Bases and Analyses Part 1 of 2*, TDR-MGR-MD-000007, Rev. 00. Las Vegas, NV: Yucca Mountain Project.
- U.S. Department of Energy, Nevada Operations Office. 1997. *Regional Groundwater Flow and Tritium Transport Modeling and Risk Assessment of the Underground Test Area, Nevada Test Site, Nevada*, DOE/NV--477. Las Vegas, NV.

- U.S. Department of Energy, Nevada Operations Office. 1999. *Corrective Action Investigation Plan for Corrective Action Units 101 and 102, Central and Western Pahute Mesa, Nevada Test Site, Nevada*, Rev.1, DOE/NV--516. Las Vegas, NV.
- U.S. Department of Energy, Nevada Operations Office. 2000a. *Underground Test Area Quality Assurance Project Plan, Nevada Test Site, Nevada*, Rev. 3, DOE/NV-341. Las Vegas, NV.
- U.S. Department of Energy, Nevada Operations Office. 2000b. *United States Nuclear Tests, July 1945 through September 1992*, Rev. 15, DOE/NV-209. Las Vegas, NV.
- U.S. Environmental Protection Agency. 1988. *Groundwater Modeling: An Overview and Status Report*, EPA/600/2-89/028 Ada, OK: Robert S. Kerr Environmental Research Laboratory.
- Um, W., and C. Papelis. 2001a. "Sorption/Desorption Behavior of Strontium and Lead on Zeolitized Tuffs from the Nevada Test Site." In *Soil Science Society of America*. Madison, WI: Soil Science Society of America, Inc.
- Um, W. and C. Papelis. 2001b. "Sorption Mechanisms of Sr(II) and Pb(II) on Zeolitized Tuffs from the Nevada Test Site as a Function of pH and Ionic Strength." In *Soil Science Society of America*. Madison, WI: Soil Science Society of America, Inc.
- Vanmarcke, E. 1983. *Random Fields: Analysis and Synthesis*. Cambridge, MA: The MIT Press.
- Wahl, R.R, D.A. Sawyer, S.A. Minor, MD. Carr, J.C. Cole, W.C. Swadley, R.J.Laczniak, R.B. Warren, K.S. Green, and C.M. Engle. 1997. "Digital Geologic Map of the Nevada Test Site Area, Nevada," USGS-OFR-97-140. Denver, CO: U.S. Geological Survey.
- Walker, G.E. 1962. *Ground Water in the Climax Stock, Nevada Test Site, Nye County, Nevada*, USGS-TEI-813. Denver, CO: U.S. Geological Survey.
- Warren, R.G. 1994a. *Structural Elements and Hydrogeologic Units of the Southwestern Nevada Volcanic Field*. Los Alamos National Laboratory informal technical report prepared for the DOE/NV Underground Test Area Project, 19 January. Los Alamos, NM: Los Alamos National Laboratory.
- Warren, R.G. 1994b. Communication to E. Price (GeoTrans) entitled, "Structural Elements and Hydrogeologic Units of the Southwestern Nevada Volcanic Field." Los Alamos, NM: Los Alamos National Laboratory.
- Warren, R.G., G.L. Cole, and D. Walther. 2000a. *A structural Block Model for the Three-Dimensional Geology of the Southwestern Nevada Volcanic Field*, LA-UR-00-5866. Los Alamos, NM: Los Alamos National Laboratory.

- Warren, R.G., D.A. Sawyer, F.M. Byers, Jr., and G.L. Cole. 2000b. A *Petrographic/ Geochemical Database and Stratigraphic and Structural Framework for the Southwestern Nevada Volcanic Field*, LA-UR-00-3791. As accessed at <http://queeg.ngdc.noaa.gov/seg/geochem/swvnf/> on July 11, 2001.
- Warren, R.G., F.C. Benedict, Jr., T.P. Rose, D.K. Smith, S.J. Chipera, E.C. Kluk, and K.M. Raven. 2002. *Alluvial Layering and Distribution of Reactive Phases Within Drill Holes ER5-4 and UE5N of Frenchman Flat*, LA-UR-02-6206. Los Alamos, NM: Los Alamos National Laboratory.
- Warren, R.G., D.A. Sawyer, F.M. Byers, Jr., and G.L. Cole. 2003. *Apetrographic, Geochemical, and Geophysical Database and Stratigraphic Framework for the Southwestern Nevada Volcanic Field*, LA-UR-03-1503. Los Alamos, NM: Los Alamos National Laboratory.
- Watermark Numerical Computing and Waterloo Hydrogeologic. 2000. *Visual PEST User's Manual (Includes PEST2000 & WinPEST) - Graphical Model-Independent Parameter Estimation*. Ontario, Canada, and Tampa, FL.
- Weast, R.C., and M.J. Astle, eds. 1982. *CRC Handbook of Chemistry and Physics*, Second edition, F-42. Boca Raton, FL: CRC Press.
- Welty, C., and L.W. Gelhar. 1989. *Evaluating of Longitudinal Dispersivity from Tracer Test Data*, R89-05, Ralph M. Parsons Laboratory Report. Cambridge, MA: Massachusetts Institute of Technology.
- Welty, C., and L.W. Gelhar. 1994. "Evaluation of Longitudinal Dispersivity from Nonuniform Flow Tracer Tests." In *Journal of Hydrology*, Vol. 153 (71-102). New York, NY: Elsevier Publishing Company.
- Wilson, M.L., J.G. Gauthier, R.W. Barnard, G.E. Barr, H.A. Dockery, E. Dunn, R.R. Eaton, D.C. Guerin, N. Lu, M.J. Martinez, R. Nilson, C.A. Rautman, T.H. Robey, B. Ross, E.E. Ryder, A.R. Schenker, S.A. Shannon, L.H. Skinner, W.G. Halsey, J.D. Gansemer, L.C. Lewis, A.D. Lamont, I.R. Triay, A. Meijer, and D.E. Morris. 1994. *Total-System Performance Assessment for Yucca Mountain-SNL Second Iteration (TSPA-1993)*, SAND93-2675. Albuquerque, NM: Sandia National Laboratories.
- Winograd, I.J., and L.R. West. 1962. *Preliminary Tracer Experiment to Demonstrate Hydraulic Continuity Between Water Wells C and C-1, Yucca Flat, Nevada Test Site*, Technical Letter NTS-20. Denver, CO: U.S. Geological Survey.
- Winograd, I.J., and W. Thordarson. 1975. *Hydrogeologic and Hydrochemical Framework, South-Central Great Basin, Nevada-California, with Special Reference to the Nevada Test Site*, USGS-PP-712-C. Denver, CO: U.S. Geological Survey.

Winterle, J.R., and P.C. La Femina. 1999. *Review and Analysis of Hydraulic and Tracer Testing at the C-Holes Complex Near Yucca Mountain, Nevada*, Center for Nuclear Waste Regulatory Analyses. San Antonio, TX: U.S.Nuclear Regulatory Commission.

Wolfsberg, K. 1978. *Sorption-Desorption Studies of Nevada Test Site Alluvium and Leaching Studies of Nuclear Test Debris*, LA-7216-MS. Los Alamos, NM: Los Alamos National Laboratory.

Wolfsberg, A., L., and J. Boryta. 2002. *Extension to the TYBO/BENHAM Modeling Study: Additional Radionuclides and Transport Processes*. Los Alamos, NM: Los Alamos National Laboratory.

Wolfsberg, A., L. Glascoe, G. Lu, A. Olson, P. Lichtner, M. McGraw, T. Cherry, and G. Roemer. 2002. *TYBO/BENHAM Model Analysis of Groundwater Flow and Radionuclide Migration from Underground Nuclear Tests in Southwestern Pahute Mesa, NTS*, LA-13977. Los Alamos, NM: Los Alamos National Laboratory.

YMP, see Yucca Mountain Project.

Yucca Mountain Project. 1996. DTN:LAIT831341AQ96.001. Radionuclide Retardation Measurements of Batch-Sorption Distribution Coefficients for Barium, Cesium, Selenium, Strontium, Uranium, Plutonium, and Neptunium, Submittal 12 November.

Yucca Mountain Project. 1997. DTN:LAIT831361AQ95.003. Transport Data of H3, Np, and Tc-95m Collected to Calculate Retardation Coefficients Using J-13 And Ue-25 P#1 Waters, Submitted 20 August.

Yucca Mountain Project. 2000. DTN:LA0003AM831341.001. Sorption Distribution Coefficient Data of Samples Taken from the Saturated Zone, Yucca Mountain, Nevada, 01/01/1993 to 03/27/2000.

Yucca Mountain Project. 2001. DTN:LA0109MD831341.001. Neptunium (Np-237) Sorption Distribution Coefficient Data in Three Types of Alluvium as a Function of Stratigraphic Position from the Nye County Early Warning Drilling Program, 08/03/1999 to 09/13/2001.

Zavarin, M., and C.J. Bruton. 2000a. *A Non-Electrostatic Surface Complexation Approach to Modeling Radionuclide Migration at the Nevada Test Site: Aluminosilicates*, Lawrence Livermore National Laboratory report attached to a memorandum to files by W. Drici (Shaw Environmental, Inc.), 13 August, 2003. Las Vegas, NV.

Zavarin, M., and C.J. Bruton. 2000b. *A Non-Electrostatic Surface Complexation Approach to Modeling Radionuclide Migration at the Nevada Test Site: Iron Oxides and Calcite*. Lawrence Livermore National Laboratory report attached to a memorandum to files by W. Drici (Shaw Environmental, Inc.), 13 August, 2003. Las Vegas, NV.

- Zavarin, M., S. F. Carle, and R. M. Maxwell. 2002. *Upscaling Radionuclide Retardation - Linking the Surface Complexation and Ion Exchange Mechanistic Approach to a Linear K_d Approach*. Lawrence Livermore National Laboratory report attached to a memorandum to files by W. Drici (Shaw Environmental, Inc.), 13 August, 2003. Las Vegas, NV.
- Zheng, C. 1990. *MT3D - A Modular Three-Dimensional Transport Model for Simulation of Advection, Dispersion and Chemical Reactions of Contaminants in Groundwater Systems*. Prepared for U.S. Environmental Protection Agency, Robert S. Kerr Environmental Research Laboratory. Ada, OK.
- Zyvoloski, G.A., B.A. Robinson, Z.V. Dash, and L.L. Trease. 1997a. *Summary of Models and Methods for the FEHM Application - A Finite-Element Heat- and Mass-Transfer Code*, LA-13307-MS. Los Alamos, NM: Los Alamos National Laboratory.
- Zyvoloski, G.A., B.A. Robinson, Z.V. Dash, and I.L. Trease. 1997b. *User's Manual for the FEHM Application - A Finite-Element Heat- and Mass-Transfer Code*, LA-13306-M. Los Alamos, NM: Los Alamos National Laboratory.



Appendix A

Hydrostratigraphic Model Supporting Information

A.1.0 Description of the Pahute Mesa-Oasis Valley Model Layers

Brief descriptions of the HSUs used to construct the PM-OV model are provided in [Table A.1-1](#). They are listed in approximate order from surface to basement, although some are laterally rather than vertically contiguous, and not all units are present in all parts of the model area. Other information supporting [Table A.1-1](#) is provided in [Table A.1-2](#) and [Table A.1-3](#).

A.2.0 References

- Bechtel Nevada. 2002. *Hydrostratigraphic Model of the Pahute Mesa-Oasis Valley Area, Nye County, Nevada*, DOE/NV/11718-646. Prepared for U.S. Department of Energy, National Nuclear Security Administration Nevada Operations Office. Las Vegas, NV.
- Ferguson, J.F., A.H. Cogbill, and R.G. Warren. 1994. "A Geophysical-Geological Transect of the Silent Canyon Caldera Complex, Pahute Mesa, Nevada." In *Groundwater*, Vol. 99 (B3): 4323-4339. Washington, DC: American Geophysical Union.
- IT Corporation. 1996. *Regional Geologic Model Data Documentation Package (Phase 1 Data Analysis Documentation, Volume I)*. Prepared for the U.S. Department of Energy, Nevada Operations Office. Las Vegas, NV.
- Slate, J.L., M.E. Berry, P.D. Rowley, C.J. Fridrich, K.S. Morgan, J.B. Workman, O.D. Young, G.L. Dixon, V.S. Williams, E.H. McKee, D.A. Ponce, T.G. Hildenbrand, WC Swadley, S.C. Lundstrom, E.B. Ekren, R.G. Warren, J.C. Cole, R.J. Fleck, M.A. Lanphere, D.A. Sawyer, S.A. Minor, D.J. Grunwald, R.J. Laczniak, C.M. Menges, J.C. Yount, and A.S. Jayko. 1999. *Digital Geologic Map of the Nevada Test Site and Vicinity, Nye, Lincoln, and Clark Counties, Nevada, and Inyo County, California*, USGS-OFR-99-554-A. Denver, CO: U.S. Geological Survey.

Table A.1-1
Hydrostratigraphic Units of the Pahute Mesa-Oasis Valley Hydrostratigraphic Framework Model
 (Page 1 of 6)

Model Layer Number ^a	Hydrostratigraphic Unit (Symbol)	Dominant Hydrogeologic Unit(s) ^b	Stratigraphic Unit Map Symbols ^c	General Description	Transport Parameter Category
46	Alluvial Aquifer (AA) (this term is also used to designate a hydrogeologic unit)	AA	Qay, QTc, Qs, Qam, QTa, QTu, Qb, Tgy, Tgc, Tgm, Tgyx, Tt	Consists mainly of alluvium that fills extensional basins such as Gold Flat, Crater Flat, Kawich Valley, and Sarcobatus Flat. Also includes generally older Tertiary gravels, tuffaceous sediments, and nonwelded tuffs (where thin) that partially fill other basins such as Oasis Valley and the moat of the Timber Mountain caldera complex.	Alluvium
45	Younger Volcanic Composite Unit (YVCM)	LFA, WTA, VTA	Typ, Tgy, Ts, Tyb, Tyr	A minor unsaturated HSU that consists of Pliocene to late Miocene basaltic rocks such as those at Thirsty Mountain and Buckboard Mesa. Also includes welded and nonwelded ash-flow tuff of the Volcanics of Stonewall Mountain. Mainly occurs in the northwestern portion of the model area.	WTA 75% VTA 25%
44	Thirsty Canyon Volcanic Aquifer (TCVA)	WTA, LFA, lesser VTA	Ttg, Tth, Tts, Ttt, Ttp, Ttc	Consists mainly of welded ash-flow tuff and lava of the Thirsty Canyon Group. Unit is very thick within the Black Mountain caldera. Also is present east and south of the caldera, including the northwestern moat area of the Timber Mountain caldera complex and the northern portion of the Oasis Valley basin.	WTA 75% LFA 25%
43	Detached Volcanics Composite Unit (DVCM)	WTA, LFA, TCU	Tf through Tq	Consists of a very complex distribution of lavas and tuffs that form a relatively thin, highly extended interval above the FC-BH detachment fault in the southwestern portion of the model area.	WTA 85% TCU 15%
42	Detached Volcanics Aquifer (DVA)	WTA, LFA	Tgyx, Tf, Tma, Tmr	Consists of welded ash-flow tuff and lava assigned to the Ammonia Tanks Tuff and units of the Volcanics of Fortymile Canyon. Although (like the DVCM) the DVA also overlies the FC-BH detachment fault, it is considered a separate HSU because of the preponderance of welded-tuff and lava-flow aquifers that compose the HSU and much smaller degree of alteration present.	WTA
41	Fortymile Canyon Composite Unit (FCCM)	LFA, TCU, lesser WTA	Tfu, Tfs, Tfd, Tfr, Tfb, Tfl, Tff	Consists of a complex and poorly understood distribution of lava and associated tuff of the Volcanics of Fortymile Canyon. Generally confined within the moat of the Timber Mountain caldera complex, where the unit forms a ring around Timber Mountain. Unit is also present in areas southwest of the Timber Mountain caldera complex.	LFA 60% TCU 30% WTA 10%
40	Fortymile Canyon Aquifer (FCA)	WTA, LFA	Tff, tuff of Cutoff Road	Composed mainly of welded ash-flow tuffs and lesser amounts of rhyolitic lava, and is generally less than 305 m (1,000 ft) thick. It is located between two composite units that are much more hydrologically diverse, although they include some of the same units as the FCA. The FCA is completely saturated.	WTA 80% LFA 20%

Table A.1-1
Hydrostratigraphic Units of the Pahute Mesa-Oasis Valley Hydrostratigraphic Framework Model
 (Page 2 of 6)

Model Layer Number ^a	Hydrostratigraphic Unit (Symbol)	Dominant Hydrogeologic Unit(s) ^b	Stratigraphic Unit Map Symbols ^c	General Description	Transport Parameter Category
39	Timber Mountain Composite Unit (TMCM)	TCU (altered tuffs, lavas) and unaltered WTA and lesser LFA	Tmay, Tmaw, Tma, Tmx, Tmat, Tmt, Tmr	Consists mainly of intra-caldera, strongly welded ash-flow tuff of the Timber Mountain Group, and is confined within the Timber Mountain caldera complex. Although consisting mainly of strongly welded tuff which is assumed to be considerably fractured and thus behave as an aquifer, the TMCM is designated a composite unit because of the potential for hydrothermal alteration within this deep intra-caldera setting. Alteration would have significantly altered the hydraulic properties of the rocks, particularly filling fractures with secondary minerals such as quartz.	TCU 75% WTA 25%
38	Tannenbaum Hill Lava-Flow Aquifer (THLFA)	LFA	Tmat	Composed entirely of rhyolitic lava of the rhyolite of Tannenbaum Hill. Occurs just outside the northwestern structural boundary of the Timber Mountain caldera complex. Tannenbaum Hill lava occurring inside the caldera complex is grouped with the TMCM.	LFA
37	Tannenbaum Hill Composite Unit (THCM)	Mostly TCU, lesser WTA	Tmat	Zeolitic tuff and lesser welded ash-flow tuff of the rhyolite of Tannenbaum Hill that occurs stratigraphically below Tannenbaum Hill lava and above the rhyolite of Fluorspar Canyon. Distribution is similar to the THLFA.	TCU 75% WTA 25%
36	Timber Mountain Aquifer (TMA)	Mostly WTA, minor VTA	Tmay, Tmaw, Tma, Tmx, Tmat, Tmt, Tmr	Consists mainly of extra-caldera welded ash-flow tuffs of Ammonia Tanks Tuff and Rainier Mesa Tuff. These rocks are the extra-caldera equivalent of the rocks comprising the TMCM. Unit occurs mostly north and west of the Timber Mountain caldera complex.	WTA 80% VTA 20%
35	Subcaldera Volcanic Confining Unit (SCVCU)	TCU	Tm, Tp, Tc, and older, undifferentiated tuffs	A highly conjectural unit that is modeled as consisting of highly altered volcanic rocks that occur stratigraphically between the Rainier Mesa Tuff and basement rocks (ATICU and RMICU) within the deeper portions of the Timber Mountain caldera complex.	TCU
34	Fluorspar Canyon Confining Unit (FCCU)	TCU	Tmrf	Consists of zeolitic, nonwelded tuff of the rhyolite of Fluorspar Canyon that generally occurs beneath the THCM, and thus has a similar distribution. Typically, the rhyolite of Fluorspar Canyon is higher structurally, and vitric in other areas.	TCU
33	Windy Wash Aquifer (WWA)	LFA	Tmw	Minor HSU consisting of the lava-flow lithofacies of the rhyolite of Windy Wash. Occurs along the western (down-thrown) side of the West Greeley fault in Area 20.	LFA

Table A.1-1
Hydrostratigraphic Units of the Pahute Mesa-Oasis Valley Hydrostratigraphic Framework Model
 (Page 3 of 6)

Model Layer Number ^a	Hydrostratigraphic Unit (Symbol)	Dominant Hydrogeologic Unit(s) ^b	Stratigraphic Unit Map Symbols ^c	General Description	Transport Parameter Category
32	Paintbrush Composite Unit (PCM)	WTA, LFA, TCU	Tmr, Tmrf, Tmn, Tp	Consists mostly of units of the Paintbrush Group that occur in the southern portion of the model area in the vicinity of the Claim Canyon caldera. Unit is dominated by thick, strongly welded Tiva Canyon Tuff within the Claim Canyon caldera. Outside the caldera this unit is more variable, consisting of welded and nonwelded tuff and rhyolitic lava assigned to various formations of the Paintbrush Group. Stratigraphically equivalent units of the Paintbrush Group that occur in the northern portion of the model area beneath Pahute Mesa have been grouped into seven separate HSUs.	WTA 75% TCU 25%
31	Paintbrush Vitric-tuff Aquifer (PVTA)	VTA	Pre-Tmr tuffs, Tp	Typically includes all vitric, nonwelded, and bedded tuff units below the Rainier Mesa Tuff to the top of a Paintbrush lava (e.g., Tpb or Tpe) but may extend to base of Paintbrush Tuff in eastern Area 19 where Tpe or Tpr lavas are not present. May also include the vitric pumiceous top of the Tpe lava. Unit occurs in the northern portion of the model area beneath Pahute Mesa.	VTA
30	Benham Aquifer (BA)	LFA	Tpb	Lava-flow lithofacies of the rhyolite of Benham. Occurs north of the Timber Mountain caldera complex and beneath the southwestern portion of Pahute Mesa.	LFA
29	Upper Paintbrush Confining Unit (UPCU)	TCU	Pre-Tmr tuffs, Tp	Includes all zeolitic, nonwelded and bedded tuffs below the Rainier Mesa Tuff to base of the rhyolite of Delirium Canyon. Unit occurs in the northern portion of the model area beneath Pahute Mesa.	TCU
28	Tiva Canyon Aquifer (TCA)	WTA	Tpc	The welded ash flow lithofacies of the Tiva Canyon Tuff in southern Area 20. May not be differentiated where thin or where sandwiched between vitric bedded tuffs as in Area 19.	WTA 70% VTA 30%
27	Paintbrush Lava-flow Aquifer (PLFA)	LFA	Tpd, Tpe, Tpr	Lava-flow lithofacies of the rhyolite of Delirium Canyon (Tpd), rhyolite of Echo Peak (Tpe), and rhyolite of Silent Canyon (Tpr). Also includes moderately to densely welded ash-flow tuff of Tpe. Unit occurs in the northern portion of the model area beneath Pahute Mesa.	LFA
26	Lower Paintbrush Confining Unit (LPCU)	TCU	Tpe, Tpp, Tpt	Includes all zeolitic nonwelded and bedded tuffs below the rhyolite of Delirium Canyon to the base of the Topopah Spring Tuff. Unit occurs in the northern portion of the model area beneath Pahute Mesa.	TCU
25	Topopah Spring Aquifer (TSA)	WTA	Tpt	The welded ash-flow lithofacies of the Topopah Spring Tuff in southern Area 20.	WTA

Table A.1-1
Hydrostratigraphic Units of the Pahute Mesa-Oasis Valley Hydrostratigraphic Framework Model
 (Page 4 of 6)

Model Layer Number ^a	Hydrostratigraphic Unit (Symbol)	Dominant Hydrogeologic Unit(s) ^b	Stratigraphic Unit Map Symbols ^c	General Description	Transport Parameter Category
24	Yucca Mountain Crater Flat Composite Unit (YMCFCM)	LFA, WTA, TCU	Tc, Th	Includes all units of the Crater Flat Group and Calico Hills Formation that occur in the southern portion of the model area in the vicinity of Yucca Mountain. Stratigraphically equivalent units that occur in the northern portion of the model area beneath Pahute Mesa have been grouped into nine separate HSUs.	WTA 75% TCU 25%
23	Calico Hills Vitric-tuff Aquifer (CHVTA)	VTA	Th (Tac)	Structurally high, vitric, nonwelded tuffs of the Calico Hills Formation. Present in the northern portion of the model area beneath the eastern portion of Area 19. May become partly zeolitic in the lower portions.	VTA
22	Calico Hills Vitric Composite Unit (CHVCM)	VTA, LFA	Th	Structurally high, lava and vitric nonwelded tuff of the Calico Hills formation. Present in the northern portion of the model area beneath the western portion of Area 19. May become partly zeolitic in the lower portions.	VTA 75% LFA 25%
21	Calico Hills zeolitic composite unit (CHZCM)	LFA, TCU	Th	Complex three-dimensional distribution of rhyolite lava and zeolitic nonwelded tuff of the Calico Hills Formation. Present in the northern portion of the model area beneath most of eastern and central Area 20.	TCU 75% LFA 25%
20	Calico Hills Confining Unit (CHCU)	Mostly TCU, minor LFA	Th	Consists mainly of zeolitic nonwelded tuff of the Calico Hills Formation. May include minor lava flows along the eastern margin. Present in the northern portion of the model area beneath the western portion of Area 20.	TCU 90% LFA 10%
19	Inlet Aquifer (IA)	LFA	Tci	Lava-flow lithofacies of the rhyolite of Inlet. Occurs as two thick isolated deposits beneath Pahute Mesa in the northern portion of the model area.	LFA
18	Crater Flat Composite Unit (CFCM)	Mostly LFA, intercalated with TCU	Th (Tac), Tc	Includes welded tuff and lava flow lithofacies of the tuff of Jorum (Tc _{pj}), the rhyolite of Sled (Tc _{ps}), and the andesite of Grimy Gulch (Tc _g). Occurs in central Area 20 in the northern portion of the model area.	LFA 75% TCU 25%
17	Crater Flat Confining Unit (CFCU)	TCU	Tc	Includes all zeolitic, nonwelded and bedded units below the Calico Hills Formation (Th) to the top of the Bullfrog Tuff (Tcb). Occurs mainly in Area 19 in the northern portion of the model area.	TCU
16	Kearsarge Aquifer (KA)	LFA	Tc _{pk}	Minor HSU that consists of the lava-flow lithofacies of rhyolite of Kearsarge. Unit is present as a small isolated occurrence in the northeastern portion of the model area.	LFA
15	Bullfrog Confining Unit (BCU)	TCU	Tcb	Major confining unit in the northern portion of the model area. Unit consists of thick intra-caldera, zeolitic, mostly nonwelded tuff of the Bullfrog Formation.	TCU

Table A.1-1
Hydrostratigraphic Units of the Pahute Mesa-Oasis Valley Hydrostratigraphic Framework Model
 (Page 5 of 6)

Model Layer Number ^a	Hydrostratigraphic Unit (Symbol)	Dominant Hydrogeologic Unit(s) ^b	Stratigraphic Unit Map Symbols ^c	General Description	Transport Parameter Category
14	Belted Range Aquifer (BRA)	LFA and WTA, with lesser TCU	Tb	Consists of welded ash-flow tuff and lava of the Belted Range Group (Tb) above the Grouse Canyon Tuff (Tbg), but may also include the lava flow lithofacies of the commendite of Split Ridge (Tbgs) and the commendite of Quartet Dome (Tbq) where present. Occurs in the northern portion of the model area.	WTA 50% LFA 50%
13	Pre-belted Range Composite Unit (PBRCM)	TCU, WTA, LFA	Tr, Tn, Tq, Tu, To, Tk, Te	Laterally extensive and locally very thick HSU that includes all the volcanic rocks older than the Belted Range Group.	TCU 75% WTA 25%
12	Black Mountain Intrusive Confining Unit (BMICU)	IICU	Tti	Although modeled as single intrusive masses beneath each of the Black Mountain, Ammonia Tanks, Rainier Mesa, Claim Canyon, and Silent Canyon calderas, and the Calico Hills area, the actual nature of these units is unknown. They may consist exclusively of igneous intrusive rocks, or older volcanic and pre-Tertiary sedimentary rocks that are intruded to varying degrees by igneous rocks ranging in composition from granite to basalt.	"TCU"
11	Ammonia Tanks Intrusive Confining Unit (ATICU)	IICU	Tmai		
10	Rainier Mesa Intrusive Confining Unit (RMICU)	IICU	Tmri		
9	Claim Canyon Intrusive Confining Unit (CCICU)	IICU	Tpi		
8	Calico Hills Intrusive Confining Unit (CHICU)	IICU	Thi		
7	Silent Canyon Intrusive Confining Unit (SCICU)	IICU	Tc, Tb		
6	Mesozoic Granite Confining Unit (MGCU)	GCU	Kg	Consists of granitic rocks that comprise the Gold Meadows stock along the northeastern margin of the model area.	
5	Lower Carbonate Aquifer - Thrust Plate (LCA3)	CA	Dg through Cc	Cambrian through Devonian, mostly limestone and dolomite, rocks that occur in the hanging wall of the Belted Range thrust fault.	

Table A.1-1
Hydrostratigraphic Units of the Pahute Mesa-Oasis Valley Hydrostratigraphic Framework Model
 (Page 6 of 6)

Model Layer Number ^a	Hydrostratigraphic Unit (Symbol)	Dominant Hydrogeologic Unit(s) ^b	Stratigraphic Unit Map Symbols ^c	General Description	Transport Parameter Category
4	Lower Clastic Confining Unit - Thrust Plate (LCCU1)	CCU	Cc, Cz, Czw, Zs	Late Proterozoic to Early Cambrian siliciclastic rocks that occur within the hanging wall of the Belted Range thrust fault.	
3	Upper Clastic Confining Unit (UCCU)	CCU	MDc, MDe	Late Devonian through Mississippian siliciclastic rocks. Present in the eastern third of the model area.	
2	Lower Carbonate Aquifer (LCA)	CA	Dg through Cc	Cambrian through Devonian mostly limestone and dolomite. Widespread throughout the model area.	
1	Lower Clastic Confining Unit (LCCU)	CCU	Cc, Cz, Czw, Zs, Zj	Late Proterozoic through Early Cambrian siliciclastic rocks. Widespread throughout the model area.	

^aPM-OV 3-D Hydrostratigraphic Framework model (BN, 2002)

^bSee [Table A.1-2](#) and [Table A.1-3](#) for definitions of HGUs

^cRefer to Slate et al. (1999) and Ferguson et al. (1994) for definitions of stratigraphic unit map symbols

Adapted from BN, 2002

Table A.1-2
Hydrogeologic Units of the UGTA Regional Model in the PM-OV Model Area

Hydrogeologic Unit	Typical Lithologies	Hydrologic Significance
Alluvial aquifer (AA) (AA is also an HSU in hydrogeologic models.)	Unconsolidated to partially consolidated gravelly sand, aeolian sand, and colluvium; thin, basalt flows of limited extent	Has characteristics of a highly conductive aquifer, but less so where lenses of clay-rich paleocolluvium or playa deposits are present
Welded-tuff aquifer (WTA)	Welded ash-flow tuff; vitric to devitrified	Degree of welding greatly affects interstitial porosity (less porosity as degree of welding increases) and permeability (greater fracture permeability as degree of welding increases)
Vitric-tuff aquifer (VTA)	Bedded tuff; ash-fall and reworked tuff; vitric	Constitutes a volumetrically minor HGU; generally does not extend far below the static water level due to tendency of tuffs to become zeolitic (which drastically reduces permeability) under saturated conditions; significant interstitial porosity (20 to 40 percent); generally insignificant fracture permeability
Lava-flow aquifer (LFA)	Rhyolite lava flows; includes flow breccias (commonly at base) and pumiceous zones (commonly at top)	Generally a caldera-filling unit; hydrologically complex, wide range of transmissivities, fracture density and interstitial porosity differ with lithologic variations
Tuff confining unit (TCU)	Zeolitic bedded tuff with interbedded, but less significant, zeolitic, nonwelded to partially welded ash-flow tuff	May be saturated but measured transmissivities are very low; may cause accumulation of perched and/or semiperched water in overlying units
Intrusive confining unit (ICU)	Granodiorite, quartz monzonite	Relatively impermeable; forms local bulbous stocks, north of Rainier Mesa, Yucca Flat, and scattered elsewhere in the regional model area; may contain perched water
Clastic confining unit (CCU)	Argillite, siltstone, quartzite	Clay-rich rocks are relatively impermeable; more siliceous rocks are fractured, but with fracture porosity generally sealed due to secondary mineralization
Carbonate aquifer (CA)	Dolomite, limestone	Transmissivity values vary greatly and are directly dependent on fracture frequency

Source: Adapted from IT (1996) and BN (2002)

Table A.1-3
Additional and Modified Hydrogeologic Units of the PM-OV Model

Hydrogeologic Unit	Typical Lithologies	Hydrologic Significance
Intra-caldera intrusive confining unit (IICU)	Highly altered, highly injected/intruded country rock and granitic material	Assumed to be impermeable. Conceptually underlies each of the SWNVF calderas and Calico Hills. Developed for this study to designate basement beneath calderas as different from basement outside calderas.
Granite confining unit (GCU)	Granodiorite, quartz monzonite	Relatively impermeable; forms local bulbous stocks, north of Rainier Mesa and Yucca Flat; may contain perched water.

Source: Adapted from BN (2002)



Appendix B

Use of Yucca Mountain Site Characterization Project Data for Developing Pahute Mesa Corrective Action Unit Model Parameter Distributions

B.1.0 Introduction

The UGTA project includes the modeling of groundwater flow and radionuclide transport in aquifers of the NTS that have been contaminated from underground testing of nuclear weapons. Modeling is used as a method of forecasting how the hydrogeologic system, including the underground test cavities, will behave over time with the goal of assessing the migration of radionuclides away from these cavities. To this end, flow and transport models are being developed over a range of scales for the UGTA CAUs. For the Central and Western Pahute Mesa CAUs, the predominant hydrologic flow pathways from the test cavities are through locally hydrologically conductive Cenozoic volcanic rocks that were erupted and deposited during multiple eruptive cycles of the Timber Mountain and Silent Canyon caldera complexes (Christiansen et al., 1977; Byers et al., 1976; Broxton et al., 1989; Byers et al., 1989; Sawyer et al., 1994). Probability distributions for flow and transport parameters for these rocks are required input for the models.

A major effort of the UGTA project is to compile and assess the suitability of the existing data for these models. Modeling of the UGTA CAUs is not a common groundwater contaminant modeling problem. Most groundwater contamination problems consist of migration of contaminants from relatively well-characterized sources over short flow paths through shallow aquifers. There is often some information about contaminant distribution as a result of monitoring and site characterization. In contrast, the Pahute Mesa CAU model will require prediction of contaminant movement through deep aquifers in a large system (tens of kilometers on a side). Seventy-six widely distributed contaminant sources must be considered for the Pahute Mesa CAU. Information about sources and radionuclide distribution in the aquifer is sparse. Test cavities on Pahute Mesa are as deep as 1,450 m, making extensive characterization of the source and contaminant migration difficult and expensive.

Using experience from other sites to reduce parameter uncertainty is an appropriate approach when developing models in a sparse data environment (Freeze et al., 1990). This approach incorporates flow and transport parameter data from investigations of similar environments when developing prior distributions for parameters to be used in modeling the study area. Utilization of such existing data can be both a cost-effective and necessary step to a modeling effort in a sparse data environment.

Volcanic rocks formed from ash or lava from the Timber Mountain, Silent Canyon, and Claim Canyon Caldera complexes comprised the host environment for the nuclear tests on Pahute Mesa. The Yucca Mountain repository site, located approximately 40 km south of the most southerly test location on Pahute Mesa

(Figure B.1-1), is composed of similar and related volcanic rocks formed by eruptions of ash or lava from volcanic vents to the south of Pahute Mesa. The YMP has implemented one of the largest hydrologic and geologic characterization studies of volcanic rocks ever conducted in any setting. The proximity and similar hydrogeologic environment of the Yucca Mountain site to Pahute Mesa make it particularly attractive as a source of potential data for the UGTA modeling effort.

The purpose of this appendix is to provide technical justification for use of YMP characterization data in determining parameter distributions for physical, hydrological, and chemical properties of volcanic rocks for use as input to flow and transport models for Central and Western Pahute Mesa CAUs:

- Section B.1.0 is the introduction.
- Section B.2.0 provides a description of the processes involved in the deposition and alteration of volcanic rocks that influence their characteristics.
- Section B.3.0 discusses the factors influencing flow and transport properties of fractured rock.
- Section B.4.0 provides the technical justification for use of YMP data in Pahute Mesa model parameter distributions.
- Section B.5.0 discusses the uncertainties associated with the use of data from other sites.
- Section B.6.0 provides a list of references used in this appendix.

B.2.0 Deposition and Alteration of Volcanic Rocks

This section provides descriptions of deposition and alteration processes for the volcanic rocks in the Yucca Mountain and Pahute Mesa areas. A discussion of these topics is essential because the flow of groundwater within the volcanic aquifers of the NTS is controlled largely by the physical characteristics of the volcanic rocks that were deposited, in general, as pyroclastic rocks (Winograd and Thordarson, 1975). The physical properties of these rocks vary systematically with the eruptive-emplacement mechanism, temperature of emplacement, and distance from the source vent of the eruptions (Smith, 1960a and b). In addition, superimposed on these properties are the jointing or fracture characteristics of the rocks and the alteration processes of devitrification, zeolitization, and hydrothermal alteration.

B.2.1 Deposition

The geology of the NTS and the surrounding area is the product of a complex history marked by major structural events. For example, the volcanic rocks of the

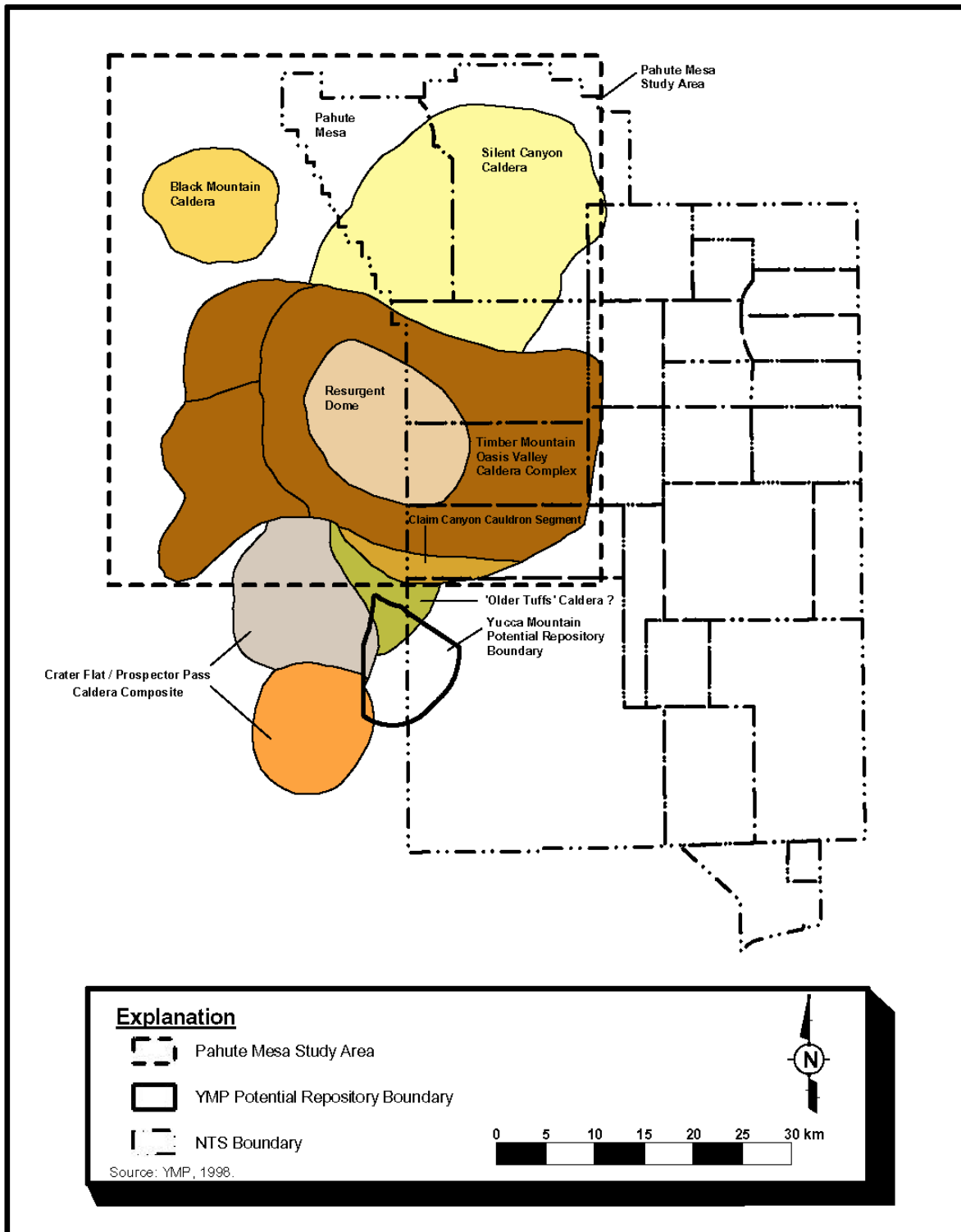


Figure B.1-1
Location of Pahute Mesa, Yucca Mountain Site, and Relevant Caldera Complexes
of the Southwestern Nevada Volcanic Field

NTS and the surrounding area were emplaced during eruptions of the SWNVF during the Tertiary Period. Successive eruptions produced at least six large and partially overlapping calderas such as the Timber Mountain and Silent Canyon Caldera complexes, Claim Canyon Caldera, and the Black Mountain Caldera that were filled with ash flows and lava flows, and blanketed surrounding Paleozoic and Precambrian rocks with vast deposits of tuff (DOE/NV, 1999). These vast tuff deposits were emplaced by processes of ballistic fallout and pyroclastic flows (ash-flow tuffs). Individual eruptive units are thickest adjacent to their source calderas and extend radially outward for distances of several tens of kilometers.

An ash fall deposit is formed after material has been explosively ejected from a vent producing an eruption column, which is a buoyant plume of tephra and gas rising high into the atmosphere (Cas and Wright, 1988). As the plume expands, pyroclasts fall back to Earth, under the influence of gravity, at varying distances from the sources, depending on their size and density (Cas and Wright, 1988). As a result, air-fall deposits mix efficiently with the atmosphere and are cooled before deposition resulting in deposits that are well sorted by grain size, if they are not altered to assemblages of clays and zeolites. Fall deposits have low densities and high porosities (20 to 35 percent).

Ash-flow tuffs, on the other hand, are the deposits left by surface flows of pyroclastic debris which travel as a high particle concentration gas-solid dispersion (Cas and Wright, 1988). They are gravity controlled and may be deposited at a variety of temperatures (less than 100 degrees celsius [°C] to temperatures approaching 800°C), dependent upon such things as the initial magmatic temperature, the specific eruption mechanism, and the transport distance of the ash-flow from the source caldera. In addition, pyroclastic flows that are deposited above the minimum annealing temperatures of volcanic glass will weld (Smith, 1960a). Welding refers to the process of compaction and cohesion of glassy fragments by viscous deformation. The extent of welding is controlled by the depositional temperature and lithostatic load. Generally, the greater the temperature and lithostatic load, the greater the degree of welding with some additional variation from the chemistry of the volcanic glass. Ash-flow tuff, when initially deposited, varies vertically in temperature due to initial variations in the eruption column dynamics (degree of mixing with the atmospheric) and conductive heat loss from the top and bottom of the pyroclastic flow.

The vertical variations in temperature and lithostatic load result in distinct zones of welding characterized by bulk density differences. Bulk densities can range from about 1.4 Megagram per cubic meter (Mg/m^3) in the outer cool and non-welded top and bottoms of an ash-flow sheet to about 2.5 Mg/m^3 in the densely welded interiors of an ash-flow tuff. Porosities are inversely correlated with density and range from greater than 30 to less than 10 percent. The vertical variations in welding of volcanic tuff also occur laterally with distance from the source vents because of heat loss during turbulent flow of the hot density currents that deposit the rocks. Generally, depositional temperatures decrease systematically with distance from vents with correlated lateral decreases in the degree of welding and density, and increases in the porosity of the tuff.

B.2.2 Alteration

Superimposed on the vertical and lateral variations in ash-flow tuff are zones of primary and secondary alteration. Primary alteration refers to devitrification, or the subsolidus recrystallization of original metastable volcanic glass. The main products of devitrification are cristobalite and alkali feldspar. The primary effect of devitrification is that stable assemblages of minerals are formed that cannot easily be affected by secondary alteration. Generally, the extent of devitrification is controlled by temperature with the hot, welded interiors of ash-flow tuff showing the greatest extent of devitrification. These densely welded, devitrified interiors of sheets of ash-flow tuff tend to maintain open fractures formed as cooling joints during the cooling of a deposit. The narrow spacing of cooling joints leads to a high fracture permeability and these types of rocks, at the NTS, tend to be some of the most productive aquifers.

Secondary alteration of non-welded ash-flow tuff consists primarily of alteration of volcanic glass to assemblages of clays and zeolites. This alteration occurs primarily in the vitric (glassy) exterior top and bottoms of the ash-flow sheets where the initial high porosities of the non-welded rocks transmit water that promotes the secondary alteration. The secondary alteration tends to dramatically reduce the conductivity and effective porosity of volcanic rocks and greatly reduces the ability of the rocks to transmit water. These rocks tend to also have a less brittle nature and a low fracture density due to the absence of cooling joints. Most of the major aquitard units of the NTS region occur in sequences of zeolitized volcanic rocks. These rocks predominate in thick sections of air-fall tuff and the distal (cool emplacement) parts of ash-flow tuff where there is limited welding of the deposits.

B.3.0 Factors Influencing Flow and Transport Parameters of Fractured Rock

The flow of groundwater beneath Pahute Mesa occurs almost exclusively through interconnected natural fractures in volcanic rocks (DOE/NV, 1997). Consequently, the parameters required to appropriately represent flow and transport in the rock mass are influenced significantly by the characteristics of the fracture system. While quantitative predictions of flow and transport parameters cannot be made from characteristics such as rock type or stress, sufficient evidence exists to identify factors that influence flow and transport parameters in fractured rock. A diagram representing these factors and their influence on flow and transport parameters is shown in [Figure B.3-1](#).

B.3.1 Influences on Flow Parameters

Flow in fractured rocks is controlled by fracture geometry and fracture connectivity. Fracture geometry includes characteristics such as orientation, spacing, aperture, and length. Geologic history, lithology, alteration, mineral precipitation or dissolution, and stress history influence fracture geometry.

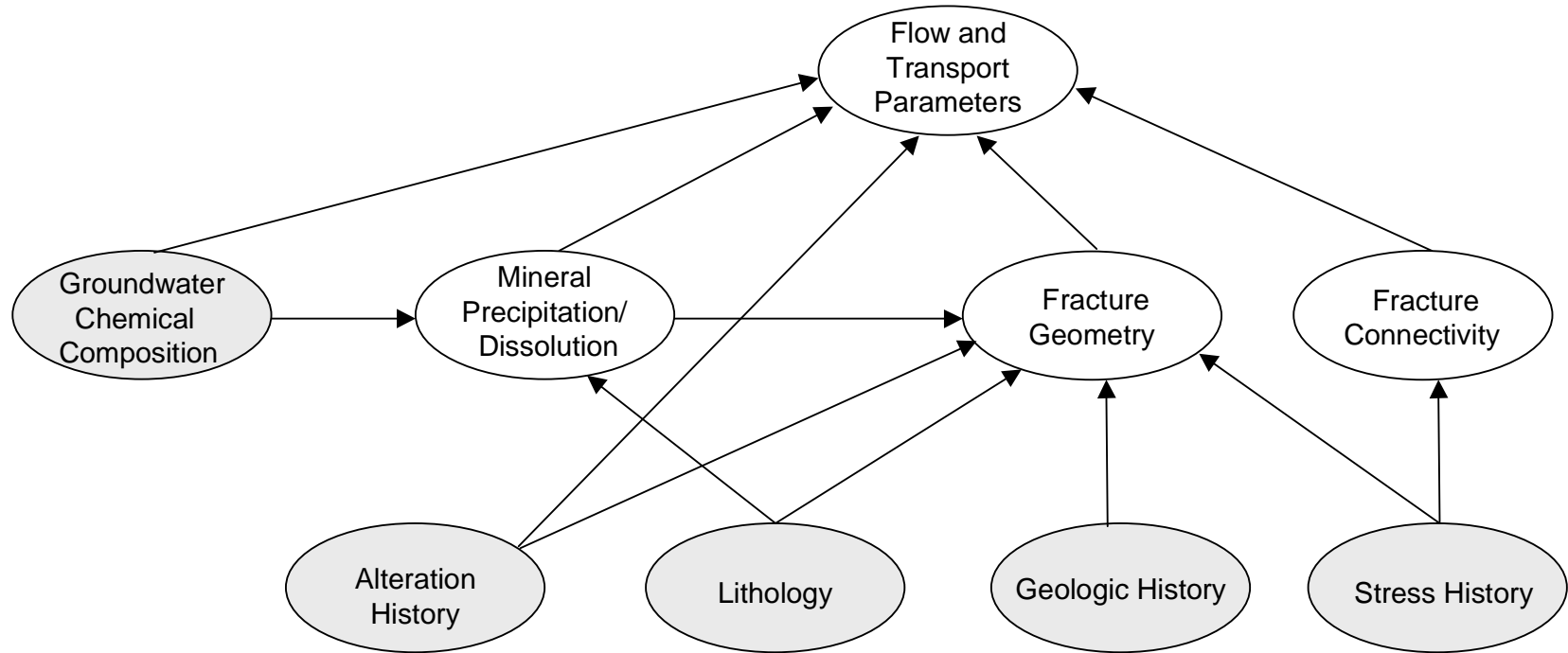


Figure B.3-1
Factors Influencing Flow and Transport Parameters in Fractured Rock

The emplacement of volcanic rocks during multiple eruptive cycles leads to stratigraphic sequences of ash-flow tuffs and magmas of varying thicknesses. Thermal stress due to cooling of these layers leads to the formation of polygonal joints.

Processes of welding and alteration following emplacement discussed in [Section B.2.0](#) influence matrix porosity and fracture geometry. The geologic and alteration histories contribute to a rock's lithologic classification.

Mineral precipitation or dissolution within fractures also influences fracture geometry and, thus, permeability. The effect on permeability can range from a reduction in permeability from filling fractures with minerals to enhancement of permeability due to fracture fillings forming bridges that prop open fractures (NRC, 1996). Mineral precipitation and dissolution are influenced by lithology and groundwater chemical composition.

Stress can influence fracture orientation and aperture distribution. Regions characterized by extensional stress tend to form extensional fractures oriented perpendicular to the intermediate stress direction. Unless the fractures are filled, fracture permeability in these regions is enhanced due to opening of the fractures (NRC, 1996).

Fracture connectivity is strongly influenced by the state of stress. The degree of connectivity is considered to be inversely related to the magnitude of differential regional stress (NRC, 1996).

B.3.2 Influences on Transport Parameters

Solute transport depends on the distribution of fluid velocities in the rock mass. Velocity distributions are influenced by fracture geometry. Solute dispersion as multiple pathways in the rock mass are encountered; thus, fracture geometry and connectivity influence dispersion.

Diffusion of solutes from fluid in fractures into fracture coatings and the rock matrix is influenced by fracture-coating characteristics, lithology, and alteration of the rock. In addition, fracture geometry influences the amount of rock surface area available for matrix diffusion.

Chemical reactions occurring within the fracture depend on chemical composition of the groundwater, the extent and composition of mineral fillings, and the nature of the rock matrix. Groundwater composition and lithology of the host rocks influence the presence and composition of mineral coatings. Lithology and the alteration history control the sorption characteristics of the rock matrix.

B.3.3 Basis for Correlation Between Sites

Similarities between factors influencing flow and transport parameters shown in [Figure B.3-1](#) provide a basis for incorporation of characterization data for volcanic rocks from other sites into prior distributions for Western and Central Pahute Mesa CAU model parameters. The rationale for use of YMP data presented in

Section B.4.0 will be based on similarities in geologic history, lithology, alteration, groundwater composition, and stress.

B.4.0 Transferability Rationale

The use of data from the YMP area and proximal CAUs on the NTS in flow and transport modeling of a specific UGTA CAU can be supported by examining specific similarities between the two areas. The previous section identified the factors that influence flow and transport parameters for fractured rock. This section considers these factors specifically for Yucca Mountain and Pahute Mesa to develop the similarities of the two areas.

B.4.1 Geologic Setting

Brief descriptions of the geologic settings of Pahute Mesa and Yucca Mountain are provided in this section.

Pahute Mesa

Pahute Mesa is an elongated, east-to-west-oriented volcanic plateau within the SWNVF and consists mainly of Miocene rhyolitic rocks that erupted from local calderas (Laczniak et al., 1996). Its eastern portion occupies the northwestern corner of the NTS, including Areas 19 and 20.

The surface of the Pahute Mesa study area consists primarily of ash-flow tuffs of the Thirsty Canyon and Timber Mountain Groups that erupted from calderas located just west and south of the area (BN, 2002). These Tertiary volcanics, along with volcanic rocks of the underlying Paintbrush Group, bury an older group of calderas that compose the Silent Canyon Caldera complex (BN, 2002). The Silent Canyon Caldera complex along with the Timber Mountain Caldera complex are the dominant geologic features in the PM-OV region. The Silent Canyon Caldera complex consists of at least two nested calderas, the Area 20 caldera and the older Grouse Canyon caldera. The Grouse Canyon caldera was formed and then filled by Tertiary eruptions of tuff and lava of the Belted Range Group. The Area 20 caldera was formed by eruptions of tuff of the Crater Flat Group, and then filled by eruptions of tuff and lava of the Crater Flat Group and Volcanics of Area 20.

The volcanic rocks of the Belted Range Group, the Crater Flat Group, and Volcanics of Area 20 are underlain by a considerable thickness of older volcanic rocks, which were probably erupted locally from unidentified calderas, some possibly beneath Pahute Mesa. In the eastern portion of Pahute Mesa outside the calderas, the Tertiary volcanic rocks probably overlie an unknown thickness of late Precambrian to Cambrian quartzites and siltstones. Paleozoic carbonates may underlie the volcanic rocks in the western portion of Pahute Mesa (BN, 2002).

Yucca Mountain

Yucca Mountain is a remnant of a Miocene-Pliocene volcanic plateau that was centered around the Timber Mountain/Oasis Valley caldera complex in the SWNVF.

Yucca Mountain consists of a series of volcanic outflow sheets that frame the southern margin of the Claim Canyon caldera. North-to-south trending basin and range faults have disrupted the volcanic plateau and formed linear mountain ranges separated by sediment-filled troughs. Yucca Mountain is an east-tilted fault block consisting of a thick sequence of tuffs erupted from the middle to late Miocene Timber Mountain-Oasis Valley caldera complex located to the north and west (Broxton et al., 1987; Byers et al., 1976; Christiansen et al., 1977).

The exposed stratigraphic sequence at Yucca Mountain is dominated by Tertiary ash-flow tuffs and ash-fall tuffs, with minor lava flows and reworked volcanic material (Broxton et al., 1987). Most tuffs are high-silica rhyolites, but two large-volume, ash-flow cooling units in the upper part of the sequence are compositionally zoned grading upward in composition from rhyolite to quartz latite. Exposed rocks at Yucca Mountain consist primarily of these two zoned tuffs, the Topopah Spring Tuff and Tiva Canyon Tuff of the Paintbrush Group (Broxton et al., 1987). The Paintbrush Group erupted from the Claim Canyon caldera just north of Yucca Mountain. According to Sawyer et al. (1994), the Topopah Spring Tuff has an age of 12.8 million years while the Tiva Canyon Tuff has an age of 12.7 million years.

Beneath the Paintbrush Group, the principal stratigraphic units are in descending order: Calico Hills Formation (Volcanics of Area 20), Crater Flat Group, Lithic Ridge Tuff of the Tram Ridge Group, Tunnel Formation, and older tuffs and Tertiary sediments. Wells on Yucca Mountain have penetrated to depths of 1.8 km without leaving volcanic rocks, and the volcanic section east of Yucca Mountain is about 1.2 km thick and overlies the Silurian Lone Mountain Dolomite (Broxton et al., 1987).

B.4.2 Lithology

Intensive studies associated with the YMP and the weapons-testing program have shown that hydrologic properties can generally be correlated with major volcanic rock types (Blankennagel and Weir, 1973; Winograd and Thordarson, 1975; BN, 2000; Prothro and Drellack, 1997). For example, Blankennagel and Weir (1973) state that ash-fall tuffs and nonwelded (or slightly welded) ash-flow tuffs have similar physical properties and hydraulic characteristics, although their origin and mode of emplacement differs. This suggests that hydrologic data gathered from field or laboratory studies of volcanic rocks at one site can be applied or transferred to another less well-studied site if it contains comparable types of volcanic rocks. This has important implications for the modeling of UGTA CAUs because the Yucca Mountain area contains comparable types of volcanic rocks that have been more extensively studied than the volcanic rocks found at the Pahute Mesa study area. For example, the widely distributed ash-flow sheets of the Timber Mountain and Paintbrush Groups that were erupted from the Timber Mountain and Claim Canyon calderas, respectively. These rocks are

generally similar in chemical composition and exhibit mostly similar patterns in their vertical and lateral variations in welding. Both groups of rocks are present in the subsurface of the Pahute Mesa study area, while the Yucca Mountain site is underlain primarily by multiple ash-flow sheets of the Paintbrush Group. This is advantageous for the modeling efforts of the Pahute Mesa study area because extensive physical properties data and hydrologic measurements of the Paintbrush Group have been obtained for the rocks along the length of Yucca Mountain. These rocks were extensively studied at Yucca Mountain because the target horizon for the location of the potential underground repository is in the densely welded, devitrified interior of the Topopah Spring Formation of the Paintbrush Group.

B.4.3 Alteration

The alteration of volcanic rocks can also influence flow and transport parameters. For example, it was seen in [Section B.3.0](#) of this appendix that alteration of volcanic rocks can directly effect fracture geometry. Therefore, any lithologic comparison between the two areas must also include an examination of possible alteration products. The transfer of data from one specific area to another is supported by demonstrating that the two areas have comparable types and degrees of alteration. Broxton et al. (1987) state that alteration of volcanic rocks at Yucca Mountain is mostly observed in nonwelded ash-flow tuff, bedded tuff, and in thin envelopes of nonwelded tuff at the top and bottom of cooling units that have densely welded, devitrified interiors. The tuffs were vitric after emplacement and were highly susceptible to alteration because of the instability of volcanic glass in the presence of groundwater. This has important implications for the modeling of UGTA CAUs because the Pahute Mesa study area has undergone similar types of alteration as the Yucca Mountain area. However, the altered volcanic rocks at Yucca Mountain have been extensively studied. For example, the alteration history of a thick sequence of vitric and zeolitized ash-fall tuffs of the Calico Hills Formation has been carefully studied as part of the YMP site characterization study. These volcanic rocks were studied extensively because they form a major vertical transport barrier between the target horizon of the Topopah Springs Formation and the water table at Yucca Mountain. These studies would provide a valuable source of comparable data for the modeling efforts of the Central and Western Pahute Mesa CAUs because related rocks of the Paintbrush Group and the Calico Hills Formation, for example, are present in the Central and Western Pahute Mesa CAUs.

B.4.4 Influence of Stress

Stress can influence fracture orientation, aperture distribution, and fracture connectivity. Extensional regions tend to form extensional fractures that are open to flow. The orientation of these open fractures is generally parallel to the intermediate stress direction. Permeability tends to be enhanced in the direction of the fracture orientation unless fractures are filled (NRC, 1996).

In addition, the interaction and linkage of joints is influenced by the state of stress. Nearby fractures tend to interact and connect if the differential regional stress is

small. When differential stress is large, the tendency to connect is weak (NRC, 1996).

Regional stress is characterized by the directions and magnitudes of the principal stresses. Directions of horizontal stress have been determined by tectonic and structural analyses and by analyses of borehole elongation. Magnitudes of the least horizontal principal stress, S_h , can be directly measured using the hydraulic fracturing method and the greatest horizontal principal stress, S_H , can be estimated indirectly from this method (Stock and Healy, 1988).

Stress Directions

A model proposed by Carr (1974) based on tectonic and structural analyses suggests the NTS region is undergoing extension with the direction of the least principal stress being North 50° West. Measurements made by Stock and Healy (1988) in four boreholes at Yucca Mountain found the direction of least principal stress to range from North 60° West to North 65° West. Stress directions were determined in seven boreholes on Pahute Mesa by Springer et al. (1984) using borehole elongation information. The distribution of orientation of borehole elongations was slightly bimodal with the major mode corresponding to a direction of least principal stress of North 56° West. The orientation of borehole elongation was evaluated in 12 additional boreholes on Pahute Mesa by Gillson (1993). The mean orientation of the direction of least principal stress from these analyses was also North 56° West. These results show good agreement between Yucca Mountain and Pahute Mesa in measured directions of least horizontal principal stress.

Stress Magnitudes

Seven measurements of the magnitude of the least horizontal principal stress (S_h) and seven corresponding estimates of the magnitude of the greatest horizontal principal stress (S_H) were obtained from three boreholes on Yucca Mountain by Stock and Healy (1988). No measurements of stress magnitude were found for Pahute Mesa; however, Carr (1974) reports two measurements of the maximum excess horizontal stress at two depths in tunnels under Rainier Mesa. These measurements along with the maximum excess horizontal stress ($S_H - S_h$) from the data of Stock and Healy (1988) are plotted in [Figure B.4-1](#).

Measurements on Yucca Mountain were made at depths ranging from 1,026 to 1,573 m. The increase in maximum excess horizontal stress with depth for the Yucca Mountain measurements can be seen in [Figure B.4-1](#). An exponential relationship was fit to the Yucca Mountain data and is shown in the figure.

Given the increase of maximum excess horizontal stress with depth evidenced by the Yucca Mountain measurements, the stress magnitudes for Rainier Mesa measured at a relatively shallow depth are consistent with stress magnitudes measured at Yucca Mountain. These similarities in the regional stress regime suggest that the influence of regional stress on fracture network characteristics is similar for Pahute Mesa and Yucca Mountain.

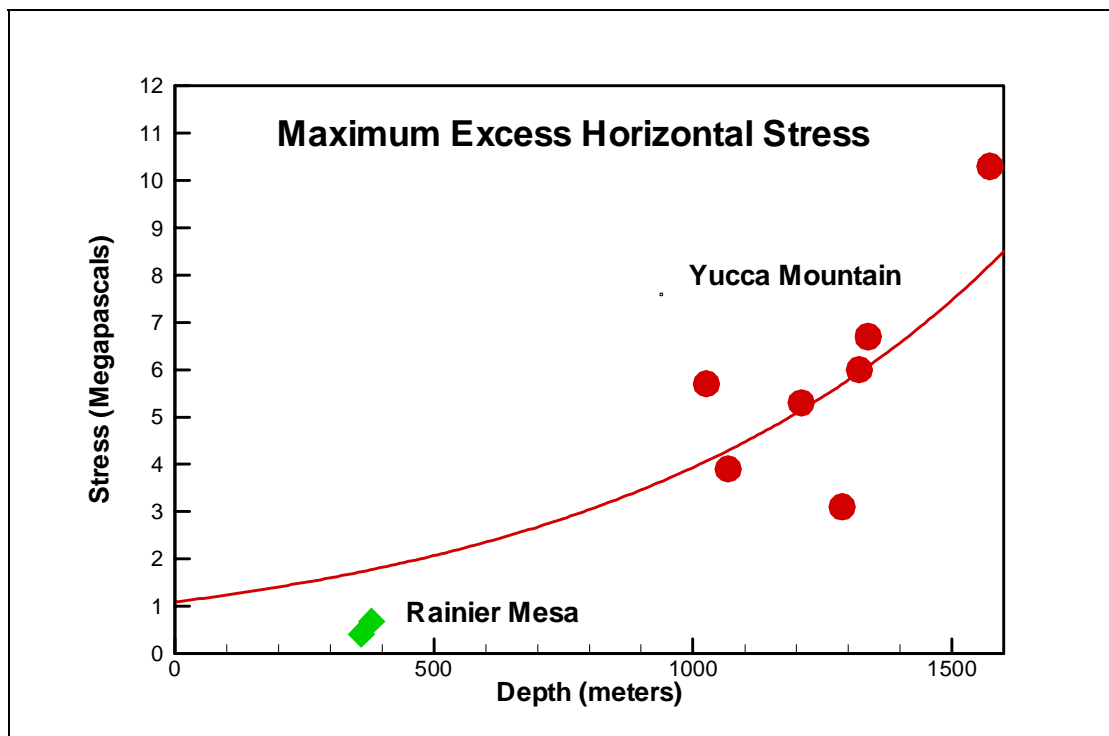


Figure B.4-1
Maximum Excess Horizontal Stress from Yucca Mountain Boreholes
(Stock and Healy, 1988) and Rainier Mesa (Carr, 1974)

B.4.5 Groundwater Chemistry

Groundwater chemistry is an important component of flow and transport models because it influences everything from mineral dissolution/precipitation reactions to fracture geometry. Examination of the groundwater chemistry for the Pahute Mesa and the Yucca Mountain areas reveals that both locations have similar geochemical signatures for wells that penetrate Tertiary volcanic rocks. This also has important implications for the transfer of data from the Yucca Mountain area to the Pahute Mesa study area because it supports the argument that both areas contain similar types of rocks.

It is well documented that groundwater acquires a chemical signature, or fingerprint, by reaction with aquifer solids along the flow path. Similar chemical signatures indicate that groundwater is flowing through similar types of aquifer material. Figure B.4-2 is a trilinear diagram showing the relative concentrations of major ions in composite groundwater samples from selected wells in the Pahute Mesa and Yucca Mountain regions. The figure contains three different plots of major-ion chemistry. The concentrations on the trilinear diagram are expressed in percent milliequivalents per liter. Trilinear diagrams are useful for illustrating various groundwater chemistry types and relationships that may exist between the types. It can be seen from the trilinear diagram that sodium is the dominant cation for both regions with minor amounts of calcium and magnesium. Further examination of the figure reveals that bicarbonate is the dominant anion for both

regions with minor amounts of sulfate and chloride. However, it can be seen from the figure, in general, the Pahute Mesa study area has greater amounts of chloride and sulfate than the Yucca Mountain area. It has been suggested that the higher proportions of chloride and sulfate in the eastern side of Pahute Mesa are a result of the interaction of groundwater with hydrothermally altered zones (Blankennagel and Weir, 1973). The Pahute Mesa study area, however, has greater amounts of chloride and sulfate than the Yucca Mountain area. Groundwater with chemical compositions such as these can be classified as sodium-potassium-bicarbonate type water. This water type is typically found in volcanic terrain and alluvium derived from volcanic material. The similarity in groundwater composition between the two areas for wells completed in the Tertiary rocks illustrates that the groundwater in both regions have a common origin and are in contact with similar types of volcanic rocks.

B.4.6 Summary

The use of data from the Yucca Mountain area to develop parameter distributions for flow and transport modeling of UGTA CAUs can be supported by examining specific similarities between the two areas.

- Both areas are located in the SWNVF.
- The volcanic rocks in both areas are the results of similar deposition processes.
- Both areas contain similar lithologic units and even lithologic units from the same source area.
- In addition, both areas have experienced similar types of alteration including devitrification and zeolitization of volcanic material.
- The two areas have also undergone similar types of regional tectonic stresses, resulting in a similarity in the two areas of regional fracture orientations.
- Finally, the two areas have similar groundwater chemistry.

B.5.0 Uncertainties in Data Transfer

While much hydrologic and transport information can be transferred from comparable sources of data, there are several cautions that must accompany the transfer and interpretation of this type of data.

First, and most importantly, hydrologic properties of volcanic tuff are strongly controlled by the fracture properties of the rocks. These properties are controlled in part by the vertical and lateral distribution of cooling joints that can be systematically related to the welding properties of the ash-flow sheets. However,

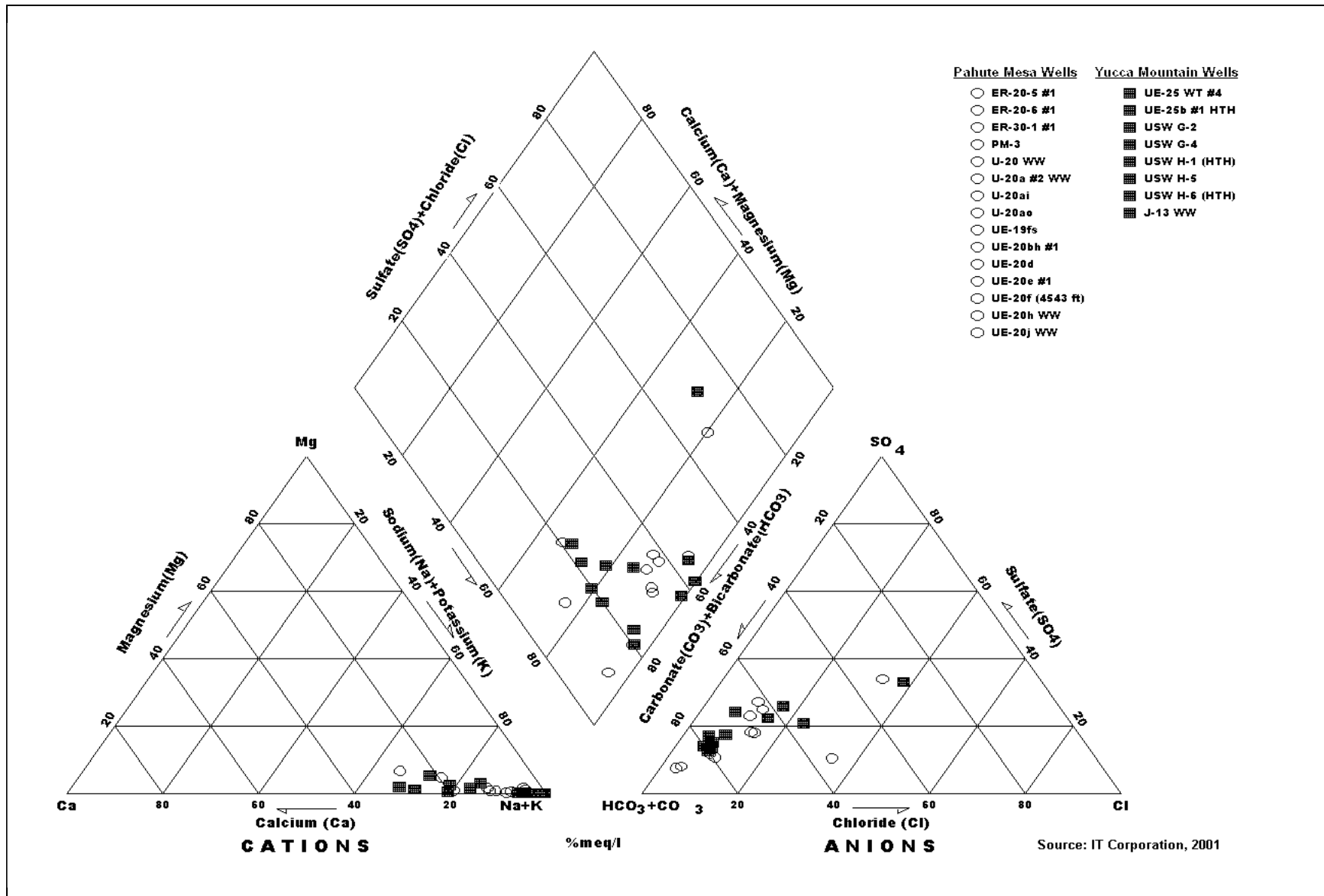


Figure B.4-2
Trilinear Diagram Showing Relative Major Ion Percentages for Groundwater from Pahute Mesa and Yucca Mountain (IT, 2001)

an additional and locally dominant component of fracture permeability is associated with tectonic fractures. These fractures are controlled by the local tectonic setting and the presence and nature of faulting, particularly basin and range faults associated with extensional faulting and basin formation. As a result, hydrologic properties of jointed volcanic rocks can vary dramatically in proximity to major fault systems. Studies of fracture frequency in the exploratory studies facility at Yucca Mountain showed that fracture frequency in the immediate vicinity of faults was influenced in a zone that ranged from less than 1 m to about 7 m (CRWMS M&O, 2000). In addition, the hydrologic properties of the faults themselves can vary significantly depending on the nature of the faulting, the presence or absence of alteration products in the fault zones, and the orientation of the faults with respect to the groundwater flow directions.

A second cause of local spatial variability of fracture properties of ash-flow tuff is the effect of paleotopography or the topography of the surface beneath the ash-flow tuff (emplacement surface). Ash-flows move as turbulent, high-particle concentration flows and are channeled by underlying topography. Consequently, the resulting thickness of local ash-flow units can change markedly by thickening in depressions and thinning over topographic highs. The general effect of ash-flow channeling is significant increases in the thickness of welded zones and the production of more intense and more closely spaced fractures that can transmit water. For example, the Topopah Springs Formation at Yucca Mountain is thickened relative to adjacent depressions from ponding in the Miocene Crater Flat tectonic basin.

Finally, the alteration history of individual sections of tuff can vary with local settings dependent on the history and access of both groundwater and hydrothermal fluids to the rocks. For example, high-porosity sections of vitric fallout and reworked tuff can decrease in porosity from alteration. Characterization studies at the YMP have also shown that sections of zeolitized tuff can vary by a factor of two or three in abundance of secondary alteration minerals. As a result, fracture permeability in both non-welded and welded tuff can change dramatically dependent on whether the fracture is filled or not filled with secondary alteration products.

B.6.0 References

BN, see Bechtel Nevada.

Bechtel Nevada. 2002. *A Hydrostratigraphic Model and Alternatives for the Groundwater Flow and Contaminant Transport Model of Corrective Action Units 101 and 102: Central and Western Pahute Mesa, Nye County, Nevada*. DOE/NV/11718-706. Prepared for the U.S. Department of Energy, National Nuclear Security Administration Nevada Operations Office. Las Vegas, NV.

Blankennagel, R.K., and J.E. Weir. 1973. *Geohydrology of the Eastern Part of the Pahute Mesa, Nevada Test Site, Nye County, Nevada*, Professional Paper 712B. Denver, CO: U.S. Geological Survey.

- Broxton, D.E., D.L. Bish, and R.G. Warren. 1987. "Distribution and Chemistry of Diagenetic Minerals at Yucca Mountain, Nye Co., Nevada." In *Clays and Clay Minerals Society*, v. 35, p. 89.
- Broxton, D.E., R.G. Warren, F.M. Byers, Jr., and R.B. Scott. 1989. "Chemical and Mineralogic Trends within the Timber Mountain-Oasis Valley Caldera Complex, Nevada: Evidence for Multiple Cycles of Chemical Evolution in a Long-Lived Silicic Magma System." In *Journal of Geophysical Research*, v. 94, 5961-5985.
- Byers, F.M., Jr., W.J. Carr, P.P. Orkild, W.D. Quinlivan, and K.A. Sargent. 1976. *Volcanic Suites and Related Cauldrons of Timber Mountain-Oasis Valley Caldera Complex, Southern Nevada*, Professional Paper 919. Denver, CO: U.S. Geological Survey.
- Byers, F.M., Jr., W.J. Carr, and P.P. Orkild. 1989. "Volcanic Centers of Southwestern Nevada: Evolution of Understanding 1960-1988." In *Journal Geophysical Research*, v. 94, pp. 5908-5924.
- Carr, W.J. 1974. *Summary of Tectonic and Structural Evidence for Stress Orientation at the Nevada Test Site*, U.S. Geological Survey Open File Report 74-176. Denver, CO.
- Cas, R.A.F., and J.V. Wright. 1988. *Volcanic Successions: Modern and Ancient*. New York, NY: Chapman & Hall.
- Christiansen, R.L., P.W. Lipman, W.J. Carr, F.M. Byers, Jr., P.P. Orkild, and K.A. Sargent. 1977. "The Timber Mountain-Oasis Caldera Complex of Southern Nevada." In *Geological Society America*, v. 88, pp. 943-949.
- CRWMS M&O, see Civilian Radioactive Waste Management System and Operating Contractor.
- Civilian Radioactive Waste Management System and Operating Contractor. 2000. *Fault Displacement Effects on Transport in the Unsaturated Zone*, ANL-NBS-HS-000020, REV 00. Las Vegas, NV.
- DOE/NV, see U.S. Department of Energy.
- Freeze, R.A., J. Massman, L. Smith, T. Sperling, and B. James. 1990. "Hydrologically Decision Analysis: 1. A Framework." In *Ground Water*, v. 28., pp. 738-766.
- Gillson III, R.G. 1993. *Analysis of Borehole Elongation in Yucca Flat and Pahute Mesa, Using the Digital Downhole Surveyor*, Thesis (M.S.). Fayetteville, AR: University of Arkansas.
- IT Corporation. 2001. *A User's Guide to the Comprehensive Chemistry Database for Groundwater at the Nevada Test Site*, ITLV/13052--070. Prepared for U.S. Department of Energy, Nevada Operations Office. Las Vegas, NV.

- Laczniak, R.J., J.C. Cole, D.A. Sawyer, and D.A. Trudeau. 1996. *Summary of Hydrogeologic Controls on Groundwater Flow at the Nevada Test Site, Nye County, Nevada*, Water-Resources Investigations Report 96-4109. Denver, CO: U.S. Geological Survey.
- NRC, see U.S. National Research Council.
- Prothro, L.B., and S.L. Drellack, Jr. 1997. *Nature and Extent of Lava-Flow Aquifers Beneath Pahute Mesa, Nevada Test Site*, DOE/NV/11718-156. Las Vegas, NV.
- Sawyer, D.A., R.J. Fleck, M.A. Lanphere, R.G. Warren, and D.E. Broxton. 1994. "Episodic Caldera Volcanism in the Miocene Southwestern Nevada Volcanic Field: Revised Stratigraphic Framework, $^{40}\text{Ar}/^{39}\text{Ar}$ Geochronology, and Implications for Magmatism and Extension." In *Geological Society of America Bulletin*, v.106, pp. 1304-1318.
- Smith, R.L. 1960a. "Ash Flows." In *Geological Society America*, Special Paper 67.
- Smith, R.L. 1960b. *Zones and Zonal Variations in Welded Ash Flows*, U.S. Geological Survey Professional Paper No. 345-F, pp. 138-143.
- Springer, J.E., R.K. Thorpe, and H.L. McKague. 1984. *Borehole Elongation and Its Relation to Tectonic Stress at the Nevada Test Site*, UCRL-53528. Livermore, CA: Lawrence Livermore National Laboratory.
- Stock, J.M., and J.H. Healy. 1988. "Stress Field at Yucca Mountain, Nevada." In *Geologic and Hydrologic Investigations of a Potential Nuclear Waste Disposal Site at Yucca Mountain, Southern Nevada*, U.S. Geological Survey Bulletin No. 1790, pp. 87-93. Carr, M.D. and J.C. Yount, eds. Denver, CO: U.S. Geological Survey.
- U.S. Department of Energy, Nevada Operations Office. 1997. *Regional Groundwater Flow and Tritium Transport Modeling and Risk Assessment of the Underground Test Area, Nevada Test Site, Nevada*, DOE/NV--477. Las Vegas, NV.
- U.S. Department of Energy, Nevada Operations Office. 1999. *Corrective Action Investigation Plan for Corrective Action Units 101 and 102: Central and Western Pahute Mesa, Nevada Test Site, Nevada*, DOE/NV--516. Las Vegas, NV.
- U.S. National Research Council. 1996. *Rock Fractures and Fluid Flow: Contemporary Understanding and Applications*. Washington DC.: National Academy Press.

Winograd, I. J., and W. Thordarson. 1975. *Hydrogeologic and Hydrochemical Framework, South Central Great Basin, Nevada-California, with Special Reference to the Nevada Test Site*, Professional Paper No. 712-G. Washington, DC.

YMP, see Yucca Mountain Project.

Yucca Mountain Project. 1998. *Yucca Mountain Project 1998 Geographic Information System CD-ROM Project*. Las Vegas, NV.



Appendix C

Description of BestFit Software

C.1.0 Introduction

A brief overview of the BestFit software is provided followed by detailed descriptions of the distributions used in this document. Detailed descriptions of the Bestfit software may be found in the user's manual (Palisade, 2002).

C.2.0 BestFit Software Overview

BestFit is a Windows program designed to find the distribution that best fits a given dataset. BestFit tests up to 28 different distribution types to find the best fit for the data. Results may be displayed as graphs or full statistical reports.

BestFit determines the optimal parameters for each distribution, performing three standard tests to determine the goodness of fit: Chi-squared, Anderson-Darling (A-D), and Kolmogorov-Smirnov (K-S). For a given dataset, the distribution fits are listed in order of goodness of fit.

BestFit fits to sample, density, or cumulative data. As many as 100,000 data points or pairs may be handled by BestFit. Outliers may be filtered out of the dataset. Parameter selection is performed using maximum-likelihood estimators and method of least squares.

The following distribution types are included in BestFit:

- BetaGeneral
- Binomial
- Chi-Square
- Error Function
- Erlang
- Exponential
- Extreme Value
- Gamma
- Geometric
- Hypergeometric
- Inverse Gaussian
- IntUniform
- Logistic
- Log-Logistic
- Lognormal
- Lognormal2
- Negative Binomial

- Normal
- Pareto
- Pareto2
- Pearson Type V
- Pearson Type VI
- Poisson
- Rayleigh
- Student's t
- Triangular
- Uniform
- Weibull

C.3.0 *Distribution Descriptions*

Detailed descriptions of the distributions used in this document are presented at the end of this section.

C.4.0 *References*

Palisade. 2002. "A Concise Summary of @Risk Probability Distribution Functions," Supplemental Document to *Guide to Using BestFit; Distribution Fitting for Windows*, Version 4.5 (included on the CD as part of the software package). Newfield, NY: Palisade Corporation.

Description of Selected Probability Distribution Functions

This description of selected probability density distribution was extracted from the BestFit software user guide (Palisade, 2002).
The descriptions are provided verbatim.

Beta (Generalized)

RISKBetaGeneral($\alpha_1, \alpha_2, \min, \max$)

Parameters:

α_1	continuous shape parameter	$\alpha_1 > 0$
α_2	continuous shape parameter	$\alpha_2 > 0$
min	continuous boundary parameter	min < max
max	continuous boundary parameter	

Domain:

$\min \leq x \leq \max$	continuous
-------------------------	------------

Density and Cumulative Distribution Functions:

$$f(x) = \frac{(x - \min)^{\alpha_1 - 1} (\max - x)^{\alpha_2 - 1}}{B(\alpha_1, \alpha_2) (\max - \min)^{\alpha_1 + \alpha_2 - 1}}$$

$$F(x) = \frac{B_z(\alpha_1, \alpha_2)}{B(\alpha_1, \alpha_2)} \equiv I_z(\alpha_1, \alpha_2) \quad \text{with } z \equiv \frac{x - \min}{\max - \min}$$

where B is the *Beta Function* and B_z is the *Incomplete Beta Function*.

Mean:

$$\min + \frac{\alpha_1}{\alpha_1 + \alpha_2} (\max - \min)$$

Variance:

$$\frac{\alpha_1 \alpha_2}{(\alpha_1 + \alpha_2)^2 (\alpha_1 + \alpha_2 + 1)} (\max - \min)^2$$

Skewness:

$$2 \frac{\alpha_2 - \alpha_1}{\alpha_1 + \alpha_2 + 2} \sqrt{\frac{\alpha_1 + \alpha_2 + 1}{\alpha_1 \alpha_2}}$$

Kurtosis:

$$3 \frac{(\alpha_1 + \alpha_2 + 1)(2(\alpha_1 + \alpha_2)^2 + \alpha_1 \alpha_2(\alpha_1 + \alpha_2 - 6))}{\alpha_1 \alpha_2 (\alpha_1 + \alpha_2 + 2)(\alpha_1 + \alpha_2 + 3)}$$

Mode:

$$\min + \frac{\alpha_1 - 1}{\alpha_1 + \alpha_2 - 2} (\max - \min)$$

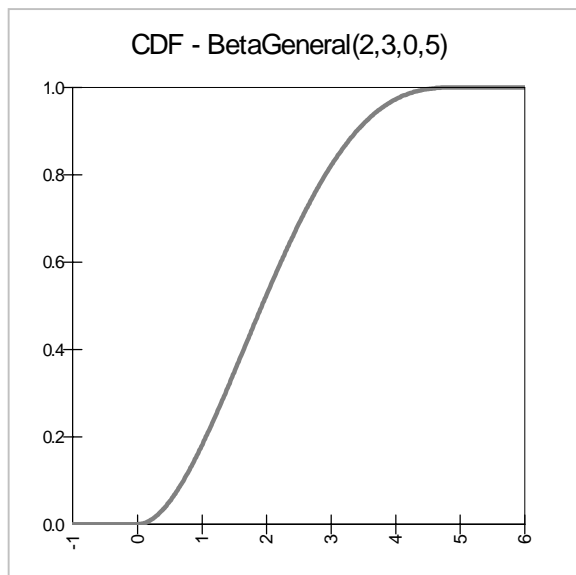
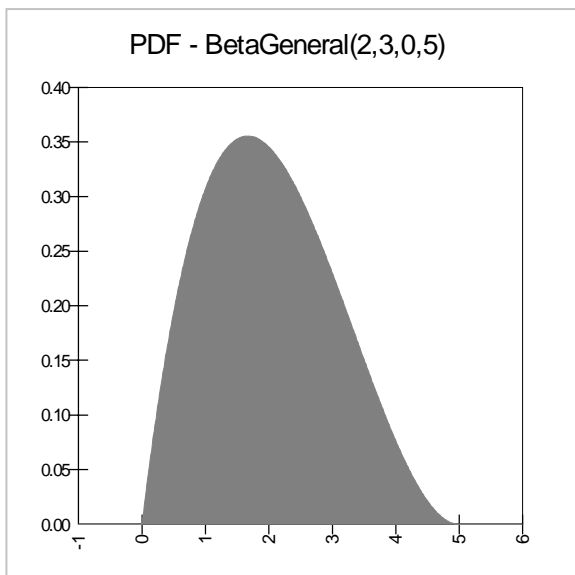
$$\alpha_1 > 1, \alpha_2 > 1$$

min

$$\alpha_1 < 1, \alpha_2 \geq 1 \text{ or } \alpha_1 = 1, \alpha_2 > 1$$

max

$$\alpha_1 \geq 1, \alpha_2 < 1 \text{ or } \alpha_1 > 1, \alpha_2 = 1$$



Chi-Squared

RISKChiSq(v)

Parameters:

v

discrete shape parameter

$v > 0$

Domain:

$0 \leq x \leq +\infty$

continuous

Density and Cumulative Functions:

$$f(x) = \frac{1}{2^{v/2} \Gamma(v/2)} e^{-x/2} x^{(v/2)-1}$$

$$F(x) = \frac{\Gamma_{x/2}(v/2)}{\Gamma(v/2)}$$

where Γ is the *Gamma Function*, and Γ_x is the *Incomplete Gamma Function*.

Mean:

v

Variance:

$2v$

Skewness:

$$\sqrt{\frac{8}{v}}$$

Kurtosis:

$$3 + \frac{12}{v}$$

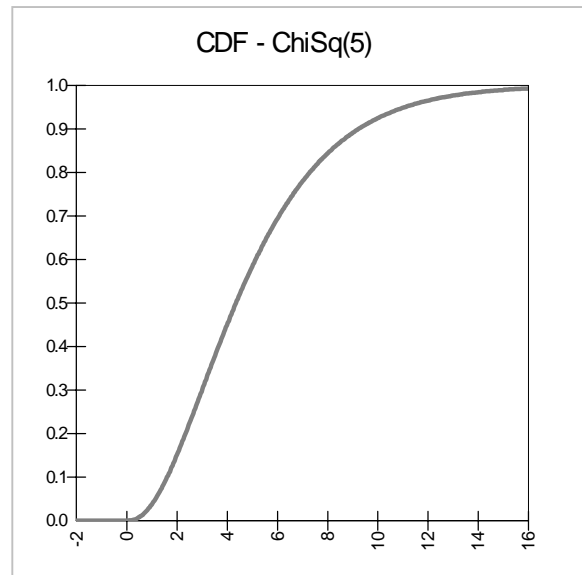
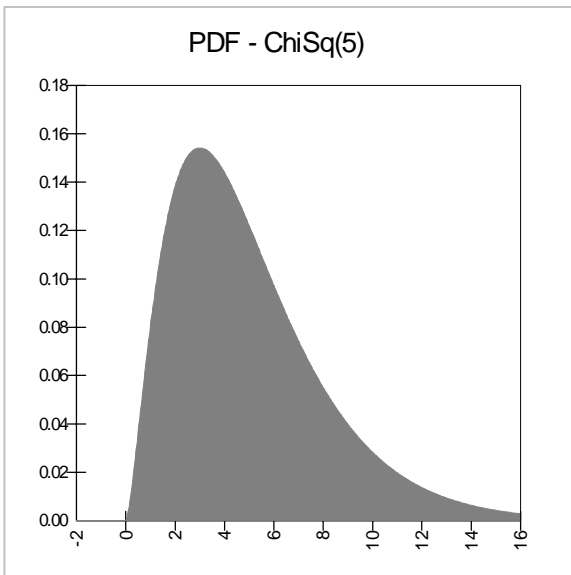
Mode:

$$v-2$$

$$\text{if } v \geq 2$$

$$0$$

$$\text{if } v = 1$$



Erlang

RISKErlang(m, β)

Parameters:

m	integral shape parameter	$m > 0$
β	continuous scale parameter	$\beta > 0$

Domain:

$0 \leq x < +\infty$	continuous
----------------------	------------

Density and Cumulative Functions:

$$f(x) = \frac{1}{\beta (m-1)!} \left(\frac{x}{\beta}\right)^{m-1} e^{-x/\beta}$$

$$F(x) = \frac{\Gamma_{x/\beta}(m)}{\Gamma(m)} = 1 - e^{-x/\beta} \sum_{i=0}^{m-1} \frac{(x/\beta)^i}{i!}$$

where Γ is the *Gamma Function* and Γ_x is the *Incomplete Gamma Function*.

Mean:

$$m\beta$$

Variance:

$$m\beta^2$$

Skewness:

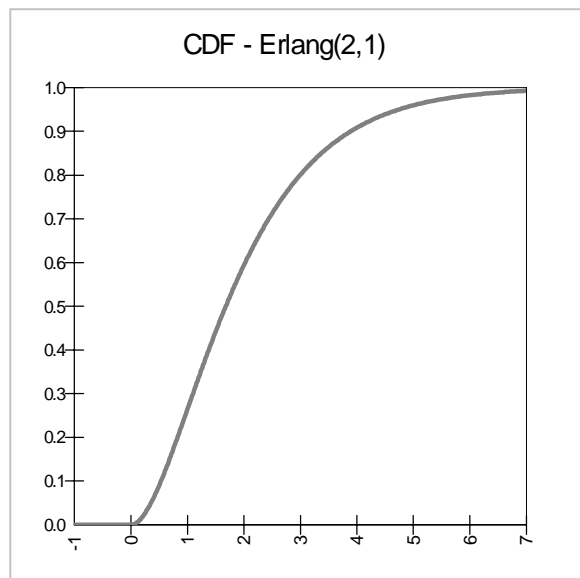
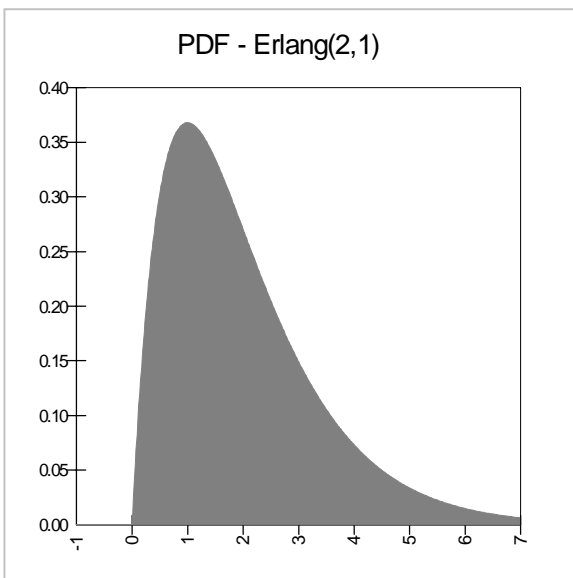
$$\frac{2}{\sqrt{m}}$$

Kurtosis:

$$3 + \frac{6}{m}$$

Mode:

$$\beta(m-1)$$



Exponential

RISKExpon(β)

Parameters:

β

continuous scale parameter

$\beta > 0$

Domain:

$0 \leq x < +\infty$

continuous

Density and Cumulative Functions:

$$f(x) = \frac{e^{-x/\beta}}{\beta}$$

$$F(x) = 1 - e^{-x/\beta}$$

Mean:

β

Variance:

β^2

Skewness:

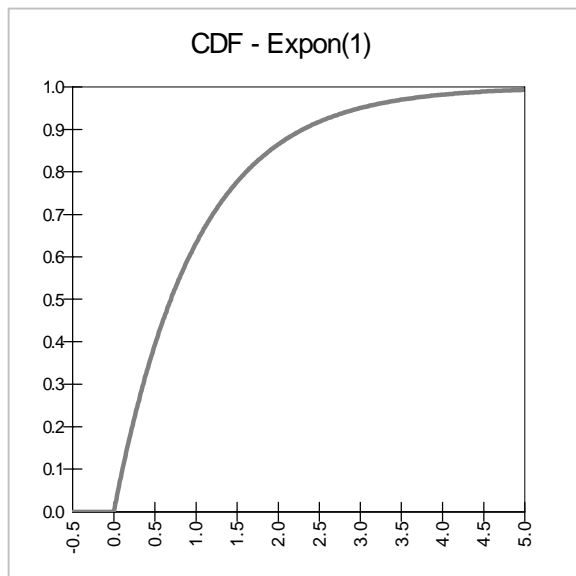
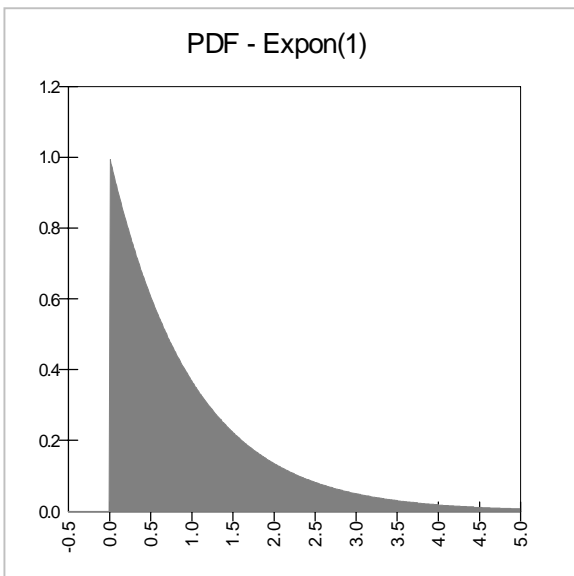
2

Kurtosis:

9

Mode:

0



Extreme Value

RISKExtValue(a, b)

Parameters:

a continuous location parameter

b continuous scale parameter $b > 0$

Domain:

$$-\infty \leq x \leq +\infty$$

continuous

Density and Cumulative Functions:

$$f(x) = \frac{1}{b} \left(\frac{1}{e^{z+\exp(-z)}} \right)$$

$$F(x) = \frac{1}{e^{\exp(-z)}}$$

where $z \equiv \frac{(x-a)}{b}$

Mean:

$$a - b\Gamma'(1) \approx a + .577b$$

where $\Gamma'(x)$ is the derivative of the *Gamma Function*.

Variance:

$$\frac{\pi^2 b^2}{6}$$

Skewness:

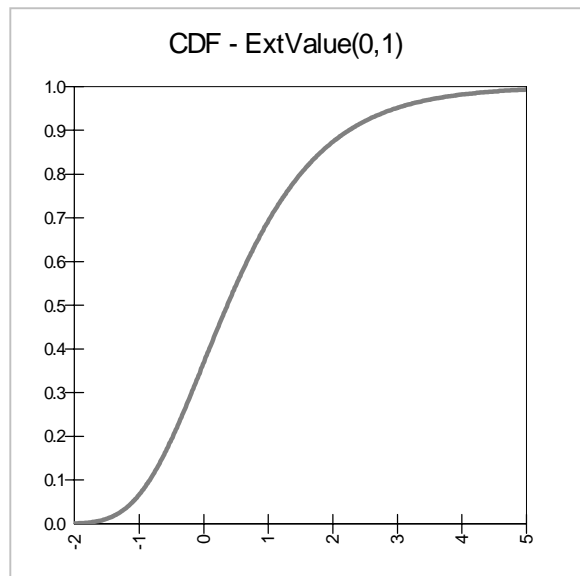
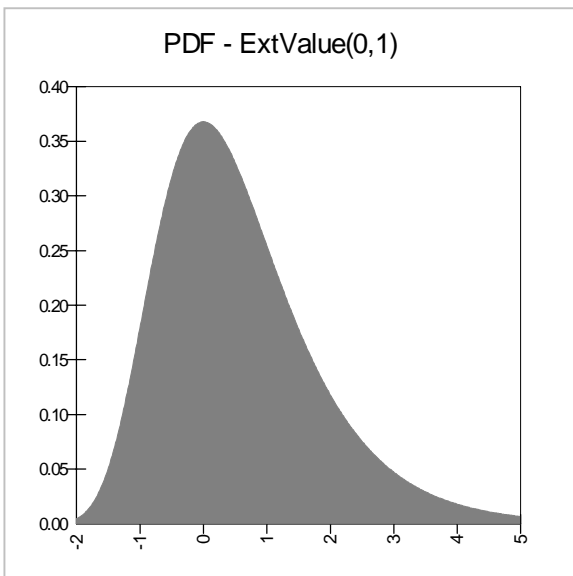
1.139547

Kurtosis:

5.4

Mode:

a



Gamma

*RISK*Gamma(α, β)

Parameters:

α	continuous shape parameter	$\alpha > 0$
β	continuous scale parameter	$\beta > 0$

Domain:

$0 < x < +\infty$	continuous
-------------------	------------

Density and Cumulative Functions:

$$f(x) = \frac{1}{\beta\Gamma(\alpha)} \left(\frac{x}{\beta}\right)^{\alpha-1} e^{-x/\beta}$$

$$F(x) = \frac{\Gamma_{x/\beta}(\alpha)}{\Gamma(\alpha)}$$

where Γ is the *Gamma Function* and Γ_x is the *Incomplete Gamma Function*.

Mean:

$$\beta\alpha$$

Variance:

$$\beta^2\alpha$$

Skewness:

$$\frac{2}{\sqrt{\alpha}}$$

Kurtosis:

$$3 + \frac{6}{\alpha}$$

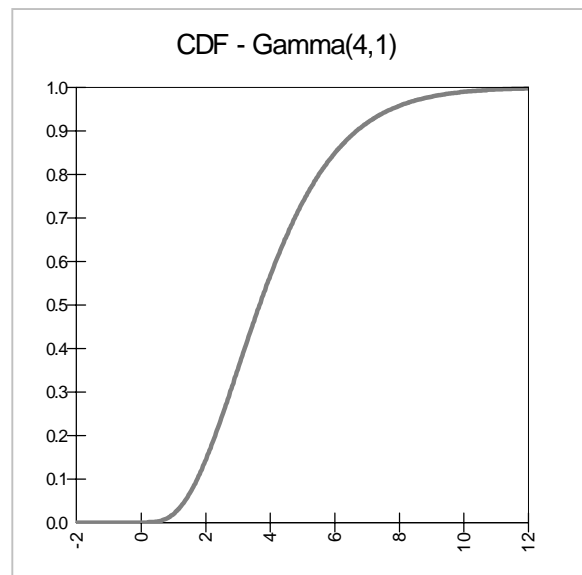
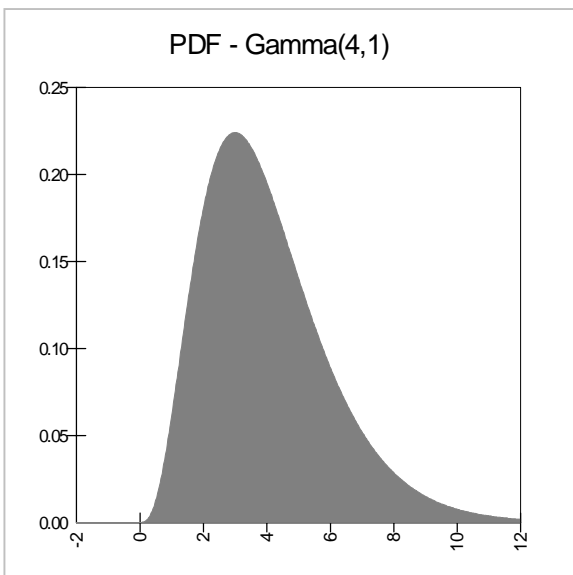
Mode:

$$\beta(\alpha - 1)$$

if $\alpha \geq 1$

Not Defined

if $\alpha < 1$



Logistic

*RISK*Logistic(α, β)

Parameters:

α continuous location parameter

β continuous scale parameter $\beta > 0$

Domain:

$-\infty \leq x \leq +\infty$

continuous

Density and Cumulative Functions:

$$f(x) = \frac{\operatorname{sech}^2\left(\frac{1}{2}\left(\frac{x - \alpha}{\beta}\right)\right)}{4\beta}$$

$$F(x) = \frac{1 + \tanh\left(\frac{1}{2}\left(\frac{x - \alpha}{\beta}\right)\right)}{2}$$

where “tanh” is the *Hyperbolic Tangent Function*.

Mean:

α

Variance:

$$\frac{\pi^2\beta^2}{3}$$

Skewness:

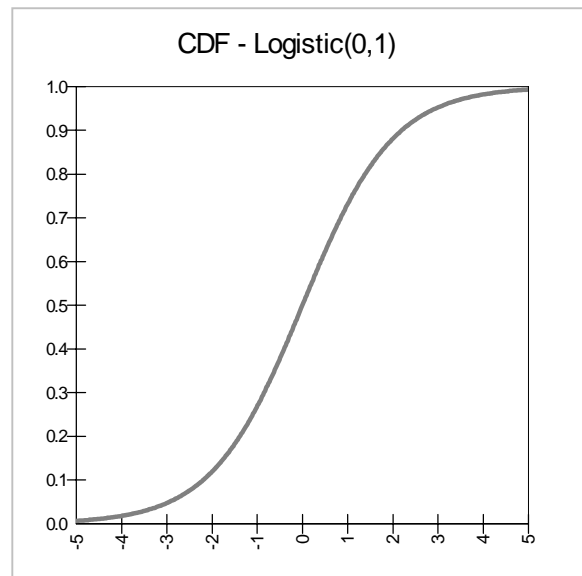
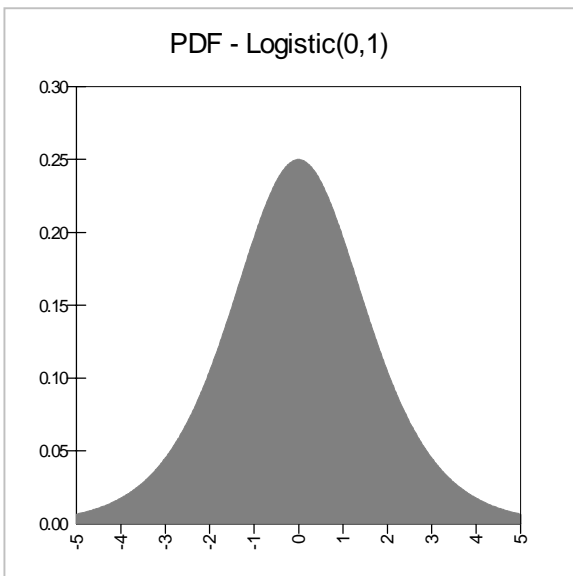
0

Kurtosis:

4.2

Mode:

α



Log-Logistic

RISKLogLogistic(γ, β, α)

Parameters:

γ	continuous location parameter	
β	continuous scale parameter	$\beta > 0$
α	continuous shape parameter	$\alpha > 0$

Definitions:

$$\theta \equiv \frac{\pi}{\alpha}$$

Domain:

$\gamma \leq x \leq +\infty$	continuous
------------------------------	------------

Density and Cumulative Functions:

$$f(x) = \frac{\alpha t^{\alpha-1}}{\beta(1+t^\alpha)^2}$$

$$F(x) = \frac{1}{1+\left(\frac{1}{t}\right)^\alpha}$$

with $t \equiv \frac{x-\gamma}{\beta}$

Mean:

$\beta\theta \csc(\theta) + \gamma$	for $\alpha > 1$
-------------------------------------	------------------

Variance:

$$\beta^2 \theta \left[2 \csc(2\theta) - \theta \csc^2(\theta) \right] \quad \text{for } \alpha > 2$$

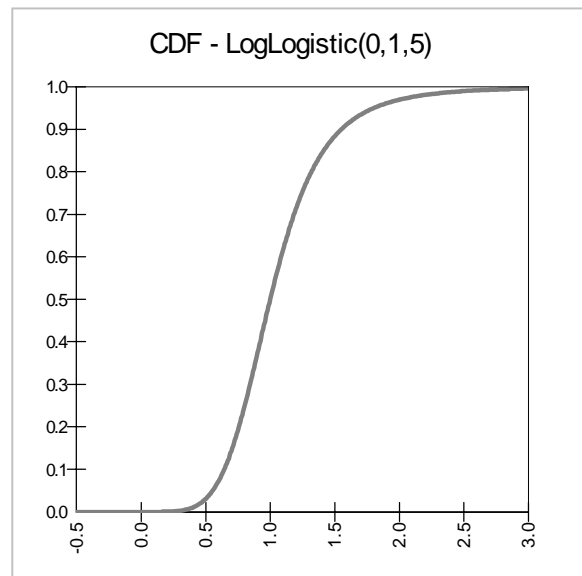
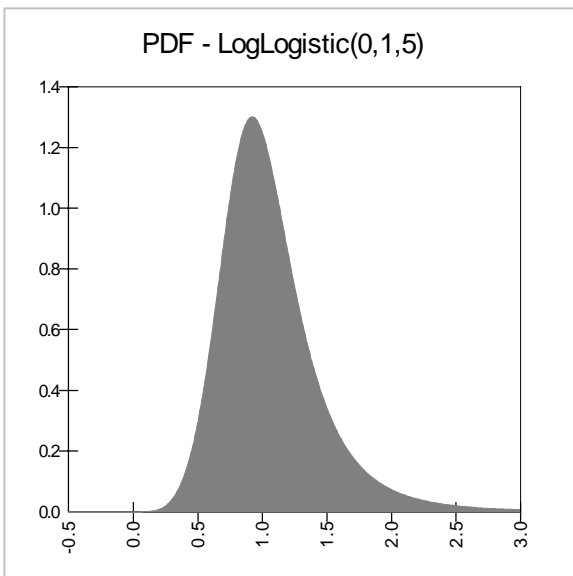
Skewness:

$$\frac{3 \csc(3\theta) - 6\theta \csc(2\theta) \csc(\theta) + 2\theta^2 \csc^3(\theta)}{\sqrt{\theta} \left[2 \csc(2\theta) - \theta \csc^2(\theta) \right]^{3/2}} \quad \text{for } \alpha > 3$$

Mode:

$$\gamma + \beta \left[\frac{\alpha - 1}{\alpha + 1} \right]^{1/\alpha} \quad \text{for } \alpha > 1$$

$$0 \quad \text{for } \alpha \leq 1$$



Lognormal (Format 1)

RISKLognorm(μ, σ)

Parameters:

μ	continuous parameter	$\mu > 0$
σ	continuous parameter	$\sigma > 0$

Domain:

$0 \leq x \leq +\infty$	continuous
-------------------------	------------

Density and Cumulative Functions:

$$f(x) = \frac{1}{x\sqrt{2\pi\sigma'}} e^{-\frac{1}{2}\left[\frac{\ln x - \mu'}{\sigma'}\right]^2}$$

$$F(x) = \Phi\left(\frac{\ln x - \mu'}{\sigma'}\right)$$

$$\text{with } \mu' \equiv \ln\left[\frac{\mu^2}{\sqrt{\sigma^2 + \mu^2}}\right] \quad \text{and} \quad \sigma' \equiv \frac{1}{2} \ln\left[1 + \left(\frac{\sigma}{\mu}\right)^2\right]$$

where Φ is the *Error Function*.

Mean:

$$\mu$$

Variance:

$$\sigma^2$$

Skewness:

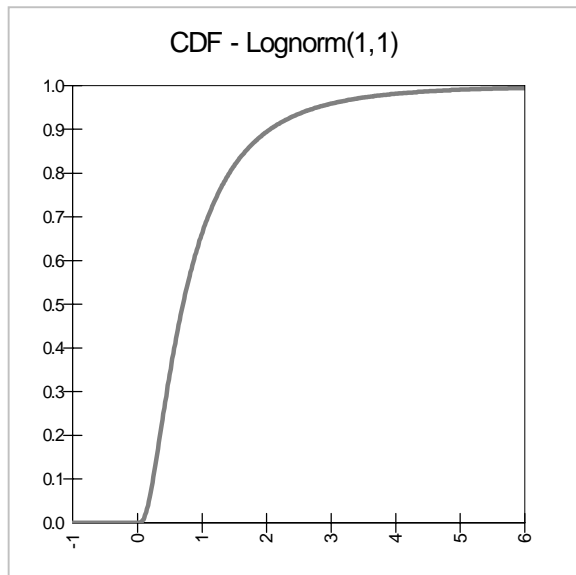
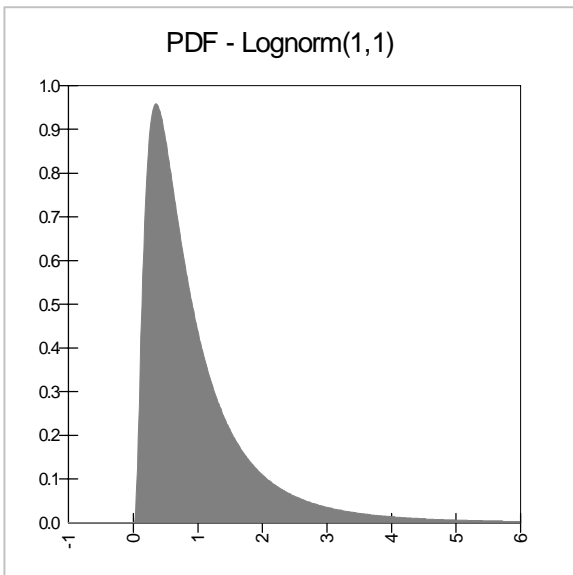
$$\left(\frac{\sigma}{\mu}\right)^3 + 3\left(\frac{\sigma}{\mu}\right)$$

Kurtosis:

$$\omega^4 + 2\omega^3 + 3\omega^2 - 3 \quad \text{with } \omega \equiv 1 + \left(\frac{\sigma}{\mu}\right)$$

Mode:

$$\frac{\mu^4}{(\sigma^2 + \mu^2)^{3/2}}$$



Lognormal (Format 2)

RISKLognorm2(μ, σ)

Parameters:

μ	continuous parameter	
σ	continuous parameter	$\sigma > 0$

Domain:

$0 \leq x \leq +\infty$	continuous
-------------------------	------------

Density and Cumulative Functions:

$$f(x) = \frac{1}{x\sqrt{2\pi\sigma}} e^{-\frac{1}{2}\left[\frac{\ln x - \mu}{\sigma}\right]^2}$$

$$F(x) = \Phi\left(\frac{\ln x - \mu}{\sigma}\right)$$

where Φ is the *Error Function*.

Mean:

$$e^{\mu + \frac{\sigma^2}{2}}$$

Variance:

$e^{2\mu}\omega(\omega-1)$	with $\omega \equiv e^{\sigma^2}$
----------------------------	-----------------------------------

Skewness:

$$(\omega + 2)\sqrt{\omega - 1}$$

with $\omega \equiv e^{\sigma^2}$

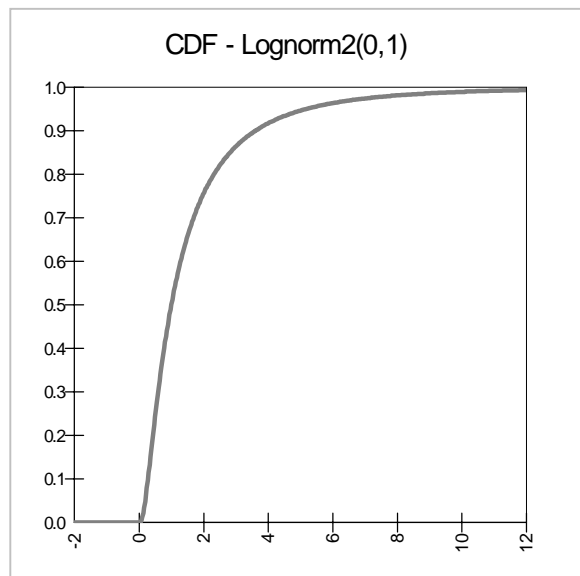
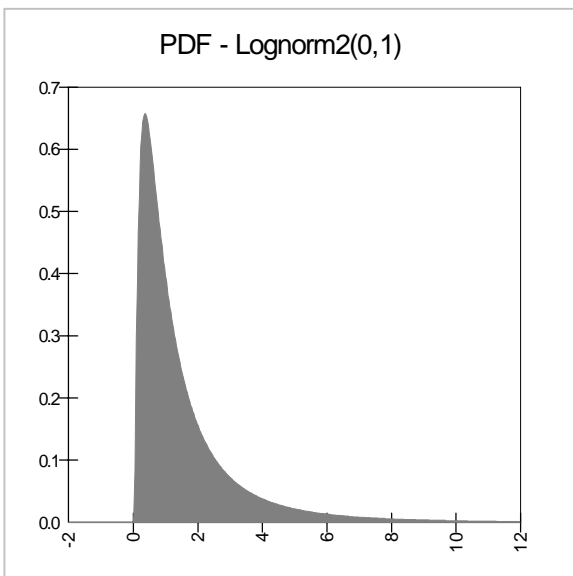
Kurtosis:

$$\omega^4 + 2\omega^3 + 3\omega^2 - 3$$

with $\omega \equiv e^{\sigma^2}$

Mode:

$$e^{\mu - \sigma^2}$$



Normal

*RISK*Normal(μ, σ)

Parameters:

μ continuous location parameter

σ continuous scale parameter $\sigma > 0$

Domain:

$$-\infty \leq x \leq +\infty$$

continuous

Density and Cumulative Functions:

$$f(x) = \frac{1}{\sqrt{2\pi}\sigma} e^{-\frac{1}{2}\left(\frac{x-\mu}{\sigma}\right)^2}$$

$$F(x) = \Phi\left(\frac{x-\mu}{\sigma}\right)$$

where Φ is the *Error Function*.

Mean:

μ

Variance:

σ^2

Skewness:

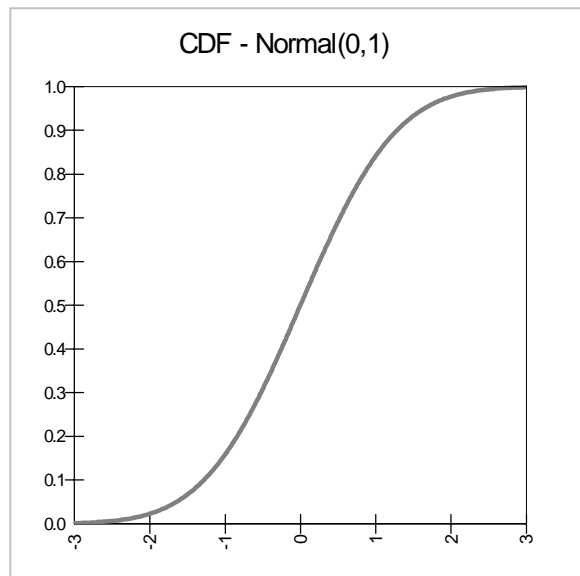
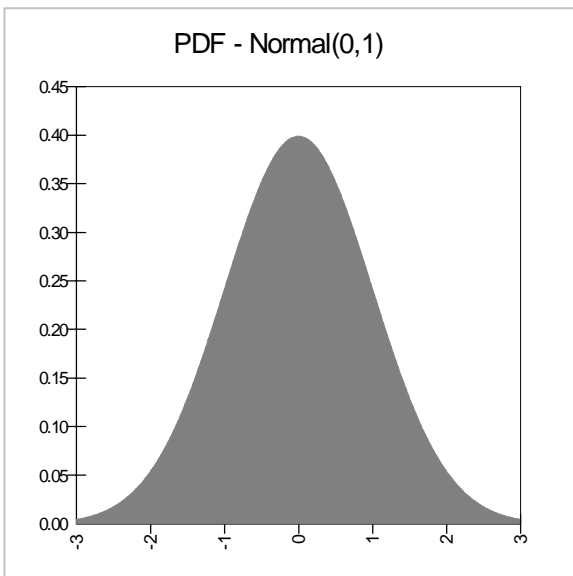
0

Kurtosis:

3

Mode:

μ



Pareto (First Kind)

Pareto(θ, a)

Parameters:

θ	continuous shape parameter	$\theta > 0$
a	continuous scale parameter	$a > 0$

Domain:

$a \leq x \leq +\infty$	continuous
-------------------------	------------

Density and Cumulative Functions:

$$f(x) = \frac{\theta a^\theta}{x^{\theta+1}}$$

$$F(x) = 1 - \left(\frac{a}{x}\right)^\theta$$

Mean:

$$\frac{a\theta}{\theta - 1} \quad \text{for } \theta > 1$$

Variance:

$$\frac{\theta a^2}{(\theta - 1)^2(\theta - 2)} \quad \text{for } \theta > 2$$

Skewness:

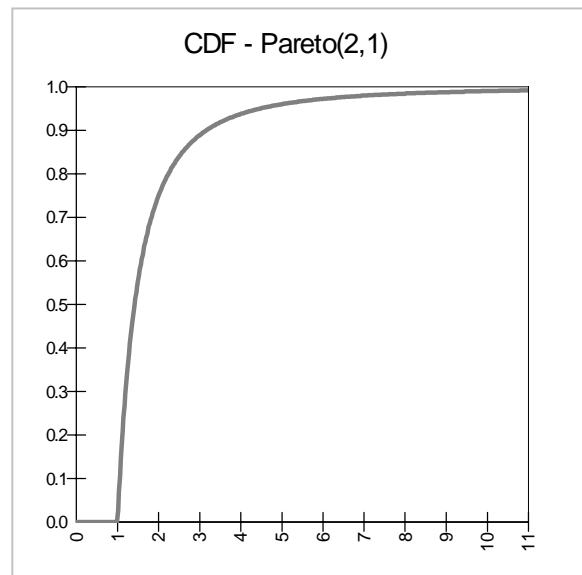
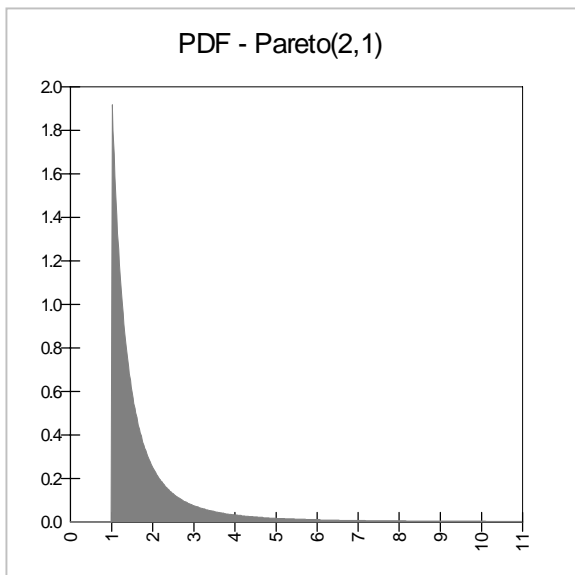
$$2 \frac{\theta+1}{\theta-3} \sqrt{\frac{\theta-2}{\theta}} \quad \text{for } \theta > 3$$

Kurtosis:

$$\frac{3(\theta-2)(3\theta^2 + \theta + 2)}{\theta(\theta-3)(\theta-4)} \quad \text{for } \theta > 4$$

Mode:

a



Pearson Type V

*RISK*Pearson5(α, β)

Parameters:

α	continuous shape parameter	$\alpha > 0$
β	continous scale parameter	$\beta > 0$

Domain:

$0 \leq x < +\infty$	continuous
----------------------	------------

Density and Cumulative Functions:

$$f(x) = \frac{1}{\beta\Gamma(\alpha)} \cdot \frac{e^{-\beta/x}}{(x/\beta)^{\alpha+1}}$$

F(x) Has No Closed Form

Mean:

$\frac{\beta}{\alpha - 1}$	for $\alpha > 1$
----------------------------	------------------

Variance:

$\frac{\beta^2}{(\alpha - 1)^2(\alpha - 2)}$	for $\alpha > 2$
--	------------------

Skewness:

$$\frac{4\sqrt{\alpha - 2}}{\alpha - 3}$$

for $\alpha > 3$

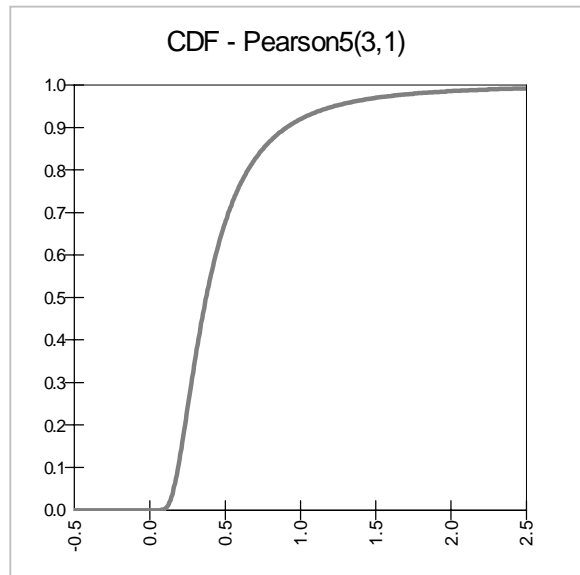
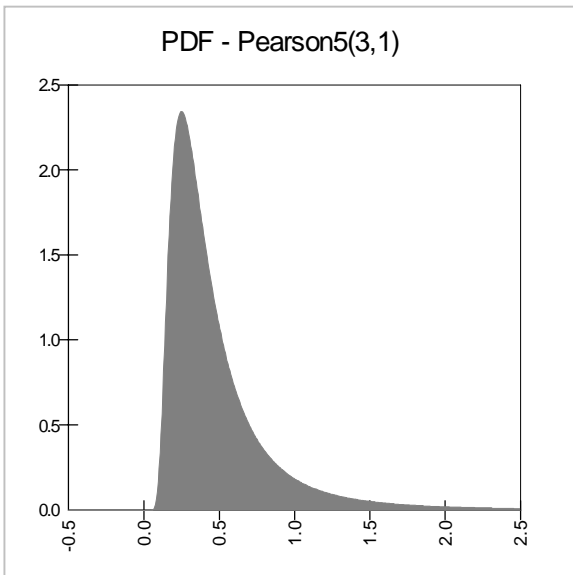
Kurtosis:

$$\frac{3(\alpha + 5)(\alpha - 2)}{(\alpha - 3)(\alpha - 4)}$$

for $\alpha > 4$

Mode:

$$\frac{\beta}{\alpha + 1}$$



Skewness:

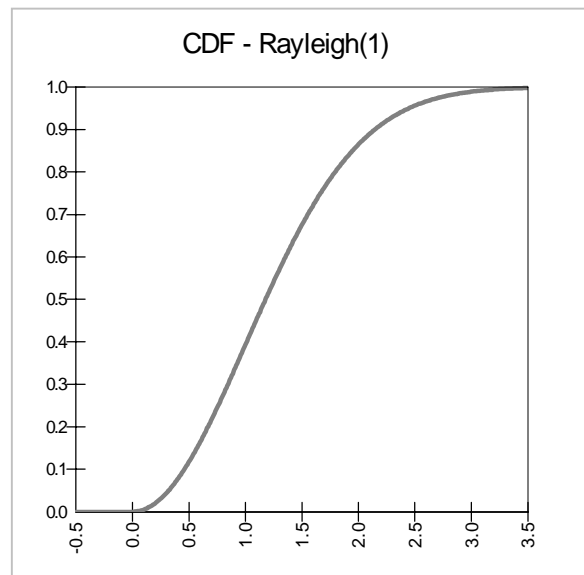
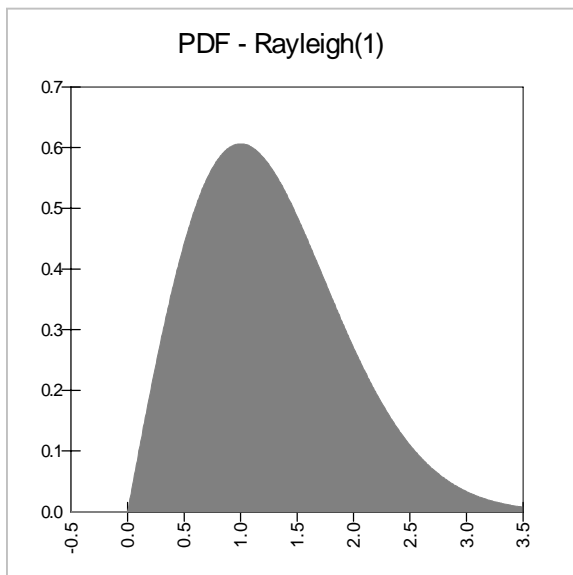
$$\frac{2(\pi - 3)\sqrt{\pi}}{(4 - \pi)^{3/2}} \approx 0.6311$$

Kurtosis:

$$\frac{32 - 3\pi^2}{(4 - \pi)^2} \approx 3.2451$$

Mode:

b



Triangular

RISKTriang(min, m.likely, max)

Parameters:

min	continuous boundary parameter	$\min < \max$
m.likely	continuous mode parameter	$\min \leq m.likely \leq \max$
max	continuous boundary parameter	

Domain:

$\min \leq x \leq \max$	continuous
-------------------------	------------

Density and Cumulative Functions:

$$f(x) = \frac{2(x - \min)}{(m.likely - \min)(\max - \min)} \quad \min \leq x \leq m.likely$$

$$f(x) = \frac{2(\max - x)}{(\max - m.likely)(\max - \min)} \quad m.likely \leq x \leq \max$$

$$F(x) = \frac{(x - \min)^2}{(m.likely - \min)(\max - \min)} \quad \min \leq x \leq m.likely$$

$$F(x) = 1 - \frac{(\max - x)^2}{(\max - m.likely)(\max - \min)} \quad m.likely \leq x \leq \max$$

Mean:

$$\frac{\min + m.likely + \max}{3}$$

Variance:

$$\frac{\max^2 + \text{m.likely}^2 + \min^2 - (\max)(\text{m.likely}) - (\text{m.likely})(\min) - (\max)(\min)}{18}$$

Skewness:

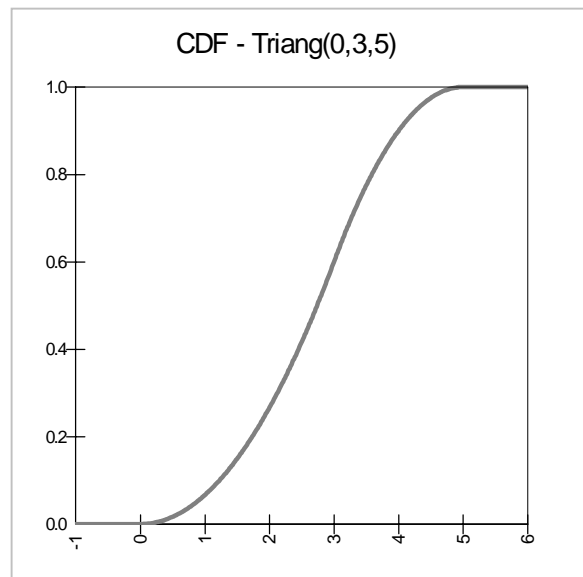
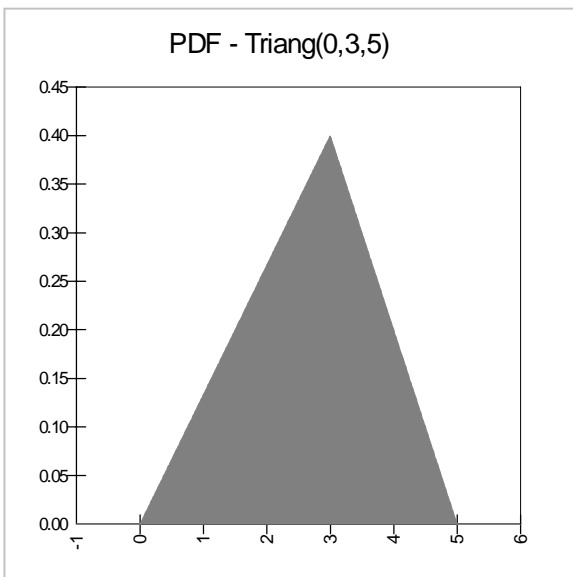
$$\frac{2\sqrt{2}}{5} \frac{f(f^2 - 9)}{(f^2 + 3)^{3/2}} \quad \text{where } f \equiv \frac{2(\text{m.likely} - \min)}{\max - \min} - 1$$

Kurtosis:

2.4

Mode:

m.likely



Uniform

RISKUniform(min, max)

Parameters:

min continuous boundary parameter min < max

max continuous boundary parameter

Domain:

$\min \leq x \leq \max$

continuous

Density and Cumulative Functions:

$$f(x) = \frac{1}{\max - \min}$$

$$F(x) = \frac{x - \min}{\max - \min}$$

Mean:

$$\frac{\max - \min}{2}$$

Variance:

$$\frac{(\max - \min)^2}{12}$$

Skewness:

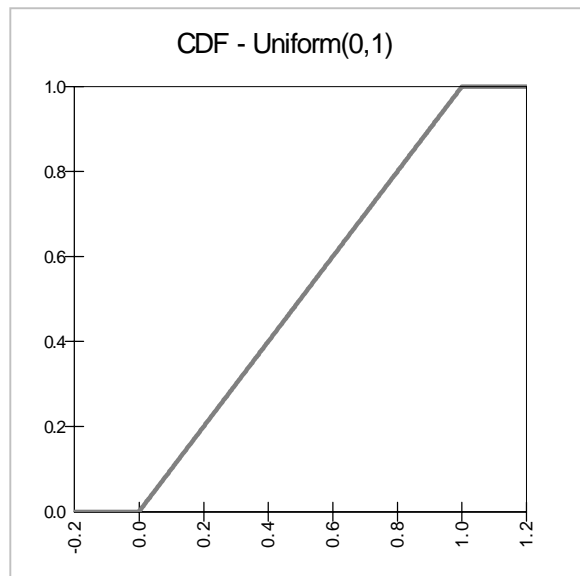
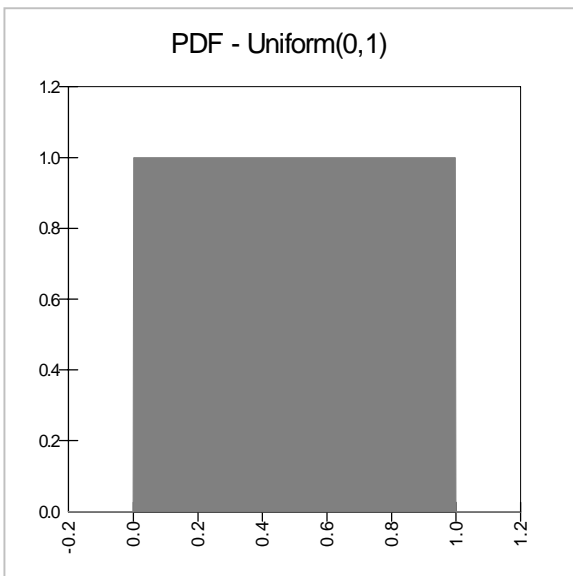
0

Kurtosis:

1.8

Mode:

Not uniquely defined



Weibull

RISKWeibull(α, β)

Parameters:

α	continuous shape parameter	$\alpha > 0$
β	continuous scale parameter	$\beta > 0$

Domain:

$0 \leq x < +\infty$	continuous
----------------------	------------

Density and Cumulative Functions:

$$f(x) = \frac{\alpha x^{\alpha-1}}{\beta^\alpha} e^{-(x/\beta)^\alpha}$$

$$F(x) = 1 - e^{-(x/\beta)^\alpha}$$

Mean:

$$b\Gamma\left(1 + \frac{1}{\alpha}\right)$$

where Γ is the *Gamma Function*.

Variance:

$$\beta^2 \left[\Gamma\left(1 + \frac{2}{\alpha}\right) - \Gamma^2\left(1 + \frac{1}{\alpha}\right) \right]$$

where Γ is the *Gamma Function*.

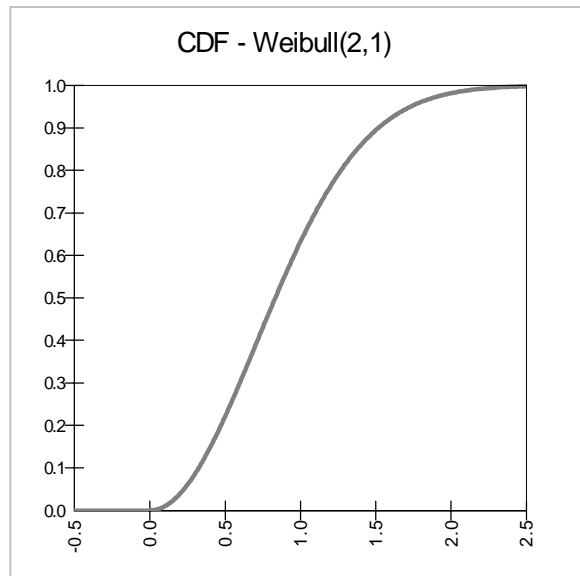
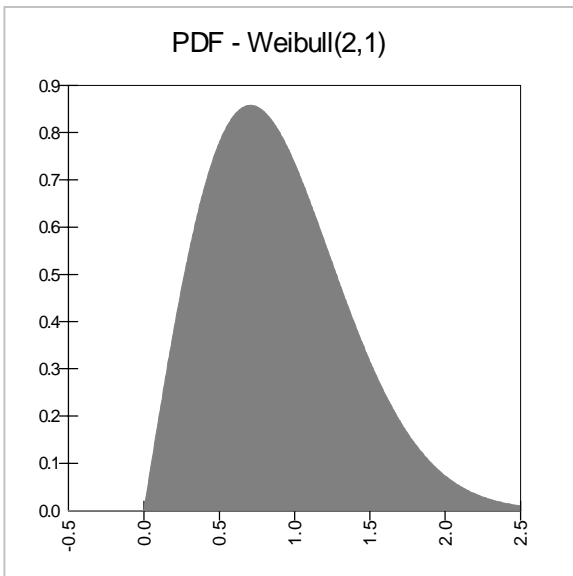
Skewness:

$$\frac{\Gamma\left(1+\frac{3}{\alpha}\right)+3\Gamma\left(1+\frac{2}{\alpha}\right)\Gamma\left(1+\frac{1}{\alpha}\right)+2\Gamma^3\left(1+\frac{1}{\alpha}\right)}{\left[\Gamma\left(1+\frac{2}{\alpha}\right)-\Gamma^2\left(1+\frac{1}{\alpha}\right)\right]^{3/2}}$$

where Γ is the *Gamma Function*.

Mode:

$$\beta\left(1-\frac{1}{\alpha}\right)^{1/\alpha} \quad \text{for } \alpha > 1$$
$$0 \quad \text{for } \alpha \leq 1$$





Appendix D

Description of Matrix Porosity Dataset

D.1.0 Introduction

Data relating to matrix porosity include measured matrix porosity values that were obtained from laboratory measurements of cores and matrix porosity values that were obtained from interpretations of geophysical logs.

This description of the matrix porosity dataset includes the following items:

- A summary of the contents of the dataset
- The structure of the table containing the dataset
- Directions on how to access the full dataset

D.2.0 Dataset Summary

Each record of the matrix porosity dataset contains information about a porosity measurement or an average porosity value for a specific interval in a well. The matrix porosity dataset contains approximately 1,856 records for roughly 71 different locations on or near the NTS. The dataset contains information about the well, the depth of samples, the method of analysis, and whether the porosity represents matrix or bulk porosity.

D.3.0 Table Structure

The matrix porosity table contains the following fields:

- Well Name - Name of the well if available
- Borehole Index identification number - The borehole index contains information about hole location, depth, and date
- Top depth for that sample - Top of the sample interval - only this value is recorded if the sample size is small
- Bottom depth for the sample - Bottom of the sample interval - blank if the sample size is small
- n(C,D) - Porosity derived from core and density logs - the core in this case generally refers to sidewall core from which particle density is

determined; the density log, combined with epithermal neutron logging produces an estimate for the dry bulk density

- n(C) - Porosity derived from core - usually the core is oven dried to determine dry bulk density, and particle density is determined from subsamples of the core; in a few rare instances, injection of other fluids into the core is used to determine porosity
- n(D) - Porosity derived from density logs - a relationship is developed that produces porosity from the log density when a particle density is assumed or measured
- n(V) - Porosity derived from velocity logs - uses a form of Wyllie's equation to calculate porosity from the sonic transit time, given per meter; in this manner, the transit time is the inverse of the sonic velocity
- n(N) - Porosity derived from neutron logs - relationship yields the porosity based on the neutron log values
- n(R) - Porosity derived from resistivity logs - based on Archie's equation, a relationship is developed that yields porosity from the formation resistivity
- average porosity - Arithmetic average of the available values
- porosity type - Matrix, bulk, or fracture - usually the core data is matrix porosity because fractured core is excluded; geophysical logs measure the entire formation and typically yields bulk porosity
- PM_DA_HSU - The hydrostratigraphic unit assigned to the interval based on the distribution of HSUs in each borehole as provided by the Bechtel Nevada geologists (Bechtel Nevada, 2002); in cases where the sample interval includes more than one HSU, multiple HSUs are recorded
- PM_DA_LAYER - Geologic model layer number for the HSU - layer numbers correspond to the layers in the Pahute Mesa-Oasis Valley hydrostratigraphic unit model (Bechtel Nevada, 2002)
- SWNVF_Strat - Stratigraphy or lithology from the Southwestern Nevada Volcanic Field Database - name of the stratigraphic unit as provided by the Bechtel Nevada geologists
- ref_Stratigraphic unit - Stratigraphy or lithology assigned by the original reference - for reference, the original designation is provided
- DDE-F - Data documentation qualifier
- Data source - Name of the entity that collected the data
- ref-id - Reference for the record

- lithology - Lithology of the rock sample or log depth - interpreted from the identification of lithology of intervals in each borehole as provided by the Bechtel Nevada geologists (Bechtel Nevada, 2002); in cases where the sample interval includes multiple lithologies, each lithology is listed
- alteration - Alteration of the rock sample or log depth - alteration such as zeolitization or argillization can change the porosity; the alteration for each borehole interval as provided by the Bechtel Nevada geologists is used as the basis for assignment of alteration (Bechtel Nevada, 2002)
- HGU - Hydrogeologic unit - the hydrogeologic unit interpreted from the hydrogeologic information provide for each borehole by the Bechtel Nevada geologists (Bechtel Nevada, 2002)

D.4.0 Access to Dataset

The full matrix porosity dataset is combined with the porosity of the alluvial and bedded volcanic units. The dataset is provided in both EXCEL and ASCII formats in the following files:

EXCEL:

- matrix_porosity.xls

ASCII:

- matrix_porosity.txt

To access the data from the paper copy of the document, use the CD provided at the end of the document and open the desired file. To access the dataset from the electronic version of the document, click on the desired file.

D.5.0 References

Bechtel Nevada. 2002. *Hydrostratigraphic Model of the Pahute Mesa - Oasis Valley Area, Nye County, Nevada*, Report DOE/NV/11718--646. Las Vegas, NV.



Appendix E

Description of Effective Porosity Dataset

E.1.0 Introduction

Data relating to effective porosity include calculated effective porosity values and fracture frequency data for fractured materials that can be used to determine effective porosity.

This description of the effective porosity and fracture frequency datasets includes the following items:

- A summary of the contents of each dataset
- The structure of the tables containing the datasets
- Directions on how to access the datasets

E.2.0 Dataset Summary

Each record of the effective porosity dataset contains information about a single measurement of effective porosity for a given borehole. The dataset is therefore, organized primarily by borehole name. The dataset contains 1,361 individual records for approximately 141 unique locations. Each record contains information about the specific interval tested, the measured porosity value, the method of measurement, and an indication of data quality.

Each record of the fracture frequency dataset contains information about a given measurement of fracture frequency for a given borehole. As a result, the fracture frequency dataset is organized primarily by borehole name. The fracture frequency dataset contains 89 records of fracture frequency for approximately 16 unique locations. Each record contains information about the interval tested, the total fracture frequency, the hydrogeologic unit, and the hydrostratigraphic unit of the interval being tested.

E.3.0 Table Structure

The effective porosity table contains the following fields:

- well_name - Borehole name
- Borehole_Index_ID - Borehole ID from the Borehole Index

- top_depth (mbgs) - Top depth in meters below ground surface of the sample. Also used when only one depth given
- bottom_depth (mbgs) - Bottom depth in meters below ground surface of the sample
- n(E,D) (%) - Porosity from electric and density logs
- n(C,D) (%) - Porosity from core and density logs
- n(N,D) (%) - Porosity from neutron and density logs
- n(C) (%) - Porosity from core
- n(D) (%) - Porosity from density logs
- n(V) (%) - Porosity from velocity logs
- n(N) (%) - Porosity from neutron logs
- n(R) (%) - Porosity from resistivity logs
- aver_poro (%) - Average of all the values reported for a given record
- porosity_type - bulk, matrix, fracture
- lithology - Lithology of the sampled rock (Bechtel Nevada, 2002)
- Alteration - Alteration of the sampled rock (Bechtel Nevada, 2002)
- HGU - Hydrogeologic Unit (Bechtel Nevada, 2002)
- PM_DA_hsu - Hydrostratigraphic Unit (Bechtel Nevada, 2002)
- PM_DA_layer - Geologic model layer number for the HSU (Bechtel Nevada, 2002)
- SWNVF_Strat - Stratigraphy or lithology from the Southwestern Nevada Volcanic Field Database
- ref_stratigraphic_unit - Stratigraphy or lithology from the reference the value came from
- DDE-F - Data Documentation Evaluation-Flag
- Remarks - Remarks for a given record
- data_source - Name of the entity which collected the data
- ref_id - Reference for the record

The fracture frequency summary table contains the following fields:

- Well - Well or location name
- Interval Top (m) - The top depth of the interval tested
- Interval Bottom (m) - The bottom depth of the interval tested
- Total Freq (m⁻¹) - The total frequency of fractures for the given interval
- HGU - The hydrogeologic unit for the interval tested
- HSU - The hydrostratigraphic unit of the interval tested
- Source - Source of the data
- ref_id - Reference for the record

E.4.0 Access to Dataset

The entire alluvial effective porosity and fracture frequency datasets are provided in both EXCEL and ASCII formats in the following files:

EXCEL:

- effective_porosity.xls
- fracture_frequency_summary.xls
- ASCII Format:
- effective_porosity.txt
- fracture_frequency_summary.txt

To access the datasets from the paper copy of this document, use the CD provided at the end of the document and open the desired file. To access the dataset from the electronic version of this document, click on the desired filename listed above.

E.5.0 References

Bechtel Nevada. 2002. *Hydrostratigraphic Model of the Pahute Mesa - Oasis Valley Area, Nye County, Nevada*, Report DOE/NV/11718--646. Las Vegas, NV.



Appendix F

Description of Dispersivity Dataset

F.1.0 Introduction

Data relating to dispersivity include measurements obtained from four transport experiments that have been performed at or near the NTS plus additional dispersivity data compiled from various literature sources.

This description of the dispersivity dataset includes the following items:

- A summary of the contents of the dataset
- The structure of the table containing the dataset
- Directions on how to access the dataset

F.2.0 Dataset Summary

Each record of the dispersivity dataset contains information about a given tracer test and the results of the data analysis following a specific method of analysis. The dataset is, therefore, organized primarily by the tracer test location and secondarily by the data analysis method. The dispersivity dataset contains approximately 150 records encompassing 70 different sites throughout the world. The dataset contains information about the specific tracer test, the method of analysis, the various dispersivity types, and an indication of the quality of the data.

F.3.0 Table Structure

The dispersivity dataset contains the following fields:

- `site_name` - Name of test, if any, and generalized location of the test
- `aquifer_material` - Geologic material the test was conducted in
- `min_avg_aquifer_thickness (m)` - The minimum average aquifer thickness in meters; if only one thickness is given, it is placed in this field
- `max_avg_aquifer_thickness (m)` - The maximum average aquifer thickness in meters

- `min_hydraulic_conductivity` (m/s) - The minimum hydraulic conductivity in meters per second for the given test material; if only one conductivity is given, it is placed in this field
- `max_hydraulic_conductivity` (m/s) - The maximum hydraulic conductivity in meters per second for the given test material
- `min_transmissivity` (m²/s) - The minimum transmissivity in square meters per second for the given test material; if only one transmissivity is given, it is placed in this field
- `max_transmissivity` (m²/s) - The maximum transmissivity in square meters per second for the given test material
- `min_eff_porosity` (%) - The minimum effective porosity in percent for the given test material; if only one porosity is given, it is placed in this field
- `max_eff_porosity` (%) - The maximum effective porosity in percent for the given test material
- `min_velocity` (m/d) - The minimum velocity in meters per day for the given test material; if only one velocity is given, it is placed in this field
- `max_velocity` (m/d) - The maximum velocity in meters per day for the given test material
- `flow_configuration` - The flow configuration for the test
- `monitoring` - The type of monitoring involved with the test
- `tracer_and_input` - The tracer used and input method for the test
- `method_of_data_interpretation` - The method of data interpretation used for the test
- `min_scale_of_test` (m) - The minimum distance of the test in meters; if only one distance is given, it is placed in this field
- `max_scale_of_test` (m) - The maximum distance of the test in meters
- `dispersivity_longitudinal_min` - The minimum longitudinal dispersivity in meters for the given test material; if only one value is given, it is placed in this field
- `dispersivity_longitudinal_max` - The maximum longitudinal dispersivity in meters for the given test material
- `dispersivity_transverse_min` - The minimum transverse dispersivity in meters for the given test material; if only one value is given, it is placed in this field

- dispersivity_transverse_max - The maximum transverse dispersivity in meters for the given test material
- dispersivity_vertical_min - The minimum vertical dispersivity in meters for the given test material; if only one value is given, it is placed in this field
- dispersivity_vertical_max - The maximum vertical dispersivity in meters for the given test material
- DQE_F - The reporting author's (see ref_id) reliability assessment of the data
- DDE_F - Data documentation flag
- data_source - The original source of the data
- ref_id - Reference for the record
- remarks - Contains additional information for a given record

F.4.0 Access to Dataset

The full dispersivity dataset is provided in both EXCEL and ASCII formats in the following files:

EXCEL:

- dispersivity.xls

ASCII:

- dispersivity.txt

To access the dataset from the paper copy of this document, use the CD provided at the end of the document and open the desired file. To access the dataset from the electronic version of this document, click on the desired filename listed above.



Appendix G

Description of Matrix Diffusion Dataset

G.1.0 Introduction

Data relating to matrix diffusion include diffusion values that were obtained from diffusion cell experiments and diffusion values obtained from fracture transport experiments.

This description of the matrix diffusion datasets includes the following items:

- A summary of the contents of each dataset
- The structure of the tables containing the datasets
- Directions on how to access the full datasets

G.2.0 Dataset Summary

Each record of the dataset for the diffusion cell experiments contains information about a given measurement in a well for a specific depth. Consequently, the dataset is organized by well name. The matrix diffusion dataset from the diffusion cell experiments contains 55 records for approximately 9 unique locations. The matrix diffusion dataset includes information on the interval tested for each site, the porosity in the tested interval, and the various diffusion parameter values.

Each record of the dataset for the fracture transport diffusion data contains information about a given measurement in a well for a specific depth. This dataset is also organized by well name and depth. The diffusion dataset from fracture transport experiments contains 52 values for approximately 7 unique well locations. The fracture transport diffusion dataset includes specific information on depth interval tested, the porosity in the tested interval, and the various diffusion parameter values.

G.3.0 Table Structure

The matrix diffusion table from the diffusion cell experiments contain the following fields:

- well_name_depth (ft) - The name of the well and the depth in feet
- porosity - The porosity of sample matrix

- log_perm (m²) - The log of the permeability in square meters
- Dm (cm²/s) - Diffusion coefficient in square centimeters per second
- Log_Dm (cm²/s) - Log of the diffusion coefficient in square centimeters per second
- Log (Por*D) - Log of the porosity multiplied by the diffusion coefficient
- comments - Comments on the data
- source - Source of the data
- ref_id - Reference for the record

The matrix diffusion data from the fracture transport tests contain the following fields:

- well_name_depth (ft) - The name of the well and the depth of the sample
- porosity - The porosity of sample matrix
- Dm (cm²/s) - Diffusion coefficient in square centimeters per second
- Log_Dm (cm²/s) - Log of the diffusion coefficient in square centimeters per second
- Log (Por*D) - Log of the porosity multiplied by the diffusion coefficient
- comments - Comments on the data
- source - Source of the data
- ref_id - Reference for the record

G.4.0 Access to Dataset

The full matrix diffusion datasets for both the diffusion cell experiments and the fracture transport calculations can be found in the following EXCEL and ASCII files:

EXCEL:

- Diffusion_Cells.xls
- Fracture_Transport.xls

ASCII:

- Diffusion_Cells.txt
- Fracture_Transport.txt

To access the data from the paper copy of the document, use the CD provided at the end of the document and open the desired file. To access the dataset from the electronic version of the document, click on the desired file.



Appendix H

Description of Matrix Sorption Parameter Datasets

H.1.0 Introduction

Data relating to matrix sorption parameters include calculated matrix sorption parameters from laboratory studies for seven different elements of concern. The laboratory studies were performed at a variety of experimental conditions such as varying lithologies, groundwater types, and atmospheric conditions.

This description of the matrix sorption parameter data includes the following items:

- A summary of the contents of each of the datasets
- The structure of the tables containing the datasets
- Directions on how to access the datasets

H.2.0 Dataset Summary

The matrix sorption parameter data is organized primarily by element type. As a result, there are eight individual matrix sorption parameter datasets. All of the tables contain roughly the same type of data; however, there are some differences between the various tables. For instance, some tables are further organized by the name of the well where the sample came from, while others are organized by the rock type used for the experimental work.

The barium sorption parameter dataset contains 24 records for 3 different well locations. The barium dataset is organized by well name and sample depth.

The cesium sorption parameter dataset contains 34 records for 3 different well locations. The dataset is also further organized by well name and sample depth.

The neptunium sorption parameter dataset contains 2,750 records for a variety of different rock types. As a result, this table is further organized by the type of material used during the experimental work.

The plutonium sorption parameter dataset contains 455 records for a variety of different rock types and well locations. This table is primarily organized by the rock type used during experimental work and secondarily by the well name, if available.

The selenium dataset is actually split into two different tables. One table contains 24 individual records for 2 different well locations. As a result, this table is primarily organized by well name and sample depth. The other table contains

222 records for a variety of different rocks types and well locations. This table is primarily organized by rock type name and secondarily by well name, if available.

The strontium dataset contains 34 records for three different well locations. The dataset is organized by well name and sample depth.

The uranium dataset contains 458 records for a number of different rocks types and well locations. As a result, the table is primarily organized by rock type name and secondarily by the well name, if available.

H.3.0 Table Structure

The matrix sorption parameter table for barium contains the following fields:

- ymp_id - Record number from original YMP sheets
- Ba_sorption_coef (mL/g) - Barium sorption coefficient in milliliters per gram
- stnd_dev (+/-) - Standard deviation of the barium sorption coefficient
- rock_type - Type of rock used in the experiment
- sample_description - Sample description is usually a function of the well name and depth
- temp (deg. C) - Temperature in degrees C
- initial_Ba_activity (dpm/g) - Initial activity for barium sample in disintegrations per minute per gram
- test_duration (days) - Number of days for the test
- sample_number - Sample number is a combination of the water used and borehole information
- experiment - Designator for the experiment
- pH - The final pH of the water
- Eh (mV) - The final Eh of the water
- remarks - Additional experiment information; originally titled 'reference' in original dataset
- Source - Source of the experiment
- ref_id - Reference for the record

The matrix sorption parameter table for cesium contains the following fields:

- ymp_id - Record number from original YMP sheets
- Cs_sorption_coef (mL/g) - Cesium sorption coefficient in milliliters per gram
- stnd_dev (+/-) - Standard deviation of the cesium sorption coefficient
- rock_type - Type of rock used in the experiment
- sample_description - Sample description is usually a function of well name and depth
- temp (deg. C) - Temperature in degrees C
- initial_Cs_activity (dpm/g) - Initial activity for cesium sample in disintegration per minute per gram
- test_duration (days) - Number of days for the test
- sample_number - Sample number is a combination of the water used and borehole information
- experiment - Designator for the experiment
- pH - The final pH of the water
- Eh (mV) - The final Eh of the water
- remarks - Additional experiment information; originally titled 'reference' in original dataset
- source - Source of the experiment
- ref_id - Reference for the record

The matrix sorption parameter table for neptunium contains the following fields:

- ymp_id - Record number from original YMP sheets
- Np_sorption_Coef (mL/g) - Neptunium sorption coefficient in milliliters per gram
- Stnd Dev (+/-) - Standard deviation of the neptunium sorption coefficient
- Np_sorption_COV (%) - This is the coefficient of variation for neptunium
- material_type - Type of material used in the experiment

- sample_description - Description of the sample
- water - Water used for the experiment
- Np (cpm/g) - Neptunium activity in counts per minute per gram
- Atmosphere - Atmosphere the experiment was conducted in
- test_duration (days) - Duration of the test in days
- sample_number - Sample number is a combination of the water used and borehole information
- experiment - Designator for the experiment
- particle_size - Sieved size of the particles
- preparation - Preparation method
- pH - Final pH of the water
- Eh (mV) - Final Eh of the water
- Remarks - Additional experiment information
- source - Source of the experiment
- ref_id - Reference for the record

The matrix sorption parameter table for plutonium contains the following fields:

- ymp_id - Record Number from original YMP sheets
- Pu_sorption_coef (mL/g) - Plutonium sorption coefficient in milliliters per gram
- Stnd Dev (+/-) - Standard deviation of the plutonium sorption coefficient
- COV (%) - Coefficient of variation
- rock_type - Type of rock used in the experiment
- sample_description - Sample description usually a function of well name and depth
- water_type - Type of water used for the experiment
- atmosphere - Atmosphere the experiment was conducted in
- test_duration (days) - Duration of the test in days

- Pu (cpm/g) - Plutonium activity in counts per minute per gram
- pH - Final pH of the water
- Eh (mV) - Final Eh in millivolts of the water
- remarks - Additional experiment information
- source - Source of the experiment
- ref_id - Reference for the record

The matrix sorption parameter table for the first selenium dataset contains the following fields:

- ymp_id - Record number from original YMP sheets
- Se_sorption_coefficient (mL/g) - Selenium sorption coefficient in milliliters per gram
- rock_type - Type of rock used in the experiment
- sample_description - Sample description usually a function of well name and depth
- selenium (cpm/g) - Initial activity of selenium sample in counts per minute per gram
- test_duration (days) - Number of days for the test
- sample_number - Sample number is a combination of the water used and borehole information
- pH - The final pH of the water
- Eh (mV) - The final Eh of the water in millivolts
- remarks - Additional experiment information; originally titled 'reference' in original dataset
- source - Source of the experiment
- ref_id - Reference for the record

The matrix sorption parameter table for the second selenium dataset contains the following fields:

- ymp_id - Record number from original YMP sheets

- Se_sorption_coef_(mL/g) - Selenium sorption coefficient in milliliters per gram
- rock_type - Type of rock used in the experiment
- sample_description - Sample description usually a function of well name and depth
- atmosphere - Atmosphere the experiment was conducted in
- Se (ppb) - Concentration of selenium used
- test_duration (days) - Number of days for the test
- sample_number - Sample number is a combination of the water used and borehole information
- experiment - Designator for the experiment
- particle_size - Particle sieved size used
- preparation - Preparation method
- pH - pH of the final water
- Eh (mV) - Eh in millivolts of the final water
- remarks - Additional experiment information; originally titled 'reference' in original dataset.
- source - Source of the experiment
- ref_id - Reference for the record

The matrix sorption parameter table for strontium contains the following fields:

- ymp_id - Record number from original YMP sheets
- Sr_sorption_coef_(mL/g) - Strontium sorption coefficient in milliliters per gram
- stnd_dev (+/-) - Standard deviation of the strontium sorption coefficient
- rock_type - Type of rock used in the experiment
- sample_description - Sample description usually a function of well name and depth
- temp (deg. C) - Temperature in degrees C

- initial_Sr_activity (dpm/g) - Initial activity for strontium sample in disintegration per minute per gram
- test_duration (days) - Number of days for the test
- sample_number - Sample number is a combination of the water used and borehole information
- experiment - Designator for the experiment
- pH - The final pH of the water
- Eh (mV) - The final Eh of the water
- remarks - Additional experiment information; originally titled 'reference' in original dataset.
- source - Source of the experiment
- ref_id - Reference for the record

The matrix sorption parameter table for uranium contains the following fields:

- ymp_id - Record identifier
- U_sorption_coef_(mL/g) - Uranium sorption coefficient in milliliters per gram
- stnd_dev (+/-) - Standard deviation of the uranium sorption coefficient
- rock_type - Type of rock used in the experiment
- sample_description - Sample description usually a function of well name and depth
- water_type - Water type used in the experiment
- atmosphere - Atmosphere the test was performed in
- U (ppb) - Uranium concentration in parts per billion
- test_duration (days) - Duration of the test in days
- sample_number - Sample number is a combination of the water used and borehole information
- experiment - Designator for the experiment
- particle_size - The sieved size of the particles in this experiment

- preparation - How the sample was prepared
- pH - pH of the final water
- Eh, mV - Eh in millivolts of the final water
- remarks - Remarks for the record
- source - Source of the information
- ref_id - Reference for the record

H.4.0 Access to Datasets

The full matrix porosity datasets are provided in both EXCEL and ASCII formats in the following files:

EXCEL:

- Barium_kds.xls
- Cesium_kds.xls
- Neptunium_kds.xls
- Plutonium_kds.xls
- Selenium_kds_a.xls
- Selenium_kds_b.xls
- Strontium_kds.xls
- Uranium_kds.xls

ASCII:

- Barium_kds.txt
- Cesium_kds.txt
- Neptunium_kds.txt
- Plutonium_kds.txt
- Selenium_kds_a.txt
- Selenium_kds_b.txt
- Strontium_kds.txt
- Uranium_kds.txt

To access the dataset from the paper copy of this document, use the CD provided at the end of the document and open the desired file. To access the dataset from the electronic version of this document, click on the desired filename listed above.



Appendix I

Description of Fracture Sorption Datasets

1.1.0 Introduction

Data relating to fracture sorption parameters include two recent studies that have sought to derive fracture retardation factors using mechanistic modeling approaches.

This description of the fracture sorption parameter datasets includes the following items:

- A summary of the contents of each dataset
- The structure of the tables containing the datasets
- Directions on how to access the full dataset

1.2.0 Dataset Summary

The first fracture sorption dataset was derived by applying a semi-mechanistic approach for estimating fracture retardation factors. The dataset is organized primarily by grouping 17 radionuclides into 5 classes. The five radionuclide classes are then organized into a low-, base-, and high-range scale. Fracture retardation factors are then estimated as a function of seven different rock types for each range scale.

The second fracture sorption dataset was derived by applying a mechanistic model using thermodynamic reaction databases to predict fracture retardation factors for several Pahute Mesa hydrostratigraphic units. The dataset is organized primarily by the element of interest. There is also an average-, low-, and high-fracture retardation factor calculated for each of the nine different elements. The fracture retardation factors in this dataset have been calculated for four different hydrostratigraphic units in the Pahute Mesa area.

1.3.0 Table Structure

The first fracture retardation dataset based on the semi-mechanistic approach contains the following fields:

- RN Class - Radionuclide class
- Range - Range associated with the fracture retardation factors
- Rock Type (bedded) - Bedded rock type

- Rock Type (non-welded) - Non-welded rock type
- Rock Type (welded) - Welded rock type
- Rock Type (lava) - Lava rock type
- Rock Type (altered) - Altered rock type
- Rock Type (fractured non-welded) - Fractured non-welded rock type
- Rock Type (bedded-altered) - bedded-altered rock type

The second fracture retardation dataset based on the mechanistic approach contains the following fields:

- RN - Radionuclide
- Range - Range associated with the fracture retardation factors
- HSU (TMA) - Timber Mountain Aquifer
- HSU (TC) - Tuff Cones
- HSU (TBA) - Belted Range Aquifer
- HSU (BAQ) - Basal Aquifer

1.4.0 Access to Datasets

The entire fracture sorption datasets are provided in both EXCEL and ASCII formats in the following files:

EXCEL:

- fracture_sorption_rocktype.xls
- fracture_sorption_hsu.xls

ASCII:

- fracture_sorption_rocktype.txt
- fracture_sorption_hsu.txt

To access the data from the paper copy of the document, use the CD provided at the end of the document and open the desired file. To access the dataset from the electronic version of the document, click on the desired file.



Appendix J

Description of Colloid-Facilitated Transport Parameter Dataset

J.1.0 Introduction

Colloid-facilitated transport parameter data can be found in five different datasets. These datasets include measured colloid concentrations and size distributions for groundwater samples, calculated colloid distribution coefficients from sorption and desorption experiments, calculated rate constants from actinide sorption and desorption experiments, and colloid filtration and retardation data obtained from both laboratory and field tracer responses.

This description of the colloid-facilitated transport parameter datasets includes the following items:

- A summary of the contents of each dataset
- The structure of the table containing each dataset
- Directions on how to access the each dataset

J.2.0 Dataset Summary

Each record in the colloid concentrations and size distribution dataset contains information about a given measurement of colloid concentrations for a given borehole. The dataset is, therefore, organized primarily by the borehole name. The dataset contains 32 colloid concentrations and size measurements for 24 different boreholes. The dataset contains information about the well name, colloid size ranges, and sources of the data.

Each record in the colloid distribution coefficients table contains distribution coefficient data for a specific actinide and colloid combination. As a result, the table is organized primarily by the sorbing actinide and secondarily by the composition of the colloid. The dataset contains 13 distribution coefficient ranges for 4 different actinides. The dataset contains information about the colloid type, the distribution coefficient range, and the source of the data.

Each record in the actinide sorption and desorption rate constants table contains forward- and reverse-rate constants for a given colloid and actinide combination. As a result, the table is organized primarily by the colloid type and secondarily by the sorbing actinide. The dataset contains 20 records of information that document rate constant ranges for both sorption and desorption of actinides onto various colloid types.

The colloid filtration and retardation datasets contain information about filtration rate constants for various wells. The data was split into two tables. The first table

contained data for laboratory tracer responses, and the second table contained data for field tracer responses. Both datasets are organized primarily by well name. The two datasets contain over 50 records for approximately 9 different locations. The datasets contain specific information on rate constants, retardation factors, and residence times.

J.3.0 Table Structure

The colloid concentration and size distribution table contains the following fields:

- well_name - Name of the well sampled
- diam_50 (nm) - Number of colloids in the 50 nm size bin
- diam_60 (nm) - Number of colloids in the 60 nm size bin
- diam_70 (nm) - Number of colloids in the 70 nm size bin
- diam_80 (nm) - Number of colloids in the 80 nm size bin
- diam_90 (nm) - Number of colloids in the 90 nm size bin
- diam_100 (nm) - Number of colloids in the 100 nm size bin
- diam_110 (nm) - Number of colloids in the 110 nm size bin
- diam_120 (nm) - Number of colloids in the 120 nm size bin
- diam_130 (nm) - Number of colloids in the 130 nm size bin
- diam_140 (nm) - Number of colloids in the 140 nm size bin
- diam_150 (nm) - Number of colloids in the 150 nm size bin
- diam_160 (nm) - Number of colloids in the 160 nm size bin
- diam_170 (nm) - Number of colloids in the 170 nm size bin
- diam_180 (nm) - Number of colloids in the 180 nm size bin
- diam_190 (nm) - Number of colloids in the 190 nm size bin
- diam_200 (nm) - Number of colloids in the 200 nm size bin
- diam_220 (nm) - Number of colloids in the 220 nm size bin
- diam_240 (nm) - Number of colloids in the 240 nm size bin
- diam_260 (nm) - Number of colloids in the 260 nm size bin
- diam_280 (nm) - Number of colloids in the 280 nm size bin
- diam_300 (nm) - Number of colloids in the 300 nm size bin
- diam_400 (nm) - Number of colloids in the 400 nm size bin
- diam_500 (nm) - Number of colloids in the 500 nm size bin
- diam_600 (nm) - Number of colloids in the 600 nm size bin
- diam_800 (nm) - Number of colloids in the 800 nm size bin
- diam_1000 (nm) - Number of colloids in the 1,000 nm size bin
- total 50-1000 - Number of colloids total in all bins
- total 50-200 - Number of colloids in the 50-200 nm bin range
- comments - Comments on the dataset; website location of the data
- source - Source of the data
- ref_id - Reference for the record

The colloid distribution coefficients table contains the following fields:

- actinide - Actinide
- colloid_type - Type of colloid

- lower_K_d_bound (mL/g) - Lower K_d bound in milliliters per gram
- upper_K_d_bound (mL/g) - Upper K_d bound in milliliters per gram
- UGTA_extension (mL/g) - Extensions to the bounds determined from U-20WW experiments
- comments - Comments on the record
- source - Source of the information
- ref_id - Reference for the record

The actinide sorption and desorption rate constants table contains the following fields:

- Colloids/Actinides - Colloid and actinide combination
- batch_kf (hr-1) - Batch sorption rate constant per hour
- batch_kb (hr-1) - Batch desorption rate constant per hour
- fracture_kf (hr-1) - Fracture sorption rate constant per hour
- fracture_kb (hr-1) - Fracture desorption rate constant per hour
- comments - Comments regarding the values
- source - Source of the information
- ref_id - Reference for the record

The colloid filtration and retardation data obtained from laboratory tracer responses contains the following fields:

- Well_name_depth (ft) - Combination of the well name and depth of the sample in feet
- Mean_res_time (hr) - Mean residence time in hours
- Filt_rate_constant (1/hr) - Filtration rate constant per hour
- Detach_rate_constant (1/hr) - Detachment rate constant per hour
- Retardation_factor - Retardation factor
- Colloid_type - Type of colloid used in the experiment
- Comments - Comments regarding the experiment
- Source - Source of the information
- Ref_id - Reference for the record

The colloid filtration rate and retardation data obtained from field tracer responses contains the following fields:

- site_name - Site name for the record
- distance (m) - Distance for the field test in meters
- mean_res_time (hr) - Mean residence time in hours
- fill_rate_constant (1/hr) - Filtration rate constant per hour
- ret_factor - Retardation factor
- probability - Probability
- comments - Additional comments regarding the record
- source - Source of the data
- ref_id - Reference for the record

J.4.0 Access to Dataset

The colloid size concentrations, distribution coefficients, actinide sorption and desorption rate constants, and colloid filtration rate and retardation data are provided in both EXCEL and ASCII formats in the following files:


EXCEL:

- Colloid_size_concentration.xls
- Colloid_Kd_Ranges.xls
- Colloid_sorption_desorption.xls
- Colloid_lab_fracture.xls
- Field_microsphere_exp.xls

ASCII:

- Colloid_size_concentration.txt
- Colloid_Kd_Ranges.txt
- Colloid_sorption_desorption.txt
- Colloid_lab_fracture.txt
- Field_microsphere_exp.txt

To access the data from the paper copy of the document, use the CD provided at the end of the document and open the desired file. To access the dataset from the electronic version of the document, click on the desired file.



Appendix K
Supplemental Information

K.1.0 Introduction

This appendix contains a description of the supplemental information provided on the CD-ROM. This information is provided to help the reader enhance their understanding of material provided in the document. The supplemental information includes a Hydrostratigraphic Unit Gallery, and Yucca Mountain Project Sorption datasets.

HSU Gallery and Descriptions

The Pahute Mesa-Oasis Valley EarthVision Hydrostratigraphic Model was completed in September 2001 (BN, 2002). The model was constructed using an existing model for Western Pahute Mesa and increasing the area of the model to include Eastern Pahute Mesa, Oasis Valley south to Beatty, to the north of the NTS boundary, and west of Beatty. This tripled the size of the original model. The model incorporated the new PM-OV series of wells along with data supplied by the Yucca Mountain Project to provide consistency with the northern end of that model. The USGS provided input for the depth to Paleozoic surface and intrusive bodies based on their gravity and magnetics studies. The model has 73 fault blocks and 48 layers. In addition, six alternative models were constructed to evaluate different conceptual models that honor the data but have different interpretations of structure and HSUs where data are not available. The EarthVision models have been exported to create meshes for the next step in the workflow, numerical modeling of groundwater flow and transport.

YMP Sorption Datasets

The Yucca Mountain Sorption datasets have been included on this CD-ROM to provide the reader faster access to the information. The original datasets and more detailed supporting information may be obtained from the Yucca Mountain Project in DTN LAIT831341AQ96.001.

K.2.0 Data Summary

HSU Gallery and Descriptions

The “HSU Model Gallery” file contains images of the HSUs with a brief description for each HSU. Additional information can be found within the “HSU Descriptions” table.

YMP Sorption Datasets

The Yucca Mountain Sorption datasets are provided in a series of eight EXCEL spreadsheets. These spreadsheets contain the YMP metadata for the dataset.

K.3.0 Access to Data

HSU Gallery and Descriptions

The HSU Model Gallery is provided in HTML format in the following file:

- Pahute Mesa-Oasis Valley HSU Gallery.html

The HSU Descriptive table is provided in EXCEL format in the following file:

- HSU-descriptions.xls

To access the gallery and associated table from the paper copy of this document, use the CD provided in this document and open the desired file within the Supplemental Information subdirectory. To access the gallery and associated table from the electronic version of this document, click on the desired filename listed above.

YMP Sorption Datasets

The Yucca Mountain Sorption datasets have been provided in EXCEL format in the following files:

- 001-Ba Sorption.xls
- 002-cesium.xls
- 003-strontium.xls
- 004-Uran Sorpt.xls
- 005-Np Conc & Sorpt.xls
- 007-Se sorption.xls
- 008-Se sorption.xls
- 009-Pu sorption.xls

To access the files from the paper copy of this document, use the CD provided at the end of the document and open the desired file within the Supplemental Information. To access the files from the electronic version of this document, click on the desired filename listed above.

K.4.0 References

Bechtel Nevada. 2002. *Hydrostratigraphic Model of the Pahute Mesa-Oasis Valley Area, Nye County, Nevada*, Report DOE/NV/11718--646. Las Vegas, NV.



Plates

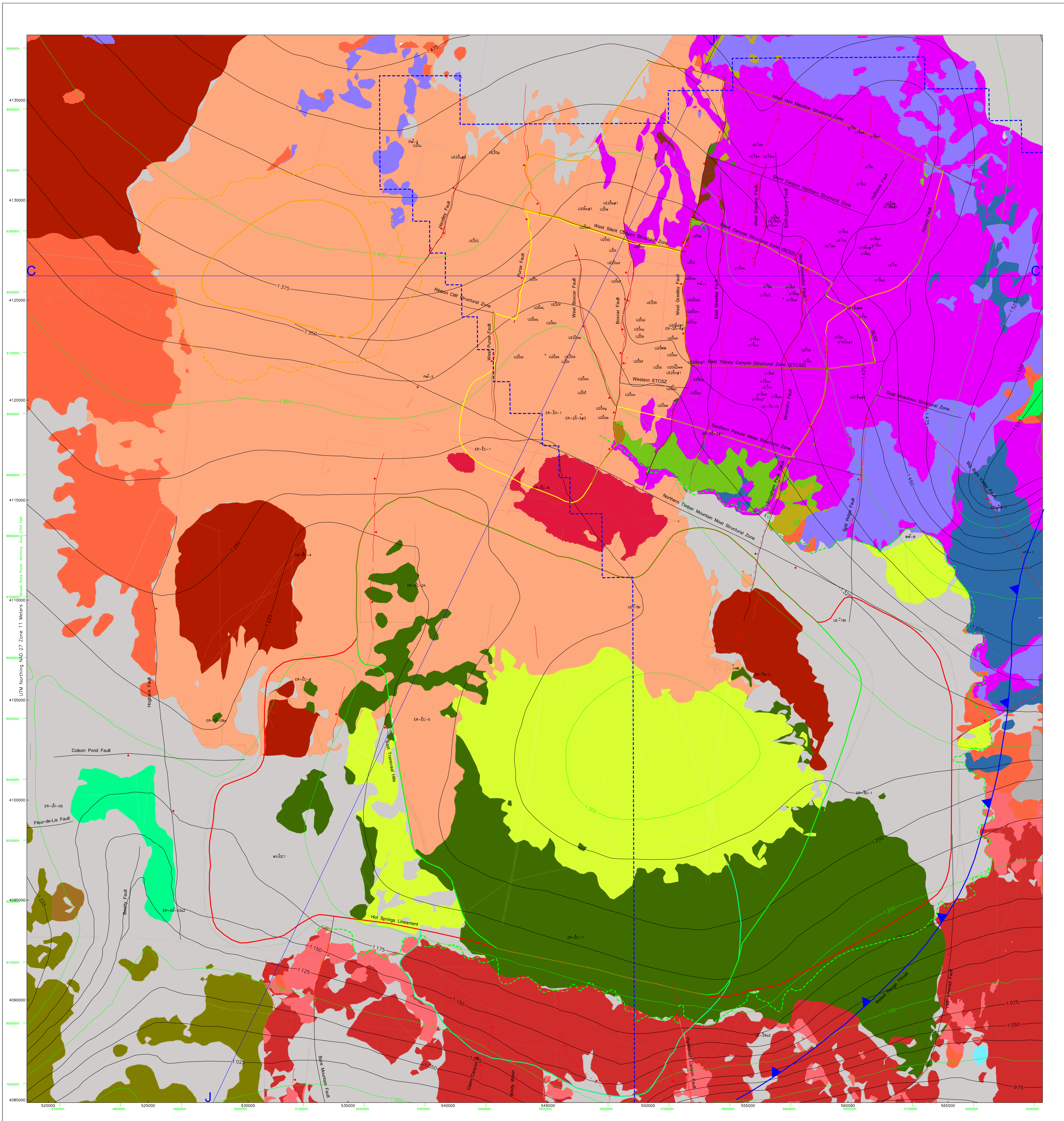


Plate 1 Hydrostratigraphic Units for the Pahute Mesa - Oasis Valley Area

EXPLANATION

- Black Mountain Caldera Topographic Margin
- Black Mountain Caldera Structural Margin (buried)
- Ammonia Tanks Caldera Structural Margin (buried)
- Timber Mountain Caldera Complex Topographic Margin (mapped, USGS)
- Common Ammonia Tanks and Rainier Mesa Structural Margins (buried)
- PM-OV Hydrogeologic Framework Model Cross Section Lines
- Borehole

Scale 1: 62,500

UTM Coordinates, NAD 27 Zone 11, Meters

Central Nevada State Plane Coordinates, Feet

--- Major Water Table Contours, elevation (m)

--- Minor Water Table Contours, elevation (m)

- NTS boundary
- Surface faults, Wahl et al., 1997, ball and bar on downthrown side
- Buried faults and structural zones
- ▲ Thrust fault, sawteeth on upper plate (buried)
- Rainier Mesa Caldera Structural Margin (buried)
- Grouse Canyon Caldera Margin (buried)
- Area 20 Caldera Margin (buried)
- Claim Canyon Caldera Margin (buried)

Hydrostratigraphic Units

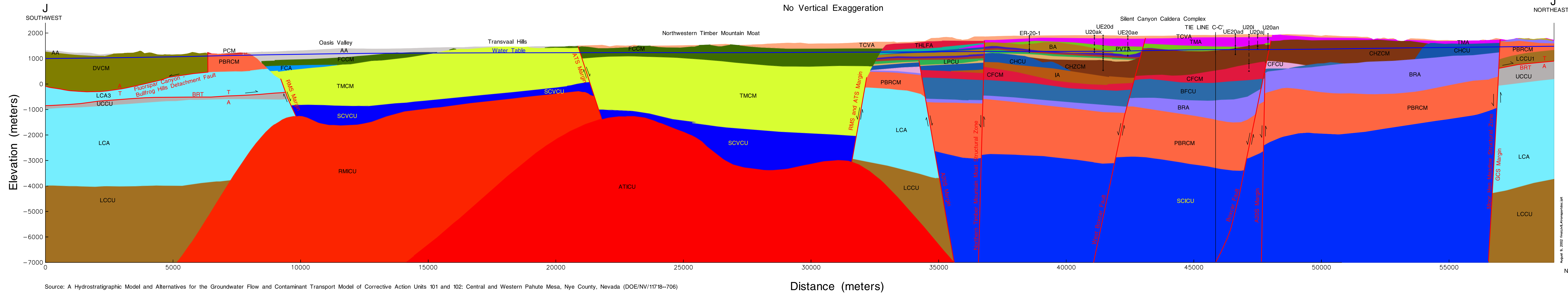
AN	TCV	PRBCW
DVA	PULFA	TRCWL
DNM	LCPU	SCOCU
YCM	TSV	LEA3
TCVA	YMEFCM	LECU1
FCCM	CHVTA	UCOU
FCA	CHVCM	LCA
THLFA	CHZCM	LCCU
THCM	CHZCU	SCOU
TMA	IA	MOCU
WVA	CFM	BCOU
PCM	CFU	CHCU
PVTA	KA	SCOU
FCU	BA	BRUCU
BA	BA	ATCU
UPCU		

August 8, 2002

Source: A Hydrostratigraphic Model and Alternatives for the Groundwater Flow and Contaminant Transport Model of Corrective Action Units 101 and 102: Central and Western Pahute Mesa, Nye County, Nevada (DOE/NV/1718-706)

Plate 2 - Southwest to Northeast Hydrostratigraphic Cross Section J-J' through the Pahute Mesa - Oasis Valley Area

Scale - 1:62,500
No Vertical Exaggeration



Hydrostratigraphic Units	
AA	CHZCM
DVA	CHCU
DVCM	IA
YVCM	CFCM
TCVA	CFCU
FCCM	KA
FCA	BFCU
THLFA	BRA
THCM	PBRCM
TMA	TMCM
WWA	SCVCU
PCM	LCA3
PVTA	LCCU1
FCCU	LCCU
BA	LCA
UPCU	LCCU
TCA	SCICU
PLFA	MGCU
LPCU	BMICU
TSA	CHICU
YMCFCM	CCICU
CHVTA	RMICU
CHVCM	ATICU

EXPLANATION

ER-20-1

 Drill hole in line of cross section. Tick marks represent tops of hydrostratigraphic units determined from drill hole data. Dashed line indicates drill hole projected into line of cross section (up to 1000 meters).

Fault with half arrows indicate sense of displacement. "T" indicates sense of movement is toward the reader. "A" indicates sense of movement is away from the reader.

TIE LINE J-J'

 Tie line indicates the location where another cross section intersects this cross section.

ATS - Ammonia Tanks caldera structural margin
 A20S - Area 20 caldera structural margin
 BMS - Black Mountain caldera structural margin
 BRT - Belted Range thrust fault
 CCS - Claim Canyon structural margin
 GCS - Grouse Canyon structural margin
 RMS - Rainier Mesa structural margin

Note: See Appendix A for definitions of hydrostratigraphic units.

Source: A Hydrostratigraphic Model and Alternatives for the Groundwater Flow and Contaminant Transport Model of Corrective Action Units 101 and 102: Central and Western Pahute Mesa, Nye County, Nevada (DOE/NV/11718--706)

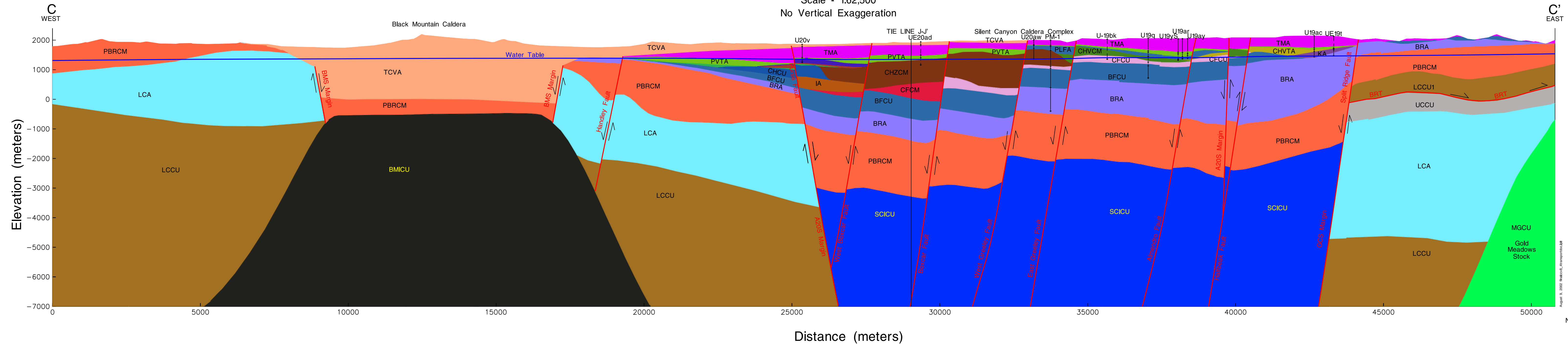
Distance (meters)

August 9, 2002 (file:///C:/Users/robert/...) [unclear]

Plate 3 - West to East Hydrostratigraphic Cross Section C-C' through the Pahute Mesa - Oasis Valley Area

Scale - 1:62,500

No Vertical Exaggeration



Hydrostratigraphic Units

AA	CHZCM
DVA	CHCU
DVCM	IA
YVCM	CFCM
TCVA	CFCU
FCCM	KA
FCA	BFCU
THLFA	BRA
THCM	PBRCM
TMA	TMCM
WWA	SCVCU
PCM	LCA3
PVTA	LCCU1
FCCU	UCCU
BA	LCA
UPCU	LCCU
TCA	SCICU
PLFA	MCCU
LPCU	BMICU
TSA	CHICU
YMCFM	CCICU
CHVTA	RMICU
CHVCM	ATICU

EXPLANATION

ER-20-1

 Drill hole in line of cross section. Tick marks represent tops of hydrostratigraphic units determined from drill hole data. Dashed line indicates drill hole projected into line of cross section (up to 1000 meters).

Fault with half arrows indicate sense of displacement. "T" indicates sense of movement is toward the reader. "A" indicates sense of movement is away from the reader.

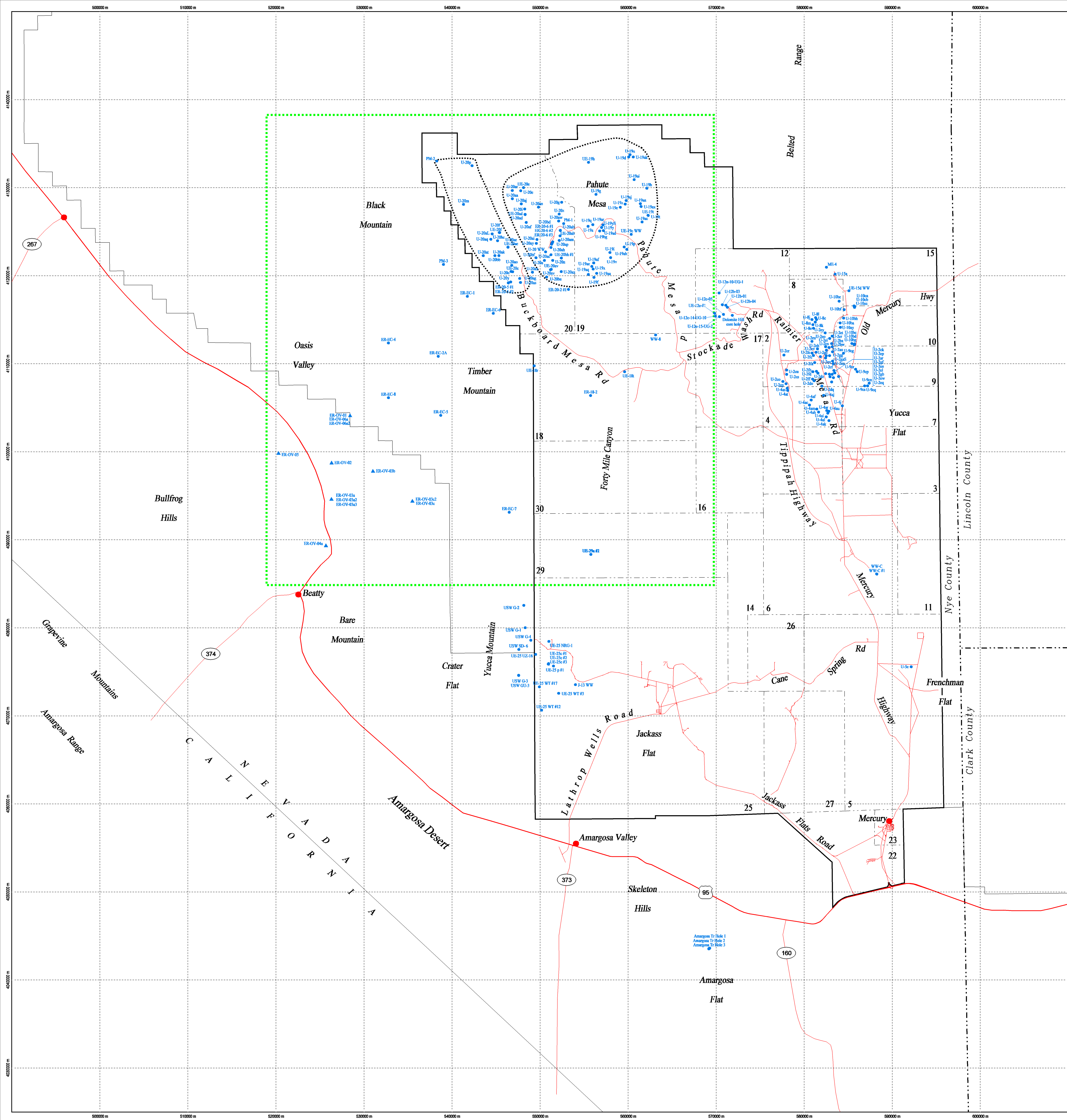
TIE LINE J-J'

 Tie line indicates the location where another cross section intersects this cross section.

ATS - Ammonia Tanks caldera structural margin
 A20S - Area 20 caldera structural margin
 BMS - Black Mountain caldera structural margin
 BRT - Belted Range thrust fault
 CCS - Claim Canyon structural margin
 GCS - Grouse Canyon structural margin
 RMS - Rainier Mesa structural margin

Note: See Appendix A for description of hydrostratigraphic units.

Source: A Hydrostratigraphic Model and Alternatives for the Groundwater Flow and Contaminant Transport Model of Corrective Action Units 101 and 102: Central and Western Pahute Mesa, Nye County, Nevada (DOE/NV/11718--706)



Borehole Name	Matrix Porosity	Effective Porosity	Dispersivity	Matrix Diffusion Parameters	Matrix Sorption Distribution Coefficients	Colloid-Facilitated Transport Parameters
Amargosa Tr Hole 1			X			
Amargosa Tr Hole 2			X			
Amargosa Tr Hole 3			X			
Dokomite Hill core hole	X					
ER-18-2		X				X
ER-20-2 #1		X				X
ER-20-5 #1		X				X
ER-20-5 #3		X				X
ER-20-6 #1	X	X	X	X		X
ER-20-6 #2		X	X			X
ER-20-6 #3		X	X			X
ER-EC-1		X				X
ER-EC-2A		X				X
ER-EC-4		X				X
ER-EC-5		X				X
ER-EC-6		X				X
ER-EC-7		X				X
ER-EC-8		X				X
U-13 WW					X	X
ME-4	X					
PM-1				X		
PM-2	X			X		X
PM-3	X			X		X
U-10ay		X				
U-10ba		X				
U-10bc		X				
U-10bd		X				
U-10be		X				
U-10bf		X				
U-10bg		X				
U-10bh		X				
U-10ca		X				
U-10cb		X				
U-10cc		X				
U-13aa		X				
U-19aa	X					
U-19ab	X					
U-19ac	X					
U-19ad	X					
U-19ae	X					
U-19af	X					
U-19ag	X					
U-19ah	X					
U-19ai	X					
U-19aj	X					
U-19ak	X					
U-19al	X					
U-19am	X					
U-19an	X					
U-19ao	X					
U-19ap	X					
U-19aq	X					
U-19ar	X					
U-19as	X					
U-19at	X					
U-19au	X					
U-19av	X					
U-19aw	X					
U-19ax	X					
U-19ay	X					
U-19az	X					
U-20 WW						X
U-20a	X					
U-20aa	X					
U-20ab	X					
U-20ac	X					
U-20ad	X					
U-20ae	X					
U-20af	X					
U-20ag	X					
U-20ah	X					
U-20ai	X					
U-20aj	X					
U-20ak	X					
U-20al	X					
U-20am	X					
U-20an	X					
U-20ao	X					
U-20ap	X					
U-20aq	X					
U-20ar	X					
U-20as	X					
U-20at	X					
U-20au	X					
U-20av	X					
U-20aw	X					
U-20ax	X					
U-20ay	X					
U-20az	X					
U-20ba	X					
U-20bb	X					
U-20bc	X					
U-20bd	X					
U-20be	X					
U-20bf	X					
U-20bg	X					
U-20bh	X					
U-20bi	X					
U-20bj	X					
U-20bk	X					
U-20bl	X					
U-20bm	X					
U-20bn	X					
U-20bo	X					
U-20bp	X					
U-20bq	X					
U-20br	X					
U-20bs	X					
U-20bt	X					
U-20bu	X					
U-20bv	X					
U-20bw	X					
U-20bx	X					
U-20by	X					
U-20bz	X					
U-20ca	X					
U-20cb	X					
U-20cc	X					
U-20cd	X					
U-20ce	X					
U-20cf	X					
U-20cg	X					
U-20ch	X					
U-20ci	X					
U-20cj	X					
U-20ck	X					
U-20cl	X					
U-20cm	X					
U-20cn	X					
U-20co	X					
U-20cp	X					
U-20cq	X					
U-20cr	X					
U-20cs	X					
U-20ct	X					
U-20cu	X					
U-20cv	X					
U-20cw	X					
U-20cx	X					
U-20cy	X					
U-20cz	X					
U-20da	X					
U-20db	X					
U-20dc	X					
U-20dd	X					
U-20de	X					
U-20df	X					
U-20dg	X					
U-20dh	X					
U-20di	X					
U-20dj	X					
U-20dk	X					
U-20dl	X					
U-20dm	X					
U-20dn	X					
U-20do	X					
U-20dp	X					
U-20dq	X					
U-20dr	X					
U-20ds	X					
U-20dt	X					
U-20du	X					
U-20dv	X					
U-20dw	X					
U-20dx	X					
U-20dy	X					
U-20dz	X					
U-20ea	X					
U-20eb	X					
U-20ec	X					
U-20ed	X					
U-20ee	X					
U-20ef	X					
U-20eg	X					
U-20eh	X					
U-20ei	X					
U-20ej	X					
U-20ek	X					
U-20el	X					
U-20em	X					
U-20en	X					
U-20eo	X					
U-20ep	X					
U-20eq	X					
U-20er	X					
U-20es	X					
U-20et	X					
U-20eu	X					
U-20ev	X					
U-20ew	X					
U-20ex	X					
U-20ey	X					
U-20ez	X					
U-20fa	X					
U-20fb	X					
U-20fc	X					
U-20fd	X					
U-20fe	X					
U-20ff	X					
U-20fg	X					
U-20fh	X					
U-20fi	X					
U-20fj	X					
U-20fk	X					
U-20fl	X					
U-20fm	X					
U-20fn	X					
U-20fo	X					
U-20fp	X					
U-20fq	X					
U-20fr	X					
U-20fs	X					
U-20ft	X					
U-20fu	X					
U-20fv	X					
U-20fw	X					
U-20fx	X					
U-20fy	X					
U-20fz	X					
U-20ga	X					
U-20gb	X					
U-20gc	X					
U-20gd	X					
U-20ge	X					
U-20gf	X					
U-20gg	X					
U-20gh	X					
U-20gi	X					
U-20gj	X					
U-20gk	X					
U-20gl	X					
U-20gm	X					
U-20gn	X					
U-20go	X					
U-20gp	X					
U-20gq	X					
U-20gr	X					
U-20gs	X					
U-20gt	X					
U-20gu	X					
U-20gv	X					
U-20gw	X					
U-20gx	X					
U-20gy	X					
U-20gz	X					
U-20ha	X					
U-20hb	X					
U-20hc	X					
U-20hd	X					
U-20he	X					
U-20hf	X					
U-20hg	X					
U-20hh	X					
U-20hi	X					
U-20hj	X					
U-20hk	X					
U-20hl	X					
U-20hm	X					
U-20hn	X					
U-20ho	X					
U-20hp	X					
U-20hq	X					
U-20hr	X					
U-20hs	X					
U-20ht	X					
U-20hu	X					
U-20hv	X					
U-20hw	X					
U-20hx	X					
U-20hy	X					
U-20hz	X					
U-20ia	X					
U-20ib	X					
U-20ic	X					
U-20id	X					
U-20ie	X					
U-20if	X					
U-20ig	X					
U-20ih	X					
U-20ii	X					
U-20ij	X					
U-20ik	X					
U-20il	X					
U-20im	X					
U-20in	X					
U-20io	X					
U-20ip	X					
U-20iq	X					
U-20ir	X					
U-20is	X					
U-20it	X					
U-20iu	X					
U-20iv	X					
U-20iw	X					
U-20ix	X					
U-20iy	X					
U-20iz	X					
U-20ja	X					
U-20jb	X					
U-20jc	X					
U-20jd	X		</			

Distribution

Paul J. Liebendorfer State of Nevada Bureau of Federal Facilities Division of Environmental Protection 333 W. Nye Lane, Room 138 Carson City, NV 89706-0851	1
Donald R. Elle State of Nevada Bureau of Federal Facilities Division of Environmental Protection 1771 E. Flamingo Rd, Suite 121-A Las Vegas, NV 89119	1
Sabrina Lawrence Environmental Restoration Division U.S. Department of Energy National Nuclear Security Administration Nevada Site Office P.O. Box 98518, M/S 505 Las Vegas, NV 89193-8518	1
Robert Bangerter Environmental Restoration Division U.S. Department of Energy National Nuclear Security Administration Nevada Site Office P.O. Box 98518, M/S 505 Las Vegas, NV 89193-8518	1
Ken Ortego Bechtel Nevada P.O. Box 98521 MS/NLV 82 Las Vegas, NV 89193	1
Chuck Russell Desert Research Institute 755 E. Flamingo Las Vegas, NV 89119	1
Ken Wall Shaw Environmental, Inc. P.O. Box 93838 Las Vegas, NV 89193	1
Jim Aldrich Los Alamos National Laboratory Box 1663, MS-J514 CST-7 Los Alamos, NM 87545	1

Gayle Pawloski Lawrence Livermore National Laboratory P.O. Box 808, L-221 Livermore, CA 94551	1
Tim Rose Lawrence Livermore National Laboratory P.O. Box 808, L-221 Livermore, CA 94551	1
Bonnie Thompson U.S. Geological Survey 160 Stephanie Street Henderson, NV 89074	1
U.S. Department of Energy National Nuclear Security Administration Nevada Site Office Technical Library P.O. Box 98518, M/S 505 Las Vegas, NV 89193-8518	1
U.S. Department of Energy Office of Scientific and Technical Information P.O. Box 62 Oak Ridge, TN 37831-0062	2 (Electronic)
Southern Nevada Public Reading Room c/o Nuclear Testing Archive P.O. Box 98521, M/S 400 Las Vegas, NV 89193-8521	2
Manager, Northern Nevada FFACO Public Reading Facility c/o Nevada State Library & Archive Carson City, NV 89701-4285	1
Sig Drellack Bechtel Nevada P.O. Box 98521 MS/NLV 82 Las Vegas, NV 89193	1 (Electronic)
Carol Bruton Lawrence Livermore National Laboratory P.O. Box 808, L-221 Livermore, CA 94551	1 (Electronic)
Jim Thomas Desert Research Institute 2215 Raggio Parkway Reno, NV 89512	1 (Electronic)

Robert Graves
U.S. Geological Survey
160 Stephanie Street
Henderson, NV 89074

1 (Electronic)

Reed Maxwell
Lawrence Livermore National Laboratory
P.O. Box 808 L-204
Livermore, CA 94551

1(Electronic)

Chuck Russell
Desert Research Institute
755 E. Flamingo
Las Vegas, NV 89119

1(Electronic)

Rick Waddell
GeoTrans, Inc.
9101 Harlan Street Suite 210
Westminster, CO 80030

1 (Electronic)

Dave Finnegan
Los Alamos National Laboratory
Box 1663, MS-J514 CST-7
Los Alamos, NM 87545

1 (Electronic)

Annie Kersting
Lawrence Livermore National Laboratory
P.O. Box 808 L-231
Livermore, CA 94551

1 (Electronic)

Andy Wolfsberg
Los Alamos National Laboratory
EES-5, MS F649
Los Alamos, NM 87545

1 (Electronic)

Paul Reimus
Los Alamos National Laboratory
Box 1663, MS-J534 CST-7
Los Alamos, NM 87545

1 (Electronic)

Ken Rehfeldt
Shaw Environmental, Inc.
P.O. Box 93838
Las Vegas, NV 89193-3838

1 (Electronic)

Warda Drici
Shaw Environmental, Inc.
P.O. Box 93838
Las Vegas, NV 89193

1 (Electronic)

Jim Watrus
Shaw Environmental, Inc.
P.O. Box 93838
Las Vegas, NV 89193-3838

1 (Electronic)

Derek Sloop
Shaw Environmental, Inc.
P.O. Box 93838
Las Vegas, NV 89193

1 (Electronic)

Shaw Environmental, Inc.
Central Files
P.O. Box 93838
Las Vegas, NV 89193

2 (Paper and Electronic)